LOCKHEED MARTIN ENERGY RESEARCH LIBRARIES

3 4456 0515742 4

ORNL-3870
UC-25 – Metals, Ceramics, and Materials
TID-4500 (45th ed.)

METALS AND CERAMICS DIVISION
ANNUAL PROGRESS REPORT
FOR PERIOD ENDING JUNE 30, 1965

OAK RIDGE NATIONAL LABORATORY
operated by
UNION CARBIDE CORPORATION
for the
U.S. ATOMIC ENERGY COMMISSION

Printed in USA. Price $7.00. Available from the Clearinghouse for Federal Scientific and Technical Information, National Bureau of Standards, U.S. Department of Commerce, Springfield, Virginia

LEGAL NOTICE

This report was prepared as an account of Government sponsored work. Neither the United States, nor the Commission, nor any person acting on behalf of the Commission:

A. Makes any warranty or representation, expressed or implied, with respect to the accuracy, completeness, or usefulness of the information contained in this report, or that the use of any information, apparatus, method, or process disclosed in this report may not infringe privately owned rights; or

B. Assumes any liabilities with respect to the use of, or for damages resulting from the use of any information, apparatus, method, or process disclosed in this report.

As used in the above, "person acting on behalf of the Commission" includes any employee or contractor of the Commission, or employee of such contractor, to the extent that such employee or contractor of the Commission, or employee of such contractor prepares, disseminates, or provides access to, any information pursuant to his employment or contract with the Commission, or his employment with such contractor.

ORNL-3870

Contract No. W-7405-eng-26

METALS AND CERAMICS DIVISION ANNUAL PROGRESS REPORT

for Period Ending June 30, 1965

J. H. Frye, Jr., Director
J. E. Cunningham, Assistant Director

Section Heads

G. M. Adamson, Jr.
B. S. Borie
D. A. Douglas, Jr.
C. J. McHargue
P. Patriarca

Compiled and Edited by Sigfred Peterson

NOVEMBER 1965

LOCKHEED MARTIN ENERGY RESEARCH LIBRARIES

3 4456 0515742 4

OAK RIDGE NATIONAL LABORATORY
Oak Ridge, Tennessee
operated by
UNION CARBIDE CORPORATION
for the
U. S. ATOMIC ENERGY COMMISSION

Reports previously issued in this series are as follows:

ORNL-28	Period Ending March 1, 1948
ORNL-69	Period Ending May 31, 1948
ORNL-407	Period Ending July 31, 1949
ORNL-511	Period Ending October 31, 1949
ORNL-583	Period Ending January 31, 1950
ORNL-754	Period Ending April 30, 1950
ORNL-827	Period Ending July 31, 1950
ORNL-910	Period Ending October 31, 1950
ORNL-987	Period Ending January 31, 1951
ORNL-1033	Period Ending April 30, 1951
ORNL-1108	Period Ending July 31, 1951
ORNL-1161	Period Ending October 31, 1951
ORNL-1267	Period Ending January 31, 1952
ORNL-1302	Period Ending April 30, 1952
ORNL-1366	Period Ending July 31, 1952
ORNL-1437	Period Ending October 31, 1952
ORNL-1503	Period Ending January 31, 1953
ORNL-1551	Period Ending April 10, 1953
ORNL-1625	Period Ending October 10, 1953
ORNL-1727	Period Ending April 10, 1954
ORNL-1875	Period Ending October 10, 1954
ORNL-1911	Period Ending April 10, 1955
ORNL-1988	Period Ending October 10, 1955
ORNL-2080	Period Ending April 10, 1956
ORNL-2217	Period Ending October 10, 1956
ORNL-2422	Period Ending October 10, 1957
ORNL-2632	Period Ending October 10, 1958
ORNL-2839	Period Ending September 1, 1959
ORNL-2988	Period Ending July 1, 1960
ORNL-3160	Period Ending May 31, 1961
ORNL-3313	Period Ending May 31, 1962
ORNL-3470	Period Ending May 31, 1963
ORNL-3670	Period Ending June 30, 1964

Highlights

Nearly all the work of the Metals and Ceramics Division may be divided into three parts. These are fundamental investigations supported by the AEC Division of Research, nonproject research on potential and actual reactor materials supported by the Division of Reactor Development and Technology, and research and development programs in support of specific reactor projects or other programs. Occasionally these lines cross, as members of diverse programs find common problems or methods. Although we made substantial progress in many areas, special achievements in a few deserve separate mention.

Our fundamental program includes both theoretical and experimental investigations of the structure of both solids and liquids, a multifaceted probe into the nature of metal deformation, and research on metal oxidation, superconducting materials including technetium, crystal growth, x-ray diffraction, the low-temperature properties of pure metal and fundamentally important alloys and the physical nature of ceramics, particularly thoria. Our program on Diffusion in Solids is now included, although the accomplishments during the reporting period, presented in Chap. 3 of this report, were made under support of the Division of Reactor Development and Technology. A highlight of the period was our hosting of the International Conference on Diffusion in Body-Centered Cubic Materials at Gatlinburg, Tennessee, Sept. 16–18, 1964. Our own research in this area, aided by our anodic sectioning technique, achieved a 10^{10}-fold range of diffusion coefficients measured for niobium in tantalum. By electron-microscopic observation of dislocation movements in niobium, we learned that stress is the major variable in determining the dislocation configuration in body-centered cubic metals. Significant strides by our program in Physical Properties included thermal conductivity measurements on iron of high purity and tungsten in a previously unattained temperature range. Both demonstrated the possibility of calculating this important property from easily measured electrical conductivity; in tungsten the lattice contributions are readily calculable from theoretical principles and in iron they are insensitive to impurity content.

To meet the materials needs of future reactors, we are exploring fundamental properties, methods of evaluation, and novel fabrication techniques for traditional and new reactor materials, with the emphasis on the increasingly important materials required for service at very high temperatures. In our research on zirconium alloys, we developed a metallographic technique for determining the anisotropy of both the structure of these materials and the orientation of precipitated hydride platelets. The method saves considerable time and equipment compared with traditional x-ray techniques. Our research on the irradiation of stainless steel has yielded a quite detailed understanding of the damage mechanism and promising alloying and heat-treatment methods for minimizing this damage. A major step in unraveling the complex corrosive interaction of molten alkali metals with refractory metals was the discovery that potassium niobates occur among the products of corrosion of niobium by potassium. We achieved very dense homogeneous uranium monocarbide by aided sintering of impure oxide-derived powder and demonstrated dramatic reductions in sintering temperatures of uranium mononitride. Developing thermochemical deposition as a method for fabricating high-temperature materials at modest temperatures, we demonstrated production of sheets of tungsten sufficiently large for property evaluation, tungsten-rhenium tubing with controlled composition and thickness, and uranium dioxide in the form of massive deposits, dendritic crystals, and very fine powder.

A substantial segment of our effort is in the support of reactor-development projects and other

programs. Activities include the development and evaluation of new and modified materials, the design and implementation of fabrication techniques, and estimation of costs and assessment of performance for fuels and other materials. The intricate first fuel core and the control elements for the High Flux Isotope Reactor were fabricated well within exacting tolerances, and under our guidance a commercial fabricator has future fuel elements in production. We have preliminary knowledge of radiation effects on the creep of INOR-8, the structural alloy of the Molten-Salt Reactor Experiment. New information on the creep of graphite under irradiation shows that this material can accommodate in-service strains at temperatures down to 150°C. The application of compatible pyrolytic carbon coatings to thorium and uranium oxide fuel particles promises simpler and less expensive fuel fabrication for high-temperature gas-cooled reactors. The 54 items of equipment for remote assembly and inspection of HFIR targets were invented, mounted, assembled in a mockup, and tested. Prototype targets fueled with $^{239}PuO_2$ demonstrated excellent stability to 97% burnup at high heat flux. For the evaluation of reactor economics, high-speed computation methods were developed to predict fabrication costs for a variety of reactor fuels; these methods have identified key design factors affecting fuel fabrication costs. New and improved metallographic techniques continue to bring fame and recognition to our Metallography Group. The cause of failure in BONUS Reactor superheater fuel elements was found, and fabrication methods are being developed to prevent recurrence.

During the report period we also hosted three meetings related to our applied programs. These meetings were the AEC-NASA Liquid Metals Corrosion Meeting, April 21–23, 1965; the 19th AEC Metallography Group Meeting, April 20–22, 1965; and the 9th AEC Coated-Particle Fuels Working Group Meeting on May 25–26, 1965.

Contents

HIGHLIGHTS iii

SUMMARY xiii

PART I. FUNDAMENTAL PROGRAMS FOR THE AEC DIVISION OF RESEARCH

1. CRYSTAL PHYSICS 3
   - The Growth of UO_2 Single Crystals Using the Floating-Zone Technique 3
   - Growth of Crystals from Molten-Salt Solutions 4
   - Hydrothermal Growth of Ferrites 4
   - Crystal Growth by Verneuil Method 5
   - Analysis of Superconducting Solenoid Magnet Design for Magnetic Susceptibility Measurements Using the Faraday Method 5
   - Physical Properties 5
     - Temperature Dependence of Lattice Constants 5
     - Optical Spectra 5
     - Magnetic Susceptibility 6

2. DEFORMATION OF CRYSTALLINE SOLIDS 7
   - Mechanism of Thermally Activated Deformation in Tantalum and Tantalum-Base Alloys 7
   - Solid-Solution Effects and Work Hardening in Tantalum and Tantalum-Base Alloys 7
   - Thermally Activated Slip in Neutron-Irradiated Copper Single Crystals 8
   - A Rate-Controlling Mechanism for Slip in Neutron-Irradiated Copper Single Crystals 9
   - Inverse Pole Figures by Numerical Methods 9
   - Rolling Textures in Face-Centered Cubic Metals 11
   - A Deformation Calorimeter 13

3. DIFFUSION IN SOLIDS 15
   - The Diffusion of Nb^{95} and Ta^{182} in Tantalum 15
   - Diffusion of Nb^{95} and Ta^{182} in Niobium (Columbium) 15
   - Diffusion of ^{181}Hf in BCC Hafnium 16
   - Diffusion of ^{44}Ti in V–20% Ti 16
   - Self-Diffusion in Chromium 16
   - Diffusion of ^{182}Ta in Titanium 18
   - Effect of Alpha Bombardment on the Diffusion of Lead in Silver 19

4. ELECTRON MICROSCOPY 20
   - Effect of Deformation Variables on Dislocation Behavior in Body-Centered Cubic Metals and Alloys 20
   - Recrystallization, Grain Growth, and Mechanical Behavior of Tungsten Sheet 22
     - Recrystallization and Grain Growth 22
     - Temperature and Grain-Size Dependence of the Lower Yield Stresses 23
     - Ductile-Brittle Transition Temperatures 23
     - Brittle Fracture Characteristics 23
     - Discussion 23

Thermally and Chemically Induced Structural Changes in Pyrolytic Carbon 23
Electron Microscopy of Pyrolytic Carbon Deposits on Fuel Particles 24
Actinide-Enhanced Structural Improvements in Pyrolytic Carbon 24
Equipment Development 25

5. ELECTRONIC PROPERTIES OF METALS AND ALLOYS 27

The Low-Temperature Specific Heats of Zirconium Alloys 27
Purification of Zirconium 32
Galvanomagnetic Properties of Zirconium 33
Observation of Mössbauer Effect Following Coulomb Excitation 35
Nickel 35
Germanium 36

6. PHYSICAL CERAMIC STUDIES 38

Creep of Thoria 38
Effect of Impurity Additions on Thoria Creep 40
Compressive Creep of Thorium Oxide 40
Compressive Strength of Thoria 41
Material Transport in Sintering 42
Inert-Gas Bubbles in Neutron-Irradiated Magnesium Oxide 42

7. PHYSICAL PROPERTIES 44

Thermal Conductivity of Inconel 702 44
Physical Properties of Iron 45
Physical Properties of Tungsten 45
Measurement of Low Thermal Conductivities 48
Stability of Temperature Transducers 48
Related Work 48

8. SOLID-STATE AND MOLECULAR THEORY 50

Paramagnetic Properties of the Rare-Earth Germanomolybdates 50
Spin-Wave Theory of α-Fe_2O_3 51
Theory of d^2 and d^8 Configurations in Arbitrary Crystalline Electric Fields 51
An Energy-Calibrated Molecular Orbital Method 52
Convergence in One-Center Expansions: H_2^+ 52
States of He and He^- 53
The *s*-Limit in Lithium 53
Molecular Geometry by One-Center Expansion 53
Electronic States of Disordered Systems 54
One-Center Expansions 54
Multicenter Expansions 55

9. SPECTROSCOPY OF IONIC MEDIA 56

Nickel(II) Centers in Molten Halide Salts: Influence of Rare-Gas-Configuration Cations in Chloride and Bromide Systems 56
Nickel(II) Centers in Binary Molten Halide Salts 56
Tetrahalonickelate(II) Complex Ions Formed in Molten Organic Salts 57
The Molten $NiCl_2$-CsCl System Up to 60 Mole % $NiCl_2$ 57
Nickel(II) Centers in Molten Oxo Salts 57
Tl^+, Pb^{2+}, and Bi^{3+} Centers in the Liquid LiCl-KCl Eutectic 57
Products of the Bi^{3+}-Bi Reaction in Acidic Chloride Media 57
Nickel(II) Centers in Halide Crystals 58
Nitrato and Chloro Complexes of Nickel(II) in Molten Dimethyl Sulfone 59

Densities of Molten Salt Mixtures 59
Furnace for the Measurement of Molten Salt Spectra 60
Apparatus for Spectroscopic Measurements on Liquids at Elevated Pressures and Temperatures 60

10. STRUCTURE OF METALS 61

Recrystallization Studies 61
Dependence of Grain-Boundary Migration Rates on Driving Force 61
The Impurity Drag Effect in Grain-Boundary Migration 61
Twinning in Columbium-Vanadium Alloys 62
Preferred Orientation of Niobium 62
Influence of Deformation Bands on Formation of $\langle 111 \rangle - \langle 001 \rangle$ Fiber Textures in Aluminum 64
Effect of Fabrication Method on Fiber Texture of Aluminum and Copper 64

11. SUPERCONDUCTING MATERIALS 65

Transformation Kinetics in Niobium-Zirconium Alloys 65
Superconducting Properties of Transformed Niobium-Zirconium Alloys 66
Technique for Measuring Critical Currents 66
Near-Surface Effects in Superconducting Niobium-Zirconium Alloys 67
Zirconium-Uranium Alloys 68
Technetium and Its Alloys 68

12. SURFACE REACTIONS OF METALS 70

Oxidation of Copper-Base Alloys 70
Aqueous Corrosion Studies 71
Refractory Metal Oxidation 71
Stress Generation in Refractory Metals During Oxidation 71
Anodic Oxide Films 72
Oxidation of Tungsten 72
Diffusion Studies 73
Treatment of Specific Heat Data 74

13. X-RAY DIFFRACTION 75

Routine Analyses 75
Crystal Structure of Mixed Oxide Compounds 76
The Crystal Structure of Calcium Beryllate ($Ca_{12}Be_{17}O_{29}$) 76
An X-Ray Diffraction Investigation of a Phase Transformation in Europium Molybdate ($Eu_{5+x}MoO_{10.5+y}$) 77
The Use of Low-Noise Preamplifiers with a Proportional Counter and a DD2 Amplifier 77
X-Ray Scattering from Irradiated BeO Single Crystals 78
The Interpretation of Diffuse X-Ray Scattering from Disordered Alloys 80

PART II. RESEARCH FOR THE AEC DIVISION OF REACTOR DEVELOPMENT

14. FUEL ELEMENT DEVELOPMENT 85

Thermochemical Deposition of Uranium Dioxide 85
Deposition of Refractory Metals 88
Tungsten-Rhenium Alloys 89
Other Tungsten Alloys 91
Rhenium 92
Molybdenum 92

Hydrogen Absorption from Water by Aluminum 93
Characterization of Fuel Dispersions 93
Fabrication of Enriched UAl_3 Dispersion Fuel Plates 96
Fabrication of Uranium Monocarbide with Intermetallic Sintering Aids 98
Aided Sintering of Uranium Nitride 99

15. HIGH-TEMPERATURE MATERIALS 102

Fabrication Development 102
Refractory Metal Extrusion 102
Fabrication of Alkali-Metal Pump Cells 104
Flow Turning of Refractory-Metal Tube Shells 105
Joining of Refractory Materials 108
Welding of Advanced Refractory Alloys 108
Brazing Alloy Development 110
Component Fabrication 111
Physical Metallurgy of Refractory Alloys 112
High-Temperature Sorption of Nitrogen by Nb–1% Zr in Ultrahigh Vacuum 112
Aging Studies on the D-43 Alloy 116
Chemical Stability of Refractory Alloys in High Vacuum 119
Recrystallization Behavior in the T-111 Alloy 119
Mechanical Properties of Refractory Alloys 122
Effect of Cold Working and Annealing on Creep Properties of Nb–1% Zr 122
Correlation of Creep Properties for Constant and Varying Stresses 122
Creep Properties of Refractory Alloys 123
Strengthening of Refractory Alloys by Carburization 123
Internal Friction Studies on Tantalum-Base Alloys 124
Compatibility of Alkali Metals with Structural Materials 124
Compatibility of Boiling Potassium with Refractory Metals 124
Corrosion of Refractory Alloys by Lithium 129
Nondestructive Evaluation of Refractory Alloys 131
Physical Properties 131
Physical Properties of Tungsten 131
Effect of Surface Treatment for Emittance of the Nb–1% Zr Alloy 133
Thermal Conductivity of D-43 and T-111 Alloys 133

16. MATERIALS COMPATIBILITY 136

Effect of Oxygen on the Corrosion of Niobium by Liquid Potassium 136
Determination of Oxygen in Potassium 138
Diffusion of Oxygen in Niobium 139

17. MECHANICAL PROPERTIES 140

Irradiation Embrittlement of Low-Boron Type 304 Stainless Steel 140
Influence of Grain Size on the Irradiation Embrittlement of Stainless Steel at Elevated Temperatures 142
Irradiation Embrittlement of Stainless Steel at Very High Temperature 142
Ductility of an Irradiated 18-8 Stainless Steel Containing Titanium 143
Influence of Neutron Irradiation on the Tensile Properties of the Aluminum Alloy 6061 144

18. NONDESTRUCTIVE TEST DEVELOPMENT 146

Electromagnetic Test Methods 146
Ultrasonic Test Methods 149
Penetrating Radiation 150

Gamma Scintillation Gaging 150
X-Ray Imaging with Closed-Circuit Television 153
X-Ray Microscope 154
Inspection Development for Problem Materials 154
Remote Inspection Development 154

19. TUNGSTEN METALLURGY 155

Thermochemical Deposition of Tungsten 155
Production of Tungsten Sheet 155
Investigation of Nodular Growths 159
Low-Temperature Deformation of Thermochemically Deposited Tungsten 159
Studies on the Brittle Behavior of Recrystallized Tungsten 161
Joining of Tungsten 162
Fusion Welding 162
Brazing 162
Joining by Thermochemical Deposition 163
High-Temperature Creep of Tungsten 163

20. URANIUM NITRIDE 164

Fabrication and Sintering Studies 164
Fabrication Development 164
Removal of Oxygen from UN 164
Sintering Studies 166
Nitrogen Solubility in Uranium Nitride 166
Microhardness Studies on Sintered UN 166
Distribution of Second-Phase Material in Uranium Nitride 168
Neutron-Activation Studies of Uranium Nitride 169

21. ZIRCONIUM METALLURGY 171

Effect of Preferred Orientation and Stress on Precipitation of Hydrides in Zircaloy-2 171
Hydride and Basal Pole Figures in Zircaloy-2 by Quantitative Metallography 172
Anisotropy in Zircaloy-2 172
Strain Anisotropy in Sheet-Type Tensile Specimens of Zircaloy-2 173
Yield Anisotropy in Zircaloy-2 174
Tubing Fabrication Analysis 177
Tube Testing Apparatus 178
Oxide Film Studies 179
Preparation of Single Crystals of Zirconium and Zirconium Alloys 181
Zone Refining of Zirconium 181
Properties of High-Purity Zirconium 182
Recrystallization 182
Oxidation of Single Crystals 182

PART III. REACTOR DEVELOPMENT SUPPORT

22. ARMY REACTORS PROGRAM 187

Corrosion Resistance of Europium Molybdate and Chemical Compatibility with Iron, Nickel, and Chromium 187
Examination of Army PM Core-I Type Fuel Tubes 188

23. DESALINATION 191

Reactor Fuel Element Fabrication Cost Estimates 191

Low-Temperature Reactors 191
Heavy-Water Organic-Cooled Reactor (HWOCR) 191
Fast Breeder Reactor with Bare Fuel 191
Evaporator-Condenser Tubing 192
Metal Fuel Evaluation 192

24. GAS-COOLED REACTOR PROGRAM 194

EGCR Support 194
Irradiation Creep of Graphite 194
Dimensional Stability of AGOT Graphite 197
Graphite Surveillance Program 198
Special Fuel Assemblies for Flux Mapping 198
Evaluation of Pneumatic Temperature-Measuring Nozzles 198
Development of Unclad Fuels 199
Pyrolytic Carbon Coating 199
Thermal Stability of Pyrolytic-Carbon-Coated Oxide Fuel Particles 201
Mathematical Simulation of Coated-Particle Behavior 202
Coated-Particle Irradiation Tests in the ETR X-Basket 202
Fueled-Graphite Fabrication 203
Impact Testing of Graphite Spheres 203
Fabrication of In-Reactor Capsules 204
Fueled-Graphite Irradiation Tests 204
Supporting Research 207
Phase Relations in the Pseudobinary UC_2-ThC_2 System 207
Welding of Advanced Alloys 207
In-Reactor Stress-Rupture Testing of Stainless Steel 208
An Evaluation of UO_2 Irradiated Above 1600°C 210
Thermal Conductivity of AGOT Graphite 210
Effects of Pyrolytic-Graphite Structure on Diffusion of Thorium 212
Effects of Deposition Conditions and Heat Treatment on the Properties of Pyrolytic Carbon 213

25. HIGH FLUX ISOTOPE REACTOR 214

Fuel Element 214
Fuel Element Manufacturing 214
Fuel Plate Fabrication 215
Boron Distribution in HFIR Inner-Annulus Fuel Plates 218
Welding and Machining 218
Uranium Homogeneity 221
Ultrasonic Detection of Nonbonds 224
Control Elements 224
Control Plate Fabrication and Preforming 224
Forming Control Element Components 225
Irradiation Testing of Europium Oxide and Europium Molybdate Dispersions 227
Mechanical Properties of Control Plate Material 228

26. HIGH FLUX ISOTOPE REACTOR TARGET DEVELOPMENT 230

Transuranium Target Fabrication Equipment 230
Design and Fabrication 231
Equipment Mockup 232
Plutonium Target Fabrication 234
Fabrication of ^{242}Pu HFIR Target Elements for Irradiation at Savannah River 234

Fabrication of HFIR Target Elements for Flow Testing 235
Welding Development 236
Irradiation Testing 237

27. MEDIUM POWER REACTOR EXPERIMENT 238

Turbine Pump Fabrication 238
Radiator Fabrication 239
Natural-Circulation Boiling-Potassium Test Loops 239
Type 316 Stainless Steel – TZM Forced-Circulation Loops 241
High-Emittance Coatings for Metals 242

28. MOLTEN-SALT REACTOR PROGRAM 243

Evaluation of MSRE Graphite 243
Reaction of INOR-8 with Impure Nitrogen 244
Mechanical Properties of INOR-8 Welds 245
Microstructures of INOR-8 Weldments 246
Joining of Graphite to Metals 248
Transition Joints 248
Brazing Alloy Development 248
Mechanical Properties of Irradiated INOR-8 249
Composition Effects in INOR-8 249
Postirradiation Creep of INOR-8 249
In-Reactor Creep of INOR-8 250
Postirradiation Metallographic Examination of MSRE In-Reactor Tests 251
Experiment ORNL MTR 47-5 251
Experiment ORNL MTR 47-6 255
Surveillance Testing 256
Dynamic Corrosion Studies 257
Corrosion Loops Circulating Molten Fluorides 257
Corrosion Loops Circulating Lead 259

29. REACTOR EVALUATION 261

Computer Programs for Calculation of Fuel Fabrication Costs 261
^{233}U Value Study 262
Effect of Variables upon Fuel Fabrication Cost 264

30. THORIUM UTILIZATION 266

Operation of a Th-^{233}U Fuel Fabrication Facility 266
BNL Fuel Rods 266
Fabrication of ^{233}U-Bearing Fuel Rods for Irradiation Tests 266
Thorium-Uranium Recycle Facility 267
Building 267
Oxide Fabrication Equipment 269
Fueled-Graphite Fabrication Equipment 269
Fueled-Graphite Development 274
Carbon-Coated Oxide Fuel Concept 274
Coated Particle Development Laboratory 274
Conversion of Sol-Gel Microspheres from ThO_2 to ThC_2 275
Gas-Solid Contact Model Studies 275
Prototype Fluidized-Bed Coater 278
Prototype Rotary-Drum Coater 280
Prototype ThO_2-ThC_2 Rotary Conversion Furnace 280

Vibratory Compaction Studies 281
Sintering and Grain Growth of Sol-Gel Thoria and Thoria-Urania 281
Sintering of Sol-Gel Oxides 282
Irradiation Studies 283
Powder-Packed Sol-Gel Oxide 283
Fission-Gas Release from Ceramic Fuels 288

PART IV. OTHER PROGRAM ACTIVITIES

31. BONUS REACTOR SUPPORT PROGRAM 293
Background on BONUS Reactor 293
In-Cell Examination of Superheater Assemblies 296
Fuel Element Fabrication 299

32. METALLOGRAPHY 300
Electron Microprobe X-Ray Analysis 300
Extended-Temperature-Range Hot-Hardness Tester 300
Metallography of Thorium Carbides 301
Francis F. Lucas Award 303
Polarized-Light Microscopy of Pyrolytic Carbon Deposits 303
Identification of Carbides, Nitrides, and Oxides of Niobium and Niobium Alloys by Anodic Staining 304
Experience with Color in Metallography 304
Accelerated Epoxy Mounting Using a Radio-Frequency Furnace 304

33. SNAP-8 CORROSION STUDIES 305
Compatibility Studies of Materials in SNAP-8 Primary System 305

34. SNAP-50 CORROSION STUDIES 308

PAPERS AND PUBLICATIONS

PAPERS AND ORAL PRESENTATIONS AT TECHNICAL MEETINGS 315

PUBLICATIONS 322

ORGANIZATIONAL CHART 331

Summary

PART I. FUNDAMENTAL PROGRAMS FOR THE AEC DIVISION OF RESEARCH

1. Crystal Physics

We have found that a geometry favorable for the growth of large high-quality UO_2 crystals may be obtained by the centrifugal distribution of an inductively melted central zone that is caused to traverse the rod. The crystal chemistry investigation of the lanthanide germanomolybdates was extended to germanotungstates. The rate of hydrothermal growth of nonucleated ferrite crystals was related to temperature, pressure, time, solvent normality, and metallic additives. Our arc-modified Verneuil system was improved. We analyzed superconducting magnet design for magnetic susceptibility measurements by the Faraday method and concluded that a properly dimensioned solenoid is very promising. The temperature dependence of magnetic susceptibilities, lattice constants, and optical absorption spectra of the lanthanide germanomolybdates is being measured and will be related by a theoretical analysis of crystal field parameters.

2. Deformation of Crystalline Solids

Flow parameters for tantalum and tantalum alloys were explained in terms of the effect of alloying on the shear modulus, which enters into the calculation of the energy of double-kink formation, the proposed rate-controlling mechanism. The temperature dependence of stage II work hardening of single crystals has been tentatively explained in terms of the difference in mobility of edge and screw dislocations, which gives rise to cell formation. The flow parameters in irradiated copper showed that the deformation is controlled by a single process, which we believe to result from the tetragonal distortions associated with small vacancy loops.

An analytical method for inverting conventional pole figures into inverse pole figures has been devised. Using it, we redetermined the texture of rolled copper and showed it to consist of ridges rather than one or more isolated orientations.

A calorimeter is being constructed to measure the increase in internal energy resulting from deformation over a wide temperature range, the partial release of this energy immediately following the deformation, and the subsequent isothermal release at higher temperatures.

3. Diffusion in Solids

Studies of diffusion in body-centered cubic metals have continued. Completed works include volume diffusion coefficient determinations for ^{95}Nb and ^{182}Ta in both pure tantalum and pure niobium, ^{181}Hf in the beta phase of reactor-grade hafnium, and ^{44}Ti in the alloy V–20% Ti. We extended diffusion data for ^{51}Cr in chromium from about 1500°C to the vicinity of the melting point and examined atmosphere effects on diffusion rates of ^{182}Ta in β-titanium. Also, we completed a combined theoretical and experimental study of the effect of alpha bombardment on the diffusion of lead in silver.

4. Electron Microscopy

Using transmission electron microscopy we have shown the dislocation configuration in deformed niobium foils to be determined primarily by the level of the applied stress and not by the temperature of deformation. We suggest that the structure of a slip band depends on the stress at which the band is formed and propose that fracture and twinning are initiated by narrow densely packed bands of dislocations generated at high stress levels.

We have studied recrystallization and grain growth, temperature and grain-size dependencies

of the lower yield stress, ductile-brittle transition temperature, and brittle fracture characteristics of tungsten sheet having a grain size range exceeding three orders of magnitude. The results are consistent with a picture of grain growth and embrittlement controlled by impurities segregated at grain boundaries.

We have extensively studied by electron microscopy various as-deposited and annealed pyrolytic carbons. Graphitization was accelerated by the presence of actinide impurities.

A procedure for preparation of specimens for electron microscopy from small highly radioactive samples is briefly outlined.

5. Electronic Properties of Metals and Alloys

Studies of the effects of niobium on the low-temperature specific heat of hexagonal zirconium have continued. In the quenched hexagonal solid solution, the sharp increase in superconducting transition temperature is a result of an increase in density of electronic states and a decrease in the Debye temperature, in agreement with theory. In the heat-treated form, the precipitation of other superconductors with high critical field and temperature depended upon alloy purity. In these dilute Zr-Nb alloys the specific heats and the resistivity both changed with 2-hr anneals at 120°C.

Niobium affected the superconductivity transition temperature, the density of electronic states, and the Debye temperature of zirconium more than do scandium and B-subgroup elements. In cubic zirconium alloys containing Mo, Re, and Ru these low-temperature properties were very nearly the same as for the hexagonal Zr-Nb alloys with the same additive content, so the low-temperature specific heat coefficients of cubic zirconium must not be very different from those of hexagonal zirconium.

We built an ion-pumped zone refining system and used it to produce zirconium crystals with resistance ratios 450 to 850 and new higher purity zone-leveled zirconium alloys for specific-heat study. The resistivity of the zirconium crystals was not a function of impurity content alone but depended on redistribution of impurities.

Galvanomagnetic properties of zirconium have been studied with additional orientations of current. The closed and compensated Fermi surface is fairly well established. Each crystal has nearly isotropic magnetoresistance with quadratic field dependence. The Hall field shows no large anisotropy but alternates in sign.

In collaboration with the Physics Division the Mössbauer effect has been observed in ^{61}Ni and ^{73}Ge following Coulomb excitation, greatly increasing the number of isotopes that can be studied by the Mössbauer effect.

6. Physical Ceramic Studies

The creep rate of thoria in the range of temperatures 1400 to 1800°C and at stresses of 4000, 7500, and 11,000 psi was measured. Formation of intergranular voids and grain-boundary sliding are associated with the deformation process. Addition of calcium oxide accelerated creep of thoria, whereas addition of aluminum oxide inhibited creep. The compressive strength of thoria is greater than indicated by current literature. The mode of failure varied from completely brittle fracture at low temperatures to essentially ductile deformation at high temperatures, although intergranular void formation was still observed during the high-temperature deformation. Rectilinear inert-gas bubbles were observed in irradiated magnesium oxide crystals.

7. Physical Properties

Measurements on iron specimens of different purity showed the thermal conductivity of any relatively pure iron to be calculable to ±1.5% to 900°C from simple electrical resistivity measurements, the Wiedemann-Franz-Lorenz relation, and our values of the lattice portion of the thermal conductivity. Our measurements on tungsten to 1000°C filled an information void concerning the temperature dependence of the thermal conductivity of this material, and the results were analyzed in terms of electronic and lattice contributions to yield a Debye temperature of 284 to 318°K. We developed a rapid method of measuring specific heat, and the results on iron show the Curie phenomenon to be a second-order transition. We obtained data at 20 to 130°C on changes in thermal conductivity in various materials due to effects of porosity, irradiation dosage and temperature, sintering, and composition.

8. Solid-State and Molecular Theory

Calculations of the magnetic properties of rare-earth germanomolybdates were consistent with experiment. The sublattice magnetization of α-Fe_2O_3 can be explained by antiferromagnetic spin-wave theory if the long-wavelength approximation is not used. We wrote a FORTRAN code to calculate the energy levels and eigenvectors of the d^2 and d^8 configurations in crystalline electric fields of arbitrary symmetry within the framework of the point charge model.

Continuing development of our general-purpose one-center expansion for atomic and molecular wave functions, we investigated the convergence of the expansion for H_2^+, examined several highly excited states of He and He^-, and attempted to determine the shape and size of CH_4^+. We are making large-scale calculations on the lithium atom, using approximate wave functions with angular interelectronic coordinates. We have invented a simple energy-calibrated molecular orbital technique and applied it to correlate ionization potentials in several groups of related compounds.

The connection between the Green's-function method and the transfer-matrix method for investigating the electronic states of disordered systems has been clarified. A nontrivial extension of the Green's-function method is being developed and applied to liquid metals.

Questions concerning the utility of the one-center expansion in relation to energy and molecular geometry calculations were studied. For certain problems, multicenter calculations promise greater accuracy.

9. Spectroscopy of Ionic Media

Optical spectroscopy is being employed to investigate the structure of molten salts. Currently the coordination geometry of Ni^{2+} ions in these media and the behavior of bismuth ions in unusual oxidation states are emphasized.

10. Structure of Metals

Copper impurity atoms interact strongly (interaction energy of 2500 to 5200 cal/mole) with a moving grain boundary in aluminum. The effective interaction distance is two atom diameters and is large relative to the width of the grain boundary. We correlated twinning tendency with dislocation substructure for niobium-vanadium alloys. This correlation suggests a model for dislocation behavior in body-centered cubic metals, which explains the effects of composition, temperature, and strain rate on flow. The major portion of the $\langle 001 \rangle$ texture in aluminum rods fabricated at low temperatures results from deformation band formation. The effects of initial orientation, temperature, and fabrication technique on preferred orientation can be explained in terms of this inhomogeneous deformation.

11. Superconducting Materials

The transformation kinetics of niobium-zirconium alloys with 25 to 60% Zr to a pearlitic structure was sluggish, only slightly sensitive to zirconium content, relatively insensitive to atmospheric contamination, and sensitive primarily to grain size. A second mode of transformation was observed in the centers of large grains.

Superconducting measurements at low fields on Nb–33% Zr alloys that had been partially or completely transformed to a pearlitic structure with interlamellar spacings of about 900 μ showed remarkably high critical currents. These specimens did not exhibit a large change in critical current caused by small changes in the applied field, as occurs in conventionally heat-treated material.

Use of the Bean technique permitted evaluation of the effects of some metallurgical variables on the critical current properties of massive niobium-zirconium alloy samples without the attachment of current leads.

In niobium-zirconium superconducting samples we detected a surface layer that has critical current densities and thicknesses near those of the London layer observed in ideal "soft" superconductors. The apparent thickness of the surface layer is not a function of the applied dc field (in the range of 6 to 40 kilogauss) and was greater in the cold-worked (735 A) than in the annealed specimens (355 A).

The delta phase of the zirconium-uranium alloy system was not superconducting at 4.2°K in zero magnetic field.

The glove-box facility constructed for the metallurgical and superconducting property studies of technetium and its alloys is in operation. A 100-g ingot was arc-melted and drop-cast. It was vacuum encapsulated in nickel and cold swaged to approximately 10% reduction in area.

12. Surface Reactions of Metals

Our major effort is directed at fundamental studies of the oxidation mechanism of metals and alloys. Alloying with small quantities of Ni, Al, and Ag caused large variations in the oxidation rate of copper single crystals; changes in the extent of lattice disregistry in the oxide films on these crystals were correlated with changes in the rate of oxidation. Small yttrium additions improved the aqueous corrosion resistance of aluminum at 200°C significantly. Studies of stress generation due to oxygen solution in the surface layers of refractory metals were continued, and an investigation of the oxidation characteristics of tungsten was initiated. Measurements of diffusion in tantalum and niobium, using the very sensitive anodic film technique, were extended in temperature and agreed well with values obtained using mechanical sectioning. Use of the anodic film method extended the range of measurable diffusion coefficients to as low as 2×10^{-19} cm^2/sec. Finally we evaluated the contribution of magnetic order to the specific heats of nickel and several Ni-Cu alloys.

13. X-Ray Diffraction

The complete crystal structure of calcium beryllate ($Ca_{12}Be_{17}O_{29}$) has been derived from x-ray diffraction data. This unusual structure contains large isolated voids over 5 A in maximum diameter, in which guest atoms could be trapped.

Studies of single crystals of BeO irradiated to fast-neutron doses in the range 0.4 to 7.1×10^{20} neutrons/cm^2 have revealed marked changes that occur in x-ray scattering patterns as this range is traversed. The significance of these changes, which we had not observed previously, is discussed in relation to the theory of the damaged structure, which was developed from data at higher doses.

By a new method, we can correct diffuse x-ray scattering from disordered alloys for contributions due to thermal motion and static atomic displacements. Unlike other techniques, it requires measurements at only one temperature and needs no models describing the character of the displacements. Its use yields the true short range order diffuse scattering, unobscured by intensity contributions due to other causes.

PART II. RESEARCH FOR THE AEC DIVISION OF REACTOR DEVELOPMENT

14. Fuel Element Development

In a one-step thermochemical process from UF_6, hydrogen, and oxygen gases at low pressures, we synthesized UO_2 as a stoichiometric solid approaching theoretical density, a dendritic needle-like deposit, or a submicron-size powder.

We showed that we can fabricate a variety of refractory metals by thermochemical techniques. With tungsten-rhenium alloys, problems have been encountered in obtaining homogeneous and uniformly thick deposits, but alloying has been accomplished at relatively low deposition temperatures, and short lengths of tubing with only moderate composition variation have been made. The products exhibited columnar grain structures, low impurity contents, and no sigma phase. A β-tungsten-type phase has been observed for the first time in this system. We have deposited both molybdenum and rhenium as smooth coatings of high density and uniform thickness, but difficulty has been encountered with uniformity and metal recovery in thick deposits.

The physical characteristics of U_3O_8 affected the quality of aluminum dispersion fuel elements made from it. The optimum oxide was dense, spherical, and low in surface area. Both arc-cast and powder-metallurgy-produced uranium-aluminum intermetallics were fabricated into acceptable aluminum-dispersion fuel plates. The powder process contains more operations but provides closer control of stoichiometry and composition.

Sintering UC with uranium silicides circumvented problems previously encountered in sintering with UAl_2 or UBe_{13} and attained densities over 96% from impure commercial UC sintered at 1575°C. The mechanisms of the improved sintering have been determined, and preliminary testing indicates the techniques may also be useful with uranium nitride.

15. High-Temperature Materials

Progress in the fabrication of refractory metals and alloys included experiments on the extrusion of tungsten and W–26% Re tube shells, use of flow turning to fabricate tubing, simplification of the fabrication of electrodynamic pump cells, develop-

ment of welding techniques, improvement of welds, development of brazed joints stable well above the brazing temperatures, and fabrication of loops and other hardware for testing compatibility with alkali metals.

Properties of high-temperature metals studied include the equilibrium and kinetics of nitrogen sorption by Nb–1% Zr, aging and recrystallization of the alloy D-43, vacuum evaporation of constituents of refractory alloys, annealing behavior of the alloy T-111, effect of cold working and annealing on creep of Nb–1% Zr, prediction of creep and rupture under variable stress, creep of refractory alloys and strengthening of these alloys by carburization, the state of oxygen in tantalum-base alloys, the resistance of refractory alloys to molten potassium and lithium, some physical properties of tungsten, including thermal conductivity from 50 to 1000°C, emittance of Nb–1% Zr and its improvement by surface treatment, and thermal conductivity of D-43 and T-111.

16. Materials Compatibility

Time, temperature, and the level of oxygen contamination enhanced corrosion and mass transfer in couples of niobium with liquid potassium. The presence of ternary compounds of the form $K_xNb_yO_z$ helps explain the complex corrosion phenomena observed.

Oxygen in potassium was determined accurately by a gettering–vacuum-fusion technique despite variations in the thermal and environmental history of the potassium.

From oxygen depletion of niobium in contact with potassium, we found diffusion coefficients of 7.9×10^{-10} and 6.4×10^{-9} cm^2/sec for oxygen in polycrystalline niobium at 600 and 815°C respectively.

17. Mechanical Properties

Recent investigations have emphasized the effects of neutron irradiation on the mechanical properties of structural alloys. The embrittlement of stainless steels at elevated temperatures by irradiation was traced to helium from not only the thermal-neutron reaction with ^{10}B but also fast-neutron reactions with the major components. Consistent with this observation, we have improved the postirradiation ductility by several methods: decreasing the grain size, increasing the amount of carbide precipitate, decreasing the boron content, and alloying with 0.2% Ti.

We found no significant effect on the mechanical properties of 6061 aluminum irradiated to doses greater than 10^{20} neutrons/cm^2.

18. Nondestructive Test Development

In continuing development of computer calculation of parameters of an induced electromagnetic field, we have studied the phase and amplitude of the vector potential, field shaping, flow of current in the specimen, and force on the specimen. The phase-sensitive eddy-current instrument has been further improved and applied to test problems for the HFIR, GCR, Fermi, HTM, and Desalination Projects.

Our work on nonbond detection has been directed toward dispersion-core fuel elements, such as used for HFIR and ATR. A device is being prepared for hot-cell examination of fuel tubes such as used for PM-1 and proposed for HWOCR. Electro-discharge machining techniques are being studied for fabricating reproducible reference notches in small-diameter tubing.

We have studied the sensitivity of our x-ray attenuation techniques and extended them to determination of total fuel content in fuel plates used for HFIR, ATR, and ORR. A scanner has been designed and built to develop techniques for measuring homogeneity of fuel rods. A photomultiplier calibration system has been assembled and is being used to optimize radiation detector operation. We are improving the sensitivity of x-ray television. We have begun assembly of a projection x-ray microscope for evaluating finely divided materials.

We are working on inspection techniques for refractory alloys based on titanium, molybdenum, tantalum, and tungsten, which are useful in space-power and other high-temperature systems.

We are modifying an ultrasonic scanner tank for use in a hot-cell facility.

19. Tungsten Metallurgy

High-purity tungsten sheet was thermochemically deposited on a partially sintered molybdenum mandrel. Deposition conditions are being investigated to enable successful deposition of new

shapes without extensive empirical adjustment of the deposition parameters. After annealing at 1000°C, thermochemical tungsten was as strong as and more ductile than recrystallized wrought powder-metallurgy tungsten. We are discovering the causes of low-temperature brittleness in tungsten, and we found that a hydrostatic prestrain improves ductility. Promising joining methods for tungsten include brazing with alloys that contain a fugitive melting-point depressant, fusion with stress relief, and thermochemical deposition of weld metal at temperatures too low to embrittle the base metal. Creep of thermochemical tungsten was similar to that of wrought material.

20. Uranium Nitride

Research and development on uranium nitride as a nuclear fuel for high-temperature reactors with high power densities has included studies of sintering kinetics and pellet fabrication, nitrogen solubility, the effect of carbon on the solubility of oxygen, relationship of microstructure to the properties of sintered material, and fission-gas release by neutron activation. Pertinent data and interpretations are presented.

21. Zirconium Metallurgy

The texture of the matrix had little effect on the orientation of hydride precipitated during cooling in unstressed fully annealed Zircaloy-2. Plastic deformation caused the hydride plates to form parallel to the tensile strain component. Hydride precipitated under elastic stress redistributed only when the tensile stress axis was parallel to a high concentration of basal poles. The redistribution of hydride increased as the stress increased.

A technique was developed for rapidly determining, by quantitative metallography, the pole figure of hydride plates in Zircaloy-2 and the crystallographic basal pole figure in close-packed hexagonal metals.

Sheet tensile specimens could not be used to characterize the three-dimensional anisotropy of Zircaloy-2. The location of the neck could be determined immediately after yielding, and the position of the neck shifted during its formation and growth.

An extrapolation of the octahedral shear stress theory predicted that the shapes of the yield loci for Zircaloy-2 in biaxial stress are elongated ellipses. This indicates that for certain conditions of biaxial stress encountered in service, the maximum permissible design stress can be increased by at least 50% by controlling the orientation of the texture relative to the applied stress geometry. Blistering encountered in fuel element cladding can probably be lessened by use of cladding material having a certain texture.

An apparatus was built for studying the strain anisotropy of Zircaloy-2 tubing in biaxial stress which allows simultaneous application of axial stress, torsional stress, and internal pressure.

The indices of refraction of anodized oxide films on zirconium decreased when they were stripped from the metal, indicating that the film in situ is strained. Similar measurements made on irradiated films showed that neutron doses up to 10^{19} neutrons/cm ^{2} did not produce defects that could be detected by such techniques, nor would they appreciably affect the rate of dissolution of the oxide in the base metal at 600°C. Such dissolution caused a strong absorption of light and caused the base metal to be strongly attacked through the oxide film by a stripping solution.

Zone refining and single crystal production was demonstrated in $\frac{3}{4}$-in.-diam as-deposited iodide zirconium bar. Recrystallization of cold-worked zone-refined zirconium was detected at 150°C and was almost complete in 100 hr at 175°C. The recrystallization behavior of material at the head differed from that at the center of a zone-refined bar, although the impurity contents did not differ more than 50 ppm total.

The interference color pattern developed by an oxide film on a single-crystal sphere of zirconium showed very graphically the variation of oxidation rate with crystallographic direction. The rate at 350°C in dry air was the highest on the basal plane, the $(10\bar{1}0)$ plane, and in a band near the $(20\bar{2}1)$, $(11\bar{2}1)$, and $(11\bar{2}2)$ planes.

PART III. REACTOR DEVELOPMENT SUPPORT

22. Army Reactors Program

We have characterized two forms that europium molybdate, a promising control or poison material, exists in depending on cooling rate. Both have good corrosion resistance and are compatible with stainless steel.

Fuel elements fabricated for PM-1 and PM-3A reactors were examined visually, radiographically, dimensionally, and metallographically to determine realistic tolerances.

23. Desalination

Our efforts are divided into three general categories: calculating fuel fabrication costs, developing fabrication processes for thin titanium tubing for evaporator-condensors, and evaluating fuel performance.

Computer codes for fuel fabrication costs were extended to include the coextrusion of Zircaloy cladding with thorium, thorium-uranium alloy, or uranium. Metal fuel performance was surveyed to help define applications of metal fuels for large desalination reactors. Methods of producing fluted titanium tubing by roll forming, tube drawing, isostatic pressing, high-energy-rate forming, and press forming are being evaluated.

24. Gas-Cooled Reactor Program

Some of our effort is in support of the Experimental Gas-Cooled Reactor. In-reactor testing of moderator graphite at temperatures of 150 to 350°C showed that irradiation-induced creep is consistent with a theoretical model and enables graphite to accommodate much greater strains without fracturing. All specimens for the graphite surveillance program were prepared. We also prepared or modified the components for several fuel assemblies to be used for flux mapping of the EGCR, and we are evaluating the dimensional stability and performance of pneumatic temperature-measuring nozzles.

A large part of our effort has been in support of unclad fuels for advanced gas-cooled reactors, especially pyrolytic-carbon-coated fuel particles for use in graphite-base fuel elements. We determined the effect of specific methane flow rate and deposition temperatures from 1300 to 2000°C on the anisotropy, density, and crystallite size of coatings on particles. These three properties along with diamagnetic susceptibility were used to characterize bulk pyrolytic carbon deposited on static substrates. We also investigated the effects of these structural properties on the diffusion of thorium in pyrolytic graphite. The thermal stability of pyrolytic-carbon-coated oxide fuel particles was demonstrated, and specimens were prepared that have shown excellent behavior under irradiation. We also initiated irradiation experiments to test mathematic simulation of coated-particle behavior. We completed the study of factors affecting the impact resistance of fueled-graphite spheres and are analyzing the results of irradiation experiments on such spheres. The thermal conductivity of fueled graphite is unaffected by irradiation, but differential neutron-induced shrinkage of fueled inserts and machined shells may complicate the removal of heat from the fuel.

Supporting research for gas-cooled reactors covers several diverse topics. We have modified our proposed phase diagram for the UC_2-ThC_2 system, using further results of dilatometry, thermal analysis, and other techniques. We have investigated the weldability of new high-strength nickel alloys. Stress-rupture properties of a British stainless steel showed that heat treatment at 800°C yields a structure that is more ductile and relatively unaffected by irradiation, although somewhat weaker. We also completed our evaluation of UO_2 specimens irradiated at high temperatures and refined the measurements of thermal conductivity of AGOT graphite.

25. High Flux Isotope Reactor

We successfully produced fuel elements for the reactor startup and prototypes for nonnuclear testing. With only minor exceptions, all elements conformed with the proposed specifications. The plate spacing for the reactor elements was held within ±3 mils for the average channel cross section and within ±6 mils for any individual spot, both of which are only about half of the permitted variations. Machining and welding techniques were developed and shown to be capable of the extremely close dimensional tolerances required.

More difficulty than had been previously experienced was encountered with dimensional variations, homogeneity, and nonbond on the reactor element. These problems were not inherent in the technique but resulted principally from excessive moisture in the aluminum powder. We obtained an acceptable boron distribution, which was a reproducible function of both the length and width coordinates of the plates.

The x-ray attenuation technique for determining fuel homogeneity has been demonstrated on a production basis. It showed differences in the fabricability of oxides produced by various vendors.

Considerable assistance has been given to the commercial fuel element fabricator. Preliminary development has been completed and plate production has started.

We fabricated two complete sets of the very complex HFIR control rods for use in reactor startup. With the large dispersion plates containing four discrete composition regions, we met close dimensional tolerances during both roll bonding and explosive forming. To avoid rupturing the brittle europium oxide–aluminum dispersion, we formed the inner cylinder under a compressive load. The 5-ft-long 18-in.-diam cylinder containing four longitudinal welds was held within a ±15-mil tolerance for the combination of diameter and straightness.

Specimens of the europium oxide–aluminum dispersion did not swell during 1 year in the ORR.

26. High Flux Isotope Reactor Target Development

We completed design, fabrication, and assembly in three simulated cells for mockup testing some 54 items that will be used to remotely fabricate the target elements. Procedures are being written for operation, disassembly, and reassembly of each unit.

Four prototype capsules were irradiated and performed satisfactorily. The one designed to operate continuously at a heat flux equivalent to the maximum instantaneous hot spot showed no detectable swelling and very little fission-gas escape from the pellets. Substantial reaction between the PuO_2 and the aluminum powder had no serious consequences. Additional elements were fabricated and are being irradiated at Savannah River. A dummy assembly of 31 elements was fabricated for hydraulic tests.

27. Medium Power Reactor Experiment

We fabricated nine turbine pumps, in which we brazed tungsten carbide bearings to refractory metals with nickel-silicon-boron alloys. Techniques were also perfected for brazing relatively thick stainless-steel-clad copper fins to tapered radiator tubes. Small stainless steel angles were first spot welded to both the tubes and the fins, holding both in a proper position while they were brazed.

We reported natural-circulation loop test results on the compatibility of conventional nickel-, iron-, and cobalt-base high-temperature alloys in boiling potassium. Haynes alloy No. 25 was superior at 980°C, and both it and type 316 stainless steel were acceptable at 870°C. TZM alloy and type 316 stainless steel interacted in refluxing potassium during 1000 hr at 1600°F.

A commercial coating improved the emittance of stainless steel at temperatures to 800°C.

28. Molten-Salt Reactor Program

Grade CGB graphite was evaluated to determine the acceptability of this material as a moderator for the Molten-Salt Reactor Experiment (MSRE). INOR-8 specimens resisted O_2-N_2 mixtures ranging from 0.03 to 5.6% O_2 for periods up to 700 hr, and reaction rates of these materials were measured.

We concluded the investigation of mechanical properties of welds of MSRE-approved heats of INOR-8. In some specimens, as-welded creep-rupture properties were comparable to wrought metal properties. Microstructures of INOR-8 weldments were analyzed and the composition of several phases is reported. Techniques were studied for making transition joints of graphite-to-INOR-8 and INOR-8-to-dissimilar metals using brazing with various fluoride-resistant brazing alloys, including a new palladium-nickel alloy.

We are determining the dose dependency of the ductility and rupture of reactor heats of INOR-8 in postirradiation creep. Boron content affected the behavior. In-reactor creep tests are in progress. Vacuum melting improved the ductility of INOR-8, and the influence of various minor elements on its properties is being investigated.

Thermal convection loops were operated to study the compatibility of several coolants and structural materials of interest to the Molten-Salt Program. Lead was found to mass transfer in steel loops at 1200°F, forming dendritic crystals of iron and chromium. For a surveillance program for studying the effects of MSRE operation on its structural materials, INOR-8 and CGB graphite specimens were fabricated to be placed in the core of the MSRE and in a control test rig that simulates the reactor thermal history.

29. Reactor Evaluation

As part of broad studies on the total cost of producing nuclear power, we are examining fabrica-

tion costs and fuel element performance as they relate to fuel cycle and other cost areas. The methodology of calculating fabrication costs and the major variables that can affect such costs are reported along with brief analyses of selected fuel element concepts.

30. Thorium Utilization

In November 1964 the Atomic Energy Commission requested that design work on equipment for the remote fabrication of metal tubular fuel elements containing ThO_2-$^{233}UO_2$ be stopped until a specific fuel element design is selected. No decision has yet been reached, so no further progress on this phase has been made. Development of equipment for fabricating graphite elements fueled with coated particles has continued. A pilot line consisting of a sol-gel sphere-forming column, a dryer, a calciner, and a coater was designed, fabricated, and placed in operation to provide experience needed to establish process control requirements and bases for automated equipment for remote fabrication.

The deposition of pyrolytic carbon on the fuel microspheres is the most expensive step in the process, primarily because of the small batch sizes that can be treated and the time required to complete each cycle. Processes for coating particles in a rotating drum and in an entrained bed were developed, and each offers potential for substantial cost reduction.

We discovered that fully dense carbide fuels could be prepared by treating calcined sol-gel oxide microspheres in a carbon bed. A scaled-down model of a production bed has been designed and is being fabricated. Also, we found that carbon-coated oxide microspheres are a promising fuel.

Fuel pellets have been pressed and fired from oxides in the gel state to densities over 90% of theoretical with good dimensional control. Differential thermal analysis of dried thoria gel has shown that crystallite growth during heating begins at about 700°C. A high radial acceleration of the tube wall is a major factor in the vibratory compaction of sol-gel oxide.

Irradiation testing of bulk oxide vibratorily compacted into metal tubes continued to demonstrate the excellent characteristics of thoria-base fuels. Relatively low fission-gas release and moderate structural changes were observed in three capsules irradiated at heat fluxes around 100 w/cm. Fission-gas release from ceramic fuels was related simply to the surface area. Platinum-rhodium thermocouples high in rhodium are satisfactory in vacuum near carbon at 1400°C.

PART IV. OTHER PROGRAM ACTIVITIES

31. BONUS Reactor Support Program

A superheater assembly that had failed prematurely in the Boiling Nuclear Superheat (BONUS) Reactor was examined in the hot cells to determine the nature and cause of failure. Two damaged Inconel-clad UO_2 fuel rods were found in the 32-rod assembly – one contained a 13-in.-long cladding rupture, while the other showed gross evidence of swelling. The cause of these failures was definitely traced to defective welding during fabrication.

Improved welding techniques have been devised and specifications modified to prevent failures of this nature from occurring in the future.

32. Metallography

A new electron microprobe analyzer was placed in operation and used to analyze microstructural constituents in nuclear fuel and structural materials. The instrument has been particularly efficient in diffusion studies connected with tests of materials compatibility.

Since being pressed into service a year ago, a new microhardness tester has performed satisfactorily at temperatures up to 2200°C. The design of the unit was based on experience accumulated during operation of a prototype model for the past several years.

New and useful metallographic techniques developed during the past year include (1) a procedure for speeding up the epoxy mounting of metallographic specimens, (2) a technique for the metallographic preparation of thorium carbide specimens in a desiccated glove box, (3) identification of carbides, oxides, and nitrides in niobium by color staining, and (4) complete technology for making routine color transparencies and prints. One reward for these efforts has been the American Society for Metals Francis F. Lucas Award for Excellence in Metallography, which we received in October 1964.

33. SNAP-8 Corrosion Studies

Materials compatibility problems associated with the primary circuit of the SNAP-8 electrical generating system were studied in forced-flow loop tests. Hydrogen contamination in the NaK coolant had no deleterious effect on corrosion. Increasing oxygen content increased the corrosion rate of iron-base alloys but not Hastelloy N. Corrosion was approximately linear with time. Carbon migrated from the hot portions of the loop to the rest of the system, severely decarburizing Croloy 9M.

34. SNAP-50 Corrosion Studies

In support of the SNAP-50 space-power program, we have started to study the nature and extent of corrosion in a NaK heat-rejection circuit made of type 316 stainless steel and Nb–1% Zr alloy. A test loop with removable specimens was built and operated for approximately 3000 hr. Examination of specimens removed from the loop after 2000 hr indicated only a minor transfer of carbon and nitrogen from the stainless steel to the niobium alloy.

Part I.

Fundamental Programs for the AEC Division of Research

1. Crystal Physics

G. W. Clark

Technological progress depends on improved understanding of presently known materials and insight into new and novel materials. Many physical phenomena can be characterized unambiguously only by study of single crystals. Suitable crystals are frequently difficult to obtain, particularly of refractory substances. Thus, we are conducting a continuing program to provide crystals needed in research, to devise and improve methods of crystal growth, and to develop increased understanding of crystal growth processes and kinetics. Crystals are being grown by several methods – by a floating-zone method, from molten-salt solvents, from supercritical aqueous systems, and by the general Verneuil method. More than ten compounds have been synthesized in single-crystal form within the past year. Some of these crystals have been used by other groups in x-ray analysis of neutron damage and in magnetic, electron-spin resonance, and optical investigations. Also, we are investigating selected physical properties, both those that relate to the crystal growth process and those important for characterizing the properties of new compounds.

THE GROWTH OF UO_2 SINGLE CRYSTALS USING THE FLOATING-ZONE TECHNIQUE[1]

A. T. Chapman G. W. Clark

We started to use the floating-zone technique to grow high-melting oxide crystals. This technique was first used on silicon by Keck and Golay[2] in 1953. Two years later a scheme called cage-zone refining was described,[3] in which an inductively melted zone was supported in a vertical ingot having longitudinal ribs, which did not melt. We have exploited the semiconducting character of UO_2 to obtain central melting (2800°C) and balanced the input power against the high radiant heat loss from the surface of the UO_2 rod to maintain a solid skin, which acted as a crucible.

Our inquiry achieved an early rather major success in that single crystals of UO_2 up to 3 cm long and 1.2 cm in diameter were grown in polycrystalline 2-cm-diam UO_2 rods by passing a molten zone through the center of each rod (see Fig. 1.1). To do this a 3–5 Mc/sec power supply was used to produce eddy-current heating in preheated rods. Multiple crystals were produced until the UO_2 rod was rotated at speeds between 200 and 800 rpm. The distribution of the molten UO_2 during rotation resulted in a geometry of the liquid-solid interface that favored the growth of one continuous crystal. Back-reflection Laue photographs exhibited sharp well-defined reflections; this indicated reasonable crystal perfection. The oxygen-to-uranium ratios of these crystals, grown in atmospheres of nitrogen or N_2–20% H_2, were between 2.000 and 2.003. No uranium metal inclusions were observed during metallographic examination up to 750×. Comparative spectrochemical analysis indicated that the major metallic impurities, initially present in the polycrystalline rod between 10 and 150 ppm each, were depleted by at least one-half in samples taken from the bottom and concentrated in samples taken from the top of the UO_2 rod.

Preliminary attempts to use this technique for growing solid-solution $(U,Th)O_2$ crystals have been encouraging.

---

[1]Abstracted in part from a note accepted for publication in the *Journal of the American Ceramic Society* and a paper presented at the American Ceramic Society Meeting, Philadelphia, May 1–6, 1965.

[2]P. H. Keck and M. J. E. Golay, *Phys. Rev.* **89**, 1298 (1953).

[3]P. H. Brace, A. W. Cochardt, and G. Comenetz, *Rev. Sci. Instr.* **26**, 303 (1955).

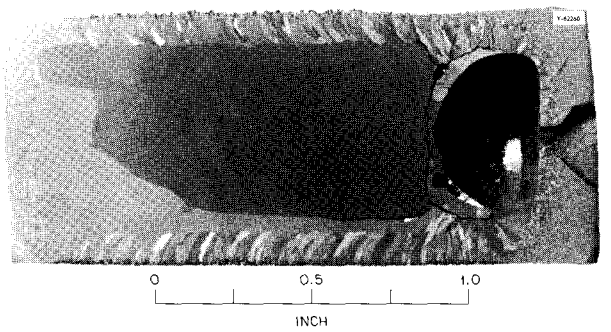

Fig. 1.1. Section of Zone-melted UO_2 Rod. Note that one grain occupies most of the cross section.

GROWTH OF CRYSTALS FROM MOLTEN-SALT SOLUTIONS

C. B. Finch G. W. Clark

Following our discovery of the lanthanide germanomolybdate family of compounds,[4] we anticipated the existence of an analogous family of tungstates, since for the same valence state the ionic radii of molybdenum and tungsten are nearly equal. Experiments to test this supposition led to the growth of both Er_2GeWO_8 and Y_2GeWO_8 crystals. Seeking to extend this family to trivalent cations smaller than the lanthanides, we could not prepare Sc_2GeMoO_8 or Fe_2GeMoO_8 (Sc^{3+} and Fe^{3+} have radii about three-fourths that of the lanthanide ions). Very limited success was had in incorporating Fe^{3+} into gadolinium germanomolybdate. Efforts to extend the crystal chemistry of this family of compounds will continue.

Two bonuses were received from these probing experiments. Since the nuclear magnetic moment contribution of tungsten is weaker and less complicated than that of molybdenum, electron-spin-resonance studies are simpler. Also, the yttrium compound is being used as a host lattice for studying the lanthanides in a dilute state in this crystal environment.

We have continued to grow pure crystals of BeO, ThO_2, and the lanthanide germanomolybdates as well as lanthanide-doped crystals of ThO_2, Y_2GeMoO_8, and Y_2GeWO_8. Research samples are selected from these for a variety of investigations.

[4]C. B. Finch, G. W. Clark, and L. A. Harris, *Metals and Ceramics Div. Ann. Progr. Rept, June 30, 1964*, ORNL-3670, p. 6.

HYDROTHERMAL GROWTH OF FERRITES

O. C. Kopp[5] G. W. Clark

Single-crystal ferrites are of technical importance. We would like to grow these complex cubic oxides of the transition elements by hydrothermal techniques, because the crystals should be more perfect than those now available and their magnetic properties depend on crystal quality. To determine appropriate conditions, the rate of growth of spontaneously nucleated ferrite crystals has been investigated as a function of temperature, pressure, time, solvent normality, and metallic additives.

Of the alkali hydroxide solvents, lithium hydroxide produced the highest growth rate. Testing various concentrations of the solvent system HCl-LiCl-LiOH, we obtained the best growth with 0.5 *N* LiOH. The added metallic ions studied were Zn, Sn, Bi, Co, Sb, Ni, and Mn. The presence of zinc or manganese distinctly enhanced growth rate. In extending this work we chose zinc as the additive to avoid complication regarding valence control. Studies by Gorter[6] and others have revealed that any fraction of the divalent ion of a pure ferrite can be replaced with other divalent ions, such as zinc. We have confirmed the incorporation of zinc in the ferrite crystals by spectrographic analysis. Also, we found that the growth rate increased with increasing temperature and pressure. Thus the highest growth rate achieved was for the highest temperature (500°C) and the highest pressure (30,000 psi) investigated. The crystal size appeared to increase linearly with growth time up to 5 weeks, but for longer times the growth rate decreased.

A detailed report of this work is in preparation, and our results will guide efforts toward seeded growth of ferrites.

[5]Consultant from the University of Tennessee.

[6]E. W. Gorter, *Nature* **165**, 798 (1950).

CRYSTAL GROWTH BY VERNEUIL METHOD

G. W. Clark

Using an oxyhydrogen Verneuil furnace,[7] we grew single crystals of NiO up to 1.5 cm in diameter and 5 cm long for a neutron-scattering experiment and titanium-doped Al_2O_3 crystals up to 0.7 cm in diameter and 3 cm long for study of mechanical properties.

The design of our arc-modified Verneuil system has been improved. With the system operating in a dual-anode transferred-arc mode, the powder for crystal growth can be injected gently into the heart of the arc, and dissimilar gases such as argon and nitrogen can be used. Powder hang-up on the anode wall continues to be troublesome.

ANALYSIS OF SUPERCONDUCTING SOLENOID MAGNET DESIGN FOR MAGNETIC SUSCEPTIBILITY MEASUREMENTS USING THE FARADAY METHOD

F. B. McLean Jr.[8] G. W. Clark

Recent progress in the construction of high magnetic field superconducting solenoid magnets has stimulated consideration of high field studies on magnetic materials. Fields equivalent to or greater than natural fields at interionic distances are economically available. We wish to measure magnetic susceptibility on small crystals in high fields. Thus we have analyzed the feasibility of using the Faraday constant-force method with solenoid magnets and finding the optimum solenoid geometry. Our analysis used zonal harmonic expansion of the field components[9] with a computer program[10] developed by the Thermonuclear Division.

We concluded from this analysis that a superconducting solenoid magnet, properly dimensioned, is a very promising means for providing high fields (50 to 100 kilogauss) in a favorable geometry for magnetic susceptibility measurements by the Faraday constant-force method. For all geometries considered, there is a sufficient volume for our estimated needs near each end of the solenoid, in which the desired magnetic force is constant (to less than 1%). The magnitude of the constant magnetic force is large and compares favorably with the better iron-core magnets described in the literature. If samples are kept closer to the axis than a distance of one-third the solenoid inner radius, the undesirable radial force is small and can be neglected.

We are preparing a report of this analysis and testing the general conclusions in our laboratory.

PHYSICAL PROPERTIES

G. W. Clark C. B. Finch
J. P. Young[11]

The physical property studies reported here are associated with the theoretical analysis reported by H. L. Davis in Chap. 8 of this report.

Temperature Dependence of Lattice Constants

The temperature dependence of the lattice constants of lanthanide germanomolybdates and lanthanide-doped thoria are being measured with an interferometric dilatometer. The temperature range covered thus far has been from 50 to 450°C. The samples for this study are about 1 mm in length along the crystallographic direction under consideration. These data on temperature dependence are to be correlated with the magnetic susceptibility and optical measurements on these same compounds.

Optical Spectra

The technique for preparing optically polished oriented crystal samples a few mils thick and greater than 15 mils in diameter has been developed.

---

[7] R. A. Lefever and G. W. Clark, *Rev. Sci. Instr.* 33, 769 (1962).

[8] Summer employee 1964, now graduate student at Brown University.

[9] M. W. Garrett, *J. Appl. Phys.* 22, 1091 (1951).

[10] M. W. Garrett, *Computer Programs Using Zonal Harmonics for Magnetic Properties of Current Systems with Special Reference to the IBM 7090*, ORNL-3318 (Dec. 4, 1962).

[11] Analytical Chemistry Division.

Absorption spectra of the lanthanide germanomolybdate crystal samples are being obtained using apparatus[12] described earlier. Preliminary spectral assignments have been made for the room-temperature spectra of Dy_2GeMoO_8.

[12]J. P. Young and G. W. Clark, *Metals and Ceramics Div. Ann. Progr. Rept. June 30, 1964*, ORNL-3670, p. 9.

Magnetic Susceptibility

The components of a superconducting solenoid magnetic susceptibility apparatus have been assembled and this system is now being calibrated. The designed temperature-range capability is from liquid helium to greater than 600°K. This design concept is being tested with a 10-kilogauss solenoid. Subject to the conclusions from this test, we plan to incorporate a solenoid capable of producing much higher magnetic fields.

2. Deformation of Crystalline Solids

R. O. Williams

The importance of plastic deformation of metals is common knowledge, but the processes that take place during and subsequent to deformation are poorly understood. We are performing research to elucidate this area. Current studies include investigations of the rate-controlling processes during deformation, the nature of the lattice reorientations, and the effect of deformation and annealing on the changes in internal energy. Other fundamental studies of deformation are reported in Chaps. 4 and 10 of this report.

MECHANISM OF THERMALLY ACTIVATED DEFORMATION IN TANTALUM AND TANTALUM-BASE ALLOYS[1]

R. J. Arsenault

The activation energies and activation volumes of tantalum and tantalum-base solid-solution alloys were obtained by both constant stress (creep) tests and constant strain-rate (tensile or compression) tests, and were investigated as a function of stress, temperature, and interstitial concentration. The agreement between the activation parameters obtained from creep and tensile or compression tests verifies many assumptions employed in the differential technique. The changes in the activation energy agree with calculations of the energy of formation of a double kink. These changes result from the effect of alloying on the shear modulus, and thus on the Peierls' stress barriers. Electron-transmission micrographs show a predominance of screw dislocations in samples deformed at large effective stresses. This is explained in terms of a larger Peierls' stress of the screw dislocations. Because the calculated change in activation energy agrees with that observed experimentally, these results support the double-kink mechanism as the rate-controlling mechanism of low-temperature deformation in body-centered cubic metals.

[1]Abstract of paper submitted to *Acta Metallurgica*.

SOLID-SOLUTION EFFECTS AND WORK HARDENING IN TANTALUM AND TANTALUM-BASE ALLOYS

R. J. Arsenault

In most of the previous investigations of solid-solution effects, face-centered cubic solid solutions have been used, and the metal became stronger on alloying. This observation does not hold for tantalum and tantalum-base alloys. The thermal component of the flow stress changes only little due to alloying, and in particular the flow stress of Ta–9.2 at.% Nb is slightly less than that of tantalum. This effect cannot be explained in terms of the solid-solution strengthening theories developed by Fleischer[2] and Mott and Nabarro.[3] In these theories the addition of any solute element increases the flow stress. The reduction of flow stress can readily be explained in terms of the double-kink (Peierls') mechanism. If the alloying addition reduces the modulus of the solid solution below that of the base metal, there will be a corresponding reduction in the activation energy of formation of a double kink, which in turn reduces the stress necessary to maintain a given strain rate.

[2]R. L. Fleischer, *Acta Met.* **11**, 203 (1963).

[3]N. F. Mott and F. R. N. Nabarro, *Proc. Phys. Soc. (London)* **52**, 86 (1940).

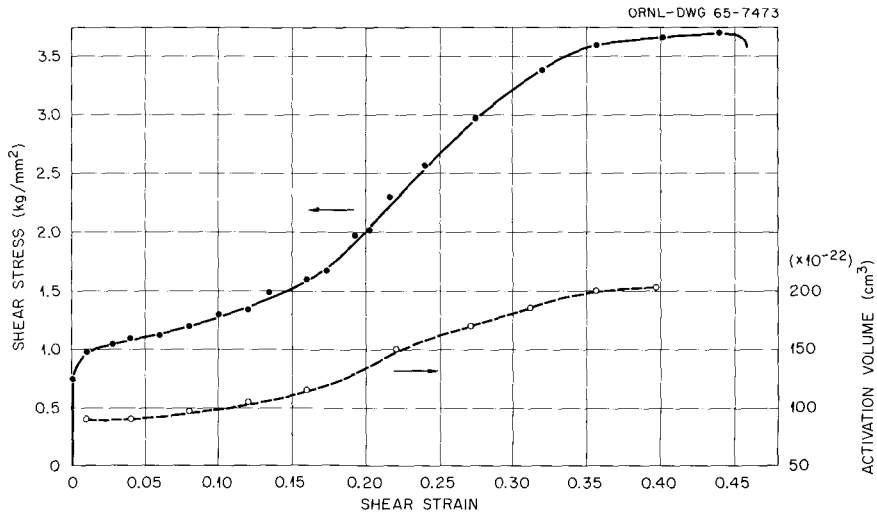

Fig. 2.1. Shear Stress vs Shear Strain for a Tantalum Sample Deformed at a Strain Rate of 5×10^{-3}/min at 448°K. The activation volumes were obtained by measuring the change in the flow stress during the test when the strain rate was changed between two values differing by a factor of 2.5.

The existence of three stages of work hardening has been observed in tantalum and tantalum-base alloys, as may be inferred from Fig. 2.1. However, the second stage of work hardening exists over a small temperature range. Figure 2.2 shows the work-hardening rate in stage II as a function of temperature. At temperatures below 273°K, stage II does not exist. Similar results have been obtained from a Ta–9.2 at. % Nb alloy, but the rate of work hardening is less. The activation volume increases slightly in stage II, as shown in Fig. 2.1, whereas in face-centered cubic metals and solid solutions the activation volume decreases in stage II.

A tentative explanation of the temperature dependence of work hardening (i.e., the existence of stage II) is based on the conclusion[2] that the mobility of screw dislocations is much less than that of edge dislocations at low temperature (i.e., at large stresses). At high temperatures the effect of the difference in mobility of screw and edge dislocations is eliminated because the athermal component contributes a larger fraction of the flow stress. As a result, interaction of edge dislocations with other dislocations is more likely, giving rise to cell structure, which causes stage II. Electron-transmission micrographs show no cell structure in samples deformed at low temperatures (high stress), but cell structure is observed in samples deformed at higher temperatures (small stress).

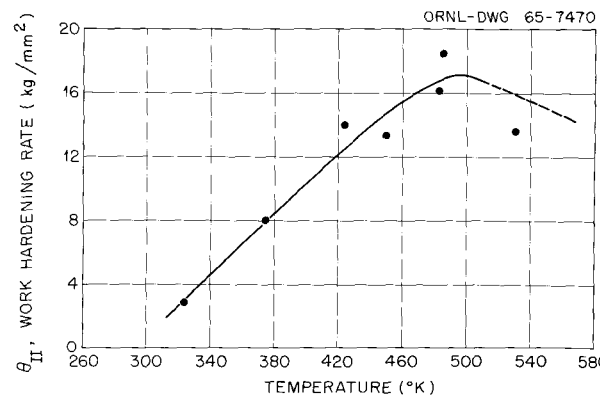

Fig. 2.2. Effect of Temperature on the Maximum Work-Hardening Rate of Tantalum in Stage II.

THERMALLY ACTIVATED SLIP IN NEUTRON-IRRADIATED COPPER SINGLE CRYSTALS[4]

R. J. Arsenault T. J. Koppenaal[5]

In developing an expression for neutron-irradiation strengthening based upon a "depleted zone"

[4]Summarized from *Appl. Phys. Letters* **6**, 159 (1965).
[5]Metallurgy Division, Argonne National Laboratory.

model, Seeger[6] assumed the existence of the rigid energy profile described by Mott and Nabarro[3] for the interaction of a dislocation with an obstacle (depleted zone). Using the quantitative expression derived by Seeger for the strengthening, several researchers have shown that in neutron-irradiated copper the theory can be successfully applied only if the activation energy for slip is assumed to be temperature dependent.[7,8] This temperature dependence of the activation energy was interpreted to arise from an obstacle-size spectrum.

In the present investigation, we directly determined experimentally the temperature dependence of the activation energy and activation volume at a constant effective stress between 200 and 290°K. Both activation parameters were independent of temperature. Figure 2.3 shows measured values of the activation energy at various temperatures. These observations contradict the rigid energy profile assumed by Seeger[6] in the development of the quantitative strengthening relationships.

[6]A. Seeger, *Proc. U.N. Intern. Conf. Peaceful Uses At. Energy, 2nd, Geneva, 1958*, vol. 6, p. 250.

[7]J. Diehl and W. Schilling, *Proc. U.N. Intern. Conf. Peaceful Uses At. Energy, 3rd, Geneva, 1964*, Paper A/Conf-471.

[8]M. J. Makin, *Phil. Mag.* **9**, 81 (1964).

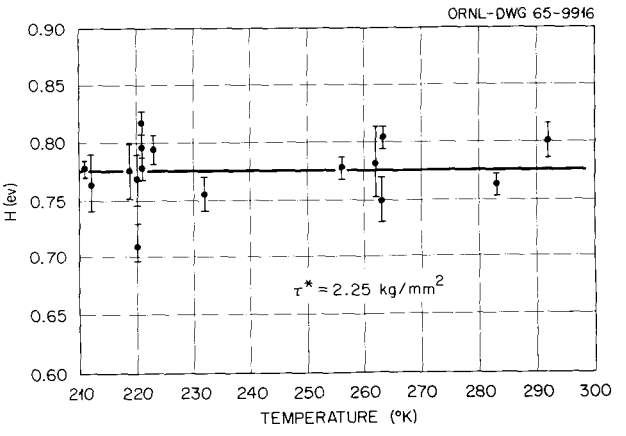

Fig. 2.3. Activation Energy for Slip in Neutron-Irradiated Copper at a Constant Effective Stress (τ^*) at Various Temperatures.

A RATE-CONTROLLING MECHANISM FOR SLIP IN NEUTRON-IRRADIATED COPPER SINGLE CRYSTALS[9]

T. J. Koppenaal[5] R. J. Arsenault

The stress dependence of the activation energy, H, and the activation volume, v^*, for slip in neutron-irradiated (8×10^{18} neutrons/cm^2) copper single crystals has been determined by tensile and creep measurements using the Conrad and Weidersich relationships. The experimental stress dependencies of both H and v^* are in excellent agreement with that predicted by Fleischer's theory for strengthening by tetragonal distortions. A number of different correlations indicate that slip in these irradiated crystals is regulated by a single rate-controlling mechanism. The activation energy for slip was temperature independent and equal to 3.0 ± 0.5 ev at zero effective stress.

We conclude that the rate-controlling mechanism for slip in these crystals is that given by Fleischer's theory. We believe the tetragonality producing the strengthening arises from the small vacancy loops found in copper that had been irradiated at room temperature.

INVERSE POLE FIGURES BY NUMERICAL METHODS

R. O. Williams

Conventional preferred-orientation data give the density of the various crystallographic poles relative to the physical directions of deformation. Conversely, the density of the physical directions can be represented relative to the crystallographic axes. Such a plot is termed an inverse pole figure and is a more accurate description of the texture. The relationship between these two representations was worked out some years ago.[10] We found that the inversion of conventional data into inverse pole figures is not a simple, direct process, but that trial-and-error methods would work.

[9]Abstract of paper accepted by *Philosophical Magazine*.

[10]L. K. Jetter, C. J. McHargue, and R. O. Williams, *J. Appl. Phys.* **27**, 368 (1956).

It was recognized very early that more powerful analytical methods might be very useful in speeding the inversion and giving better results. Considerable work has been done on this problem but has failed so far to give satisfactory inversions for various reasons. We decided that the original approach[10] after suitable modification should be checked more carefully, and this work is described here.

The basic relation is illustrated in Fig. 2.4, which shows the relation between the experimentally measurable x-ray data and the desired function that covers the crystallographic triangle. Thus we have

$$I_{hkl,\phi} = \overline{T} , \tag{1}$$

where I is the normalized intensity for the hkl plane at an angle ϕ, and $\overline{T}$ is the average value of the desired function along path β, which is ϕ degrees from the pole hkl. We may choose to represent the function as the sum of peaks. That is, at some point i

$$T_i = k \sum_j aS ; \tag{2}$$

where k is a constant such that

$$k \sum_j a = 1 ; \tag{3}$$

a is the profile of the peak, which we have taken to be

$$a = (1 + \cos x\gamma)/2 \tag{4}$$

for $x\gamma \leqq 2\pi$ and otherwise zero; and S is the strength of a peak. The distance from the peak center is γ. If we substitute Eq. (2) into Eq. (1), we have

$$I_{hkl,\phi} = \frac{k}{\beta} \sum_j S \int_\beta a \, d\beta , \tag{5a}$$

or more simply

$$I_i = \sum_j b_{ij} S_j . \tag{5b}$$

If $i \geqq j$, then this set of equations can be inverted to a new set where

$$S_i = \sum_j c_{ij} I_j , \tag{6}$$

and

$$T_i = k \sum_j a_{ij} c_{ij} I_{ij} , \tag{7a}$$

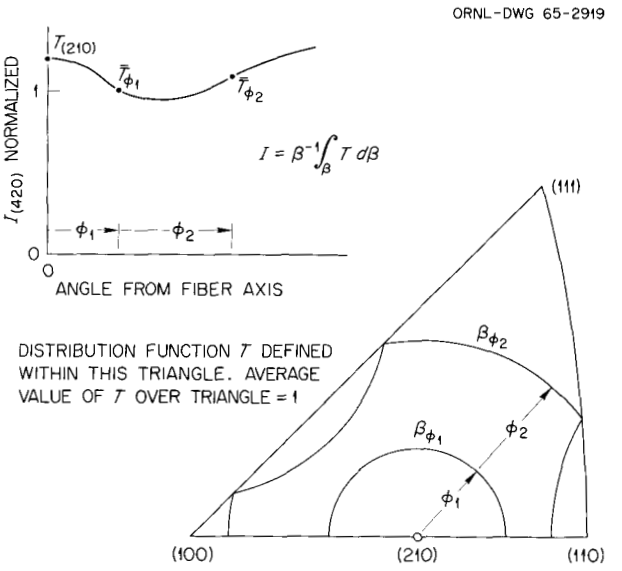

Fig. 2.4. The Relation Between the Density of a Direction over the Crystallographic Unit Triangle and the Corresponding Pole Figure for the (420) Plane.

or

$$T_i = \sum_j d_{ij} I_j . \tag{7b}$$

The difference between the experimental values of I and those calculated from Eq. (5) using values of S from Eq. (6) is called the residue and is designated by δI. If i is greater than j in Eq. (5), the inversion is done in the least-squares sense; that is, $\sum(\delta I)^2$ is minimized. There are standard computer programs for this operation.

Using 36 uniformly spaced peaks over the unit triangle for the cubic system, we derived 56 equations. These were then inverted, but the resulting c matrix was poorly behaved; that is, the elements were generally so large that the values of S and hence T exhibited large variations; there were even some negative values of T, which have no physical meaning. The values of S, nevertheless, gave small residuals and thus mathematically the solution was entirely satisfactory. We never established why this should be true, although the inversion process in no sense controls the range of values of the elements of the inverted matrix.

Various attempts to reduce the magnitude of elements of the inverted matrix met with a notable lack of success. Finally, additional sets of equations were written of the form

$$\sum_j f_{ij} S_j = 0 \ , \tag{8}$$

where matrix elements for successive peaks are generally equal in magnitude but opposite in sign. Always

$$\sum_j f_{ij} = 0 \ . \tag{9}$$

An equation was written for all peaks within a row, and seven rows were used to give seven additional equations. The values of the f's were not critical; values between about 0.01 and 0.04 were satisfactory. When these control equations are included in the set that is inverted, the resulting c matrix is much better behaved and gives a good reduction of the data.

It will be appreciated that these control equations limit the difference between adjacent peaks in the rows. The inversion does not require that these equations be satisfied exactly, only that the error be comparable to the residuals for the intensities. The inclusion of these additional equations cannot avoid increasing the residuals.

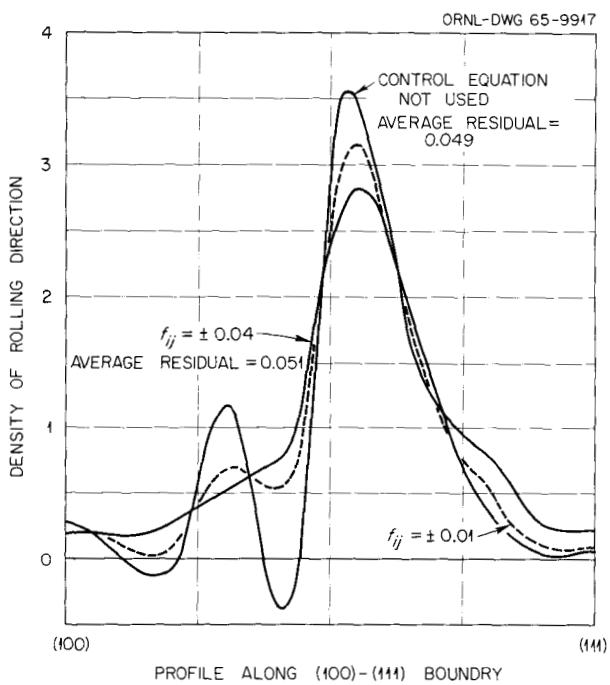

Fig. 2.5. The Calculated Values of the Density of the Rolling Direction Along the (100)–(111) Boundary Showing the Value of the Control Equations in Obtaining a Useful Inversion.

The effectiveness of these additional equations is illustrated in Fig. 2.5, which is a profile of the unit triangle along the (100)–(111) side for the rolling direction of an aluminum sheet. A value of 0.04 for the $|f_{ij}|$ in the control equations increased the size of residual only 4% but markedly improved the inversion.

ROLLING TEXTURES IN FACE-CENTERED CUBIC METALS

R. O. Williams

It has been well established that rolled face-centered cubic metals and alloys have either of two different textures. The copper type is characteristic of pure metals other than silver and the brass type is characteristic of silver and alloys with low stacking-fault energies. There is less agreement as to what orientations make up these textures. An investigation has been conducted to better define these textures.

Samples of copper, nickel, brass, and aluminum were rolled to 95% reduction and suitably fabricated into spherical samples, and the (111) pole figures were obtained. A comparison with published data established that the present textures were the same as obtained by others. The copper, brass, and aluminum were run as fiber textures around the three principal directions, and the data were inverted using in part the method described above.

The identity of the textures is established when the components of the three inverse pole figures are properly associated. This is done by separating the inverse figures on a common stereographic plot. Examination of the inverse pole figures suggests that the orientations are made up of continuous ridges and the texture is considered solved when the components of the ridges that are mutually perpendicular are identified. The resulting figure of copper is shown in Fig. 2.6 and the agreement with the (111) pole figure is shown in Fig. 2.7.

Aluminum is very similar to copper, although differences have been identified. The brass texture is rather different and more complex. The (111) pole figures showed nickel to be the same as copper.

ORNL-DWG 65-4311R

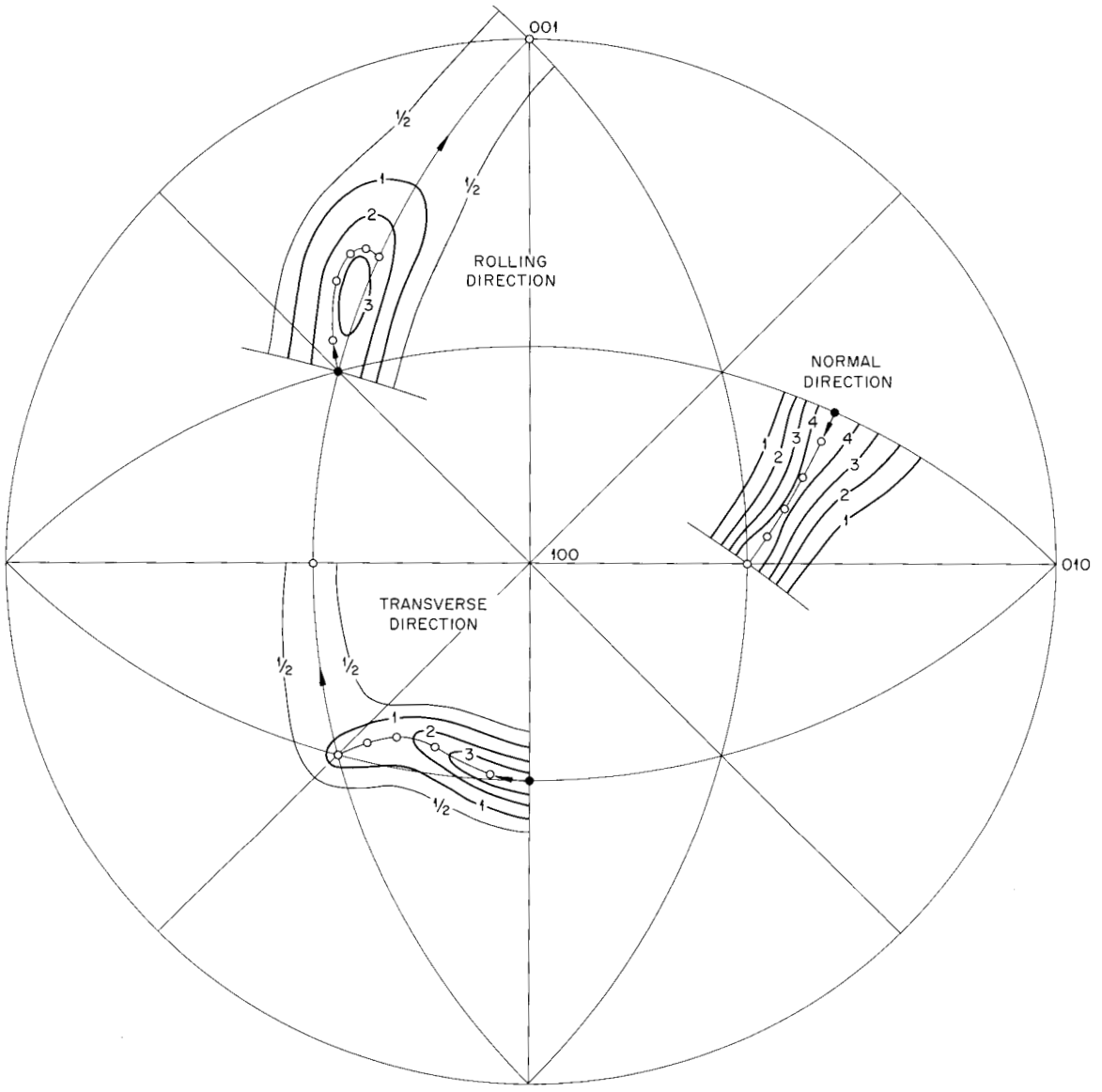

Fig. 2.6. An Arrangement of the Inverse Pole Figures for Copper Sheet Showing the Texture. Note that the texture is composed of ridges, in which the corresponding points are indicated.

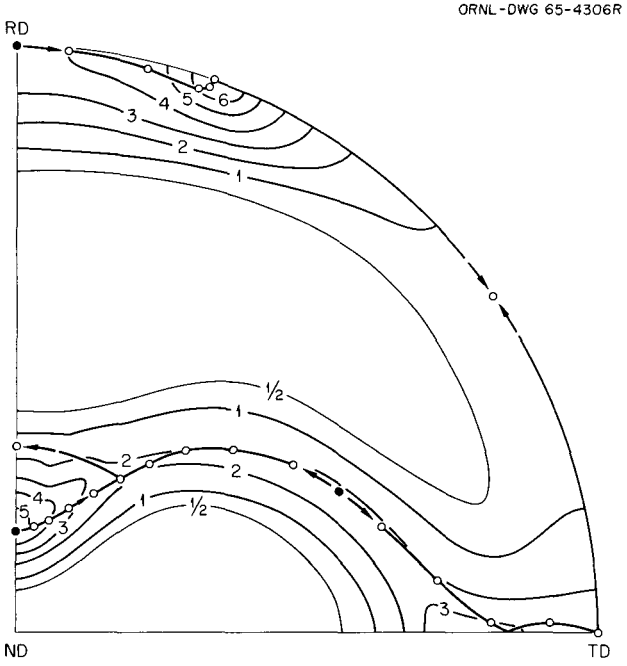

Fig. 2.7. A Comparison of the Proposed Texture (Heavy Line with Points Indicated) in Fig. 2.6 with the Conventional (111) Texture (Contours) for Copper Sheet.

A detailed comparison of these data with published data is not attempted here because of the complexity. The agreement is good in some cases but poor in others. In particular, no set of previously proposed orientations has accounted for the (111) pole figure as well as is shown in Fig. 2.7.

A DEFORMATION CALORIMETER

A. Wolfenden[11]

Advances have been made[12,13] in the measurement of the energy relations involved in the deformation of metals by the construction of calorimeters operating with good sensitivity and accuracy. The data obtained so far have permitted a certain amount of interpretation of the stored energy in terms of the dislocation structures of deformed metals. Although direct measurements of dislocation patterns have been made[14] by electron-transmission microscopy, these suffer two handicaps. By this technique alone, the significant reactions of thermally activated motion cannot be uncovered. Also, as shown by Ham,[15] serious errors may arise from the loss of dislocations during thinning of the sections. Additional information on the structure of cold-worked metals and on the recovery mechanisms is obtained by investigation of the kinetics of the release of stored energy.

For the reasons outlined above, a calorimeter is under construction to measure the energy relations involved in the deformation of metals as a function of deformation temperature, and to measure the immediate and subsequent releases of energy when the specimens are heated. Using the data from the annealing kinetics of the deformed samples, we expect to be able to identify the defects mobile at room temperature in copper. Impact compression inside the calorimeter was chosen as the mode of deformation, since the strain is simple and readily evaluated, and since energy measurements can, with the proposed instrument, start immediately after deformation without need for transfer of the sample.

The apparatus is shown schematically in Fig. 2.8 and consists essentially of a tungsten carbide hammer positioned by guide rails and a tungsten carbide anvil set in a massive block, all under vacuum. Deformation takes place when the hammer is driven rapidly into contact with the specimen against the inertia of the heavy block. The hammer is accelerated by the action of compressed air on the piston.

The internal energy of the sample immediately after impact will be deduced from the mechanical energy expended during deformation, and the temperature rise measured by a thermocouple spot-welded to the specimen. The subsequent heating of the sample to measure the energy release will be controlled by heaters placed in the block. Impact velocity, which must be measured to evaluate the work done in the deformation process, will be determined with two electromagnetic pick-ups feeding an oscillograph. The temperature rise of the sample both immediately after impact and on subsequent annealing will be recorded automatically to obtain the desired annealing kinetics.

[11] Noncitizen employee from England.

[12] A. L. Titchener and M. B. Bever, *Progr. Metal Phys.* 7, 247–338 (1958).

[13] R. O. Williams, *Rev. Sci. Instr.* 31, 1336–41 (1960); 34, 639–43 (1963).

[14] J. E. Bailey and P. B. Hirsch, *Phil. Mag.* 5, 485 (1960).

[15] R. K. Ham, *Phil. Mag.* 7, 1177 (1962).

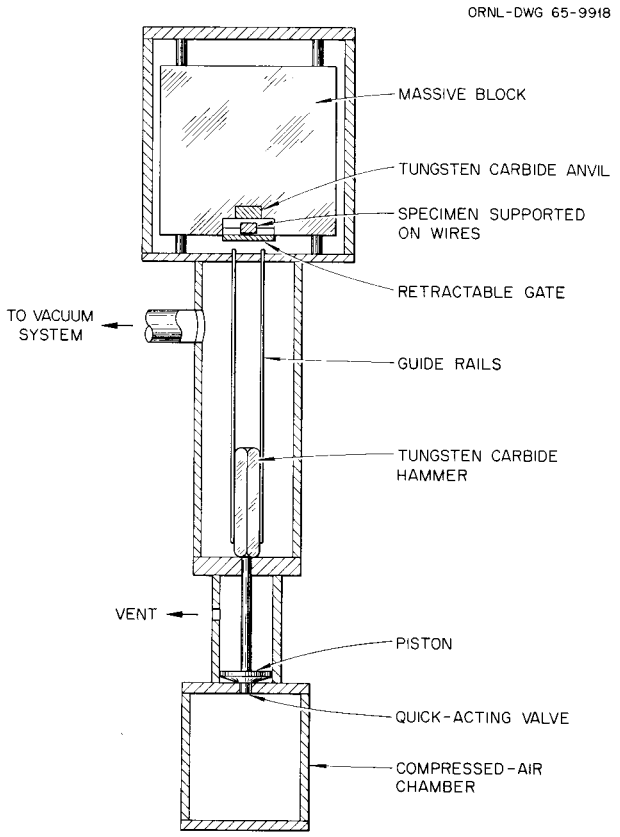

Fig. 2.8. Deformation Calorimeter.

3. Diffusion in Solids[1]

T. S. Lundy

Our purpose is to provide information concerning mechanisms and rates of diffusion processes that are important in the development of materials for high-temperature applications. We have completed several studies on diffusion in body-centered cubic metals and one on the effect of alpha bombardment on the diffusion of lead into silver. Some of our research utilizes the anodic sectioning technique for niobium and tantalum developed jointly with the Reactions at Metal Surfaces Group. Chapter 12 of this report includes a more complete report of this application. The diffusion of oxygen in niobium and thorium in pyrolytic carbon, measured in other programs, is reported respectively in Part II, Chap. 16, and Part III, Chap. 24, of this report.

THE DIFFUSION OF Nb^{95} AND Ta^{182} IN TANTALUM[2]

R. E. Pawel[3] T. S. Lundy

Diffusion constants were obtained for Nb^{95} and Ta^{182} in tantalum over the temperature range 920–2500°C making use of lathe, grinding, and anodic film sectioning techniques. Over this temperature range, the lattice diffusion coefficients were observed to vary from about 2.5×10^{-19} cm^2/sec to about 4×10^{-9} cm^2/sec for Nb^{95} in tantalum. The Ta^{182} diffusion coefficients were about half those for Nb^{95} at all temperatures. The apparent variation in the activation energy for Nb^{95} diffusion in tantalum was about 6000 cal/mole over the whole temperature range; thus the Arrhenius relationship was seen to apply exceptionally well to this system. The expression $D = 0.23 \exp(-98{,}700/RT)$ cm^2/sec describes the data within 20%.

DIFFUSION OF Nb^{95} AND Ta^{182} IN NIOBIUM (COLUMBIUM)[4]

T. S. Lundy F. R. Winslow
R. E. Pawel[3] C. J. McHargue

The volume diffusion coefficients of Nb^{95} and Ta^{182} in niobium have been measured over the temperature range 878 to 2400°C. High-temperature specimens ($T \gtrsim 1500°C$) were sectioned by conventional lathe and grinding techniques while low-temperature specimens were sectioned by an anodizing and stripping technique previously described. Over a range of more than ten orders of magnitude in diffusivity, the self-diffusion data are well represented by the equation

$$D = (1.1 \pm 0.2) \exp[-(96{,}000 \pm 900)/RT] \text{ cm}^2/\text{sec} .$$

Upward deviations from this line are explained by short-circuit diffusion in combination with the loss of resolution of the sectioning techniques. Oxygen contamination within the range 100 to 450 ppm was found to have little or no effect on the self-diffusivity of niobium.

In a limited number of measurements, the diffusivity of Ta^{182} in niobium was found to be about half that of Nb^{95} in niobium. These data may be described by

$$D = \left(1.0 \begin{smallmatrix}+0.9\\-0.5\end{smallmatrix}\right) \exp[-(99{,}300 \pm 2400)/RT] \text{cm}^2/\text{sec} .$$

---

[1]Support for this program shifted from the AEC Division of Reactor Development to the Division of Research on July 1, 1965.

[2]Abstract from *Phys. Chem. Solids* **26**, 937–42 (1965).

[3]Reactions at Metal Surfaces Group.

[4]Abstract of *Trans. Met. Soc. AIME* **233**, 1533–38 (1965).

DIFFUSION OF ^{181}Hf IN BCC HAFNIUM[5]

F. R. Winslow T. S. Lundy

Self-diffusion coefficients in reactor-grade hafnium (2.1% Zr) have been measured over the temperature range 1795 to 1995°C using ^{181}Hf and standard lathe sectioning techniques. The diffusivity can be represented by:

$$D = \left(1.2 \begin{smallmatrix}+0.7\\-0.5\end{smallmatrix}\right) \times 10^{-3} \exp\left[-(38{,}700 \pm 1000)/RT\right] \text{ cm}^2/\text{sec} .$$

Some scatter in the data precludes a firm conclusion as to the existence of curvature in the Arrhenius plot, but the very low values of D_0 and Q indicate that β-hafnium is in the same anomalous class as β-Ti, β-Zr, and γ-U with respect to diffusion behavior.

In addition to the specimens annealed in the beta range, two specimens were annealed at 1745°C. These specimens, unlike the others, showed non-Gaussian penetration behavior – evidence that diffusion occurred in the hexagonal close-packed alpha phase. The highest possible D value calculated from the curved penetration plots is more than one order of magnitude lower than the D value at 1795°C. Thus, the α-β transformation temperature for hafnium is 1770 ± 25°C, in substantial agreement with values by other workers.

DIFFUSION OF ^{44}Ti IN V–20% Ti

J. F. Murdock

The diffusion of ^{44}Ti in the alloy V–20 wt % Ti was studied in the temperature range of 1100 to 1650°C in a further effort to characterize the non-Arrhenius behavior previously reported in β-titanium and vanadium[6,7] and to note the effect of composition on diffusion in body-centered cubic materials. The data are summarized on an Arrhenius-type plot shown in Fig. 3.1 and appear to be best fitted by a straight line from 1100 to 1350°C and a line of continuous curvature from 1350 to 1650°C.

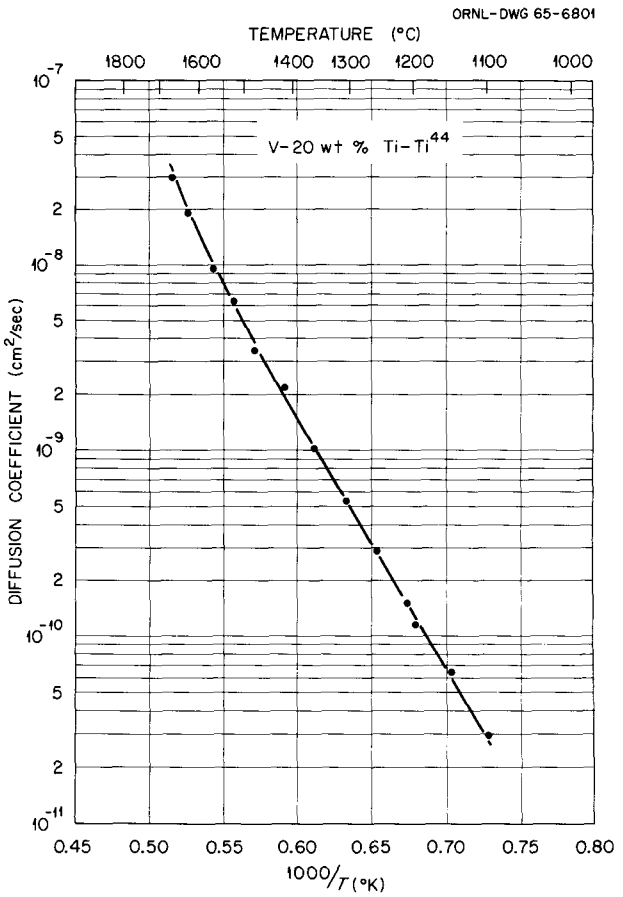

Fig. 3.1. Temperature Dependence of the Diffusion of ^{44}Ti in V–20% Ti.

SELF-DIFFUSION IN CHROMIUM

J. Askill[8]

Recent data[9] from 1000 to 1550°C on the diffusion of ^{51}Cr in chromium have shown that, at least within this temperature range, self-diffusion does not exhibit the nonlinear dependence of log D on $1/T$ that has recently been established for the body-centered cubic metals Ti, Zr, and U. In

[5]Summary of a Technical Note to be published in *Transactions of the Metallurgical Society of AIME.*

[6]J. F. Murdock, T. S. Lundy, and E. E. Stansbury, *Acta Met.* **12**, 1033–39 (1964).

[7]T. S. Lundy and C. J. McHargue, *Trans. Met. Soc. AIME* **233**(1), 243–44 (1965).

[8]Noncitizen employee from England.

[9]J. Askill and D. H. Tomlin, *Phil. Mag.* **11**(111), 467–74 (1965).

the present study the temperature range has been extended to the melting point (about 1900°C).

Diffusion samples ½ in. in diameter and ⅜ in. long of 99.98% chromium were subjected to grain-growth anneals in argon at temperatures of about 1600°C for a few hours, resulting in grain sizes of 2 to 3 mm. Diffusion anneals were then carried out in argon at a pressure of about 2 atm, and the samples were analyzed by hand grinding as previously described.[9] Penetration curves (log concentration vs distance squared) for temperatures below 1200°C were all curved, due to grain-boundary diffusion.[9] Between 1200 and 1700°C the plots were linear over two to three logarithmic cycles in concentration. Above 1700°C, however, in every case the penetration plot consisted of two distinct parts and yielded two diffusion coefficients. A typical penetration plot in each of the three temperature regions is shown in Fig. 3.2. An Arrhenius plot showing data from 1000°C to the melting point is shown in Fig. 3.3. The data from 1000 to 1700°C can be represented by the equation $D = 1.6 \exp(-81{,}000/RT)$ cm^2/sec.

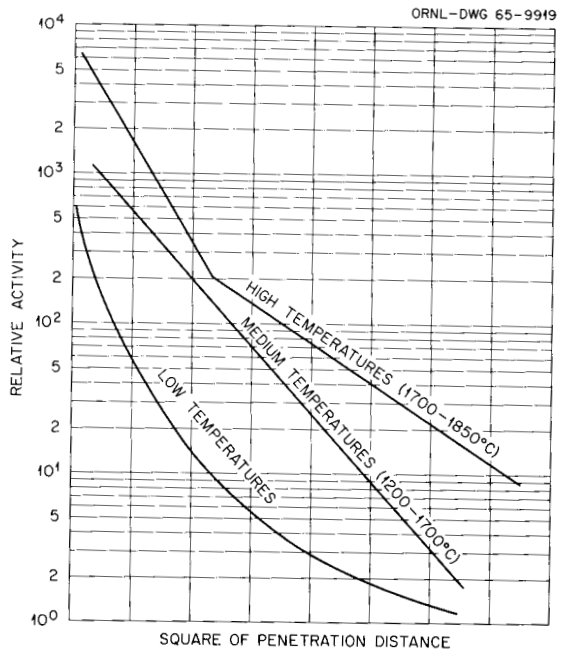

Fig. 3.2. Typical Penetration Plots for Self-Diffusion in Chromium.

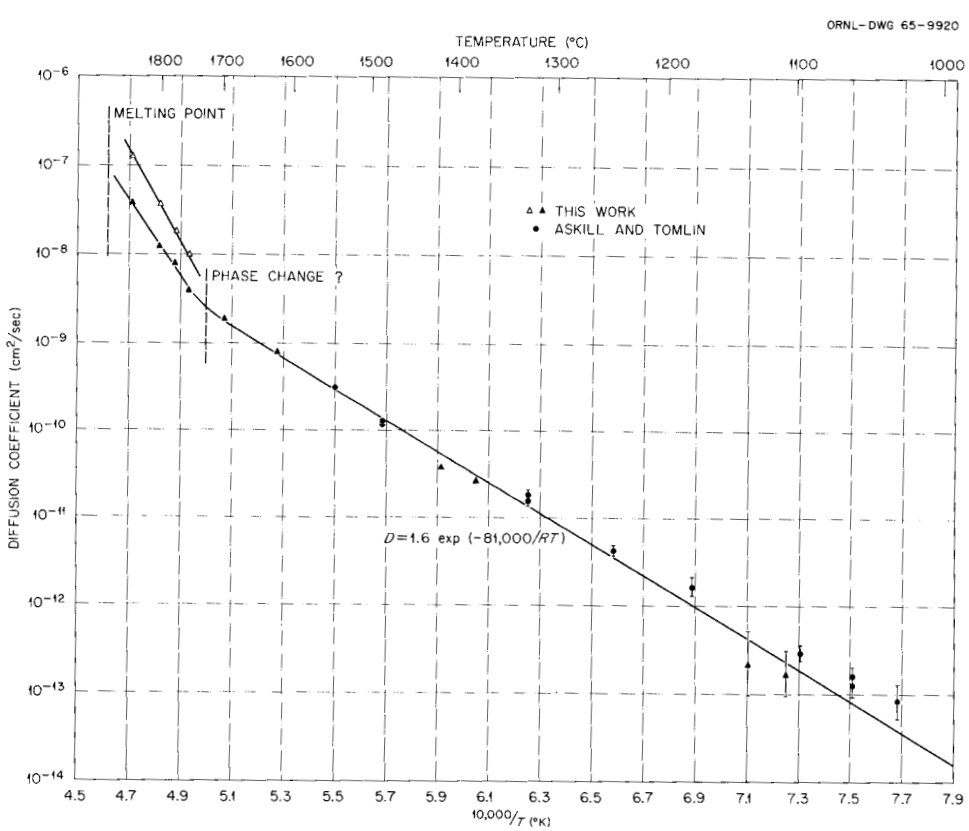

Fig. 3.3. Temperature Dependence of the Diffusion of ^{51}Cr in Chromium.

The transition temperature from the single to two-part penetration plots was 1725 ± 25°C.

The change in diffusion characteristic at 1725°C may be associated with a structure change in chromium. However, x-ray work at these temperatures has not given any decisive information. We plan to investigate the diffusion of ^{51}Cr in both Cr–10% Ni and Cr–20% Ni alloys at temperatures near the melting point and also to carry out some x-ray studies on these alloys to try to clarify the nature of the transition.

DIFFUSION OF ^{182}Ta IN TITANIUM

J. Askill[8]

Anomalous diffusion in the body-centered cubic phases of Ti, Zr, and U is now well established. Kidson[10] has suggested that the unusually large diffusion coefficients result from an enhancement of the vacancy concentration by impurity oxygen atoms forming oxygen-vacancy complexes. To test this hypothesis, diffusion experiments from 1000 to 1600°C under various annealing conditions were carried out using the isotope ^{182}Ta. Tantalum was chosen as the solute because no data were available for the diffusion of tantalum in titanium, although there are data on the diffusion of 12 other metals in titanium.

The specimens were annealed (1) under 1 to 2 atm of 99.995% pure argon, (2) in a normal laboratory vacuum of about 5×10^{-5} torr, and (3) in a high vacuum of 8×10^{-9} torr. One sample was annealed in high vacuum after a high-vacuum preanneal and another annealed in a normal vacuum after a high-vacuum preanneal. All others were annealed either in a normal vacuum or in argon after a normal laboratory vacuum preanneal. In each case the temperature was measured with a calibrated optical pyrometer and the pressure was measured at the diffusion-anneal temperatures. The diffusion samples were analyzed by customary lathe sectioning techniques, and penetration plots linear over two to three logarithmic cycles in concentration were obtained. Diffusion coefficients are shown as a function of temperature in Fig. 3.4. Shown for comparison is the graph of ^{99}Mo diffusion in titanium, reported by Gibbs, Graham, and Tomlin.[11] The results gave a curved Arrhenius plot as expected for diffusion in β-titanium and an analysis into the two exponential terms:

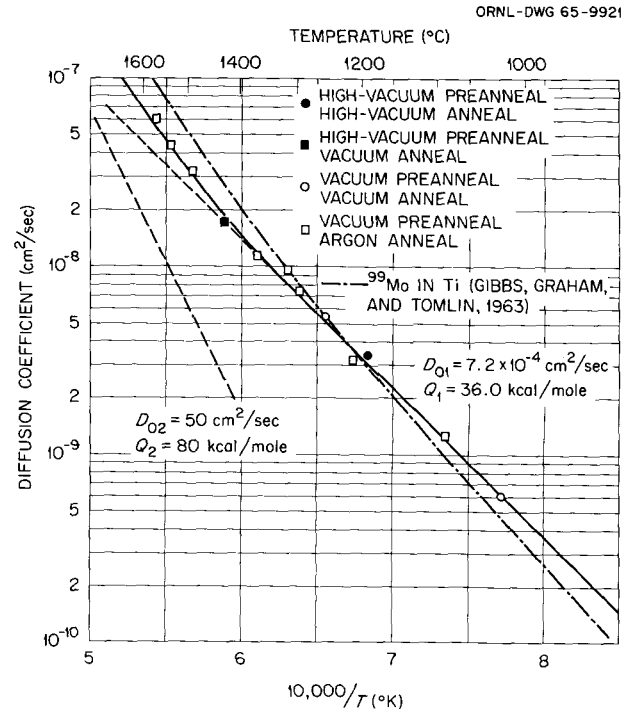

Fig. 3.4. Arrhenius-Type Plot Showing Atmosphere Effects on the Diffusion of ^{182}Ta in β-Titanium.

$$D = D_{01} \exp(-Q_1/RT) + D_{02} \exp(-Q_2/RT) ,$$

where

$D_{01} = 7.2 \times 10^{-4}$ cm^2/sec,

$Q_1 = 36.0$ kcal/mole,

$D_{02} = 50$ cm^2/sec,

$Q_2 = 80$ kcal/mole.

Chemical analyses of one sample that had undergone a normal vacuum anneal and one that was used in the high-vacuum experiment showed approximately 100 ppm O in each. This is much less than the concentration required if there is one-to-one correspondence between the oxygen impurity atoms and the extrinsic vacancies (those causing the high diffusion coefficients at lower temperatures in the beta phase). Within experimental error the different annealing condition had no noticeable effect on the diffusion rates. This suggests, then, that the enhanced diffusion

[10] G. V. Kidson, *Can. J. Phys.* **41**, 1563 (1963).

[11] G. B. Gibbs, D. Graham, and D. H. Tomlin, *Phil. Mag.* **8**(92), 1269–81 (August 1963).

rates do not result from oxygen impurity already in the material or absorbed during the anneal but are due to some intrinsic property of titanium itself.

EFFECT OF ALPHA BOMBARDMENT ON THE DIFFUSION OF LEAD IN SILVER[12]

D. Heitkamp[13] W. Biermann[14]
T. S. Lundy

The theory of radiation-enhanced diffusion has been extended to include the effect of annihilation of point defects (vacancies and interstitials) at a free surface. Predictions are then made for the magnitude of the effect of alpha bombardment on self-diffusion in silver. Experimental values for ^{212}Pb diffusion in silver, obtained by the alpha-recoil method of Hevesy and Seith, were found to be in agreement with predictions from a theory that excludes the surface as a sink for point defects.

---

[12]Abstract of an article submitted for publication in *Acta Metallurgica*.

[13]Visitor from Germany, now at Institut für Radiochemie, Karlsruhe, Germany.

[14]Visitor from Germany, now at Babcock and Wilcox Company, Atomic Energy Division, Oberhausen, Germany.

4. Electron Microscopy

J. O. Stiegler

We are using the electron microscope as a primary research tool to correlate microstructure on a fine scale with various properties of solids. In addition to our own research program, in which we are attempting to understand the deformation mechanisms of body-centered cubic metals and alloys, we are developing information on other materials of interest to groups in the Division, such as structural features of pyrolytic carbons, radiation effects in stainless steels and UO_2, and elevated-temperature fracture of nickel and nickel-base alloys.

EFFECT OF DEFORMATION VARIABLES ON DISLOCATION BEHAVIOR IN BODY-CENTERED CUBIC METALS AND ALLOYS

J. O. Stiegler K. Farrell[1]
B. T. M. Loh[2]

One of the distinctive features of the body-centered cubic transition metals is a strong increase in yield or flow stress in a standard tensile test as the deformation temperature is lowered. We showed this increase in stress to be accompanied by an increase in the ratio of screw to edge dislocation components as observed in electron micrographs. For very low deformation temperatures, only straight screw segments are observed, indicating that the thermally activated motion of screw dislocations is the rate-controlling process in the low-temperature deformation of body-centered cubic metals. The temperature range in which screw motion becomes dominant appears to be a function of composition, purity, and heat treatment. Similar effects are noted in body-centered cubic alloys at higher temperatures.

Strain rate is the variable that is held constant in a standard tensile test; an increased stress is necessary to maintain this constant rate as the deformation temperature is lowered. The corresponding change in microstructure suggests that either the increased stress or the lowered temperature is significantly changing details of

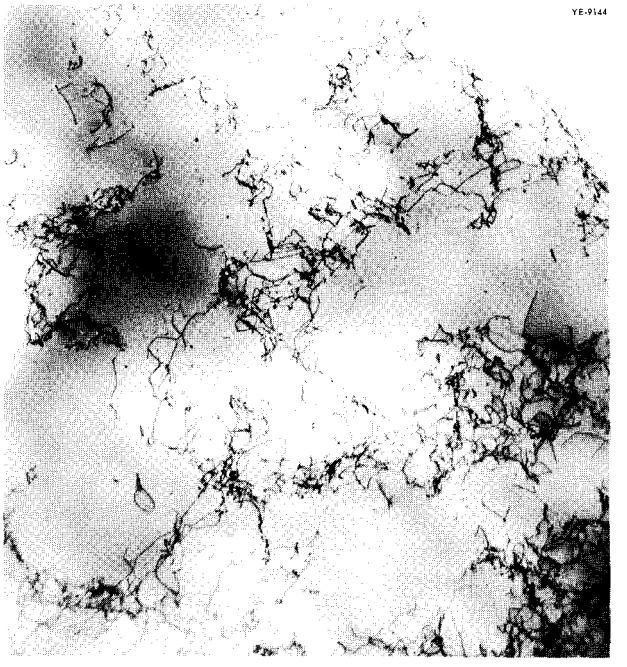

Fig. 4.1. Transmission Electron Micrograph of Niobium Deformed About 2.5% in Tension at 23°C. The tensile stress at the point at which the test was stopped was about 8800 psi. 25,000×. Reduced 55%.

[1]Noncitizen employee from England.

[2]Noncitizen employee from Taiwan.

the deformation process. In order to assess the relative importance of these two variables we deformed a series of niobium specimens at various strain rates at 23 and –70°C. The resulting microstructures shown in Figs. 4.1 to 4.3 indicate that applied stress (or strain rate) is the dominant variable. The specimen deformed at a standard rate of 0.050/min at 23°C showed considerable tangling and a well-developed cell structure, whereas the one deformed at –70°C exhibited a uniform distribution of short predominantly screw segments accompanied by a high density of loops and other debris. A specimen strained about 2% at –70°C at a constant stress of 8400 psi, the maximum stress reached in the standard room-temperature test, showed tangling, definite cell formation, and a low density of loops. This demonstrates clearly that temperature is not the controlling factor. Thus, by altering external loading conditions to maintain a constant strain rate in a standard tensile test, we are in turn altering the fine-scale details of the deformation process and are promoting those processes that favor brittle fracture and twinning.

If the activation energy for cross slip were higher than that for dislocation motion alone, cross slip of screw components should be retarded at low temperatures relative to screw motion. The strong similarity in microstructure between the creep specimen deformed at low temperature and the room-temperature tensile specimen shows that cross slip of screw segments is not significantly retarded at low temperatures. The presence of the large number of loops in slip bands formed at low temperatures also indicates that a considerable amount of cross slip has occurred since all proposed mechanisms for loop production involve cross slip.

To show that cross slip was occurring frequently at low temperatures or in disordered alloys, we tested and examined an Fe–21 at. % Al alloy treated to produce short-range order. In such an alloy, cross slip should be largely inhibited, since movement of a segment of a dislocation off an established slip plane disorders more of the lattice and, consequently, requires a higher stress than

Fig. 4.2. Transmission Electron Micrograph of Niobium Deformed About 2.5% in Tension at –68°C. The strain rate was identical to that used in testing the specimen shown in Fig. 4.1, but the applied tensile stress was about 20,000 psi. Note the uniform distribution of straight dislocation segments and the high density of loops. 25,000×. Reduced 55%.

Fig. 4.3. Transmission Electron Micrograph of Niobium Deformed at –68°C Under a Constant Tensile Load of About 8400 psi. 37,500×. Reduced 55%.

movement of the dislocation on the previously disordered slip plane. Electron microscope examination of the alloy showed that after light deformation the dislocations were confined to planar arrays and that the slip bands were free of loops. After more extensive deformation had occurred and large volumes had been disordered, dislocation tangles and loops were observed. This substantiates our belief that frequent although not extensive cross slip occurs at low temperatures or in random alloys and that the changes in dislocation pattern and behavior are largely a result of the high applied stress required to move screw dislocations.

The apparent suppression of cross slip at low temperatures or in random solid-solution alloys, evidenced by narrow slip bands and straight slip lines, may be a consequence of the high applied stress required for deformation under these circumstances. In general, the structure of a slip band will depend on the stress at which the band is nucleated, because of the multiple cross-slip mechanism of multiplication. Jogs on screw dislocations formed by cross slip are able to act as sources of new dislocations when the applied stress is high enough that the newly formed edge components can glide past one another. At low temperatures or in some alloys the flow stress is extremely high due to the difficulty in moving screw dislocations; multiplication consequently occurs for relatively small jogs. That is, slip bands are very narrow since multiplication occurs without extensive cross slip.

Twinning and fracture may be a result of high stress concentrations produced by narrow slip bands formed suddenly at high stress levels. The observation that prestraining at elevated temperatures suppresses twinning at lower temperatures reinforces our belief that this dynamic effect is responsible for these deformation phenomena. Although slip bands formed at low temperatures in prestrained materials also are narrow, the dislocation density in the band and the stress concentration resulting from the band are built up slowly enough to be relieved by slip. The large shear produced suddenly by a slip band created at a high stress level can, on the other hand, be most easily relieved by twinning and fracture.

Present work is aimed at clarifying the role of interstitial elements in the deformation process. Type, amount, and distribution of interstitial elements in niobium are being varied systematically and their effect on mechanical properties and dislocation behavior studied. Similar studies also will be conducted on substitutional solid solutions. Micro-yield behavior will be studied using etch-pitting techniques on polycrystals in an attempt to understand the role of grain boundaries in the production of initial mobile dislocations. We are also preparing to study precipitation processes in this crystal system in order to control the type, size, and distribution of precipitates to optimize mechanical behavior at elevated temperatures.

RECRYSTALLIZATION, GRAIN GROWTH, AND MECHANICAL BEHAVIOR OF TUNGSTEN SHEET

K. Farrell[1] J. T. Houston
A. C. Schaffhauser[3]

Tungsten in single crystal form is quite ductile at room temperature. However, when grain boundaries are introduced into the specimens, they become brittle even at temperatures as high as 300°C. We suspect that this effect is caused by the segregation of impurity atoms at the grain boundaries. We have, therefore, examined indirectly the insidious effects of such segregation on grain growth and the mechanical properties of polycrystalline tungsten.

Recrystallization and Grain Growth

The rolled sheet was made by a powder-metallurgical process. In the as-received condition it had a fibrous structure composed of equiaxed subgrains with an average diameter of 1.4 μ. When the material was annealed, primary recrystallization began at 1250°C and was rapid at 1300°C, giving a mean grain size of about 15 μ. Thereafter, at temperatures up to about 2000°C very little primary grain growth occurred.

At 2000°C and above, extensive grain growth, or secondary recrystallization, occurred. This growth began at one surface of the specimen and then spread through the specimen thickness. The resulting grain size was highly heterogeneous, with the larger grains exceeding 5 mm in diameter on annealing at 2800°C.

---

[3]Physical Metallurgy Group.

Temperature and Grain-Size Dependence of the Lower Yield Stresses

In the temperature region between 450°C and the ductile-brittle transition temperatures, the lower yield stresses in bend tests increased exponentially with decreasing test temperature. The temperature exponents (at constant strain rate) corresponded to pseudoactivation energies of between 4000 and 4500 cal/mole for the annealed materials and 1130 cal/mole for the as-received material.

The yield stress depended strongly on the recrystallized grain size. However, because of heterogeneous grain sizes and distribution in some of the specimens, the precise relationship between grain size and lower yield stress is not yet clear.

Ductile-Brittle Transition Temperatures

In the bend tests, as-received and partially recrystallized material displayed a change from ductile to brittle behavior in the temperature region 155 to 190°C. In material recrystallized at 1300°C the ductile-brittle transition temperature was 245°C. Specimens annealed at higher temperatures up to 2500°C had ductile-brittle transitions in the temperature range 245 to 285°C, the highest value being for material annealed at 2100°C. There was a suggestion of a fall in transition temperatures at the largest grain sizes. The lowest transition temperatures were associated with the fine subgrains.

Brittle Fracture Characteristics

In the recrystallized specimens annealed at temperatures below 2100°C and tested below the ductile-brittle transition temperatures, fracture was largely intergranular. Isolated transgranular cleavage facets did occur, but these rarely exceeded one or two grains in size, and often they terminated within a grain, the fracture path then jumping to an adjacent grain boundary. Examination of the fracture surfaces showed a sparse distribution of small precipitate particles on the parted grain boundaries.

In those specimens annealed above 2100°C, the large grains failed by cleavage, but fracture through small-grained areas was intergranular. Since the large grains predominated, the general fracture surface was composed largely of cleavage facets. Many of these cleavage cracks appear to originate at grain boundaries.

Discussion

The results are consistent with a picture of embrittlement controlled by impurities segregated at grain boundaries. Such segregated material prevents grain growth on annealing until the temperature is sufficiently high to disperse or dissolve the impurity. Secondary recrystallization then occurs. We believe that these impurities also inhibit the operation of grain-boundary dislocation sources and provide strong barriers to the transmission of slip from grain to grain. This results in highly localized stress concentrations, which are released suddenly by cracking at the boundaries. The cracks follow an intergranular path when grain-boundary impurity segregation is strong. They become transgranular when the degree of segregation is reduced but appear in general to originate at grain boundaries.

THERMALLY AND CHEMICALLY INDUCED STRUCTURAL CHANGES IN PYROLYTIC CARBON

J. O. Stiegler R. B. Evans III[4]

Results are summarized of a study using electron microscope and electron diffraction techniques to clarify the nature of pyrolytic carbon in the deposited and annealed states, and to investigate the effect of actinide impurities on the annealing process. Contrast variations in transmission micrographs of the as-deposited materials were due to thickness variations in the cleavage flakes arising from roughness of the deposition surface and from the presence of microvoids about 100 A in diameter. No microstructural changes occurred during a 24-hr anneal at 2400°C, but the structure improved, as evidenced by a sharpening of the diffraction rings. Anneals at higher temperatures resulted in the formation of graphite crystallites about 1000 A in diameter by about 100 A thick and in the elimination of the fine-scale wrinkling. Surface diffusion or evaporation and condensation gave rise to the formation of mounds of material having the two-dimensional pyrolytic structure and

[4]Reactor Chemistry Division.

to a filling of the microvoids at free surfaces. At temperatures below which structural changes occur, uranium diffusion down growth-cone boundaries promoted an unidentified microstructural change in the region adjacent to the boundaries and eliminated the microvoids.

ELECTRON MICROSCOPY OF PYROLYTIC CARBON DEPOSITS ON FUEL PARTICLES[5]

J. O. Stiegler C. K. H. DuBose
J. L. Cook[6]

Electron microscopy and diffraction techniques were used to characterize structural features of various pyrolytic carbons deposited on fuel particles in a fluidized bed at temperatures between 1400 and 1800°C. The as-deposited materials consisted of turbostratically stacked monolayers having the hexagonal graphite structure. The average diameter of the layers ranged between about 50 and 150 A, and the bulk density varied from 1.42 to 2.08 g/cm^3, depending on the deposition conditions. Using direct transmission microscopy on cleaved flakes, we showed the low-density deposits to contain microvoids about 100 A in diameter. The density of microvoids increased as bulk density decreased, but the crystallite size did not significantly change with density. Surface replicas showed distinctive features that are characteristic of the different deposits but which cannot be interpreted directly in terms of the structure of the deposits as revealed by transmission techniques.

ACTINIDE-ENHANCED STRUCTURAL IMPROVEMENTS IN PYROLYTIC CARBON

J. O. Stiegler R. B. Evans III[4]

Pyrolytic carbon has been shown to be unstable at temperatures somewhat above the deposition temperature. We found that the presence of actinide elements significantly lowers the temperature range in which structural improvements leading to graphitization occur. To characterize the actinide-enhanced structural changes, we used transmission electron microscopy and diffraction on cleavage flakes extracted from various regions of a pyrolytic carbon–uranium carbide diffusion couple that had been held 100 hr at 2000°C.

We observed no structural changes in the host pyrolytic carbon located outside the diffusion zone. Within the diffusion zone at least three phases coexisted, often in contact with one another. The fringes in isolated regions of Fig. 4.4 arise from diffraction effects from thin platelets of graphite, and the black areas are a thick nonplatelike substance, probably uranium carbide or its reaction product formed after exposure to the atmosphere. The diffraction pattern from this area, shown in Fig. 4.5, exhibits sharp diffraction spots from the graphite platelets superimposed on smooth nearly uniform rings from material retaining the pyrolytic carbon structure. This indicates that a nearly continuous layer of pyrolytic carbon must be present in this area. There is some indication of material having the appearance of pyrolytic carbon in several areas free of the fringe

Fig. 4.4. Transmission Electron Micrograph of a Cleavage Flake Extracted from Within the Diffusion Zone of a Couple of Uranium Carbide with Pyrolytic Carbon Held 100 hr at 2000°C. 37,500×. Reduced 56%.

[5]Abstract of paper presented at the Seventh Biennial Conference on Carbon, to be submitted for publication.

[6]Ceramics Group; present address, IBM Corp., Lexington, Ky.

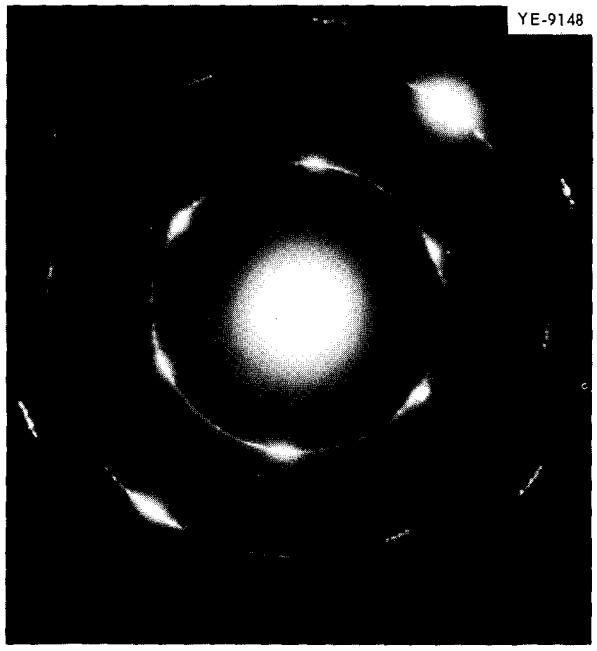

Fig. 4.5. Selected Area Electron Diffraction Pattern from the Area Shown in Fig. 4.4. Reduced 14%.

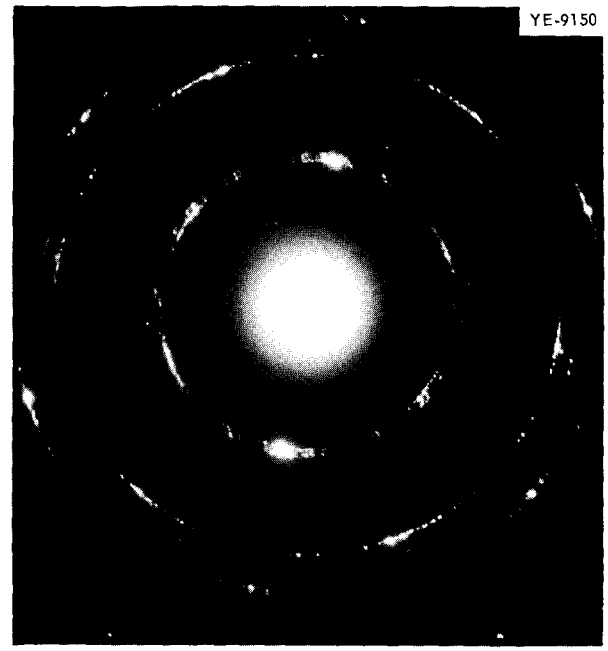

Fig. 4.7. Selected Area Electron Diffraction Pattern from the Area Shown in Fig. 4.6. Reduced 14%.

Fig. 4.6. Transmission Electron Micrograph of Graphite Flakes Extracted from the Diffusion Zone of a Uranium Carbide–Pyrolytic-Carbon Couple Held 100 hr at 2000°C. 37,500×. Reduced 55%.

patterns, but we are unable to say whether it contains any uranium. Most likely the area shown in Fig. 4.4 contains a continuous layer of material possessing the pyrolytic structure, with graphite platelets and uranium carbide particles distributed over it. Figures 4.6 and 4.7 show well-developed graphite platelets produced in some regions of the diffusion zone. Uncatalyzed formation of a similar structure would require a temperature above 2700°C.

EQUIPMENT DEVELOPMENT

C. K. H. DuBose T. M. Gayle[7]

It has become increasingly evident that an understanding of irradiation-induced effects on properties of materials can benefit greatly from electron microscope observations on the nature, distribution, and behavior of defect clusters. However, the normal techniques for microscopy must be modified since the materials for examination are

[7]Instrumentation and Controls Division.

highly radioactive. This means that very small specimens must be used, and they must be prepared with as little handling as possible.

To satisfy these requirements we have developed a simple semiremote technique. Specimens are cut, in a hot cell if necessary, to a thickness of about 0.1 mm and a maximum diameter of 3 mm. These are "dimpled" on both sides by an electrolytic jet technique to reduce the thickness of the center of the specimen to about 0.01 mm. Final polishing, until a hole forms in the prethinned area, is accomplished in a standard electropolishing cell in which breakthrough is detected by an extremely sensitive photocell device. Incident light is piped to the specimen and transmitted light is delivered to the photocell by a fiber optics system. This provides an intense light beam and also eliminates interference from thermal fluctuations of the polishing solution and radiation effects from the specimen. Activation of the photocell stops the polishing.

With this technique we can detect extremely small holes, which usually are surrounded by reasonably large areas transparent to electrons. The technique is extremely rapid compared to standard techniques using large foils; it does not require close attention of the operator and it generally yields usable samples.

5. Electronic Properties of Metals and Alloys

J. O. Betterton

We have continued transition-metal studies by low-temperature specific heats, galvanomagnetic properties, and Mössbauer effect. Additional laboratory equipment was put into operation and should serve us well in the future. For example, our low-temperature calorimeter now operates in fields to 40,000 gauss; this will permit much information to be obtained on superconductors. We have solved many of the problems of specimen purity by construction of a 10^{-10}- to 10^{-11}-torr zone refiner, with which we have prepared the especially pure single crystals needed for galvanomagnetic studies, and can also remove magnetic and other impurities from superconductors and superconducting alloys for more careful study of the role of impurities in superconductivity. We have put into operation a complete Mössbauer facility including a preparation laboratory and have started the construction of a helium cryostat and superconducting magnet for Mössbauer studies.

THE LOW-TEMPERATURE SPECIFIC HEATS[1] OF ZIRCONIUM ALLOYS

J. O. Betterton J. O. Scarbrough

The superconducting transition temperatures of Group IVA elements are increased in all known cases by addition of other transition metals to the right of them in the Periodic Table. We have studied this increase in transition temperature by measurement of the specific heats of zirconium-niobium alloys (0 to 5 at. % Nb) in the temperature range 1.5 to 4.5°K. Alloys were prepared with two levels of purity: cast alloys, with the sum of niobium and zirconium 99.95%, and alloys zone leveled in the high-vacuum apparatus, with the sum of niobium and zirconium 99.99%. Each was studied in two conditions of heat treatment, quenched (hexagonal solid solution) and annealed (hexagonal + second phase). Each material was measured at zero magnetic field and in one or two fields up to 40 kilogauss so that the properties of both the normal and the superconduction states could be inferred separately. Typical specific heat results of this type are illustrated in Figs. 5.1 and 5.2.

The upper curves of Figs. 5.1 and 5.2 represent the quenched condition of a pure alloy containing 2.3 at. % Nb and a less pure alloy containing 4 at. % Nb respectively. The superconducting transitions of these quenched alloys correspond to ideal bulk superconductivity in the sense that they quench with the application of a modest magnetic field, and most of the volume appears to transform, based on the size of the specific heat discontinuity. The temperature width of the transformation is considerably broadened in these alloys compared to pure-metal superconductors. A transition temperature T_c was based on the mean specific heat value between normal and superconducting states. The electronic specific heat coefficient γ and the Debye temperature θ_D for the normal state are obtained from the specific heats measured in a magnetic field. The variation of these coefficients with niobium content is shown in Fig. 5.3. By use of the theoretical expression[2,3]

$$T_c = 0.85\ \theta_D \exp\left(-1/NV_{BCS}\right)$$

and the expression $\gamma = 2\pi^2 k^2 N/3$, where k is Boltzmann's constant and N is the density of electronic states of one spin only, the interaction

[1]The term "specific heat" is used in this discussion to denote the heat capacity per gram-atom of metal or alloy.

[2]J. Bardeen, L. N. Cooper, and J. R. Schrieffer, *Phys. Rev.* **108**, 1175 (1957).

[3]Pierre Morel, *Phys. Chem. Solids* **10**, 277 (1959).

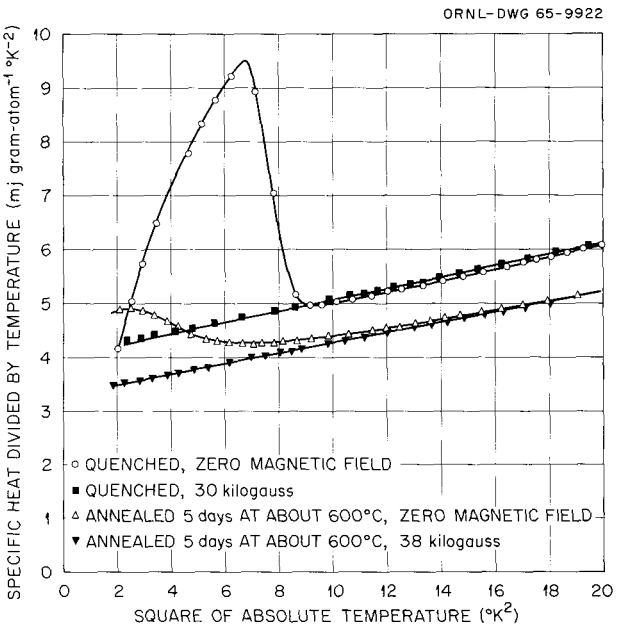

Fig. 5.1. Low-Temperature Specific Heat of Zone-Leveled Zr–2.3 at. % Nb.

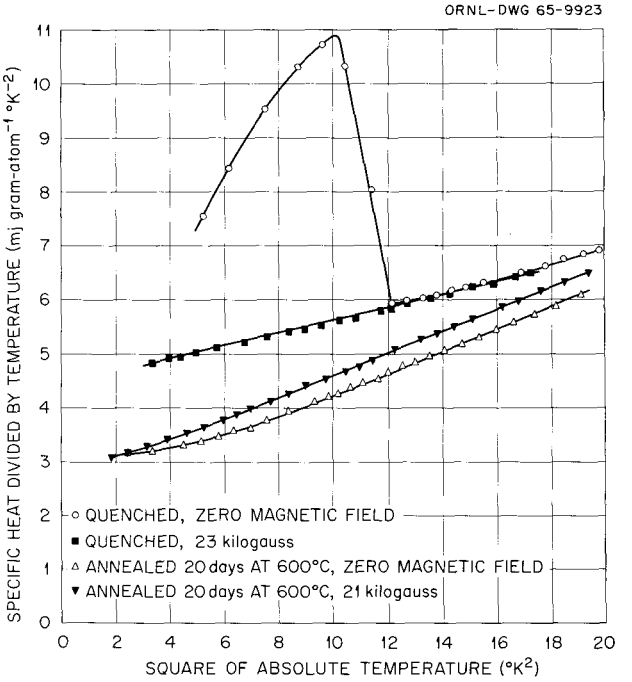

Fig. 5.2. Low-Temperature Specific Heat of Cast Zr–4 at. % Nb.

constant V_{BCS} has been evaluated and also plotted in Fig. 5.3.

The effect of the niobium is to increase N and T_c and to decrease θ_D of zirconium sharply. This occurs in such a manner that the interaction constant changes only little and the increase in T_c results from the changes in N and θ_D. Comparison of the larger effects on N and θ_D with niobium additions to zirconium with effects that had been observed from B-subgroup elements[4] or from scandium[5] shows that the zirconium-niobium alloys do not agree with the others when the properties are related to the average number of electrons per atom.

The change in minor impurities between the cast alloys and the zone-leveled alloys slightly changed the specific heats of the quenched alloys, as can be seen by comparison on Fig. 5.3 of the zone-leveled 2.3 at. % Nb alloy with the cast alloys. On the other hand, after the alloys were annealed at 600°C the specific heats of the less pure alloys differed from those of the pure alloys in more remarkable manner. The hexagonal solid solution forms a second phase, which in the pure alloys produces a long tail on the superconducting transition. This is illustrated by the lower curves for the alloy 2.3 at. % Nb on Fig. 5.1. The magnetic field quenches the superconductivity in this case.

With impurities such as Fe, Ni, Mn, and Cr in the cast alloys, the precipitate is much harder to quench. In the 4% Nb alloy shown on Fig. 5.2, the specific heats seem to show that about 30% of the volume of the sample is a second phase with a uniform transition temperature above 4.5°K. A magnetic field of 21 kilogauss did not quench this superconductivity. Since the second phase could not be seen in either optical microscopy or with x rays, an extension of the superconducting volume beyond the phase boundaries of this finely divided second phase may be indicated.

The following results illustrate the sensitivity of quenched zirconium-niobium alloys to low-temperature heat treatments. The alloy containing 3 at. % Nb and quenched from the cubic state had an electronic specific-heat coefficient $\gamma = 4.166$ mj gram-atom^{-1} °K^{-2}; annealing 2 hr at 120°C decreased this to 3.596 mj gram-atom^{-1} °K^{-2}. The Debye temperature was practically unchanged (263.5 to 264.1°K). The resistivity of the 5 at. % Nb alloy quenched from 1000°C was 25.03 μohm-cm at 4.2°K before annealing and only 22.10 μohm-cm

[4]G. D. Kneip, Jr., J. O. Betterton, and J. O. Scarbrough, *Phys. Rev.* 131, 2425 (1963).

[5]J. O. Betterton, Jr., and J. O. Scarbrough, *Metals and Ceramics Div. Ann. Progr. Rept. June 30, 1964*, ORNL-3670, p. 51.

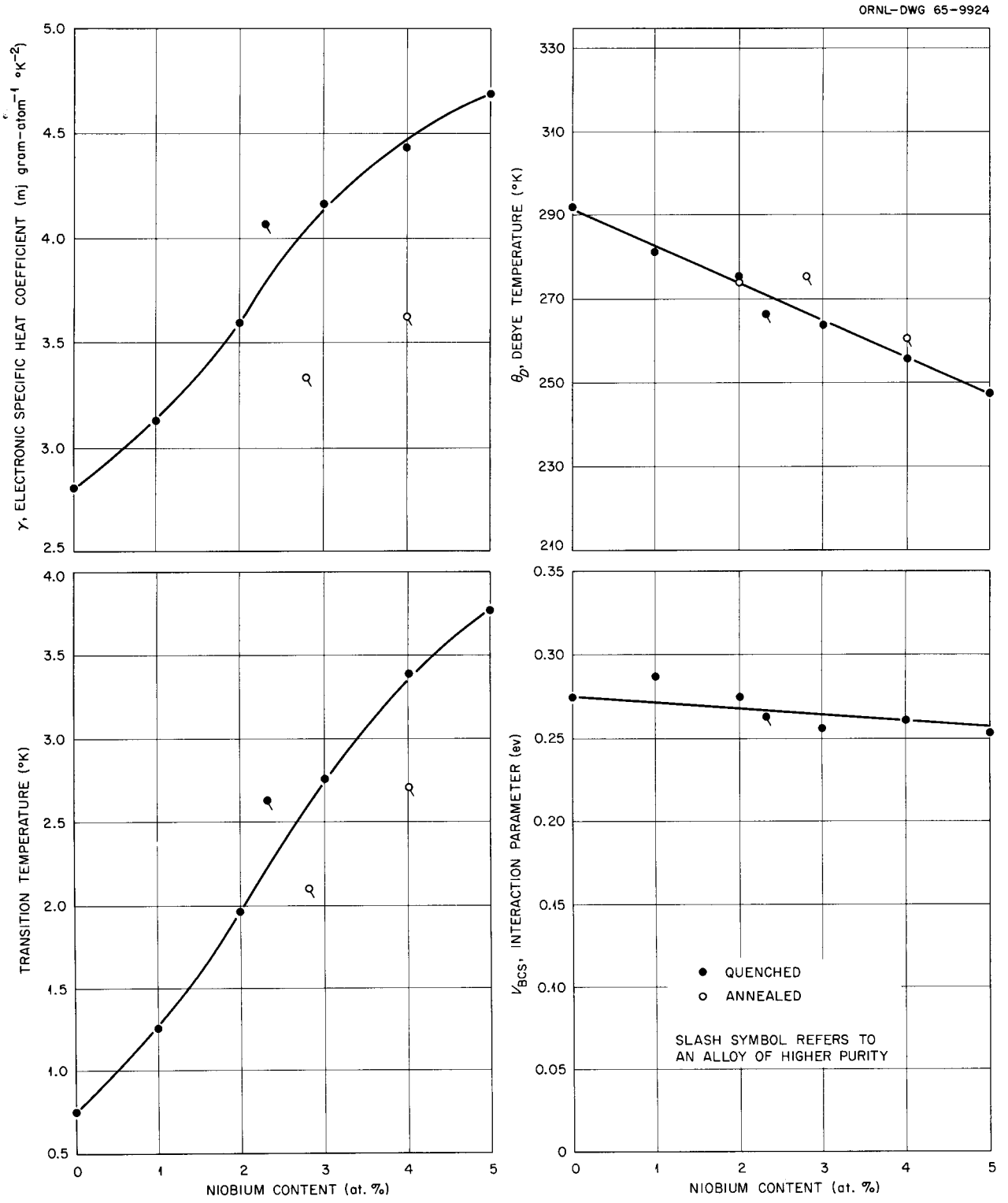

Fig. 5.3. Electronic Specific Heat Coefficient, Debye Temperature, Superconducting Transition Temperature, and the Interaction Constant as Functions of Niobium Content in Zirconium-Niobium Alloys.

after annealing 2 hr at 120°C. The decreases in electrical resistivity and in electronic specific heat were 12 and 14%, respectively, which we associate with fast precipitation reactions and depletion of niobium from the matrix phase.

Low-temperature specific heats were measured for dilute Zr-Mo, Zr-Re, and Zr-Ru alloys in the body-centered cubic structure retained after quenching. The alloys were cast, using 99.99% zone-refined zirconium. Superconductivity was observed in all of these alloys, as shown by the specific heats plotted in Fig. 5.4. The transitions are of the bulk type, which are quenched with external magnetic fields of 25 and 35 kilogauss, although the transition temperature width is still of the order of 0.5 to 1.0°K. An interesting point about these alloys is that the low-temperature specific-heat coefficients γ and θ_D, the transition temperature, and the interaction constant are all close to the values for hexagonal zirconium-niobium alloys with the same solute content. This is shown in Fig. 5.5, where the present values for Zr-Mo, Zr-Re, and Zr-Ru are plotted with the solid curves representing the values for zirconium-niobium alloys. Extrapolation to pure cubic zirconium gives values close to those for hexagonal zirconium. On this basis the allotropic transition in zirconium arises from differences in the specific heat of the two forms at elevated temperatures.

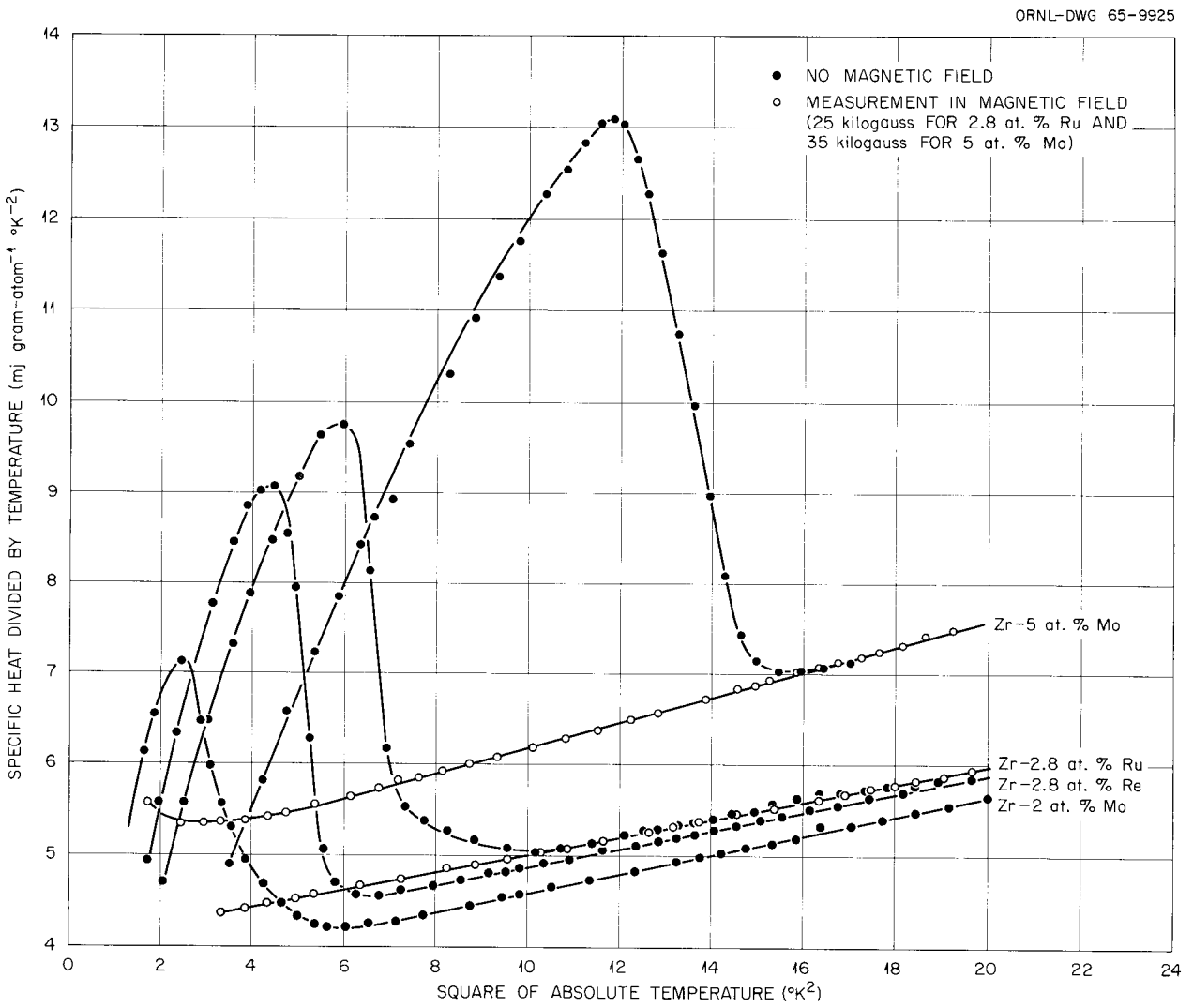

Fig. 5.4. Specific Heats of Zr-Mo, Zr-Re, and Zr-Ru Alloys.

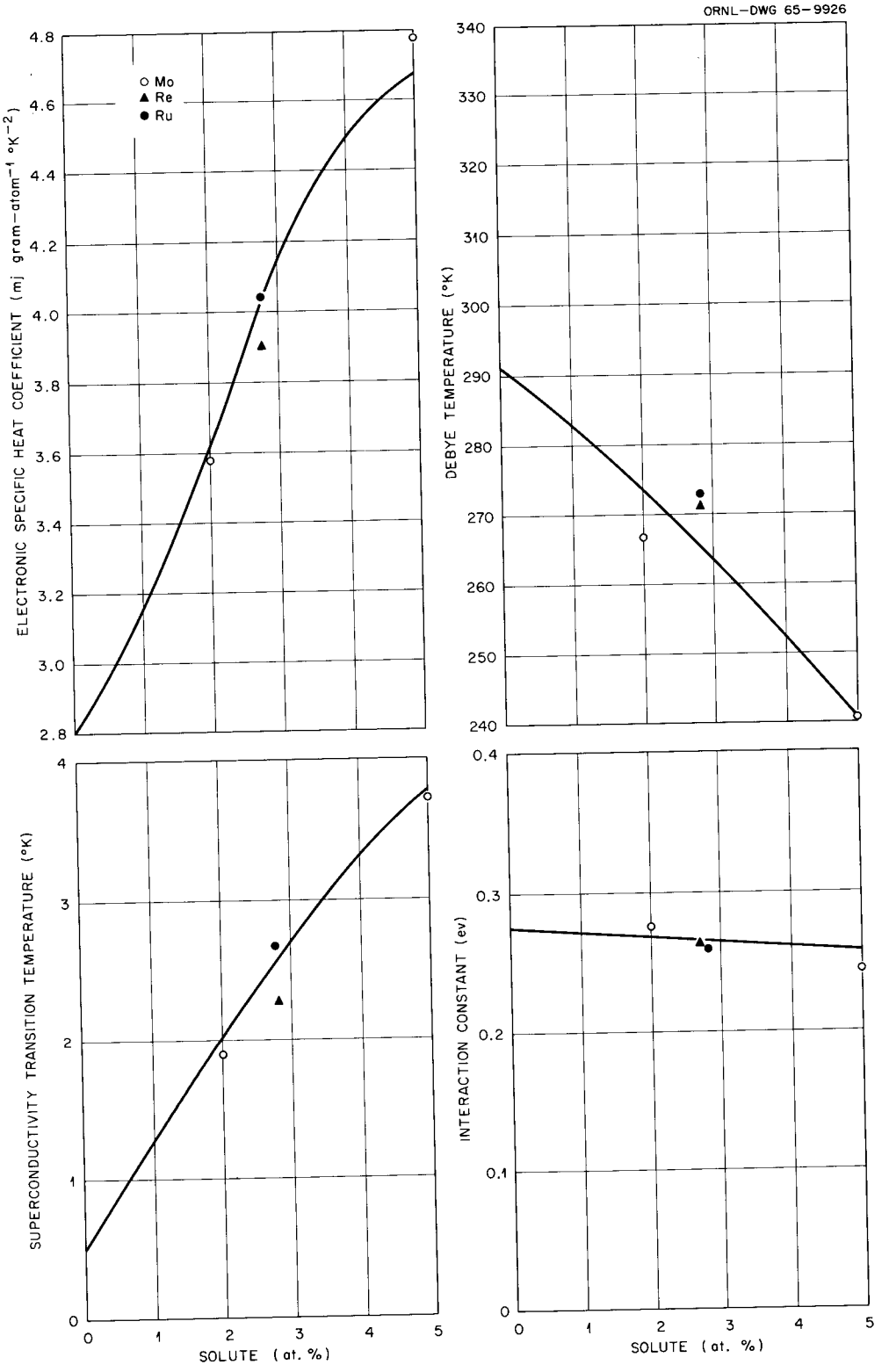

Fig. 5.5. Comparison of Low-Temperature Properties of Zr-Mo, Zr-Re, and Zr-Ru Cubic Alloys to Those of Hexagonal Zr-Nb (Solid Curve).

PURIFICATION OF ZIRCONIUM

D. S. Easton J. O. Betterton

Pure crystals of zirconium are required for galvanomagnetic studies in high magnetic fields. Hopes for obtaining this material were renewed when Wilson[6] showed that resistance ratios as high as 450 could be attained by zone refining in a 10^{-8}-torr vacuum. We built an apparatus to determine the purity obtainable at 10^{-10} torr by use of sputter-ion and titanium-sublimation pumping and to prepare crystals of Zr, Ti, Hf, V, Nb, and Ta for galvanomagnetic investigation.

The apparatus is shown in Fig. 5.6. It consists of independently movable specimen supports, movable electron gun, stainless steel bell jar, and sputter-ion and titanium-sublimation pumps. The elevators are coupled magnetically and driven by an automatic programmer, which also controls the electron-beam power supply for overnight operation. The whole system is baked overnight at 200 to 400°C and the walls are refrigerated during use. The experiment showed that it is not only feasible to use an ion-pumped zone refiner but highly desirable, since the system maintained satisfactory vacuums even with large gas loads resulting from zirconium starting material that contained 0.4 at. % H. The pressure of 10^{-10} torr in the system during the final passes of zone refining includes no back-streaming oil, and zirconium rods were made with resistance ratios in the range 600 to 850 after zoning and in range 400 to 700 after alpha annealing. The usual zone-refining profile is modified by evaporation, which occurs during vacuum zone refining in a system with refrigerated walls. For zirconium most condensable impurities have solidus-to-liquidus ratios less than unity, and their evaporation is enhanced by their enrichment in the liquid zone. Theoretically, a nearly constant and low impurity value would exist in the zoned region after a few passes. The only impurities in zirconium with solidus-to-liquidus ratios significantly greater than one are oxygen and nitrogen. That of hafnium is only slightly greater than unity, and analytical results for carbon show that its solidus-to-liquidus ratio is less than unity. When this ratio is greater than unity, as for oxygen and nitrogen, the liquid zone will be lower in concentration than the solid during zone refining and these impurities will be difficult to evaporate. Further, because oxygen, hydrogen, and nitrogen are noncondensable, they will be present around the liquid as the main residual gases in the vacuum system, in forms such as O_2, N_2, CO, CO_2, H_2O, and hydrocarbons. Contamination of the liquid from the gases is likely and will reduce the efficiency of the zone-refining process.

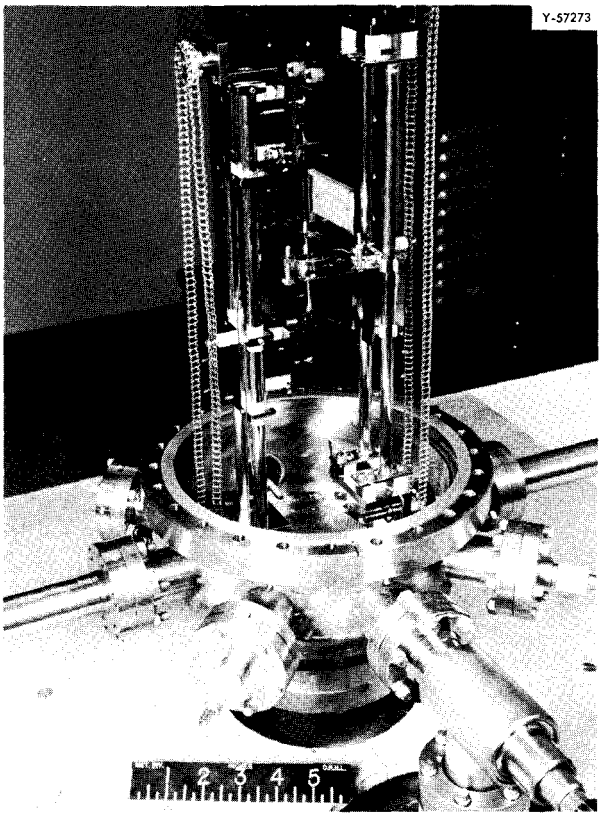

Fig. 5.6. Interior of Zone-Refining Apparatus.

The purity of the zirconium was increased from 99.95 to greater than 99.99% by zoning. The concentration of the major impurities before and after zoning is shown in Fig. 5.7. Only oxygen, carbon, and hafnium remain in any significant amounts. Hafnium is not separated by zoning, as expected from its solidus-to-liquidus ratio near unity, and it is not evaporated, in accord with its low vapor pressure. The carbon analysis showed an indication of zone refining, with carbon moving

[6] J. C. Wilson, *Metals and Ceramics Div. Ann. Progr. Rept. June 30, 1964*, ORNL-3670, pp. 155–59.

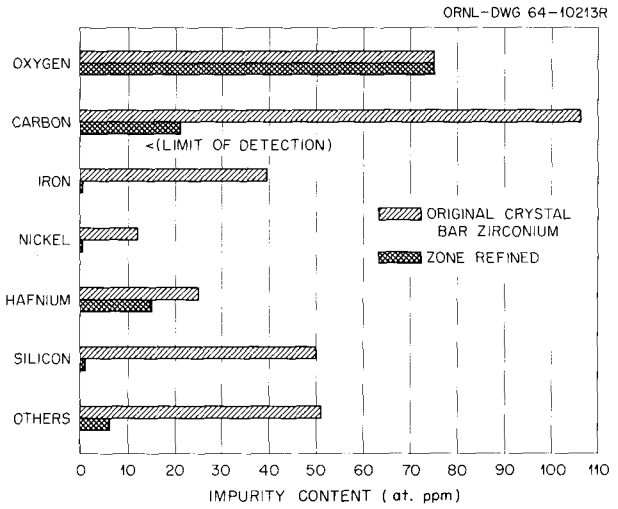

Fig. 5.7. Concentration of Impurities in Zirconium Before and After Zone Refining. Carbon was not detected in the zoned material; the bar shows the limit of detection.

towards the end that corresponds to solidus-to-liquidus ratio less than unity. This provides information on the zirconium-carbon phase diagram in support of depression of the zirconium melting temperature by carbon. Often carbon evaporates appreciably from the unmelted ends, indicating that carbon in the solid state may oxidize and be removed as CO and CO_2. The carbon was reduced in the central zoned sections to below the analytical detection limits. Although there is large scatter in the analysis, on the average the oxygen content is nearly constant throughout the zoned region and equal to the concentration present in the original material.

In the preparation of single crystals we have found that an imperfect crystal is often formed during slow solidification, that this crystal can be cooled successfully through the beta-to-alpha transformation in a sharp temperature gradient, and that it must be annealed at temperatures just under the allotropic transformation to reduce low-angle boundaries and distortions. Crystals as large as 3.5×0.4 cm produced in this manner had sharp Laue patterns. The above annealing procedure has always reduced the resistance ratio, and this had been attributed to contamination during the annealing. Recently, with 10^{-10}-torr vacuums we have continued to find the same reduction in ratios as with the earlier 10^{-8}-torr systems. Thus we conclude that not annealing contamination at 800°C but some other mechanism, such as collection or dispersion of oxygen from the low-angle boundaries and dislocations, reduces the ratio. Other impurities could also be involved, but only oxygen is present in large enough quantities to account for 25 to 50% reduction in the ratio. This work has shown that we must interpret resistance ratios carefully in zirconium, since for some conditions of annealing the ratios are no longer inversely proportional to impurity content.

GALVANOMAGNETIC PROPERTIES OF ZIRCONIUM

J. O. Betterton D. S. Easton

Galvanomagnetic properties of zirconium were measured with five different current directions at 4.2°K in transverse magnetic fields to 32 kilogauss. The results for each current direction, interpreted by means of Lifshitz theory,[7–9] showed that the zirconium Fermi surface is closed and compensated. Compensation is based on a near quadratic field dependence of the magnetoresistivity for all magnetic field directions. The closed surface is based on a near isotropy during magnetic field rotation.

The magnetoresistivity showed small minima whenever the magnetic field was normal to a direction in the basal plane, and this effect increased as the crystal axis approached the c axis. The theoretical work of Altmann and Bradley[10] shows that a narrow angle of open orbits is possible near the $\langle 10\bar{1}0 \rangle$ directions of the basal plane. The minima may be related to these orbits, and we are preparing new crystals with axes $\langle 0001 \rangle$, $\langle 10\bar{1}0 \rangle$, and $\langle 2\bar{1}\bar{1}0 \rangle$ to investigate this effect.

Each of the five zirconium crystals already studied had a Hall field with a very similar rosette pattern with the lobes alternating in sign. The Hall field is the odd component (upon magnetic field reversal) of the electric field perpendicular

[7] I. M. Lifshitz, M. Ia. Azbel′, and M. I. Kaganov, *Soviet Phys. JETP (English Transl.)* **4**, 41–54 (1957).

[8] I. M. Lifshitz and V. G. Peschanskii, *Soviet Phys. JETP (English Transl.)* **8**, 875–83 (1959).

[9] N. E. Alekseevskii *et al.*, *Soviety Phys. JETP (English Transl.)* **12**, 837–46 (1961).

[10] S. L. Altmann and C. J. Bradley, *Phys. Rev.* **135**, A1253 (1964); *Phys. Letters* **1**, 336 (1962).

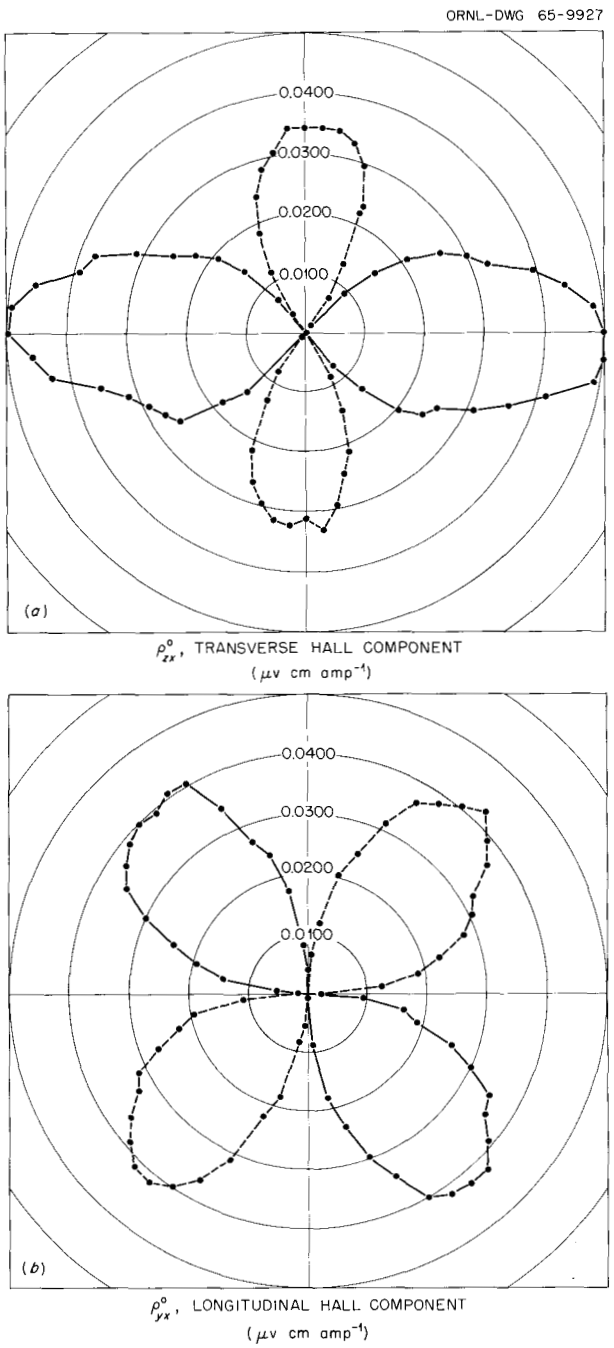

Fig. 5.8. Polar Diagrams Showing the Effect of Magnetic Field Direction on Hall Field Components of a Pure Zirconium Crystal at 4.2°K at 31 Kilogauss, and with Current in the Direction $\langle 3\bar{1}\bar{2}3\rangle$. (*a*) Transverse component, ρ^0_{yx}. (*b*) Longitudinal component, ρ^0_{zx}. The dashed lines represent negative values.

to the current. Both the ρ^0_{yx} and ρ^0_{zx} components, were equally large and alternated similarly in sign. These components are illustrated in Fig. 5.8 for a crystal with the axis $\langle 3\bar{1}\bar{2}3\rangle$. In contrast to a metal such as tungsten where the Hall electric field remains about 90° behind the magnetic field during rotation and only positive ρ^0_{yx} is observed, the behavior in zirconium can be best described by counter-rotation of a nearly constant Hall field vector and a magnetic field vector in the same plane. The alternation in sign is in agreement with both hole and electron surfaces in a compensated metal. The absence of any sharp variations in Hall field supports only closed sections of the Fermi surface for the crystals studied up to now.

The field dependences of the magnetoresistance and of the Hall field deviate from perfect quadratic and linear behavior respectively. This deviation is apparently not related to impurities, since it has not been changed by recent improvement in zirconium purity. Koehler's rule, on the other hand, is farily well obeyed with allowance for anisotropy due to current direction.

Fawcett[11] has pointed out that transition metals with even atomic number should have compensated galvanomagnetic behavior. The reason is the same as that for ordinary metals, in that the same numbers of electrons should be in partly filled upper bands as holes in unfilled lower bands. This argument is reasonable when the bands do not overlap too much in energy. In the transition metals of Groups IIIA to VIIA the electronic specific heat coefficient has minima[12] at even Groups IV and VI, and zirconium is thus in that part of the Periodic Table where the bands overlap little and the numbers of electrons and holes would be expected to be equal.

Longitudinal magnetoresistivity was measured for currents in the directions $\langle 15\bar{6}\bar{9}2\rangle$, $\langle 3\bar{1}\bar{2}3\rangle$, and $\langle 10\bar{1}1\rangle$ and was found to be about one-tenth the transverse magnetoresistivity. Variation of the longitudinal magnetoresistivity with orientation is related, by means of a complicated integral,[13] to the geometry of the Fermi surface

[11] E. Fawcett, *Advan. Phys.* **13**, 139 (1964).

[12] K. A. Gschnidner, Jr., *Solid State Phys.* **16**, 275 (1964).

[13] A. B. Pippard, "The Dynamics of Conduction Electrons," pp. 98–99 in *Low Temperature Physics Lectures at Les Houches Summer School of Theoretical Physics*, Gordon and Breach, New York, 1962.

and the variation of the mean free path over the Fermi surface. We hope that by systematic study some information will be obtained on the extent to which the mean free path varies with current direction.

OBSERVATION OF MÖSSBAUER EFFECT FOLLOWING COULOMB EXCITATION

Gordon Czjzek
Felix E. Obenshain[15]
Dietrich Seyboth[14,15]
J. L. C. Ford, Jr.[15]

The Mössbauer effect following Coulomb excitation has been observed with ^{61}Ni and ^{73}Ge. Both nuclides were excited by 25-Mev oxygen ions from the ORNL tandem Van de Graaff, and the same chamber was used to hold the target and absorber at liquid nitrogen temperature. Our discovery that the Mössbauer effect can be observed after Coulomb excitation greatly extends the number of metallurgical systems that can be studied by Mössbauer spectroscopy.

Nickel[16]

The target was a layer of nickel, enriched to 92% ^{61}Ni, electroplated on a copper plate. The absorber was a disk of natural nickel.

The observed Mössbauer spectrum was fitted with a theoretical curve (Fig. 5.9). The theoretical spectrum, both of emitter and absorber, consists of 12 lines; the folded spectrum consists of 35 lines. Each line is characterized by three parameters: position, maximum absorption, and width at half height. In fitting process, the following parameters were varied:

1. The position of the central line (determined by the isomer shift),
2. The distance between the lines (determined by the internal field),
3. The intensity of the central line,
4. The width of the central line.

The remaining 101 parameters were made dependent on these four parameters by theoretical relations. The resulting parameters are listed in Table 5.1 with the corresponding parameters from a fit to the Mössbauer spectrum obtained by Obenshain and Wegener[17] using the radioactive source

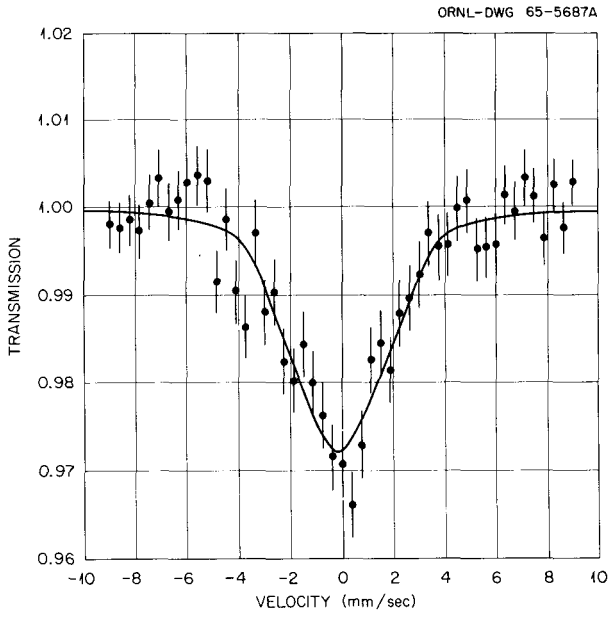

Fig. 5.9. Mössbauer Spectrum of ^{61}Ni Following Coulomb Excitation.

$$^{61}\mathrm{Co} \xrightarrow[99\ \mathrm{min}]{\beta^-} {}^{61}\mathrm{Ni}^* .$$

These results show that no isomer shift occurs; that is, the electronic surroundings of the Coulomb-excited nuclei are on the average the same as in the regular lattice. The internal field is on the average the same as in the undisturbed lattice. But the intensities of the individual lines are halved and their widths are doubled. The total absorption, defined by the total area under the absorption dip, is the same within the accuracy of the measurements.

From these results we conclude that the average Debye-Waller factor in our target does not differ by more than about 10% from that in an undisturbed nickel crystal. However, the Coulomb-excited nuclei in their final positions sample a wider

[14]Visitor from University of Erlangen, Germany.

[15]Physics Division.

[16]Reported in part by D. Seyboth, F. E. Obenshain, and G. Czjzek, *Phys. Rev. Letters* **14**, 954 (1965).

[17]F. E. Obenshain and H. Wegener, *Phys. Rev.* **121**, 1344 (1961).

Table 5.1. Parameters of the Mössbauer Spectra of ^{61}Ni Obtained with Coulomb Excitation and with a Radioactive Source

	Coulomb Excitation	Radioactive Source[a]
Isomer shift, mm/sec	0.12 ± 0.12	0.02 ± 0.03
Internal field, kilogauss	75 ± 6	72 ± 5
Intensity of central line, %	0.701 ± 0.035	1.466 ± 0.027
Width of central line, mm/sec	1.48 ± 0.66	0.76 ± 0.05
Total area, % mm sec^{-1}	14.8 ± 2.4	16.0 ± 1.0

[a]F. E. Obenshain and H. Wegener, *Phys. Rev.* **121**, 1344 (1961).

distribution of magnetic fields, electronic charge densities, electric field gradients, and binding energies than do nuclei in an undamaged nickel crystal.

Germanium

The Mössbauer effect in ^{73}Ge has not been observed previously. This isotope is not accessible by the conventional method, since the only level with a high enough transition probability to the ground state, the one at 67.0 kev, is not populated by radioactive decay.

The target was a layer of germanium, enriched to 84% ^{73}Ge and evaporated on a nickel plate. The absorber was put together from pieces cut parallel to a (110) plane from a germanium single crystal.

The Mössbauer spectrum measured with 67.0-kev gamma rays showed a small absorption dip centered at zero velocity. This dip was fitted with a single line of Lorentz shape. Figure 5.10 shows the measured spectrum with the fitted curve. The parameters of the fitted line are:

1. position 0.11 ± 0.14 mm/sec,
2. maximum absorption 0.64 ± 0.04%,
3. width at half a maximum 4.4 ± 0.6 mm/sec.

From these data, we can conclude that the isomer shift is zero within the accuracy of the measurement. Also, from the maximum absorption a crude estimate of the recoilless fraction f is possible. From the Debye model and an average Debye temperature of 360°K (values given in the literature vary between 350 and 380°K), the value $f = 0.12$ is expected. If we assume that this is

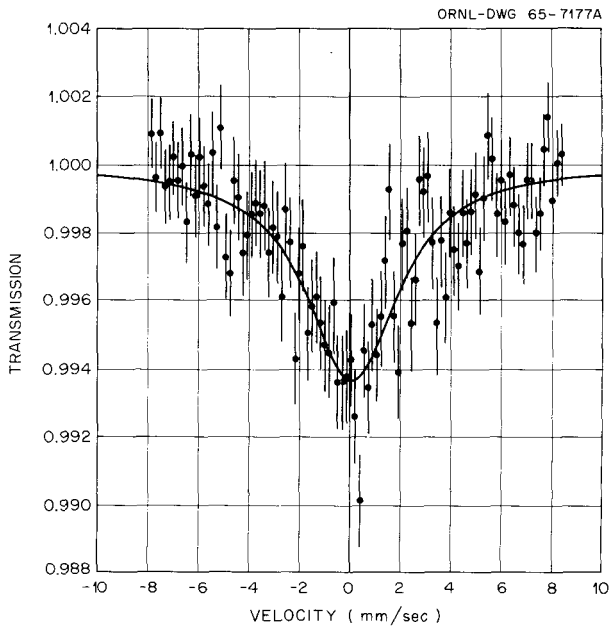

Fig. 5.10. Mössbauer Spectrum of ^{73}Ge Following Coulomb Excitation.

actually the recoilless fraction in the absorber, the f value of the target can be calculated to be $f \cong 0.01$. Three interpretations of this low apparent f value are possible. First, many of the Coulomb-excited nuclei could end in a position with a weak binding energy. This would mean that the average effective Debye temperature of these atoms would be only about 220°K. Another explanation would be that the heat generated in the slowing-down process of the Coulomb-excited nuclei cannot dissipate fast enough, and that the effective temperature at the emitting nucleus is

higher than 80°K. With θ_D as given for germanium and the estimated f value we obtain $T_{eff} \cong 250°K$. The third possibility is that the observed line originates only from those nuclei that find a final position at a regular lattice site, and that a large fraction of the nuclei comes to rest with a wide distribution of electronic densities and field gradients, leading to a smeared-out spectrum that could not be observed.

The width of the line is greater by a factor (1.8 ± 0.3) than the width expected from the mean lifetime $\tau = (2.33 \pm 0.20) \cdot 10^{-9}$ sec of the excited state. If the f value calculated from the Debye temperature of the absorber is correct, this broadening is due to the thickness of the absorber.

These results and conclusions can be considered as only preliminary. More experimental work is necessary to establish with certainty the f values of target and absorber. But the results show that important information on the effects of radiation damage in germanium can be obtained by this method.

6. Physical Ceramic Studies

C. S. Yust C. S. Morgan

Ceramic materials are potentially useful for applications at very high temperatures, but generally they are not considered for structural members because of poor mechanical properties. A better understanding of the factors controlling the strength and plasticity of ceramics may provide information from which the mechanical behavior of ceramics may be optimized. For this reason, the deformation mechanism in thorium dioxide, the highest melting refractory oxide, is being carefully investigated. We have thus far studied the creep behavior and compressive strength properties of thoria. We are embarking on a study of the effects of impurity additions to thoria and have some preliminary results on these effects. Ultimately, this study will be broadened to include other variables, such as the influence of atmosphere and stoichiometry. Additional studies on the kinds of defects produced by various treatments of fluorite-type materials are being initiated.

CREEP OF THORIA

C. S. Yust L. E. Poteat[1]

Creep in thoria was studied in specimens prepared from high-purity thoria powder. Solid cylinders were formed by isostatic pressing at 35,000 psi and firing in air at 1800°C for 2 hr and had densities of 97.5% of theoretical and an average grain diameter of approximately 10 μ. The specimens were tested in compression by application of a constant load in the range of 4000 to 11,000 psi at temperatures from 1400 to 1800°C.

Results of the creep-rate measurements are summarized in Fig. 6.1. An activation energy calculated for the process from these data is 112 ± 7 kcal/mole.

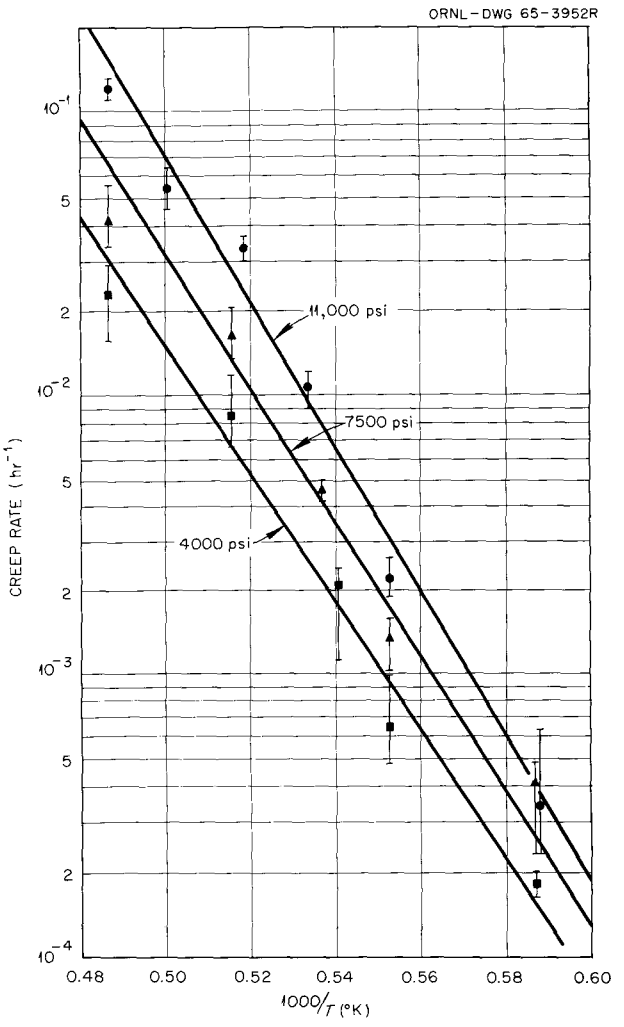

Fig. 6.1. Creep Rate of Thoria.

[1]Summer Research Participant in 1963 and 1964 from North Carolina State University.

The microstructure after deformation reveals that intergranular void formation and grain-boundary shearing are associated with creep deformation. Figure 6.2 depicts a specimen deformed 8.3% in compression and shows the size and distribution of intergranular voids at this stage of compression. Figure 6.3 presents evidence of grain-boundary shearing, indicated by displacement of the scratch across grain boundaries, in a specimen deformed 4.5%.

Deformation in polycrystalline single-phase ceramics involves one or more of the following mechanisms: (1) diffusional processes, (2) slip within grain lattices, and (3) grain-boundary shearing. Processes (2) and (3) are intimately related, since grain-boundary shearing without grain deformation is not possible. In addition, the kinetics of processes (2) and (3) may be identical to those of purely diffusional processes, since dislocation motion during steady-state creep is determined by dislocation climb – a diffusional process. Differentiation of the three types of mechanisms that may be responsible for creep in thoria is therefore not easily accomplished, if at all possible.

If a polycrystalline body is to deform without the creation of intergranular voids, each grain in the aggregate must be capable of deforming in a general manner. The analysis of the principal slip system in the fluorite lattice structure by Groves and Kelley[2] indicates that sufficient independent slip systems to permit general shape change are not present in thoria, and thus the formation of intergranular voids would be explained. However, secondary slip systems might become operative under the influence of stresses encountered in the deforming polycrystal, and the existence of such systems in the fluorite structure has been reported.[2]

[2]G. W. Groves and A. Kelley, *Phil. Mag.* 8(85), 877–87 (1963).

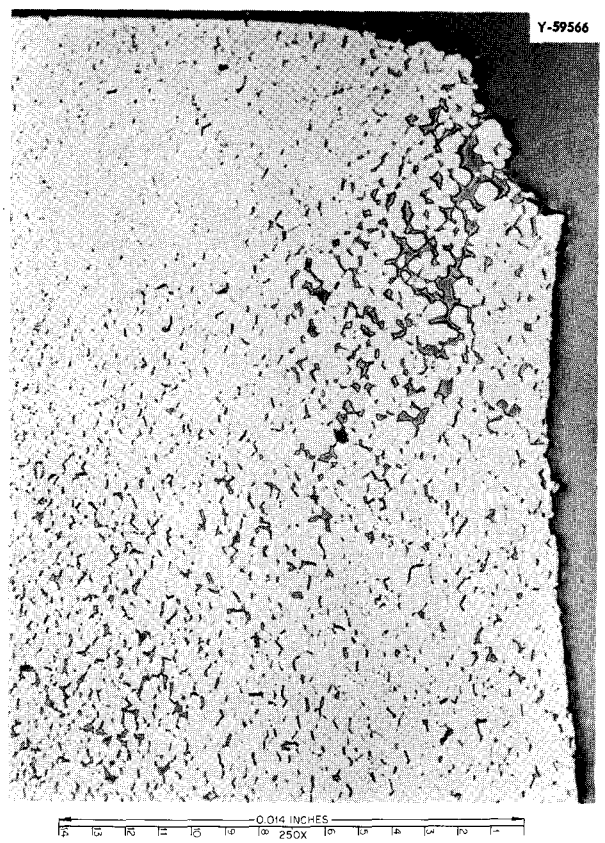

Fig. 6.2. Intergranular Voids in a Thoria Creep Specimen Compressed 162 hr at 1430°C and 11,000 psi. Compression axis is vertical and specimen is unetched. Reduced 32%.

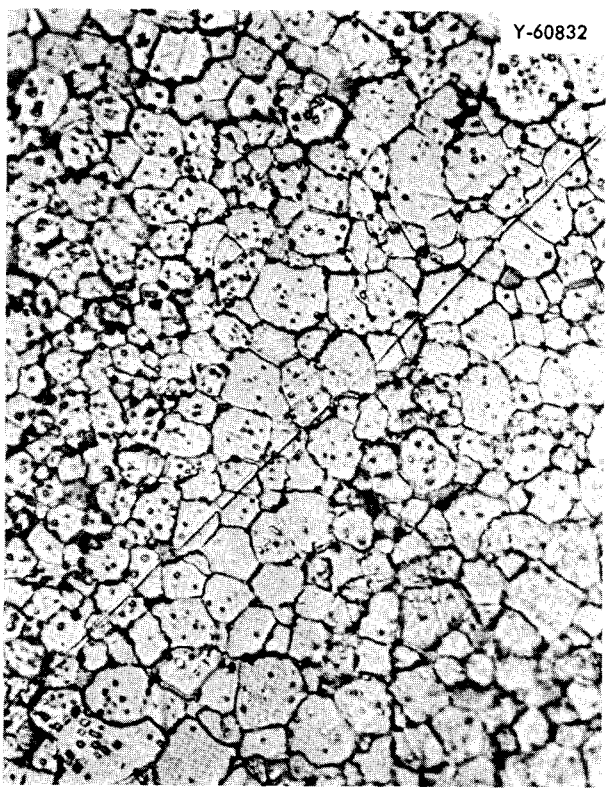

Fig. 6.3. Grain-Boundary Shear in Thoria Is Illustrated by Displacement of Scratch on a Polished Surface of Compression Creep Specimen. The specimen was compressed 35 hr at 1535°C and 7500 psi.

If sufficient independent slip systems for general deformation are available, an alternative mechanism for intergranular void formation might be extensive local shear in grain-boundary regions. The extent of shear in a boundary varies with the orientation of the boundary; hence, the junction of boundaries may be the site of very high hydrostatic tensile stress, which may cause cracks at grain-boundary junctions. The pileup of dislocations at a grain boundary is also a potential source of grain-boundary voids. The application of shear stress to boundaries may result in the application of tensile stresses to boundary jogs in such a manner that the jogs open into boundary voids.

Comparison of the thoria creep data with results for UO_2 is appropriate, since these two materials have the same lattice structure. Creep in bending of stoichiometric and nonstoichiometric UO_2 has been reported by Armstrong and Irvine.[3] For stoichiometric UO_2 they report an activation energy of 91 ± 8 kcal/mole, which agrees well with the value reported here for thoria. They also report the appearance of intergranular voids, but the nonstoichiometric UO_2 showed a greatly lessened tendency to form intergranular voids. Scott, Hall, and Williams[4] have reported that the excess oxygen in UO_2 increases the plasticity of this material. Since the addition of excess oxygen to UO_2 diminishes intergranular void creation in creeping UO_2, lack of sufficient lattice plasticity is probably a major factor in the creation of intergranular voids in creeping thoria.

EFFECT OF IMPURITY ADDITIONS ON THORIA CREEP

C. S. Yust

We are evaluating the effect of impurity additions on the creep rate of thoria and on the creep mechanism. At present, two additives (calcium oxide and aluminum oxide) are being investigated. The calcium oxide forms a complete solid solution with thorium dioxide and, due to valency differences, results in the formation of an anion-deficient structure. Preliminary measurements indicate that the creep rate of these specimens is greater than that of pure thoria. The surface of these thoria creep specimens appears markedly different from that of pure thoria, although the significance of this observation is not yet understood.

Additions of alumina to thoria result in the formation of a mixture of thoria and alumina crystallites. Specimens prepared from mechanical mixtures of the two powders had regions of pure thoria distributed through a lattice of mixed alumina and thoria grains. The grain size in the pure thoria areas was about 10 μ, while in the mixed-grain region the presence of the alumina prevented thoria grain growth and kept the grain size to about 2 to 3 μ. The creep rate of this material was significantly lower than that of pure thoria. The intergranular cracking observed in pure thoria was evident in the pure thoria regions of the specimen but not in the mixed crystal regions. The study of creep in alumina-containing thoria will be continued on specimens fabricated from coprecipitated alumina and thoria powders, which should yield a more homogeneous specimen and allow the effects of microstructure to be clarified.

COMPRESSIVE CREEP OF THORIUM OXIDE[5]

C. S. Morgan L. L. Hall

Compressive creep tests at elevated temperatures have been carried out on polycrystalline thoria and thoria-calcia specimens. At 1465°C a stress of 8000 psi caused appreciable long-term creep in ThO_2 bushings. At the same temperature, specimens that contained small quantities of calcium oxide deformed initially at an order of magnitude lower stress. The creep rate of the calcia-containing material decreased steadily with time, and after several hundred hours was about the same as that of "pure" ThO_2 specimens. Metallographic examination of the specimens after creep test revealed evidence of polygonization in ThO_2 specimens and grain growth in ThO_2-CaO specimens.

[3] W. M. Armstrong and W. R. Irvine, *J. Nucl. Mater.* 7(2), 133–41 (1962); *J. Nucl. Mater.* 9(2), 121–27 (1963).

[4] R. Scott, A. R. Hall, and J. Williams, *J. Nucl. Mater.* 1, 39–48 (1959).

[5] Abstract of paper submitted for publication in *Transactions of the British Ceramic Society.*

COMPRESSIVE STRENGTH OF THORIA

C. S. Yust L. E. Poteat[1]

The compressive strength of thoria at temperatures from 1100 to 1900°C was determined on specimens prepared from high-purity thoria powder. Solid cylinders were formed by isostatic pressing at 35,000 psi and firing in air at 1800°C for 2 hr and had densities of 97.5% of theoretical and an average grain diameter of approximately 10 μ. The creep results indicate that the compressive strength of thoria is substantially greater than that reported in current literature; hence, reevaluation of the compressive strength of thoria as well as study of the deformation mechanism of compressive failure of thoria is desirable. The results of the compressive strength tests are presented in Fig. 6.4 and are compared with recently published[6] compressive strength data for thoria. The decrease of strength with temperature increase is linear in the range 1100 to 1500°C. Above 1500°C the strength decreases with increasing temperature at a significantly lower rate. This change in slope of the strength-vs-temperature curve is associated with a macroscopic change in the deformation mode from brittle to plastic. Figure 6.5 depicts the

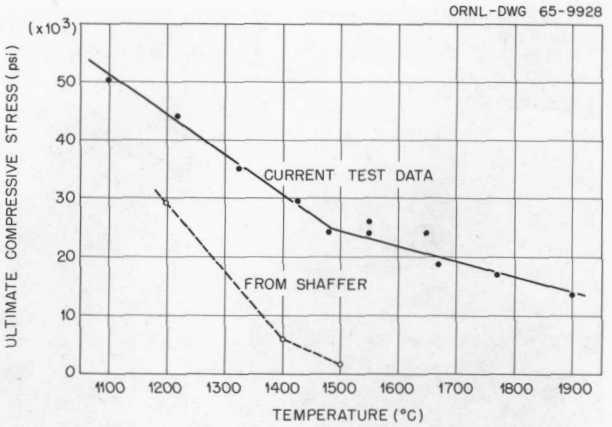

Fig. 6.4. Variation of the Compressive Strength of Thoria with Temperature.

[6]P. T. B. Shaffer, *Plenum Press Handbooks of High-Temperature Materials, No. 1, Materials Index*, p. 360, Plenum, New York, 1964.

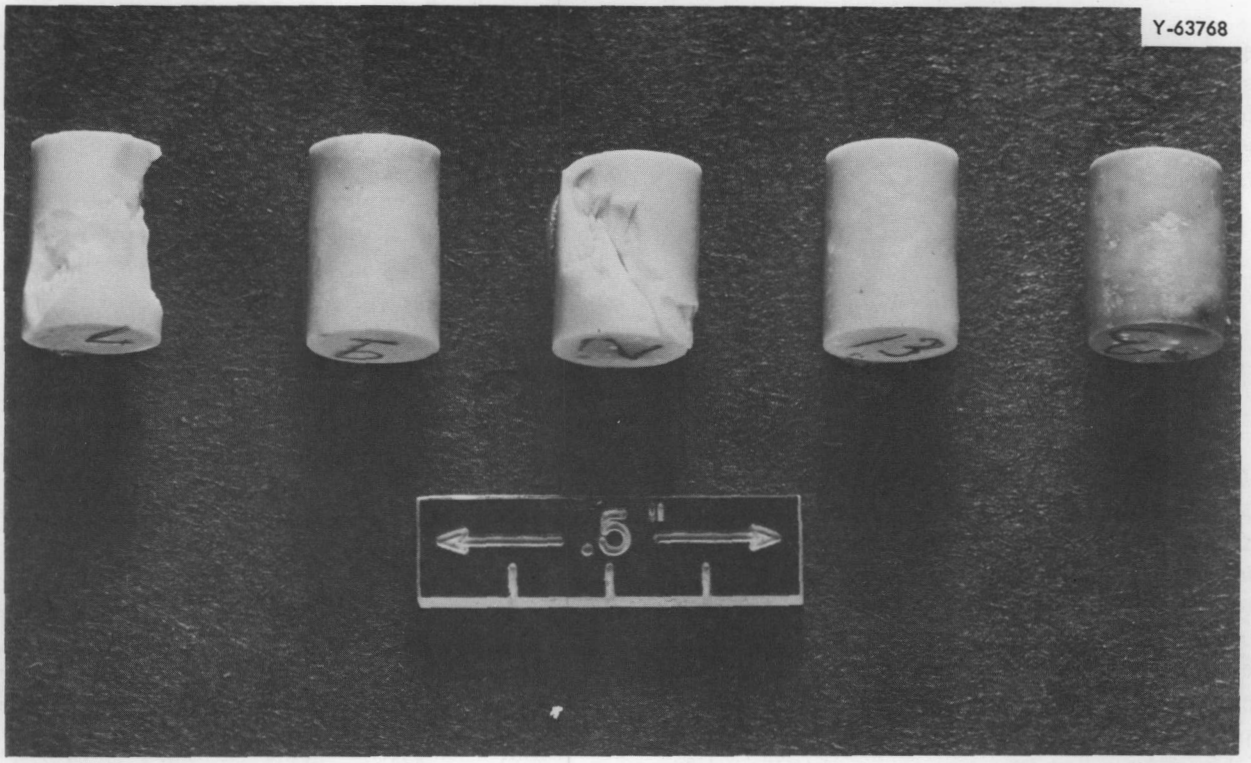

Fig. 6.5. Thoria Compression Specimens Deformed at 0.05/min at Temperatures of (from Left to Right) 1100, 1325, 1650, 1770, and 1900°C.

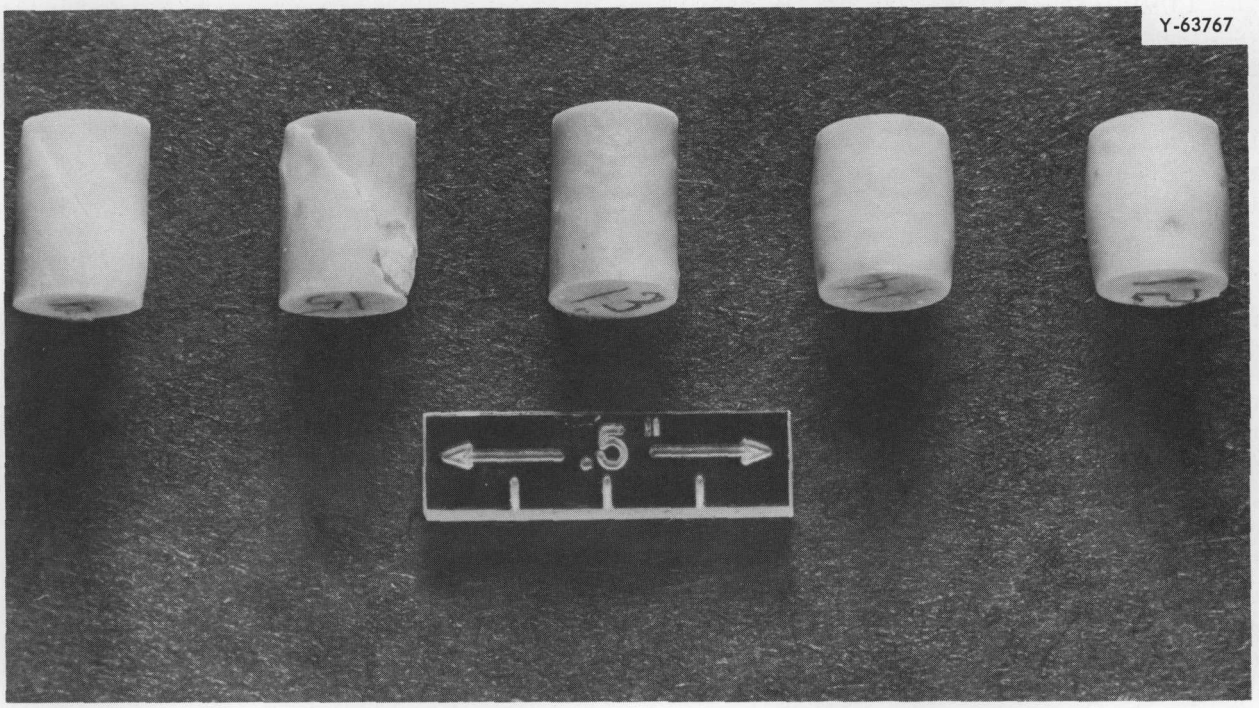

Fig. 6.6. Thoria Compression Specimens Deformed at 1770°C at Strain Rates of (from Left to Right) 0.5, 0.2, 0.05, 0.02, and 0.005/min.

appearance of a series of specimens that demonstrate the change in fracture mode as the temperature is increased. The effect on the specimens of variation of strain rate at a constant temperature is shown in Fig. 6.6.

MATERIAL TRANSPORT IN SINTERING[7]

C. S. Morgan C. J. McHargue
C. S. Yust

Investigation of the densification kinetics of ThO_2 powder compacts containing varying amounts of coprecipitated CaO indicates that the initial densification, as the temperature is being raised, is primarily by dislocation movement, as is thought to be the case with pure ThO_2. The ThO_2-CaO compacts sinter more readily than pure ThO_2 compacts. The extent to which dislocation transport of material continues after attainment of isothermal conditions is considered. Reasons are advanced to show that model study results indicating volume diffusion transport of material do not rule out a substantial dislocation contribution.

INERT-GAS BUBBLES IN NEUTRON-IRRADIATED MAGNESIUM OXIDE[8]

C. S. Morgan D. H. Bowen[9]

In magnesium oxide irradiated with neutrons at 150, 600, and 1000°C, rectilinear bubbles have been observed by transmission electron microscopy for doses greater than 10^{20} neutrons/cm^2 (>1 Mev) and for annealing temperatures above 1500°C. The bubbles had {100} surfaces and sides ranging from 40 to 400 A, and measurements of the residual growth of the crystals after annealing have been correlated with the volume occupied by the bubbles.

Electron-microscope and gas-release studies indicate that the bubbles form primarily by vacancy condensation and subsequently act as sinks for the diffusion of neon and helium produced by the transmutation of magnesium and oxygen. We sug-

[7]Abstract of paper accepted for publication in *Transactions of the British Ceramic Society*.

[8]Abstract of paper submitted to *Philosophical Magazine*. Work done at Metallurgy Division, AERE, Harwell, while C. S. Morgan was on attachment from ORNL.

[9]Metallurgy Division, AERE, Harwell.

gest that mechanical release of these gases when the crystals are crushed at room temperature can take place by two processes: the intersection of bubbles by cleavage cracks, and pipe diffusion along irradiation-induced dislocations.

In a crystal irradiated at 1000°C, large precipitates were formed that, on annealing, dissolved, leaving behind bubbles up to 2000 A in size and having a variety of crystallographic shapes.

7. Physical Properties

D. L. McElroy

We are trying to understand heat transport in solids by analysis of careful measurements of physical properties of selected materials over a broad temperature range. Eventually we hope to predict the thermal conductivity of solids either from first principles or from model approximations that use easily measured properties. So far our approach has been to measure as accurately as possible a series of related physical properties on the same sample or on a group of samples. We now have a capacity to measure the temperature dependence of the following related physical properties: thermal conductivity, electrical resistivity, thermoelectric power, specific heat, and thermal radiative properties.

Accurate physical property measurements are sometimes quite elusive, due to equipment idiosyncrasies and temperature measurement difficulties. These difficulties may be partially soluble; however, their detection requires constant surveillance and intercomparison of several methods of measuring the same property. Once we have obtained satisfactory measurements, they are used to separate the total thermal conductivity into parts, each dependent on a particular heat-transport mechanism. The behavior of the individual parts is examined theoretically to reveal the influence on the scattering mechanism of such variables as temperature, impurity concentration, defect structure, and other selected changes.

THERMAL CONDUCTIVITY OF INCONEL 702

J. P. Moore W. P. Murray[1]
W. Fulkerson

The thermal conductivity of Inconel 702 was measured[2] in the radial heat flow apparatus over the range 50 to 930°C. Although the alloy is subject to at least two complex reactions that affect the thermal conductivity, age-hardening and "K-state" formation, the measurements of three laboratories, ORNL, National Research Council (Canada),[3] and National Bureau of Standards,[4] agree to within ±2% and to within ±1% for the same structural state in the alloy, as shown in Fig. 7.1. The thermal conductivity of the solution-

[1]Co-op student, University of Cincinnati.

[2]The Inconel 702 specimen was supplied by the National Bureau of Standards as part of its attempt to find a suitable standard in the thermal conductivity range 0.1 to 0.5 w cm^{-1} $°C^{-1}$.

[3]M. J. Laubitz and K. D. Cotman, *Can. J. Phys.* **42**, 131–52 (1964).

[4]D. R. Flynn and H. E. Robinson, "The National Bureau of Standards High Temperature Absolute Cut-Bar Apparatus," pp. 353–90 in the *Proceedings of the 3rd Conference on Thermal Conductivity, Gatlinburg, Tennessee, October 16–18, 1963* (limited distribution).

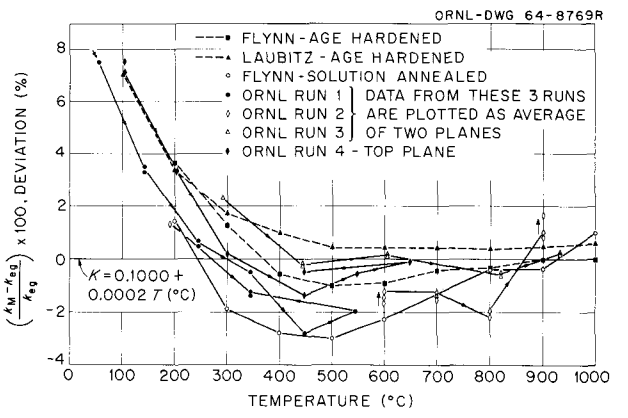

Fig. 7.1. Percentage Deviation from the Indicated Equation of the Thermal Conductivity of Inconel 702 in the Age-Hardened and Solution-Annealed Conditions.

annealed alloy is approximately 2% lower than that of the aged alloy. We are measuring other properties of Inconel 702 to study the effects of these conditions on the electron and phonon contributions.[5]

This remarkable measurement agreement has precipitated the need for a long-range coordinated thermal conductivity program among several laboratories that have the capability and desire for making precise measurements. As a guide for selecting materials for this study we have used available data for all the solid elements and several theoretical formulas to calculate the lattice portion of the thermal conductivity as a function of temperature. These calculations take into account phonon-phonon and phonon-electron mechanisms to give realistic order-of-magnitude results for temperatures above the Debye characteristic temperature.

PHYSICAL PROPERTIES OF IRON

J. P. Moore W. Fulkerson
T. G. Kollie

The effects of temperature, purity, magnetic state, and crystal structure on the thermal conductivity, electrical resistivity, and Seebeck coefficient of iron were obtained from measurements on Armco iron (99.5% pure, $\rho_{300}/\rho_{4.2} = 11.0$) and a high-purity iron (99.95% pure, $\rho_{300}/\rho_{4.2} = 26.2$). The most probable determinate errors of the measurements were: thermal conductivity ±1.5%, electrical resistivity ±0.1%, and Seebeck coefficient ±0.8%, with slightly larger absolute errors. Details and interpretation of this work are reported elsewhere.[6] One useful result is that the thermal conductivity of iron can be calculated to ±1.5% between 0 and 900°C from simple electrical-resistivity measurements, and the lattice portion of the thermal conductivity determined in this study.

The specific heat of iron was determined in a novel extension of the total hemispherical emittance apparatus.[7] The circuit for the new technique is shown in Fig. 7.2, and allows controlled heating of an instrumented rod contained in a constant-temperature black-body vacuum chamber. Emittance and electrical resistivity data were obtained with the specimen at a constant temperature, the specimen power was then increased, and a high-speed digital voltmeter (Millisadic) recorded the specimen power and temperature changes as a function of time. A specific heat run required about 5 sec; the Millisadic records 350 readings per second. The data collected in a run were decoded with a digital computer to provide specific heat values as a function of temperature. The results on iron were reproducible to ±0.5% to 850°C and are within ±1% of results from several other studies.[8–11] Our values for the specific heat of iron show the Curie phenomenon to be a second-order transition, as illustrated by the discontinuity in Fig. 7.3.

PHYSICAL PROPERTIES OF TUNGSTEN

J. P. Moore W. Fulkerson
R. S. Graves

Advanced fabrication techniques allowed us to obtain a fine grained relatively pure tungsten ($\rho_{300°K}/\rho_{4°K} = 35$) of 99.8% theoretical density for use in apparatuses requiring large samples. We measured thermal conductivity (50 to 1000°C, in the radial heat flow apparatus), thermoelectric power (to 1000°C in the radial heat flow apparatus;

[5]Modified abstract, J. P. Moore and W. P. Murray, "The Thermal Conductivity of Inconel 702," *Proceedings of Fourth Conference on Thermal Conductivity, San Francisco, California, October 13–16, 1964* (limited distribution).

[6]J. P. Moore, W. Fulkerson, T. G. Kollie, and D. L. McElroy, *Comparison of the Thermal Conductivity, Electrical Resistivity, and Seebeck Coefficient of a High-Purity Iron and an Armco Iron to 1000°C* (journal article in preparation).

[7]This work is reported in more detail by T. G. Kollie, *The Development of a Pulse Heating Calorimeter Technique for Measuring the Specific Heat of Electrical Conductors and Its Application to Pure Iron from 100 to 1200°C*, M. S. thesis, University of Tennessee, August 1965; ORNL-TM-1178.

[8]D. L. McElroy, *Calorimetry of High Purity Iron and Steels*, unpublished Ph. D. thesis, the University of Tennessee, 1957.

[9]D. C. Wallace, P. H. Sidles, and G. C. Danielson, *J. Appl. Phys.* **31**, 168–76 (1960).

[10]P. R. Pallister, *J. Iron Steel Inst. (London)* **161**, 87–90 (1949).

[11]R. Hultgren *et al.*, *Selected Values of Thermodynamic Properties of Metals and Alloys*, Wiley, New York, 1963.

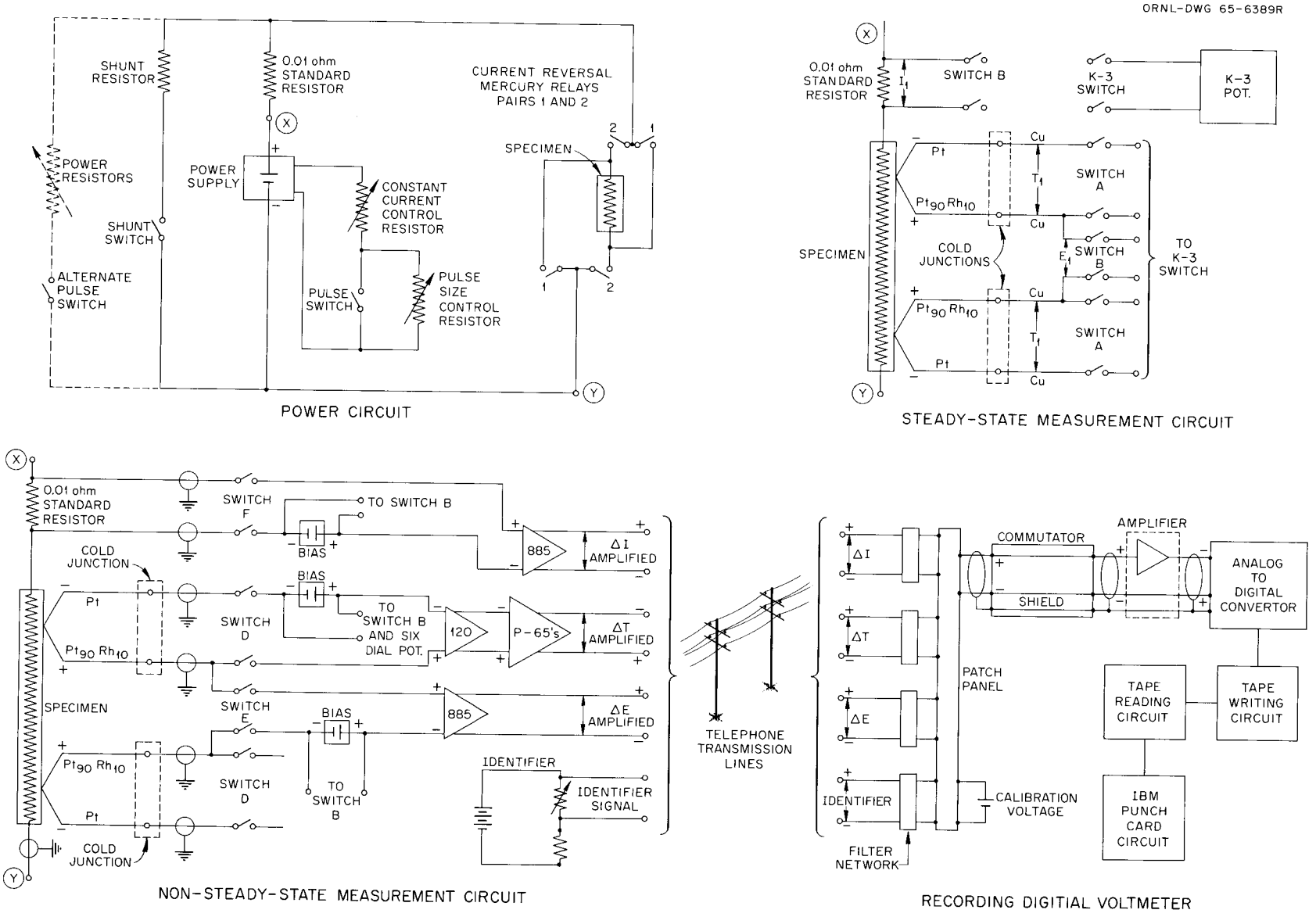

Fig. 7.2. Schematic Representation of the Circuit for Specific Heat Measurement by Pulse Heating.

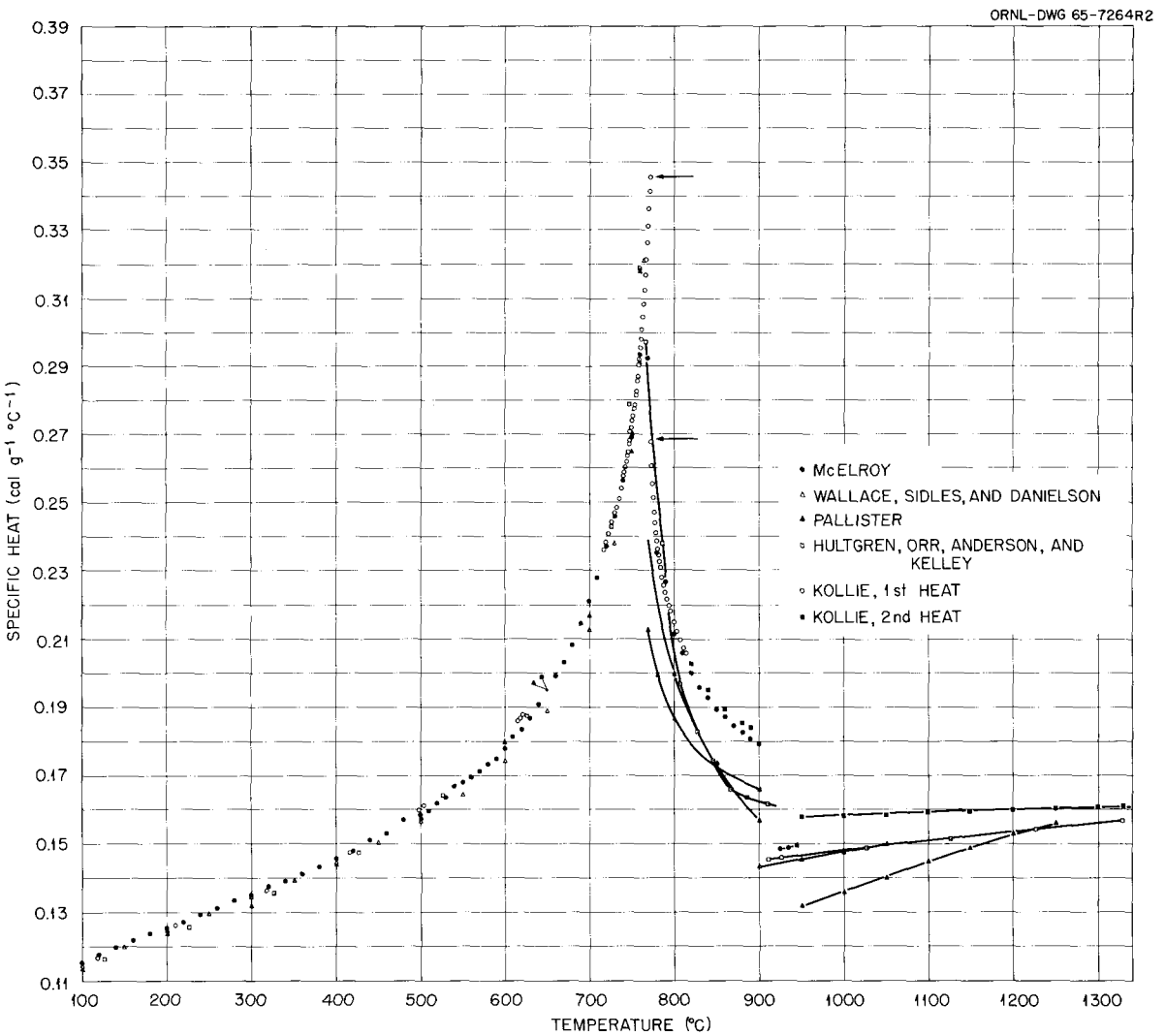

Fig. 7.3. The Specific Heat of Iron as a Function of Temperature, as Measured by a Pulse-Heating Method. Note the specific heat discontinuity at the Curie point, indicated by arrows pointing to points representing two measurements at essentially the same temperature in the same experiment.

to 1300°C in the resistivity apparatus), and electrical resistivity (to 1400°C in the resistivity apparatus). The results obtained are tabulated and contrasted to the results of others in Part II, Chap. 15 of this report. The total thermal conductivity of tungsten decreases with temperature and may be treated as if composed of two terms: an electronic portion, calculable with the Wiedemann-Franz-Lorenz relation from the measured electrical resistivity, and a lattice portion, obtained by subtracting the electronic portion from the total thermal conductivity. The temperature dependence of the lattice thermal resistance is described to within ±2% by

$$W_L = 2.612 + 2.77 \times 10^{-3}\ T - 1.185 \times 10^{-4}\ T^{-2}\ ,$$

where T is the absolute temperature (°K) and W_L is in cm °C w^{-1}. Above 600°C the T^{-2} term contribution is less than 2% of the total and the linear term yields, by the Leibfried-Schlömann analysis,[12] a Debye characteristic temperature of 318°K. This compares favorably with values

[12] G. Leibfried and E. Schlömann, "Wärmeleitung in Electrisch Isolierenden Kristallen (Heat Conduction in Electrically Insulating Crystals)," *Nachr. Akad. Wiss. Goettingen, Math.-Physik. Kl, IIa. Math.-Physik.-Chem. Abt.* **1954**, 71–93 (translated as AEC-tr-5892).

of 291 to 388°K obtained by other means.[13] For temperatures below the Debye temperature, ln (W_L/T) was linear in $1/T$, as expected by Ziman's[14] analysis, and this linearity yielded a Debye characteristic temperature of 284°K. The average mean free path of the phonons was calculated by a single-phonon gas model and decreased from 80 A at 100°C to 36 A at 1000°C. The reasonableness of these results lends credit to extrapolation of the results to higher temperatures, as we have done in Chap. 15 of this report.

MEASUREMENT OF LOW THERMAL CONDUCTIVITIES[15]

N. N. Engel[16] D. L. McElroy

A radial-heat-flow system that uses a single movable thermocouple to measure the radial temperature distribution was developed for measuring the thermal conductivity of insulators to 1000°C. Initial measurements were completed on a low-density thermal insulation (carbon felt, type VDF) in vacuum to 600°C, in air to 300°C, and in helium to 1000°C. The results in vacuum were fitted by an $A + BT^3$ relation. The first term implies a constant heat transport contribution from the carbon felt. The T^3 term implies a radiation dependence that was only 40% of the exchange calculated for radiation in the absence of the specimen. By adding the known thermal conductivities of the two gases to this expression, we obtained equations that represented well the thermal conductivity measured with the gases present. Thus, carbon-felt insulation blocks direct radiation transport and gaseous convection but not gaseous conduction.

STABILITY OF TEMPERATURE TRANSDUCERS[17]

T. G. Kollie J. P. Moore
W. Fulkerson R. S. Graves

Temperature measurement difficulties constitute a major experimental limitation to accurate physical property determinations. During the past year we have observed several significant and unexpected changes in the thermal emf characteristics of Pt–10% Rh, Pt thermocouples. Between 200 and 1000°C, cold-worked 0.005-in.-diam thermocouples showed a −8°C error, but this could be reduced to less than 1°C by annealing. When the radial heat flow system contained Inconel, Al_2O_3, and helium, errors as great as 90°C were noted due to the transfer of Al, Si, Ca, and Mg to the thermoelements. In radial heat flow measurements above 800°C on tungsten in helium, we noted deleterious contamination of the Pt–10% Rh, Pt thermocouples with copper, which came from the constantan thermoelements of another measuring plane. When these thermoelements were deleted from the system, satisfactory operation to 1000°C was achieved.

On the encouraging side, W–5% Re, W–26% Re thermocouples showed negligible changes in calibration at 1400°C in the high-temperature vacuum furnace. Furthermore, our measurements of the electrical resistivity of tungsten and W–26% Re wires indicated that these materials are useful high-temperature transducers. Since it is useful to obtain physical property data over the widest possible temperature range without reinstrumentation of specimens, we measured the thermal emf of a Platinel thermocouple to −200°C. We obtained a sensitivity at −200°C of 7.8 μv/°C, which is 40% greater than that of Pt–10% Rh, Pt at 0°C, and sufficient to be useful to −200°C. Finally, we have obtained an automatically balancing optical pyrometer for extending physical property measurements to higher temperatures.

RELATED WORK

J. P. Moore R. K. Williams
R. S. Graves N. N. Engel[16]
W. Fulkerson

The physical properties of various solids are of interest in the design and operation of numerous

---

[13] K. A. Gschneidner, Jr., *Solid State Phys.* **16**, 275–426 (1964).

[14] J. M. Ziman, *Electrons and Phonons; the Theory of Transport Phenomena in Solids*, 3d ed., Clarendon, Oxford, 1963.

[15] Condensed from "An Apparatus to Measure the Thermal Conductivity of Poor Conductors to 1000°C," *Proceedings of Fourth Conference on Thermal Conductivity, San Francisco, California, October 13–16, 1964* (limited distribution).

[16] Summer research participant in 1964 from Georgia Institute of Technology, Atlanta.

[17] Brief summaries of parts of a compilation by N. H. Briggs and D. L. McElroy, *High-Temperature Thermometry Work at the Oak Ridge National Laboratory*, to be published as part of a TID report of the proceedings of the AEC High-Temperature Thermometry Meeting, AEC Headquarters, Washington, D.C., Feb. 24–26, 1965.

high-temperature devices. Although the high-temperature characteristics are of primary interest, often data do not exist at low temperatures, and such data can be informative and helpful for planning more extensive studies. The development of a longitudinal heat flow apparatus that does not require specimen instrumentation has proved useful in providing data accurate to ±3% on numerous specimens between 20 and 130°C. Pursuant to more extensive studies, we have obtained data on poly- and single-crystal silicon, chromium, SrF_2, D-43 (Nb–10% W–1% Zr–0.1% C), T-111 (Ta–8% W–2% Hf), and several commercial sintered aluminum products.

Interesting thermal conductivity changes have been noted in BeO, irradiated BeO, MgO, Speer 780 graphite, and cermets of aluminum and UO_2. The observed thermal conductivity behavior due to the effects of porosity, irradiation dosage and temperature, sintering, Néel temperature, and composition will be reported elsewhere.[18]

We have two apparatuses under development for extending our measurement capabilities. One apparatus, now being tested, is designed to measure directly the difference in thermal conductivity to 600°C of two small uninstrumented specimens. The power to an instrumented probe resting on each specimen is adjusted to create the same temperature difference across the two specimens. The difference in the power needs for the two probes yields the difference in the thermal conductivity of the two specimens. This method should be useful in determining directional effects and effects due to heat treatment. A second apparatus is a vacuum furnace in which numerous physical properties may be measured. It has been operated to 1700°C at a vacuum of 5×10^{-6} torr with tantalum concentric tube furnace. The useful working space, 3.5 in. in diameter by 20 in. long, was initially used to intercompare various means of measuring high temperatures, including thermocouples, resistance thermometers, and optical pyrometers. This large system is currently being adapted to extend our radial heat flow measurements on tungsten to 1600°C.

Our measurements of the thermal conductivity of graphite are reported in Part III, Chap. 24 of this report.

---

[18] J. P. Moore, *Thermal Conductivity Measurements with Simple Longitudinal Heat Flow Apparatus* (report in preparation).

8. Solid-State and Molecular Theory

J. S. Faulkner

Our research interests are reasonably well illustrated by the summaries that appear in this report. The primary purpose is to carry out quantum-theoretical investigations of the properties of solids and molecules, but we have also been able to furnish some needed theoretical help for other groups and individuals in the Division.

PARAMAGNETIC PROPERTIES OF THE RARE-EARTH GERMANOMOLYBDATES

H. L. Davis

A number of rare-earth germanomolybdates (R_2GeMoO_8 with R = Pr, Nd, Tb, Dy, Ho, Er, Yb) have been synthesized,[1] and qualitative features concerning their paramagnetic properties have been observed.[1,2] Perhaps the most striking feature of these optically transparent crystals is their strong paramagnetic anisotropies. The crystals all have a body-centered tetragonal (scheelite) structure. The crystals containing Pr, Nd, Tb, Dy, and Ho align in a magnetic field with their c-axes parallel to the field, whereas those containing Er and Yb align with their c-axes perpendicular to the field. We have now theoretically understood these anisotropic properties by considering the effect of the crystalline electric fields on the lowest J multiplet of the free R^{3+} ion, as explained below.

Though the R^{3+} ion sees a crystalline field of C_{4h} symmetry, a very minor approximation allows calculations to be performed with the much simpler D_{4h} symmetry. With this approximation, the lowest J-multiplet energy levels of the free R^{3+} ion will be perturbed by the crystalline electric field Hamiltonian:

$$H_{cf} = \langle r^2 \rangle \alpha A_2^0 O_2^0 + \langle r^4 \rangle \beta \, [A_4^0 O_4^0 + A_4^4 O_4^4] + \langle r^6 \rangle \gamma \, [A_6^0 O_6^0 + A_6^4 O_6^4] \, .$$

The symbols used are standard and have been defined by Hutchings.[3] The parameters A_n^m have been obtained from a point-charge model of the eight neighboring O^{2-} ions about an R^{3+} ion, while the $\langle r^n \rangle$ have been taken over from the free R^{3+}-ion Hartree-Fock results.[4] This enables the lowest lying energy levels of the R^{3+} ion in the crystal and their behavior in a magnetic field to be calculated. From these results we have theoretically estimated the susceptibilities for each of the crystals and give them in Table 8.1 along with the experimental[1,2] powder susceptibilities. The theoretical directional susceptibilities agree precisely with the alignment behavior described above. At the same time, the powder susceptibilities agree reasonably for those systems where data are available. As more precise data become available (e.g., the temperature dependence of the directional susceptibilities and optical absorption spectra), we expect our simple point-charge model to require some modifications.

[1] C. B. Finch, G. W. Clark, and L. A. Harris, *Metals and Ceramics Div. Ann. Progr. Rept. June 30, 1964*, ORNL-3670, p. 6.

[2] G. W. Clark, E. Sonder, and A. T. Chapman, *Metals and Ceramics Div. Ann. Progr. Rept. June 30, 1964*, ORNL-3670, p. 9.

[3] M. T. Hutchings, *Solid State Phys.* **16**, 227 (1965).

[4] A. J. Freeman and R. E. Watson, *Phys. Rev.* **127**, 2058 (1962).

Table 8.1. Magnetic Susceptibilities[a] of Compounds R_2GeMoO_8

Rare Earth, R	Susceptibility (10^{-4} emu/g)			
	Theoretical			Experimental
	Parallel	Perpendicular	Powder	Powder
Pr	0.40	0.07		
Nd	0.29	0.16		
Tb	2.75	0.57	1.30	1.20
Dy	2.96	0.84	1.55	1.56
Ho	2.08	1.26	1.53	1.52
Er	0.82	1.42	1.22	1.17
Yb	0.11	0.35		

[a]Measured at 297°K with an applied magnetic field of 1750 gauss.

SPIN-WAVE THEORY OF α-Fe_2O_3

H. L. Davis

At temperatures low compared to the Néel temperature, the sublattice magnetization, $M(T)$, for α-Fe_2O_3 has been experimentally found[5,6] to depend approximately on temperature according to

$$M(T)/M(0) = 1 - aT^n ,$$

with $n = 5/2$ to within experimental error. Though α-Fe_2O_3 is a weak ferromagnet, to first order one would expect the experimental result to approximate $n = 2$, the spin-wave result[7] for a Heisenberg antiferromagnet. We have found that this disagreement between theory and experiment is due to the long-wavelength approximation used in standard[7] antiferromagnetic spin-wave theory and not to the inability of the spin-wave formalism to describe the α-Fe_2O_3 spin system. In particular, our calculations on α-Fe_2O_3 point out the existence of Brillouin zone-boundary effects in antiferromagnets; in the same manner such effects have been demonstrated to be of importance in ferromagnetic spin-wave theory.[8] When the zone-boundary effects are allowed for in the spin-wave theory of α-Fe_2O_3, it agrees with the empirical relation for $M(T)$.

[5]D. H. Anderson, *Bull. Am. Phys. Soc.* **7**, 537 (1962).

[6]F. E. Obenshain, L. D. Roberts, and J. O. Thomson, *Bull. Am. Phys. Soc.* **8**, 558 (1963).

[7]R. Kubo, *Phys. Rev.* **87**, 568 (1952).

THEORY OF d^2 AND d^8 CONFIGURATIONS IN ARBITRARY CRYSTALLINE ELECTRIC FIELDS

H. L. Davis

In the study of systems whose magnetic and optical properties are due to Ni^{2+} and V^{3+} ions in crystalline electric fields of less than cubic symmetry, heretofore the experimental data have been customarily correlated with theoretical results obtained by use of perturbation methods on results for these ions in cubic environments. Since the energy levels of these ions are not always widely separated, such perturbation methods are not necessarily applicable. To avoid perturbation methods, we have considered the general theory of d^2 and d^8 configurations in crystalline electric fields of arbitrary symmetry within the framework of the point-charge model.

[8]H. L. Davis and A. Narath, *Phys. Rev.* **134**, A433 (1964).

These considerations have enabled us to formulate a FORTRAN code that directly calculates the energy levels and eigenvectors of the d^2 and d^8 configurations without recourse to perturbation theory. This code uses as input the Slater integrals, a spin-orbit coupling parameter, and parameters describing the arbitrary crystalline field. We anticipated that this code will be used to interpret optical data, obtained by the Spectroscopy of Ionic Media Group (Chap. 9 of this report), on the Ni^{2+} ion in molten-salt and solid-state environments.

AN ENERGY-CALIBRATED MOLECULAR ORBITAL METHOD[9]

C. E. Melton[10] H. W. Joy

In almost any form of simple molecular orbital calculation,[11] which represents molecular orbitals as linear combinations of atomic orbitals ("LCAO-MO"), the secular equation $\det[H_{ij} - S_{ij}E] = 0$ must be solved to find the expansion coefficients and eigenvalues E. Here the H_{ij} are taken to be matrix elements of some effective one-electron Hamiltonian operator over the atomic orbitals, and the S_{ij} are atomic orbital overlap integrals. Because the nature of the effective Hamiltonian has yet to be properly elucidated, many different schemes have been reported for assigning values to these matrix elements, all of them empirical in one way or another and often open to criticism. Using a computer we have been able to construct another scheme wherein we make the approach as empirical as needed in each application.

If these one-electron molecular-orbital schemes are correct, then the calculated occupied energy levels must be the same as the real energy levels of the molecule, and if we only knew the effective Hamiltonian we could calculate the proper elements of the secular equation and get the correct energy levels. But since hopes of finding a good effective Hamiltonian are not very bright, we have turned the problem inside out. We take a set of observed energy levels and by an iterative least-squares technique find a set of matrix elements that gives them. Our computer program allows us to arbitrarily assign values to all the elements of a given secular equation and to specify which of them are to be held fixed and which are to be varied to fit the data. The problem of using the program to do simple molecular-orbital calculations then becomes one of searching for reasonable molecular models from which we can set up a secular equation, and the computer is our means of experimentally testing whether a particular model will adequately represent molecular features of interest. We have found that some very simple models provide good correlations of ionization potentials of straight-chain hydrocarbons, straight- and branched-chain hydrocarbon free radicals, halogen-substituted methanes, and xenon halides.

CONVERGENCE IN ONE-CENTER EXPANSIONS: H_2^+ (ref. 12)

H. W. Joy G. S. Handler[13]

We have recently[14] made a one-center expansion for the ground ($1s\sigma_g$) state of H_2^+, of the form

$$\psi = \sum_l c_l R_l(r) P_l(\cos\theta),\ l \text{ even},$$

wherein each $R_l(r)$ is expanded in terms having the form $r^n \exp(-\alpha r)$, and we have found that at equilibrium internuclear separation the l expansion converges approximately as $1/l^4$ for large l. We now give evidence that each $R_l(r)$ expansion converges exponentially as a function of number of terms in the expansion, and that the rate of convergence is essentially the same in the $l = 0$ and $l = 2$ shells of the ground state and the $l = 1$ shell of the $2p\sigma_u$ (l odd) excited state. We show that Cohen's[15] l-expansion for this excited state

[9]Reported more fully in *J. Chem. Phys.* **42**, 1986, 2982 (1965).

[10]Chemistry Division.

[11]J. D. Roberts, *Molecular Orbital Calculations*, W. A. Benjamin, New York, 1962.

[12]Condensed from a paper accepted for publication by the *Journal of Chemical Physics*.

[13]Consultant from the University of California, San Diego, La Jolla.

[14]H. W. Joy and G. S. Handler, *J. Chem. Phys.* **42**, 3047 (1965).

[15]M. Cohen, *Proc. Cambridge Phil. Soc.* **58**, 130 (1962).

also converges approximately as $1/l^4$. We suggest that if this approach can be extended to finding convergence laws in multielectron problems, then we might be able to obtain fairly good values of various molecular properties from a few simple one-center calculations.

STATES OF He AND He$^-$

H. W. Joy

There has been some recent interest in autoionizing states of helium and resonances apparently due to He$^-$, both of which are observed in electron scattering experiments.[16] To help sort out some of these states, several calculations have been made with our general-purpose one-center expansion program.[17] We are examining all possible stationary states of helium and He$^-$ that can be represented by Slater determinants containing simple 1*s*, 2*s* (orthogonalized to 1*s*), and 2*p* Slater-type orbitals. The results to date indicate that those states having a single 1*s* electron are located near 20 ev and those with no 1*s* electron near 60 ev above the $1s^2$ ground state, and that there are no states with energies in between. Except for the ground state, the calculated energies agree with available experimental data to within about 1 ev.

THE *s*-LIMIT IN LITHIUM

G. S. Handler[13] H. W. Joy

An antisymmetric wave function constructed[18] from a sum of terms, each having the form

$$\phi(1,2,3) = r_1^I r_2^J r_3^K \exp(-Ar_1 - Br_2 - Cr_3) \times P_L(\cos\theta_{12}) P_M(\cos\theta_{13}) P_N(\cos\theta_{23}) ,$$

appears to adequately represent the wave function for the ground state of the lithium atom. When $L = M = N = 0$ in all terms, the best resulting function provides a measure of the extent of the radial contribution (the *s*-limit) to the correlation energy. The evidence of our computations so far suggests that the expansion will converge to the *s*-limit in about six to eight terms.

MOLECULAR GEOMETRY BY ONE-CENTER EXPANSION

H. W. Joy

The one-center expansion technique,[17] while perhaps not capable of producing the very best approximations to the true molecular wave functions, is nonetheless a well-founded variational approach and is quite adequate for obtaining much useful information. We believe that molecular shapes and sizes can be determined in many cases by means of relatively small one-center expansions, and we are presently examining the molecule CH_4^+.

Bishop[19] has published a single-determinant wave function for CH_4 having the one-center configuration $1s^2 2s^2 2p_x^2 2p_y^2 2p_z^2$. In forming ground-state CH_4^+, one would remove either a 2*s* electron or one of the 2*p* electrons, and thus the resulting wave function would be a linear combination of the (almost) degenerate configurations

$$1s^2 2s 2p_x^2 2p_y^2 2p_z^2 ,$$

$$1s^2 2s^2 2p_x 2p_y^2 2p_z^2 ,$$

$$1s^2 2s^2 2p_x^2 2p_y 2p_z^2 ,$$

$$1s^2 2s^2 2p_x^2 2p_y^2 2p_z .$$

If the Jahn-Teller theorem is true, the molecule will distort at least somewhat from full tetrahedral symmetry in an effort to remove the degeneracy. We have given our computer program these four configurations to work with and allowed it to start with Bishop's orbital parameters and tetrahedral geometry. It has varied the orbital parameters and the geometry and come up with evidence that strongly suggests that CH_4^+ is neither tetrahedral nor distorted tetrahedral; it seems to be square planar instead, with slightly greater C – H bond distances than those in CH_4.

---

[16] J. F. Burns, Health Physics Division, private communication.

[17] H. W. Joy, *Metals and Ceramics Div. Ann. Progr. Rept. May 31, 1963*, ORNL-3470, p. 11.

[18] G. S. Handler, *Journal of Chemical Physics* (in press).

[19] D. M. Bishop, *Mol. Phys.* **6**, 305 (1963).

ELECTRONIC STATES OF DISORDERED SYSTEMS

J. S. Faulkner

The Green's-function[20–22] method for calculating the electronic states of disordered systems has the advantages that it is systematic and general. It is relatively easy to keep track of the terms that are included and omitted in a particular calculation, so that the level of approximation can be systematically improved. The generality of the method allows one to apply it as well in principle to three-dimensional problems of physical interest as to one-dimensional models where the mathematical framework is more clear. Sometimes in practice, the actual calculation that one is led to by the Green's-function method is identical with one that has been previously obtained by another method, but the advantages of the Green's-function method outlined above make it interesting to see how this comes about.

During the past year we have reformulated in terms of Green's functions a calculation of the density of electronic states of a one-dimensional liquid metal that we had carried out using transfer matrices.[23] By doing this we have been able to see why the result we obtained using the average trace of the transfer matrix is identical with the highest approximation so far worked out using Green's functions, the Klauder, Matsubara, and Toyozawa (KMT) approximation.[21,22] We also clarified the general connections between Green's functions and transfer matrices.

In the field of Green's functions themselves, we have worked out a nontrivial extension of the KMT approximation for liquid metals. Our extension takes into account the interference terms that arise when the electron is scattered by pairs of atoms.

ONE-CENTER EXPANSIONS

R. M. Rutledge[24] A. F. Saturno[25]

Although one-center expansion (OCE) is usually not considered a feasible general approach to polyatomic molecular wave functions, previous results for species of the type XH_n have been on a par with other methods. The appeal of the OCE approach is the ease of formulation and computing compared to multicenter approaches. In fact, only recently have the much more laborious multicenter calculations[26,27] yielded better results than the OCE method for CH_4. Our first work[28] was a study of CH_3^-, CH_4, and CH_5^+. Wave functions expressed by configuration interaction of the singly excited states of a closed-shell ground state were calculated. The basis set consisted of Slater-type orbitals (STO's) through $l = 4$, belonging to the irreducible representations spanned by the σ-bonding representation. As the geometry of CH_3^- and CH_5^+ is unknown, these species were calculated as a function of nuclear geometry. The calculations indicated that both ions have a D_{3h} configuration rather than CH_3^- having C_{3v} and CH_5^+ having C_{3v} or C_{4v}.

In the above work the CH_4 calculations were done as a function of order of the expansion. For a given l_{max} all possible configurations of the above type were included having STO's with $l \leq l_{max}$. Four different expansions ($l_{max} = 1$, 2, 3, and 4) were done. A plot of the ground state energy vs l_{max} indicated that an extension of the above calculations to around $l_{max} = 12$ might yield results close to recent successful multicenter calculations.[26,27] The extension of the previous calculations on CH_4 through $l_{max} = 8$ gave much less improvement than was expected. The addition of extra radial terms to the s, p, and d orbitals did not indicate that much improvement could be obtained by this means.

The energy barrier calculation for the inversion of NH_3 by Moccia,[29] using OCE-SCF (self-consistent field) wave functions, attracted our attention for two reasons. First, the energy barrier

---

[20] S. F. Edwards, *Phil. Mag.* **3**, 1020 (1958).

[21] J. R. Klauder, *Ann. Phys. (N.Y.)* **14**, 43 (1961).

[22] T. Matsubara and Y. Toyozawa, *Progr. Theoret. Phys. (Kyoto)* **26**, 739 (1961).

[23] J. S. Faulkner, *Phys. Rev.* **135**, A124 (1964).

[24] Postdoctoral Fellow.

[25] Consultant from the University of Tennessee.

[26] B. J. Wuznick, *J. Chem. Phys.* **40**, 2860 (1964).

[27] Morris Krauss, *J. Res. Natl. Bur. Std., A* **68**, 635 (1964).

[28] R. M. Rutledge and A. F. Saturno, *Journal of Chemical Physics* (to be published).

[29] R. Moccia, *J. Chem. Phys.* **40**, 2176 (1964).

calculated was low, and, second, the nonplanar wave function was calculated with only partial minimization of the parameters and the planar wave function with no minimization of the parameters. From our experience the value of Moccia's energy barrier was in the range of variation due to parameter changes. Probably, minimization of the planar wave function would have given a lower barrier. The above observations and the poor results on CH_4 led us to question the OCE configuration determination of NH_3. Calculations similar to our previous one on CH_3^- indicated that the configuration of NH_3 is D_{3h} rather than C_{3v} for l_{max} = 1, 3, 4. However, C_{3v} was observed rather than D_{3h} for l_{max} = 2 with the angle between the C_3 axis and an N–H bond being 113.5° (exptl 112°). Until these results are explained, the usefulness of OCE configuration studies is uncertain.

MULTICENTER EXPANSIONS

R. M. Rutledge[24] A. F. Saturno[25]

In the immediate future, study of Gaussian-type orbitals offers promise in light of Krauss's recent results.[27,30] The use of Gaussian orbitals alleviates much of the computation difficulties of the traditional STO's in the multicenter approach.

Semiempirical methods are at present the only practical means of performing calculations on any but the simplest species. Several calculations of organic molecules using a simple Hückel molecular-orbital approach have been made. The work now under way is on better self-consistent-field molecular-orbital methods such as the Pariser-Parr or Pople calculations.

[30] Morris Krauss, *J. Res. Natl. Bur. Std.*, *B* **68**, 35 (1964).

9. Spectroscopy of Ionic Media

G. P. Smith

This chapter describes studies of the absorption spectra of molten-salt systems and supporting research. In studies of systems containing Ni^{2+} ions, the $d \rightarrow d$ absorption bands are used as a probe of coordination geometry. These include investigations of systems containing very high Ni^{2+} concentrations that are beginning to provide answers on the extent to which the coordination geometry of a crystalline transition metal compound is preserved on melting. We report studies of the spectra of posttransition metal ions in molten salts, in which interest centers on the discovery of extraordinary oxidation states for bismuth.

NICKEL(II) CENTERS IN MOLTEN HALIDE SALTS: INFLUENCE OF RARE-GAS-CONFIGURATION CATIONS IN CHLORIDE AND BROMIDE SYSTEMS[1]

G. P. Smith C. R. Boston

Absorption spectra of dilute solutions of nickel(II) halides in melts of CsCl, RbCl, KCl, NaCl, LiCl, $MgCl_2$, CsBr, KBr, and LiBr were measured to determine the influence of surrounding solvent cations on the spectra and coordination geometry of color centers formed by nickel in these systems. Measurements on CsCl, LiCl, $MgCl_2$, and LiBr solutions extended from 4 to 40 kK (kilo-Kaysers[2]) and included both $d \rightarrow d$ and charge-transfer bands, whereas the remaining systems were studied from 4 to between 22 and 26 kK and covered only the $d \rightarrow d$ absorptions. Substantial differences were found in these spectra and correlated with the solvent cation size. Analysis of the spectra of nickel centers in CsCl, CsBr, RbCl, KCl, and KBr showed the coordination geometry of halide ions about nickel to be approximately tetrahedral. Although the coordination geometry of centers in sodium, lithium, and magnesium salts was not unambiguously determined, there was evidence that at least two different types of nickel centers were present, one of which may be approximately tetrahedral.

[1]Abstract of a paper to be submitted for publication.

[2]The Kayser is the unit wave number (1 K = 1 cm^{-1}).

NICKEL(II) CENTERS IN BINARY MOLTEN HALIDE SALTS

J. Brynestad[3] C. R. Boston
G. P. Smith

We are undertaking a systematic study of the spectra of nickel(II) centers at low concentrations in the molten LiCl-KCl, $MgCl_2$-KCl, and $MgCl_2$-CsCl systems as a function of composition (isothermal) and temperature. This logical extension of our previous study of nickel(II) centers in chloride media has as its purpose to correlate the spectra of nickel(II) centers in chloride media with different cation environments and to see if the correlations are consistent with other properties of the systems.

[3]On leave from the Advanced Teachers Institute of Norway, Trondheim.

TETRAHALONICKELATE(II) COMPLEX IONS FORMED IN MOLTEN ORGANIC SALTS[4]

G. P. Smith T. R. Griffiths[5]
S. von Winbush[6]

Optical absorption spectroscopy was used to study the formation of halo complexes of Ni^{2+} in melts of nine quaternary organic chloride, bromide, and iodide salts containing dissolved nickel halides. The system tri-*n*-butyl-benzylphosphonium chloride/nickel chloride was investigated at $NiCl_2$ concentrations up to 33.3 mole %, and the remaining systems were examined only at low nickel halide concentrations. For all systems at all compositions nickel(II) was present exclusively in the form of tetrahalonickelate(II) complex ions.

THE MOLTEN $NiCl_2$-CsCl SYSTEM UP TO 60 MOLE % $NiCl_2$

G. P. Smith C. R. Boston

We are measuring the absorption spectra of liquid mixtures of $NiCl_2$ with CsCl at nickel chloride concentrations that range from very dilute up to 60 mole %. There are two binary compounds in the $NiCl_2$-CsCl system, Cs_3NiCl_5 with a tetrahedral arrangement of four chloride ions about Ni^{2+}, and $CsNiCl_3$ with an octahedral arrangement of six chloride ions about Ni^{2+}. We are interested in determining to what extent the coordination geometry that prevails in the melts is correlated with that in the crystalline compounds.

NICKEL(II) CENTERS IN MOLTEN OXO SALTS

C. H. Liu[7] G. P. Smith

We are measuring the absorption spectra of nickel(II) centers in various molten nitrate and sulfate salts to determine the coordination geometry and electronic structure. Preliminary data indicate that a distorted octahedral geometry occurs in all systems with unusually low values of the ligand-field parameter.

[4]Abstract of paper presented at the Electrochemical Society Meeting, San Francisco, California, May 1965.

[5]Visitor from England, now at The University of Leeds, England.

Tl^+, Pb^{2+}, AND Bi^{3+} CENTERS IN THE LIQUID LiCl-KCl EUTECTIC[8]

G. P. Smith D. W. James[9]
C. R. Boston

Absorption spectra from 1.7 to 5.7 ev were measured for dilute solutions of TlCl, $PbCl_2$, and $BiCl_3$ in the molten LiCl-KCl eutectic at 440 and 640°C. The Tl^+ and Pb^{2+} centers showed one band each, and the Bi^{3+} showed two bands. Band parameters at 440°C and assignments in terms of a point-ion model are the following: for Tl^+, 5.01 ev, 4.7×10^3 liters $mole^{-1}$ cm^{-1} ($f = 0.09$), assigned to ${}^1S_0 \rightarrow {}^3P_1$; for Pb^{2+}, 4.49 ev, 6.9×10^3 liters $mole^{-1}$ cm^{-1} ($f = 0.13$), assigned ${}^1S_0 \rightarrow {}^3P_1$; for Bi^{3+}, 3.75 ev, 7×10^3 liters $mole^{-1}$ cm^{-1} ($f = 0.12$), assigned to ${}^1S_0 \rightarrow {}^3P_1$, and 5.4 ev, approximately 27×10^3 liters $mole^{-1}$ cm^{-1}, assigned to ${}^1S_0 \rightarrow {}^1P_1$. These results are compared with the spectra of Tl^+, Pb^{2+}, and Bi^{3+} centers in alkali chloride crystals.

PRODUCTS OF THE Bi^{3+}-Bi REACTION IN ACIDIC CHLORIDE MEDIA[10]

N. J. Bjerrum[11] C. R. Boston
G. P. Smith

Bismuth metal reacts with dilute solutions of $BiCl_3$ in molten NaCl-$AlCl_3$ and NaCl-$ZnCl_2$ mixtures to form at least three very unusual ions. One of these is probably Bi^+, which has a partially filled *p*-electron shell. The other two ions appear to involve bismuth-bismuth bonds and remarkably low oxidation states.

Most of the experiments have been done in a eutectic mixture of $AlCl_3$-NaCl (63 mole % $AlCl_3$)

[6]Summer Research Participant in 1964 from the Agricultural and Technical College of North Carolina, Greensboro.

[7]Department of Chemistry, Polytechnic Institute of Brooklyn, New York.

[8]Abstract of "Optical Spectra of Tl^+, Pb^{2+}, and Bi^{3+} in the Molten Lithium Chloride-Potassium Chloride Eutectic," *J. Chem. Phys.* **42**(6), 2249–50 (1965).

[9]Presently with Chemistry Department, University of Queensland, Brisbane, Australia.

[10]Preliminary report.

[11]On leave from the University of Copenhagen, Denmark.

Table 9.1. Absorption Bands of Products of the Bi^{3+}-Bi Reaction in $NaCl-AlCl_3$ Eutectic Melts

Species 1		Species 2		Species 3	
Wave Number (kK)	Extinction (liters $mole^{-1}$ cm^{-1})	Wave Number (kK)	Extinction (liters $mole^{-1}$ cm^{-1})	Wave Number (kK)	Extinction (liters $mole^{-1}$ cm^{-1})
14.5	200	11.4	95	18.2	275
15.1	200	13.4	95	22.2	530
17.1	500	25.6	1600	28.6	1000

over a temperature range of 130 to 250°C. The resulting absorption spectra, measured between 7 and 40 kK, can be interpreted in terms of at least three ionic species. Parameters of the absorption bands for these species are shown in Table 9.1. The species are numbered according to the order in which they appear when the Bi/Bi^{3+} ratio is increased. The extinction coefficients for the first two species are derived on the basis of added bismuth metal, while the extinction coefficients for the third species are calculated according to the total number of bismuth atoms in the melt.

We have little doubt about the oxidation state of the first species. The ratio of charge to number of atoms is very close to 1, which shows that the formula for this species is Bi_n^{n+}. We have been unable to measure directly the oxidation state of the second species. The measurements so far show an oxidation state in the range one-third to one-seventh for the third species.

The equilibrium between the first two species has been intensely studied at 130°C. The presence of two isosbestic points shows that when the concentration of $BiCl_3$ is sufficiently high the system can be treated according to a two-species model.

In going from the first to the second species, a high degree of polymerization takes place, approximately six, which is somewhat higher than found previously[12,13] in the binary $BiCl_3$-Bi system. We are still not certain whether the same species are present in the two systems. The equilibrium also depends on the $BiCl_3$ concentration. The reaction is apparently 6 Bi_n^{n+} (species 1) $\rightleftharpoons Bi_{6n-1}^{6n-3}$ (species 2) + Bi^{3+}. The value of n cannot be determined easily in the $AlCl_3$-NaCl solvent, since any excess of bismuth metal will use all available $BiCl_3$ and form the third species. However, the reaction

$$l\mathrm{Bi} + \mathrm{Bi}^{3+} \rightleftharpoons 3\mathrm{Bi}^{+}_{(l+1)/3}$$

was found in a eutectic mixture of KCl–54 mole % $ZnCl_2$, and the product of this reaction had a spectrum similar to that of the first species. Since the first species is in the +1 oxidation state, it should consequently have the formula Bi^+. The second species will have the formula Bi_5^{3+} if n is equal to 1. This result fits well with the reaction

$$m\mathrm{Bi} + \mathrm{Bi}^{3+} \rightleftharpoons \mathrm{Bi}_{m+1}^{3+},$$

found in the eutectic mixture $ZnCl_2$–28 mole % KCl.

These deductions must be taken with some reservations. While the absorption band at 11.4 kK is at the same position in both $AlCl_3$ and $ZnCl_2$ melts, the absorption bands at 15.1 and 17.0 kK in the $AlCl_3$ melt should correspond to bands at 13.8 and 17.9 kK, respectively, in the $ZnCl_2$ melt. Since this is a rather large shift, the same species may not be present in both systems.

NICKEL(II) CENTERS IN HALIDE CRYSTALS

J. Brynestad[14] G. P. Smith

For our research on nickel(II) centers in molten chloride media, we need the spectra of nickel(II) centers with fairly well-defined geometry. As a preliminary study, we have been growing nickel(II)-

[12] C. R. Boston and G. P. Smith, *J. Phys. Chem.* **66**, 1178 (1962).

[13] C. R. Boston, L. C. Howick, and G. P. Smith, *J. Phys. Chem.* **67**, 1849 (1963).

[14] On leave from the Advanced Teachers Institute of Norway, Trondheim.

doped single crystals of congruently melting compounds in the $MgCl_2$-AlkCl and $ZnCl_2$-AlkCl (Alk = Cs, Rb, K) systems, and we have preliminary information on the spectra at room temperature of Ni(II) centers in these crystals.

Theoretical work on the point-charge model of Ni^{2+} in crystalline fields is reported in Chap. 8 of this report.

NITRATO AND CHLORO COMPLEXES OF NICKEL(II) IN MOLTEN DIMETHYL SULFONE

C. H. Liu[15] G. P. Smith

We are studying the formation of NO_3^- and Cl^- complexes of Ni^{2+} in molten dimethyl sulfone as solvent, to determine the spectra and formation constants of the successive complexes. This information will help us evaluate spectroscopic data on nickel(II) centers in molten chloride and nitrate salts. Molten dimethyl sulfone is particularly suitable for this study, because it forms such weak solvo complexes with Ni^{2+} that the relatively weak nitrato and chloro complexes can form.

DENSITIES OF MOLTEN SALT MIXTURES

C. R. Boston G. P. Smith

Densities were determined at several temperatures and compositions for the systems, tri-*n*-butylbenzylphosphonium chloride-$NiCl_2$ and CsCl-$NiCl_2$. The technique used was that described by Smith and Petersen[16] and modified by Griffiths.[17] The results are summarized in Table 9.2.

[15]Department of Chemistry, Polytechnic Institute of Brooklyn, New York.

[16]G. P. Smith and G. F. Petersen, *J. Chem. Eng. Data* **6**, 493 (1961).

[17]T. R. Griffiths, *J. Chem. Eng. Data* **8**, 568 (1963).

Table 9.2. Density Equations for Molten Chloride Mixtures

$NiCl_2$ or $AlCl_3$ Concentration (mole %)	$\rho = \alpha - \beta t$		Experimental Temperature Range (°C)	Standard Deviation (g/cm^3)
	α (g/cm^3)	β ($g\ cm^{-3}\ °C^{-1}$)		
		$NiCl_2$-Tributylbenzylphosphonium chloride system		
		$\times 10^{-3}$		$\times 10^{-3}$
33.44	1.180	0.78	121–164	1.1
20.76	1.081	0.53	134–183	0.6
10.10	1.048	0.54	157–178	0.7
5.03	1.028	0.51	161–183	1.0
0.00[a]	1.021	0.548	178–240	0.2
		$NiCl_2$-CsCl system		
60.00	3.209	0.94	807–847	1.2
40.06	3.165	0.87	754–843	2.0
20.09	3.286	0.93	548–773	1.6
		$AlCl_3$-NaCl system		
100.00	1.723	2.3	202–221	1.9
73.00	1.760	0.92	183–337	1.0
61.80	1.796	0.86	162–275	1.0
52.00	1.841	0.85	124–294	0.8

[a]T. R. Griffiths, *J. Chem. Eng. Data* **8**, 568 (1963).

Densities have been determined at several temperatures for mixtures of NaCl with 52 and 62 mole % $AlCl_3$, and measurements on NaCl–73 mole % $AlCl_3$ are in progress. The density of molten $AlCl_3$ has been redetermined and found to differ substantially from the literature value. Table 9.2 summarizes the results.

To measure density, we observed the rise and fall with temperature of calibrated quartz "floats" in a melt that was sealed off in a quartz capsule. To assure accurate temperature control and to eliminate temperature gradients, the entire capsule was held either in a silicone oil bath or a large aluminum block.

Plots of molar volume against composition showed extremely large negative deviations from linearity. For example, at 50 to 60 mole % $AlCl_3$ the deviation is about 20%, whereas most molten salt mixtures deviate only 1 to 3%.

FURNACE FOR THE MEASUREMENT OF MOLTEN SALT SPECTRA[18]

C. R. Boston G. P. Smith

A resistance-heated furnace is described which may be used with the Cary model 14-H spectrophotometer for measuring the absorption spectra of liquid systems at temperatures up to 1450°C. The furnace accommodates a 10-mm-square absorption cell and has a platinum liner to contain accidental release of corrosive liquids. The heating element is made of Pt–20% Rh alloy.

APPARATUS FOR SPECTROSCOPIC MEASUREMENTS ON LIQUIDS AT ELEVATED PRESSURES AND TEMPERATURES[19]

D. W. James[20] G. P. Smith

A pressure vessel and furnace for measuring absorption spectra of liquid systems at elevated temperatures and pressures is described. At 600°C the assembly will operate at 300 atm. This apparatus was designed for use with either the Cary model 11 or the Cary model 14-H spectrophotometer. The liquid sample is held in a standard 1-cm-square absorption cell with a wide neck attached.

---

[18] Abstract of "Furnace for Molten Salt Measurements on the Cary Model 14-H Spectrophotometer up to 1450°C," *Rev. Sci. Instr.* **36**, 206 (1965).

[19] Abstract of paper submitted for publication.

[20] Presently with Chemistry Department, University of Queensland, Brisbane, Australia.

10. Structure of Metals

C. J. McHargue

We are seeking the principles underlying the atom movements that occur during deformation, annealing, and phase transformation in solids. We use these principles to correlate the physical and mechanical properties with microstructure and to obtain microstructures with specific properties by suitable thermal and mechanical treatments. During this report period, we studied migration of grain boundaries during annealing and the deformation of body-centered and face-centered cubic metals and alloys.

RECRYSTALLIZATION STUDIES

R. A. Vandermeer

Dependence of Grain-Boundary Migration Rates on Driving Force[1]

Most theories of grain-boundary migration rates predict that the rate should be proportional to the driving force. In recrystallization studies on aluminum, Gordon and Vandermeer[2] generated data that could provide the first experimental test of this proportionality. Their analysis, however, incorrectly related the average instantaneous boundary migration rate of the recrystallized grains to the measured rate of increase of the recrystallized fraction of the specimen volume. We have pointed out the error and modified the analysis so that a more proper average boundary migration rate can be calculated from the experimental data. The earlier data were reevaluated and confirmed the theoretically proposed linear relationship.

[1]Summary of work published in *Trans. Met. Soc. AIME* **233**, 265 (1965).

[2]P. Gordon and R. A. Vandermeer, *Trans. Met. Soc. AIME* **224**, 917–28 (1962).

The Impurity Drag Effect in Grain-Boundary Migration

The experimental boundary migration rate data of Gordon and Vandermeer[2] on zone-refined aluminum alloys containing copper were reevaluated in terms of an improved impurity-drag theory by Cahn.[3] Three regions of migration behavior are expected on theoretical grounds – a high velocity regime, a low velocity regime, and a transition region between the two. Some experimental data fell into each category. In the low velocity range, where most of the data were obtained, the reciprocal of the boundary velocity was proportional to the concentration of copper, in excellent agreement with theory. The transition between the high and low velocity regimes was continuous, although theoretically it should have been discontinuous. In this transaction region, however, the theory suggests that a boundary can have two stable velocities. We can rationalize the apparent discrepancy if we recognize that a boundary in the transition state can oscillate between these two velocities. Thus, since we can really observe only the macroscopic and, hence, the average behavior of the boundary, the measured velocities should be intermediate between the two predicted velocities. Such was the case.

By fitting all the experimental data to the theory until an internal consistency was reached, we arrived at reasonable values for the parameters in Cahn's theory that relate to the fundamental atomic phenomena involved in the boundary migration process (e.g., interaction potential and diffusivity of impurity atoms). Our interpretation indicates a rather strong interaction (interaction energy of 2500 to 5200 cal/mole) between the

[3]J. W. Cahn, *Acta Met.* **10**, 789–98 (1962).

copper impurity atoms and a moving grain boundary in aluminum. The effective interaction distance is about two atom diameters and is large relative to the width (about one-half atom diameter) of the disordered region of the boundary, in which the diffusivity of the impurity atom is high.

TWINNING IN COLUMBIUM-VANADIUM ALLOYS[4]

D. O. Hobson[5] J. O. Stiegler[6]
C. J. McHargue

The effects of alloy composition, deformation temperature, heat treatment, and interstitial contamination on the occurrence of deformation twins were studied. The twinning transition temperature varied with composition. The temperature range of the transition was very narrow. Alloys of 20 to 70% V could be cold rolled and exhibited profuse twinning. The alloys that did not twin at room temperature (10, 80, and 90% V) could not be cold rolled. Oxygen additions systematically lowered the transition temperature for all vanadium contents. The transition temperature for a 30% V alloy increased with annealing temperature, apparently due to changes in dislocation density and configuration. Twinning did not nucleate fracture in any specimen in the 20 to 60% V composition range.

PREFERRED ORIENTATION OF NIOBIUM

J. C. Ogle R. A. Vandermeer

We started to determine the deformation and recrystallized textures of niobium rolled at room temperature and at liquid-nitrogen temperature. Previously, we showed that niobium single crystals that had undergone extensive cross twinning recrystallized initially at twin intersections and at a higher rate than did crystals that did not contain such intersections. These recrystallized grains had an orientation relationship not only to the parent crystal but also to the intersecting twins. These new grains grew more rapidly into the twins than into the parent crystal. These results suggest that different recrystallized textures may be developed in niobium fabricated under different conditions.

The large-grain structure of electron-beam-melted pancakes of niobium was partially broken up by compressing and recrystallizing prior to rolling. Two pieces were rolled at room temperature and two pieces were rolled at liquid-nitrogen temperature to obtain the maximum amount of twinning. All specimens were reduced approximately 90% in thickness. Figures 10.1 and 10.2 are typical of the microstructures of the material rolled at the two temperatures. The material rolled at liquid-nitrogen temperature recrystallized completely in 0.5 hr at 1125°C, and its microstructure is shown in Fig. 10.3. The grains grew mainly in a direction parallel to the layers that are seen in the as-rolled material in Figs. 10.1 and 10.2. The annealing temperature for the material rolled at room temperature was approximately 200°C higher than that of material rolled at the lower temperature.

Spherical preferred-orientation specimens were machined from blocks of laminated sheets and the

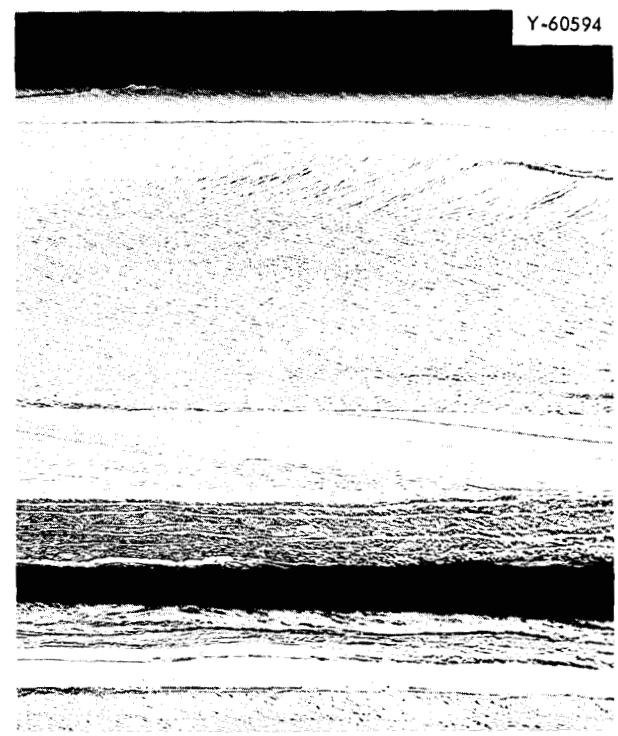

Fig. 10.1. Polycrystalline Niobium Reduced 90% in Thickness by Rolling at Room Temperature. 100×.

[4]Abstracted from *Trans. Met. Soc. AIME* 233, 1138–45 (1965).

[5]Now in Zirconium Metallurgy Group.

[6]Electron Microscopy Group.

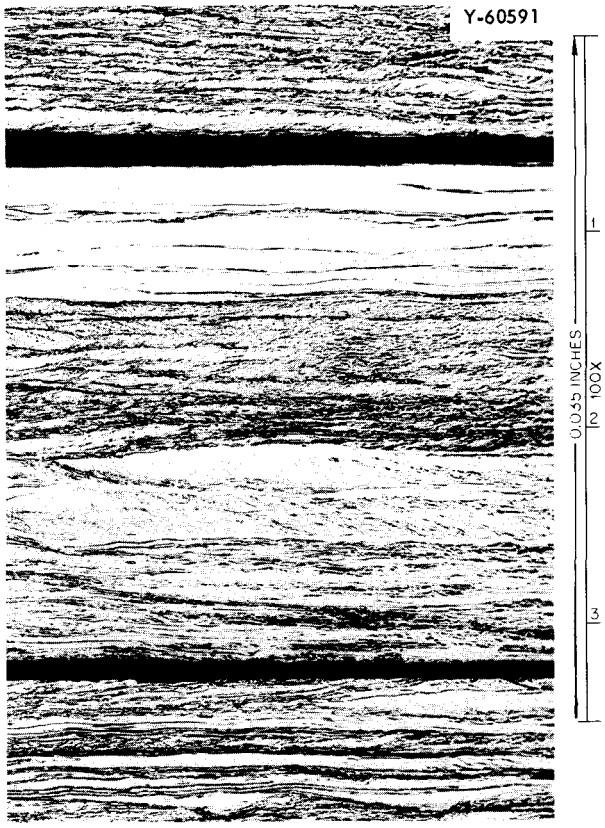

Fig. 10.2. Polycrystalline Niobium Reduced 90% in Thickness by Rolling at 77°K. 100×.

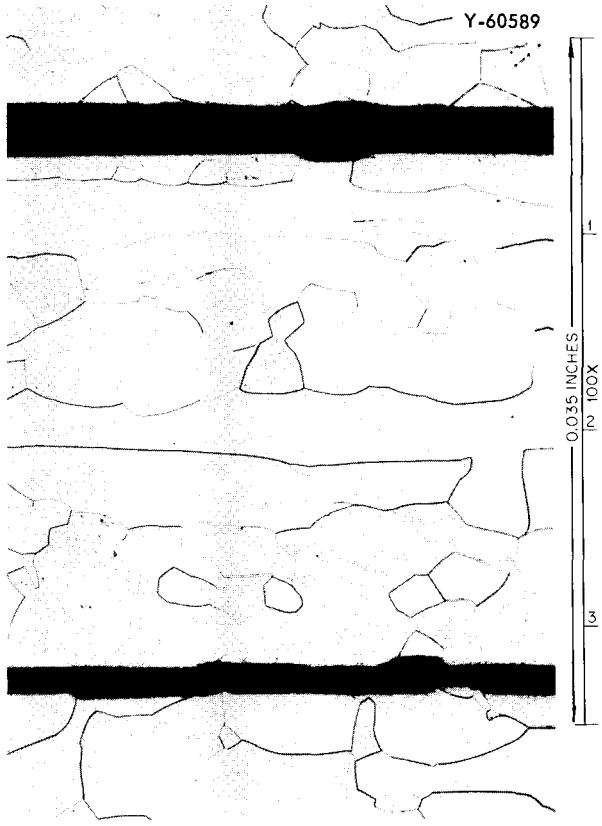

Fig. 10.3. Polycrystalline Niobium Reduced 90% in Thickness by Rolling at 77°K and then Annealed in Vacuum 0.5 hr at 1125°C. 100×.

textures determined by using the ORNL technique. The texture was not the same on both sides of the sheet. X-ray diffraction patterns of opposite sides of several pieces of rolled material showed a very high concentration of (200) planes and very few, if any, (222) planes parallel to one side of the sheet. The opposite side of the sheet contained a high concentration of (222) planes and very few, if any, (200) planes parallel to the rolling plane. We think these inhomogeneities are associated with the laminated microstructures of Figs. 10.1 and 10.2, which in turn, can be traced to the coarse-grained starting material. The grain size apparently was large enough for each grain to deform approximately as a single crystal.

By use of a spherical x-ray specimen that provided data from both sides of the rolled sheet, the textures are provisionally identified as follows:

1. Rolled at liquid-nitrogen temperature – (001) $[\bar{1}10]$ + (112) $[\bar{1}10]$ + unidentified texture.
2. Rolled at room temperature – (001) 10° off $[\bar{1}10]$ + (112) 10° off $[\bar{1}10]$ + unidentified texture. These textures are not as sharp as those in the material rolled at liquid-nitrogen temperature.
3. Rolled at liquid-nitrogen temperature and annealed 0.5 hr at 1125° – (112) $[\bar{1}10]$. The $[\bar{1}10]$ direction is spread toward the transverse direction.
4. Rolled at room temperature and annealed 0.5 hr at 1325°C. Possibly (111) $[11\bar{2}]$ + unidentified textures.

Another series of polycrystalline specimens was rolled from fine-grained randomly oriented starting stock and the textures and annealing kinetics are being determined. These will be compared to the reorientation of single crystals during rolling. The kinetics of recovery and recrystallization in rolled single crystals will be determined and correlated with changes in the substructure.

INFLUENCE OF DEFORMATION BANDS ON FORMATION OF ⟨111⟩ – ⟨001⟩ FIBER TEXTURES IN ALUMINUM[7]

R. E. Reed[8] C. J. McHargue

Single crystals of aluminum were extruded 90% at 296 and 77°K. The resultant double fiber texture had a strong ⟨111⟩ texture component with a weak ⟨001⟩ texture component that varied with starting orientation. Decreasing the temperature of deformation increased the amount of ⟨001⟩ component. The starting orientation and temperature of deformation strongly affected the morphology of the ⟨001⟩ component. A model based upon the formation of deformation bands in aluminum was proposed to explain the effects of orientation and temperature upon the distribution of the ⟨001⟩ texture component present in the double fiber texture of the extruded aluminum single crystals.

[7]Abstract of paper submitted to *Transactions of the Metallurgical Society of AIME*.

EFFECT OF FABRICATION METHOD ON FIBER TEXTURE OF ALUMINUM AND COPPER[9]

R. E. Reed[8] C. J. McHargue

The effect of the mode of fabrication on fiber textures was illustrated by extruding, drawing, and swaging rods of aluminum with an initial diffuse ⟨001⟩ texture. After reductions of 89% at room temperature, the rods contained from 17 to 75% ⟨001⟩ orientations.

Rods of copper and aluminum fabricated from materials with initially random textures showed only minor differences for the same forming methods and temperatures.

[8]Now in Solid State Division.

[9]Summary of paper submitted to *Transactions of the Metallurgical Society of AIME*.

11. Superconducting Materials

M. L. Picklesimer

We are studying the effects of metallurgical variables on the properties of superconducting materials. Of concern are the effects on current-carrying capacity in a magnetic field of such things as morphology, compositions, and spacings of two-phase structures; mechanical strain; preferred orientation; aging and transformation reactions; and fabrication procedures and heat treatment. This study requires sufficient knowledge of the physical metallurgy of the systems of interest, many of which have never been studied. We need to establish a background of information on the transformation kinetics and products, morphologies, phase diagrams, precipitation and aging reactions, and rates of formation of intermetallic compounds. We have reported previously some results on Zr-Nb, Nb-Sn, Tc, and Tc-Zr alloys and compounds. This work has continued and broadened to include more experimental techniques and materials.

TRANSFORMATION KINETICS IN NIOBIUM-ZIRCONIUM ALLOYS

G. R. Love M. L. Picklesimer

The work described last year on the transformation kinetics of niobium-zirconium alloys[1] has been completed and will be reported in detail elsewhere.[2] The separate influences of cold working, zirconium content, grain size, and atmospheric contamination on the rate of transformation from the high-temperature single-phase body-centered cubic structure to the two-phase structures within the miscibility gap were determined. The principal mode of reaction yielded a lamellar structure composed of two body-centered cubic phases of different zirconium content. A time-temperature-transformation (T-T-T) diagram representative of the pearlitic transformation in these alloys is shown in Fig. 11.1 for Nb–33% Zr alloys previously annealed at 1050°C for 1 hr to produce a grain size of 8 to 10 μ. This reaction is relatively sluggish for all zirconium contents; the nose of the curve is displaced only to half the time in an Nb–60% Zr alloy. Cold working, however, decreases the incubation time to about one-tenth in all alloys. Increases in grain size up to about 800 μ increase the incubation time up to tenfold.

In the larger grained samples, a second mode of reaction was observed at the longer times of transformation. The high-temperature beta phase reacted by the precipitation of uniformly distributed particles, which, though detectable metallographically,

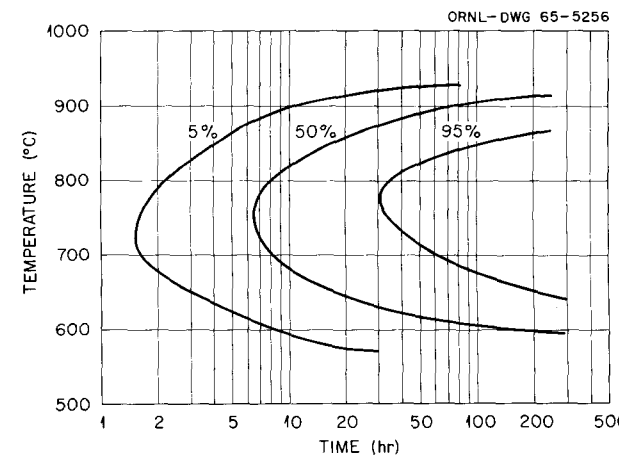

Fig. 11.1. Time-Temperature-Transformation Curves for an Annealed Nb–33% Zr Alloy. Annealed 1 hr at 1050°C. Grain size 8 μ. No detectable contamination.

[1] G. R. Love and M. L. Picklesimer, *Metals and Ceramics Div. Ann. Progr. Rept. June 30, 1964*, ORNL-3670, pp. 21–22.

[2] M. L. Picklesimer and G. R. Love, *Transformation Kinetics in Niobium-Zirconium Alloys* (submitted for publication).

never grew to a size large enough to permit determination of the morphology or composition. Nucleation of these particles was very slow, but they seemed to approach complete reaction faster than the pearlitic transformation. This reaction is observed in the larger grained, annealed materials because the pearlitic structure nucleates only at grain boundaries and grows slowly toward the grain center. Thus, there is still untransformed material in the centers of large grains, in which the second mode of reaction can nucleate. In the finer grained material, the grain center is consumed by the pearlitic reaction before the second mode can nucleate.

Examination of a series of samples contaminated by reaction with a small amount of air at 1400°C indicated that nitrogen and oxygen contamination has little or no effect on the kinetics of the pearlitic transformation. The oxygen content varied appreciably from the surface to the center of the specimen and from grain boundary to grain center in grains near the surface. The transformation kinetics did not vary in these specimens either from surface to center of grains or throughout the specimens on either a macroscopic or microscopic scale.

SUPERCONDUCTING PROPERTIES OF TRANSFORMED NIOBIUM-ZIRCONIUM ALLOYS

J. A. Wheeler, Jr. G. R. Love

Several characteristics of the transformation of the high-temperature body-centered cubic single phase in niobium-zirconium alloys are of particular significance to the investigation of their superconducting properties. This reaction produces a lamellar structure of two body-centered cubic phases of different compositions, in which the thickness and spacing of the individual lamellae can be varied over a range of 250 to 10,000 A by choice of ingot composition and transformation temperature. The apparent superconducting penetration depth in niobium-zirconium alloys of this composition range is between 350 and 700 A (described in the following section), and current densities of as much as 1.2×10^7 amp/cm^2 have been induced to flow within this penetration depth. Therefore, materials capable of carrying remarkably high current densities may be produced by suitable choice of fabrication and heat-treatment procedures. The information obtained in the studies of the transformation kinetics discussed above allows us to produce these lamellar structures with controlled thicknesses and spacings by a suitable choice of transformation temperature, with controlled orientation relative to the postulated current path by a choice of the fraction reacted, with independent matrix hardening due to the second mode of transformation by a choice of the original grain size, and with auxiliary cold work in the transformed structure. Our initial experiments have been concerned with the variation of critical current density in the sample as a function of the total volume fraction reacted to the pearlitic structure.

Initially the critical current density is being determined as a function of volume fraction transformed in Nb–33% Zr alloys. The variation of current-carrying capacity as a function of applied magnetic field was determined for selected levels of volume fraction transformed. The data are incomplete but indicate that the heat-treated samples carried remarkably high critical current densities at relatively low applied fields. The fully transformed pearlitic specimens had essentially the same properties whether the starting material was fully annealed or cold worked. Since complete transformation requires 168 hr in the annealed material and only 48 hr in the cold-worked material, use of the latter considerably reduces the possibility of contamination during heat treatment. The mean lamellar thickness in these samples was about 900 A, about twice the apparent penetration depth for annealed untransformed material.

TECHNIQUE FOR MEASURING CRITICAL CURRENTS

G. R. Love J. A. Wheeler, Jr.

Most critical current measurements are made on wire specimens, with nonsuperconducting leads (such as copper) used to conduct the test current into and out of the cryostat. The problem of reproducibly making adequate noninterfering joints for carrying large currents between normal and superconducting materials has not been solved to

our satisfaction. While the Boom-type joints[3] are acceptable for niobium-zirconium wire samples, they have not been established as adequate for other arbitrarily selected alloy samples. Since the connection of leads and the manufacture of wire specimens are often difficult or impossible, we have examined testing techniques that utilize relatively massive samples and preferably do not require the direct attachment of any leads to the specimen.

A number of techniques might be used to compare the current-carrying ability of bulk samples. All have the advantage that they magnetically induce the currents to flow in the sample and therefore do not require leads to be attached. All have the disadvantage that they involve one or more implicit assumptions about the spatial variation of magnetic fields, and hence of currents, in the samples. We are preparing equipment for magnetic susceptibility measurements in superconductors, but the results we now report were obtained using the ac-magnetization technique first discussed by Bean.[4] The critical assumption of the Bean experiment is that in simultaneous coaxial ac and dc magnetic fields, the magnetization of a sample of superconducting material will trace a minor hysteresis loop as the applied ac field varies. A Fourier analysis of the induced field at the sample surface indicates that it will consist of the applied field and its odd harmonics. The magnitude of these harmonics has been simply related to the magnitude of the critical currents induced to flow in the sample surface by the applied ac field. When the dc field is large relative to the ac field, this induced critical current is essentially the critical current characteristic of the applied dc field. In practice, the applied ac field rarely exceeds a few hundred gauss while the dc field ranges from 1 to 100 kilogauss.

The Bean technique has been tested by measurements on both cold-worked and annealed niobium-zirconium samples 3 mm in diameter and 30 mm long. We prepared 0.010-in.-diam wire samples in each of these conditions and attached Boom-type joints for current leads to them. The directly measured current densities (on the wire samples) were compared to those calculated to flow according to the Bean model. Although we observed the same relative performance in both the heat-treated wire samples and the Bean measurements, the latter always indicated somewhat higher current-carrying capacity. In a sense, this difference should be expected, since the critical current of the wire is limited to that of the poorest section of the wire, while the Bean critical current is an average over a much larger current-carrying cross section. These results lend confidence to the assumption that the Bean measurement does indicate at least relative critical current densities as the sample conditions are varied.

NEAR-SURFACE EFFECTS IN SUPERCONDUCTING NIOBIUM-ZIRCONIUM ALLOYS

H. Ullmaier[5] G. R. Love

An additional benefit of the Bean measurement described above is that it can yield significant new information concerning the surface layers of a superconductor. When the amplitude of the applied ac field is small, essentially all shielding of the applied field occurs within a few hundred angstroms of the sample surface. For field penetrations less than some critical depth, δ, this layer apparently has homogeneous properties. Analysis of the measurements can give, for a single sample, the value of the critical current induced in the surface layer, the thickness of this layer, and the value of the bulk critical current. The values derived for the thickness of the layer and its critical current density in both cold-worked and annealed Nb–33% Zr alloys are compared in Table 11.1 with the London depths and current densities calculated for several ideal "soft" superconductors. In view of the pronounced differences in all the other physical properties between these soft superconductors and the niobium-zirconium alloys, the similarity in properties of the surface layers is remarkable. The apparent thickness of this near-surface layer in niobium-zirconium alloys is not a function of the applied dc field, and the change in apparent thickness with cold work is in the direction predicted from the changes produced in electronic mean free path by cold work.

[3]A compression joint of copper on the specimen wire, suggested by R. W. Boom, formerly of the Electronuclear Division. For a discussion of difficulties with this joint, see: G. R. Love and J. A. Wheeler, Jr., *Metals and Ceramics Div. Ann. Progr. Rept. June 30, 1964*, ORNL-3670, p. 22.

[4]C. P. Bean, *Rev. Mod. Phys.* **36**, 31 (1964).

[5]Thermonuclear Division.

Table 11.1. A Comparison of London Depths and Nominal Critical Current Densities Within the London Layer in Soft Superconductors with the Observed Thickness and Current Densities in Nb–33% Zr

Material	Reference	London Depth (A)	Critical Depth δ (A)	Critical Current Density (amp/cm^2)
				$\times 10^7$
Sn	*a*	510		1.77
Al	*a*	492		0.59
Pb	*b*	390		6.03
In	*b*	640		1.34
Hg	c	710		1.40
Nb–33% Zr (annealed)			355	~1.9
Nb–33% Zr (cold worked)			735	1.15

[a]T. E. Faber and A. B. Pippard, *Proc. Roy. Soc. (London), Ser. A* **231**, 336 (1955)

[b]J. Lock, *Proc. Roy. Soc. (London), Ser. A* **208**, 391 (1951).

[c]A. B. Pippard, *Proc. Roy. Soc. (London), Ser. A* **191**, 399 (1947).

A detailed description and interpretation of these experimental results will be presented elsewhere.[6]

ZIRCONIUM-URANIUM ALLOYS

J. A. Wheeler, Jr. G. R. Love

We surveyed the phase diagram and transformation kinetics of zirconium-uranium alloys in the range 20 to 40 at. % U, using both metallographic observation and continuous measurement of electrical resistivity throughout programmed temperature cycles. These investigations confirmed the general form of the phase diagram suggested by Holden and Seymour.[7] We also noted that the transformation of the high-temperature body-centered cubic phase to the delta phase is quite rapid. Free cooling from 800°C in vacuum (about 30°C/min near the transformation temperature) supercooled the specimen no more than 50°C and produced recalescence when the transformation began. The temperature coefficient of electrical resistivity for the delta phase was negative, approximately −0.024/°C, throughout the temperature range of 50 to 590°C. No measurements were made below 50°C.

This alloy system is of considerable metallurgical interest, both for its multitude of solid-state reactions and for the possibility of introducing damage into the lattice by nuclear fission products, which might affect the superconducting properties. A sample of the delta-phase alloy was tested using our ac susceptibility technique and a ballistic magnometer in the equipment of S. T. Sekula and R. W. Kernohan of the Solid State Division. In both tests the sample was not superconducting in zero field at 4.2°K. At the present time, no further work is planned on this alloy system.

TECHNETIUM AND ITS ALLOYS

J. A. Wheeler, Jr. G. R. Love
M. L. Picklesimer

The glove-box facility constructed for the metallurgical study and preparation of technetium-base alloys is in essentially full-scale operation. This facility will be used to study both the physical metallurgy and superconducting properties of technetium and its alloys.

With the assistance of the Melting and Casting Group of the Division and the Superconductivity Group of the Solid State Division, we made the largest casting of pure technetium yet obtained. The casting, shown in Fig. 11.2, with boss weighed approximately 100 g.

Technetium powder of nominal purity 96.8 to 99.4% (remainder primarily oxygen) was obtained from the Isotopes Division. It was cold pressed at 30,000 psi in our glove-box facility to pellets

[6]G. R. Love, *Near-Surface Measurements on Superconducting Niobium-Zirconium Alloys* (to be submitted for publication).

[7]A. N. Holden and W. E. Seymour, *Trans. AIME* **206**, 1312 (1956).

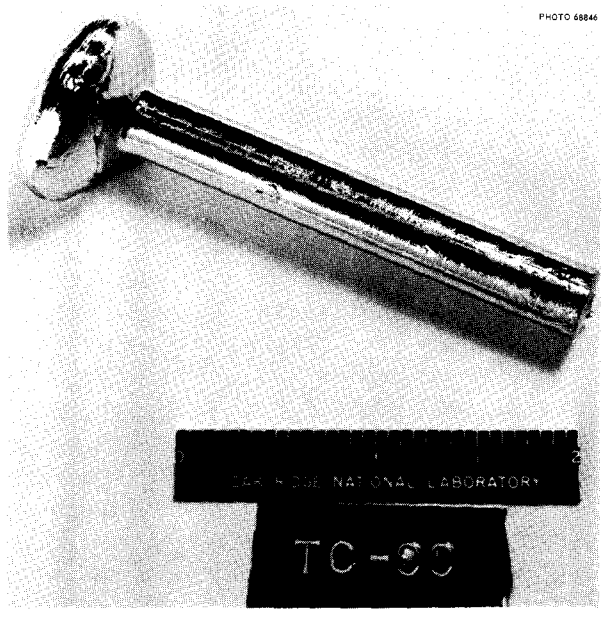

Fig. 11.2. As-Cast Ingot of Purified Technetium. Approximately 100 g in weight.

$\frac{1}{2}$ in. high and $\frac{1}{2}$ in. in diameter (approximately 4 g). Batches of five or six pellets were further purified of oxygen by sintering in pure flowing hydrogen for 4 hr at 1000°C in the muffle furnaces attached to one of the glove boxes. The pellets were then transferred in about 25-g quantities to the Melting and Casting Laboratory, where they were arc melted (nonconsumable electrode) to dense buttons. Four of these dense buttons were charged into an arc drop-casting furnace and melted several times without dropping to ensure thorough outgassing. The charge was then drop-cast into a chilled copper mold. The ingot was $\frac{3}{8}$ in. in diameter and 2.5 in. long and had a large boss on top to act as a feeder to prevent a shrinkage cavity in the top of the cylindrical section. The primary impurity in the as-received powders was oxygen retained from the purification and metal powder-production steps. The weight losses observed during sintering were only slightly greater than could be explained by the removal of oxygen. After the sintering operation, the total weight loss for all melting steps was less than 1%. The contamination of the melting furnace was minimal and decontamination required less than one man-day.

This technetium ingot has been cut from its boss, inserted into an evacuated nickel-tube capsule, and cold swaged to about 10% reduction in area. Further working was stopped when a crack was discovered in the sealing weld in the end of the capsule. All operations except for the swaging were carried out in the glove-box facility.

The glove boxes containing facilities for cutting, mounting, polishing, and etching metallographic specimens of technetium-base alloys are now also in full operation.

12. Surface Reactions of Metals

J. V. Cathcart

Most metals and alloys are prevented from undergoing catastrophic oxidation through the formation of thin oxide films on their surfaces. These films restrict further oxidation to an extent that depends largely upon the properties of the films at various stages of their development. Our primary task is to investigate the mechanism of film formation, to study the properties of the films, and to determine the factors that control their degree of protectiveness.

The major feature of our research continues to be an investigation of the influence of stresses generated during the course of oxidation on the mechanism of oxidation. For example, one project involves a study of stress generation resulting in refractory metals from the solution of oxygen in the surface layers of the metal. A second project consists of a study of the thin film stage of oxidation of dilute copper-base alloys where regions of lattice disregistry in the oxide films are of importance because they provide paths of easy diffusion through the oxide. Other work in the group includes an investigation of the corrosion of aluminum- and iron-base alloys in high-temperature water, a study of diffusion in tantalum and niobium, and an evaluation of the contribution of magnetic order to the specific heats of nickel and several nickel-copper alloys.

OXIDATION OF COPPER-BASE ALLOYS

J. V. Cathcart G. F. Petersen

Our previous investigations[1] of the early stages of oxidation of pure (99.999%) copper single crystals led to the conclusion that paths of easy diffusion, associated with regions of lattice disregistry in the oxide, play an important role in the transport of cations across the oxide films. A study of the thin-film stage of oxidation of dilute alloys was undertaken to provide a further means of testing this hypothesis and to obtain a better understanding of the fundamentals of alloy oxidation.

Single-crystal specimens of copper containing from 0.1 to 2.0 at. % Ni, Ag, Al, or Fe were grown in the form of spheres, annealed for 200 hr at 1000°C, and oxidized for 30 min at 250°C and 1 atm oxygen pressure. Specimens of this type have the advantage of revealing all possible crystallographic planes a maximum number of times and of permitting a ready qualitative comparison of the relative rates of oxidation of different crystal orientations. The influence on the oxidation rate of even small additions of the second metal was surprisingly large. Depending on the crystal plane and alloy composition, changes in oxidation rate up to a factor of 5 relative to pure copper were observed.

We are beginning a more detailed study of the oxide films formed on these alloys. X-ray and reflection electron diffraction studies of the oxide formed on the (111) of a Cu–0.4 at. % Ni alloy detected no NiO. This plane oxidized half as fast as in pure copper, and the initial x-ray results indicated that this reduction in rate was in part due to a reduction in the degree of lattice disregistry in the oxide film. However, considerable additional work will be required before the structural details of these films are completely understood.

[1] J. V. Cathcart and G. F. Petersen, *Metals and Ceramics Div. Ann. Progr. Rept. June 30, 1964*, ORNL-3670, pp. 27–28.

AQUEOUS CORROSION STUDIES

J. V. Cathcart

Previous studies[2] of the air oxidation at high temperatures of iron-base alloys containing 6 to 25% Cr and 4 to 6% Al showed that the surface oxide was Al_2O_3 and that the addition of 1% Y served to stabilize the Al_2O_3 layer, making it highly adherent. In cooperation with the Metal Forming and Casting Group we attempted to determine whether or not small yttrium additions produced a similar beneficial effect during the aqueous corrosion of aluminum alloys in high-temperature water.

Aluminum alloys containing from 2 to 10% Y were tested in an autoclave at 200°C and approximately 180 psi, and the results were compared with those for 99.999% pure aluminum. The characteristic features of the corrosion of pure aluminum in distilled water are the extensive intergranular attack and the marked physical deformation of the specimens. Yttrium additions greatly reduced the overall corrosion rate of the specimens, and in particular, eliminated the intergranular attack. A minimum rate of corrosion was observed for an yttrium concentration of approximately 2%.

As a further test of the effect of the presence of a second phase on the corrosion of aluminum alloys, we also investigated the corrosion of an Al–20% Zn alloy at 200°C. As in the case of the aluminum-yttrium system, a second phase was present in the alloy at the test temperature, and the overall corrosion rate was significantly reduced relative to that of pure aluminum. Also, intergranular attack was reduced.

Pure yttrium is anodic with respect to aluminum as is, in all probability, the intermetallic YAl_3, which constitutes the second phase in the Al–2% Y alloy. The increased corrosion resistance of yttrium-aluminum alloys may thus be attributable to the second phase acting as a sacrificial anode.

Zinc, on the other hand, is cathodic with respect to aluminum, and a different explanation is required for the enhanced corrosion resistance exhibited by the Al–20% Zn alloy. The results obtained with this alloy are phenomenologically similar to those obtained earlier by Draley[3] in his studies of aluminum-base alloys containing iron and nickel. Draley suggested that the intergranular attack in pure aluminum is caused by the precipitation of dissolved hydrogen in the grain boundaries, whereas the improved corrosion resistance of the Al-Fe-Ni specimens could be explained by noting that even small additions of iron or nickel to aluminum produced a second phase that is cathodic with respect to the matrix. The nascent hydrogen liberated at the surface of the second phase does not dissolve in the matrix, but recombines, presumably catalytically, at the surface.

Thus the chief role of the zinc-rich phase in aluminum-zinc alloys appears to be that of preventing excessive amounts of hydrogen from going into solution in the aluminum matrix. The YAl_3 phase may also serve a similar function in the aluminum-yttrium alloys.

[2]C. S. Wukusick and J. F. Collins, *Mater. Res. Std.* 4, 637–46 (1964).

[3]J. E. Draley and W. E. Ruther, *Corrosion* 12, 480t–90t (1956).

REFRACTORY METAL OXIDATION

R. E. Pawel J. V. Cathcart

Our activities have centered upon the study of self-induced stresses produced during oxidation of many refractory metals. These stresses, which exist in the substrate metal as well as in the oxide film, can affect the nature of the resulting oxide product and, consequently, the oxidation kinetics. Several phases of this investigation are presently in progress.

Stress Generation in Refractory Metals During Oxidation

Studies of the generation of surface stresses during oxidation by measuring the flexure of thin metal specimens oxidized on one side were continued. This work now includes flexure measurements for tantalum specimens while they are oxidized at 350 to 550°C and for niobium specimens at 400 to 425°C. Our original model,[4] in which stress was related to the oxygen solution process in the surface layers of the metal, was reasonably consistent with the new experimental results up to oxidation times sufficient to produce voluminous pentoxide scales on the surface of the

[4]R. E. Pawel, J. V. Cathcart, and J. J. Campbell, *J. Electrochem. Soc.* 110, 551 (1963).

specimens. For tantalum, these times were greater than 200 hr at 350°C and ranged to approximately 30 min at 550°C. In niobium, deviations from the behavior predicted by the model were more closely associated with the "breakaway" phase of the oxidation process than for tantalum. An unambiguous explanation is not yet available; however, the importance of stresses associated with the oxide films themselves apparently increases and becomes dominant as the rate of film formation increases.

Additional corroborating evidence for the proposed stress generation model was obtained from flexure experiments conducted on anodized specimens. Since the anodic film permits the passage of oxygen into the metal without thickening of the film (see next section), any change in flexure should be independent of the possible influence of the film *per se*. Since specimens indeed bent under these conditions, where oxygen solution in the metal was the principal event, it is reasonable to ascribe stress buildup to this source. The flexure, translated into maximum bending stress values, for an anodized tantalum specimen is compared to the oxidation rate curve for oxidation at 500°C and 1 atm pressure in Fig. 12.1. Although the rather uncertain boundary conditions controlling the precise distribution of oxygen in the metal prevented an analytical evaluation of the maximum surface stress under these conditions, metallographic and x-ray evidence indicated that surface stress levels equivalent to those in unanodized tantalum were generated (i.e., approximately 50,000 psi compression).

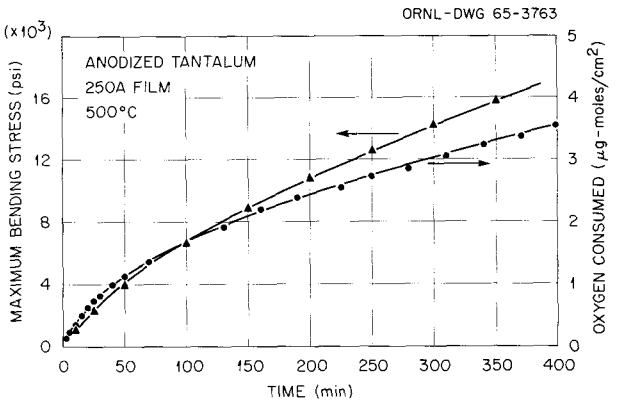

Fig. 12.1. Bending-Stress vs Time Compared with the Oxidation Rate Curve for an Anodized Tantalum Specimen.

Anodic Oxide Films

In order to further characterize the effect of the physical state of the oxide film on the oxidation process for the refractory metals, our studies involving anodic oxide films were continued. Results of the investigation of structure and crystallization phenomena in stripped anodic films have recently been published.[5,6] Quantitative measurements of the effect of the presence of anodic films upon the gaseous oxidation rate have been completed for tantalum for temperatures from 400 to 575°C with anodic film thicknesses from 75 to 4000 A. At a given oxidation temperature, anodic films generally decreased the gross oxygen consumption rate compared to that of unanodized tantalum and also delayed the appearance of "breakaway" (an abrupt increase in the oxidation rate common to tantalum, niobium, and several other metals). However, considerable amounts of oxygen were consumed at a rate that varied inversely with the anodic film thickness, dissolving in the metal without changing the thickness of the anodic film. Anodic films as thin as 40 A could exert a substantial influence on the normal course of gaseous oxidation of electropolished tantalum.

In addition, from the data obtained thus far we estimated oxygen permeation rates as a function of temperature for the amorphous anodic films. The temperature dependence of the permeation rate expressed in Arrhenius form corresponded to an activation energy of about 45 kcal/mole. Unless an unusual temperature dependence of the oxygen concentration is involved, this value is quite low compared to that estimated for diffusion through crystalline oxide.

Oxidation of Tungsten

In preliminary experiments, we examined the oxidation kinetics and oxide morphology in the thin-film oxidation stage for tungsten at temperatures in the range 400 to 600°C. Specimen preparation procedures were established and the reproducibility of both kinetics and morphology appeared

[5]R. E. Pawel, *Rev. Sci. Instr.* **35**, 1066 (1964).

[6]R. E. Pawel and J. J. Campbell, *J. Electrochem. Soc.* **111**, 1230 (1964).

to be satisfactory. As in the cases of tantalum and niobium, the early-stage oxidation kinetics indicated that the mechanism changes during this part of the process. However, other qualitative observations indicate substantial deviations in the general characteristics of oxidation from those exhibited by tantalum and niobium.

DIFFUSION STUDIES

R. E. Pawel T. S. Lundy[7]

The investigation of tracer diffusion in tantalum by means of the anodic film sectioning technique[8,9] was extended both to higher temperatures, where the results could be compared with those obtained by lathe machining and grinding, and to lower temperatures, where the direct determination of diffusion profiles and coefficients is most difficult. The technique was also used to supplement data for diffusion in niobium.[10]

Because the *maximum* thickness of a single section using the anodic film technique is limited to about 1000 A, it was practical to compare results with the other techniques only over very narrow temperature ranges. The overlap in our case occurred over the temperature range 2000–2300°C. The data from different methods agreed within the limits of reproducibility of a single method. Although the anodic film sectioning technique is obviously most useful for these metals at low temperatures where diffusion distances are exceedingly small, it competed favorably in accuracy and convenience with the grinding techniques for obtaining diffusion coefficients in the range of 10^{-10} to 10^{-11} cm^2/sec. In addition, the lower temperature limit of our diffusion data for ^{95}Nb in tantalum was pushed to 920°C, at which a lattice diffusion coefficient of 2.5×10^{-19} cm^2/sec was measured.

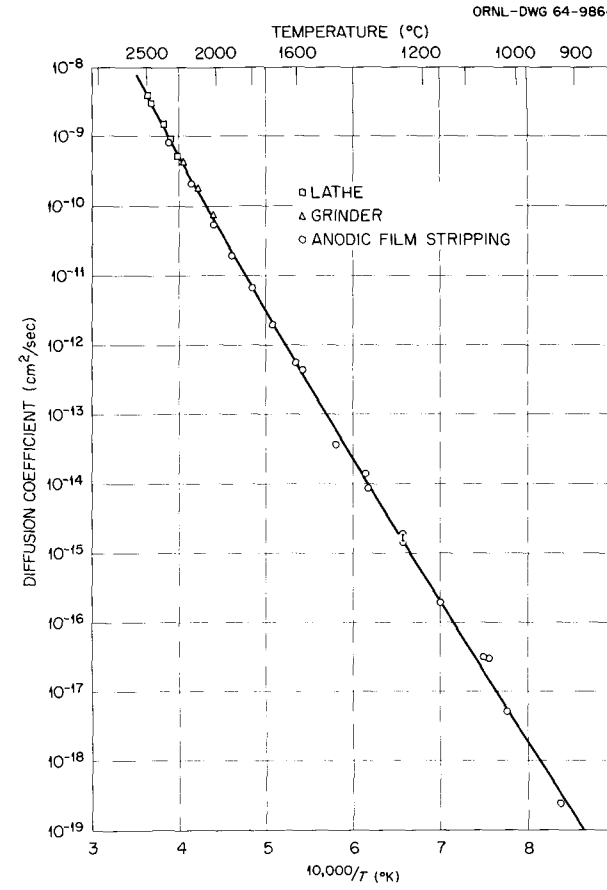

Fig. 12.2. Arrhenius Plot of the Diffusion Coefficients for ^{95}Nb in Ta. *Note overlap of data obtained by lathe, precision grinder, and anodic film stripping techniques.*

Our results for the diffusion of ^{95}Nb in tantalum[11] are summarized in Fig. 12.2, in which a 10^{10}-fold variation in the diffusion coefficient is shown in Arrhenius form. These results indicate only a slight deviation from ideal behavior; thus, the equation $D = 0.23 \exp(-98{,}700/RT)$ described the temperature dependence of the diffusion coefficient over the whole temperature range within 20%. Data were also obtained for the diffusion of ^{182}Ta in tantalum over a slightly shorter range of temperature, 1250–2200°C. The ratio of the diffusion constants for niobium and tantalum in tantalum was constant within experimental error at $D_{Nb}/D_{Ta} = 1.85 \pm 0.15$. Therefore, substitutional diffusion in

[7]Solid Reactions Studies Group.

[8]R. E. Pawel and T. S. Lundy, *Acta Met.* 13, 345 (1965).

[9]T. S. Lundy, J. I. Federer, R. E. Pawel, and F. R. Winslow, "A Summary of ORNL Work on Diffusion in Beta Zirconium, Vanadium, Columbium and Tantalum," pp. 35–49 in *Diffusion in Body-Centered Cubic Metals*, American Society for Metals, Metals Park, Ohio, 1965.

[10]T. S. Lundy, F. R. Winslow, R. E. Pawel, and C. J. McHargue, "Diffusion of Nb-95 and Ta-182 in Niobium," accepted for publication in *Transactions of AIME*.

[11]R. E. Pawel and T. S. Lundy, *Phys. Chem. Solids* 26, 937–42 (1965).

tantalum is apparently not subject to an anomalous temperature dependence such as that observed in the body-centered cubic systems β-zirconium and β-titanium. Other work on diffusion is reported in Chap. 3 of this report.

TREATMENT OF SPECIFIC HEAT DATA

R. E. Pawel E. E. Stansbury[12]

The specific heat contribution due to magnetic order in pure nickel and several nickel-copper alloys was determined by subtracting the theoretical specific heat, computed on the basis of no magnetic effects, from recently determined experimental values.[13–15] The energy and entropy changes associated with the ferromagnetic transition were calculated and, at least for pure nickel, found to be low compared to those predicted through the use of popular electronic models. The magnitude of the discrepancy between the predicted and observed energy and entropy of magnetic order could be greatly reduced if the measured average number of unpaired spins per atom in metallic nickel is accounted for by distributions of $3d^8$ and $3d^{10}$ electron configurations rather than by $3d^9$ and $3d^{10}$.

[12]Consultant from the University of Tennessee.

[13]R. E. Pawel and E. E. Stansbury, *Phys. Chem. Solids* **26**, 607 (1965).

[14]R. E. Pawel and E. E. Stansbury, *Phys. Chem. Solids* **26**, 757 (1965).

[15]R. E. Pawel and E. E. Stansbury, accepted for publication in *Journal of Applied Physics*.

13. X-Ray Diffraction

H. L. Yakel

The activities of the X-Ray Diffraction Group are equally divided between service functions, in which we support other programs of the Laboratory, and several basic research programs of our own. These activities are not mutually exclusive and their interaction has often provided new stimuli in both areas.

Our laboratory maintains the capability to handle a large volume of service problems whose nature and complexity may cover a wide spectrum of experimental techniques and analytical procedures. Lattice parameter estimations, crystal orientation and perfection studies, investigations of thermally induced phase transitions, and complete crystal structure determinations are examples of the variety of problems treated during the past year.

Fundamental research programs are concerned with diffraction studies of departures from perfection in real crystalline structures. Causes of these imperfections include solid-solution formation, precipitation in crystalline solids, and radiation damage. Both experimental observation and theoretical interpretation of experiment have been advanced within the period of this report.

ROUTINE ANALYSES

O. B. Cavin R. M. Steele
L. A. Harris H. L. Yakel

Samples submitted to the X-Ray Diffraction Laboratory for routine analysis during the period of this report exceeded 1000 in number. While results pertinent to the work of other programs of the Division are cited elsewhere in this report, crystallographic data for previously unreported compounds and alloys are collected in Table 13.1.

Diffraction studies of irradiated MgO and Al_2O_3 powders were initiated for the Reactor Chemistry Division. Lattice expansions occurred, and Bragg maxima tended to become broad at high fast-neutron doses, but no anomalous diffuse intensity, such as was observed in irradiated-BeO powder patterns, appears.

Investigation of phases present in vapor-deposited tungsten-rhenium alloys demonstrated[1] the presence of an A15-type structure in as-deposited alloys with 13 to 45% Re. Heat treatment of an as-deposited 37% Re alloy at 1500°C for 1 hr partially converted the A15-type structure to α-tungsten (A2 type) and a sigma phase (tetragonal, $a_0 = 9.63$ A, $c_0 = 4.985$ A).

Preliminary single-crystal diffraction data for $KMgCl_3$ were obtained at the request of the Spectroscopy of Ionic Media Group, who are examining the absorption spectrum of nickel substituted for magnesium in this compound. The data indicate a pseudo-tetragonal orthorhombic unit cell with

$$a_0 = 6.955 \pm 0.003 \text{ A},$$

$$b_0 = 6.971 \pm 0.004 \text{ A},$$

$$c_0 = 9.922 \pm 0.003 \text{ A}.$$

The structure is a distortion of the ideal perovskite-type structure, such as has been reported[2] for $GdFeO_3$. Although twinning makes the collection of accurate intensity data difficult, we plan an analysis of detailed atom positions in this structure.

Our continuing study of the UC_2-ThC_2 pseudobinary system has centered on the eutectoid composition of approximately 38% ThC_2 to more

[1] J. I. Federer and R. M. Steele, *Nature* **205**, 587 (1965).

[2] S. Geller and E. A. Wood, *Acta Cryst.* **9**, 563 (1956).

Table 13.1. Crystallographic Data for New Alloys and Compounds

Composition (% are atomic)	Crystal System	Lattice Parameters (A)	Comments
50% Tb–25% Cu–25% Zn	Cubic	3.54 ± 0.01	B2(CsCl)-type
50% Tb–25% Ag–25% Pd	Cubic	3.551 ± 0.005	A2-type bcc
50% Tb–37.5% Ag–12.5% Pd	Cubic	3.578 ± 0.005	A2-type bcc
50% Tb–20% Ag–30% In	Cubic	3.69 ± 0.01	A1-type fcc
50% Tb–30% Ag–20% In	Cubic	3.68 ± 0.01	A1-type fcc
50% Tb–40% Ag–10% In	Cubic	3.65 ± 0.01	A1-type fcc
25% Tb–50% Ag–25% La	Cubic	3.705 ± 0.005	A2-type bcc
25% Tb–50% Ag–25% Y	Cubic	3.610 ± 0.005	A2-type bcc
Co_3Cr	Cubic	3.55 ± 0.01	A1-type fcc
$TbRh_2$	Cubic	7.492 ± 0.005	C15($MgCu_2$)-type
$(NH_4)_2TcF_6$[a]	Hexagonal	a_0 = 5.994 ± 0.005 c_0 = 4.800 ± 0.005	Isomorphous with $(NH_4)_2ReF_6$

[a]D. E. LaValle, W. T. Smith, and R. M. Steele, "Rhenium Nitrogen Fluoride and Rhenium Tetrafluoride," accepted for publication in *Journal of Inorganic and Nuclear Chemistry*.

accurately determine the transition temperatures, the existence of a proposed miscibility gap within the high-temperature face-centered cubic phase field, and the kinetics of transformation. High-temperature powder-diffraction data obtained in the period of this report failed to disclose a miscibility gap in the face-centered cubic phase field near 38% of ThC_2, and suggest that the eutectoid transformation cannot be suppressed by quenching. Long-period anneals of ThC_2 at temperatures below the monoclinic-cubic (or tetragonal) transition temperature produced materials whose diffraction patterns were sharp and had well-resolved $K\alpha_1$-$K\alpha_2$ doublets at the highest observable scattering angles. Monoclinic unit cell parameters determined from a pattern recorded with Cr $K\alpha$ radiation ($\bar{\lambda}$ = 2.29092A) were

$$a_0 = 8.269 \pm 0.005 \text{ A},$$

$$b_0 = 4.232 \pm 0.002 \text{ A},$$

$$c_0 = 10.583 \pm 0.006 \text{ A},$$

$$\beta = 90.23 \pm 0.04\ ^\circ.$$

CRYSTAL STRUCTURE OF MIXED OXIDE COMPOUNDS

The Crystal Structure of Calcium Beryllate[3] ($Ca_{12}Be_{17}O_{29}$)

L. A. Harris H. L. Yakel

Calcium beryllate crystallizes in the cubic system with a_0 = 14.023 ± 0.05 A. Its crystal structure has been determined by standard three-dimensional Patterson and difference Fourier methods. Refinement of the structure in the acentric space group $F\bar{4}3m$ by iterative structure factor-least-squares calculations gave a final error index R = 0.066. The ideal composition of the compound was found to be $Ca_{12}Be_{17}O_{29}$ (four formula weights per unit cell) as a result of this analysis.

The structure is described as composed of rods of close atom packing running parallel to $\langle 110 \rangle$ crystal directions and intersecting at 4*b* sites of

[3]Abstract of paper submitted for publication in *Acta Crystallographica*.

$F\bar{4}3m$. As the rods diverge from the 4*b* sites, large (5.4 A free diameter) holes are left centered at 4*a* positions.

Two types of calcium-oxygen coordinations are found; one has eight oxygen atoms in the form of a rectangular prism about a calcium atom while the other is a sixfold grouping similar to that reported in cubic rare-earth oxides. Of the 68 beryllium atoms per unit cell, 20 have nearly normal tetrahedral oxygen atom coordination, 32 have three short and one long oxygen atom contact, and the remaining 16 have an unusual trigonal oxygen atom coordination.

An X-Ray Diffraction Investigation[4] of a Phase Transformation in Europium Molybdate ($Eu_{5+x}MoO_{10.5+y}$)

L. A. Harris A. T. Chapman[6]
R. A. Potter[5]

A compound $Eu_{5+x}MoO_{10.5+y}$ ($x \cong 0.3$; $y \cong 0.2$) has been synthesized by solid-state methods. A high-temperature x-ray diffractometer was used to observe a phase transformation in this compound. The transformation involves the inversion of a low-temperature rhombohedral phase to a cubic one above 1550 ± 25°C. The phase transformation is readily reversible in air and appears to fit Buerger's "displacive transformation" classification.

Optical and powder x-ray film data were obtained for both phases. Structure factor calculations carried out for several critical reflections of the high-temperature phase suggested that it is an anion-defect fluorite structure. Diffraction experiments using Cu Kα and Cr Kα radiations for extended exposure times failed to reveal any superlattice reflection, which would have indicated a possible pyrochlore-type structure.

[4]Abstract of paper presented at the Philadelphia Meeting of the American Ceramic Society, May 1–6, 1965.

[5]Ceramics Laboratory.

[6]Crystal Physics Group.

THE USE OF LOW-NOISE PREAMPLIFIERS WITH A PROPORTIONAL COUNTER AND A DD2 AMPLIFIER

R. W. Hendricks

In many problems of x-ray analysis either a proportional counter or a scintillation counter is needed to eliminate pulses generated by radiation of undesired energy. To perform this electronic separation as efficiently as possible, the resolution of the counter tube and amplification system must be optimized.

A Reuter-Stokes RSG-30A proportional counter and a DD2 Linear Amplifier were chosen as basic components. To these were added as preamplifiers either a White Cathode Follower, an ORTEC 105XL, or a TENNELEC 100B charge-sensitive low-noise preamplifier. Radiation sources were ^{55}Fe, ^{75}Se, and ^{109}Cd isotopes, which emit 5.90 kev (Mn Kα), 10.54 kev (As Kα), and 22.16 kev (Ag Kα) x rays respectively.

Table 13.2. Resolutions[a] Obtained with Several Preamplifiers at Three X-Ray Energies

Isotope	Energy (kev)	Best Resolution Attained (%)			
		Reuter-Stokes Data	White Cathode Follower	ORTEC 105XL	TENNELEC 100B
^{55}Fe	5.90	16.4	16.8	16.2	16.2
^{75}Se	10.54			12.3	12.3
^{109}Cd	22.16	8.3	11.1	8.6	8.6

[a]Resolution is defined as the full width of half maximum of the pulse-height distribution peak divided by the peak position.

The resolution achieved by the various instrument combinations is compared quantitatively in Table 13.2 together with the resolution quoted by Reuter-Stokes where possible. Examination of these data permitted the following major conclusions to be drawn:

1. The use of a low-noise preamplifier in conjunction with an RSG-30A proportional counter and a DD2 linear amplifier provides the optimum conditions for operation of the counting system.
2. Either of the charge-sensitive low-noise preamplifiers examined achieves these conditions.
3. Experiments with amplifiers other than the DD2 (e.g., ORTEC-221, TENNELEC TC200) showed no substantial advantage for these instruments over the DD2 for the type of single-channel analysis usually required in x-ray diffraction problems.

X-RAY SCATTERING FROM IRRADIATED BeO SINGLE CRYSTALS

H. L. Yakel

An increasing volume of evidence[7] suggests that, in the range of fast-neutron doses from 10^{20} to 10^{22} neutrons/cm^2, x-ray diffraction patterns of irradiated BeO show a pronounced decrease in the intensities of the sharp Bragg maxima of reflections $hk{\cdot}l$ with $l \neq 0$. This decrease, which might be considered as an anomalous anisotropic thermal vibration effect in the **c*** direction of reciprocal space, is more severe the greater $l^2/(h^2 + k^2 + hk)$ and the greater the dose. One can achieve doses so large that no $hk{\cdot}l$ reflection with $l \neq 0$ would produce an observable sharp Bragg maximum, and in such a case all the scattered intensity near any reciprocal lattice point with $l \neq 0$ would be interpreted as diffuse scattering.

One may also conclude that, as fast-neutron dose increases, the sharp Bragg maxima of nonprism reflections shift toward much smaller $l\mathbf{c}^*$ values than those characteristic of the diffuse intensity near $hk{\cdot}l$. If the $|\mathbf{c}^*|$ value associated with the sharp Bragg maxima is associated with the average c_0 spacing of the entire crystal or crystallite, then the c_0 spacings so computed may rise to 4.5 to 4.6 A ($\Delta c/c$ = 3 to 5%) in the 10^{21} to 10^{22} neutrons/cm^2 dose range. Correlation of observed density decrease and unit cell expansion would therefore improve, as demonstrated by Australian workers.[8]

One may note that the theory proposed by Yakel and Borie[9] to account for powder pattern line shapes from BeO irradiated to 3.6×10^{21} neutrons/cm^2 at 110°C also gives an average c_0 spacing of the entire crystal through the relation

$$c_0 = (1 - \alpha)c + \alpha(1 + \epsilon)c = (1 + \alpha\epsilon)c ,$$

where α is the probability of occurrence of a spacing anomaly, ϵ is the fractional expansion which occurs at an anomaly, and c is twice the average spacing between layers when no anomaly is present. With $\alpha = 0.05$, $\epsilon = 0.4$, and $c = 4.44$, c_0 is 4.53 A.

We have reexamined our powder and single-crystal diffraction data in the light of the new evidence discussed above and have found substantial agreement with it in our powder data. Unfortunately, we have not irradiated single crystals of BeO to what is apparently the critical dose range for the weakening, shifting, and eventual disappearance of the sharp Bragg maxima of reflections such as the 00·2. This range is surprisingly narrow and lies between about 1×10^{20} and 7×10^{20} neutrons/cm^2. We have, however, been able to study a flux-grown BeO crystal irradiated to 3.7×10^{20} neutrons/cm^2 at <100°C, which was generously supplied by S. B. Austerman.[10] A 2θ scan of the 00·2 reflection from this crystal is compared in Fig. 13.1 with similar scans of the same reflection from crystals that we had irradiated to 0.4×10^{20} and 7.1×10^{20} neutrons/cm^2. A profile of the 00·2 reflection from an unirradiated crystal is shown at the right; all data were collected in (+1, +1) double-crystal geometry with Cu Kα radiation monochromatized by first-order reflection from 111 planes of a flat nearly perfect germanium crystal.

[7] D. G. Walker, R. M. Mayer, and B. S. Hickman, *J. Nucl. Mater.* 14, 147–58 (1964).

[8] B. S. Hickman, D. G. Walker, and R. J. Hemphill, *J. Nucl. Mater.* 14, 167–74 (1964).

[9] H. L. Yakel and B. S. Borie, *Acta Cryst.* 16, 589 (1963).

[10] Atomics International Corporation, Canoga Park, Calif.

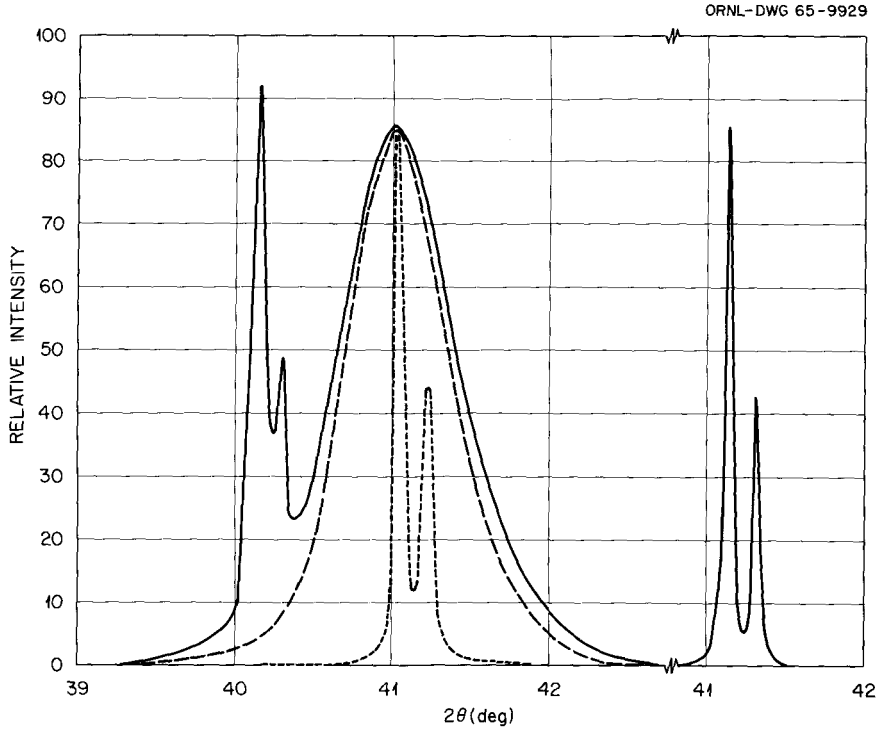

Fig. 13.1. The 2θ Profiles of 00·2 Reflections from BeO Single Crystals Irradiated to 0.4×10^{20} neutrons/cm^2 at 147°C (Broken Curve), 3.7×10^{20} neutrons/cm^2 at <100°C (Solid Curve), and 7.1×10^{20} neutrons/cm^2 at 147°C (Dashed Curve). The 00·2 2θ profile from an unirradiated BeO crystal is shown displaced to the right. All intensities have been normalized to a maximum of 85 to 95.

In Fig. 13.1 we note the pronounced change in profile with increasing dose. Starting from a relatively sharp Bragg maximum, it changes to a two-component reflection with a relatively sharp Bragg maximum at low scattering angle and a broad diffuse maximum at a higher scattering angle. Finally, it becomes a diffuse reflection with no observable trace of the Bragg maximum. We computed an apparent c_0 spacing of 4.48 A from the sharp component of the reflection from the crystal irradiated to 3.7×10^{20} neutrons/cm^2.

The interpretation of such data in terms of a model of the damaged crystal lattice probably involves the rather sudden loss of long-range regularity of lattice sites in the **c** direction. Before the regularity drops to the extent that Bragg maxima are not observable, the c_0 spacing corresponding to these maxima increases by as much as 5%, reflecting the large expansion of interlayer spacing caused by isolated defects and clusters. At the same time, highly damaged sections of the structure are growing in size and assuming a degree of local order within, and perhaps between, themselves. It is the diffuse scattering from such sections that is observed near every reciprocal lattice site $hk{\cdot}l$ with $l \neq 0$. The interpretation of the features of this diffuse scattering can, in large part, follow that given previously,[9] with the additional assumption of random C-type layers to account for the streaks in directions hk with $h - k \neq 3n$.

The identification and description[11] of a high-temperature form of BeO has naturally led to consideration of the possibility that the atomic configuration in highly damaged sections may approach that of the β-BeO structure. To date, we have not found experimental evidence to support this hypothesis.

[11] D. K. Smith, C. F. Cline, and S. B. Austerman, UCRL-7539, Rev. I (Jan. 14, 1964).

THE INTERPRETATION OF DIFFUSE X-RAY SCATTERING FROM DISORDERED ALLOYS

B. Borie C. J. Sparks, Jr.

Measurements of diffuse x-ray scattering from a disordered substitutional alloy provide the only direct information about the detailed atomic arrangement. However, this useful information is obscured by contributions to the scattering from other sources. Always present is temperature diffuse scattering (TDS), resulting from the thermal motion of the atoms. Another diffuse scattering component is caused by small static displacements of the atoms from the sites of the ideal lattice. These displacements are a consequence of the disorderly distribution of atoms of two different sizes on the atomic sites.

Previous efforts to correct measured intensities to obtain only the scattering due to local order have been inadequate. Usually one tries to remove the TDS by assuming that it varies linearly with temperature and extrapolating to absolute zero from measurements at two temperatures. This is at best crude since (1) the TDS depends linearly on temperature only at temperatures higher than those normally used, (2) its theoretical justification is derived from a treatment of thermal motion in a perfectly periodic medium rather than the aperiodic disordered alloy, and (3) the assumption that other components of the diffuse scattering are temperature independent is of questionable validity. Corrections for the diffuse scattering due to the static displacements have been even more primitive.

We devised a new method for separating the diffuse scattering into its various components for a cubic material. No models or assumptions about the character of either the dynamic or static atomic displacements are necessary, except that the displacements are assumed to be small.

In general, one may write for the scattered intensity I in electron units,

$$I = \sum_m \sum_n f_m f_n \exp\left[ik\cdot(r_m - r_n)\right] . \qquad (1)$$

The position vector and atomic scattering factor of the mth atom are r_m and f_m, and the vector k is $2\pi(s - s_0)/\lambda$, s and s_0 being unit vectors defining the directions of the scattered and incident radiation. If the atomic positions correspond exactly to the sites of the average lattice, then for a disordered alloy Eq. (1) gives only the sharp fundamental Bragg maxima and the local order diffuse scattering. The Fourier transform of this diffuse intensity yields the short-range order parameters, which describe the local atomic arrangement.

However, if the atoms are displaced, either dynamically or statically, their positions are given by $r_m + \delta_m$, where δ_m is a small vector from the ideal site to the actual atomic position. The intensity is then given by

$$I = \sum_m \sum_n f_m f_n \exp\left[ik\cdot(r_m - r_n) + ik\cdot(\delta_m - \delta_n)\right] .$$

Consider the contribution to I of, say, all pairs of atoms a distance $r_m - r_n$ apart, with an A atom at m and a B atom at n. Let this contribution be I_{mn}^{AB} and let the total number of such pairs be N_{mn}^{AB}. Then

$$I_{mn}^{AB} = N_{mn}^{AB} f_A f_B \exp\left[ik\cdot(r_m - r_n)\right] \times \left\langle \exp\left[ik\cdot(\delta_m - \delta_n)\right]\right\rangle . \qquad (2)$$

The average indicated in Eq. (2) is both a spatial average, since the displacements of different mn pairs may be different, and a time average, since a component of δ_m is dynamic due to thermal motion. If $k\cdot(\delta_m - \delta_n)$ is sufficiently small that all terms in the series expansion of the exponential beyond the quadratic term may be neglected, Eq. (2) may be written

$$I_{mn}^{AB} = \psi_{mn} + \phi_{mn} ,$$

where

$$\psi_{mn} = N_{mn}^{AB} f_A f_B \exp\left[ik\cdot(r_m - r_n)\right]$$

and

$$\phi_{mn} = N_{mn}^{AB} f_A f_B \exp\left[ik\cdot(r_m - r_n)\right] \times \left\langle ik\cdot(\delta_m - \delta_n) - \frac{1}{2}\left[k\cdot(\delta_m - \delta_n)\right]^2 \right\rangle . \qquad (3)$$

Here, ψ_{mn} is that part of the intensity that would have been observed if there were no atomic displacements. The problem of concern here is to understand ϕ_{mn} so that it may be removed from the measurements.

Let the vector displacement δ_m be written in terms of the unit cell vectors a_1, a_2, and a_3:

$$\delta_m = x_m a_1 + y_m a_2 + z_m a_3 ,$$

where x_m, y_m, and z_m are small pure numbers. We may write k in terms of the reciprocal vectors b_1, b_2, and b_3:

$$k = 2\pi(h_1 b_1 + h_2 b_2 + h_3 b_3) ,$$

where h_1, h_2, and h_3 are continuous variables that are essentially the coordinates of a point in reciprocal space. Then

$$k \cdot \delta_m = 2\pi(h_1 x_m + h_2 y_m + h_3 z_m) ,$$

and Eq. (3) may be written

$$\phi_{mn} = N_{mn}^{AB} f_A f_B \exp[ik\cdot(r_m - r_n)] \{2\pi i(h_1 \langle x_m - x_n \rangle + h_2 \langle y_m - y_n \rangle + h_3 \langle z_m - z_n \rangle)$$
$$- 2\pi^2(h_1^2 \langle [x_m - x_n]^2 \rangle + h_2^2 \langle [y_m - y_n]^2 \rangle + h_3^2 \langle [z_m - z_n]^2 \rangle + 2h_1 h_2 \langle [x_m - x_n][y_m - y_n] \rangle$$
$$+ 2h_2 h_3 \langle [y_m - y_n][z_m - z_n] \rangle + 2h_3 h_1 \langle [z_m - z_n][x_m - x_n] \rangle)\} .$$

Define three functions, periodic in h_1, h_2, and h_3, whose Fourier series representations are given by

$$B'(h_1 h_2 h_3) = \sum_n N_{mn}^{AB}\, 2\pi i \langle x_m - x_n \rangle \exp[ik\cdot(r_m - r_n)] ,$$

$$C'(h_1 h_2 h_3) = -\sum_n N_{mn}^{AB}\, 2\pi^2 \langle [x_m - x_n]^2 \rangle \exp[ik\cdot(r_m - r_n)] ,$$

$$D'(h_1 h_2 h_3) = -\sum_n N_{mn}^{AB}\, 4\pi^2 \langle [x_m - x_n][y_m - y_n] \rangle \exp[ik\cdot(r_m - r_n)] .$$

If ϕ_{mn} is summed over n to obtain Φ, the contribution to the intensity of all AB pairs for any $r_m - r_n$, we obtain

$$\Phi/f_A f_B = h_1 B'(h_1 h_2 h_3) + h_2 B'(h_2 h_3 h_1) + h_3 B'(h_3 h_1 h_2) + h_1^2 C'(h_1 h_2 h_3) + h_2^2 C'(h_2 h_3 h_1)$$
$$+ h_3^2 C'(h_3 h_1 h_2) + h_1 h_2 D'(h_1 h_2 h_3) + h_2 h_3 D'(h_2 h_3 h_1) + h_3 h_1 D'(h_3 h_1 h_2) . \quad (4)$$

Similar expressions may be developed for AA and BB pairs and the result combined to give the total contribution to the diffuse intensity due to the static and dynamic atomic displacements. The precise character of the resultant periodic functions is unimportant for our purpose here. To separate the intensity distribution into its various components, we need only to know that the contribution due to the atomic displacements may be written in terms of such functions as in Eq. (4).

For the sake of simplicity we illustrate the separation into two dimensions, though its extension to three is obvious. Suppose we confine our attention to the $h_1 h_2 0$ plane in reciprocal space. Let $A(h_1, h_2)$ represent the periodic short-range order diffuse scattering. Then, by analogy with Eq. (4), the total diffuse intensity after removal of the form factor dependence may be written

$$I(h_1 h_2) = A(h_1 h_2) + h_1 B(h_1 h_2) + h_2 B(h_2 h_1)$$
$$+ h_1^2 C(h_1 h_2) + h_2^2 C(h_2 h_1) + h_1 h_2 D(h_1 h_2) . \quad (5)$$

Let the operator $\Delta_1 I(h_1 h_2)$ be defined by

$$\Delta_1 I(h_1 h_2) = I(h_1 h_2) - I(h_1 - 1, h_2) .$$

Then

$$\Delta_1 I(h_1 h_2) = B(h_1 h_2) + (2h_1 - 1)C(h_1 h_2) + h_2 D(h_1 h_2) \quad (6)$$

and

$$\Delta_1^2 I(h_1 h_2) = 2C(h_1 h_2) ,$$

$$\Delta_2 \Delta_1 I(h_1 h_2) = D(h_1 h_2) .$$

Having recovered C and D, we may substitute in Eq. (6) to obtain B:

$$B(h_1 h_2) = \Delta_1 I(h_1 h_2) - \left(h_1 - \frac{1}{2}\right) \Delta_1^2 I(h_1 h_2) - h_2 \Delta_2 \Delta_1 I(h_1 h_2) .$$

It is then straightforward to recover A by substitution of B, C, and D in Eq. (5).

Limitations of the method include the requirement that the separation be performed near the origin in reciprocal space, so that higher order terms in the series expansion remain small. Since the separation depends on intensity differences, it is very sensitive to the accuracy of the measurements. The required manipulations of the data are such that access to a computer is useful, particularly if a three-dimensional separation is to be attempted. Measurements at only one temperature are needed, however, and the technique provides the most complete correction for intensity contributions associated with static atomic displacements.

Part II.

Research for the AEC Division of Reactor Development

14. Fuel Element Development

G. M. Adamson, Jr.

The prime goal of the fuel element development program has continued to be the development of new or improved fabrication techniques for both fuels and cladding materials. At present, our emphasis is on thermochemical deposition, both for the conversion of uranium hexafluoride to uranium dioxide by a one-step high-temperature hydroreduction reaction and as a means for fabricating difficult cladding materials.

The high-temperature fuel cladding materials we are fabricating by thermochemical reduction of halides include tungsten-rhenium alloys, other tungsten alloys, molybdenum, and rhenium. Development of thermochemical production of pure tungsten is reported in Chap. 19 of this report.

Improvements in aluminum-base dispersion fuel elements are being sought through studies of fabrication behavior and the mechanism of hydrogen absorption.

THERMOCHEMICAL DEPOSITION OF URANIUM DIOXIDE

R. L. Heestand C. F. Leitten, Jr.

The overall reaction $UF_6 + O_2 + 3H_2 \rightarrow UO_2 + 6HF$ may be used to synthesize uranium dioxide directly by thermochemical techniques.[1] We analyzed the thermodynamic and kinetic factors that affect the rate and efficiency of the one-step reaction and concluded that low operating system pressure, temperatures sufficiently high to limit formation or condensation of intermediate compounds, and excess oxygen and hydrogen should favor the reaction.

Experiments were run to confirm the predicted effects of temperature, pressure, and gas composition on the reaction products. Figure 14.1 shows schematically the experimental apparatus. It was necessary to inject the UF_6 directly into the hot zone of the furnace to prevent loss of uranium by preliminary formation of the solid intermediate products UO_2F_2 or UF_4 in the cold zones. Figure 14.2 shows the arrangement of the resistance-heated Pt–40% Rh furnace, the water-cooled injector used to introduce the UF_6 into the hot zone of the system, and the low-density alumina deposition substrate, which was used to facilitate removal of samples. In addition, argon is used as a blanket to separate the reactants at the injector tip and prevent buildup of UO_2 on the injector.

The ranges of experimental conditions consisted of reaction temperature from 900 to 1500°C, pressure from 2 to 20 torrs, and gas-feed compositions from 30 to 80 vol % H_2, 10 to 70 vol % O_2 or steam, and 1 to 10 vol % UF_6. System parameters have not been optimized in regard to all variables; however, several trends are apparent. In the temperature range of 1200 to 1500°C at pressures below 10 torrs, UO_2 is formed when gas composition limits are held within 60 to 80 vol % H_2, 10 to 40 vol % O_2 or steam, and 1 to 10 vol % UF_6. When UF_6 is injected directly into the hot zone so that mixing occurs in the desired temperature range, the deposit may be obtained as either a highly dendritic crystal growth or as a solid dense uniform deposit. A typical dendritic crystalline growth, shown in Fig. 14.3, was obtained with a gas composition of 78 vol % H_2, 20 vol % steam, and 2 vol % UF_6 at 6 torrs and 1250°C.

[1] R. L. Heestand and C. F. Leitten, Jr., "Thermochemical Reduction of Uranium Hexafluoride for the Direct Fabrication of Uranium Dioxide," to be published in *Nuclear Applications*.

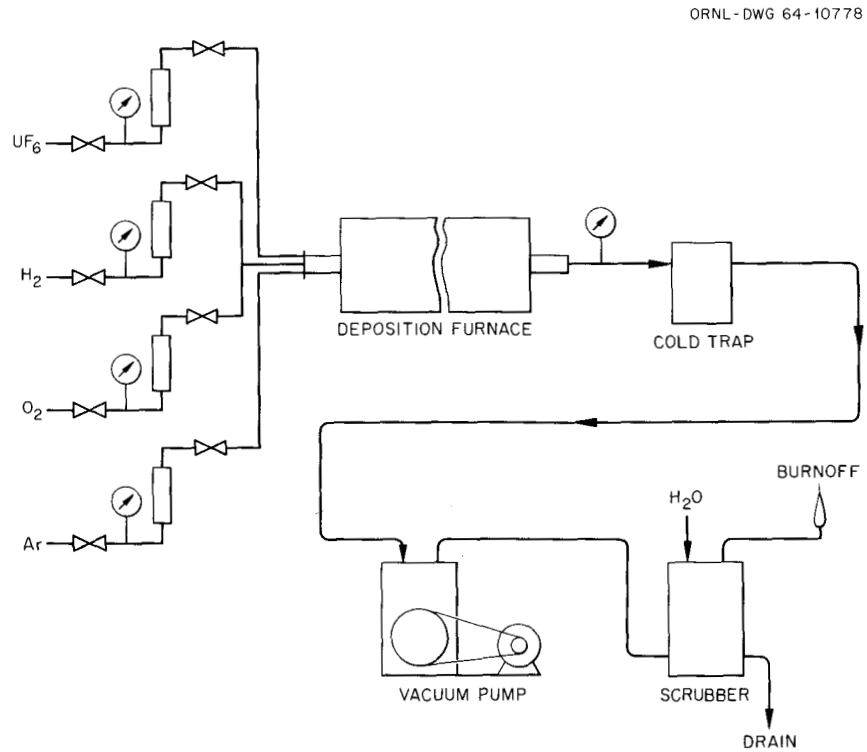

Fig. 14.1. Schematic of Apparatus for Thermochemical Deposition of Uranium Dioxide from Uranium Hexafluoride.

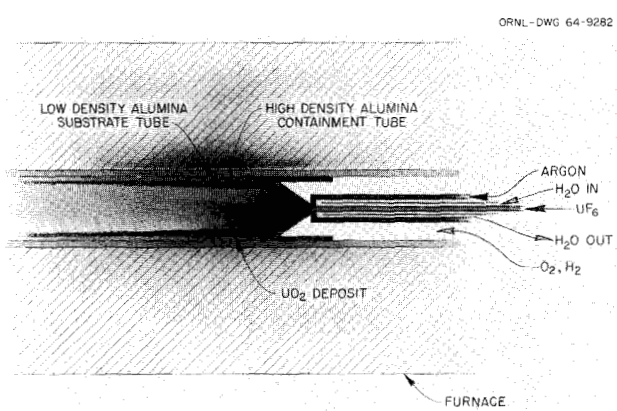

Fig. 14.2. Arrangement of Water-Cooled Injector for Introducing Uranium Hexafluoride.

Deposits of this type have oxygen-to-uranium ratios, determined polarographically, in the range 2.000 to 2.003 and fluorine contents less than 10 ppm. These deposits are readily removed from the alumina substrate and are easily crushed to powder.

Using the same method of fuel injection, we obtained a dense uniform deposit when the pressure was reduced to 2 to 3 torrs and the UF_6 content of the gas was increased above 3%. Figure 14.3 also shows an approximately 0.040-in.-wall UO_2 tube, which was deposited at 1300°C and 3 torrs at a rate of 6 mils/hr with a feed rate of 40 cm^3/min UF_6, 45 cm^3/min O_2, and 550 cm^3/min H_2. The bulk density closely approximated the theoretical x-ray density of UO_2 (10.96 g/cm^3).

We have adjusted the stoichiometry of the solid deposits by varying the feed gas composition, primarily the oxygen content, at a given temperature and pressure. Figure 14.4 shows the range of microstructures obtained for different oxygen concentrations. The increasing amount of second phase is typical of precipitation of U_4O_9.

Although our principal effort has been directed toward obtaining massive deposits, we found that submicron size powders, as shown in the background of Fig. 14.3, may be obtained if the gases mix at lower temperatures. We believe that an intermediate fluoride is formed on mixing and subsequently reduced to UO_2 in the hot zone.

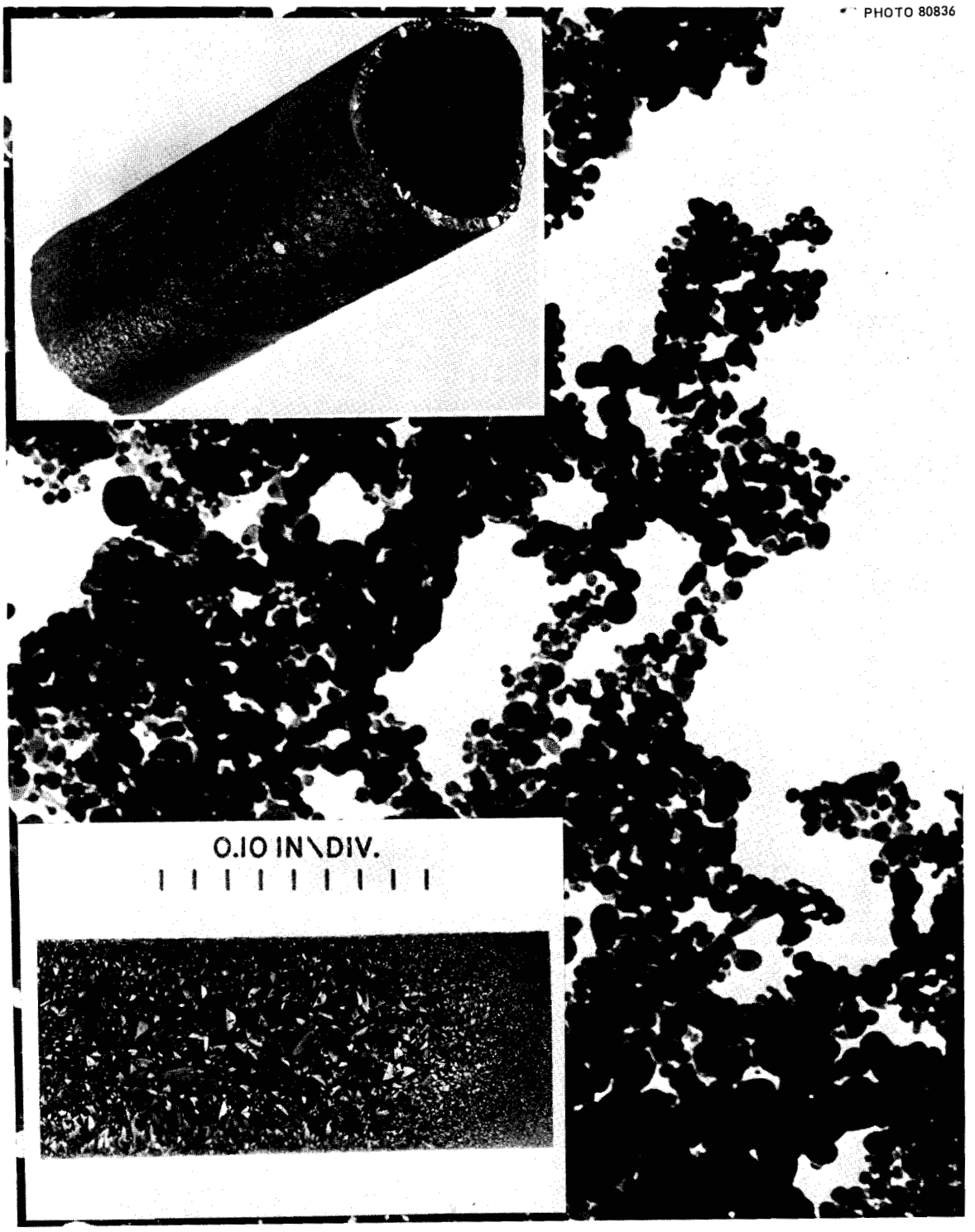

Fig. 14.3. Samples of Uranium Dioxide Prepared by Vapor Deposition. At the lower left is a dendritic deposit of deep red translucent crystals. At the top is a section of UO_2 tube, 0.750-in.-diam × 0.040-in. wall, deposited at 1300°C from UF_6, O_2, and H_2 in 6 hr, 5×. The background is an electron micrograph of extremely fine powder, 165,000×. Reduced 16%.

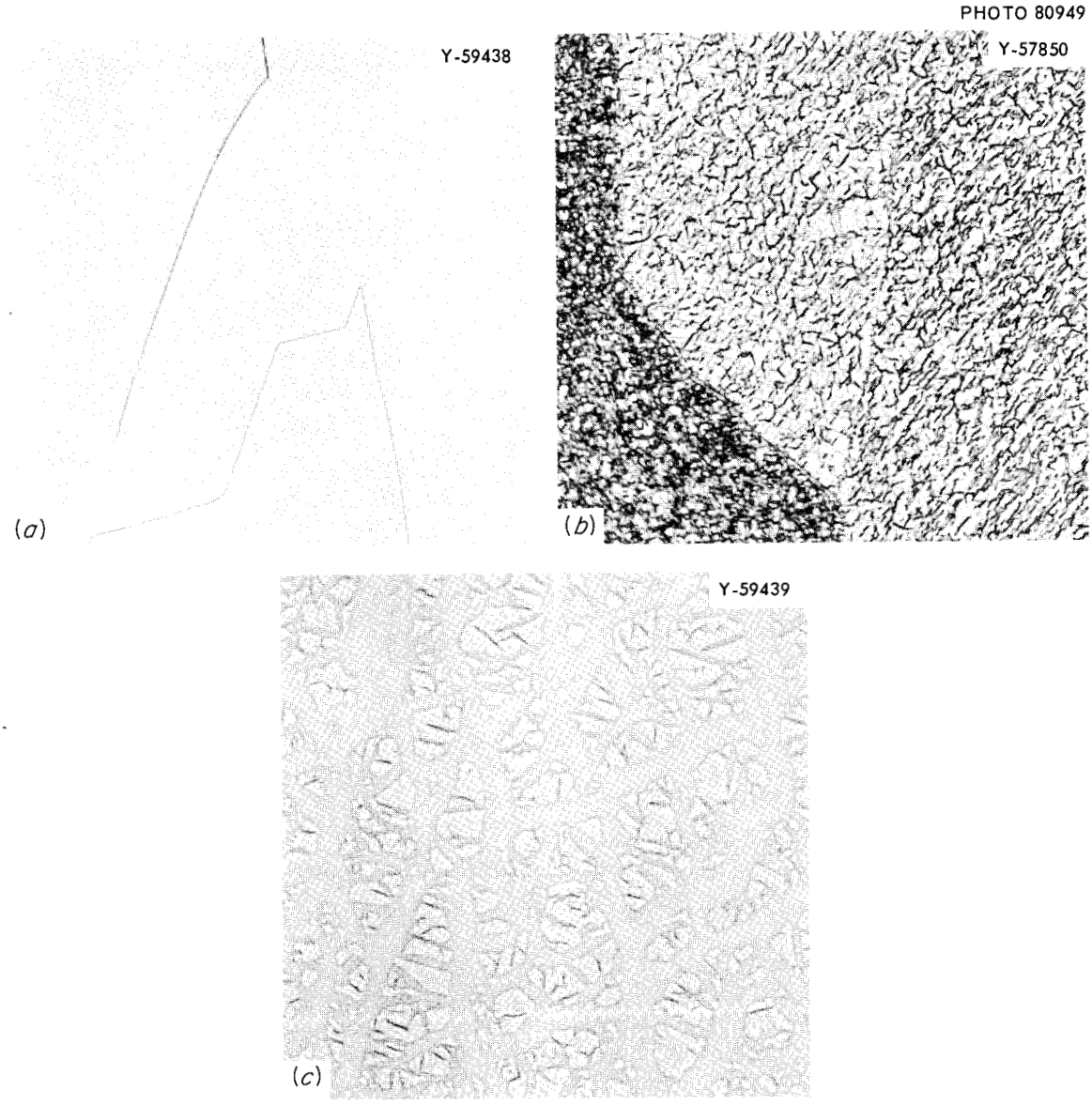

Fig. 14.4. Microstructure of Solid UO_2 Deposits Obtained at 1300°C and 3 torrs. Gas compositions by volume and oxygen-to-uranium ratios were (*a*) 9% O_2–85% H_2–6% UF_6, 2.001; (*b*) 10% steam–86% H_2–4% UF_6, 2.008; and (*c*) 12% O_2–81% H_2–7% UF_6, 2.166. Etchant: 70% H_2O, 20% H_2O_2 solution (30%), and 10% concd HNO_3. 250×.

DEPOSITION OF REFRACTORY METALS

J. I. Federer C. F. Leitten, Jr.

The preparation and fabrication of various refractory metals by thermochemical deposition has continued. Our goals include the deposition of these metals as both claddings and free-standing shapes. The major effort has been directed at the deposition of tungsten-rhenium alloys. Obtaining fine-grained tungsten by the simultaneous deposition of tungsten and minor alloying additions is also being sought. Deposition of unalloyed tungsten, which was formerly a part of this program, is reported in Chap. 19 of this report. Other refractory metals now being deposited include rhenium and molybdenum.

Tungsten-Rhenium Alloys

The preparation of tungsten-rhenium alloys by the simultaneous hydrogen reduction of tungsten and rhenium hexafluorides has continued.[2] The alloying studies have shown both the feasibility of codeposition and the problems involved. The equipment used has been described previously.[3]

Due to metering difficulties, the actual ReF_6 flow rates were not well known in early experiments; however, the characteristic codeposition behavior for stationary hot zones was established.[2] With the high deposition temperature used (700°C), easier reduction of ReF_6 than WF_6 resulted in rhenium-rich deposits near the inlet of the reaction zone. Subsequently, the metering difficulties were eliminated by the use of mass flowmeters,[4] and codeposition was further investigated.[5] The typical deposition behavior is shown by the composition profiles in Fig. 14.5, wherein the rhenium content of the deposits is plotted against distance from the inlet of the reaction zone. The deposition conditions and metal-recovery values are included. The recovery values are determined by comparing the metal content of both metered fluorides with the weight of deposit obtained.

The curve labeled WRe-16 is typical of deposits prepared at 500 to 700°C, exhibiting a high rhenium content near the inlet followed by a rapid decrease in rhenium with distance from the inlet. The curves labeled WRe-18 and WRe-19 represent deposits prepared under the same conditions as WRe-16 except that argon was included with the reacting gases. Although the mechanism is not clear, argon improves the uniformity of the distribution of rhenium in the deposit. The rhenium

[2]J. I. Federer and C. F. Leitten, Jr., *Metals and Ceramics Div. Ann. Progr. Rept. June 30, 1964*, ORNL-3670, pp. 68–70.

[3]R. L. Heestand, J. I. Federer, and C. F. Leitten, Jr., *Preparation and Evaluation of Vapor-Deposited Tungsten*, ORNL-3662 (Aug. 1964).

[4]Hastings-Raydist, Inc., Hampton, Virginia.

[5]J. I. Federer and C. F. Leitten, Jr., "Vapor Deposition and Characterization of Tungsten-Rhenium Alloys," to be published in *Nuclear Applications*.

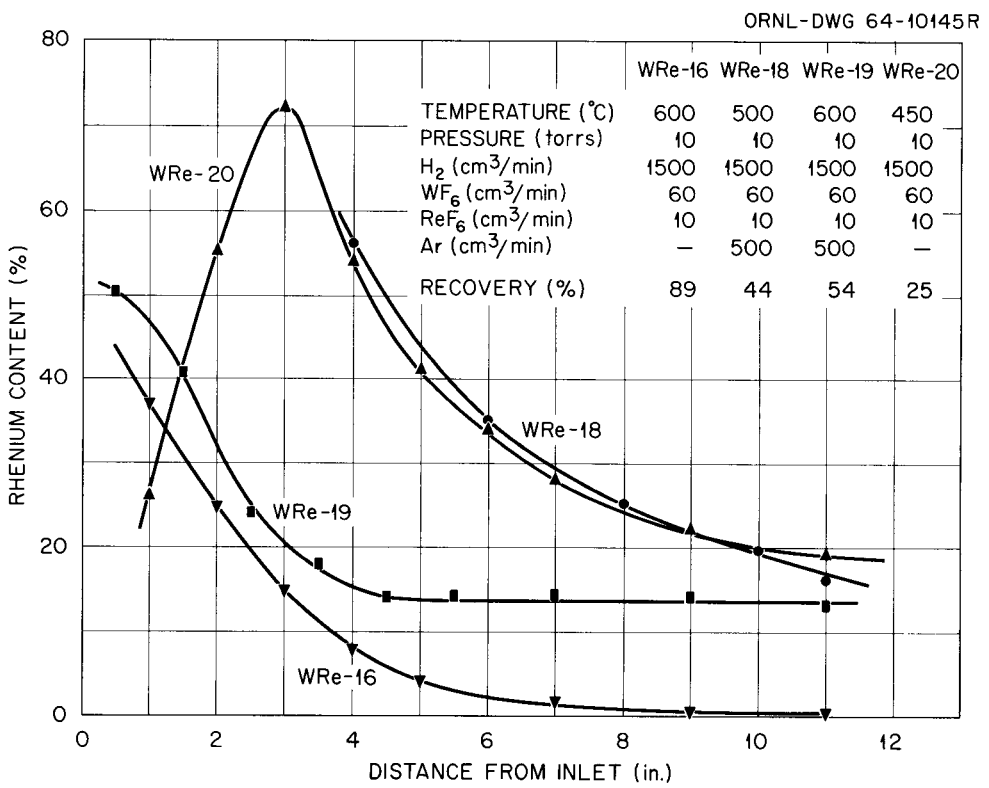

Fig. 14.5. Variation of Rhenium Content with Distance from the Inlet of the Reaction Furnace.

content in WRe-19 was substantially increased throughout the deposit and was constant over the distance from 5 to 12 in. from the inlet. The presence of argon, however, lowered the metal recovery from 89 to 54%. Lowering the deposition temperature to 450°C also significantly changed the rhenium distribution, as shown by the curve labeled WRe-20. Analysis of the composition profiles for several deposits revealed that a greater proportion of the rhenium was recovered in the deposits than of the tungsten. In general deposition rates also were higher near the inlet than farther downstream. Consequently, deposits prepared with a stationary hot zone were both thicker and richer in rhenium near the inlet.

In an alternate arrangement, we attempted to alleviate the axial variation in thickness and rhenium content by substituting a short moving hot zone for the relatively long stationary hot zone. Adjusting the gas composition controlled the alloy composition and regulating the rate of movement of the hot zone controlled the thickness. In the initial experiments with a moving hot zone, an 8-in.-long furnace was moved 4 to 5 in. along the deposition tube in $\frac{1}{4}$-in. increments every 15 min. The conditions and results of these experiments, WRe-26 and WRe-28, are shown in Fig. 14.6. The moving hot zone maintained a relatively high rhenium content throughout a greater length of deposit than had been obtained previously. Metal recoveries varied from 36% at 600°C to 93% at 800°C. As the deposition temperature was increased, the fraction of tungsten recovered increased; this increased tungsten recovery may be seen in the lower rhenium content of specimen WRe-28.

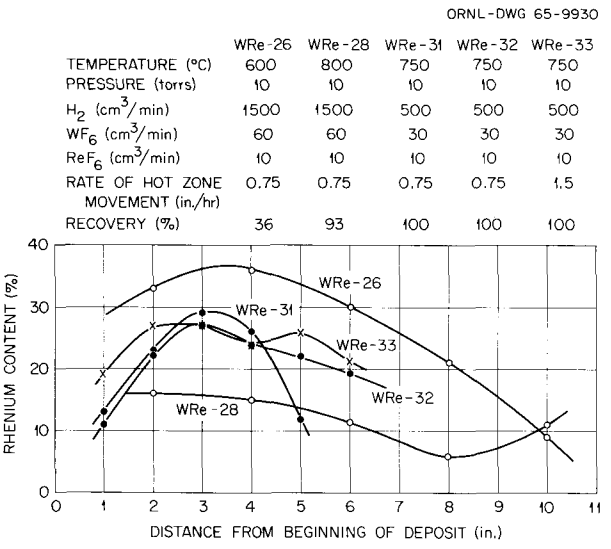

Fig. 14.6. Variation of Rhenium Content in Tungsten-Rhenium Deposits Prepared with a Moving Hot Zone.

Since the moving hot zone was 8 in. long in the initial experiments, a range of compositions was still being deposited throughout the deposition zone. Subsequently, the furnace was replaced with a 1-in.-long induction coil. A mechanical device moved the deposition tube through the induction coil at a constant rate of 0.75 in./hr, and the gases were preheated to about 300°C. The other conditions of these experiments, WRe-31, -32, and -33, and the results are shown in Fig. 14.6. In these experiments, the total feed rate of WF_6 and ReF_6 was reduced and 100% of the metal was recovered. The axial variations in composition cannot be completely evaluated because of the short length of the deposits and the relatively large end effects due to temperature gradients. Nevertheless, the high metal recoveries and the correlation between gas composition (25% ReF_6, exclusive of H_2) and the maximum rhenium content of the deposits (27 to 29%) is encouraging. Definite improvements in uniformity of deposition were observed. In experiment WRe-33, a 7-in.-long deposit was prepared at a constant deposition rate of 4.3 mils/hr over the middle 4 in. of the deposit. Although not yet optimized, the moving hot zone technique appears to have potential for depositing alloys of uniform composition and thickness.

The interstitial and metallic impurity contents of alloy deposits are similar to those of unalloyed vapor-deposited tungsten. Typical impurity contents are <20 ppm C, <5 ppm N and H, 5 to 35 ppm O, and traces of several metals including copper, boron, and silicon. The grain structure, shown in Figs. 14.7 and 14.8, is typically columnar with a tendency towards more needle-like grains in alloys containing greater than 25% Re. Figure 14.7 shows long columnar grains, containing considerable fine structure, in a W–32% Re deposit. A columnar structure resembling unalloyed tungsten is shown in the W–12% Re deposit in Fig. 14.8. Columnar grain structures now appear predominant in alloys containing up to 50% Re.

Hardness values increased from 450 DPH for unalloyed tungsten to about 1800 DPH for alloys containing 25 to 30% Re. X-ray diffraction results

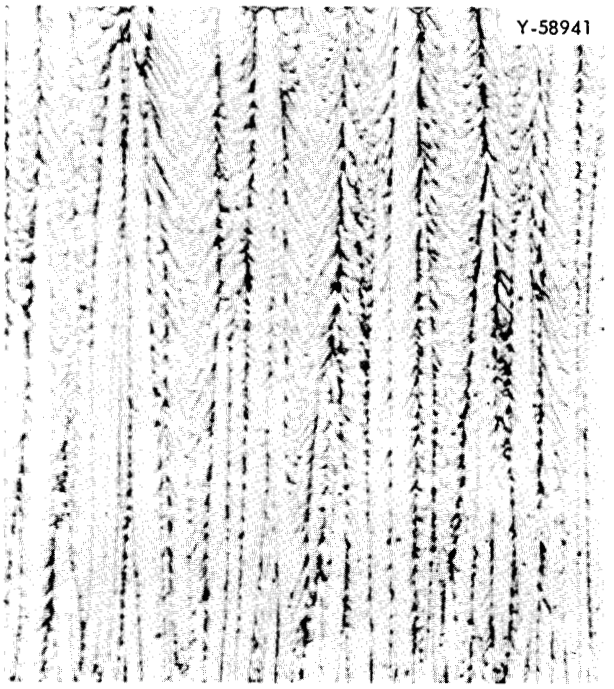

Fig. 14.7. Vapor-Deposited W–32% Re Alloy. Etchant: 1 concd NH_4OH, 1 H_2O_2 (30%), 4 H_2O. 500×.

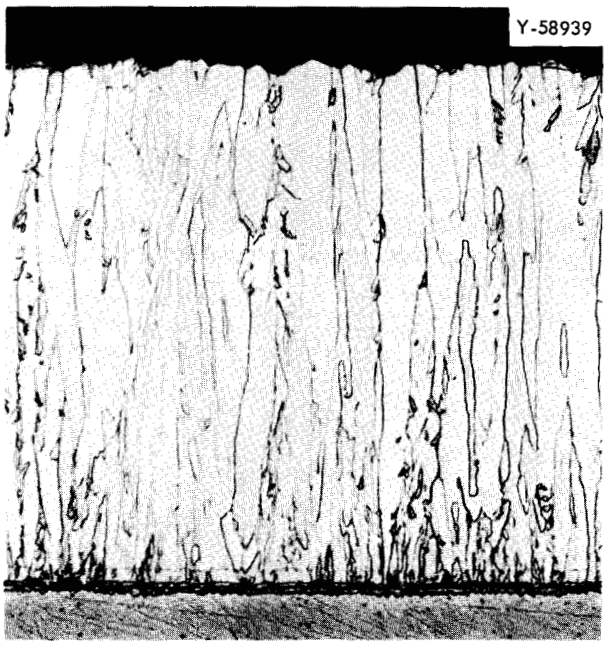

Fig. 14.8. Vapor Deposited W–12% Re Alloy. Etchant: 1 concd NH_4OH, 1 H_2O_2 (30%), 4 H_2O. 250×.

indicate that the hardness increase is associated with an increasing amount of β-tungsten-type structure (cubic), which coexists with a solid solution (body-centered cubic) of rhenium in tungsten.[6] The solid solution is observed principally in deposits with low rhenium contents, whereas the β-tungsten structure is associated with high rhenium contents. The latter phase does not appear in published phase diagrams,[7,8] which have not been established below 1200°C. Neither sigma phase, which is reported to occur in alloys containing 26 to 63% Re, nor elemental rhenium has been found in any as-deposited alloys.

Other Tungsten Alloys

The deposition of fine-grained rather than the usual columnar-grained tungsten has been attributed to unintentional contamination with vanadium.[2] In continuing deposition experiments, small amounts of certain alloying elements are being added to tungsten by coreduction of the mixed fluorides. The objective is to study methods for adding known quantities of the elements to tungsten.

In preliminary experiments, coreduction at 600, 700, and 800°C of a mixture containing about 0.06% VF_5 in WF_6 resulted in vanadium contents ranging from less than 10 to 75 ppm but no change in structure. Subsequently we tried to add boron, molybdenum, and vanadium to tungsten by using binary mixtures of WF_6 with BCl_3, MoF_6, and VF_5 at higher concentrations under the following conditions.

Temperature	600, 700, 800°C
Pressure	10 torrs
H_2	1000 cm^3/min
WF_6 + 0.5% BCl_3	50 cm^3/min
WF_6 + 2.1% VF_5	50 cm^3/min
WF_6 + 0.5% MoF_6	50 cm^3/min
Deposition mandrel	$\frac{7}{8}$-in.-OD × $\frac{3}{5}$-in.-ID × 12-in.-long copper tube (for internal deposit)

[6] J. I. Federer and R. M. Steele, *Nature* **205**, 587–88 (1965).

[7] P. Greenfield and P. A. Beck, *Trans. AIME* **206**, 265–76 (1956).

[8] J. J. English, *Binary and Ternary Phase Diagrams of Columbium, Molybdenum, Tantalum, and Tungsten*, DMIC-152, p. 92 (April 1961).

The WF_6 + BCl_3 mixture was metered at 38°C, the temperature at which the vapor pressures of the two constituents are equal. The other two mixtures were metered at the boiling points of VF_5 (50°C) and MoF_6 (35°C).

Each additive suppressed tungsten deposition. For example, no deposit was obtained at 600°C with the VF_5 mixture and only 50% recovery was obtained at 600°C with the BCl_3 mixture. Metal recoveries, however, increased with increasing deposition temperature. Boron additions, if any, were less than the limit of spectroscopic detection (50 ppm). Vanadium contents ranged from 880 to 1130 ppm and molybdenum from less than 20 to 1000 ppm.

The microstructures of samples prepared with fluoride mixtures containing BCl_3 and MoF_6 were columnar with a very fine precipitate at the grain boundaries and, to a lesser extent, within the grains. No other characteristic microstructural features were observed. Several of the samples prepared with a mixture containing VF_5 had regions of VF_3 included in the microstructure. The vanadium contents of these samples were not included in the range of values mentioned above. The microstructures of two samples from two different deposits prepared at 800°C were unlike any previously observed, being neither columnar nor equiaxed. The grains were elongated in the growth direction but did not extend completely through the deposits. The columnar structure apparently was disrupted by the frequent nucleation of new grains as deposition proceeded.

These experiments have demonstrated the feasibility of adding small amounts of alloying additions to tungsten by vapor deposition, but the process is subject to the nonuniformity problem previously discussed for the deposition of tungsten-rhenium alloys. Several methods are being considered to minimize this problem, including deposition on a male mandrel contained in a mixing chamber and the use of a moving hot zone.

Rhenium

Studies of deposition of unalloyed rhenium by hydrogen reduction of rhenium hexafluoride (ReF_6) have continued. The purpose is to determine the conditions required to prepare uniform deposits for applications of the unalloyed metal and to establish baseline information for deposition of alloys containing rhenium.

Deposition studies have been conducted under conditions included within the limits indicated below.

Temperature	500 to 800°C
Pressure	2 to 50 torrs
H_2/ReF_6	10 to 200
Flow rates	
H_2	250 to 2000 cm^3/min
ReF_6	10 to 25 cm^3/min
Substrate	Copper
Geometry	$\frac{3}{4}$ in. OD × 12 in. long

Although the optimum conditions for deposition of uniform high-density metal have not been determined, several general trends are evident. The efficiency of reduction of ReF_6 is enhanced by high values of the three principal variables – temperature, pressure, and H_2/ReF_6 ratio. Under conditions of high reduction efficiency, the deposits consist of nodular growths, mechanically interlocked crystals having considerable grown-in porosity, and some smooth coating. Deposits of high density and uniform thickness occur under conditions of low reduction efficiency. Ductile coatings of high-density metal, 1 to 2 mils thick and 10 in. long, have been deposited at 600°C with an H_2/ReF_6 ratio of about 12 (250 cm^3/min H_2 and 20 cm^3/min ReF_6) and a system pressure of 10 torrs. The deposition rate was about 0.5 mil/hr and the reduction efficiency was 25%. The grain structure of this material was typically columnar but less needle-like than that of vapor-deposited tungsten grains.

Molybdenum

Molybdenum also is being deposited by the hydrogen reduction of MoF_6. Preliminary results indicate that slightly higher temperatures are required for this reaction than for deposition of either tungsten or rhenium. All the bad features of rhenium deposits also appear to be present in molybdenum deposits, but some smooth coatings have been prepared at 800 and 900°C. The grain structure of molybdenum deposited at 900°C, H_2/MoF_6 ratio of 40, and a system pressure of

10 torrs is columnar and similar in appearance to that of vapor-deposited tungsten.

HYDROGEN ABSORPTION FROM WATER BY ALUMINUM

M. M. Martin C. F. Leitten, Jr.

In fabricating aluminum-base fuel plates, we infrequently observe blisters in the aluminum cladding even though the initial stock has been acceptable in annealing tests. Desorption of atomic hydrogen from free internal surfaces produces the majority of blisters in aluminum. A source of atomic hydrogen is thought to be atmospheric water that reacts and discolors aluminum surfaces in normal heat-treating operations.[9] We determined the effect of time (2 to 10 hr), temperature (450 to 550°C), and annealing-air dewpoint (0 to 39°C) on the hydrogen absorption by types 6061 and 1199 aluminum.

Previous studies centered on establishing sample preparation and a procedure for vacuum fusion analysis of internal hydrogen in aluminum. In general, degassed and machined cylinders of the two alloys were exposed to humid air at high temperature and then melted in a vacuum-fusion rig to determine the amount of absorbed hydrogen. The cylinders were prepared from $\frac{3}{4}$-in.-diam rods of the materials, which had been annealed at less than 10^{-3} torr for 24 hr at a temperature near their melting point. Immediately prior to analysis, the specimens were remachined and heated in vacuum to 400°C for 1 hr to reduce the surface gas contributions.

Table 14.1 summarizes the initial hydrogen contents for unreacted cylinders. The degassing treatments reduced significantly the amount of hydrogen in type 1199 aluminum but did not affect the level in type 6061 aluminum. We also noted considerable variation in the results for 6061 aluminum.

The hydrogen content of 1199 aluminum on reaction increased two- to tenfold from the original 0.04 $cm^3/100$ g. The changes, however, were independent of the experimental variables. Surprisingly, the hydrogen content of reacted 6061 aluminum remained essentially constant within the range found in the degassed material. The alloy additions that affect the oxide film undoubtedly control the diffusion of hydrogen into and out of the specimens.

Table 14.1. Hydrogen Content of Types 1199 and 6061 Aluminum After Various Treatments to Lower the Surface Gas[a]

Treatment	Hydrogen Content ($cm^3/100$ g)	
	1199 Al	6061 Al
Turned in lathe, about 0.062 in. removed from diameter	0.45	0.74
Degassed and turned	0.11	0.15 to 1.01
Degassed and turned, then heated to 400°C at $<10^{-2}$ torr		
60 min	0.054	0.47
120 min		0.64
360 min	0.038	0.57

[a]All values are the average of two determinations except where range is shown.

CHARACTERIZATION OF FUEL DISPERSIONS

D. O. Hobson C. F. Leitten, Jr.

We completed work on the characterization of various types of U_3O_8 powders dispersed in aluminum matrices. The purpose was to discover the effects fabrication variables had on fuel plates containing various types of oxide fuel. Such knowledge should help us determine what properties to specify when ordering commercial fuel. Another purpose was to find a suitable way to quantitatively evaluate fragmentation and stringering in the material under consideration and to propose a model that can be used to predict the fabrication behavior of similar fuel dispersions.

Samples of commercial powders were ordered from three vendors. The as-received properties of the three oxides are listed in Table 14.2, and Fig. 14.9 shows their microstructures. Each powder was powder-metallurgically dispersed in type X8001 aluminum powder and roll bonded with type 6061 aluminum to form fuel plates. Previously developed ATR fabrication procedures were

[9]M. M. Martin, *Metals and Ceramics Div. Ann. Progr. Rept. June 30, 1964*, ORNL-3670, p. 75.

Table 14.2. Properties of Commercial Powders of U_3O_8

Oxide	Sieve Cut	Analysis (%)	Density[a] (g/cm^3)	Surface Area[b] (m^2/g)	Uranium Analysis (%)
N	−80 +100	0.009	8.28	0.026	84.60
	−100 +140	21.9			
	−140 +200	33.9			
	−200 +270	21.8			
	−270 +325	15.2			
	−325	7.2			
S	−80 +100	0.19	8.26	0.058	84.72
	−100 +140	25.6			
	−140 +200	33.3			
	−200 +270	20.8			
	−270 +325	12.9			
	−325	7.2			
D	+100	0.005	8.28	0.107	82.89
	−100 +140	7.3			
	−140 +200	37.0			
	−200 +270	39.8			
	−270 +325	13.2			
	−325	2.7			

[a]Vacuum impregnation.
[b]Static BET krypton adsorption.

followed.[10] Representative longitudinal microstructures of the three oxides in the as-fabricated condition are shown in Fig. 14.10.

Since the fuel particles were highly fragmented, we wanted to use a counting method that did not depend upon line or point count methods, or upon random counting methods for the determination of fragmentation. A very simple expedient was used, namely the counting of every particle and every fragment in the field of view. The distinction between a small fragment of a large particle and an original fine particle was often difficult to determine and was solely dependent upon the judgement of the investigator. Employing this counting procedure yielded fragmentation ratio values for three different oxides, as shown in Table 14.3, together with the raw data.

On the basis of this analysis, the S-type oxide showed a wider range in the fragmentation index between samples than either the D- or N-type oxides. In addition, the S oxide had the lowest density and the highest amount of fragmentation of the three oxides tested. Both these factors relate to the initial condition of the oxide. The as-received powder contained numerous cracks and had an angular, almost acicular, shape. When this oxide was fabricated, each particle readily broke up into small fragments.

The fragmentation values for the D oxide do not take into account the material contained in the stringered tails as shown in Fig. 14.10. This material was too finely divided to be resolved in the photographs. Further, we believe these fine particles are not a manifestation of fragmentation but result from the removal of individual fines agglomerated on the surface of many of the original oxide particles. The large surface area of this powder reflects the presence of these fines. Thus, the D oxide values represent only a measure of the integrity of the central particles seen in the structure and do not include the material scoured from the surface.

The fragmentation index for the N-type oxide is slightly higher than that for the D type; however,

[10]D. O. Hobson *et al.*, *Fabrication Development of U_3O_8-Aluminum Composite Fuel Plates for the Advanced Test Reactor*, ORNL-3644 (July 1964).

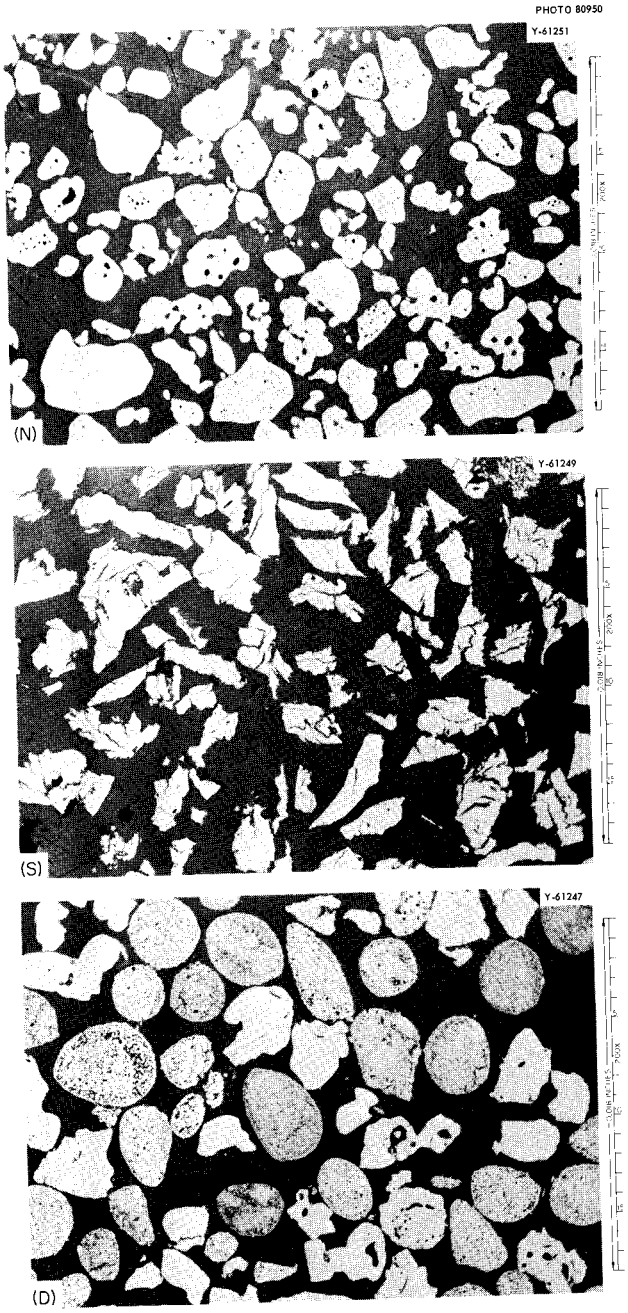

Fig. 14.9. Three Commercial U_3O_8 Samples in the As-Received Condition. The letters N, S, and D denote material from different suppliers. As polished. 200×. Reduced 50%.

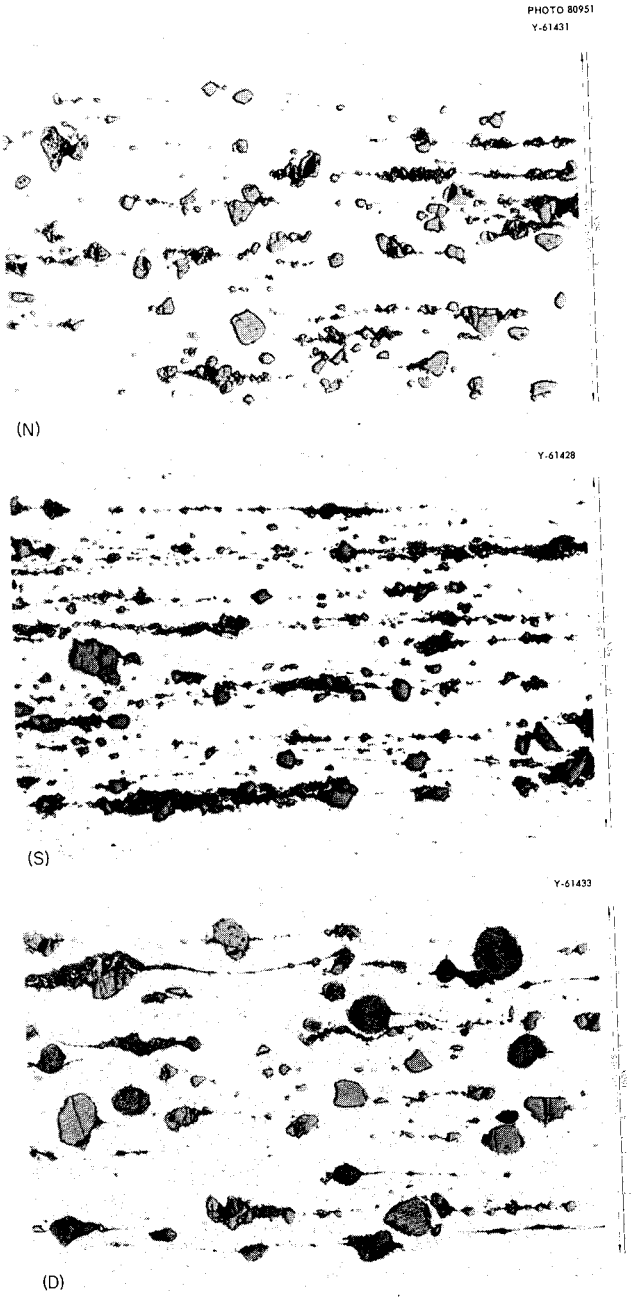

Fig. 14.10. Microstructure of Fuel Plates Fabricated from Three Commercial Oxides. The letters N, S, and D identify oxide from different suppliers. Hot straight rolled to a reduction ratio of 11.4, cold rolled 1.08, total reduction 12.3. As polished. 150×. Reduced 50%.

as shown in Fig. 14.10, the degree of stringering is noticeably less. This effect we attribute to the low surface area of the N-type oxide, resulting from the greater integrity and the more spherical shape of the particles.

In summary, we have found that the fabrication behavior of oxide particles can be qualitatively predicted on the basis of the physical properties of the oxide and the particle shape. The degree

Table 14.3. Experimental Fragmentation Data on Commercial Oxides

Oxide	View Number	Number of Original Particles	Number of Fragments	Fragmentation Index	Average
N	C-9-N (1)	450	3049	6.78	
	(11)	501	3384	6.75	6.90
	(21)	508	3359	6.61	
	(31)	554	4092	7.39	
S	C-7-S (1)	622	5812	9.34	
	(11)	561	5746	10.24	10.01
	(21)	556	5341	9.61	
	(31)	482	5328	11.05	
D	C-11-D (1)	491	2758	5.62	
	(11)	465	2561	5.51	5.86
	(21)	352	2252	6.40	
	(31)	511	3095	6.06	

of fragmentation increased with decreasing oxide density. In addition, particle shape affected fragmentation; spherical particles resisted fragmentation during fabrication more than particles having irregular shapes. We recommend the specification of high density U_3O_8 (>8.27 g/cm^3) as spherical particles with low surface areas (<0.05 m^2/g) to eliminate excessive cracking and the tailing of fines from the surface of the particles. The application of our characterization method to dispersions of UO_2 in stainless steel is described in Part III, Chap. 22 of this report.

FABRICATION OF ENRICHED UAl_3 DISPERSION FUEL PLATES

W. J. Werner J. H. Erwin
M. M. Martin C. F. Leitten, Jr.

A number of problems are anticipated with fuels for very high performance aluminum-water research reactors. The need for incorporating burnable poisons in fuel plates precludes the use of alloy fuels, since large and erratic boron losses have been experienced during melting. The metastable nature of the oxide dispersions and the large gas releases that could accompany the reactions under irradiation potentially restrict their use.[11] Since the uranium-aluminum intermetallics are stable under these conditions,[12] a limited amount of work was performed to determine the feasibility of intermetallic fuel and fuel-plate preparation. High-performance aluminum-base fuel plates containing either arc-cast UAl_2-UAl_3 mixtures or stoichiometric compounds produced by powder-metallurgical processes could be fabricated into fuel plates by conventional techniques with no deleterious effects. This work will be augmented by irradiation of the intermetallics in the form of ORR fuel elements. Because of the variable UAl_2-UAl_3 composition of material produced by casting, which severely restricts the production of large quantities of plates of equal fuel volume, the powder metallurgy route with UAl_3 was chosen for the irradiation experiment.

The UAl_3 was prepared in the following manner. High-purity uranium metal was hydrided to produce finely divided particles (3 to 4 μ average particle size). This material was then intimately mixed with the proper amount of high-purity aluminum powder (−325 mesh) by oblique dry blending. The blend was placed in a graphite die and the hydrogen removed from the mixture by the application of heat and vacuum. The mixture was then hot pressed under a low pressure of high-purity

[11] A. E. Richt, C. F. Leitten, Jr., and R. J. Beaver, "Radiation Performance and Induced Transformations in Aluminum-Base Fuels," p. 469 in *Research Reactor Fuel Element Conference, Sept. 17–19, 1962, Gatlinburg, Tennessee*, TID-7642, book 2 (1963).

[12] G. W. Gibson and D. R. deBoisblanc, "Uranium-Aluminum Alloy Powders for Use as Nuclear Reactor Fuels," paper presented at 1963 Fall Meeting of the Metallurgical Society of AIME, Oct. 21–25, 1963.

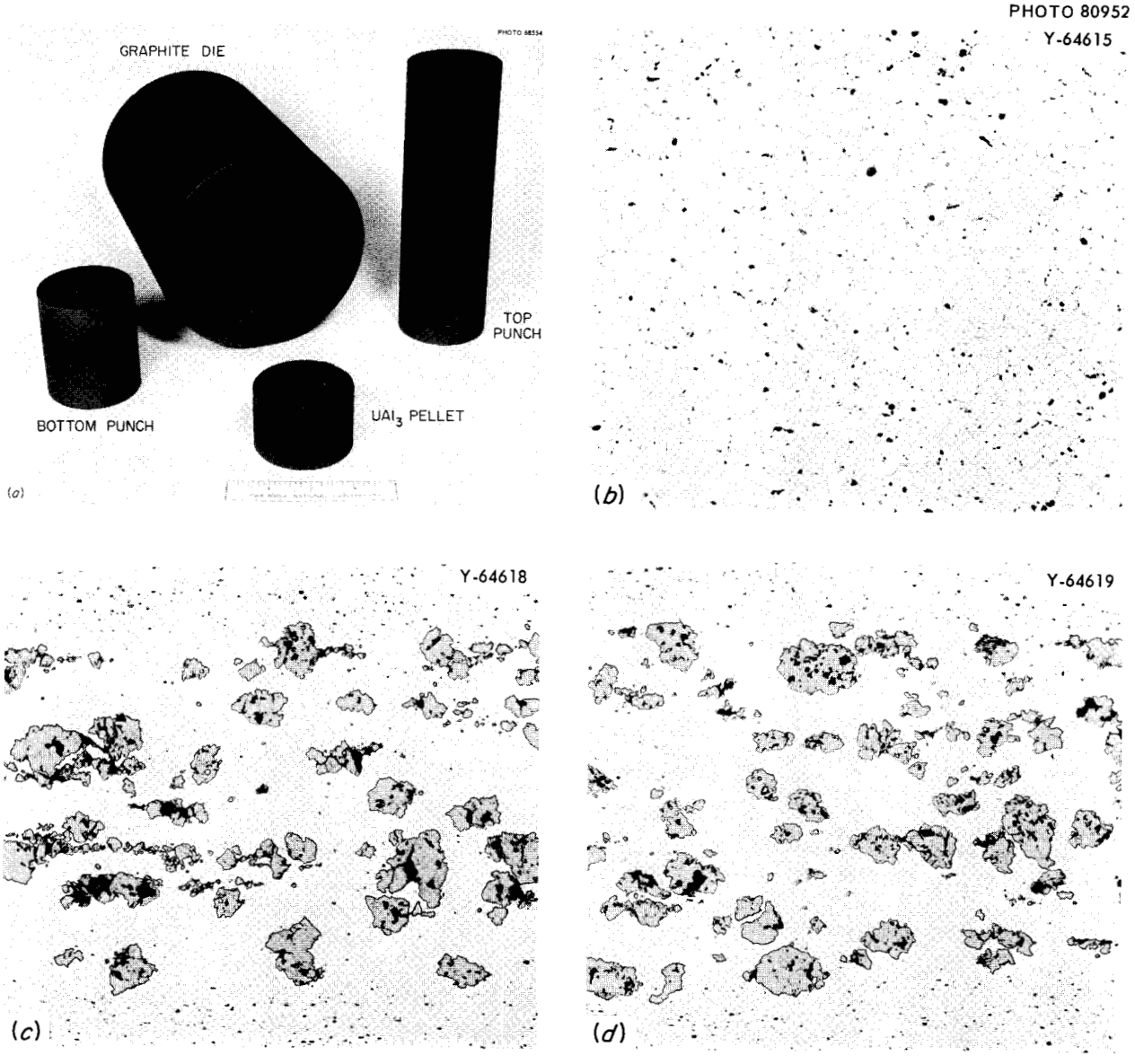

Fig. 14.11. UAl_3 in Various Stages of Plate Fabrication. (*a*) Pellet and die parts used in hotpressing. (*b*) Microstructure of pellet. Etchant 5% concd HF. 100×. (*c*) Longitudinal section of rolled fuel plate. As polished. 100×. (*d*) Transverse section of rolled plate. As polished. 100×.

argon at 1000°C for 2 hr. Figure 14.11 is a composite showing a UAl_3 pellet and associated graphite die, a photomicrograph of the hot-pressed pellet, and longitudinal and transverse sections of a finished UAl_3 dispersion plate. The dark appearance of the as-pressed pellet is a surface effect believed to have arisen during ejection of the pellet from the die. The UAl_3 hot pressings were hand-crushed to the proper particle size (−170 +325 mesh). High-quality blister-free plates of appropriate dimensions were fabricated from these intermetallics by conventional picture-frame techniques.

Chemical, spectrographic, and x-ray analyses were performed on the starting, intermediate (UH_x), and final materials. These analyses showed no

major impurities or impurity pickup during processing. Chemical and x-ray analyses of the starting materials and final sized product are shown in Table 14.4.

Table 14.4. Chemical and X-Ray Analyses of UAl_3 Starting Materials and Final Product

Measurement	Material		
	Al	U (metal ingot)	UAl_3 (powder)
Oxygen, %	0.24	0.018	0.1318
Nitrogen, %	0.0041	0.0027	0.024
Carbon, %	0.005	0.004	0.041
Density (toluene pycnometer), g/cm^3			6.7369
BET surface area, m^2/g			0.20
Weight fraction uranium			0.72932
Moisture content, %	<0.03		0.0361
X-ray UAl_3 content, %			95–97

FABRICATION OF URANIUM MONOCARBIDE WITH INTERMETALLIC SINTERING AIDS

J. P. Hammond

Uranium monocarbide as a nuclear fuel has excellent properties for a number of reactor types, but difficulties encountered in fabrication impose serious economic restrictions on its use. Ordinary sintering gives inadequate density and requires excessively high temperature. Over the last several years we have investigated[13,14] sintering aids that alleviate this problem without impairing fuel performance by introducing debilitating secondary constituents. Both volatilization and dissolution in the matrix were used as means for eliminating additive constituents. Table 14.5 summarizes our results.

The uranium intermetallics used as sintering aids (7.5% UAl_2, 0.75% UBe_{13}, and 0.75% U_3Si_2) are attractive because they are easily prepared as relatively air-stable fine powders and their secondary elements are of low thermal-neutron absorption cross section. With high-purity carbide powder as charge material, each of these processes can produce highly dense stoichiometric single-phase products (Table 14.5). The method using UAl_2 as the additive, for example, gives densities in excess of 97% of theoretical at a sintering temperature of only 1375°C.

When the carbide powder is impure, as it is when synthesized from UO_2 by carbon reduction, or contains excessive carbon, densification is impaired and secondary phases are retained whether UAl_2 or UBe_{13} is used as the additive. For the U_3Si_2 process, however, this is not the case. When sintering with U_3Si_2, we achieved best results with the UO_2-derived uranium monocarbide containing high oxygen, and the density was not appreciably influenced by a small excess in carbon content.

To aid interpretation of the sintering mechanisms for these processes, we determined pertinent pseudobinary diagrams and derived tentative ternary isotherms at the sintering temperatures.[15] An important feature of these processes was an initial stage in which reactive metal vapor issued from the additive and promoted shrinkage by scavenging the carbide powder of sinter-inhibiting oxide films. When highest densities were obtained, this stage was generally followed by liquid-phase sintering. Single-phase compacts were ultimately achieved when the residual constituent either dissolved in the matrix or carburized.

When powder of hyperstoichiometric carbon or high-oxygen content was sintered, the ability to form liquid as an intermediate step appeared to

[13] J. P. Hammond, J. D. Sease, and C. Hamby, Jr., "Uranium Monocarbide Fabrication with UAl_2 as Sintering Aid," pp. 145–53 in *The Fourth Uranium Carbide Carbide Conference, East Hartford, Conn., May 20–21, 1963*, TID-7676 (1964).

[14] J. P. Hammond and G. M. Adamson, Jr., "Fabrication of Uranium Monocarbide with a Volatile Sintering Temperature Depressant," *Symposium on Carbides in Nuclear Energy, Harwell, England, Nov. 5–7, 1963*, MacMillan, London, 1964.

[15] J. P. Hammond and G. M. Adamson, Jr., "Activated Sintering of Uranium Monocarbide," 1965 International Powder Metallurgy Conference, June 14–17, 1965 (to be published).

Table 14.5. Results of Sintering UC with Intermetallic Aids

Sintering Aid (wt %)	Type of UC Charge		Sintering Temperature (°C)	Sintered Density (% of theoretical)	Description of Product and Aid Elimination
	% C	Preparation			
7.5 UAl_2	4.8	Arc cast[a]	1375	>97	Near stoichiometric single-phase product; additive volatilized
	4.8	UO_2 derived[b]	1375	~75	
	4.9	Arc cast[a]	1375	~90	
0.75 UBe_{13}	4.8	Arc cast[a]	1525	~95	Stoichiometric single-phase product; additive dissolved
	4.8	UO_2 derived[b]	1525	~77	
	4.9	Arc cast[a]	1525	~86	
0.75 U_3Si_2	4.8	Arc cast[a]	1575	~96	Stoichiometric single-phase product; additive dissolved
	4.8	UO_2 derived[b]	1575	>97	
	5.1	Arc cast[a]	1575	~95	

[a]High-purity carbide prepared from spectrographic carbon and uranium containing <40 ppm C, <50 ppm N, and 75 ppm O.

[b]Carbothermally prepared UC with purposely introduced oxygen: 0.7 wt % O_2 as ground.

be the key to successful consolidation. With UAl_2 and UBe_{13}, reactions seemed to occur that prevented liquid from forming. With U_3Si_2, on the other hand, consolidation probably was promoted by the uranium dicarbide, present as a secondary constituent in the carbide powder, reacting with the silicide additive to give grain-wetting liquid phases.

Figure 14.12 illustrates microstructures observed when arc-cast UC is sintered with U_3Si_2. The densities indicated are based on a 100% UC product. With a stoichiometric starting powder, 1% U_3Si_2 as the additive results in a microstructure of uranium carbide with a few dicarbide needles (Fig. 14.12*a*). With substantial excess carbon in the charge, almost pore-free structures with some secondary microconstituents were obtained (Fig. 14.12*b*). By appropriately balancing the amount of additive against the excess in carbon, the secondary phase can be limited to silicon carbide (Fig. 14.12*c*), which is stable to around 1700°C in uranium monocarbide.[15] With insufficient silicide additive, both U_2C_3 and SiC form as secondary phases.

We demonstrated that with not undue attention to control of composition, essentially single-phase products can be consistently achieved from carbide powders synthesized from UO_2 by reduction with carbon.

AIDED SINTERING OF URANIUM NITRIDE

J. P. Hammond

Like uranium carbide fuel, uranium mononitride has the advantages of higher thermal conductivity and uranium density than those of UO_2, but fabrication is even more difficult than it is for the carbide.[16] Studies were initiated to examine various aids for sintering uranium mononitride along the lines carried out for uranium monocarbide (preceding section).

Shown in Table 14.6 are some of the more interesting results from preliminary experiments conducted to date. These rather promising results were obtained for uranium mononitride starting powder analyzing 93.68% U, 5.58% N, 0.01% C, and 0.102% O. Material from three separate batches of uranium mononitride was studied, and the sintered density improved with purity of the starting material. The good result listed last in Table 14.6 is attributed to scavenging of contaminants by the aluminum vapor and the extreme fineness of the uranium mononitride powder. Chemical analysis indicated that a 12% loss of nitrogen resulted from the fabrication. The microstructure (Fig. 14.13) showed trace amounts of an unidentified finely distributed constituent.

[16]E. O. Speidel and D. L. Keller, *Fabrication and Properties of Hot-Pressed Uranium Mononitride*, BMI-1633 (May 30, 1963).

PHOTO 69398

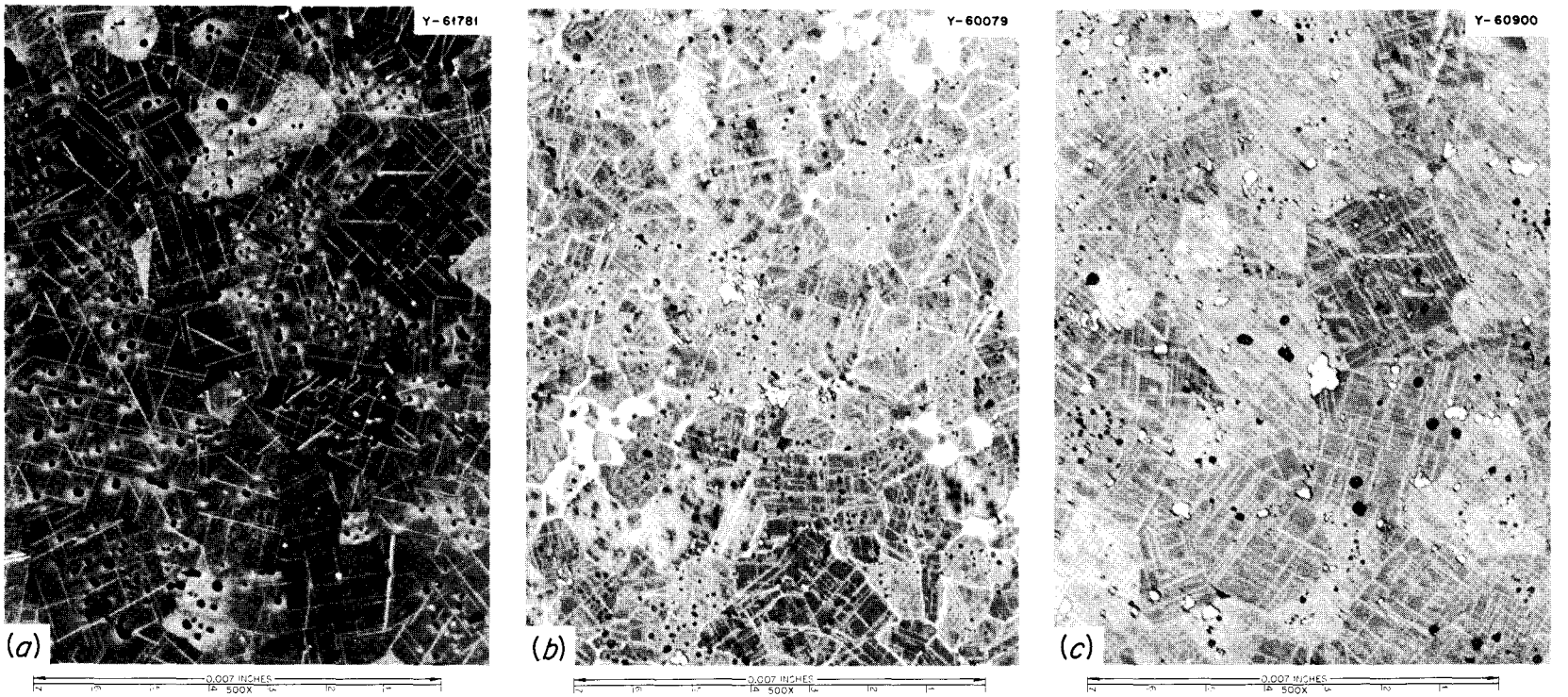

Fig. 14.12. Microstructures of UC Sintered with U_3Si_2 3 hr at 1600°C. (*a*) Starting carbide contained 4.8% C, sintered with 1% U_3Si_2, final density 96.3% of theoretical, no second phases observed. (*b*) 5.1% C, 1.5% U_3Si_2, density 94.9%, U_2C_3 and SiC present. (*c*) 5.1% C, 3.9% U_3Si_2, density 94.3%, SiC present. Reduced 37%.

Table 14.6. Sintering Results for Uranium Nitride[a]

Sintering Temperature (°C)	Sintering Aid (wt %)	Ball Milling Time[b] (days)	Sintered Density (% of theoretical)[c]	Secondary Constituents	
				Amount	Kind
1500	2 UAl_2	2	89.2	Very slight	Sizeable particle
1500	4 UAl_2	2	89.8	Very slight	Sizeable particle
1600	2 UAl_2	2	94.9	Slight	
1600	4 UAl_2	2	93.1	Very slight	
1550	Al vapor[d]	6	95.0	Trace	Fine, uniformly dispersed

[a]Pressed as $^5/_{16}$-in.-diam pellets at 25 tsi with 2% camphor binder and fired 3 hr in vacuum in tungsten-lined tantalum crucible.

[b]Tungsten carbide balls in rubber-lined drum, 4-μ starting powder.

[c]Average of two tests.

[d]Provided by distillation from 10% (of charge) UAl_2 powder introduced on hearth of crucible.

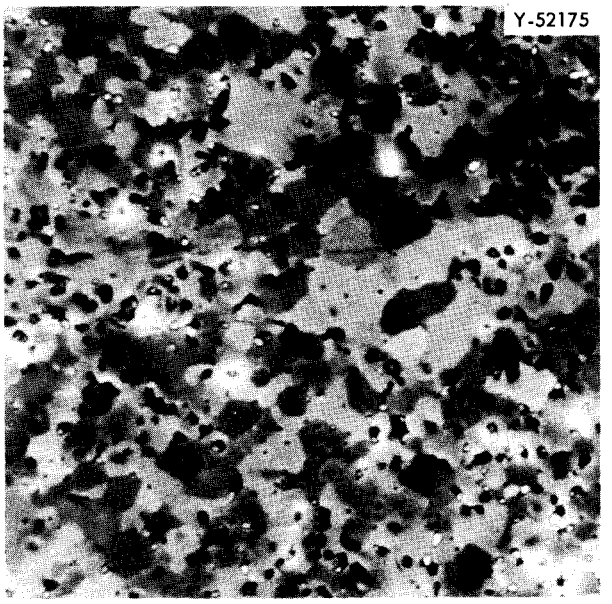

Fig. 14.13. Microstructure of Uranium Nitride Sintered 3 hr at 1550°C in Presence of Aluminum Vapor. Swabbed in equal parts lactic and concd nitric acids, followed by immersion in a mixture of 30 ml lactic acid, 10 ml concd HNO_3, and 2 ml concd HF. 1000×.

15. High-Temperature Materials

W. C. Thurber W. O. Harms

Our goal is to develop an advanced materials technology on a sufficiently broad base and an appropriate time scale so that engineers concerned with the design and development of advanced reactor systems will have sufficient information on high-temperature materials when required. This should greatly reduce the amount of development needed for specific systems and accelerate their realization. Within this broad framework we have focused our attention on those high-temperature systems that will require refractory metals for the containment of molten alkali metals. The program includes development and inspection of refractory-metal tubing, studies of joining methods, measurement of the mechanical and physical properties of refractory alloys, studies of physical metallurgy, and an appraisal of the compatibility of refractory metals with alkali metals. Significant portions of this work are covered in detail elsewhere.[1–3] Programs on the specific materials tungsten and uranium nitride are reported in Chaps. 19 and 20, respectively, and more basic studies on materials compatibility in Chap. 16.

In the text that follows, frequent reference is made to commercial refractory-metal alloys by their trade designations. The nominal compositions of these alloys are listed in Table 15.1.

Table 15.1. Compositions of Refractory-Metal Alloys

Designation	Base	Additives (wt %)
B-66	Niobium	5 Mo, 5 V, 1 Zr
C-129Y	Niobium	10 Hf, 10 W, 0.1 Y
Cb-752	Niobium	10 W, 2.5 Zr
D-43	Niobium	10 W, 1 Zr, 0.1 C
FS-85	Niobium	27 Ta, 10 W, 1 Zr
T-111	Tantalum	8 W, 2 Hf
TM	Molybdenum	0.5 Ti
TZM	Molybdenum	0.5 Ti, 0.08 Zr

FABRICATION DEVELOPMENT

C. F. Leitten

Refractory Metal Extrusion

R. E. McDonald G. A. Reimann

Work has continued on the extrusion of tungsten billets to produce sound tube shells for subsequent processing into thin-wall large-diameter tubing. In view of our previous experience with tungsten extrusion, we again attempted to extrude uncoated tungsten using the mandrel technique. To evaluate the effect of increased billet density on extrusion parameters, we prepared billets from $3\frac{1}{4}$-in. bar stock that had been extruded from $5\frac{7}{8}$-in. powder-metallurgy billets. Table 15.2 summarizes the pertinent data obtained. The billets prepared from the preextruded bar stock required greater extrusion loads because of their greater density. The optimum extrusion temperature for both powder-metallurgy

[1] W. C. Thurber *et al.*, ORNL-TM-980 (October 1964) (classified).

[2] W. C. Thurber *et al.*, ORNL-TM-1050 (March 1965) (classified).

[3] W. C. Thurber, W. O. Harms, *et al.*, ORNL-TM-1140 (July 1965) (classified).

billets and wrought bars was found to be 1700°C for a reduction ratio of 5.8.

To produce tube shells more compatible with the required final tube size, we tried to increase the reduction ratio by employing a mandrel with a smaller diameter. As shown in Table 15.2, incomplete extrusions were encountered at a reduction ratio of 8.8 and temperatures of 1850 and 1925°C. In both cases, the $\frac{3}{4}$-in.-diam mandrel "necked" and failed as a result of tensile stresses. Figure 15.1 shows the mandrel failures. An additional billet (No. 1449) was extruded at 2000°C and yielded a satisfactory shell $1\frac{1}{2}$-in. OD × $\frac{1}{4}$-in. wall with good surface characteristics. The high surface quality of this extrusion is shown in Fig. 15.2.

The possibility of extruding uncoated W–26% Re alloys was investigated in a joint venture with the Albany Metallurgy Research Center, U.S. Bureau of Mines, Albany, Oregon. Machined billets of both sintered and cast material are supplied by that organization. We measured the rate of oxidation of the alloy and studied the nature of the oxide formed. The W–26% Re alloy was substantially more resistant to oxidation than unalloyed tungsten in the extrusion temperature range of interest. The effectiveness of the bare extrusion process depends upon the lubricity of the oxide layer that develops

Table 15.2. Tungsten and Tungsten-Alloy Extrusion Data

Billet No.	Method of Billet Fabrication	Billet Type	Billet Density (% of Theoretical)	Billet Temperature (°C)	Time to Reach Temperature (min)	Extrusion Time (sec)	Reduction Ratio	Load (tons)		Remarks
								Break-through	During Extrusion	
1190[a]	Sintered	Tube shell	92	1850	25	12.5	5.8	480	405	Outer surface good; inner surface superior.
1191[a]	Sintered	Tube shell	92	1700	23	10.6	5.8	405	380	Outer and inner surfaces superior.
1362[a]	Wrought bar	Tube shell	>99	1650	23	8.0	5.8	600	515	Outer surface good, some tearing; inner surface superior.
1363[a]	Wrought bar	Tube shell	>99	1700	23	8.0	5.8	555	510	Outer surface good, minimum tearing; inner surface superior.
1447[a]	Wrought bar	Tube shell	>99	1700	21	15	5.8	545	535	Outer surface good; inner surface superior.
1448[a]	Wrought bar	Tube shell	>99	1850[b]	20	18	8.8	645	600	Incomplete extrusion; mandrel failed; outer surface good; inner surface superior.
1449[a]	Wrought bar	Tube shell	>99	2000[b]	23	13	8.8	580	540	Outer surface good; inner surface superior.
1450[c]	Arc cast	Bar	>99	2100[b]	25	15	10	660	580	Incomplete extrusion; bar ratcheted and broke.
1451[a]	Wrought bar	Tube shell	>99	1925[b]	22	15	8.8	600	580	Incomplete extrusion; mandrel failed; outer surface good, inner surface superior.
1491[c]	Arc cast	Bar	>99	2800	23	13	6.1	670	510	Incomplete extrusion; bar ratcheted and broke.
1492[c]	Sintered	Sheet bar	92	2200	26	18	8.5	645		Partial extrusion; surface good.
1493[c]	Arc cast	Sheet bar	>99	2200	26	21	5.3	630		Partial extrusion; surface good.

[a]Tungsten.
[b]Not measured accurately.
[c]W–26% Re alloy.

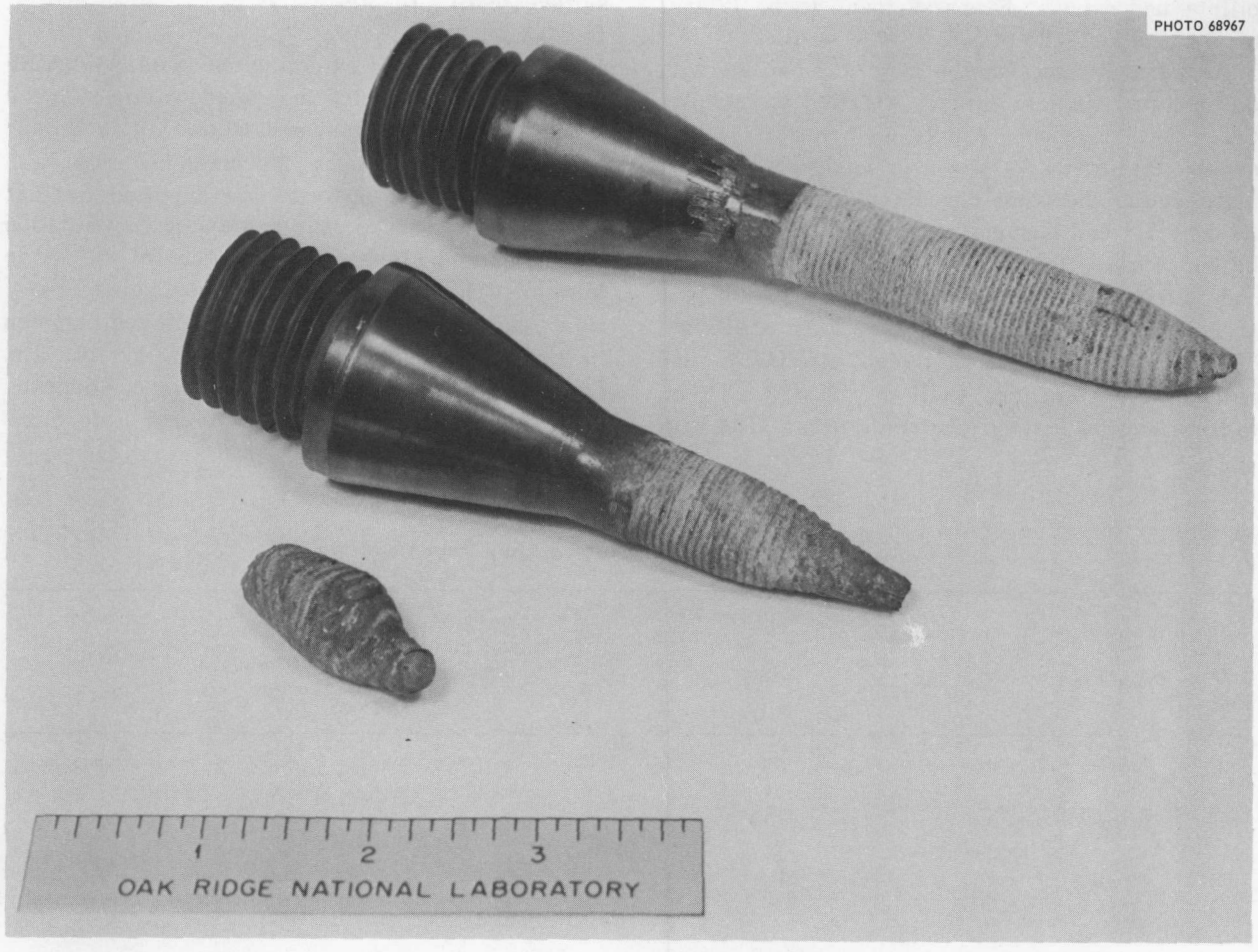

Fig. 15.1. Tube Shell Mandrels that Failed in Tension During Extrusion of Tungsten at 1870–1925°C.

during transfer of the billet from the furnace to the extrusion press. The effect of rhenium on the oxidation characteristics has raised doubts regarding the effectiveness of this method of lubrication for the alloy. Because we lacked sufficient data on the minimum amount of oxide required for an uncoated extrusion, we attempted two uncoated bar extrusions, using arc-cast W–26% Re billets. As shown in Table 15.2, billets Nos. 1450 and 1491 failed to extrude. Severe surface ratcheting was encountered in both extrusions. Further attempts to extrude W–26% Re sheet bar stock were made using a high-temperature glass lubricant. Partial extrusions were accomplished at 2200°C at reduction ratios of both 8.5 and 5.3. The latter yielded considerably more extruded bar stock. In both cases, the surface of the extruded material was of good quality. Further lowering of the reduction ratio yielded complete extrusions of the alloy.

Fabrication of Alkali-Metal Pump Cells

R. E. McDonald K. E. Toomey

An electrodynamic pump cell designed for use in liquid-metal pumped loops was fabricated from Nb–1% Zr alloy. An Inconel can was required to protect the alloy from oxidation during use. Because of the many problems associated with conventional fabrication techniques due to warpage and materials compatibility, a more simplified design was proposed. Aluminum-powder-filled epoxy dies were developed to form the two Inconel covers by explosive forming. A completed pump cell is shown in Fig. 15.3.

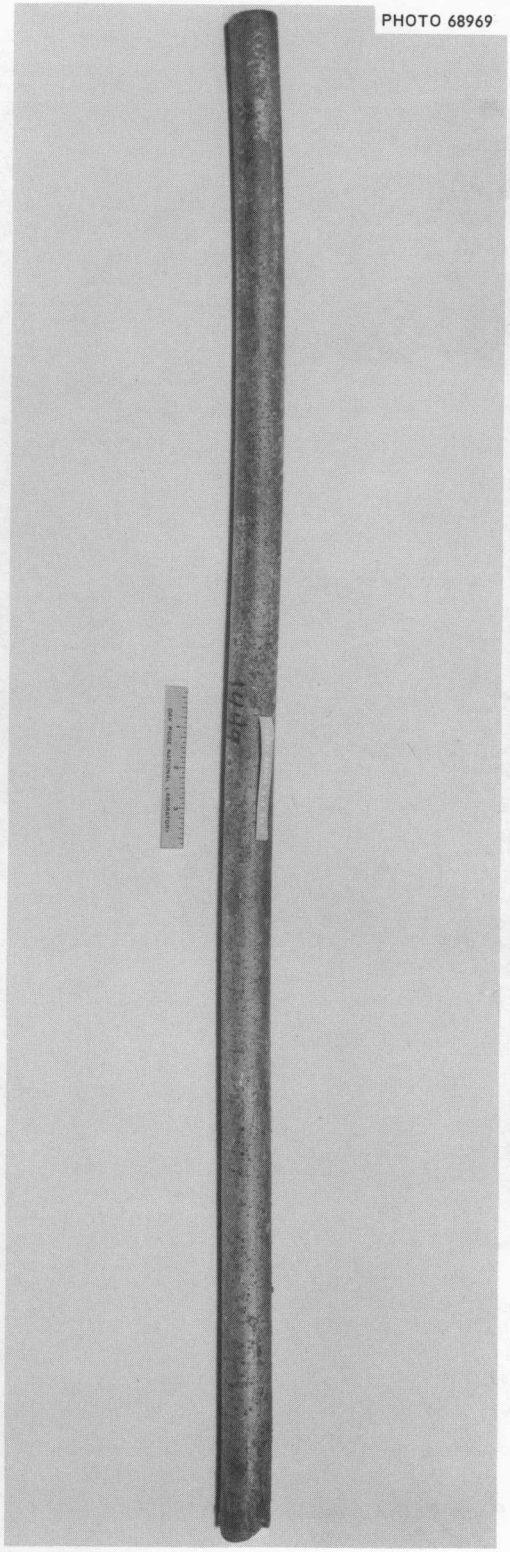

Fig. 15.2. Tube Shell Extrusion of Pure Tungsten (Billet No. 1449, 1980°C, Reduction Ratio 8.8) Showing Excellent Surface Obtainable from Uncoated Billets.

The pump cell was fabricated by forming a loop of Nb–1% Zr tubing and wrapping this tubing in molybdenum foil to protect it from the Inconel covers. Figure 15.4 is a positive radiograph showing the dark Nb–1% Zr tubing restrained by pins inside the welded Inconel covers. The dark lines in the lower right portion are two Inconel baffles to prevent the liquid conductor bar from rotating in the magnetic field during operation.

Flow Turning of Refractory-Metal Tube Shells

R. E. McDonald

Feasibility was demonstrated for producing niobium- and tantalum-base alloy tube shells by the flow turning technique at room temperature. Two hollow cylinders of the cast tantalum-base alloy T-111 were successfully flow turned to tube shells and subsequently tube reduced and drawn to finished tubing. The inner surface was inferior but the tubing was otherwise sound. The inferior surface is due at least in part to the relatively large grain size in the initial cast cylinder and to frictional drag during movement of the material along the mandrel during flow turning. The quality of the final inner surface of the as-flow-turned shell was improved when a copper insert sleeve in a Nb–1% Zr alloy hollow was employed during the flow turning operation. This technique could also be used to improve the inner surfaces of T-111 alloy tube shells.

Attempts to lightly flow turn welded thin-walled cylinders of D-43 and Cb-752 alloys were unsuccessful due to catastrophic failures in the heat-affected zone. The purpose of this effort was to establish the feasibility of producing tube shells by rolling plate material, seam welding, and lightly working the weld area prior to sending the material to a tubing manufacturer.

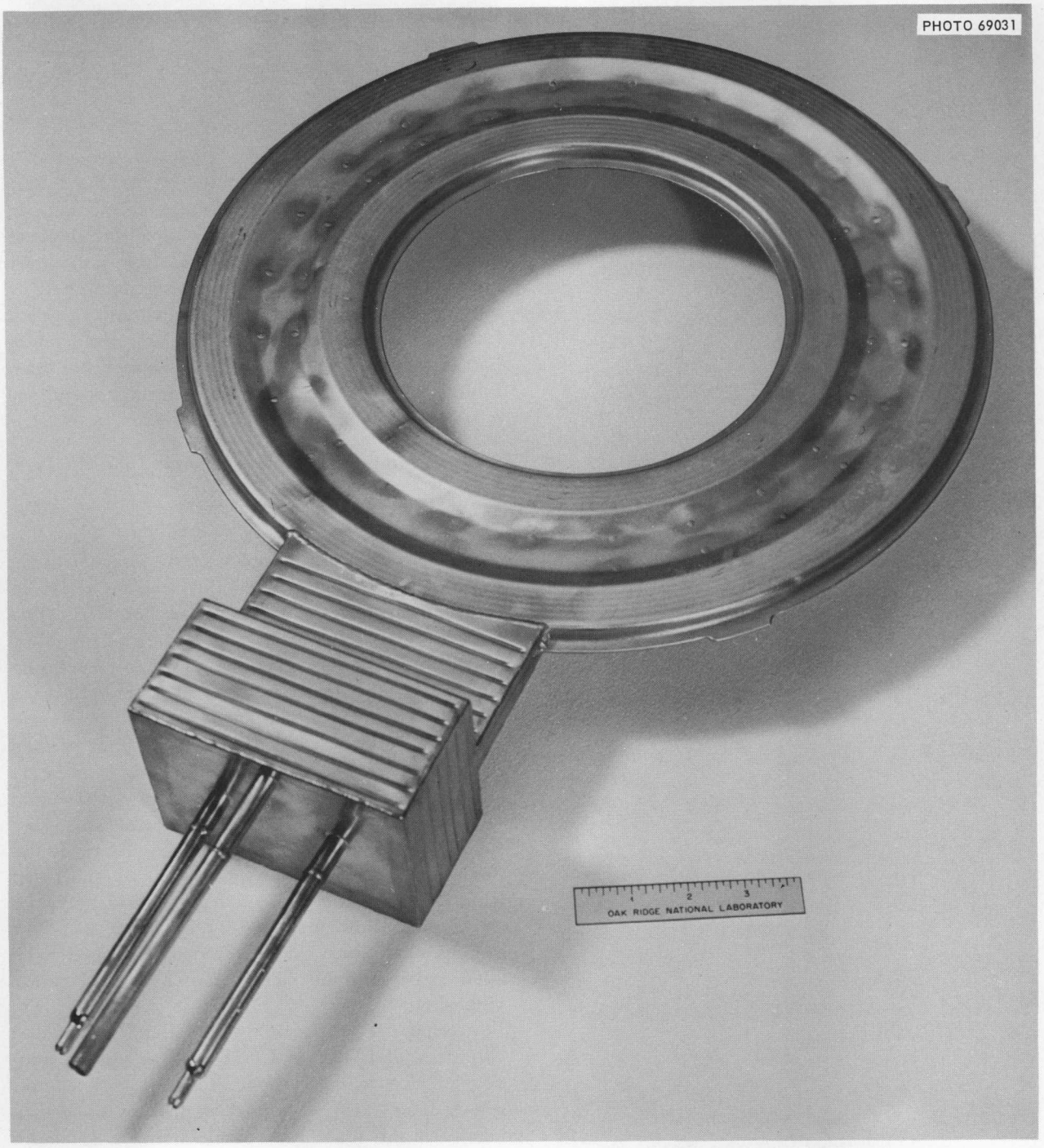

Fig. 15.3. Completed Liquid-Metal Pump Cell Assembly.

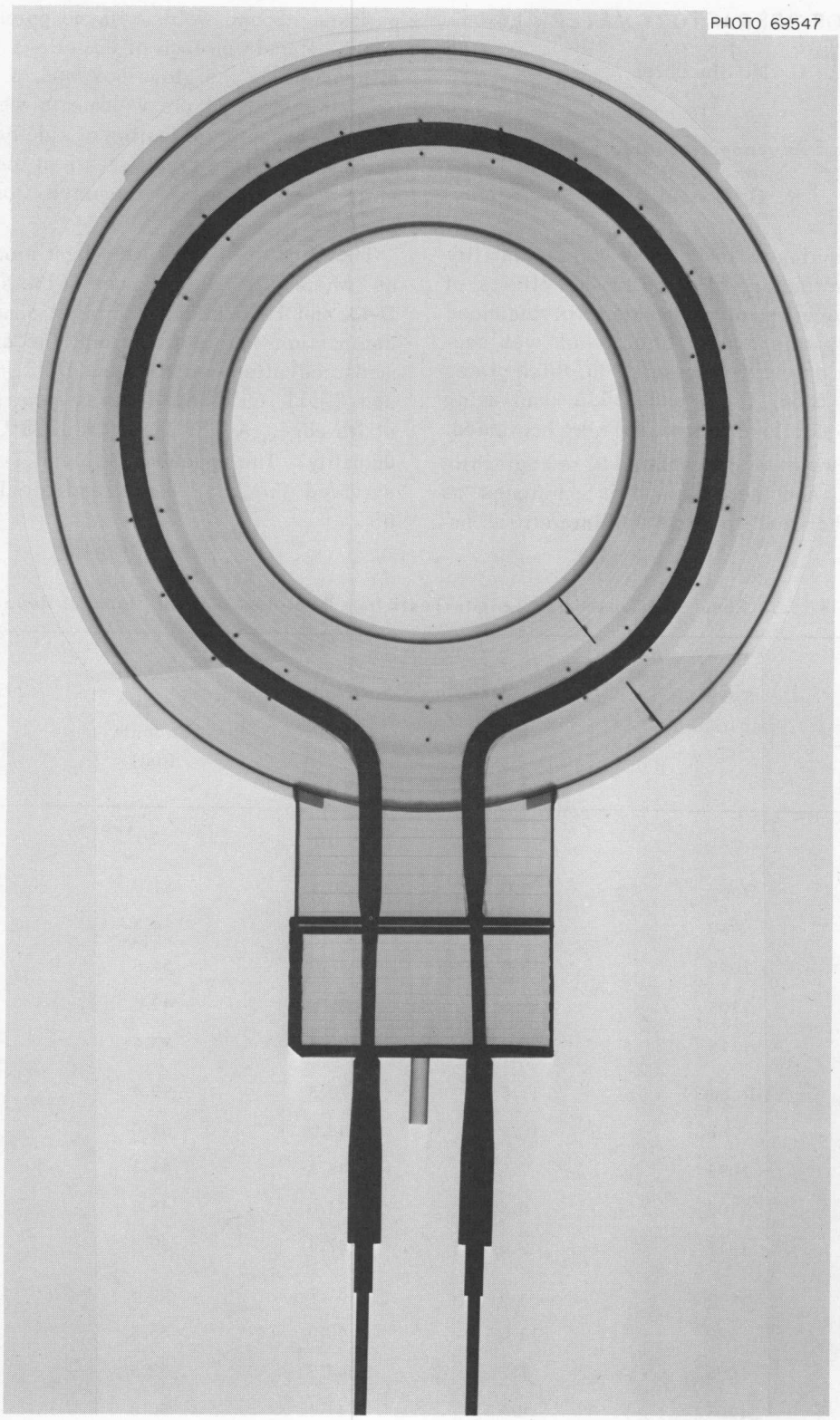

Fig. 15.4. Positive Radiograph of Completed Pump Cell Assembly.

JOINING OF REFRACTORY MATERIALS

G. M. Slaughter

Welding of Advanced Refractory Alloys

R. G. Donnelly

We are continuing to investigate the weldability of advanced refractory alloys and the effects of aging on the properties of weldments involving these alloys. During this report period, work was centered primarily on the welding of ½-in.-thick plates of the alloys B-66, D-43, and T-111, and aging studies on FS-85 alloy sheet welds were continued.

These plate welds were evaluated by radiographic, dye-penetrant, and metallographic techniques as well as by chemical analysis for interstitial impurities. Sound welds with no porosity or cracks could be made in each of the alloys if the welding atmosphere in the glove box was of a high purity. The properties of the weldments were determined by room-temperature testing of side-bend specimens and by transverse tensile tests at elevated temperatures on specimens machined from the welded plates.

The bend specimens were bent around a $2T$ radius, where T is the thickness of the specimen. The D-43 and B-66 alloys exhibited almost no plastic deformation before fracturing; the angles of bend measured after fracture were D-43, 5°; B-66, 15°; and T-111, 65°. All failures were in the weld or at its edge. A 2-hr anneal at 1315°C improved the ductility. The annealed D-43 and T-111 specimens survived the 105° bends and the B-66 failed at 65°.

Table 15.3. Results of Transverse Tensile Tests from ½-in.-thick Welded Plates of Refractory Alloys

Alloy	Test Temperature (°C)	Elongation (%)	Yield Strength at 0.2% Offset (psi)	Ultimate Tensile Strength (psi)	Location of Failure[a]
			$\times 10^3$	$\times 10^3$	
D-43	Room	5.0	60.8	81.0	B-W
	980	8.5	35.1	54.4	B
	1095	10.0	37.0	51.5	B
	1205	13.0	39.9	42.0	B
	1315	10.0	29.8	33.4	B-W
B-66	Room	11.5	76.3	99.4	W
	980	10.0	48.9	63.0	B
	1095	7.5	45.3	41.1	B
	1205	6.5	41.0	43.8	B-W
	1315	9.0	37.4	39.5	B
T-111	Room	5.0	82.7	90.5	W
	980	11.0	40.0	55.5	B-W
	1095	7.5	41.9	52.5	W
	1205	8.0	41.1	50.8	W
	1315	10.0	37.7	43.9	W

[a]W, weld; B, base metal.

The results of transverse tensile tests to 1315°C are listed in Table 15.3 and indicate that the elongations for welded plates are significantly lower than those reported previously for unwelded sheet material,[4] especially at the higher temperatures. This difference probably is due to the higher restraining effect of the weld metal in the center of the gage length of the thicker weldments. In ultimate tensile strength, the B-66 alloy was stronger than D-43 and also stronger than the tantalum alloy up to 980°C. Above 1095°C, the T-111 alloy had the highest ultimate strength.

In the niobium alloys, the failures were either in the base metal or partially in the weld and partially in the base metal. The T-111 alloys, however, always failed in weld metal even though chemical analysis showed no contamination of the weld metal by interstitials.

The effects of aging at 815, 980, and 1205°C on the longitudinal bend ductility of FS-85 alloy sheet welds are shown in Fig. 15.5. Each specimen was doubly wrapped, once in tantalum and once in molybdenum, and then aged in either a vacuum furnace or a quartz capsule. The specimens encapsulated in quartz became embrittled sooner and did not recover as did the specimens aged in the vacuum furnace. Examination of the encapsulated specimens by the laser probe technique revealed surface contamination high in silicon content. As a result of this observation, all future specimens will be aged in vacuum furnaces with high-density Al_2O_3 muffles.

The aging results for D-43 alloy sheet welds are compiled in Fig. 15.6. We studied the effects of time, temperature, and environment of aging and

[4]G. E. Gazza and T. S. DeSisto, *Evaluation of Refractory Metal Sheet Alloys*, U.S. Army Materials Research Agency, Technical Report AMRA-TR-64-16, pp. 15–16 (July 1964).

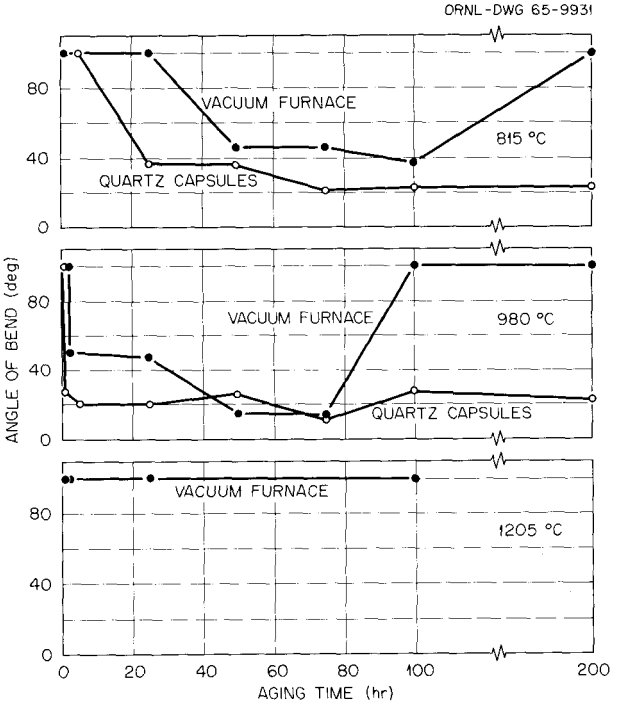

Fig. 15.5. Influence of Aging Time and Environment at Various Temperatures on the Bend Ductility of FS-85 Alloy Welds.

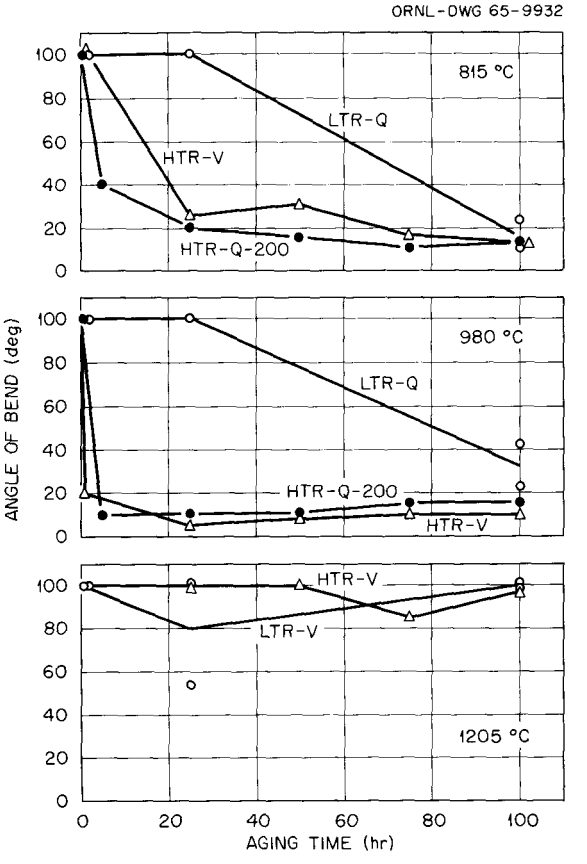

Fig. 15.6. Influence of Aging Time, Temperature, and Environment and of Processing History on the Room-Temperature Bend Ductility of D-43 Alloy Welds. Aging environments: Q, quartz capsule; V, vacuum furnace. Maximum processing temperatures: HTR, 1425°C; LTR, 1205°C. Specimens designated HTR-Q-200 were tested at 93°C.

processing history. Two different heats of the alloy were investigated and are designated as HTR or high-temperature-route (maximum processing temperature 1425°C) and LTR or low-temperature-route (maximum processing temperature 1205°C). The HTR material had a higher interstitial content (1070 ppm C, 210 ppm O, 70 ppm N, 2 ppm H) than the LTR material (950 ppm C, 64 ppm O, 38 ppm N, 1 ppm H). The data at the two lower aging temperatures show that the welds in the specimens with high interstitial content aged faster, regardless of whether they were aged in a vacuum furnace or in quartz capsules. The HTR-Q-200 curve (test temperature, 93°C) shows that these embrittled specimens exhibited a ductile-to-brittle transition temperature above 93°C even though unwelded companion specimens were all ductile after aging.

We have found no aging reaction for alloy T-111 at 815, 980, or 1205°C for 1, 2, 25, or 100 hr. It is the only refractory alloy investigated in this program that has not shown an aging reaction.

Brazing Alloy Development

R. G. Gilliland

We are developing brazing alloys to produce joints in refractory-base alloys with a service capability of 1900°C. Preliminary results on the ternary systems Ti-V-Ta and Nb-V-Ta were reported previously.[5] Selected alloy compositions from these ternary systems were tested for stability in a vacuum to 1370°C for 500 hr, mechanical properties, and remelt temperatures.

Microstructures of braze joints for alloys from each ternary system are shown in Fig. 15.7. The structure of the 65% V–30% Nb–5% Ta alloy indicates that the braze joint consists of a single phase; we believe the reaction zone at the brazing alloy–base metal interface in both aged joints is caused by diffusion during the aging treatment.

[5]R. G. Gilliland, *Metals and Ceramics Div. Ann. Progr. Rept. June 30, 1964*, ORNL-3670, pp. 79–82.

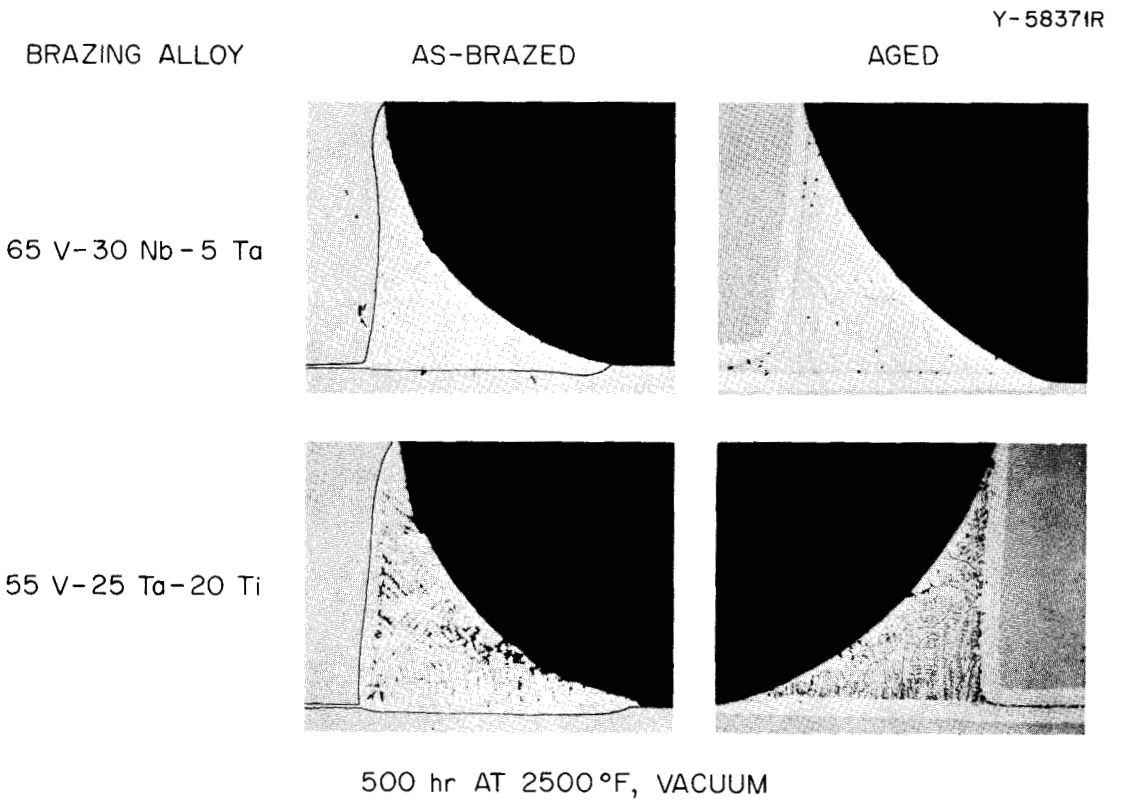

Fig. 15.7. Cross Sections of Tantalum T-Joints in the As-Brazed and Aged Conditions. Excellent joint soundness is in evidence. As polished. 50×.

Microhardness readings taken across the brazing alloy–base metal interface of these T-joint specimens showed an overall increase in brazing alloy hardness as a result of aging; the hardness profile rose slightly in the interfacial reaction zone.

Table 15.4. Shear Strength of V-Ta-Ti and V-Ta-Nb Brazed Joints Tested at 1370°C in Vacuum

Brazing Alloy Composition (wt %)	Brazing Temperature (°C)	Shear Strength[a] (psi)
		$\times 10^3$
50 V–25 Ta–25 Nb	1870	17.0 (3)
40 V–30 Ta–30 Nb	1930	18.8 (2)
65 V–5 Ta–30 Nb	1820	14.3 (1)
65 V–30 Ta–5 Ti	1840	14.6 (2)
55 V–25 Ta–20 Ti	1840	11.9 (1)
50 V–20 Ta–30 Ti	1760	20.3 (2)
TZM[b]	1870	44.2 (1)

[a]Numbers in parentheses indicate number of samples tested.

[b]Specimen material blank heated through brazing cycle prior to testing.

Table 15.5. Results of Brazing Alloy Remelt Study

Brazing Alloy Composition (wt %)				Brazing Temperature (°C)	Remelt Temperature (°C)	Approximate Rise in Melting Temperature (°C)
V	Ta	Nb	Ti			
50	25	25		1870	2500	630
40	30	30		1930	2000	70
65	30	5		1870	2300	430
65	5	30		1810	2300	490
65	30		5	1840	2400	560
55	25		20	1840	2200	360
50	20		30	1760	2400	640
40	10		50	1760	2400	640

We have used Miller-Peaslee type test specimens[6] to determine the shear strengths of these brazing alloys at 1370°C with TZM alloy as the base metal. The results are presented in Table 15.4. Further tests are being performed at 1200 and 1650°C.

We have also determined the remelt temperatures of brazed joints formed by alloys from these ternary systems. The results are presented in Table 15.5. All brazing-alloy melting temperatures increased significantly except for the V–30% Ta–30% Nb alloy. The greatest effects (greater than 600°C) were exhibited by the V–25% Ta–25% Nb, V–20% Ta–30% Ti, and V–10% Ta–50% Ti alloys.

Component Fabrication

E. A. Franco-Ferreira

Refractory Metal Loops. – Numerous small natural-circulation loops of Nb–1% Zr, D-43, and T-111 were fabricated for materials compatibility studies. The general techniques used in this work have been described previously.[7]

A large pumped loop for boiling-potassium service was made of Nb–1% Zr alloy. This loop, shown in Fig. 15.8, measures approximately 1.5 by 10 ft and contains 72 welds. Specialized jigs and fixtures were developed for the various welding operations.

Liquid Metal Pumps. – Two pump cells, each based on a different design, were fabricated from Nb–1% Zr alloy for use in the large pumped loop program.

Sealing of Refluxing Capsules. – Capsules made of various refractory alloys for containing refluxing liquid metals at elevated temperatures are used in the materials compatibility testing program. For this application, the void space in the capsules must be evacuated to 10^{-5} to 10^{-7} torr before the final sealing operation. Since handling complications precluded the use of an electron-beam welder for this job, a specialized resistance-welding process and the requisite equipment were developed. The process developed consists of welding a refractory-metal plug into a pumpout nipple in the upper end cap of the refluxing capsule.

[6]F. M. Miller and R. L. Peaslee, *Welding J. (N.Y.)* 37(4), 144s–50s (1958).

[7]E. A. Franco-Ferreira, *Metals and Ceramics Div. Ann. Progr. Rept. June 30, 1964*, ORNL-3670, pp. 82–83.

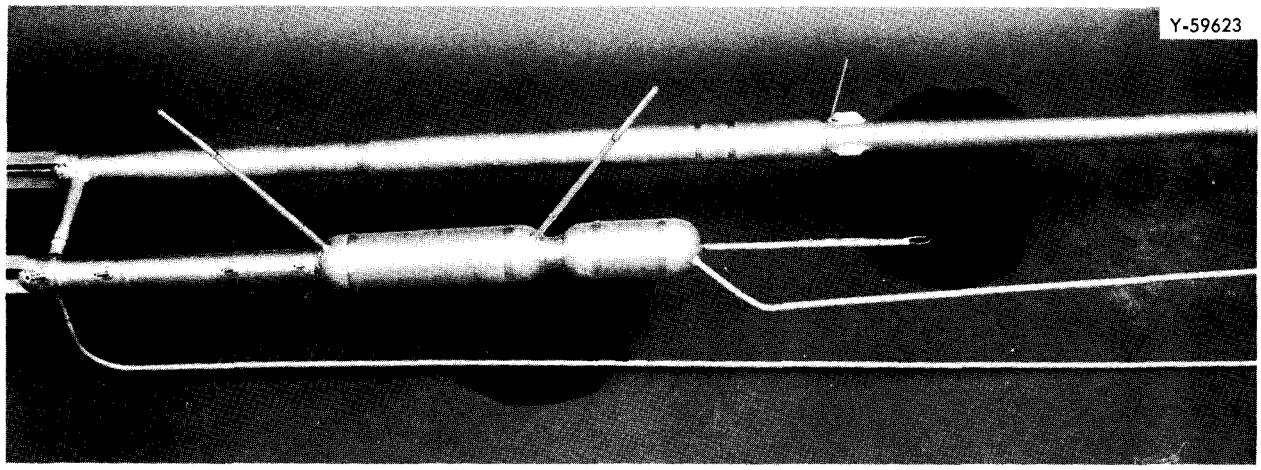

Fig. 15.8. Nb–1% Zr Pumped Loop.

This is accomplished by resistance heating of the two joint components while the entire capsule assembly is in a vacuum chamber under high vacuum. The apparatus is shown in Fig. 15.9. A large motor-generator power supply (not shown) was connected across the power terminals, and when a suitable vacuum was obtained, the refractory-metal plug was brought into contact with the nipple by means of the plunger. The power supply was then short-circuited and the joint heated rapidly. When a sufficiently high temperature was reached, additional pressure was applied to the plunger, and the power was turned off.

A view of a sealed capsule with the plug in place is shown in the upper left inset of Fig. 15.9. A longitudinal cross section of a typical upper end cap of the capsule, including the plug weld, is shown in the lower left inset of the figure.

PHYSICAL METALLURGY OF REFRACTORY ALLOYS

H. Inouye

High-Temperature Sorption of Nitrogen by Nb–1% Zr in Ultrahigh Vacuum

H. Inouye

Nitrogen in the Nb–1% Zr alloy is unstable in ultrahigh vacuum at high temperatures. The rate at which the nitrogen content changes depends upon the deviation from equilibrium between nitrogen in the gas phase and nitrogen in the alloy. We have established the conditions for equilibrium and the kinetics of the sorption process.

The equilibrium conditions for the system N_2/Nb–1% Zr–N for alloys containing up to 278 ppm N between 1200 and 1800°C are shown in Fig. 15.10. The straight line portions of the curves are parallel with a slope of two and thus represent solid solutions of nitrogen in the alloy that obey Sieverts' law. Deviations from this law are shown by the dashed curves. Based on the published data[8] for the solubility of nitrogen in unalloyed niobium, 1% Zr in niobium lowers the nitrogen solubility by at least an order of magnitude (e.g., 2300 ppm in niobium compared to about 200 ppm in the alloy at 1200°C).

The partial molar heats of solution $\overline{\Delta H}$ of nitrogen in the alloy were determined from the plot of log P_{N_2} vs $1/T$ shown in Fig. 15.11 to be –51.3 kcal/gram-atom N above 1400°C and –35.0 kcal/gram-atom N below this temperature when the nitrogen content of the alloy is less than 100 ppm. At nitrogen contents near 275 ppm $\overline{\Delta H}$ was –51.3 kcal/gram-atom between 1200 and 1800°C. We think the change in $\overline{\Delta H}$ at 1400°C for alloys containing 100 ppm N or less is due to an interaction of the nitrogen with the carbon or the oxygen in the alloy.

[8]W. M. Albrecht and W. D. Goode, Jr., *Reaction of Nitrogen with Niobium*, BMI-1360 (July 6, 1959).

ORNL-DWG 65-2931R

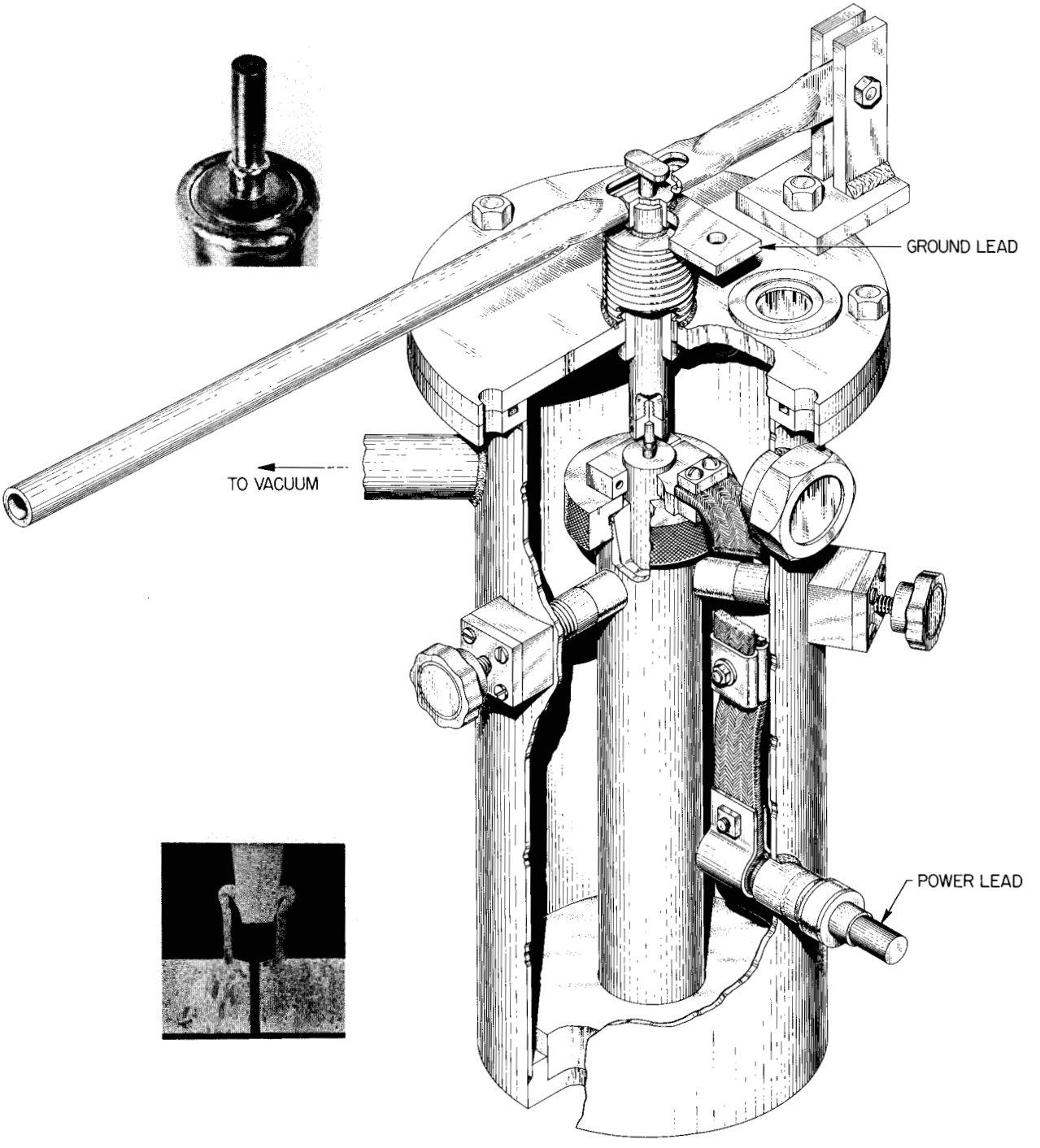

Fig. 15.9. Apparatus for Sealing Refluxing Capsules in Vacuum. Upper left: sealed capsule. Lower left: photomacrograph of plug-nipple joint, 6× (reduced 64%).

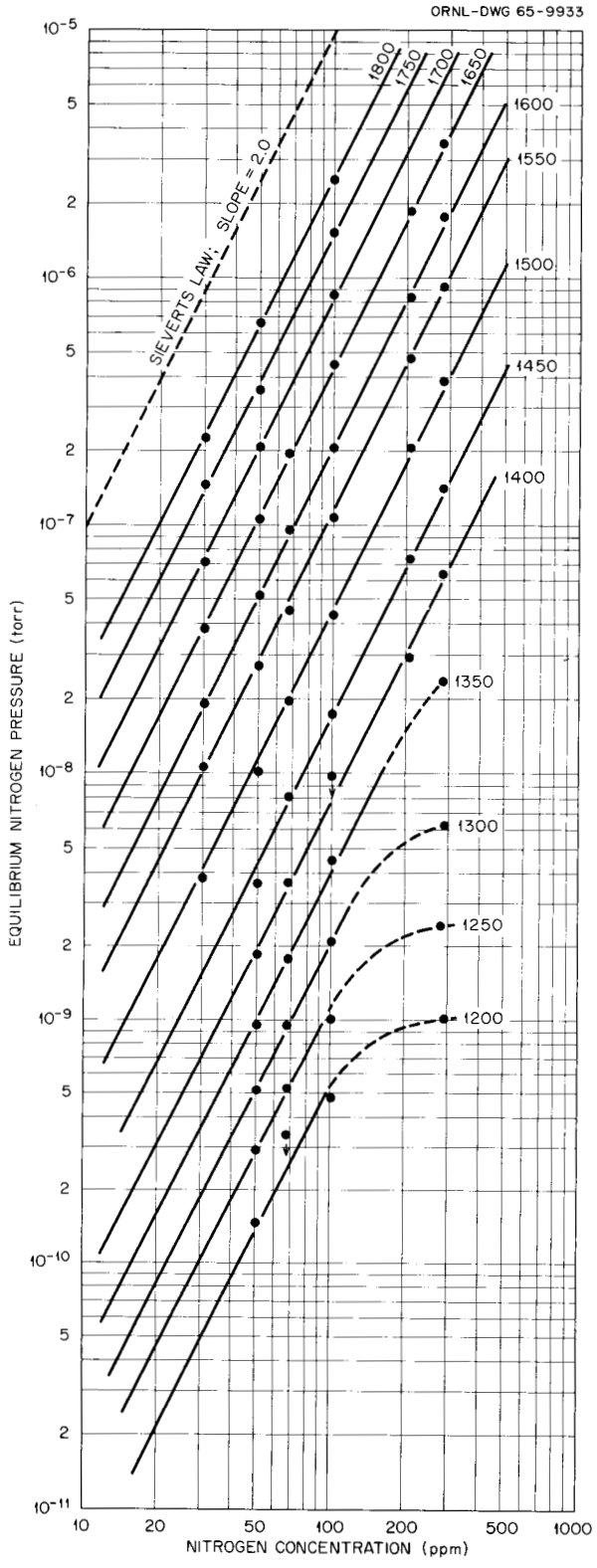

Fig. 15.10. Pressure-Temperature-Composition Diagram for the Nb–1% Zr–N Terminal Solid Solutions. The isotherms are labeled with the temperature in °C.

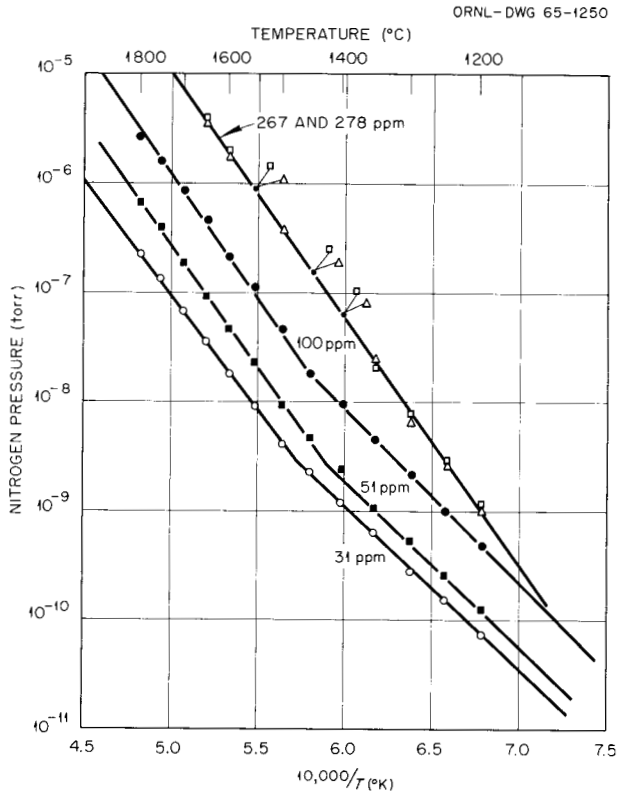

Fig. 15.11. The Dependence of the Equilibrium Nitrogen Pressure on the Absolute Temperature for Nb–1% Zr–N Solid Solutions.

The process by which nitrogen is sorbed by the Nb–1% Zr alloy in ultrahigh vacuum involves chemisorption of the gas as atoms on the surface and subsequent diffusion of these atoms into the alloy. We postulate that the chemisorbed nitrogen (denoted as N) is in a state of dynamic equilibrium with both the gas phase and the nitrogen in solution (denoted as N) in accordance with reactions

$$\tfrac{1}{2}\,N_2 \underset{\text{chemisorption}}{\overset{\text{desorption}}{\rightleftharpoons}} \text{N (atoms on the surface)}\,, \tag{1}$$

and

$$\text{N} \underset{\text{solution}}{\overset{\text{dissolution}}{\rightleftharpoons}} N\ \text{(nitrogen in solution)}\,. \tag{2}$$

The net reaction,

$$\tfrac{1}{2}\,N_2 \underset{\text{sorption}}{\overset{\text{degassing}}{\rightleftharpoons}} N\ \text{(Sieverts law)}\,, \tag{3}$$

is consistent with the Sieverts law behavior shown in Fig. 15.10. The reactions have been shown to be reversible by experiment; additional supporting evidence is presented below.

A measure of the equilibrium for reaction (1) is the sticking probability α, which is defined as that fraction of gas incident on the surface that is chemisorbed. The magnitude of α during a 10-min sorption period and its variation with temperature is shown in Fig. 15.12 for a filament degassed to 59 ppm N. At a given test pressure, α characteristically goes through a minimum, then goes through a maximum, and eventually becomes zero. To the left of the maxima shown in Fig. 15.12, α is independent of the pressure; that is, the sorption rate is proportional to the pressure, as shown in Fig. 15.13. Because the maximum gas uptake during these experiments was only 0.05 ppm, the reaction proceeding to the right predominated.

At temperatures higher than that corresponding to the maximum in α, reaction (2), proceeding increasingly to the left, exerts its effect and gives rise to a decrease in the sorption rate in proportion to the deviation from equilibrium. The intersections of the curves in Fig. 15.12 with the abscissa represent the approximate equilibrium pressures and temperatures for the alloy containing 51 ppm N, as shown in Fig. 15.10.

With increased sorption times the nitrogen content of the alloy increases and the dynamic equilibria, reactions (1) and (2), tend to shift to the left. The rate of increase in the amount of nitrogen sorbed (ΔC) decreases with time, as shown in Fig. 15.14. Alternatively, α decreases as the nitrogen content increases, as shown in Fig. 15.15. The variations in α with the nitrogen content reflect the changes in the dynamic equilibrium existing at the surface. These changes arise from changes in the diffusion rates of nitrogen in the alloy with temperature and pressure.

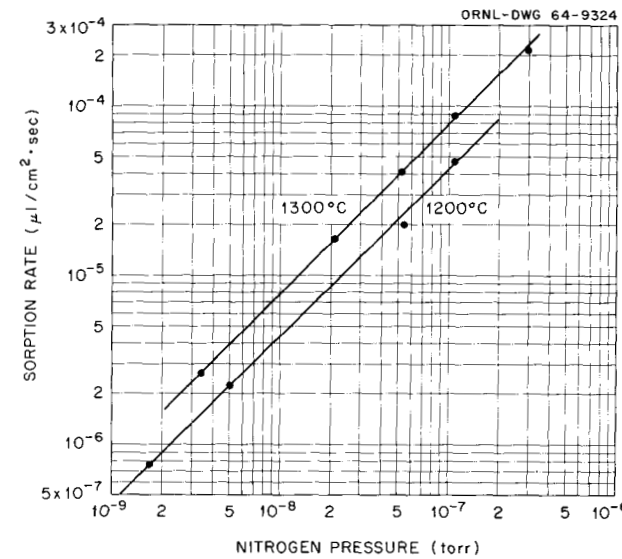

Fig. 15.13. The Dependence of the Sorption Rate of Nitrogen by Nb–1% Zr on the Nitrogen Pressure.

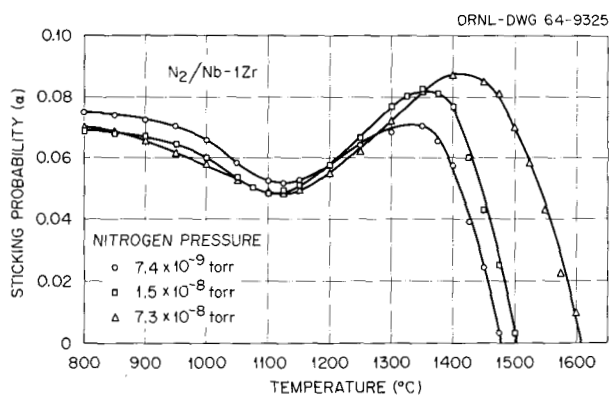

Fig. 15.12. The Dependence of the Sticking Probability on Temperature for Three Nitrogen Pressures.

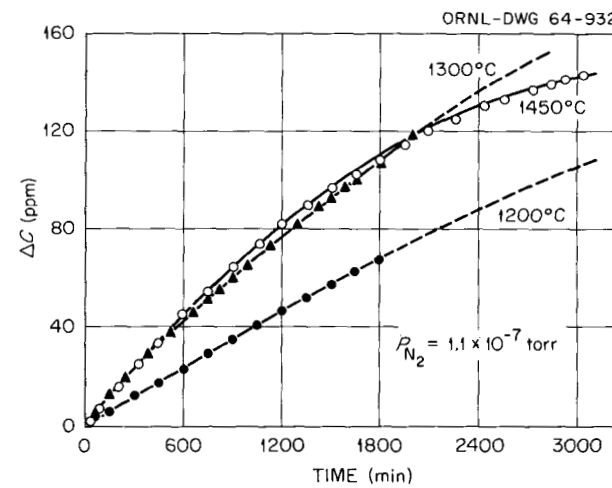

Fig. 15.14. The Variation in Amount (ΔC) of Nitrogen Sorbed with Time.

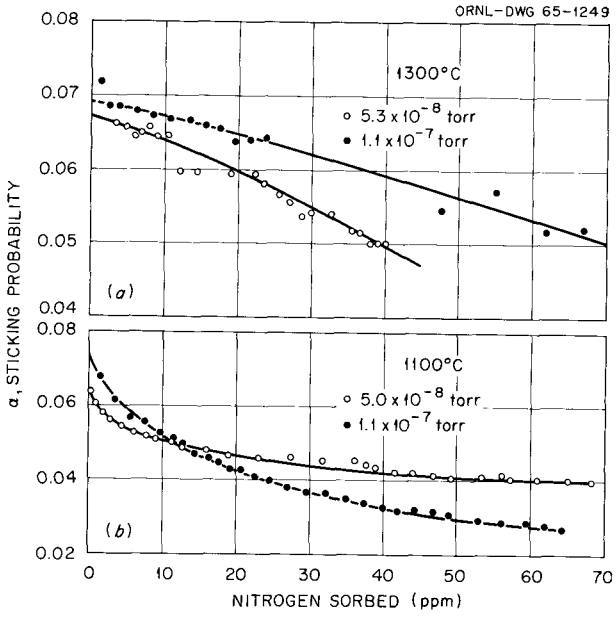

Fig. 15.15. The Dependence of Sticking Probability on the Nitrogen Pressure and Nitrogen Content at Two Temperatures.

Aging Studies on the D-43 Alloy

T. K. Roche

The relatively high strength of the D-43 alloy is attributed to the presence of dispersed carbides. At least two carbide phases have been reported. One of these is a high-temperature modification, occurring above approximately 1600°C as platelets and identified as hexagonal Nb_2C; the other, occurring below 1600°C as finely dispersed particles, has been identified as a cubic niobium-zirconium carbide.

In earlier experiments we demonstrated that the D-43 alloy responds to heat treatment.[9] For example, the alloy hardened when annealed at 1815°C and then aged by heat treatment at 1095°C. In addition, elongations determined from room-temperature tensile tests on specimens annealed at 1540 and 1815°C were found to be 24 and 6% respectively. We tried to correlate the effects of these heat treatments with the type and morphology of the carbide precipitate in the microstructure of the alloy. It now appears that these earlier correlations were probably not valid.

We systematically determined the extent of deterioration in room-temperature ductility of the alloy as a function of annealing temperature and determined the kinetics of the recovery in room-temperature ductility after annealing for 2 hr at 1815°C and aging between 980 and 1425°C. Tensile specimens with a 1.0 × 0.250-in. gage section were prepared from 0.040-in.-thick strips of the alloy. All heat treatments were carried out in vacuum and tensile tests were conducted at a strain rate of 0.05/min.

The effect of annealing temperature on the room-temperature ductility of the alloy is shown in Fig. 15.16. These results were extremely dependent upon the cooling rate from the annealing temperature. For comparison, the times for cooling through the temperature range from 1600 to 1300°C were approximately 20 sec for "fast" cooling and 80 sec for "slow" cooling. The elongation of fast-cooled specimens decreased from about 32 to 20% as the annealing temperature increased from 1540 to 1840°C. We attribute this ductility

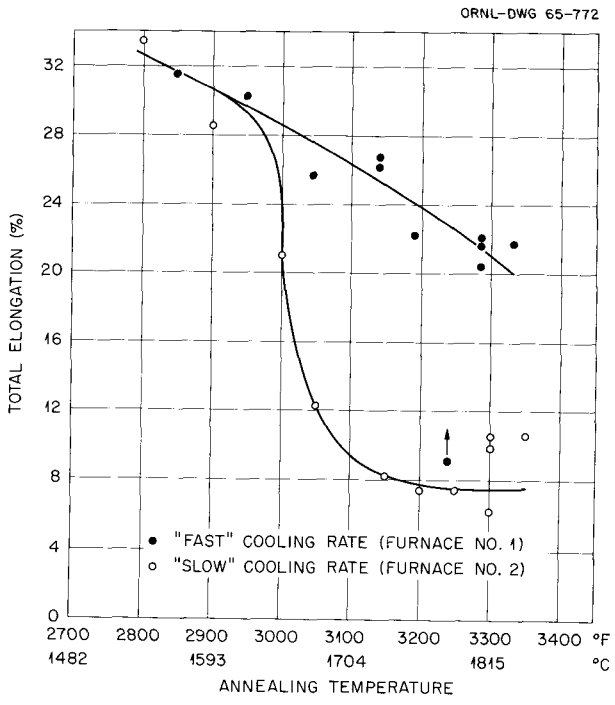

Fig. 15.16. Effect of Cooling Rate from Annealing Temperature on the Room-Temperature Ductility of the D-43 Alloy.

[9]T. K. Roche, *Metals and Ceramics Div. Ann. Progr. Rept. June 30, 1964*, ORNL-3670, pp. 96–99.

loss to the increase in grain size and the presence of larger amounts of Nb_2C in the specimens annealed at the higher temperature. In contrast, slow cooling caused a sharp drop in ductility to about 8%. This additional ductility loss has been attributed to an aging process during the slow cool from the annealing temperature. However, we could detect in the microstructures essentially no effect of cooling rate that would explain the wide difference in ductility. These microstructures are shown in Fig. 15.17.

PHOTO 80953

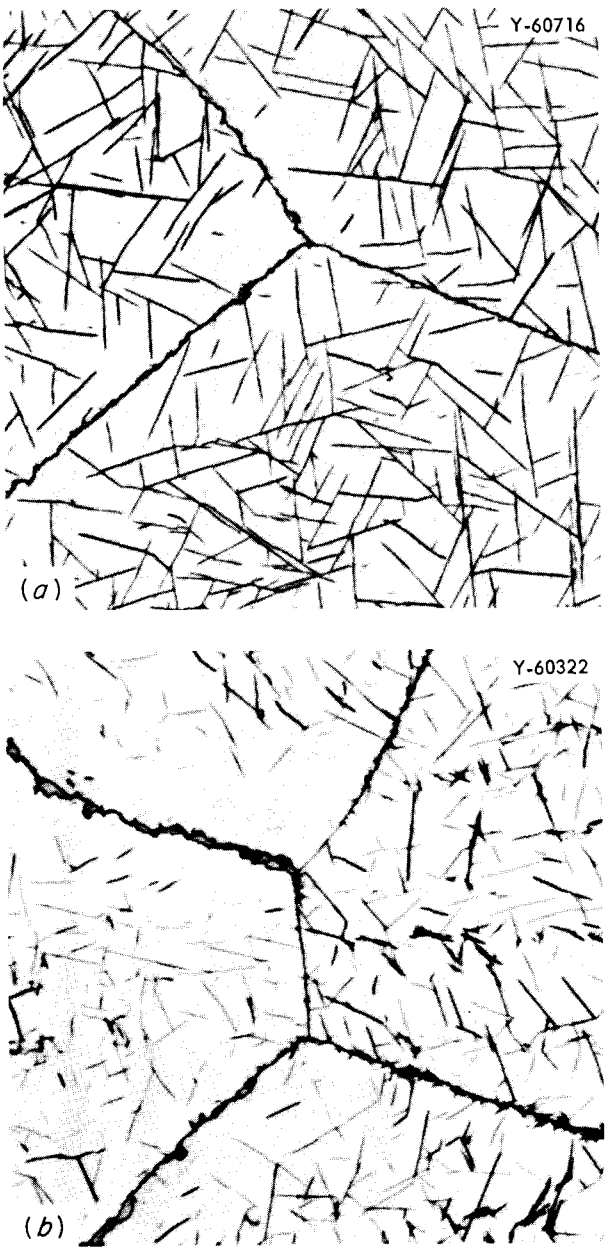

Fig. 15.17. Microstructures of D-43 Alloy Annealed 2 hr at 1815°C Followed by Fast and Slow Cooling. 500×. Etchant: 10 ml H_2SO_4, 10 ml concd HNO_3, 25 ml concd HF, 50 ml H_2O. (*a*) Fast cool, elongation 21.4%. (*b*) Slow cool, elongation 8.6%.

The aging or recovery kinetics of the embrittled alloy slow cooled from 1815°C as a function of aging temperature is shown in Fig. 15.18. Recovery in ductility started after approximately 200, 50, and 5 hr at 980, 1095, and 1200°C respectively. At the higher temperatures ductility was restored within 2 hr. The interstitial content of the alloy (Heat No. 1) after the 1815°C anneal was 780 ppm C, 23 ppm O, and 28 ppm N. The aging kinetics of annealed and fast-cooled specimens are shown in Fig. 15.19. These specimens were obtained from a different heat (Heat No. 2) of the alloy and contained 860 ppm C, 17 ppm O, and 33 ppm N. The characteristic loss in ductility of these specimens on aging, which is absent in the slow-cooled specimens, confirms that the cooling-rate effect observed in Fig. 15.16 is associated with an aging phenomenon.

Two distinct differences between the results in Fig. 15.19 for Heat No. 2 and those shown in

ORNL-DWG 65-774R

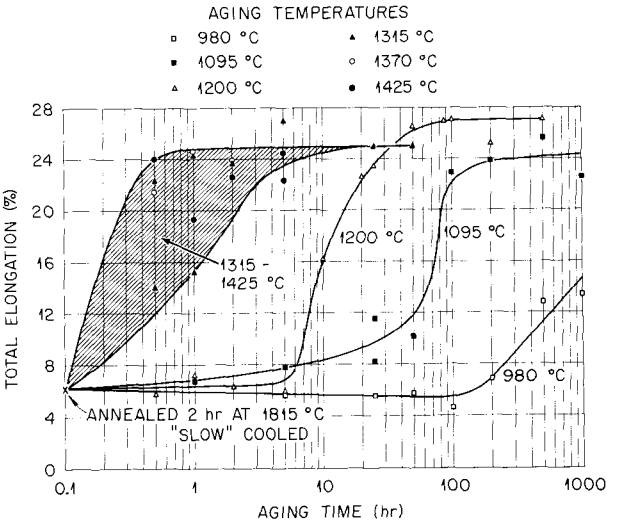

Fig. 15.18. Recovery in Room-Temperature Ductility of the D-43 Alloy (Heat No. 1) by Aging Between 980 and 1430°C After Slow Cooling from 1815°C.

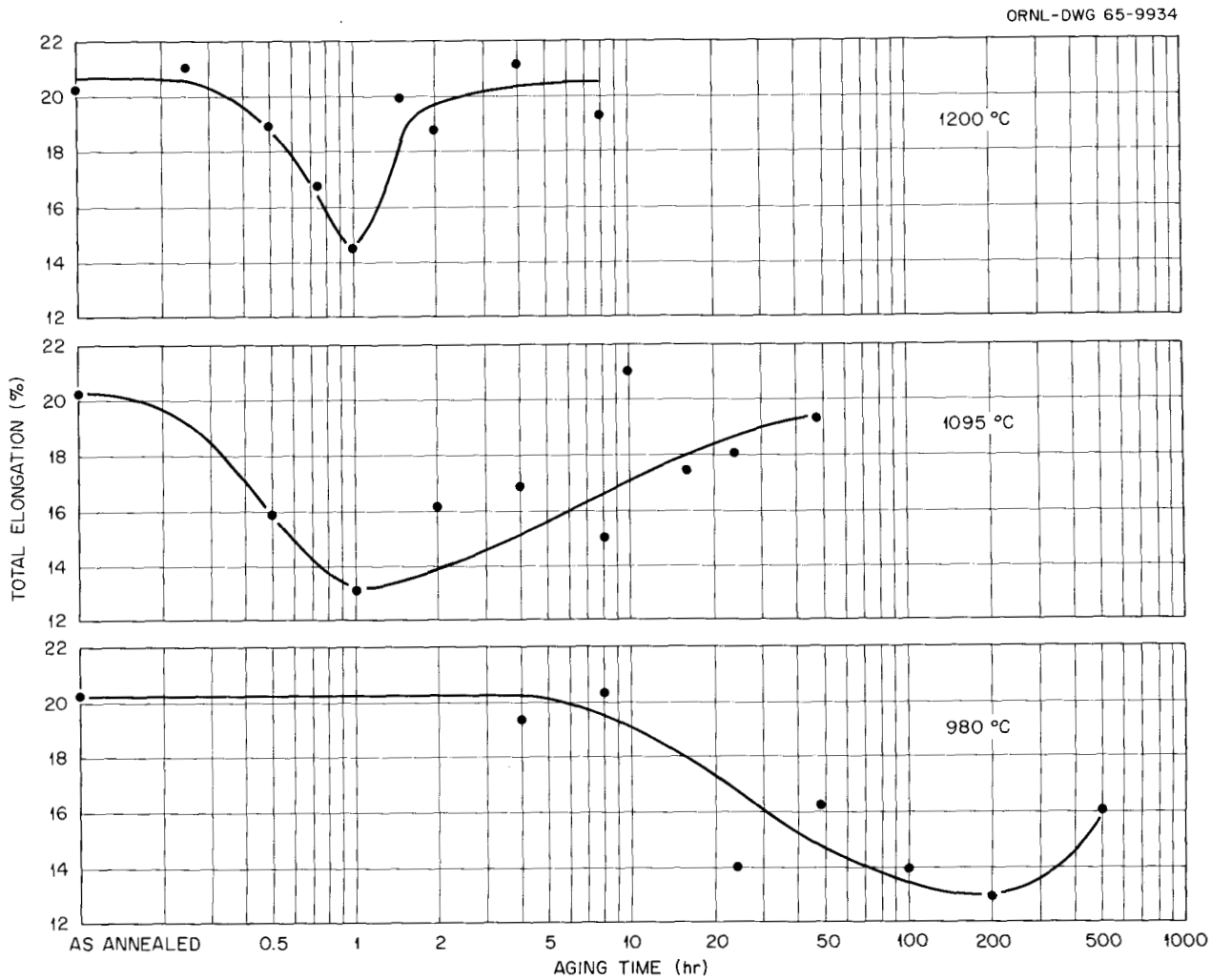

Fig. 15.19. Effect of Aging at 980, 1095, and 1200°C on the Room-Temperature Ductility of the D-43 Alloy (Heat No. 2) After Fast Cooling from 1815°C.

Fig. 15.18 for Heat No. 1 are: (1) Heat No. 2 was embrittled less than Heat No. 1 (14 vs 8% elongation), and (2) overaging or recovery occurred faster for Heat No. 2 than for Heat No. 1 (less than 2 hr vs 5 to 10 hr at 1200°C).

In a recent set of experiments, specimens were rapidly cooled (more rapidly than for the fast cool discussed above) from 1815°C in an induction apparatus where the vacuum was better than that used previously (10^{-7} as compared to 10^{-6} torr). The interstitial content of these annealed specimens was 820 ppm C, 7 ppm O, and 22 ppm N, and the tensile elongation was 25%. As shown in Table 15.6, only slight embrittlement was noted on aging at 1200°C, and this occurred after 45 min when the ductility decreased only to 20.5%. An exception was noted for one specimen aged 48 hr that was contaminated when the furnace tube failed during the aging treatment. The interstitial content of this specimen was increased to 960 ppm C, 110 ppm O, and 150 ppm N, and the specimen became severely embrittled (1.8% elongation). The microstructures of the aged specimens in this series were identical to those observed previously for both heats of the alloy (i.e., conversion of the Nb_2C platelets to the dot-like dispersion of the cubic niobium-zirconium carbide). Furthermore, comparison of the microstructures of the two specimens aged 48 hr at 1200°C showed no observable effect due to the increased contamination.

Table 15.6. Room-Temperature Tensile Ductility of D-43 Alloy After Rapid Cooling from 1815°C in Induction Apparatus and Aging at 1200°C

Aging Time (hr)	Total Elongation (%)	Aging Time (hr)	Total Elongation (%)
0	25.1	8	25.1
0.25	24.3	16	28.0
0.5	23.0	24	25.6
0.75	20.5	48	1.8[a]
1	23.9	48	26.6
2	25.6	72	29.2
4	24.7		

[a]Specimen contaminated during aging.

Thus, the following tentative conclusions can be drawn regarding the aging characteristics of the D-43 alloy: (1) Embrittlement does not appear to be caused by the carbide conversion *per se*; (2) the degree of embrittlement and the recovery kinetics appear to be related to other interstitials (oxygen and nitrogen), and the aging mechanism may possibly involve a complex interaction of interstitials with the zirconium present in the alloy. We are continuing this work in an effort to more clearly understand this aging phenomenon.

Chemical Stability of Refractory Alloys in High Vacuum[10]

D. T. Bourgette

Evaporation losses of the refractory alloys T-111, Nb–1% Zr, FS-85, B-66, C-129Y, and D-43 were determined for various periods of time at temperatures between 1200 and 1500°C and at pressures ranging from 7×10^{-7} to 6×10^{-10} torr.

In general, evaporation from these alloys was not serious, especially at temperatures of 1200 to 1300°C. The alloys that exhibited the greatest evaporation losses contained the more volatile elements such as vanadium, zirconium, and hafnium. For example, B-66, the most volatile alloy studied, lost 1.70 mg/cm^2 at 1500°C and 7×10^{-9} torr in 316 hr, while at 1200°C and 6×10^{-10} torr it lost 0.077 mg/cm^2 in 513 hr. Vanadium and zirconium contributed 95% of the total weight loss. Evaporation occurred only at the surfaces; no subsurface voids were detected nor did evaporation occur at any preferential sites, such as grain boundaries or impurity inclusions at or near the surfaces.

The total weight change in the specimens appeared to be pressure- and composition-dependent. At 1200 to 1300°C and 10^{-7} torr, the niobium-base alloys Nb–1% Zr and D-43, containing only zirconium as the evaporating element, gained weight, while at the same temperature and 10^{-9} torr they lost weight. We attributed this behavior to interstitial contamination at 10^{-7} torr and purification at 10^{-9} torr. Alloys containing more than one evaporating species, such as B-66 and C-129Y, lost weight at both the high and low test pressures at 1500°C. The evaporation losses in these cases overshadowed the changes in the interstitial contents.

Changes in the interstitial concentrations were dependent on the pressure. At 1500°C and pressures of 10^{-9} torr or lower, carbon was retained while oxygen, nitrogen, and hydrogen were evolved. At a higher pressure of 10^{-7} torr and 1500°C, carbon was lost while oxygen and nitrogen were picked up. We believe that the reaction of carbon and oxygen resulted in the loss of carbon at the higher pressures, while at 10^{-9} torr insufficient oxygen was present to appreciably reduce the carbon concentrations.

[10]Summary of paper presented at the Eighth Annual Conference on Vacuum Metallurgy and to be published in the conference transactions.

Recrystallization Behavior in the T-111 Alloy

D. T. Bourgette

Recovery and recrystallization following deformation play important roles in the practical control of mechanical properties of metals. Therefore, we need an understanding of these processes to optimize the properties for high-temperature service.

The recovery and recrystallization of T-111 that had been annealed at 1800°C for 1 hr, cold rolled 25, 50, 75, and 90%, and then annealed again for 1 hr at various temperatures are graphically presented in Fig. 15.20. The as-worked hardness values and the initial slopes of the hardness curves indicate that recovery occurred below 800°C, the lowest temperature at which specimens were treated after rolling. Recovery without recrystallization also continued above 800°C.

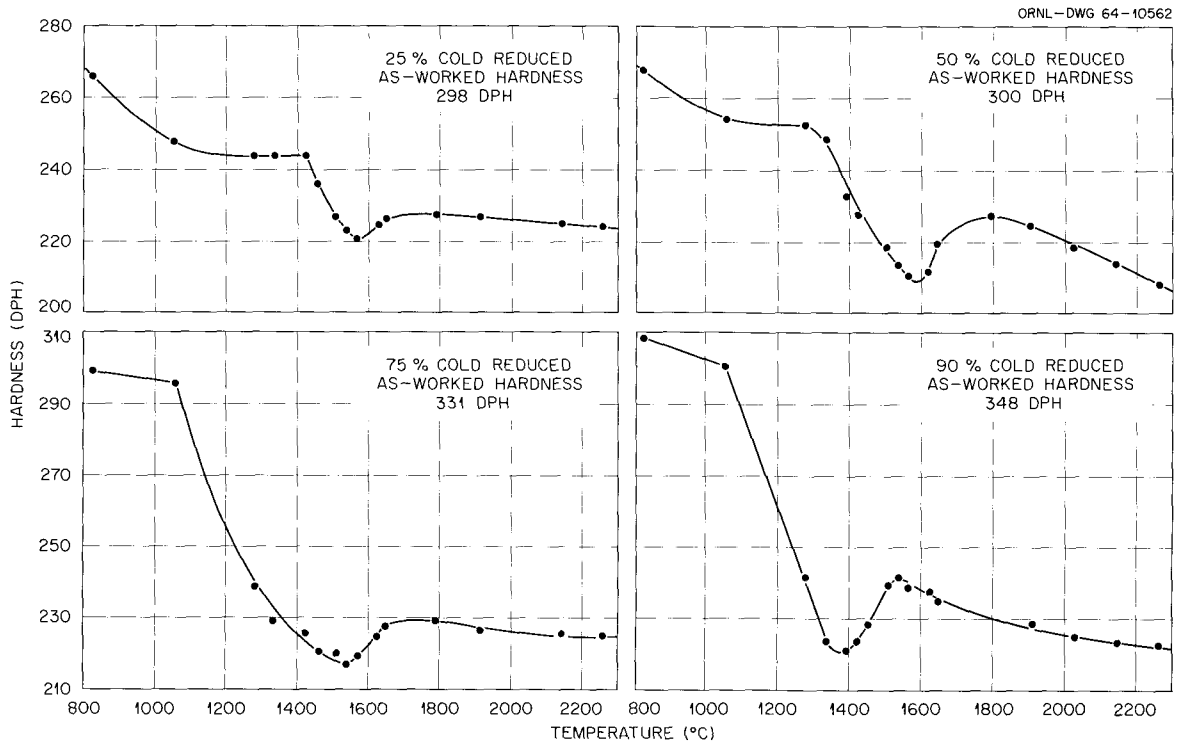

Fig. 15.20. Effect of Annealing Temperature on the Hardness of Cold Worked T-111.

Metallographic examination showed that recrystallization began at temperatures corresponding approximately to the temperatures at which the magnitude of the negative slopes of the hardness curves increased sharply, and was complete at temperatures corresponding to the minima in the hardness curves for the different levels of cold work.

As the amount of cold work increased, the grain size of the fully recrystallized material became finer, as illustrated in Fig. 15.21. Moreover, for higher levels of cold work, the precipitate that was present after the reference anneal redissolved more readily at temperatures at which grain growth occurred. For example, Fig. 15.21 shows that for 90% cold work the precipitate has completely dissolved, while for 25% cold work the precipitate particles are arrayed in the original grain boundaries.

With increasing annealing temperatures beyond the minima on the hardness curves (Fig. 15.20), grain growth continued with an increase in hardness. We postulate that the increase in hardness is due to submicroscopic reprecipitation of a second phase during cooling. At the 90% level of cold work this reaction occurs simultaneously with the dissolution of the microscopic phase that precipitated during the reference anneal. This behavior is not uncommon and is analogous to the hardening reaction in the Nb–7.5 at. % W system as observed by electron microscopy.[11] Within the recrystallization range the hardness of cold-worked T-111 increased with time to a maximum after initial softening. The time necessary to show this increase in hardness decreased with an increase in temperature. For material worked 50% Fig. 15.22 illustrates this behavior and shows that the hardness started to rise after 10 hr at 1260°C and 2 hr at 1480°C.

We plan to determine the volume fraction of recrystallized material for the various heat treatments. This will help us determine more accurately the temperatures at which recrystallization starts, the rate of recrystallization, and the rate of grain growth as a function of cold work and temperature.

[11] J. O. Stiegler, ORNL, personal communication, Oct. 16, 1964.

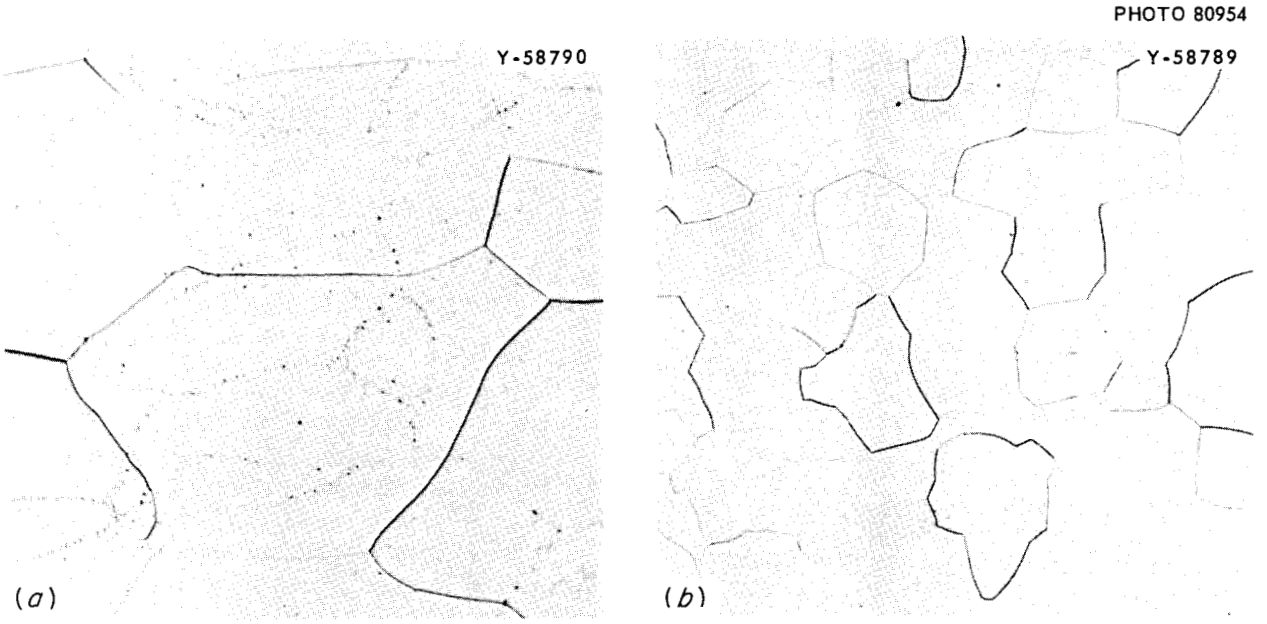

Fig. 15.21. Microstructures of T-111 Annealed 1 hr at 1650°C. 350×. Etchant: 30 g NH_4HF_2 + 50 ml concd HNO_3 + 20 ml H_2O. (*a*) 25% cold work; DPH = 227. (*b*) 90% cold work; DPH = 238.

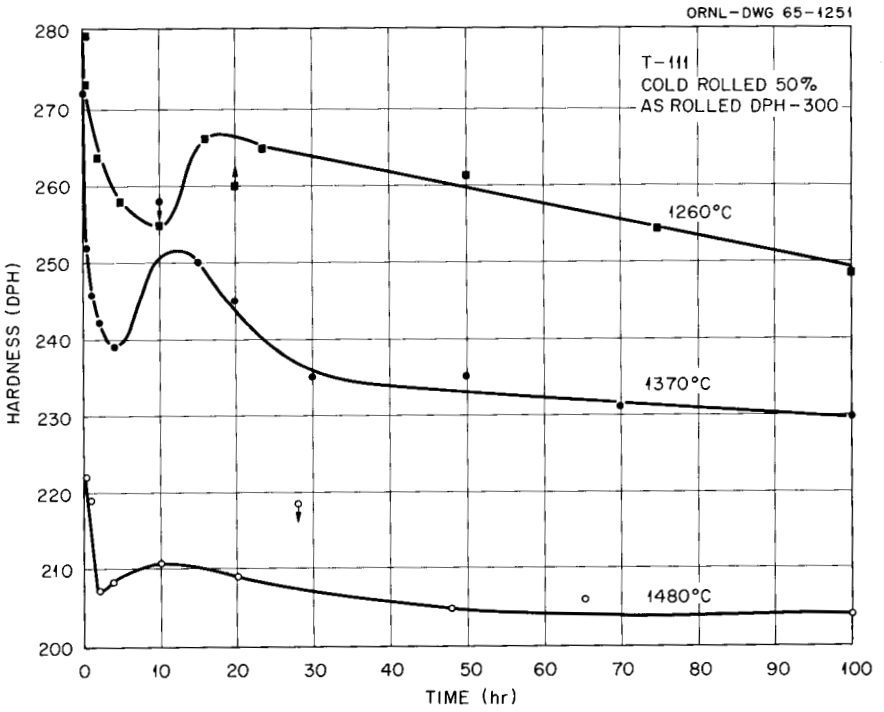

Fig. 15.22. Characteristic Change in Hardness of T-111 Alloy Cold Worked 50% and Heat Treated at the Indicated Temperatures.

MECHANICAL PROPERTIES OF REFRACTORY ALLOYS

J. R. Weir

Effect of Cold Working and Annealing on Creep Properties of Nb–1% Zr[12]

H. E. McCoy

We determined the combined effects of cold working and annealing on the creep properties of the Nb–1% Zr alloy. The material was initially recrystallized by annealing 1 hr at 1200°C and was then cold worked various amounts up to 80%. Some of the material was tested in the cold-worked condition and some after an additional anneal at 1200, 1350, 1500, or 1700°C. Creep tests were performed at 980 and 1200°C.

In general, the creep strength increased as the annealing temperature was increased. At a test temperature of 980°C the rupture life was increased by about tenfold and the time required to reach 1% strain was increased more than hundredfold by annealing at 1700°C. In contrast, annealing at 1200°C changed these properties little. At a test temperature of 1200°C a similar trend was observed, although the effect was somewhat less pronounced. The 1700°C anneal increased the rupture life sixfold and the time to 1% strain hundredfold.

Cold working changed the creep strength somewhat less than did annealing. For a given postworking annealing treatment, the rupture lives for the complete range of cold working never varied by more than twofold. However, the time to reach small strains was influenced more. The time to 2% strain reached a maximum at about 10% cold working and decreased sharply with greater amounts of working. The variations in strength due to cold working decreased as the postworking annealing temperature was increased. Similar effects were noted at both test temperatures, although the magnitude was considerably less at the higher temperature. The fracture ductility was not significantly affected by any of the annealing and cold-working treatments employed.

We also determined the recrystallization temperature of Nb–1% Zr for various amounts of cold working and obtained information on the kinetics of recrystallization at 980 and 1200°C. Metallographic and x-ray diffraction studies were conducted to determine microstructural changes that occurred as a result of cold working and annealing.

Correlation of Creep Properties for Constant and Varying Stresses

H. E. McCoy

Although creep properties are normally determined under a condition of constant load, materials are often subjected in service to varying loads. The cladding on nuclear fuel elements, for example, is subjected to continually increasing stresses under normal stable operation, as the fuel is burned and fission gases are released.

The rupture life under conditions of constant stress and constant stress rate has been found for several iron- and nickel-base alloys to be correlated by the relationship:[13]

$$A^n = \dot{\sigma}^n t_r^{\,n+1}/(n+1) \qquad (1)$$

where A and n are constants determined from conventional creep tests and defined by the relationship $t_r = (A/\sigma)^n$, σ is the stress, $\dot{\sigma}$ is the stress rate, and t_r is the rupture life.

We examined the applicability of this expression to refractory metals, with reference to its use for describing rupture and its accuracy for describing times to various amounts of strain. Creep results were determined by conventional constant-load tests and compared with the creep behavior obtained in constant stress-rate tests.

Test results were obtained for alloys T-111, Nb–1% Zr, D-43, and FS-85 at 1200°C. For the first three alloys the data from either type of test could be used to predict the creep behavior from 1% strain to rupture for the other type of test. The creep data for the FS-85 alloy are not described by the relationship $t_r = (A/\sigma)^n$ and hence cannot be analyzed by the use of Eq. (1).

[12]Condensed in part from "Creep Properties of the Nb–1% Zr Alloy," *J. Less-Common Metals* 8, 20–35 (1965).

[13]C. R. Kennedy, *Metals and Ceramics Div. Ann. Progr. Rept. May 31, 1962*, ORNL-3313, pp. 44–45.

Creep Properties of Refractory Alloys

R. L. Stephenson

Our object is to provide creep-rupture data to 1000 hr so that promising refractory metal alloys can be compared. We tested the Cb-752, FS-85, Ta–10% W, and TZM alloys and continued previous work on D-43 and TM alloys. Figure 15.23 compares the 1000-hr rupture stresses of several alloys.

As previously reported,[14] heat treating the D-43 alloy for 300 hr at 980°C diminishes the improvement in properties that resulted from solution annealing, cold working, and aging. More recently we observed that creep-rupture properties of specimens held 500 hr at 980°C prior to testing are actually inferior to those of the as-received material. The same effect was observed for welded specimens and specimens that had been recrystallized by a 1-hr anneal at 1540°C.

[14]R. L. Stephenson, *Metals and Ceramics Div. Ann. Progr. Rept. June 30, 1964*, ORNL-3670, p. 85.

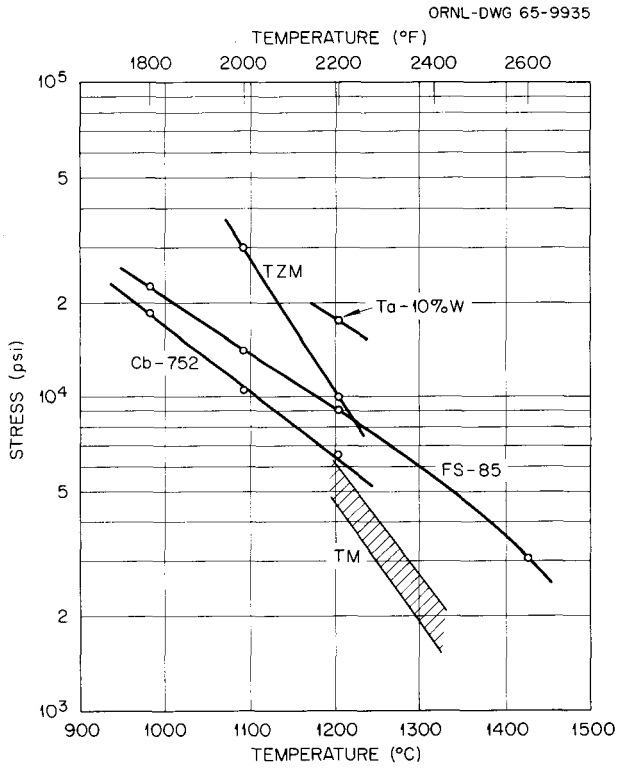

Fig. 15.23. Variation of 1000-hr Rupture Stress with Temperature for Refractory Alloys.

The effect of annealing temperature on the creep-rupture properties was investigated for the FS-85 and Cb-752 alloys. In both cases, the creep-rupture properties improved with increasing annealing temperature up to approximately 1600°C. Above this temperature the material became weaker and much less ductile. An unidentified second phase was visible in specimens of each alloy that had been annealed at 1760°C. Specimens of each alloy have been annealed at 1590°C (the apparent optimum annealing temperature) and are being tested to determine whether the improved properties are stable for long times.

Strengthening of Refractory Alloys by Carburization

H. E. McCoy

There are two reasons for studying the solid-state carburization of refractory metals. First, it is often desirable to treat the surface of a finished part for improved hardness and wear resistance but retain the ductility of the "core" of the part. Second, fabrication of a refractory-base alloy that contains a strong carbide-former followed by addition of carbon to the fabricated part seems to be an attractive approach to obtaining the strength of a high-carbon alloy, while obviating the normal fabrication and welding problems for these alloys.

A technique was developed for carburizing refractory metals by exposing the heated metal to a mixture of hydrogen and benzene. The hydrogen is passed over benzene and the benzene content is determined by the temperature of the liquid benzene. This mixture is then passed through a furnace that contains the material to be carburized.

The amount of carbon absorbed by the material is a function of its temperature and the carburizing potential of the gas. We evaluated the effects of benzene content from 0.01 to 1 vol % and specimen temperatures of 1000 to 1350°C for Nb–1% Zr and T-111 alloys. Metallographic studies have shown that the temperature of the material during carburization not only influences the quantity of carbon absorbed but also the morphology of the carbide precipitates. Lower temperatures favor the formation of a fine precipitate and higher temperatures result in a coarser precipitate.

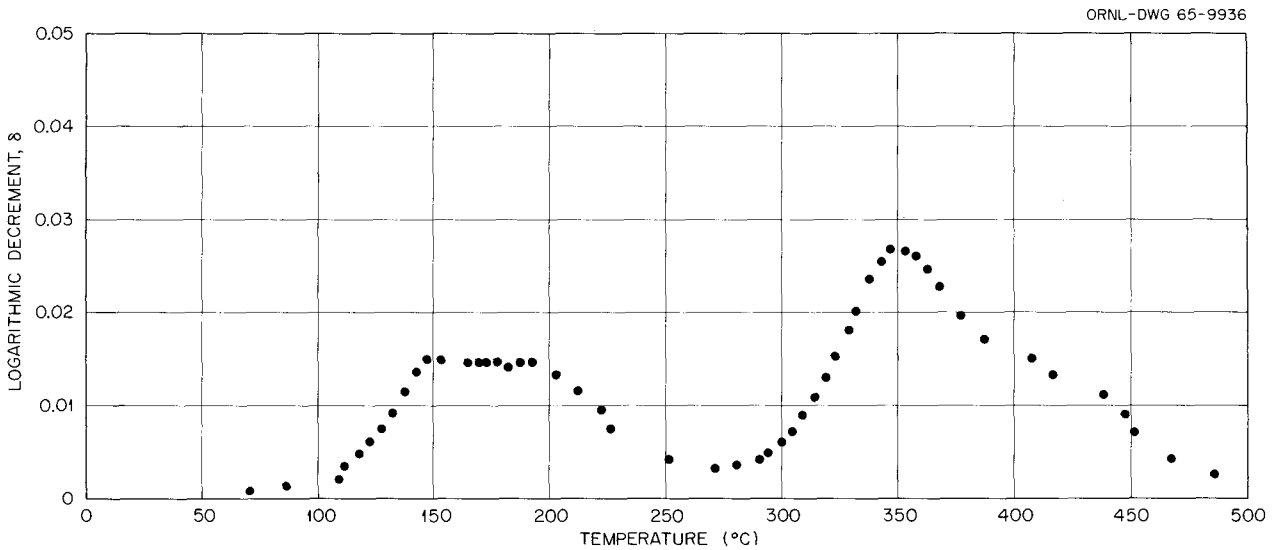

Fig. 15.24. Internal Friction Spectrum of Ta–0.2% Hf Alloy Annealed at 2300°C.

Internal Friction Studies on Tantalum-Base Alloys

R. L. Stephenson

Internal friction is recognized as an excellent tool for determining the solubilities and precipitation kinetics of interstitial solutes in body-centered cubic metals. We are applying this technique to Ta-Hf and Ta-W alloys to learn the behavior of interstitials in the T-111 alloy.

Figure 15.24 shows the internal friction spectrum of a Ta–0.2% Hf alloy that had been annealed at 2300°C. The peaks near 150 and 350°C are due to the stress-induced ordering of oxygen and nitrogen atoms, respectively, in the tantalum matrix.[15,16] The peaks near 190 and 410°C appear to be due to the stress-induced ordering of oxygen and nitrogen atoms, respectively, in the neighborhood of hafnium atoms. Aging experiments intended to determine the solubility and precipitation kinetics of interstitials in this alloy have yielded contradictory results.

[15]R. W. Powers, *Acta Met.* **3**, 135 (1955).

[16]T. S. Ke, *Phys. Rev.* **47**, 914 (1948).

COMPATIBILITY OF ALKALI METALS WITH STRUCTURAL MATERIALS

J. H. DeVan

Compatibility of Boiling Potassium with Refractory Metals

J. H. DeVan J. R. DiStefano
D. H. Jansen

Light weight efficient power plants are needed to supply the auxiliary electrical and ion-propulsion requirements of space vehicles. Design studies have indicated that high performances can be achieved with a system consisting of a nuclear reactor mated to a Rankine-cycle turbine generator.[17] Potassium was concluded to be the best choice for a single working fluid to cool the reactor, power the turbine, and lubricate the turbine, generator, and pump. Since the service temperatures for such a system would exceed 1000°C, refractory metals and their alloys are being considered for use as structural materials for nozzles, turbine blades, and fuel-element

[17]A. P. Fraas, *Nucleonics* **22**(1), 72 (1964).

ORNL-LR-DWG 75699R

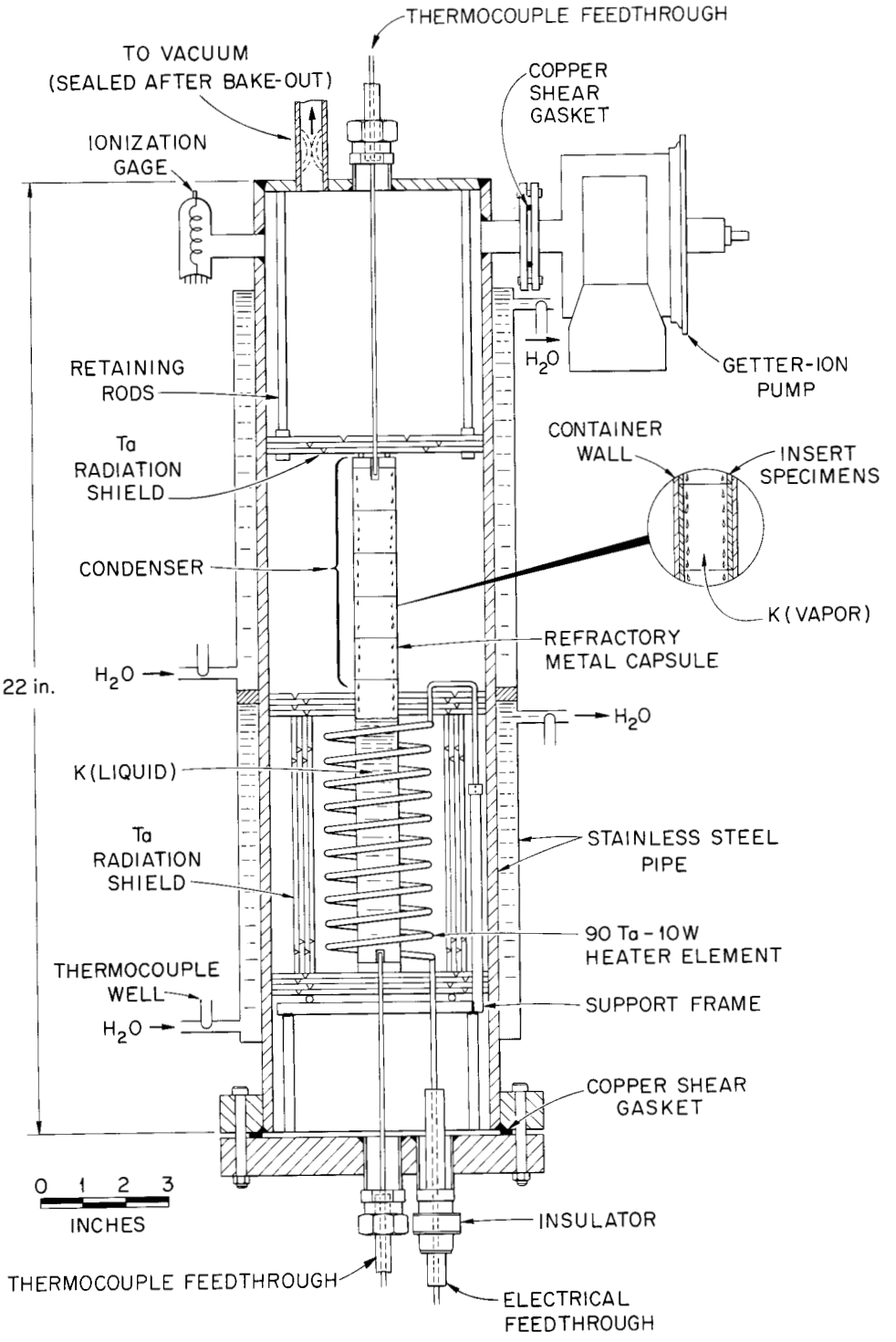

Fig. 15.25. Capsule for Testing Refluxing Potassium in Refractory Alloys.

cladding. In view of these considerations, a threefold test program consisting of refluxing capsules, natural-circulation loops, and forced-circulation loops was undertaken to study the behavior of several of the more promising refractory-metal alloys in boiling potassium in the range 1100 to 1300°C. The alloys chosen for the first phase of this investigation were Nb–1% Zr, D-43, FS-85, T-111, and TZM.

The purpose of the refluxing capsules and natural-circulation loops is to provide quantitative data on the rates of dissolutive attack by potassium as a function of temperature and condensing rate. Refluxing capsules, shown in Fig. 15.25, contain machined and weighed inserts within the condenser area. Natural-circulation loops, illustrated by Fig. 15.26, contain sleeve-type inserts in the liquid region below the condenser as well as in

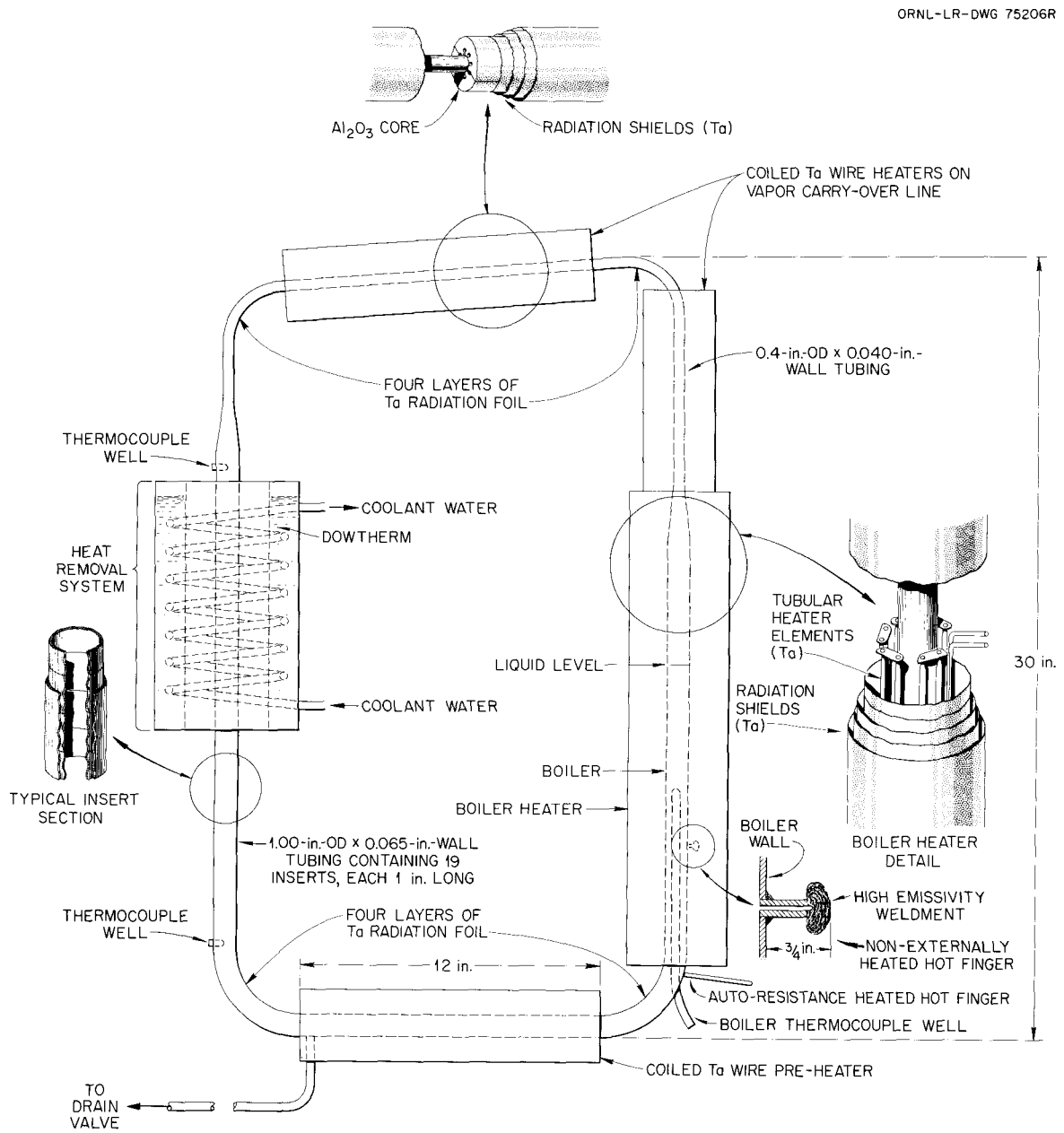

Fig. 15.26. Natural-Circulation Loop for Testing Boiling Potassium in Refractory Alloys.

the condenser. Pumped loops, typified by Fig. 15.27, have test sections designed to provide information on the corrosion-erosion resistance of potential nozzle and turbine blade materials. In each type of test the heat of condensation is carefully monitored by a heat sink placed directly around the condenser section. Measurement of the flow rate of the heat-sink coolant, combined with its heat content, yields a direct measure of the heat of condensation and, hence, the condensing rate of potassium. Test materials are evaluated from weight changes, metallographic examination, and chemical and x-ray diffraction analysis.

Table 15.7 summarizes the conditions and results of boiling-potassium capsule and loop tests that we have thus far operated with refractory metals. All tests were conducted under vacuum in the range 10^{-7} to 10^{-9} torr. Initial oxygen content in the potassium analyzed 70 to 200 ppm by the gettering-vacuum-fusion method[18] and 20 to 50 ppm by the amalgamation method.[19]

[18] A. P. Litman and J. W. Prados, *The Partitioning of Oxygen Between Zirconium and Liquid-Potassium*, ORNL-TM-1039 (April 1965).

[19] J. C. White, A. S. Meyer, and Gerald Goldberg, *Anal. Chem. Div. Ann. Progr. Rept. Dec. 31, 1961*, ORNL-3243, p. 41.

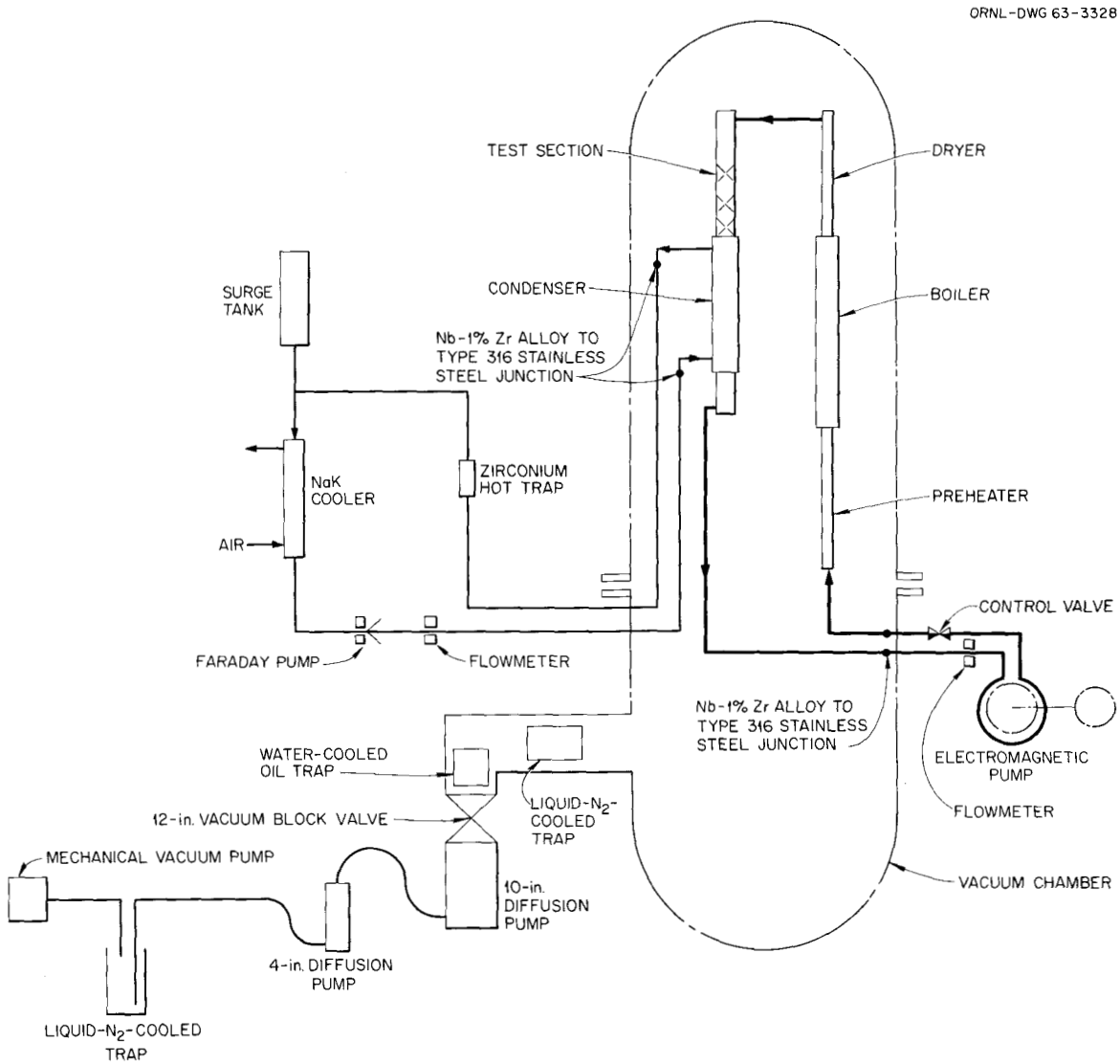

Fig. 15.27. Forced-Circulation Loop for Testing the Action of Potassium on Structural Materials.

Table 15.7. Summary of Boiling-Potassium Refractory-Metal Compatibility Tests

No. of Tests	Material		Temp (°C)		Time per Test (hr)	Condensing Rate (g min^{-1} cm^{-2})	Weight Change (mg/cm^2)	Results	
	Specimen	Container	Max	Min				Chemical	Metallographic
					Refluxing Capsules				
1	TZM	TZM	1260		5000	0.27	+7 to −0.4	Increase in concentration of Ti and Mo in K.	No attack
3	D-43	D-43	1200–1310		850–5000	0.27–0.57	+1.7 to −0.002	Oxygen transfer from top to bottom of capsule. Some decarburization at bottom. No Nb, Zr, or W in K after test.	No attack. ZrO_2 layer on surface of end-plug weld.
4	Nb–1% Zr	Nb–1% Zr	1100–1220		600–5000	0.17–0.28	+0.8 to −0.1	Oxygen transfer from top to bottom of capsule.	No attack
					Natural-Circulation Loops				
1	Nb–1% Zr	Nb–1% Zr	1140	650	2800		+0.13 to +0.01	No significant change in specimens from condenser or subcooler.	No attack
1	Nb–1% Zr	Nb–1% Zr	1200	675	1200	0.19	+0.7 to −0.2	Increase in oxygen concentration of specimens in subcooler.	No attack
1	D-43	D-43	1200	835	3000	0.35	+0.6 to +0.2	Increase in oxygen of specimen in subcooler.	No attack
1	T-111	T-111	1250	1040	3000			Test being examined.	
1	TZM	D-43	1250	~1000				Test in progress.	
					Forced-Circulation Loops				
1	Nb–1% Zr	Nb–1% Zr	1100	355	3000	270 g/min		Increase in oxygen concentration in boiler and condenser regions. No increase in concentration of Nb or Zr in K.	~1 mil erosion damage, second stage blade
1	TZM	Nb–1% Zr	1100					Test under construction.	

Metallographic examination of boiler and condenser sections from the refluxing capsule tests disclosed no evidence of dissolutive attack.[20–22] The expectation of weight losses in the condensing region, reflecting dissolution of the alloy by the condensing vapor, was not realized. Both losses and gains were observed, depending on specimen location in the condenser, but the total gains outweighed the losses. In tests with niobium-base alloys, changes in oxygen content were of the same magnitude as the weight changes, and therefore, the weight changes appear to be symptomatic of migration of oxygen rather than metal dissolution. Weight changes in a TZM capsule (+7 to −2 mg/cm^2) were larger than those found for niobium-base alloys and were more indicative of dissolution, since there was very little evidence of interstitial migration. Both titanium and molybdenum concentrations in the potassium increased.

Corrosion effects in the natural-circulation loops correlated in all respects with the effects observed in corresponding refluxing capsule tests.[20,21,23] Weight changes, when corrected for the migration of interstitial elements, showed negligible dissolution of the condenser walls and no evidence of mass transfer of metallic elements to the subcooler.

[20] J. R. DiStefano and J. H. DeVan, ORNL-3683, pp. 202–11 (classified).

[21] J. H. DeVan *et al.*, ORNL-TM-1050, pp. 41–50 (classified).

[22] J. H. DeVan *et al.*, ORNL-TM-1140, pp. 29–40 (classified).

[23] D. H. Jansen and E. E. Hoffman, *Niobium–1% Zirconium, Natural-Circulation Boiling-Potassium Corrosion Loop Test*, ORNL-3603 (May 1964).

Table 15.8. Design Conditions of Test Section of Nb–1% Zr Boiling-Potassium Forced-Circulation Loop[a]

	Temperature (°C)	Pressure (psia)	Vapor Velocity (fps)	Vapor Quality (%)
First-stage (convergent nozzle)				
Nozzle entrance	1093	140	1.5	
Nozzle exit	1032	100	1390	96
Blade surface	1071	100		
Second-stage (convergent-divergent nozzle)				
Nozzle entrance	1032	100	1.7	
Nozzle exit	743	12	3080	83
Blade surface	932	12		
Third-stage (convergent nozzle)				
Nozzle entrance	743	12	15	
Nozzle exit	693	7	1430	96
Blade surface	718	7		

[a]Operated 3000 hr.

One Nb–1% Zr forced-circulation loop with Nb–1% Zr nozzle and turbine-blade specimens in the test section was operated under the conditions shown in Tables 15.7 and 15.8. Results of examination of components from the test section are summarized below.

Test Section Component	Results
First-stage nozzle	Nonmetallic-appearing layer 1 to 2 mils thick on throat, resulting in a 4-mil decrease in throat diameter.
First-stage blade	Nonmetallic deposit on concave portion of blade; no attack or erosion observed; some discoloration at impingement area.
Second-stage nozzle	Nonmetallic deposit 0.5 mil thick on exit portion of convergent-divergent nozzle, resulting in a 1-mil decrease in throat diameter.
Second-stage blade	Erosion, or attack, or both, approximately 1 mil deep at impingement area; metallic crystalline deposit 1 mil thick on concave portion (see Fig. 15.28).
Third-stage nozzle	No deposit on surface; irregularities observed.
Third-stage blade	Crystalline deposit 0.5 mil thick; appears similar to deposit on second-stage blade.

Metallographic examination of the Nb–1% Zr alloy used in the boiler, condenser, and subcooler showed no evidence of attack or deposits, and no significant pickup of niobium or zirconium by the potassium was found.

Corrosion of Refractory Alloys by Lithium

C. E. Sessions J. H. DeVan

The compatibility of advanced refractory alloys with lithium at elevated temperatures has been studied under both static and dynamic flow conditions. The static tests were designed to study the effects of oxygen in the alloy, heat treatment,

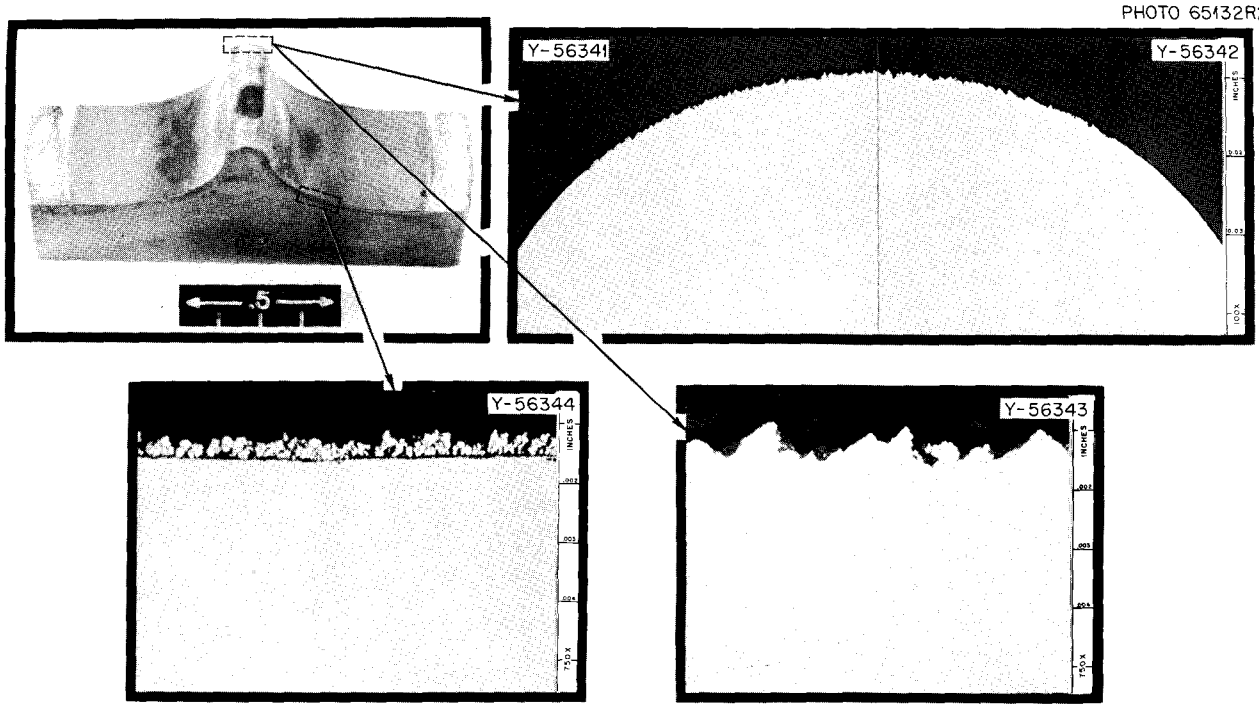

Fig. 15.28. Nb–1% Zr Blade Specimen from Second Stage of Boiling Potassium Pumped Loop. Test conditions: vapor temperature, 743°C; vapor quality, 83%; vapor velocity, 3080 fps; test duration, 3000 hr. Specimens as polished.

and test temperature in line with prior indications[24] that oxygen contamination was particularly detrimental to the corrosion resistance of niobium and tantalum-base alloys. Dynamic tests using thermal convection loops were operated to determine the extent of dissolution and mass transfer of the refractory alloys at elevated temperatures in a polythermal system.

The static corrosion tests have shown that the effects of oxygen in the advanced refractory alloys D-43, B-66, FS-85, CB-752, and T-111 are quite similar to those observed for Nb–1% Zr. That is to say, specimens of the refractory alloys that were exposed to lithium following an internal oxidation treatment exhibited either a transgranular Widmanstätten attack or intergranular corrosion attack, depending on the exposure temperature. For most of these alloys the predominant mode of attack changed from transgranular at the lower test temperature, 500°C, to intergranular at the higher test temperature, 1000°C. Fortunately, the susceptibility to oxygen-accelerated attack by the lithium could be eliminated if contaminated specimens were heat treated in the temperature range 1300 to 1600°C after oxidation but prior to exposure to lithium. The corrosion resistance that results after heat treatment is attributed to the precipitation of the oxygen as a thermodynamically stable oxide (ZrO_2 or HfO_2), which is not reduced by the high-temperature lithium. Thus, the corrosion by lithium of advanced refractory alloys follows very closely the corrosion mechanism proposed[24,25] for Nb–1% Zr relative to the effect of oxygen contamination.

One new phenomenon that was observed in the static compatibility tests was the presence of transgranular cracks in several of the refractory alloy coupons after exposure to high-temperature lithium. The cause of the cracking was attributed to hydrogen embrittlement that occurred when lithium was being removed with water after the test. However, several observations suggest that the phenomenon observed is related more to crack propagation of a clean surface in the presence of

[24] J. R. DiStefano, *Corrosion of Refractory Metals by Lithium*, ORNL-3551 (March 1964).

[25] J. R. DiStefano, *Metals and Ceramics Div. Ann. Progr. Rept. June 30, 1964*, ORNL-3670, p. 107.

hydrogen than to conventional hydrogen embrittlement. The advanced alloys cracked near room temperature in the absence of an applied stress. The cracks were not propagated as a result of hydride formation, since no hydride was observed in the microstructure, even for hydrogen-content increases as large as 1200 ppm. Also, the susceptibility to cracking depended on the thermal history of the alloy. For example, samples that were recrystallized or aged and exposed to lithium at 1000°C were more susceptible to cracking than samples exposed to lithium at 500°C. Additional work is in progress to further define the fracture mechanism of this process.

Two thermal convection loops have been evaluated after circulating lithium for 3000 hr at a maximum temperature of 1200°C with a temperature drop of 120°C. The results of the first loop, which was an all Nb–1% Zr alloy loop containing Nb–1% Zr inserts, provided a weight-change profile to be used as baseline data for comparing with dissolution tendencies of advanced refractory alloys in lithium. The second Nb–1% Zr alloy loop contained TZM alloy inserts and provided a measure of the dissimilar-metal reactions that result when niobium- and molybdenum-base alloys are used in a common circuit. The results of these two loops show that in the hot leg the refractory alloys lose oxygen, nitrogen, carbon, and zirconium to the lithium, and in the cold leg gold-colored zirconium nitride (ZrN) crystals deposit. The magnitude of the weight change was quite small in the Nb–1% Zr single-alloy loop but significantly larger in the dissimilar-metal (Nb–1% Zr, TZM) loop. Also, in the dissimilar-metal loop the major alloying constituents transferred. Niobium was transferred to the TZM alloy and molybdenum was picked up by the Nb–1% Zr, with larger transfers of both occurring at the highest temperatures. Thus, the results of the dynamic tests showed transfer of predominantly interstitial impurities in both loops, but larger quantities and more species were transported in the dissimilar-metal loops.

NONDESTRUCTIVE EVALUATION OF REFRACTORY ALLOYS

R. W. McClung

We have nondestructively evaluated tubing, sheet, plate, and bar of several refractory alloys, including B-66, Cb-752, Nb–1% Zr, FS-85, D-43, W–26% Re, TZM, and T-111. The specific techniques employed were selected according to the materials and their configurations. Fluorescent penetrants were used to evaluate the outer surfaces of the alloys, and very few significant discontinuities were detected by this procedure. At least one ultrasonic technique was used for the detection of internal flaws, and in some instances radiography and eddy currents were also applied.

Nondestructive evaluation was completed on a quantity of T-111 and B-66 alloy tubing produced under an Air Force contract in connection with a joint AF-NASA-AEC project. In general, the quality of the B-66 alloy was somewhat superior to that of the T-111 alloy. The results of this evaluation program have been reported in detail.[26]

A large portion of our work was devoted to the preparation of appropriate reference standards and subsequent evaluation of materials under study. For the ultrasonic evaluation of sheet, plate, bar, and tubing, we have found that electro-discharge machining yields the most accurate and reproducible reference notches. Details on the development of techniques for the preparation of reference standards are presented in Chap. 18 of this report.

PHYSICAL PROPERTIES

D. L. McElroy

This phase of the program is concerned with the measurement and correlation of high-temperature thermophysical properties of high-temperature materials. Thermal conductivity, thermoelectric power, electrical resistivity, and total hemispherical emittance are measured and evaluated as required to understand the behavior of these materials from both an applied and a theoretical point of view.

Physical Properties of Tungsten

W. Fulkerson J. P. Moore
R. S. Graves

We have completed a series of high-temperature physical property measurements on tungsten to resolve some major inconsistencies in values

[26]K. V. Cook and R. W. McClung, *Nondestructive Evaluation of T-111 and B-66 Alloy Tubing*, ORNL-TM-990 (February 1965).

reported in the literature and to provide accurate data over temperature ranges where none existed. We measured thermal conductivity from 50 to 1000°C, thermoelectric power from 0 to 1300°C, and electrical resistivity from −269 to 1400°C. The tungsten specimens were machined from wrought material derived from extrusions of pressed-and-sintered billets, and the bulk density was 99.8% of theoretical. The electrical resistivity ratio ($\rho_{300°K}/\rho_{4°K}$) was 35. The results of our measurements are given in Table 15.9, and the theoretical implications of these results are presented in Part I, Chap. 7 of this report. The thermal conductivity results are contrasted with those of previous investigators in Table 15.10 and Fig. 15.29. A large gap in the existing data between 300 and 800°C and the large discrepancies among reported values at temperatures greater than 1300°C are readily apparent.

The thermal conductivity of tungsten can be written as the sum of electronic, k_e, and lattice, k_l, components:

$$k = k_e + k_l \,. \tag{1}$$

If k_e is related theoretically to electrical resistivity, then

$$k = LT/\rho + k_l \,, \tag{2}$$

where L is the Lorenz number, T is the absolute temperature in degrees Kelvin, and ρ is the electrical resistivity. Between 500 and 1400°C, ρ, in μohm-cm, is given by the equation

$$\rho = -3.022 + (2.517 \times 10^{-2})T + (2.611 \times 10^{-6})T^2 \tag{3}$$

to within ±0.2%. If Eqs. (2) and (3) are used with measured thermal conductivity values, we find that the lattice thermal resistance $1/k_l$ becomes linear above 500°C. Thus, the measurements show that above 500°C

$$k = \frac{LT \times 10^6}{-3.022 + (2.517 \times 10^{-2})T + (2.611 \times 10^{-6})T^2} + \frac{1}{2.612 + (2.77 \times 10^{-3})T} \,. \tag{4}$$

This equation was used to extrapolate our results. The extrapolated values are given in Table 15.10 and are plotted in Fig. 15.29. They agree well with the high-temperature data of other investigators presented in Table 15.10.

Table 15.9. Results of Physical Property Measurements on Wrought Tungsten

Temperature (°C)	Thermal Conductivity (w cm^{-1} °C^{-1})	Electrical Resistivity (μohm-cm)	Thermoelectric Power (mv/°C)
0		4.05	5.0
100	1.602	7.33	10.9
200	1.479	9.80	16.2
300	1.389	12.42	20.9
400	1.322	15.16	25.3
500	1.267	18.01	29.2
600	1.221	20.93	32.8
700	1.184	23.93	35.8
800	1.152	27.01	38.5
900	1.123	30.09	40.7
1000	1.100	33.25	42.4
1100		36.49	43.9
1200		39.71	45.0
1300		42.99	45.8
1400		46.40	

Table 15.10. Collected Data on Thermal Conductivity of Tungsten

Temperature (°C)	Thermal Conductivity (w cm^{-1} °C^{-1})				
	ORNL	Rudkin[a]	Osborn[a]	Tye[a]	Langmuir and Taylor[a]
0					1.658
100	1.602			1.680	1.518
200	1.479			1.520	1.411
300	1.389			1.380	1.331
400	1.322				
500	1.267				
600	1.221				
700	1.184				
800	1.152			Wheeler[a]	Gumenyuk and Lebedev[a]
900	1.123	1.150	1.157		1.151
1000	1.100	1.109	1.139	1.102	1.118
1200	1.055[b]	1.063	1.108	1.062	1.103
1400	1.019[b]	1.042	1.077	1.033	1.063
1600	0.987[b]	0.976	1.047	1.012	0.975
1800	0.959[b]	0.946		0.996	0.942
2000	0.932[b]	0.917		0.982	0.921
2200	0.909[b]	0.900		0.971	0.904
2400	0.887[b]			0.962	
2600	0.868[b]			0.956	
2800	0.848[b]				
3000	0.831[b]				
3200	0.814[b]				
3400	0.798[b]				

[a]For references, see Fig. 15.29.
[b]Extrapolated values, see text and Eq. (4).

Effect of Surface Treatment for Emittance of the Nb–1% Zr Alloy

T. G. Kollie

The total hemispherical emittance of a material can be influenced by surface treatment and temperature. We have determined the effect of surface treatment on the emittance of the Nb–1% Zr alloy between 200 and 800°C and obtained the smoothed results given in Table 15.11.

The emittance of the pickled alloy was doubled by grit blasting. Grit blasting and dimpling slightly more than doubled the emittance. We attributed these changes to the greater geometric radiating area of the rougher surfaces. Note that all the surface treatments yielded emittances greater than those obtained for a smooth thermally etched rod.

Thermal Conductivity of D-43 and T-111 Alloys

J. P. Moore W. Fulkerson

The thermal conductivity of ½-in.-thick by ½-in.-diam specimens of D-43 and T-111 alloys was measured over a limited temperature range in the longitudinal heat flow apparatus. The smoothed results are compared to those of Hedge[27] in Table

[27]J. C. Hedge, C. Kostenko, and J. I. Lang, *Thermal Properties of Refractory Alloys*, ASD-TDR-63-597 (June 1963).

15.12. Our values are lower than Hedge's by 13 to 15% for D-43 and by 5 to 6% for T-111. The thermal conductivity of both alloys increased with temperature; D-43 is a better conductor of heat than is T-111. For the temperature range studied, the lattice portion of both alloys decreased with temperature, as is observed generally for all materials at high temperatures. However, when Hedge's high-temperature data are similarly treated, the lattice portion increases. To resolve this discrepancy, we have specimens of the alloys that will permit us to measure their thermal conductivities at high temperatures in the radial heat flow apparatus.

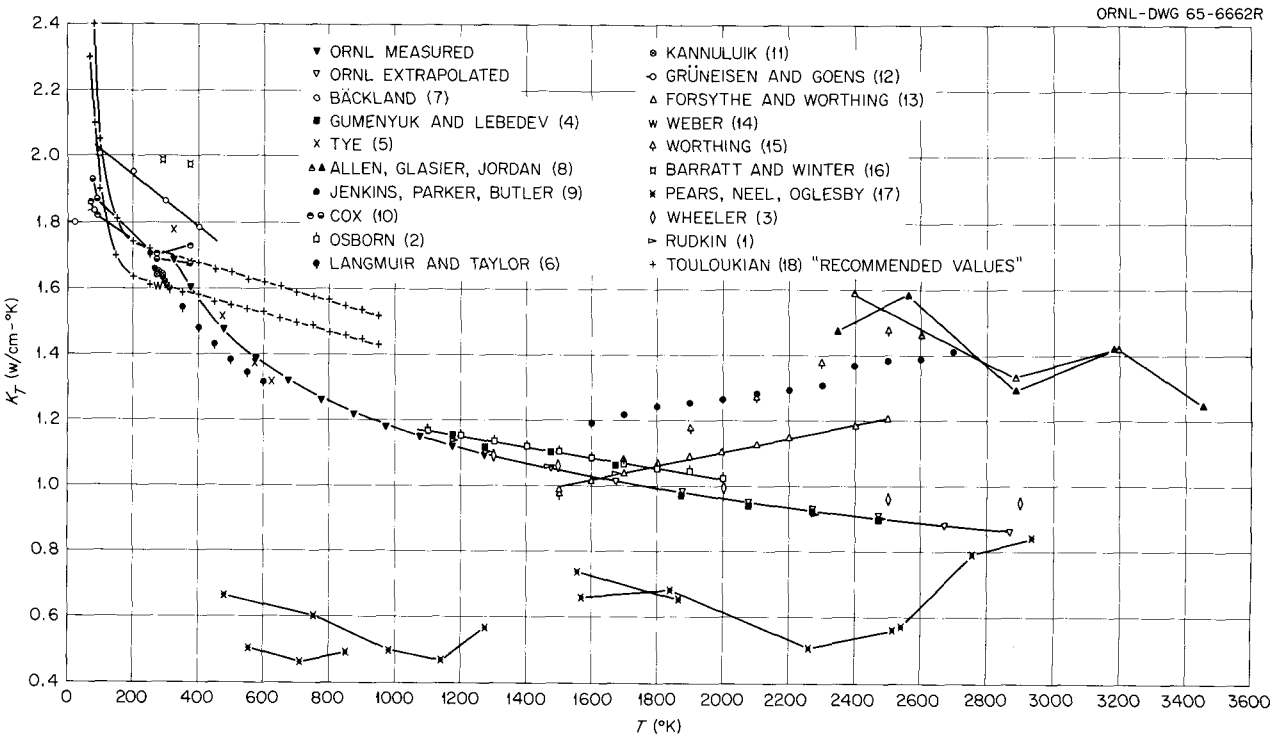

Fig. 15.29. Thermal Conductivity of Tungsten. References to literature values follow. (1) Rudkin, Parker, and Westover, USNRDL-TR-419 (1960). (2) Osborn, *J. Opt. Soc. Am.* 31, 428 (1941). (3) Wheeler, "Thermal Diffusivity at Incandescent Temperatures by a Modulated Electron Beam Technique," presented at the Natl. Phys. Lab. Intern. Conf. on Thermal Conductivity, Teddington, England, July 1964. (4) Gumenyuk and Lebedev, *Fiz. Met. i Metaloved.* 11, 29 (1961); translated as NP-tr-733. (5) Tye, pp. 169–79 in Niobium, Tantalum, Molybdenum, and Tungsten, Elsevier, 1961. (6) Langmuir and Taylor, *Phys. Rev.* 50, 68–87 (1936). (7) Bäckland, "Measurement and Analysis of the Thermal Conductivity of Tungsten and Molybdenum at 100 to 400°K," presented at the Natl. Phys. Lab. Intern. Conf. on Thermal Conductivity, Teddington, England, July 1964. (8) Allen, Glasier, and Jordan, *J. Appl. Phys.* 31, 1382 (1960). (9) Jenkins, Parker, and Butler, USNRDL-TR-348, pp. 1–24, 1959 (AD-226896). (10) Cox, *Phys. Rev.* 64, 241 (1943). (11) Kannuluik, *Proc. Roy. Soc. (London), Ser. A* 131, 320 (1931). (12) Grüneisen and Goens, *Z. Physik* 44, 615 (1927). (13) Forsythe and Worthing, *Astrophys. J.* 61, 146 (1925). (14) Weber, *Ann. Physik* 54, 165 (1917). (15) Worthing, *Phys. Rev.* 4, 535 (1914). (16) Barratt and Winter, *Proc. Phys. Soc. (London)* 26, 347 (1914). (17) Neel, Pears, and Oglesby, WADD-TR-60-924 (February 1962). (18) *Metallic Elements and Their Alloys*, Thermophysical Properties Research Center Data Book, vol. 1, p. 1029R, Purdue University, LaFayette, Indiana.

Table 15.11. Total Hemispherical Emittance of Nb–1% Zr Alloy

Temperature (°C)	Total Hemispherical Emittance[a]			
	Smooth Rod Thermally Etched at 1500°C	Pickled Strip	Pickled and Grit-Blasted Strip	Pickled, Dimpled, and Grit-Blasted Strip
200	0.12	0.16	0.33	0.36
400	0.10	0.16	0.37	0.40
600	0.11	0.18	0.41	0.43
800	0.12	0.22	0.45	0.47

[a]Determined in a vacuum of 1×10^{-7} torr.

Table 15.12. Results of Thermal Conductivity Measurements on D-43 and T-111 Alloys

Temperature (°C)	Thermal Conductivity (w cm^{-1} $°C^{-1}$)			
	Measured	Electronic Contribution[a]	Lattice Contribution	Hedge
D-43 Alloy				
30	0.419	0.408	0.011	0.482
60	0.428	0.420	0.008	0.493
90	0.438	0.431	0.007	0.502
120	0.447	0.442	0.005	0.520
T-111 Alloy				
30	0.391	0.362	0.029	0.414
60	0.398	0.373	0.025	0.422
90	0.407	0.384	0.023	0.431
120	0.416	0.395	0.021	0.439

[a]Calculated from Lorenz's number and electrical resistivity.

16. Materials Compatibility

J. H. DeVan

Since refractory metals have exhibited better corrosion resistance to liquid alkali metals than have the more conventional metals and alloys, they are being considered as containment materials for alkali metals in high-temperature nuclear reactor systems. The most important corrosion problems in alkali metal systems have generally stemmed from impurities such as carbon, oxygen, and nitrogen. Our current program has been oriented to analyze these impurities in alkali metals and to study their effects on newly developed refractory-metal container materials. Impurities in alkali metal–refractory metal systems include those initially present in the alkali metal and those "gettered" by the alkali metal from the refractory metal.

Other work on corrosion by liquid alkali metals is reported in Chap. 15, in Chap. 27 of Part III, and in Chaps. 33 and 34 of Part IV.

EFFECT OF OXYGEN ON THE CORROSION OF NIOBIUM BY LIQUID POTASSIUM[1,2]

A. P. Litman

The behavior of unalloyed niobium in liquid potassium under static conditions at constant temperatures of 200, 600, and 815°C was influenced by oxygen in the components, temperature, and exposure time. Adjusting the oxygen content of either the potassium or the niobium produced various manifestations of corrosion, including the production of surface and subsurface corrosion products, illustrated in Fig. 16.1, and the mass transfer of oxygen, niobium, and potassium. All the corrosion processes were enhanced by higher temperatures and longer exposures.

The surface scales were predominantly niobium dioxide, but niobium metal, other niobium oxides, potassium metaniobate, and unidentified species were sometimes present. The subsurface product, tentatively identified as niobium dioxide, was never observed when the initial oxygen content of the niobium was less than 1000 ppm. Higher initial oxygen concentrations in the niobium or the potassium resulted in more rapid thickening of the surface scales.

Significant weight losses (0.3 to 2.4 mg/cm^2) occurred for oxygen-doped niobium specimens exposed to potassium at 600 and 815°C, but weight changes were insignificant at 200°C. We found that oxygen transfer was controlling in determining the magnitude of the weight losses. Typical oxygen-loss patterns, obtained by vacuum fusion analysis of the niobium, are shown in Fig. 16.2 for specimens initially containing 2600 ppm O. Similar oxygen losses occurred for specimens initially containing much lower levels of oxygen.

Other evidence of component mass transfer was afforded by chemical analysis of the potassium. As illustrated by Table 16.1, the niobium concentration in the potassium increased with temperature and initial oxygen concentration in the potassium. The temperature dependence of the niobium content at the higher oxygen levels showed a discontinuity below 400°C, suggesting a change in the corrosion mechanism at this temperature.

The redistribution of potassium in the test system was determined by stepwise acid leaching

[1]Condensed from the University of Tennessee M.S. Thesis of A. P. Litman, *The Effect of Oxygen on the Corrosion of Niobium by Liquid Potassium*, ORNL-3751 (July 1965).

[2]Summary of papers presented at the NASA–AEC Liquid-Metals Information Meeting, Gatlinburg, Tennessee, April 21–23, 1965 and the 14th AEC Corrosion Symposium, Augusta, Georgia, May 26–28, 1965.

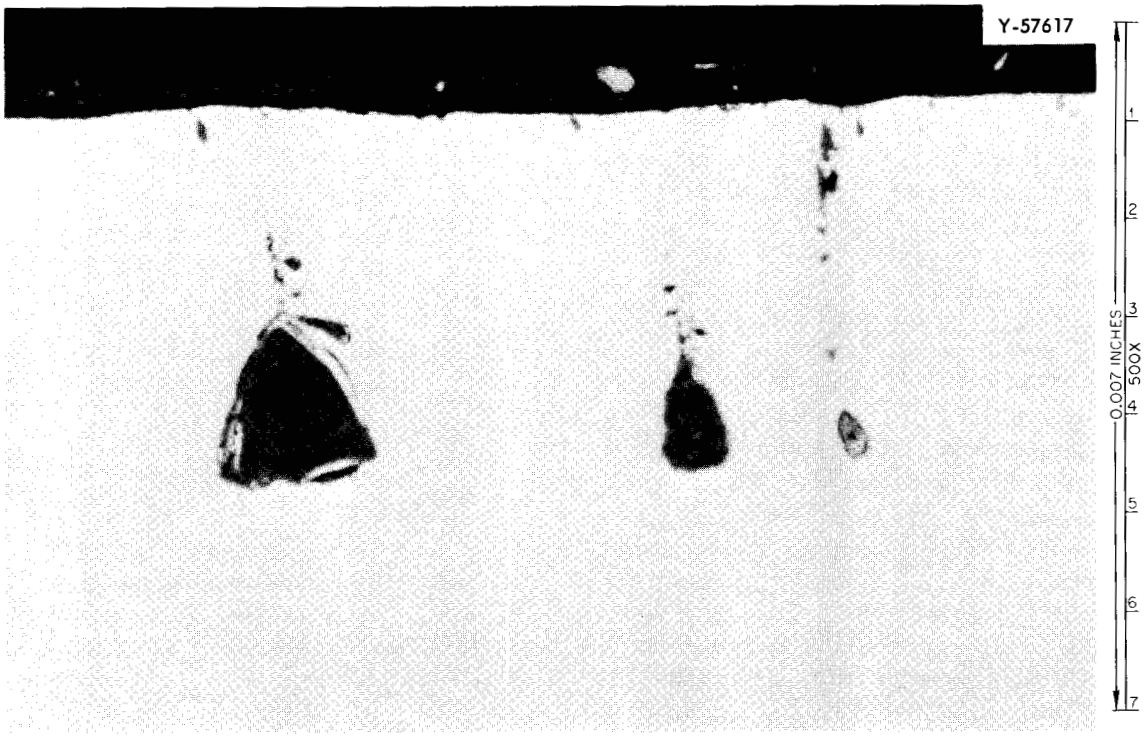

Fig. 16.1. Surface and Subsurface Corrosion Products Formed on a Niobium Specimen Containing 2400 ppm O After Exposure at 815°C to Potassium Containing 50 ppm O. As Polished. 500×.

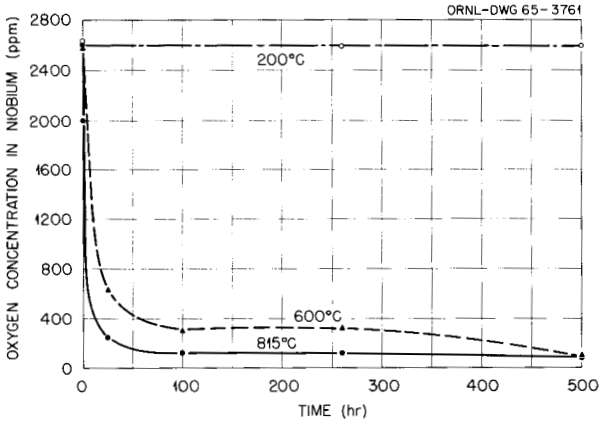

Fig. 16.2. Effect of Time and Temperature on the Migration of Oxygen from Niobium in Contact with Potassium.

Table 16.1. Effect of Temperature and Initial Oxygen Concentration on the Niobium Content of Potassium Exposed for 48 hr to Nb–0.017% O

Temperature (°C)	Niobium Content in Potassium (ppm)		
	Initial Content of Oxygen in Potassium		
	50 ppm	450 ppm	600 ppm
200	50	75	
400	75	425	750
600	150	450	925
800	375	475	

of the surface and separate analyses of the surface corrosion products, substrates, and matrices. A portion of the results is presented in Table 16.2. The transfer of potassium in these tests was primarily associated with the growth of a surface corrosion product.

The observations from these experiments were impossible to rationalize in terms of a simple model based only on the binary oxides of niobium and potassium. Such a model could not account for the marked depletion of oxygen in niobium at 600 and 815°C, which occurred independently of the initial oxygen concentration in either the niobium or potassium. This depletion also contradicted the finding of niobium dioxide and potassium in the surface and subsurface corrosion products. Further, we found that pure niobium dioxide is unstable in excess potassium. To account for these observations, we had to postulate the existence of one or more ternary compounds of the form $K_xNb_yO_z$ with a thermodynamic stability sufficiently high to reduce the chemical potential of the oxygen in solution considerably below its value for equilibrium with binary oxides. Further, we proposed that these species disproportionate on cooling to yield the corrosion products observed at room temperature.

Table 16.2. Potassium Contents of Nb–0.017% O Test Specimens Exposed to Potassium for 500 hr

Temperature (°C)	Potassium Content (ppm)		
	Surface Corrosion Product	Substrate[a]	Matrix[b]
200	53	12	<2
600	215	12	<2
815	2530	128	<2

[a]Includes subsurface corrosion product.

[b]Specimen region below subsurface corrosion product.

DETERMINATION OF OXYGEN IN POTASSIUM

A. P. Litman J. W. Prados[3]

Distribution ratios for oxygen between zirconium and liquid potassium at 815°C have been determined experimentally,[4] and the results for 100-hr exposures, as a function of zirconium specimen thickness, are summarized in Fig. 16.3. These ratios and an oxygen mass balance were used in the determination of oxygen levels in oxygen-doped potassium by the gettering–vacuum-fusion (GVF) technique. In these experiments, the oxygen-doped potassium was heated variously in molybdenum, nickel, and niobium containers at temperatures from 200 to 815°C and for periods of 1 to 100 hr. The results are presented in Table 16.3 and show that at oxygen levels from 60 to 2900 ppm GVF analysis is accurate despite variations in the thermal and environmental history of the potassium. The amalgamation and vacuum distillation techniques failed to yield a satisfactory measure of oxygen in doped potassium after similar exposures.[5,6]

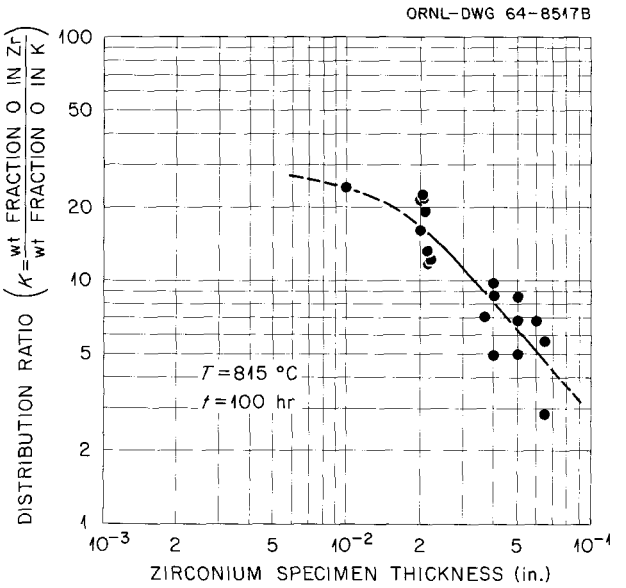

Fig. 16.3. Distribution Ratio for Oxygen Between Zirconium and Potassium After 100 hr at 815°C Under Static Conditions, as a Function of Thickness of the Zirconium Specimen.

[3]Consultant from the University of Tennessee.

[4]A. P. Litman and J. W. Prados, "The Partitioning of Oxygen Between Zirconium and Liquid Potassium," ORNL-TM-1039 (April 1965); accepted for publication in *Electrochemical Technology*.

[5]A. P. Litman and G. Goldberg, *Metals and Ceramics Div. Ann. Progr. Rept. May 31, 1963*, ORNL-3470, pp. 64–66.

[6]A. P. Litman, J. E. Strain, and G. Goldberg, *Metals and Ceramics Div. Ann. Progr. Rept. June 30, 1964*, ORNL-3670, pp. 113–14.

Table 16.3. Oxygen Recovered from Potassium by the GVF Technique[a]

Oxygen Added (ppm)	Total Oxygen[b] (ppm)	Temperature[c] (°C)	Oxygen Found (ppm)	Oxygen Recovery (%)
905[d]	955	200	960	102
1045[d]	1095	200	1135	104
15[d]	65	600	60	92
155[e]	205	600	225	110
340[e]	390	800	355	91
1100[e]	1225	800	1210	99
1375[e]	1500	800	1650	110
2780[e]	2905	800	2820	97
250[d]	300	815	275	92
610[d]	745	815	740	99
1380[d]	1430	815	1565	109

[a]Sample exposed to 0.020- to 0.065-in.-thick zirconium specimen for 100 hr at 815°C.

[b]Includes oxygen initially present in the potassium.

[c]Temperature at which oxygen-doped potassium was heated in molybdenum, nickel, or niobium containers for times varying from 1 to 100 hr before analysis by GVF technique.

[d]Oxygen added by contacting with niobium containing dissolved oxygen.

[e]Oxygen added as K_2O.

DIFFUSION OF OXYGEN IN NIOBIUM[7]

A. P. Litman

In connection with the compatibility studies described in this chapter, the diffusivities of oxygen in polycrystalline niobium were determined at 600 and 815°C. The diffusivity measurements were based on the observation that oxygen diffused from the niobium in contact with potassium to form complex corrosion products at the niobium-potassium interface, and that the reaction afforded a reproducible and constant surface oxygen concentration. By analyzing the oxygen depletion in the niobium as a function of time and applying the appropriate solution in Fick's second law, we found the diffusion coefficients to be 7.9×10^{-10} and 6.4×10^{-9} cm^2/sec at 600 and 815°C respectively. These values are slightly smaller than, but in reasonable agreement with, recent literature[8] values, which were calculated from the rate at which oxygen penetrated niobium that was exposed to oxygen gas at a pressure of 760 torrs.

[7]Abstract from Short Note accepted for publication in *Physica Status Solidi*.

[8]R. I. Jaffee, W. D. Klopp, and C. T. Sims, *Trans. Am. Soc. Metals*, 51, 282–98 (1959).

17. Mechanical Properties

J. R. Weir, Jr.

Our general objectives center around studies of the effects reactor service environments have on the engineering mechanical properties of materials. Our work is so oriented that having observed important effects on the properties of materials we investigate potential ways to eliminate the deleterious effects. Our research in the past year has emphasized the elevated-temperature radiation-induced embrittlement of engineering alloys. Our approaches should result in practical solutions to the problem.

Investigations of mechanical properties of materials for specific applications are reported in Chaps. 15, 19, and 21 and several chapters of Part III.

IRRADIATION EMBRITTLEMENT OF LOW-BORON TYPE 304 STAINLESS STEEL

W. R. Martin

A growing literature[1-7] describes the magnitude and characteristics of the irradiation-induced embrittlement of alloys at elevated temperatures. These data appear to be consistent with the hypothesis that the grain-boundary embrittlement is due to the helium generated by the $^{10}B(n,\alpha)^{7}Li$ thermal-neutron capture reaction.[1,8,9]

We studied the effect of very small concentrations of boron on the embrittlement of type 304 stainless steel irradiated to a high exposure in a thermal-neutron test reactor. These steels generally contain in excess of 1 ppm B, and it was necessary to electron-beam remelt a commerical heat of steel to reduce the concentration of this element to 0.015 ppm.

The postirradiation ductilities are listed in Table 17.1 for deformation at 704 and 842°C. Only small differences are found among the ductilities of all the electron-beam melted heats, although the concentrations of boron span an order of magnitude. The largest difference in ductility exists between the commercial alloy and the electron-beam remelted alloys. The concentrations of helium were calculated for the $^{10}B(n,\alpha)$ reaction for each of the alloys and are given in Table 17.2. If helium arises only from the (n,α) reactions due to thermal neutrons, these data suggest that either helium is not responsible for the embrittlement or the embrittlement is quite independent of helium concentrations in the range of 0.13 to 1.1×10^{-7} atom fraction. However, if one includes the concentration of helium due to fast-neutron (n,α) reactions for all the elements present in stainless steel, the data appear more compatible with an irradiation embrittlement mechanism based on helium. Table 17.2 also gives the concentration of helium due to

[1] N. E. Hinkle, *Am. Soc. Testing Mater. Spec. Tech. Publ.* 341, 344 (1963).

[2] P. C. L. Pfiel and D. R. Harries, "Effect of Irradiation on Austenitic Steels and Other High Temperature Alloys," paper presented at the American Society for Testing and Materials Symposium on Flow and Fracture of Metals and Alloys in Nuclear Environment, Chicago, June 21–26, 1964 (to be published).

[3] W. R. Martin and J. R. Weir, "The Effect of Irradiation Temperature on the Postirradiation Stress-Strain Behavior of Stainless Steel," paper presented at the American Society for Testing and Materials Symposium on Flow and Fracture of Metals and Alloys in Nuclear Environment, Chicago, June 21–26, 1964 (to be published).

[4] A. N. Hughes and J. R. Caley, *J. Nucl. Mater.* 10, 60 (1963).

[5] J. Fennell and A. C. Roberts, *J. Nucl. Mater.* 12, 167 (1964).

[6] W. R. Martin and J. R. Weir, *Nucl. Appl.* 1(2), 160–67 (1965).

[7] F. A. Comprelli *et al.*, *Trans. Am. Nucl. Soc.* 7(2), 455 (1964).

[8] R. S. Barnes, *Some Mechanism of Radiation Induced Mechanical Property Changes*, AERE-R-4655 (July 1964).

[9] J. Moteff, F. C. Robertshaw, and F. D. Kingsbury, "Effect of Neutron Irradiation on the Stress-Rupture Properties of High-Temperature Precipitation Hardening Alloys," Paper No. 64-364 from American Institute of Aeronautics and Astronautics 1st Annual Meeting, Washington, D.C., June–July, 1964.

Table 17.1. Embrittlement of Stainless Steel Irradiated[a] at 700°C

Tensile Test Temperature (°C)	Natural Boron Concentration (ppm)	Ductility			
		True Uniform Strain[b]		Total Elongation	
		Irradiated (%)	Unirradiated (%)	Irradiated (%)	Unirradiated (%)
704	0.015	13.7		19.1	
	0.023	12.7	30.9	23.3	56.2
	0.107	13.1		21.6	
	0.130	12.7	19.6	19.6	60.4
	3.9	11.2	18.0	13.1	40.2
842	0.015	3.1		6.1	
	0.023	2.9		6.1	
	0.107	2.9	13.8	5.6	46.6
	0.130	3.3	18.2	6.1	57.2
	3.9	1.5	16.0	3.0	43.0

[a]Irradiated at B-8 position of the ORR to a neutron dose of 4.5×10^{20} neutrons/cm^2 (thermal) and 3.5×10^{20} neutrons/cm^2 (>1 Mev).

[b]Specimens strained at a rate of 0.2%/min.

the (n,α) reactions with fast neutrons, taken from the work of Bush *et al.*[10] When the helium from all sources is considered, the lack of variation in ductility among the electron-beam melted heats is more easily explained, since they differ so little in total helium concentration. This suggests that the irradiation of these electron-beam melted alloys to a lower fast-neutron dose would result in a greater variation in the ductilities. This is confirmed in Table 17.3, which compares the effects of two widely different doses.

Table 17.2. Approximate Helium Concentration from All (n,α) Reactions

Natural Boron Concentration (ppm)	Helium Concentration (Atom Fraction)		
	Due to ^{10}B and Thermal Neutrons	Due to Fast Neutron Reactions	Total
	$\times 10^{-6}$	$\times 10^{-6}$	$\times 10^{-6}$
0.015	0.013	0.3	0.31
0.023	0.020	0.3	0.32
0.107	0.091	0.3	0.39
0.130	0.110	0.3	0.41
3.9	3.3	0.3	3.6

We conclude that removing the ^{10}B from the alloy is not the ultimate solution for improving the ductility of irradiated alloys, because even in thermal-neutron reactors (n,α) reactions with fast neutrons are significant for materials containing low boron concentrations.

[10]S. H. Bush, J. Moteff, and J. R. Weir, "Radiation Damage in Fast Reactor Components," presented at American Nuclear Society Topical Meeting on Fast Reactor Technology, Detroit, Michigan, April 26–28, 1965 (to be published).

Table 17.3. Effect of Boron Content of Type 304 Stainless Steel at Low and High Doses

Exposure (neutrons/cm^2)	B Content (ppm)	Elongation (%)		Helium Concentration (ppm)		Total
		704°C	842°C	$^{10}B(n,\alpha)$	Fast (n,α)	
High exposure,	0.11	22	6	0.091	0.3	0.4
$\sim 5 \times 10^{20}$	3.9	13	3	3.3	0.3	3.6
Low exposure,	0.11	39	41	0.00004	0.00006	0.0001
$\sim 5 \times 10^{16}$	3.9	40	29	0.00150	0.00006	0.0016

INFLUENCE OF GRAIN SIZE ON THE IRRADIATION EMBRITTLEMENT OF STAINLESS STEEL AT ELEVATED TEMPERATURES[11]

W. R. Martin

Low[12] and McLean[13] have shown that grain size affects the process of grain-boundary fracture. The finer the grain size, the higher the applied stress necessary to nucleate a crack and the lower the rate of crack propagation. We therefore studied the influence of grain size in the range of ASTM 3 to 10 on the postirradiation ductility of stainless steels. Typical data are given in Table 17.4. The ductility of irradiated materials may be increased significantly by reducing the grain size. Stainless steel having a grain size of ASTM 8 to 10 is at least twice as ductile as material having a grain size of ASTM 3.

We also investigated the contribution of grain-boundary sliding to the total strain at fracture. Using the technique of Rachinger,[14] we analyzed the strain at fracture for irradiated and unirradiated material in terms of grain-boundary sliding, slip within the grain matrix, and the strain attributable to widening of cracks. Irradiated materials fractured at strains for which no grain-boundary sliding could be detected. The elongation due to separation of cracks was also reduced, particularly for the fine-grained material.

[11]Condensed from article submitted to *Journal of Nuclear Materials*.

[12]J. R. Low, Jr., "The Fracture of Metals," No. 1 in *Progress in Materials Science*, vol. 12, ed. by B. Chalmers, Macmillan, New York, 1963.

[13]D. McLean, *Grain Boundaries in Metals*, p. 336, Clarendon, Oxford, 1957.

[14]W. Rachinger, *J. Inst. Metals* **81**, 33 (1952–53).

IRRADIATION EMBRITTLEMENT OF STAINLESS STEEL AT VERY HIGH TEMPERATURE

W. R. Martin

We showed previously that the postirradiation ductility of type 304 stainless steel at elevated temperatures is practically independent of irradiation temperature up to 700°C. Our studies of irradiation temperature have now been extended into the temperature range of 700 to 900°C for the steels containing 0.02 and 0.06% C. The total elongations from tests at 650, 704, 775, and 842°C are listed in Table 17.5 for the irradiated specimens and the unirradiated controls. The preirradiation ductilities of the low- and high-carbon steels were not significantly different. However, except for irradiation at 900°C, the postirradiation ductility of the high-carbon heat was significantly better than that of the low-carbon heat. In general, the ductility of the irradiated alloy decreases when either the test temperature or the irradiation temperature is increased. Deformation temperature appears to have a greater influence than irradiation temperature. Since the influence of irradiation temperature might be associated with grain growth or carbon redistribution, the largest effect is noted at 900°C, the temperature at which all the carbon is in solution in both heats.

The higher ductilities observed for the high-carbon alloy may be due to several factors. The concentration of the helium generated from (n,α) reactions is approximately 20% lower in the high-carbon heat, due to a lower concentration of ^{10}B (0.6 to 0.8 ppm). However, we believe that the improved ductility is related to the distribution and agglomeration of grain-boundary carbides. Weaver[15,16]

[15]C. W. Weaver, *J. Inst. Metals* **88**, 296 (1959–60).

[16]C. W. Weaver, *Acta Met.* **8**, 343 (1960).

Table 17.4. Influence of Grain Size on Irradiation Embrittlement

ASTM Grain Size	Total Elongation (%)			
	At 704°C		At 842°C	
	Unirradiated	Irradiated	Unirradiated	Irradiated
3	30	19	23	8
5	39	23	36	11
8–10	58	42	47	16

Table 17.5. Elevated-Temperature Ductility of Unirradiated and Irradiated AISI Types 304L and 304 Stainless Steel

Tensile Test Temperature (°C)	Irradiation Temperature (°C)	Total Elongation (%)			
		Unirradiated[a]		Irradiated[b]	
		0.02% C	0.06% C	0.02% C	0.06% C
650	700	42.2	36.8	16.9	28.5
	800	39.8	41.7	17.6	29.9
	900		37.4	11.3	12.4
704	700	38.9	41.5	13.1	23.0
	800	36.2	36.6	13.3	20.3
	900	31.4	28.0	6.4	
775	700	33.0	40.7	9.1	15.7
	800	30.0	40.0	7.2	12.6
	900		31.7	2.9	4.0
842	700	38.4	31.9	6.7	10.6
	800	36.8	39.0	4.0	8.8
	900	24.5	25.6	2.2	3.0

[a]Control specimens were held at the irradiation temperature for a period equal to the irradiation time.
[b]Alloys irradiated to a dose of 3.5×10^{20} neutrons/cm^2 (>1 Mev) and 4.5×10^{20} neutrons/cm^2 (thermal).

Table 17.6. Effect of Grain-Boundary Carbides on Elevated-Temperature Embrittlement of Irradiated Stainless Steel[a]

Preirradiation Heat Treatment	Tensile Test Temperature (°C)	Total Elongation (%)
1 hr at 1036°C	704	20.5
1 hr at 1036°C and 100 hr at 800°C	704	30.5
1 hr at 1036°C	842	7.6
1 hr at 1036°C and 100 hr at 800°C	842	13.9

[a]Type 304 stainless steel containing 0.06% C irradiated at 50°C to a dose of 7×10^{20} neutrons/cm^2 (>1 Mev) and 9×10^{20} neutrons/cm^2 (thermal), and strained at a rate of 0.2%/min.

has shown that heat treatment of a nickel-base alloy to produce a coherent precipitate in the grain boundaries improved the ductility. If the strength of the interface between the carbide and the matrix is large compared to the cohesive strength of the boundary, grain-boundary precipitates that reduce the length of the sliding interface can increase the stress necessary to cause triple-point cracks. Weaver observed that the precipitate in the nickel-base alloy restricted the propagation of these cracks to intercarbide spaces.

One can apply this reasoning to the variation of irradiation embrittlement observed for the 0.02 and 0.06% C stainless steels. Hence, if the high-carbon steel is heat treated before irradiation to agglomerate the carbides, the ductility is improved. Examples are given in Table 17.6.

DUCTILITY OF AN IRRADIATED 18-8 STAINLESS STEEL CONTAINING TITANIUM

W. R. Martin

Since boron normally segregates to the grain boundaries in alloys, most of the helium from transmutation is generated at these boundaries. If one could form a stable boron compound that is in-

Table 17.7. Influence of Titanium on the Elevated-Temperature Irradiation Embrittlement of 18-8 Stainless Steel[a]

Titanium (wt %)	Total Elongation[b] (%)		
	650°C	700°C	842°C
0.0	31.0	31.5	20.0
0.2	40.0	38.0	45.1
0.3	34.7	28.5	35.2
0.4	31.5	26.5	25.0
0.5	28.8	21.5	19.0
0.6	24.1	19.5	17.9
0.8	22.9	20.5	19.1
1.0	30.6	23.5	23.5
1.2	29.8	23.0	28.5

[a]Specimens irradiated to a dose level of 1×10^{20} (thermal) and 1.5×10^{19} neutrons/cm^2 (>1 Mev).

[b]Measured for 1-in. gage length in tests at a strain rate of 2%/min.

soluble either in the melt or after solidification, one could get a homogeneous distribution of this compound. Then helium generated would stay at the precipitate-matrix interface and much less would form at the grain boundaries. Having an incoherent interface, these precipitates would also serve as a depository for helium generated from reaction of other elements with fast neutrons. Thus, in principle the introduction of a strong boride former such as titanium should result in material with a lower susceptibility to elevated-temperature embrittlement in thermal- and fast-neutron environments.

We have now accumulated data from two different irradiations of type 304 stainless steel, and typical data are given in Table 17.7. Small additions of titanium obviously improve greatly the ductility of the stainless steel. Titanium additions at the level required to meet the composition specifications for type 321 stainless steel are above the range for maximum ductility.

Titanium additions in the range up to 0.2% greatly reduce the magnitude of irradiation embrittlement in type 304 stainless steel. Although the alloys containing titanium have smaller grains than the unstabilized alloys, we believe the effect of titanium to be as hypothesized earlier. We plan to investigate the properties of this alloy in more detail.

INFLUENCE OF NEUTRON IRRADIATION ON THE TENSILE PROPERTIES OF THE ALUMINUM ALLOY 6061

H. E. McCoy

For improved strength, aluminum alloys are often used in the age-hardened and cold worked states. Although the rates of overaging and recovery at various temperatures are known reasonably well for most aluminum alloys, how irradiation alters these rates is not known. Adair, Hook, and Garrett[17] indicate that some very large effects might be expected.

In three experiments, we irradiated the aluminum alloy 6061 in the "O" (annealed), T-6 (age-hardened), and cold worked (20%) conditions. In the first two experiments, the dose varied from 2.9×10^{20} to 0.8×10^{20} neutrons/cm^2 (thermal) and 2.9×10^{19} to 0.4×10^{19} (fast, >2.9 Mev), and the irradiation temperature ranged from 110 to 490°C. The wide flux range was due to the large area covered by the specimens. Representative specimens were tensile tested at 25°C and at the irradiation temperature. In the third experiment, specimens were irradiated at 43°C to an integrated dose of 7.4×10^{19} (thermal) and 2.9×10^{18} neutrons/cm^2 (fast, >2.9 Mev). All the specimens were tested at 25°C after being given various isochronal anneals to determine the temperature required to restore the preirradiation properties.

The results of the first and second experiments indicated that, under the conditions of flux and irradiation temperature studied, the properties of the alloy in the "O," T-6, and cold worked conditions were not altered by irradiation. The tensile tests at elevated temperatures indicated that the rates of overaging and recovery were each identical for the irradiated and unirradiated materials.

The results from the third experiment exhibited considerable scatter but indicated the following trends. The yield stress of the alloy in the "O" condition was increased approximately 10% by irradiation, the ultimate stress was increased 4.5%, and the fracture elongation was reduced approximately 20%. Annealing 0.5 hr at 200°C appeared sufficient to recover the preirradiation properties. The irradiated cold worked material exhibited no

[17]A. M. Adair, R. E. Hook, and H. J. Garrett, *Radiation Induced Overaging of a 2024-T3 Aluminum Alloy*, ARL-132 (September 1961).

increase in yield stress, a 10% increase in tensile stress, and a 50% increase in fracture elongation. Annealing for 0.5 hr at 200°C appeared sufficient to recover the preirradiation properties. The yield and tensile stresses of the material in the T-6 condition increased about 2.5 and 4%, respectively, and the ductility was unaltered. The yield and tensile strengths exhibited some unusual changes as a function of postirradiation annealing temperature; however, these properties were always within 5% of the properties of the control specimens. The rupture ductility was also quite erratic but never varied more than 10% from that of the control material.

We conclude that the properties of the 6061 alloy do not appear to be altered drastically by irradiation doses of the order of 10^{20} (thermal) and 10^{19} neutrons/cm^2 (fast).

18. Nondestructive Test Development

R. W. McClung

The nondestructive test development program has been designed to develop new and improved methods of evaluating reactor materials and components. To achieve this we have conducted studies on the various physical phenomena, developed instrumentation and other equipment, devised application techniques, and designed and fabricated reference standards. Among the methods being actively pursued are electromagnetics (with major emphasis on eddy currents), ultrasonics, and penetrating radiation. In addition to the programs oriented to particular methods, we have programs aimed at applying these and other methods to the inspection of problem materials and to the remote inspection of radioactive materials.

ELECTROMAGNETIC TEST METHODS

C. V. Dodd

We have continued research and development concerning electromagnetic phenomena on both analytical and empirical bases. As part of the program, we are studying the mathematical determination of the vector potential of a coil as a function of coil dimensions, frequency, specimen conductivity, and coil-to-specimen spacing (lift-off). This electromagnetic boundary-value problem is solved by a relaxation technique on a digital computer. The differential equation for the vector potential is approximated by finite difference terms. By making a number of correcting calculations, we can make the value of the vector potential converge to agreement with the differential equation at every point. We anticipate that this method will be of value not only for the design of eddy-current test methods but also for other applications of electromagnetic induction. The first uses appear to be in the thermonuclear project and in the development of sintered aluminum products.

We have applied this technique to the problem of a long coil above a conducting plane. Figure 18.1 shows the variation of the phase and amplitude of the vector potential. (This is a cross section taken from the coil axis in the radial direction.) After we have determined the vector potential, we can calculate any physically observable electromagnetic phenomenon, such as the coil impedance,

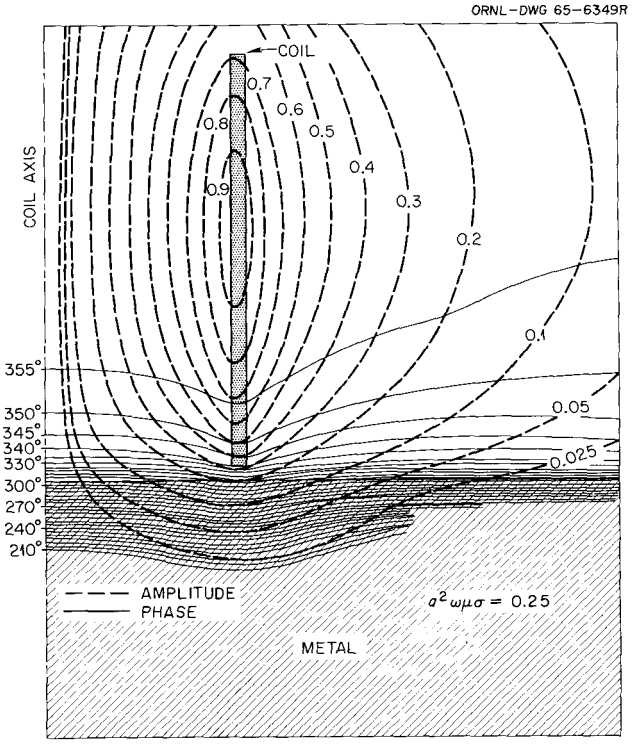

Fig. 18.1. Phase and Amplitude Variations in the Vector Potential Associated with Long Coil Above a Conducting Plane.

ORNL-DWG 64-11708

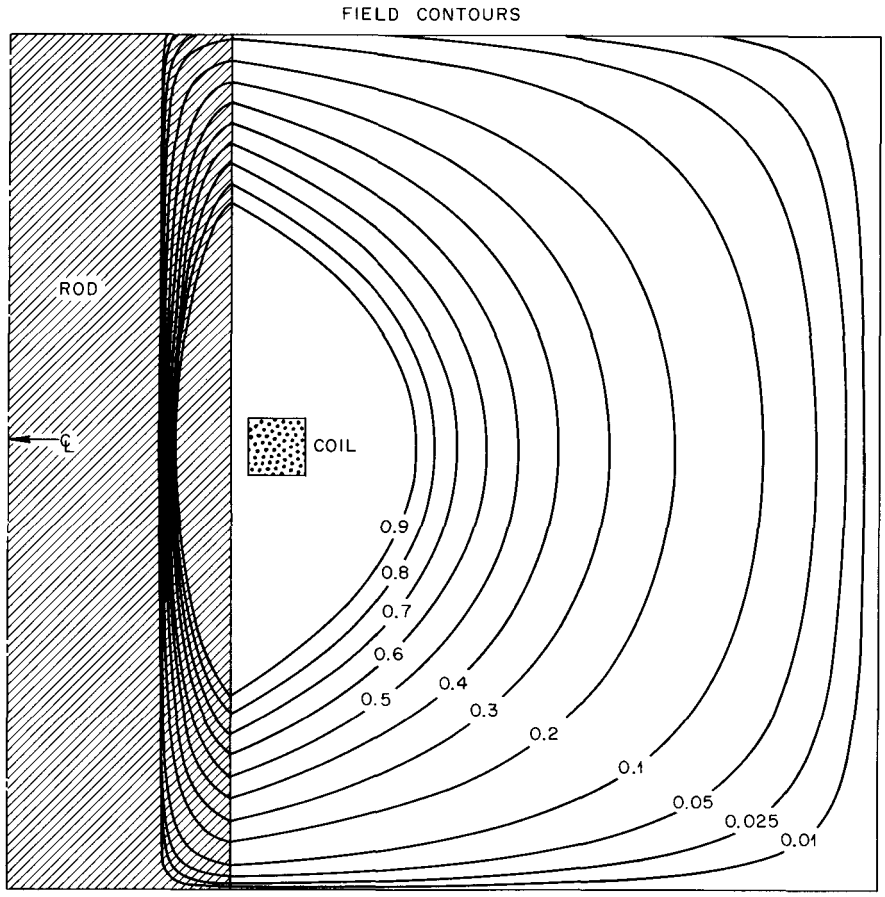

Fig. 18.2. Equipotential Contours of the Vector Potential in a Ferromagnetic Rod Inside an Encircling Coil.

the eddy currents in the metal, the rate of eddy-current heating in the metal, or the eddy-current forces on the metal. Since the eddy-current flow is proportional to the vector potential, the contours in the metal in Fig. 18.1 are also contours of eddy-current flow.

We have also applied this technique to ferromagnetic materials. Figure 18.2 shows the variation in vector potential of a coil encircling a ferromagnetic rod with a relative permeability of 200. Note the lack of penetration into the rod and the sharp cutoff of the current inside the rod. We have calculated the shaping of the eddy-current flow inside a metal through the use of ferrite with the coil. Figure 18.3 shows how the contours of vector potential and eddy-current flow are "squeezed" in toward the coil axis. We hope that this technique can be used to focus the current flow inside the metal and provide greater sensitivity to defects.

As stated earlier, from the vector potential we can calculate other phenomena. Figure 18.4 shows contours of equal eddy-current heating density. The equations have also been derived to calculate both eddy-current and magnetic forces. In addition a new relaxation equation has been calculated for pulses of current in nonlinear magnetic materials. These new equations are being programmed for computer solution.

We are continuing the development and applications of the phase-sensitive eddy-current instrument[1] developed at ORNL. Harmonic distortion is one of the factors limiting the sensitivity of the

[1]C. V. Dodd, *Mater. Evaluation* **22**(6), 260 (1964).

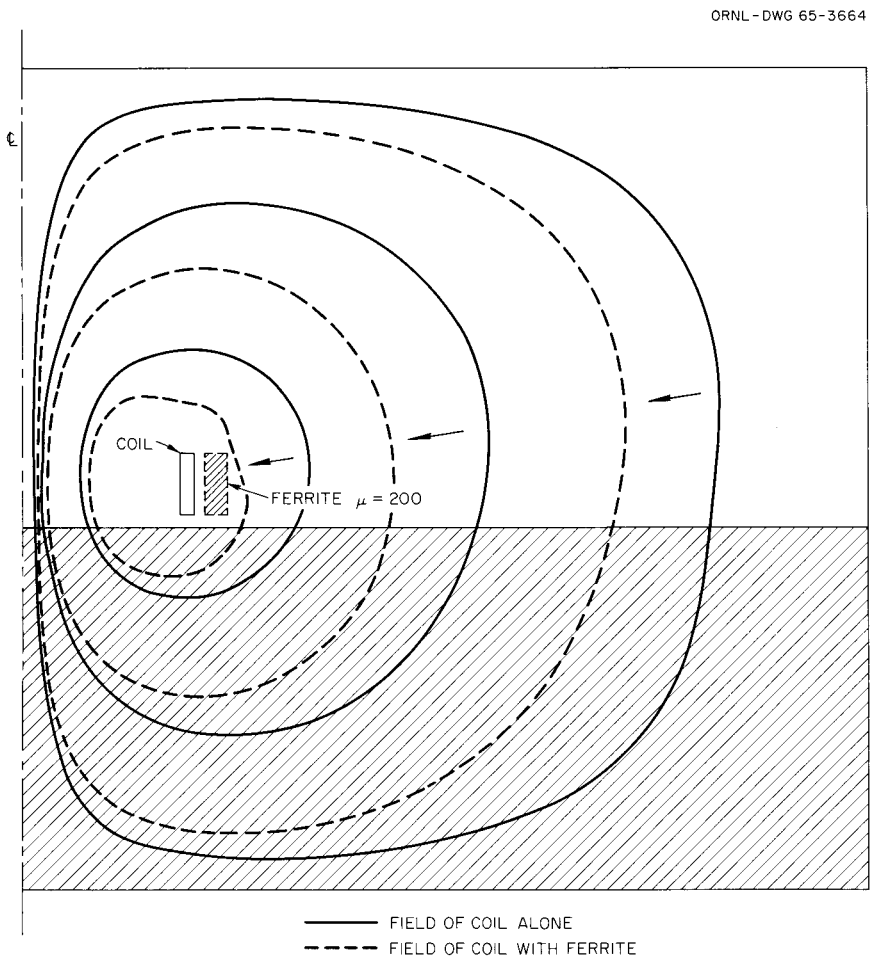

Fig. 18.3. Equipotential Contours of the Vector Potential and the Eddy-Current Flow with a Ferrite Ring Around the Coil.

instrument. The amplifiers and the oscillators of the system are being redesigned to minimize distortion, to increase the frequency range, and to permit use of inexpensive transistors. A power amplifier and video amplifiers have been designed with a 10-Mc bandwidth and 0.2% total harmonic distortion to 750 kc (the limit of our present distortion-measuring equipment). The instrument previously had 1-, 2-, 5-, 10-, 20-, 50-, 100-, and 200-kc oscillators. We have designed 500-, 1000-, 2000-, and 5000-kc oscillators, which should allow more sensitive inspections to be made of thin low-conductivity materials.

The phase-sensitive instrument has been applied to test problems for the HFIR, gas-cooled reactors, the Fermi Reactor, the High-Temperature Materials Program, and the Desalination Project.

We have designed and built time-differentiating circuits that selectively amplify rapidly changing signals from discontinuities without affecting the slowly changing signals from dimensional variations. Successful utilization of the new circuits requires that the inspections be made at constant speed, but an increase of tenfold or more has been seen in the sensitivity to defects. To achieve this greater sensitivity to flaws in manual inspections, we have constructed a hand-held probe that vibrates at a fixed frequency. We shall determine its optimum frequency and amplitude of vibration.

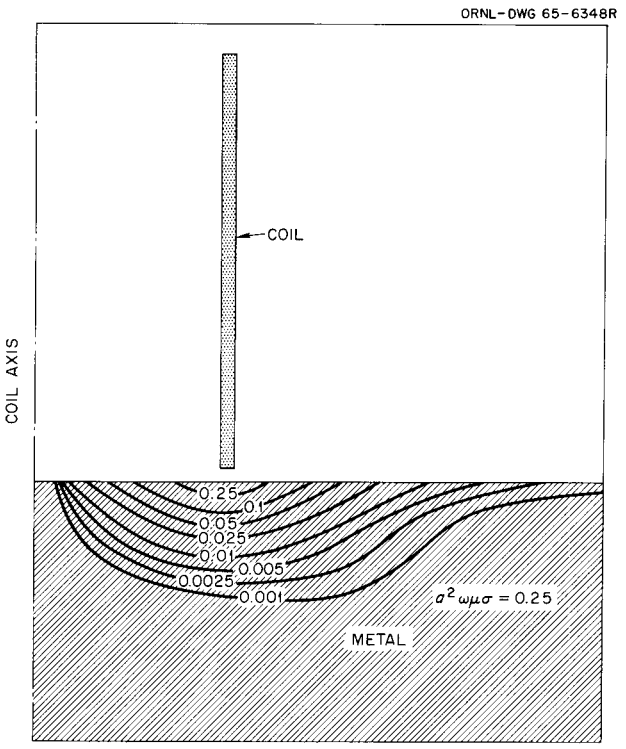

Fig. 18.4. Contours of Equal Eddy-Current Heating Density.

ULTRASONIC TEST METHODS

K. V. Cook R. W. McClung

We have continued our studies on the behavior of ultrasound in thin sections; our principal effort is the detection of nonbonds in cladding structures. The through-transmission ultrasonic method has been used successfully to detect nonbonds in thin fuel plates by monitoring changes they cause in transmitted intensity. A problem with such a system is the possible presence of other conditions causing ultrasonic attenuation and erroneous interpretation as a nonbond. Of particular concern is the detection of nonbond in aluminum-clad dispersion-core fuel plates, such as those for the HFIR and the Advanced Test Reactor. Our work on such plates with dispersions of U_3O_8, UAl_3, and niobium-coated UO_2 has indicated that the UAl_3 dispersion cores show very little variation in attenuation, permitting reliable inspection. The oxide cores have higher and more variable attenuation. One source of this variation is related to the final shape of the stringered fuel particles; the highest attenuation variation is due to laminar stringering produced in both transverse and longitudinal directions during fuel plate fabrication. This will reduce the expected nonbond sensitivity or increase the spurious rejection rate. We have also observed that severe particle cracking (with little stringering) associated with segregation can produce a nonbond indication. However, segregation alone does not produce such indications.

The immersed through-transmission technique was successfully applied to the evaluation of fuel tubes containing a cylindrical core of enriched UO_2 dispersed in stainless steel. A small probe was placed inside the tube for use as the receiver; the two transducers were moved in tandem along the tube as it rotated, accomplishing a helical scan. Positive writing on a helical recorder provided a map showing the size and location of nonbonds. This method is convenient to use in a cold (low-radiation-level) laboratory; however, we want to be able to evaluate such fuel elements in a hot laboratory using remote handling methods. Preliminary mockup studies have shown that a through-transmission reflection ultrasonic inspection is feasible and could simplify the mechanical "jigging" requirements. In this method, the same transducer serves as both transmitter and receiver. The ultrasonic energy is transmitted through the tube wall and across the interior of the tube (which is filled with water), then reflected from the inner surface of the opposite tube wall and thence back along the same path to the receiver. Thus, any nonbond will attenuate the sound as it is transmitted through the wall in both directions. We determined optimum dimensions for a Teflon guide block being made to maintain proper alignment between the transducer and the specimen and allow evaluation in a hot cell.

We are studying ways to make realistic reproducible reference notches. Thus far, we have used electrical discharge machining (EDM). Ratios of notch depth to tool wear have been established for a number of materials, principally refractory alloys for space-power and other high-temperature applications. (A typical curve for Mo–0.5% Ti is shown in Fig. 18.5.) Curves have been prepared for molybdenum, Mo–0.5% Ti, D-43 (Nb–10% W–1% Zr), B-66 (Nb–5% Mo–5% V–1% Zr), Nb–1% Zr, FS-85 (Nb–27% Ta–10% W–1% Zr), Inconel, stainless

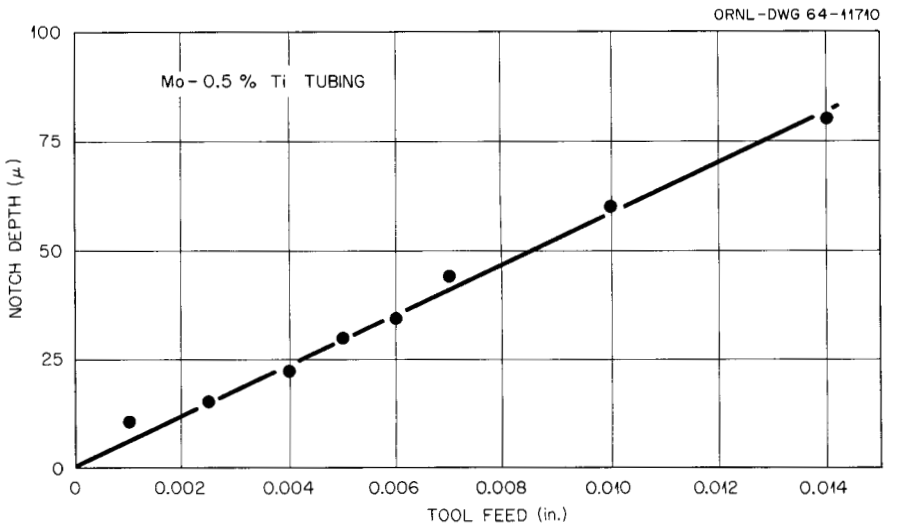

Fig. 18.5. Calibration Curve for Machining of Notches in Mo–0.5% Ti Tubing.

steel (types 304 and 347), TZM (Mo–0.5% Ti–0.08% Zr), and T-111 (Ta–8% Hf–2% W). These curves were established for similar notches with both the eroding voltage and the electrode arm configuration held constant. We are also determining the deviations from these ratio curves that occur when one or more fixed conditions are altered. Knowing these ratios and the effect of any deviation from the fixed conditions, reference notches can be fabricated to predetermined sizes with greater confidence.

We have demonstrated that notches as small as $\frac{1}{8}$ in. long × 0.001 in. deep × 0.0025 in. wide can be fabricated reproducibly. Notches have been placed on the outer and inner surfaces of tubing as small as $\frac{1}{8}$-in. OD × 0.020-in. wall. A differential-focusing microscope technique is used to measure the depth of outer-surface notches. For inner-surface notches we have developed techniques for casting rubber replicas of the defects and measuring the replica with the microscope.

PENETRATING RADIATION

Gamma Scintillation Gaging

B. E. Foster S. D. Snyder

We are continuing the application of x- and gamma-ray attenuation to the evaluation of fuel elements. Variation in transmitted intensity can be monitored by scintillation gaging and related through proper calibration to the fuel content within the area of the radiation beam. Recent work has been directed toward measurement of ultimate sensitivity of this type system and application of the method for the determination of total fuel content within a fueled configuration. This latter consideration is quite important because of the need to know total fuel quantities for both criticality prediction and accountability. The preliminary experiments to determine total fuel content were performed on 18 irradiation test plates fabricated at ORNL. Ten of the specimens contained U_3O_8-aluminum dispersion cores with aluminum cladding. The remaining eight were aluminum-clad dispersions of niobium-coated UO_2-ZrO_2 particles in aluminum. Calibration curves (milligrams uranium vs chart reading) were obtained for each of the above types of fuel plates by use of chemical analyses of scanned sections in conjunction with the calibration curve previously developed[2] for HFIR fuel plate homogeneity evaluations. Our technique requires multiple scans on the fuel plate, determination of average scan values, planimeter measurement of the projected fuel area, and calculations from the results of these measurements. Our experimentally determined fuel content deviated less than 0.5% on the average from the actual core loading. This

[2]B. E. Foster, S. D. Snyder, and R. W. McClung, *Continuous Scanning X-Ray Attenuation Technique for Determining Fuel Homogeneities in Dispersion Core Fuel Plates*, ORNL-3737, p. 13 (January 1965).

technique now enables rapid nondestructive assay of fuel plates for the HFIR, ATR, and other reactors.

To measure the maximum sensitivity, we determined the minimum specimen thickness change and the minimum radiation intensity change that could be detected above the background noise level. When the apparatus operated under conditions similar to those of recent homogeneity determinations in HFIR- and ATR-type fuel plates, thickness changes and intensity changes of about 0.2% were detected at a signal-to-noise ratio of 2. These values will facilitate later calculations of system capability for evaluation of specific materials with theoretical mass attenuation coefficients.

We are in the preliminary stages of developing scintillation detector probes to be inserted into hollow cylindrical specimens for determination of fuel homogeneity by x-ray attenuation. These probes will consist of $\frac{1}{4}$-in.-diam NaI(Tl) crystals coupled to Lucite light pipes of the same diameter. The other end of the light pipe is tapered to 1 in. in diameter for coupling to a 1-in.-diam photomultiplier tube. We have fabricated two light pipes. One is 13 in. long and was machined to a $\frac{1}{4}$-in. diameter over an 11-in. length; the other was made by gluing a 36-in.-long $\frac{1}{4}$-in.-diam Lucite rod to a 1-in.-diam rod that was machine tapered to a $\frac{1}{4}$-in. diameter over a 1-in. length. The glue, made by dissolving Lucite shavings in ethylene chloride, provides a joint with no change in refractive index. Both pipes were sprayed with a reflective paint, except on the coupling ends.

We have recently designed and fabricated a scanner, shown in Fig. 18.6, for the investigation of fuel homogeneity in fuel rods. Rods with outside diameters from 0.250 to 0.750 in. can be

Fig. 18.6. Scanner Used to Determine Fuel Homogeneity in Fuel Rods.

moved longitudinally through collimated radiation beams at speeds of 2, 4, 8, 16, and 24 in./min. The maximum continuous scan length is 5 ft and the minimum is 6 in. The various scan speeds are obtained through a rack and pinion drive system with a Slo-Syn motor driver and a series of interchangeable pinion gears.

We have equipped the scanner with two radiation sources, 2 curies ^{60}Co and 5 curies ^{137}Cs, housed in a single container with approximately 6 in. of lead separating them. Also, for versatility of the beam collimation we have provided six different lead collimators with rectangular openings $\frac{1}{16} \times \frac{3}{16}$ in., $\frac{1}{16} \times \frac{1}{4}$ in., $\frac{1}{16} \times \frac{1}{2}$ in., $\frac{1}{8} \times \frac{1}{8}$ in., $\frac{1}{8} \times \frac{1}{4}$ in., and $\frac{1}{8} \times \frac{1}{2}$ in. The rod-centering and guide rollers are an integral part of each collimator assembly to assure good alignment of rod diameter with collimator center line. Collimator support plates that slide out of the radiation beam allow for easy and safe interchange of collimators. The detectors, each a NaI(Tl) crystal optically coupled to a photomultiplier, are housed above each collimator and are accessible from the back of the housing. With this system we shall be able to determine the optimum source, collimator size, and scanning speed for fuel homogeneity inspection in any particular type of fuel rod.

Specifications on fuel distribution within an element are becoming more stringent. The area of interest for fuel homogeneity in a fuel plate has been less than 0.005 in.^{2} in some instances. Interrogation for this small spot size requires rapid scanning speeds to avoid an excessive inspection time per fuel element. These requirements thus place a severe burden on the radiation detector and associated circuitry. The detector must be designed for optimum operation with little deviation.

Fig. 18.7. System for Optimum Calibration of Photomultiplier Tubes for Gamma Scintillation.

To assure ourselves that the detectors are operating properly, we designed and fabricated a photomultiplier calibration chamber and assembled it with a single-channel analyzer as shown in Fig. 18.7. With this system we can tune the detectors for optimum operation and, through routine observations, note any deterioration of the detector system.

The system consists of a standard single-channel analyzer and a lead-shielded chamber lined with both copper and cadmium. The radiation detector is a NaI(Tl) crystal optically coupled to a photomultiplier tube. The output from the pulse-height analyzer goes to a linear count-rate meter and finally to a recorder. Also, a decade scaler and timer are included to permit the operator to determine the count rate at any point within the gamma spectrum for any time period up to 10^6 sec. A photomultiplier divider network has been constructed and installed in the lead chamber. The features of the divider network include potentiometers for adjusting the accelerating and focusing potentials of individual photomultiplier tubes. These potentials are measured with electrostatic voltmeters. After the potentials are determined for optimum operation of the photomultiplier tube, the resistance values can be determined for fabrication of the permanent divider network for that particular detector.

X-Ray Imaging with Closed-Circuit Television

W. H. Bridges

The use of an x-ray sensitive closed-circuit television has been described previously.[3] The images obtained in that work were essentially black and white. The use of such a system for radiographic inspection, however, places a demand for "gray"; that is, the sensitivity to radiation must be good enough to detect the small changes resulting from a defect in the material under study. We are determining the minimum contrast that we can ascertain with our present system so that a comparison can be made with the high-resolution system to be delivered shortly.

We have learned that the operating voltages applied to the x-ray sensitive vidicon may be adjusted to give extremely good sensitivity but an extremely poor image. Figure 18.8 illustrates the response of a beryllium-window vidicon to 100-kv constant potential x rays without regard to image quality. The change in slope to negative values for the –50 beam-volt curve is the result of a rapidly increasing background current, and the sensitive element of the vidicon becomes saturated. When this occurs, the image is no longer useful.

In order to establish the "defect sensitivity," a rather unusual aluminum penetrameter has been made. It is about 7.5 in. in diameter and 30 mils thick, with indentations ranging from 1 mil in diameter and 1 mil deep to 20 mils in diameter and 20 mils deep. The holes are arranged in concentric circles, with all those of the same depth in one circle and with the depth varying with radius. The circular pattern was chosen so that the specimen can be rotated while the telemonitor is watched. The motion makes the "defect" easier to see, and also the smallest indentation that can be seen is

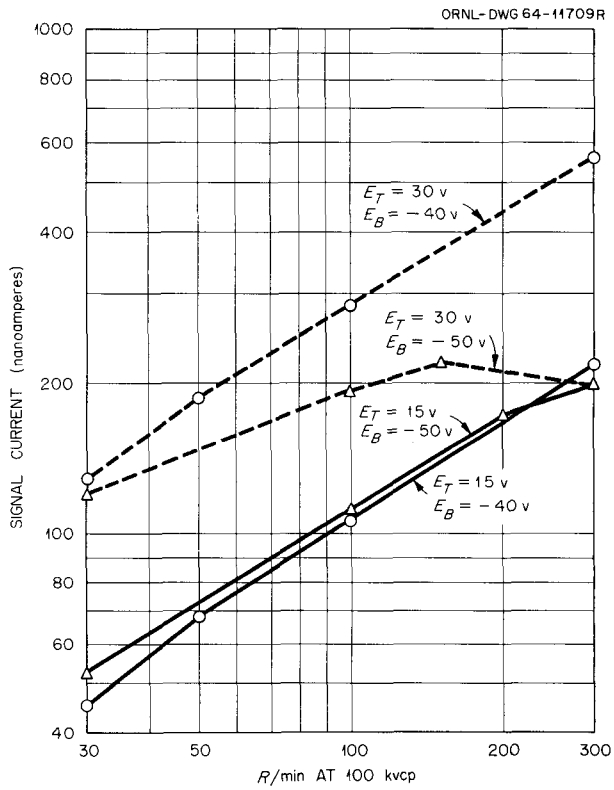

Fig. 18.8. Response of X-Ray-Sensitive Vidicon to Radiation Rate for Various Beam (E_B) and Target (E_T) Voltages.

[3]W. H. Bridges, *Metals and Ceramics Div. Ann. Progr. Rept. June 30, 1964*, ORNL-3670, p. 126.

relatively easy to locate. Using this penetrameter, we shall be able to establish proper operating conditions for many varieties of radiographic inspection.

X-Ray Microscope

W. H. Bridges

Projection x-ray microradiography offers several advantages over contact microradiography. Contact microradiography is limited by the grain size of the recorded image and the light optics used to examine the image. However, when a specimen is examined with a divergent beam from a small source, such limits are not imposed and the resolution depends directly on the size of the x-ray source. Recently several electron-optical components became available. These are being modified and assembled into an x-ray projection system. Preliminary testing of the various parts to determine their characteristics is complete. They have been assembled as a unit and a target holder is being made to allow the introduction of several different x-ray targets during operation.

INSPECTION DEVELOPMENT FOR PROBLEM MATERIALS

K. V. Cook R. W. McClung

We have continued to work on nondestructive tests for unusual materials that are difficult to inspect and on new materials that have no evaluation history. This has included such items as graphite and refractory alloys based on tantalum, molybdenum, niobium, titanium, and tungsten, used in space-power and other high-temperature systems. We found that conventional penetrant, radiographic, and ultrasonic techniques could be applied to D-43 (Nb–10% W–1% Zr),[4] T-111 (Ta–8% W–2% Hf),[5] and B-66 (Nb–5% Mo–5% V–1% Zr)[5] alloy tubing. Excessive noise levels have been encountered with encircling-coil eddy-current examinations, particularly on very thin wall tubing. We believe much of the noise to be associated with localized dimensional variations.

REMOTE INSPECTION DEVELOPMENT

K. V. Cook R. W. McClung

We have made a preliminary checkout of a remote scanning facility to be used to perform ultrasonic and eddy-current nondestructive testing in a hot cell. The system has been modified to allow incremental transverse movements of the search tube when operated manually. Previously, small quantitative well-controlled transverse movements on the search tube could be made only in the automatic modes of operation, in which each stepping operation is followed by a longitudinal movement of the search tube. With this modification the amount of stepping across a reference defect can be varied in increments as small as 0.001 in.

Another modification was made that allows an *x-y* plotter to be used as a "C" scan recorder or as a slave device for indicating the location of the search tube in the scanning tank in the hot cell. There is some hysteresis with change of direction, contributed principally by the gears in the mechanical system. Other mechanical modifications are necessary before the system can be tested further. Work in progress for hot-cell application of nonbond testing on fuel tubes is described briefly in ULTRASONIC TEST METHODS, this chapter.

---

[4]R. W. McClung and K. V. Cook, *Nondestructive Evaluation of D-43 Alloy Tubing by Oak Ridge National Laboratory*, ORNL-TM-843 (June 1964).

[5]K. V. Cook and R. W. McClung, *Nondestructive Evaluation of T-111 and B-66 Alloy Tubing*, ORNL-TM-990 (February 1965).

19. Tungsten Metallurgy

W. C. Thurber W. O. Harms

Vapor deposition of tungsten and tungsten alloys is being studied as a fabrication method for high-temperature reactor components. An important advantage of the process is the ability to fabricate objects with diverse and intricate shapes. Moreover, many refractory alloy materials can, in principle, be synthesized and formed at lower temperatures and with simpler equipment than required for more conventional procedures. We are defining the optimum conditions for deposition of pure tungsten and tungsten-base alloys, evaluating the deposited material for creep properties and bend-transition temperatures, and developing joining methods.

Solutions to the basic problem of brittleness in tungsten are being investigated on more conventionally prepared tungsten-base materials through the introduction of mobile dislocation sources in the form of a finely dispersed stable second phase.

Experiments on the extrusion of tungsten and results of physical property measurements on tungsten are presented in Chap. 15 of this report. Chapter 14 describes experiments on the vapor deposition of tungsten alloys, principally with rhenium. An electron-microscopic study of recrystallization and grain growth in tungsten is reported in Part I, Chap. 4 of this report.

THERMOCHEMICAL DEPOSITION OF TUNGSTEN

F. H. Patterson W. C. Robinson, Jr.
C. F. Leitten, Jr.

Studies were continued on basic techniques for thermochemical deposition (TCD) of tungsten[1] of high chemical purity according to the reaction

$$WF_6(g) + 3H_2(g) \xrightarrow[\text{Excess } H_2]{\text{Heat}} W(s) + 6HF(g) . \quad (1)$$

Tungsten sheet stock was produced for subsequent physical and mechanical evaluation. Specific investigations centered on the improvement of deposition substrates, the elimination of nodular growths within deposits, and optimization of the deposition parameters.

We successfully scaled up our procedures for small cylindrical laboratory deposits to uniformly thick 12- × 1.5- × 0.06-in. test sheets. This type of flat uniform deposit was necessary for establishing reference data on the physical and mechanical properties of TCD tungsten.

Production of Tungsten Sheet

Deposition Mandrels. – Tungsten sheet for evaluation of physical and mechanical properties was deposited on the inside surfaces of molybdenum mandrels. This substrate material was selected because of its favorable coefficient of thermal expansion and chemical properties. Powder metallurgy afforded a relatively inexpensive technique for the fabrication of the required flat substrate surfaces. Figure 19.1 shows the molybdenum mandrel encased in a copper vacuum chamber complete with contoured feed-gas inlet and by-product outlet. Insert A presents a more detailed view of the flat substrate surfaces of the mandrel. Insert B is a photomicrograph of the cross-sectional area of the partially sintered molybdenum compact. Partial sintering provided a high-density smooth surface for subsequent tungsten deposition. The bulk of the compact remained at a lower density, thus facilitating dissolution of the mandrel from the deposit.

[1]D. O. Hobson and C. F. Leitten, Jr., *Metals and Ceramics Div. Ann. Progr. Rept. June 30, 1964*, ORNL-3670, p. 132.

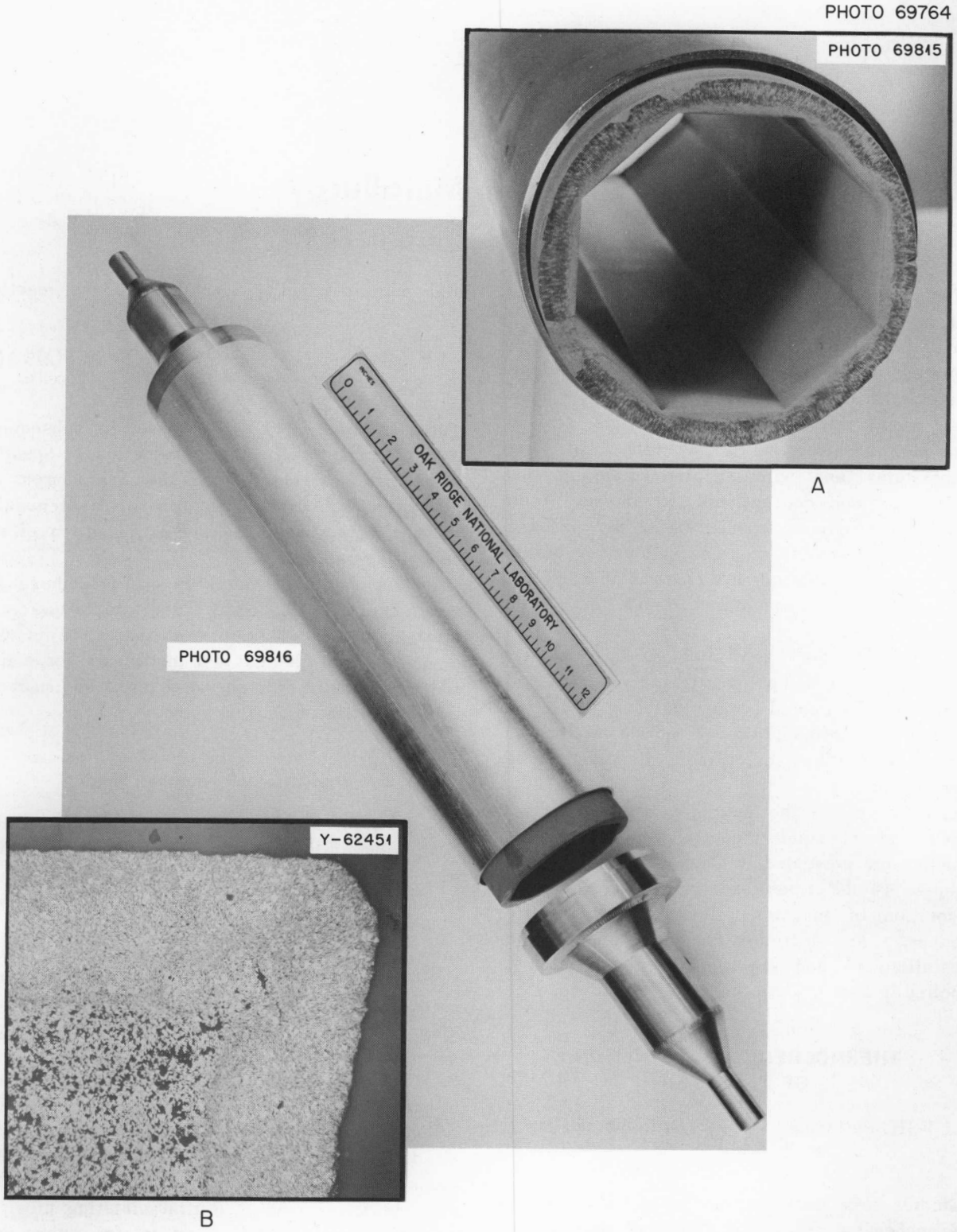

Fig. 19.1. Partially Assembled Molybdenum Mandrel and Deposition Chamber. Insert A, detail of the flat deposition surfaces. Insert B, photomicrograph of partially sintered molybdenum, showing high-density deposition surface and low-density base material, 100×.

The mandrel was fabricated by vibratory-compaction of −325-mesh molybdenum powder around an octagonal type 304L stainless steel mold. A unichrome rubber sleeve served as the outer form. A green density of about 86% was obtained when the compact was isostatically pressed at 30,000 psi. The mandrel was partially sintered in place for 16 hr at 700°C under a hydrogen partial pressure of 1 torr. Each octagonal mandrel afforded flat deposition surfaces for the production of eight 16- by 1.5-in. tungsten sheets.

Improvement of Thickness Uniformity. – The thickness uniformity of thermochemically deposited tungsten sheet is highly dependent on gas concentration and temperature. First, the feed gases are depleted downstream as the deposit progresses down a long uniformly heated tube. Second, the deposition rate is lowered at the leading end by the cold feed gases and reaches a maximum at some optimum distance along the tubular deposition substrate.

To improve the uniformity of thickness, a tube furnace affording a properly profiled temperature gradient was used to heat the deposition substrate. To counteract feed-gas depletion, the temperature was lowered at the section where the deposition rate in the gas-rich region normally is a maximum. Subsequently, the temperature was progressively raised downstream to maintain a constant deposition thickness as the feed gases were depleted. The increased temperatures downstream also provided more thermal agitation of the progressively increasing boundary layer of hydrogen fluoride being generated on the deposition surface. Heating the premixed feed gases further improved both deposition uniformity at the mandrel inlet and overall efficiency. A temperature of 350°C adequately reduced the initial chilling effect with only a small loss of material in the preheater. Feed-gas preheating also nearly doubled the deposition rate and probably helped remove residual impurities in the feed gases as well; however, this has not been confirmed by chemical analyses. The deposition schedule is given below.

H_2 gas flow, cm^3/min	3000
WF_6 gas flow, cm^3/min	200
Chamber pressure, torrs	5
Gas preheater temperature, °C	350
Deposition chamber temperature, °C	
Zone 1	565
Zone 2	560
Zone 3	570
Zone 4	580

The H_2:WF_6 molar ratio of 15 proved adequate to limit residual fluorine in the deposit and afford complete reduction of the WF_6. Sheet was deposited having an oxygen, fluorine, and carbon contamination level of less than 5, 9, and less than 10 ppm respectively. A deposition rate of about 3.2 mils/hr was realized at an efficiency of about 76%. Efficiency was calculated on the basis of useful sheet obtained per gram of tungsten in the WF_6 used.

A photograph of the resultant TCD tungsten sheet is presented in Fig. 19.2. Insert A is a photomicrograph of a section perpendicular to the deposition surface and shows the well-ordered deposition characteristic in the [100] direction. Insert B is a photomicrograph of a section parallel to the substrate. Deposit thickness measurements are presented below at 1-in. increments of distance from the gas-entrance end for a typical 1.5-in.-wide tungsten sheet. A difference of only 0.007 in. was observed along the 12-in. length.

Distance from Gas-Entrance End (in.)	Sheet Thickness (in.)
0–¼	0.061
1	0.062
2	0.064
3	0.065
4	0.066
5	0.066
6	0.066
7	0.066
8	0.067
9	0.066
10	0.066
11	0.063
12¼	0.060

An improved multiple-heating-zone tube furnace was fabricated recently and is being installed. This furnace consists of five independently heated tubular elements in sequence and is designed to further improve thickness uniformity.

PHOTO 69765

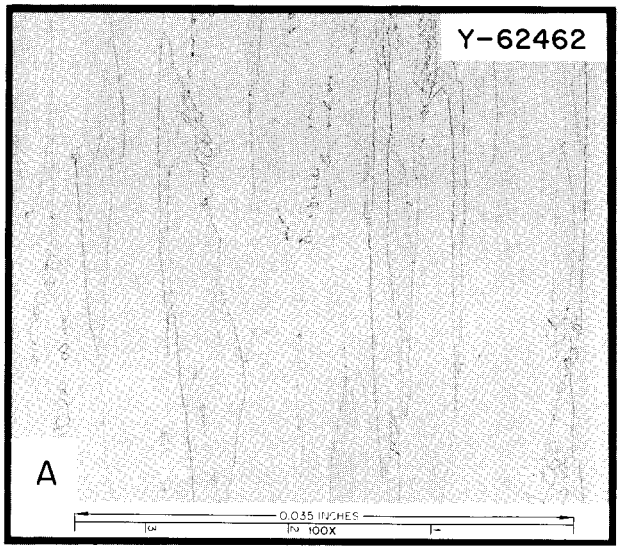

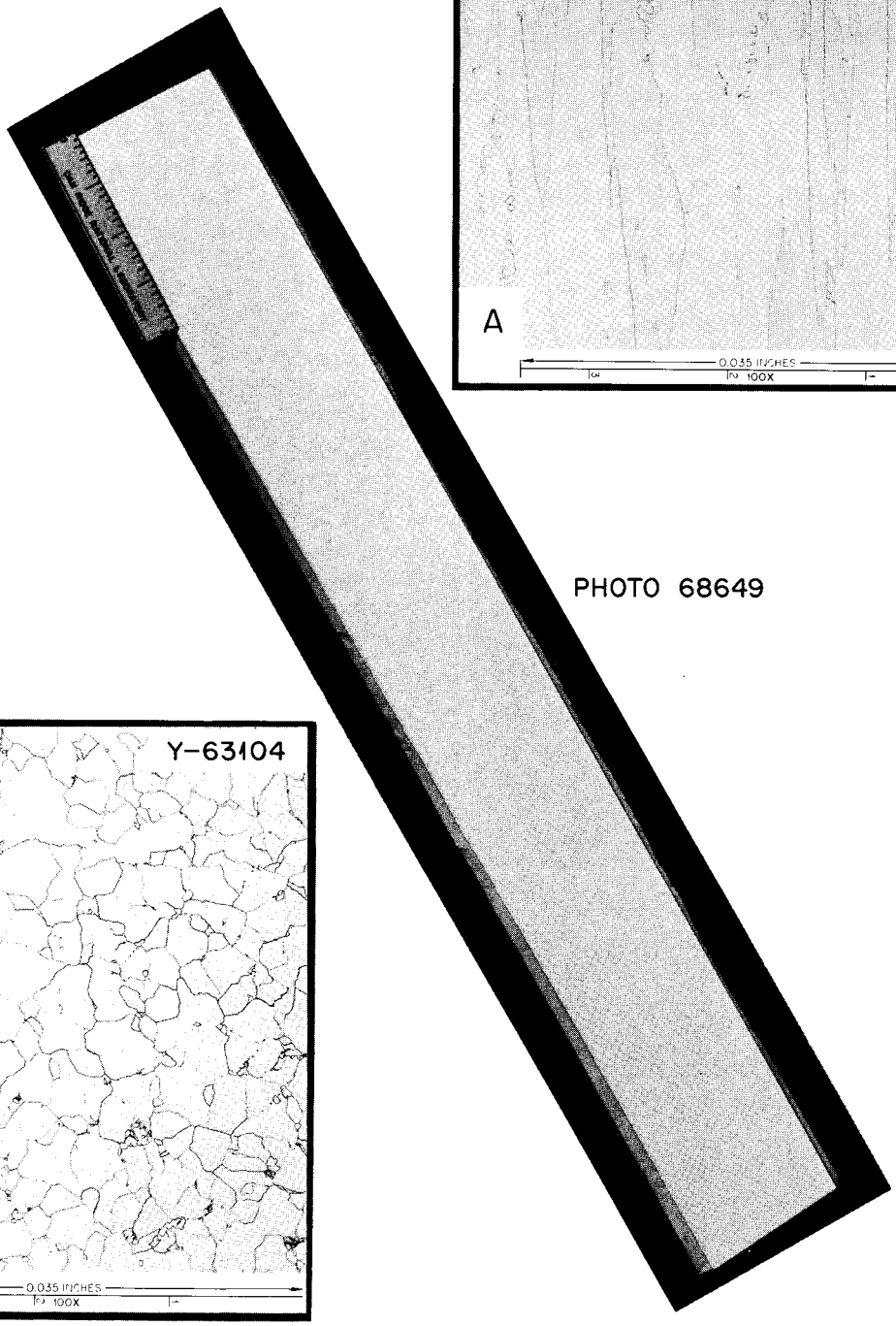

PHOTO 68649

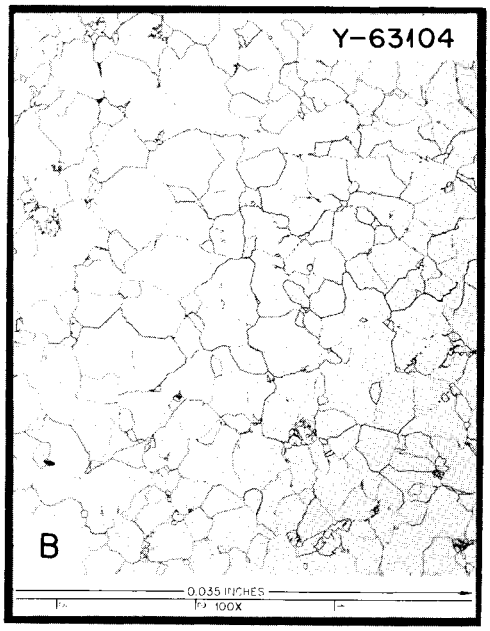

Fig. 19.2. Thermochemically Deposited Tungsten Sheet. Insert A, photomicrograph of this material perpendicular to the deposition surface. Insert B, photomicrograph viewed normal to the deposition surface.

Investigation of Nodular Growths

As reported elsewhere,[2,3] rough nodular growths have been observed in TCD tungsten. These nodules grow at rates many times that of the bulk deposit and give rise to abrupt changes in such properties as density, purity, and grain orientation. The processing conditions and mechanisms that lead to nodular growth must be understood if we are to produce TCD components with uniform properties and dimensions without having to rely on empirical adjustments of the deposition parameters.

It is now clear that the growths result from heterogeneous nucleation by compounds or metallic particles that become incorporated in the deposit at some stage of the deposition process. We have demonstrated[3] that nuclei of this type can arise from at least three sources: the formation of complex oxyfluorides in the presence of oxidizing contaminants, incomplete reduction of WF_6 due to local HF buildup in turbulent-to-laminar flow regions, and the occlusion of randomly oriented tungsten particles that had precipitated homogeneously in the gas phase, usually at elevated temperatures.

The conditions that promote the formation of these nuclei are interrelated, and for given specific substrate geometries the problem has been solved empirically in a reasonably educated manner. A systematic, parametric type study has been undertaken, however, to provide a better understanding of the complex phenomena involved and thereby remove the empiricism associated with selection of optimum conditions for a given experimental or production situation.

[2]F. H. Patterson and C. F. Leitten, Jr., ORNL-TM-1050, p. 98 (classified).

[3]F. H. Patterson, W. C. Robinson, Jr., and C. F. Leitten, Jr., ORNL-TM-1140, pp. 90–92 (classified).

LOW-TEMPERATURE DEFORMATION OF THERMOCHEMICALLY DEPOSITED TUNGSTEN

A. C. Schaffhauser

We are investigating the factors controlling the low-temperature deformation behavior of TCD tungsten by determining the yield strength and the ductile-to-brittle transition temperature. These properties of TCD material are compared in Fig. 19.3 with similar properties[4] determined on conventional wrought material derived from powder metallurgy (PM) billets.

The as-received PM material (stress relieved 5 min at 1150°C) is stronger and more ductile than the as-deposited TCD tungsten. However, after a 1-hr anneal at 1000 or 1800°C the TCD material is more ductile and its strength is comparable to that of the crystallized (2100°C heat treated) PM tungsten.

We believe that the decrease in ductility of recrystallized PM tungsten is due to the annihilation and pinning of dislocations and to the segregation of interstitial impurities to the grain boundaries, preventing the grain boundaries from acting as dislocation sources during low-temperature deformation. Evidence supporting this hypothesis is presented in the next section. Therefore, the higher purity of TCD tungsten as seen in Table 19.1 could account for its greater ductility compared to recrystallized PM tungsten.

[4]A. C. Schaffhauser, *Metals and Ceramics Div. Ann. Progr. Rept. June 30, 1964*, ORNL-3670, pp. 134–38.

Table 19.1. Chemical Analysis of TCD and Wrought (PM) Tungsten

Specimen Description	Impurity Content (ppm)				
	C	O	N	H	F
TCD, as-deposited	<10	17	<5	<1	22
TCD, 1 hr at 1000°C	<10	10	<5	<1	8
TCD, 1 hr at 1800°C	<5	12	<5	<1	4
Wrought (PM), as-received	23	13	<5	3	
Recrystallized—wrought (PM) treated 1 hr at 2100°C	21	19	<5	4	

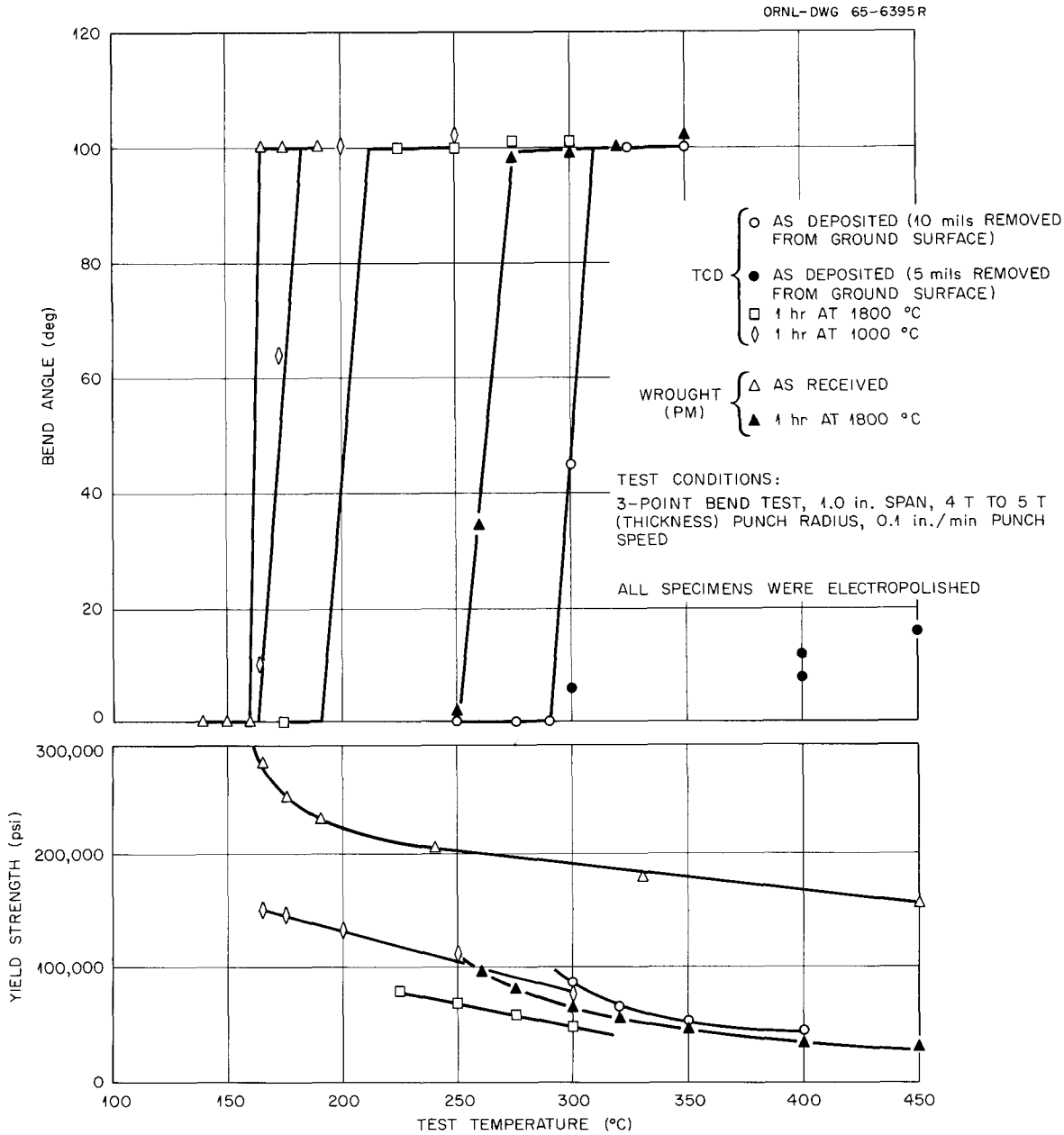

Fig. 19.3. Strength and Ductility of TCD and Wrought (PM) Tungsten Sheet.

The large increase in ductility obtained by annealing TCD tungsten is most likely due to stress relief, especially for the low-temperature anneals. Thus, the low-temperature ductility of TCD tungsten is controlled primarily by the residual stresses and the purity of the material. The columnar grain structure of the pyrolytic material does not appear to be detrimental to ductility.

The importance of very careful specimen preparation is evident from the results shown in Fig. 19.3. We had to remove over 0.005 in. from the as-ground surface of the bend specimens by lapping to remove the surface cracks that prevented the specimens from bending through angles greater than 20° at test temperatures as high as 450°C.

Fig. 19.4. Transmission Electron Micrograph of Recrystallized Commercial-Purity Tungsten, Hydrostatically Prestrained. 42,500×.

STUDIES ON THE BRITTLE BEHAVIOR OF RECRYSTALLIZED TUNGSTEN

A. C. Schaffhauser

We are studying the factors controlling the ductile-to-brittle transition in recrystallized tungsten. Although segregation of small amounts of interstitial impurities to the grain boundaries has long been the accepted cause of embrittlement, the precise mechanisms involved are not well understood. Our experiments have shown that the low ductility of recrystallized tungsten is due largely to the lack of mobile dislocations and the inability to generate dislocations at low temperatures.

A large hydrostatic pressure can produce localized yielding around precipitates in impure chromium and iron due to the difference in compressibility between the precipitate and the bulk material.[5,6] We have seen evidence of this effect in tungsten. Figure 19.4 shows dislocations generated at a precipitate in a grain boundary of recrystallized commercially pure tungsten (0.002% C) that had been subjected to a hydrostatic pressure of 150,000 psi at room temperature.

The ductility of prestained material is believed to be enhanced because the thermal activation necessary for deformation is lowered by the generation of mobile dislocations prior to testing.[7] Thus, the amount by which the transition temperature is lowered should depend on the number of grains containing mobile dislocations prior to testing. The number of dislocation sources activated by hydrostatic pressurization has been shown to be a function of the amount, size, and distribution of precipitate particles within the material.[6]

Recrystallized bend specimens of commercial purity tungsten and a W–0.5% Hf–0.2% C alloy were subjected to the hydrostatic treatment described above. The decrease in transition temperature obtained by this hydrostatic prestain prior to testing is shown in Fig. 19.5. The testing

[5]F. P. Bullen *et al.*, *Phil. Mag.* **9**, 803 (1964).

[6]S. V. Radcliffe and H. Warlimot, *Phys. Status Solidi* **7**, K67 (1964).

[7]H. Conrad, *Guiding Principles for Lowering the Ductile-to-Brittle Transition Temperature in the BCC Metals*, ATN-64(9236)-4 (Dec. 10, 1963).

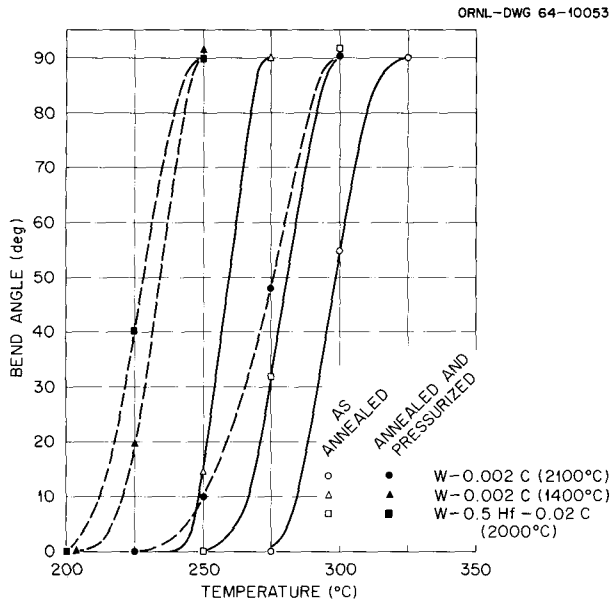

Fig. 19.5. Effect of Hydrostatic Prestrain on Bend Ductility of Tungsten.

conditions were the same as those described in the preceding section of this chapter. The figure shows that the hydrostatic prestain lowered the transition temperature of the alloy to a greater extent than it did for the commercially pure material. The volume of carbide precipitate in the alloy was approximated ten times that in the pure material.

The effect of grain size on the ductility and yield behavior of tungsten is being investigated to determine the relation of grain boundary segregation to the lack of dislocation sources during deformation at low temperatures. This work is described in Part I, Chap. 4 of this report.

JOINING OF TUNGSTEN

R. G. Gilliland

The usefulness of tungsten and its alloys at elevated temperatures depends upon the development of suitable joining techniques to provide joints comparable in properties to the base metal. We are developing methods for welding and brazing tungsten in an effort to attain this goal.

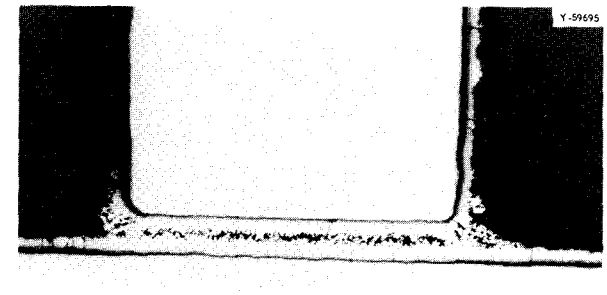

Fig. 19.6. Tungsten Joint Brazed at 1350°C with Al–18% Ta Alloy. Aluminum was volatilized by evacuation of the furnace during the brazing cycle. As polished. 150×. Reduced 49%.

Fusion Welding

The results of early tungsten-arc welding studies on sheet material derived from both arc-cast and powder metallurgy billets have been reported.[8] More recent studies have indicated that a 1-hr stress relief of the fusion welds in 0.060-in.-thick sheet reduces the ductile-to-brittle transition temperature from 475 to 350°C. As in the past, we used 4*T* (*T* = thickness) single-joint bend-testing apparatus.

We fusion welded 0.060-in.-thick material prepared by thermochemical deposition at ORNL using techniques identical to those we developed for conventional tungsten. Specimens are currently being machined for further evaluation of this material.

Brazing

We have been trying to develop methods and procedures for brazing tungsten below its recrystallization temperature so as to create joints serviceable above the recrystallization temperature. The method used is based on the concept that evaporating a low-melting component from a two- or three-component melt will leave a solidified material that remelts at a much higher temperature.

We are testing brazing alloys from the aluminum-tantalum and aluminum-tungsten binary systems. The joint shown in Fig. 19.6 was brazed by causing Al–18% Ta alloy to flow into the joint at

[8]R. G. Gilliland, *Metals and Ceramics Div. Ann. Progr. Rept. June 30, 1964*, ORNL-3670, pp. 139–40.

1350°C under argon at 1 atm. Evacuation after reaching temperature caused aluminum evaporation, resulting in a tantalum-rich joint. Other joints have been made in a similar manner with an Al–20% W alloy at 1150°C. These preliminary studies indicate that this innovation is sufficiently attractive to justify further studies of the process variables and techniques.

Joining by Thermochemical Deposition

R. L. Heestand R. G. Gilliland
B. F. Shuler[9]

Deposition of tungsten metal by thermochemical reduction of tungsten hexafluoride with hydrogen has been investigated as a method for joining of tungsten components. The process for depositing tungsten in the form of tubing has been described in detail,[10] and only minor changes in fixturing and reactant flow distribution were necessary to produce joints suitable for demonstrating the present application of the process. The process differs from the more conventional joining methods, fusion welding and brazing, in that low temperatures, in the range of 500 to 650°C, are used; therefore, recrystallization and embrittlement of the wrought tungsten-base metal are avoided. Several joint designs, including flat plate and tube-end closures, were fabricated and samples were prepared for ductile-to-brittle transition testing.

In one experiment a sheet of wrought tungsten was joined to a sheet of thermochemically deposited (TCD) sheet of equal thickness. The specimens were placed within the deposition tube with appropriate fixturing and masking to give deposits in the desired areas. The finished joint, after dissolution of the copper deposition mandrel, contained excess pyrolytic tungsten, which was then removed by grinding. Deposition onto an angle of approximately 90° gave a crack at the grain intersections. When the joint configuration was changed by grinding the wrought tungsten to a radius of 0.5 in. tangent to the root of the weld, it did not crack, and no fracture or gross impurity buildup could be detected on examination of the interface at higher magnifications. We demonstrated joining end caps to tubes by thermochemically depositing a tube with a closed end, cutting off the end, and rejoining the end by thermochemical deposition. No attempt was made to grind off the excess tungsten. End closures of this type were tested by a helium mass spectrometer leak detector and found to be leak tight.

Several flat plate specimens of both TCD tungsten and wrought tungsten were joined to wrought tungsten by the TCD techniques, for bend testing. Evaluation of these joints is not complete.

[9]Summer employee.

[10]R. L. Heestand, J. I. Federer, and C. F. Leitten, Jr., *Preparation and Evaluation of Vapor Deposited Tungsten*, ORNL-3662 (August 1964).

HIGH-TEMPERATURE CREEP OF TUNGSTEN

H. E. McCoy

Many of the projected applications of tungsten and its alloys require high-temperature creep data for periods of time of at least 1000 hr and a good knowledge of the structural stability under these conditions.

Pure wrought tungsten fabricated from powder has been creep tested at temperatures of 1650 and 2200°C at stresses that resulted in rupture lives of up to 1000 hr. The creep properties were independent of the orientation of the test specimen in the sheet of material from which it had been cut. Abnormal grain growth was noted in the stressed sections tested at 2200°C.

Several lots of sheet prepared by thermochemical deposition (TCD) from WF_6 have been studied at the same temperatures. This material is characterized by large columnar grains oriented normal to the plane of the sheet. The rupture life of this material was generally equivalent to that of the pure wrought tungsten, although considerable scatter was present in the test results. The TCD material exhibited very low fracture ductilities at 1650°C, and most of the measured elongation resulted from the formation of intergranular cracks. At 2200°C the ductility of the TCD material was comparable to that of the pure wrought tungsten.

One lot of the W–0.5% Hf–0.02% C alloy (Sylvania A) has been evaluated. At 1650°C this alloy is stronger than pure tungsten, although the fracture ductility is considerably less. At 2200°C the rupture life and rupture ductility were both less for the alloy than for pure tungsten. However, the grain size of the alloy was more stable at 2200°C than that of the pure tungsten.

20. Uranium Nitride

W. O. Harms W. C. Thurber

Uranium mononitride is an attractive nuclear fuel because of its high uranium density and high thermal conductivity. Unlike uranium monocarbide, it does not hydrolyze rapidly in moist air. Our research and development program on this compound has continued and includes studies of sintering kinetics and pellet fabrication, nitrogen solubility in sintered UN, the effect of carbon on the solubility of oxygen in UN, effects of microstructure on the properties of sintered material, and fission-gas release by neutron activation. Other portions of this program have been summarized in appropriate progress reports.[1-3] Aided sintering of uranium nitride studied in another program is described in Chap. 14 of this report.

FABRICATION AND SINTERING STUDIES

R. A. Potter

We developed techniques for fabricating UN test specimens and, when applicable, effectively removing oxygen contamination from the specimens during the fabrication process. In addition, initial-stage sintering mechanisms were investigated.

Fabrication Development

The fabrication scheme consisted of prepressing the powder at 10 tsi, screening to pass 40 mesh, and final pressing at 50 tsi. The pieces were heat treated in a tungsten resistance furnace at 1500°C and 5×10^{-5} to 5×10^{-6} torr. Clean nitrogen was then introduced at 1 atm pressure and the temperature was raised to 2220°C and maintained for a period of time. The temperature was then lowered to 1500°C, the pressure was reduced to 5×10^{-5} torr, and the system was cooled to room temperature. To vary bulk densities and microstructures of the sintered products, the time at temperature (2220°C) was varied, and in some instances the sintering cycle was repeated. Small additions of graphite to the powder, as discussed below, enabled us to vary oxygen contents in the sintered pieces from 450 to 5000 ppm.

Specimens fabricated as described above were furnished for other portions of the program, such as hot hardness measurements, thermal conductivity measurements, oxygen solubility studies, and neutron activation measurements.

Removal of Oxygen from UN

An inherent problem associated with UN powders obtained from several vendors was the presence of 1000 to 5000 ppm O impurity.

In an experiment designed to remove the oxygen contaminant, approximately 0.3% graphite was added to a UN powder containing 2400 ppm O and 700 ppm C. The mixture was cold pressed into pellets, which were then sintered 80 min at 2220°C in 1 atm N_2 to average densities 86% of theoretical (14.32 g/cm^3), compared to 89% without the graphite. Chemical analyses showed the sintered pellets to contain 450 ppm O and 1500 ppm C. The microstructure of such a pellet is compared in Fig. 20.1 with that of a pellet fabricated from the as-received powder. Although the addition was effective in removing oxygen, there was some sacrifice in density.

[1] ORNL-TM-980, pp. 106–24 (classified).
[2] ORNL-TM-1050, pp. 81–97 (classified).
[3] ORNL-TM-1140, pp. 70–88 (classified).

PHOTO 80955

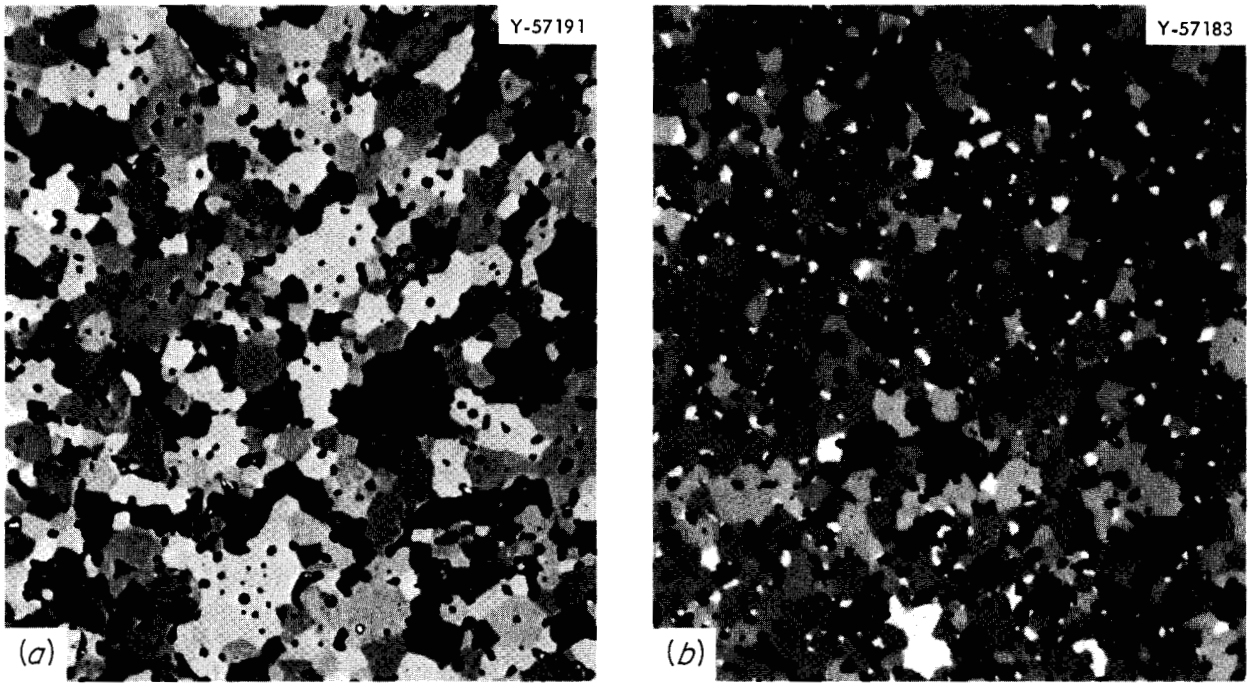

Fig. 20.1. Microstructure of Pellets Fabricated from UN Powder Containing Approximately 2400 ppm O. Etchant: 30 lactic acid, 10 concd HNO_3, 1 concd HF. 500×. (*a*) Microstructure of UN pellet fabricated from powder containing 0.3% C addition. Density: 86% of theoretical. (*b*) Microstructure of pellet fabricated from as-received powder. Density: 89% of theoretical.

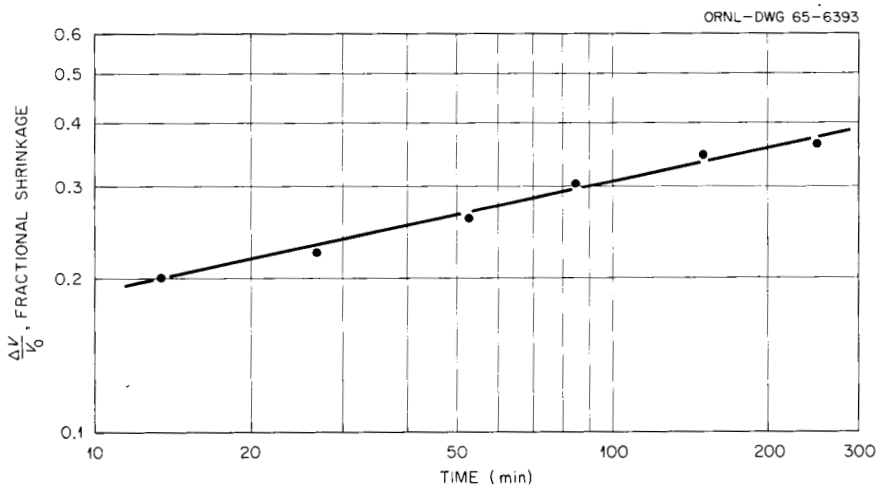

Fig. 20.2. Effect of Time on Volumetric Shrinkage of Cold-Pressed UN at 1700°C.

Sintering Studies

We are presently investigating early-stage sintering kinetics of UN containing various amounts of oxygen in combination with carbon. Data were obtained from an isothermal series of sintering experiments designed to indicate the time dependence of the process. The logarithmic plot of volume against time at 1700°C in Fig. 20.2 has a slope of 0.22, indicating that grain-boundary diffusion is the controlling sintering mechanism[4] in UN containing approximately 1700 ppm O and 300 ppm C.

NITROGEN SOLUBILITY IN URANIUM NITRIDE

T. G. Godfrey

The possible solubility of nitrogen in sintered UN was studied.[5] The main conclusion drawn from this work was that UN specimens routinely fabricated in this Laboratory[6] contain excess nitrogen in the form of second-phase U_2N_3 and possibly also in solution in UN. As-fabricated pellets were free of x-ray-detectable (<1 to 2%) U_2N_3, but pellets annealed in an argon-filled static capsule at 1000°C acquired a detectable concentration of U_2N_3 on exterior surfaces. Pre- and postanneal photomicrographs revealed no apparent changes in the internal microstructure of the pellets, which typically showed a three-phase structure of UN, U_2N_3, and UO_2. The U_2N_3 phase was invariably associated with UO_2 at grain-boundary intersections. Examination of pellets doped with graphite during fabrication to remove oxygen by carbothermic reduction showed that U_2N_3 was not present in the absence of UO_2. This observation suggests a possible interaction between oxygen and excess nitrogen.

MICROHARDNESS STUDIES ON SINTERED UN

T. G. Godfrey G. Hallerman[7]

Our purpose is to determine the effect of impurity levels and fabrication variables on the strength of sintered UN as reflected by room-temperature and elevated-temperature microhardness measurements. The specimens for this study were typical of material supplied by several vendors and represented a wide range of variables, including oxygen and carbon contents, density, and grain size.

Room-temperature diamond pyramid hardness (DPH) measurements, made with a 136° sapphire indenter at a 2-kg load, are shown in Fig. 20.3. The data plotted represent average values and ranges for three to six measurements on each specimen. The specimens of primary interest were those with widely differing oxygen contents, but because of the wide range in densities of these specimens, a series of seven specimens from one batch of material was included in order to establish the hardness-density relationship at constant oxygen content. The line in Fig. 20.3 represents the least-squares equation

$$\mathrm{DPH} = 1018.4\, d - 534.8 \qquad (1)$$

for this series, where d is the fraction of theoretical density.

Three of the specimens for which data are plotted in Fig. 20.3 had been doped with graphite powder during fabrication to reduce the oxygen content by carbothermic reduction of the oxide impurity during sintering.[6] Several other specimens had moderately high carbon contents, presumably introduced during synthesis of the UN powder. In Fig. 20.3 the majority of the points lie reasonably close to the line. The major exceptions are the triangular points representing two specimens with 6000 ppm C and 1000 to 1600 ppm O and two specimens with 600 ppm C and 4700 ppm O.

Precise lattice parameters given in Table 20.1 were determined for these and other specimens, from x-ray diffraction patterns obtained from metallographically prepared surfaces of the pellets. The specimens that contained 600 to 700 ppm C (2600 and 4700 ppm O respectively) yielded a parameter very close to that obtained for pure UN by other workers.[8] Specimens with greater carbon contents, on the other hand, showed significant lattice expansions. Application of Vegard's law to the UN-UC system[8] yielded an estimate of the mole fraction of UC in these specimens, as shown in Table 20.1.

---

[4] D. L. Johnson and I. B. Cutler, *J. Am. Ceram. Soc.* **46**(11), 541–45 (1963).

[5] T. G. Godfrey, ORNL-TM-1050, pp. 90–93 (classified).

[6] R. A. Potter, ORNL-TM-980, pp. 106–8 (classified).

[7] Metallography Group.

[8] A. E. Austin and A. F. Gerds, *The Uranium-Nitrogen-Carbon System*, BMI-1272 (June 1958).

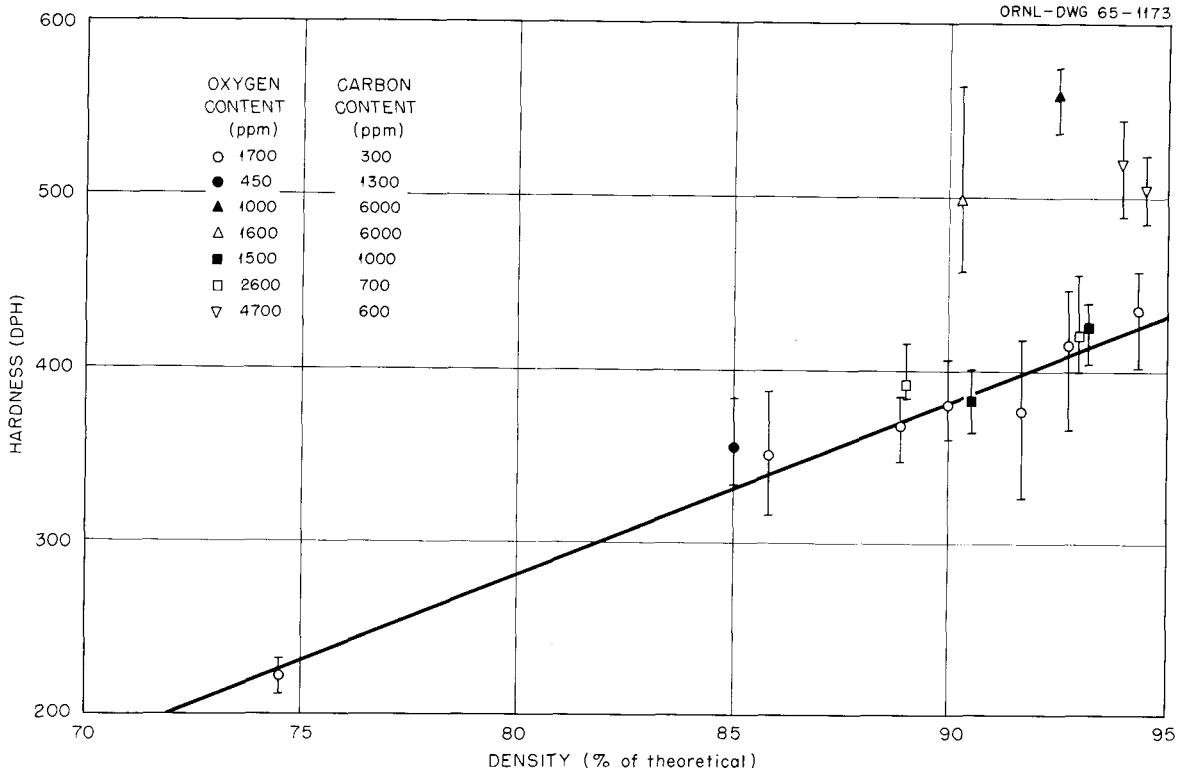

Fig. 20.3. Room-Temperature Hardness of Sintered Uranium Nitride as a Function of Density, Showing Effects of Oxygen and Carbon Contents. Line represents least-squares fit of average values for pellets with 1700 ppm O and 300 ppm C.

Table 20.1. Effect of Carbon Content on Lattice Parameter of UN and Estimate of UC in Solid Solution

Carbon Content[a] (ppm)	Lattice Parameter[b] (A)	UC Content[c] (mole %)
600	4.8886	0
700	4.8884	0
1000	4.8894	1
1300	4.8919	4
6000	4.8982	13

[a]By chemical analysis.
[b]Precision of measurement, ±0.0005 A.
[c]Based on application of Vegard's law.

Microstructural examination of all specimens showed that those with carbon content equal to or greater than 1000 ppm are free of second-phase UO_2 while all others contain UO_2 in amounts corresponding roughly to the oxygen content indicated by chemical analysis.

The implications of these results are as follows: (1) The hardness of UN is relatively unaffected by low to moderate oxygen content (450 to 2600 ppm), (2) the hardness is slightly increased by high oxygen content (4700 ppm), and (3) the solution of 13 mole % UC in UN markedly increases the hardness but a 4 mole % solution essentially does not. A related observation is that the addition of carbon to UN reduces the oxygen content, both as determined by chemical analysis and as evidenced by the absence of UO_2 in the microstructure. Since the amount of oxygen still present in these samples is comparable to that of other specimens that do show UO_2 in the microstructures, the oxygen must be either in solution in UN or present as a very fine dispersion of UO_2 within the UN grains and not resolvable by optical metallography. This

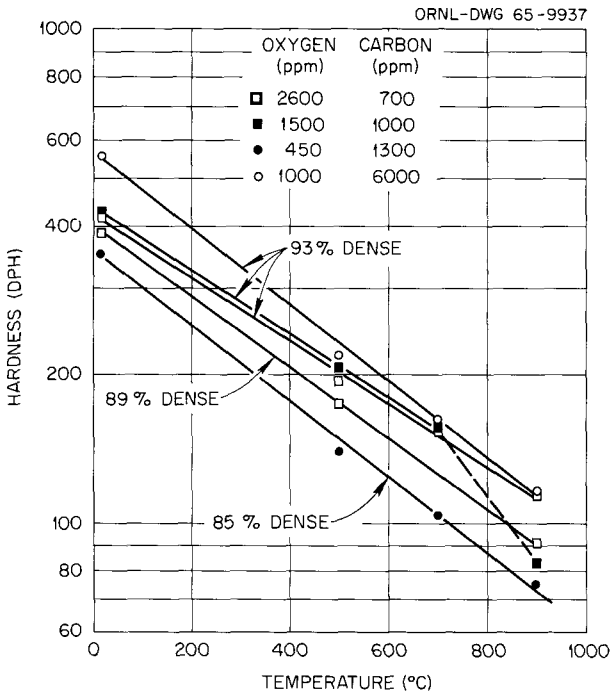

Fig. 20.4. Hot Hardness of Sintered Uranium Nitride of Various Densities and Purities.

question is considered further in the following section.

The hot-hardness of five specimens, determined to 900°C, is shown in Fig. 20.4. When the density correction, Eq. (1), is applied to the two lower density specimens, all have essentially the same hardness up to 700°C except for the sample with 1000 ppm O and 6000 ppm C. This sample was considerably harder at room temperature, but it softened at a faster rate and its hardness had decreased to that of the other samples at 900°C. The hardness at 900°C of the specimen containing 1500 ppm O and 1000 ppm C is considerably lower than would be expected. This specimen contains (see next section) a fine dispersion of UO_2 (approximately 10^{15} particles/cm^3). Since dispersions of this concentration would be expected to increase hardness, the 900°C data are questionable until more results at higher temperatures are obtained.

DISTRIBUTION OF SECOND-PHASE MATERIAL IN URANIUM NITRIDE

T. G. Godfrey J. O. Stiegler[9]

A fine dispersion of stable particles is beneficial in a reactor fuel material, since properly dispersed particles act as pinning sites for fission-gas bubbles.[10–14] For a given concentration of fission gas, the formation of many fine bubbles leads to considerably less swelling than does the formation of a few large bubbles.[14] Dispersed particles impede the movement of the bubbles to free surfaces under the application of mechanical stresses or thermal gradients.

In view of the importance of fine dispersions in nuclear fuels, we examined uranium nitride specimens of various carbon and oxygen contents prepared from material of various origins and histories. Experimental techniques employed were electron microscopy of replicated fracture surfaces, optical metallography, x-ray diffraction, and chemical analysis. Five sets of specimens were examined, and from the results a hypothesis was developed to explain qualitatively the relationship between composition, temperature, and resultant microstructure.[15]

Various observations of the relationships between composition, microstructure, and properties have shown that the solubilities of oxygen and carbon in uranium nitride are interrelated and complex.

The compounds UN and UC form a continuous solid solution and the low-temperature solubility of oxygen or the hypothetical compound UO in UN is very low, although in UC it may[16] extend to

[9]Electron Microscopy Group.

[10]A. T. Churchman, R. S. Barnes, and A. H. Cottrell, *J. Nucl. Energy* **7**, 88 (1958).

[11]G. W. Greenwood, *J. Nucl. Mater.* **6**, 26 (1962).

[12]D. Kramer, W. V. Johnson, and C. G. Rhodes, *J. Inst. Metals* **93**, 104–52 (1964–65).

[13]M. V. Speight, *J. Nucl. Mater.* **12**, 216–20 (1964).

[14]R. S. Barnes, *J. Nucl. Mater.* **11**, 135–48 (1964).

[15]T. G. Godfrey and J. O. Stiegler, ORNL-TM-1140, pp. 74–83 (classified).

[16]F. Anselin *et al.*, "On the System (UPu)(CNO) as Applied to Sintered Carbides, Carbonites, and Oxycarbides," pp. 113–61 in *Carbides in Nuclear Energy*, vol. I, ed. by L. E. Russell *et al.*, Macmillan, London, 1964.

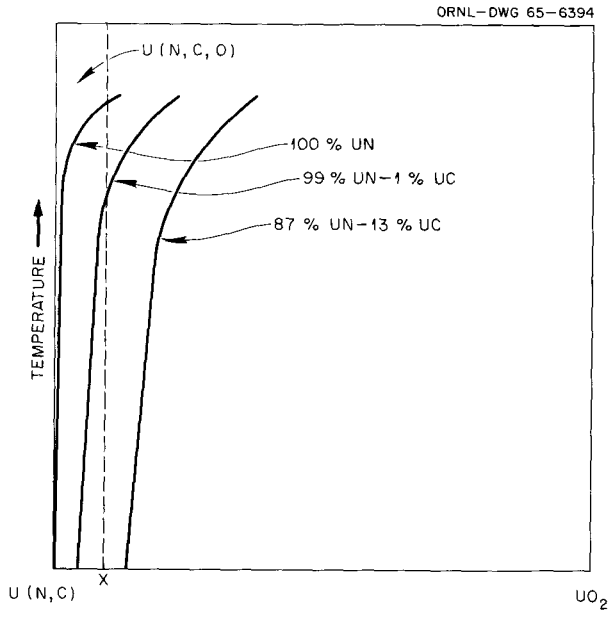

Fig. 20.5. Representation of the Possible Phase Relationship in the U(N,C)-UO_2 System. See text for explanation of dashed line.

about 36 mole %. For UN-UC solid solutions, the solubility of UO is proportional to the concentration of UC; the UN acts as an inert diluent.[16]

The presence of a fine dispersion indicated that the precipitated phase was in solution at some higher temperature. A simplified representation of a possible temperature-composition diagram for the U(N,C)-UO_2 system, showing increased solubility at high temperature, is given in Fig. 20.5. For an oxygen content represented by UO_2 concentration *x* in pure UN, UO_2 would precipitate at a temperature sufficiently high to enable it to migrate to the more energetically favorable grain-boundary locations, where it would precipitate as a relatively massive phase. The incorporation of carbon into the system to form a U(N,C) phase would increase the solubility of the oxide at all temperatures and, therefore, would lower the precipitation temperature. At this lower temperature, the mobility of the oxygen would be so reduced that migration could occur only over short distances during the short time provided by the normal cooling rate of the sintering cycle. Hence, a finely dispersed precipitate results. A prolonged anneal slightly below the solution temperature would promote consolidation of the fine precipitate particles into coarser ones to reduce the total surface area of the system. When sufficient carbon has been incorporated into the UN, the solution would persist at all temperatures.

If the foregoing explanation for the appearance or nonappearance of a precipitate or dispersion in UN is correct, we should be able, through subtle adjustments in composition, to produce a desired microstructure in UN with no gross changes in the standard sintering schedule. Implementation of this idea will require a more detailed knowledge of the basic solubility limits as a function of temperature in the U-N-C-O system.

NEUTRON-ACTIVATION STUDIES OF URANIUM NITRIDE

R. B. Fitts

We are studying the fission-gas retention characteristics of uranium mononitride for comparison with those of the established nuclear fuels such as UO_2. We are also evaluating the influence of small amounts (<5000 ppm) of oxygen and carbon on the fission-gas-release behavior. In addition, we are checking our ability to predict with our postirradiation test the in-reactor release of fission gas from UN reactor fuels during extended irradiation. The low-temperature neutron-activation, postirradiation-annealing, and ^{133}Xe-monitoring techniques employed have been reported previously.[17,18]

In earlier work[19] our UN samples contained UO_2, UN_2, and U_2N_3 on surfaces and within the samples. The dissociation of the higher nitrides at elevated temperatures prevented the measurement of normal fission-gas release characteristics. These phases are now removed by a 15-hr vacuum anneal at 1200°C prior to irradiation. This treatment yields samples that show the expected diffusional-type release.

On samples of five new batches of uranium nitride (one arc-cast and four of sintered pellets), we are evaluating the diffusion coefficient and activation energy for ^{133}Xe release. These samples all con-

[17] *GCR Program Quart. Progr. Rept. Dec. 31, 1959*, ORNL-2888, p. 68.

[18] D. F. Toner and J. L. Scott, *Am. Soc. Testing Mater., Spec. Tech. Publ.* **306**, 86 (1961).

[19] R. B. Fitts, *Metals and Ceramics Div. Ann. Progr. Rept. June 30, 1964*, ORNL-3670, pp. 144–45.

tain about 1000 ppm O. The data from the first three tests of each batch have confirmed our earlier conclusion,[19] that the release of fission-gas from UN at 1400°C is comparable to that from UO_2 for samples having densities the same percentage of theoretical. This conclusion is now based on tests of samples from 12 different batches of UN, representing material made by arc casting, the Dynapak process, and the standard sintering techniques applied to UN powder obtained from four different sources.

21. Zirconium Metallurgy

M. L. Picklesimer

We are investigating zirconium-base alloys of potential use as structural materials in water-cooled or moderated reactor systems. The principal projects are: (1) studies of the physical metallurgy, consisting of transformation kinetics and morphologies, mechanical properties, phase diagrams, and heat treatment; (2) the development, evaluation, and utilization of preferred orientation and strain anisotropy in α-zirconium alloys during both fabrication and service; (3) the determination of the effects of composition, temperature, and environment on the oxidation-corrosion rates in the thin-film stages of oxide growth; (4) a study of the effects of alloy composition and oxidation environment on the structural properties of thin oxide films in situ; and (5) investigation of the stress orientation of precipitated hydride in Zircaloy-2.

EFFECT OF PREFERRED ORIENTATION AND STRESS ON PRECIPITATION OF HYDRIDES IN ZIRCALOY-2

P. L. Rittenhouse

Hydrogen absorption during the corrosion of α-zirconium alloys is a major deterrent to their use as reactor materials, since the concentrations of hydrogen soluble at operating temperatures are sufficient to cause precipitation of zirconium hydride platelets when the alloys are cooled from that temperature. The effect of these hydride platelets on ductility depends on their orientation relative to the applied stress and is nearly zero in Zircaloy-2 of relatively low hydrogen content when the stress axis is parallel to the platelets.[1] That the stress can affect the orientation of the hydrides during precipitation has been shown;[2] this reorientation can either enhance or lower the ductility.

The present research reexamines a previous conclusion[3,4] that hydride precipitated under elastic stress appreciably redistributes only when a preferred orientation is present and the stress is parallel to a concentration of basal poles. Schedule J Zircaloy-2 was selected for study because it has a high concentration of basal poles parallel to the transverse direction.[5] Hydrogen content was varied to determine its effect on the hydride distribution.

The specimens were hydrided to levels of 120, 170, or 280 ppm hydrogen and loaded elastically (20,000 psi maximum) at 400°C. The hydride was allowed to precipitate under the applied stress during furnace cooling. The hydride pole figures were determined by the technique described in a following section, and the number of hydride plates per unit area and the volume fraction of hydride were determined for each specimen.

The hydride trace data, the hydride pole distribution figures, and the quantitative metallographic

[1] R. P. Marshall and M. R. Louthan, Jr., *Trans. Am. Soc. Metals* **56**, 693–700 (1963).

[2] R. P. Marshall, *Hydride Orientation and Mechanical Properties of Thin-Walled Zircaloy Tubing*, DPST 63-74-8 (October 1963).

[3] P. L. Rittenhouse and M. L. Picklesimer, *The Effect of Preferred Orientation and Stress on the Directional Precipitation of Hydrides in Zircaloy-2*, ORNL-TM-844 (June 1964).

[4] P. L. Rittenhouse, *Metals and Ceramics Div. Ann. Progr. Rept. June 30, 1964*, ORNL-3670, pp. 148–49.

[5] P. L. Rittenhouse and M. L. Picklesimer, *Metallurgy of Zircaloy-2: Part I – The Effects of Fabrication Variables on the Anisotropy of Mechanical Properties*, ORNL-2944 (Oct. 13, 1960); *Part II – The Effects of Fabrication Variables on the Preferred Orientation and Anisotropy of Strain Behavior*, ORNL-2948 (Jan. 11, 1961).

data will be reported elsewhere.[6] The principal conclusions are: (1) the preferred crystallographic orientation had little if any influence on the orientation of hydride plates in as-received fully annealed material, and most hydride plates lay parallel to the rolling plane; (2) the hydride plates that precipitated after plastic deformation tended to be aligned with the tensile strain component and were perpendicular to the compressive strain component; (3) hydride plates redistributed only when they had precipitated under an elastic stress that was perpendicular to a high concentration of basal planes; (4) hydride distribution figures treated in terms of percent of plates present can be misleading; the data are best treated in terms of the number of plates per unit area. Data so treated indicate that there may be preferred sites for hydride precipitation that are occupied at low hydrogen levels, and higher hydrogen levels force less favorable sites to be occupied; (5) the number of hydride plates at any given orientation in unstressed annealed material was a function of hydrogen content, but the fraction at each orientation was identical for the three hydrogen contents examined; (6) as the hydrogen content increased, the number of hydride plates reoriented by stress increased, but the fraction reoriented decreased; (7) the average hydride particle size was essentially independent of the hydrogen content in these tests; (8) the redistribution of hydrides increased as the stress increased; and (9) the fraction reoriented increased with increased stress and decreased with increased total hydrogen content.

HYDRIDE AND BASAL POLE FIGURES IN ZIRCALOY-2 BY QUANTITATIVE METALLOGRAPHY[7]

M. L. Picklesimer P. L. Rittenhouse

A technique was developed for rapidly determining by quantitative metallography the pole figure of hydride plates in Zircaloy-2 and the basal pole figure of close-packed hexagonal metals. Approximately 200 trace angles are measured on each of three orthogonal surfaces, and smoothed histograms of the data are plotted. A trial-and-error approximation is used to determine the pole figure. An eyepiece goniometer equipped with electrical readout is used to measure and record the angle between specific reference directions and the traces of the hydride plates on the specimen surface. A polarized-light metallurgical microscope equipped with a sensitive tint plate and electrical readout of the stage angle is used for locating and recording the basal plane trace in close-packed hexagonal metals. The trace angle data in both determinations are collected on an x-y recorder with a remote pen action at a rate of 500 to 800 points per hour. A pole figure can be determined in less than 2 hr on metallographically prepared specimens. The technique permits an easier quantitative study of preferred orientation in close-packed hexagonal metals and determination of the interrelationships between stress axis, crystallographic preferred orientation, and stress orientation of hydrides in Zircaloy-2.

ANISOTROPY IN ZIRCALOY-2

P. L. Rittenhouse M. L. Picklesimer

The increasing use of zirconium alloys for fuel-element cladding and for structural members of nuclear reactors and the demand for the maximum service from a minimum of material at higher operating temperatures and pressures demand that the strength of these alloys be increased. Although this might be accomplished by alloying, it may be accomplished sooner and at less cost by increasing the strength of Zircaloy-2 and Zircaloy-4 through the control and utilization of strongly developed preferred orientation and the resulting strong anisotropy of mechanical properties. The maximum permissible design stress in Zircaloy-2 pressure tubing may be increased at least 50% by such control and utilization of texture.[8]

The same research[8] showed that no presently available theory can explain or predict the stress-strain anisotropy observed in α-zirconium alloys.

[6] P. L. Rittenhouse and M. L. Picklesimer, report in preparation.

[7] Abstract of paper presented at the 19th AEC Metallographic Group Meeting, April 20–22, 1965 at Oak Ridge National Laboratory, Oak Ridge, Tennessee (proceedings to be published as ORNL-TM-1161).

[8] M. L. Picklesimer, "A Preliminary Examination of the Formation and Utilization of Texture and Anisotropy in Zircaloy-2," *Proceedings of the USAEC Symposium on Zirconium Alloy Development, Castlewood, Pleasanton, Calif., Nov. 12–14, 1962*, GEAP-4089, vol. II (Nov. 30, 1962), ORNL-TM-460 (Feb. 28, 1963).

Stress analysts and structural design engineers cannot use such theories in dealing with the stress-strain behavior of inherently anisotropic metals in even simple stress conditions. No one yet knows how to specify what anisotropy is desirable in a given case, what anisotropy is undesirable, or how to produce a specific anisotropy in a given shape for a given application.

An understanding of the effects of texture on the flow of material during tube manufacturing should permit a larger mill yield of defect-free material having any specified texture. An understanding of the relationships between texture and the stress-strain anisotropy should permit the designer to take advantage of such anisotropy, to use the higher strength material despite its lower apparent ductility, and to avoid situations wherein the texture with low yield strength could cause a service failure due to misuse of the inherent anisotropy.

Some results on the anisotropy of properties under uniaxial stress in Zircaloy-2 as a function of crystallographic preferred orientation have been previously reported.[5] We now have an accelerated program under way to determine such behavior under biaxial stress. In addition, we shall examine the deformation systems operating in material being plastically strained under selected restraints, how texture is developed during mill manufacture of shapes, and the sequence, amounts of deformation, and types of forming operations necessary to produce desired textures in mill products. The data collected will also be used to set test criteria and engineering specifications, to provide stress analysts and design engineers with quantitative design data, and to provide theorists with part of the information they need to develop and test theories of anisotropy in non-cubic metals.

Strain Anisotropy in Sheet-Type Tensile Specimens of Zircaloy-2

Studies of the anisotropy in Zircaloy-2 conducted by this group in the past[5] used round tensile specimens. Preliminary studies had shown that the necessary information on anisotropy could not be obtained on sheet-type tensile specimens. The relation between specimen geometry and test results has been reexamined for highly textured Zircaloy-2 because much of the material to be tested is available only in sheets too thin to permit machining of round specimens.

Sheet tensile specimens were cut with axes parallel to the rolling and transverse directions from strongly textured (basal poles parallel to the normal direction) Zircaloy-2 sheet $\frac{1}{8}$ in. thick. Width-to-thickness ratios ranged from 10 to 0.6 with the "thickness" direction always being the original thickness direction of the sheet. All specimens were vacuum annealed at 650°C after machining. A grid of lines, 0.050 in. apart, was applied by anodizing (using Kodak Photo Resist as a mask) over the entire reduced section of the specimen and well onto at least one grip section. The specimens were tested at a head rate of 0.1 in./min in an Instron tensile machine. Polaroid transparencies were made of the grid on each specimen as assembled in the tensile machine and after various degrees of strain.

The yield strengths in the rolling and transverse directions were low and almost identical. A small but definite increase in yield strength was observed with decreased cross-sectional area, independent of the width-to-thickness ratio. Both ultimate strength and the reduction in area seemed to be relatively insensitive to the width-to-thickness ratio and to the cross-sectional area. Elongations at maximum load were also insensitive, but differences were observed in the values of total elongation; however, no definite trend could be established. Such mechanical properties are to be expected in Zircaloy with this degree and type of texture.

Similar conclusions cannot be reached as to the effects of specimen geometry on the anisotropy of strain and strain ratios. The transparencies of the specimens were projected, and the intersections of the enlarged grid patterns were marked off on tracing paper. The movement of these intersections during straining could then be followed by overlaying the sheets of paper on a light box. A typical strain sequence is shown in Fig. 21.1 for three positions along a tensile specimen, all patterns being centered on the center line of the final fracture. Folding of such tracings about apparent center lines demonstrated that the strain was symmetrical except for those specimens in which the neck formed near one shoulder. In the latter specimens, restraint by the shoulder was made evident by the asymmetry across the fracture line.

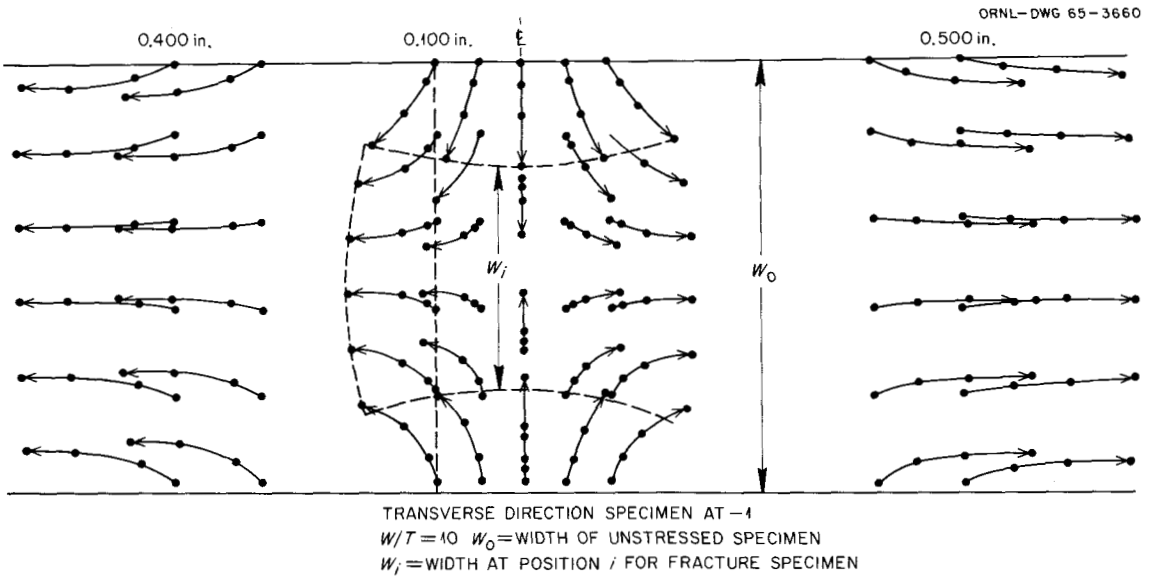

Fig. 21.1. Movement of Grid Points Near the Fracture Region of a Sheet Tensile Specimen of Zircaloy-2.

The width strains (both micro and average) along the length of the specimen from the fracture towards each shoulder were measured. At no point along the length did the microwidth strains vary across the width of the specimen. Thus, the differences observed in microlength strains across any width position reflected differences in microthickness strains. The lines of grid points bowed away from the fracture center, as shown in Fig. 21.1, because the thickness strains were greater in the center of the specimen than along the edge.

One measure of strain anisotropy previously developed is the k value[5] (i.e., the ratio of contractile strain to the axial strain for each of the principal fabrication directions). In the round tensile specimens used in that study, the k values were constant for any given test condition, being independent of the amount of axial strain that had occurred, over a range of natural strain from at least 0.002 to 0.6. The k values thus could be used to characterize the strain anisotropy of each material. Typical plots of k vs distance from the fracture for the sheet-type specimens are shown in Fig. 21.2. Obviously, the strain ratios (k values) vary with total strain. Intercomparison of the data for several specimens shows that the k values vary in no recognizable pattern with width-to-thickness ratio and specimen axis direction. This study showed conclusively that strain ratios determined on sheet-type tensile specimens cannot be used to characterize the anisotropy of the material in a simple manner, at least at the larger strains, which can be measured more precisely.

Perhaps the most interesting observation was that the position of the neck could be detected at strains just beyond yielding. The neck was very obvious by the time the maximum load was reached, the point at which necking is usually assumed to begin. Total width strains as functions of distance from the center line of the fracture are shown in Fig. 21.3 for three conditions of test. These curves and similar curves for many other specimens show that the center of the neck region can shift during the early stages of plastic strain and that multiple necking frequently occurs. The asymmetry of curves 2 and 3 in Fig. 21.3 was caused by the proximity of the right-hand shoulder during neck formation.

Yield Anisotropy in Zircaloy-2

In the classical octahedral shear stress theory of plastic flow,[9] a yield ellipse is predicted for plane (i.e., biaxial) stress in an isotropic material. The yield stress in tension is assumed identical to that in compression, regardless of the test direction in the material. Such behavior generally occurs in the cubic metals, and a typical yield

[9] A. Nadai, *Theory of Flow and Fracture of Solids*, vol. 1, 2d ed., pp. 209–13, McGraw-Hill, New York, 1950.

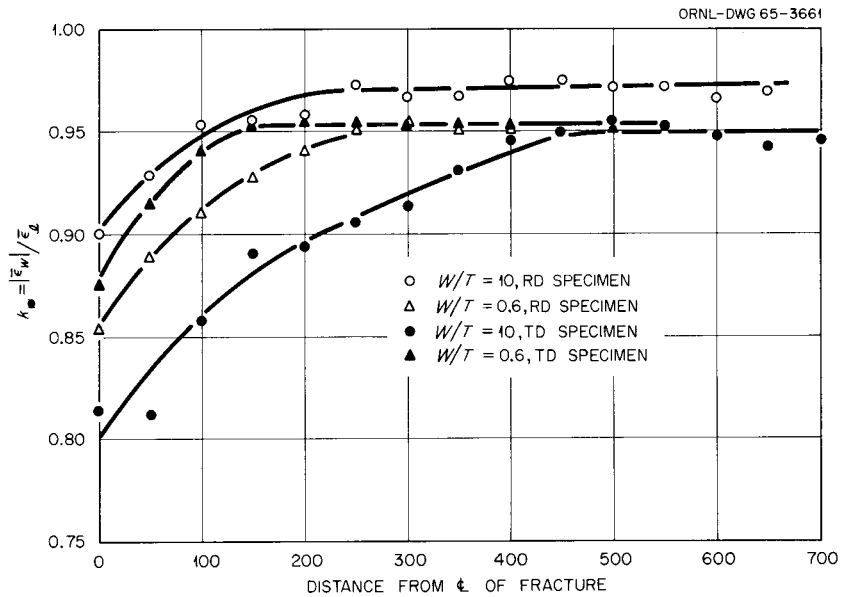

Fig. 21.2. Variation of Values of Strain Ratio k with Distance from Fracture in Sheet Tensile Specimens of Zircaloy-2.

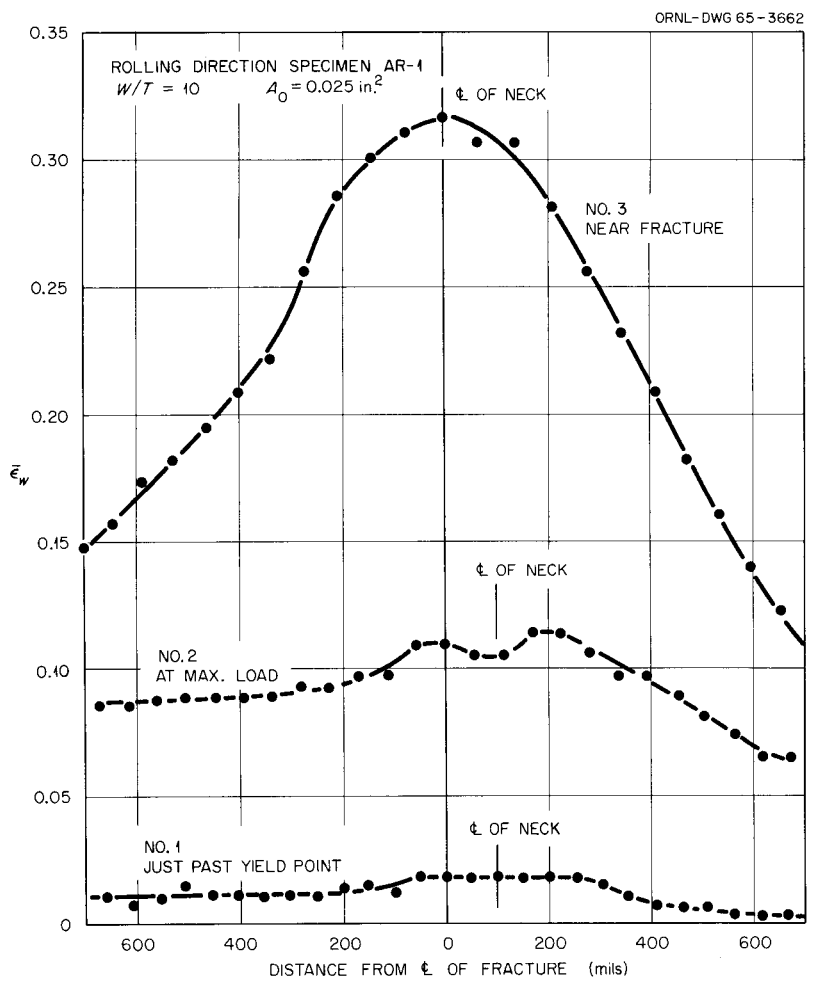

Fig. 21.3. Total Width Strains as Functions of Distance from the Center Line of Fracture in a Sheet Tensile Specimen of Zircaloy-2.

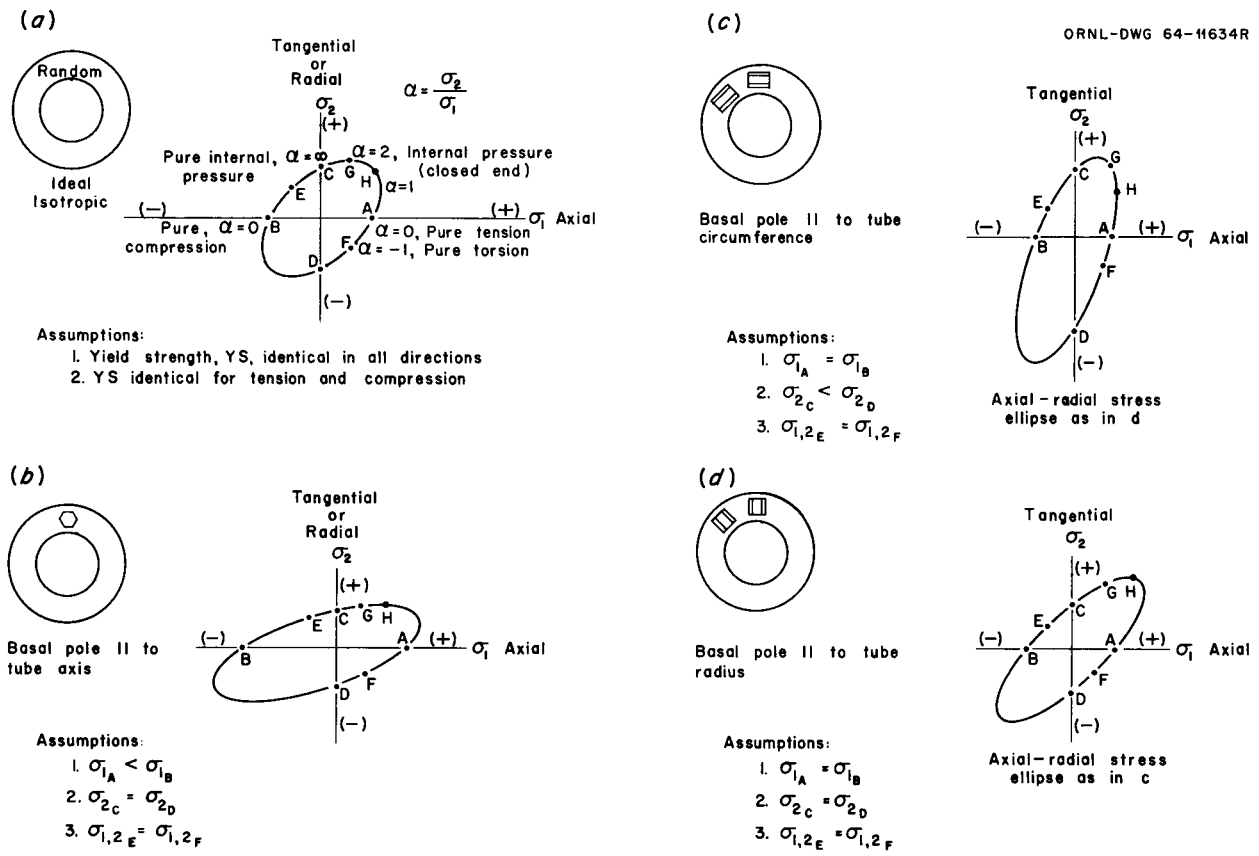

Fig. 21.4. Possible Biaxial Yield Stress Ellipses for Zircaloy-2.

ellipse is shown in Fig. 21.4*a*. The yield strength in biaxial stress is the distance from the center to the ellipse boundary. Several cases of particular stress conditions ($\alpha = \sigma_2/\sigma_1$) are indicated on the figure by the letters A through H.

If the material has a cubic crystal structure and can be made to have an anisotropy of yield stress in uniaxial tension, the yield ellipse is rotated and the ellipticity can be increased. The center of the ellipse is, however, still at the center of the reference axes.

We have attempted to determine what the shapes and orientations of the yield ellipse could be for certain textures in Zircaloy-2 tubing, assuming that the octahedral shear stress theory can be modified to allow a material to have a yield strength in tension appreciably different from that in compression, and to allow the differences to vary greatly as the stress directions are moved relative to the crystallographic directions. We postulated three textures in the tubing (basal poles concentrated in the axial, tangential, and radial directions) and used yield values previously obtained[8] for certain crystallographic directions in highly textured Zircaloy-2 sheet. The results are shown in Fig. 21.4*b*, *c*, and *d*.

If the above assumptions are even approximately valid, the yield ellipses for basal poles concentrated in the axial and tangential directions are not centered on the reference axes and are rotated so that the maximum yield strengths in biaxial stress do not occur for $\alpha = 1$ (internal pressure in a spherical pressure vessel) as is the case for isotropic material and for radially concentrated basal poles. In addition, the ellipticity of the yield loci is considerably greater than that found for the most anisotropic cubic metal. It is gratifying that recently reported data on burst testing of Zircaloy-2 tubing[10] and on constraint tests in commercially pure titanium[11] have shown that

[10] R. C. Aungst, *Stress Rupture Tests of Zircaloy-2 Pressure Tubes*, BNWL-8 (January 1965).

[11] W. A. Backofen, private communication on work in progress.

the behavior predicted from the above analysis is correct.

Some important conclusions can be drawn as to the effects of the textures for certain stress conditions encountered in service. Consider the case of an internally pressurized tube with a closed end as a bulge or blister begins to form in the wall. For the main portion of the tube, the stress condition is such that $\alpha = 2$ (point G). In the bulge itself, the stress condition approaches that of $\alpha = 1$ (point H) as the bulge or blister forms. If the basal poles are concentrated in the axial direction (Fig. 21.4*b*), the yield strength will be relatively low and, as the bulge forms, the stress required to yield will increase moderately rapidly (neglecting strain hardening and considering stress geometry alone). If the basal poles are concentrated in the tangential direction (Fig. 21.4c), the formation of the bulge will be catastrophic, since the stress required for yielding in the bulge ($\alpha = 1$) is considerably less than that required for the yielding to begin in the original wall position ($\alpha = 2$). This will be so even if a moderate amount of strain hardening occurs with increased plastic flow. This texture is the one most commonly found in Zircaloy-2 tubing made for use as pressure tubing and fuel element cladding. The texture most resistant to bulging is that having basal poles concentrated in the radial direction (Fig. 21.4*d*) as the stress required for yielding increases rapidly as α goes from 2 to 1 (from the main part of the tubing to the bulge).

One of the surprising results of the past studies of anisotropy in Zircaloy-2 plate and sheet[5] was that the tensile strength was essentially independent of texture (i.e., the material was almost isotropic in tensile strength). If now a "tensile strength ellipse" is plotted on the same axes as the yield stress ellipse, one can readily see that the "flow stress" ellipses must progressively rotate and move toward the center of the reference axes as plastic strain occurs. The "flow stress" ellipses increase in size with plastic strain because the flow stresses that are required to continue strain increase as the material work hardens.

Tubing Fabrication Analysis

Analysis of the problem of controlling texture during manufacture of tubing leads to a critical question, whether or not the texture of the final material is independent of the strain path when material with a given starting shape and texture is deformed into a given final shape. A corollary question is whether or not a given shape change can be accomplished by successive complete operations of the deformation systems known to operate in single crystals. Limited answers to both questions have been found, but the generality of these answers remains to be determined.

Consider the problem as presented in Fig. 21.5. First, assume that the specimen is a single-crystal cube with the basal plane parallel to one of the cube faces. The cube is to be distorted into some shape that can be obtained by a simple sequence of successive twinning and/or slip operations. Next, one determines the changes that occur in shape and dimensions when the cube is strained by a path such as A of Fig. 21.5. Also, the new orientation of the basal pole is determined. The problem is to determine if exactly this shape and dimensional change can be accomplished by another sequence of twinning and/or slip operations, and if the location of the basal pole is the same or different. In this example, exactly the same changes can be made by path B, which gives a difference of essentially 90° in basal pole orientations. The dimensions of the shapes by the two paths are within 0.2% and the face angles agree within 0.5°.

Many combinations of final shapes and dimensions and of strain paths were examined. In general, the final basal pole orientations were within 10° of each other if the final shapes and dimensions were the same, although two apparently different deformation paths were used. In many cases, no second path could be found that could produce the same shape and dimensional changes. Thus, only qualified and limited answers can yet be given to the two critical questions.

This analysis has shown some of the questions that must be continually asked during the planning of a fabrication sequence that is expected to control texture. For the particular sequences of Fig. 21.5, the two paths can be readily produced by mill equipment. However, only a specific and quite limited deformation of tubing can be obtained by these particular paths. Thus, we expect that the reduction or strain pattern of each step of the fabrication sequence will be controlled by the amount that will produce the desired change in texture and not by the amount of cold work the material can withstand before annealing is required.

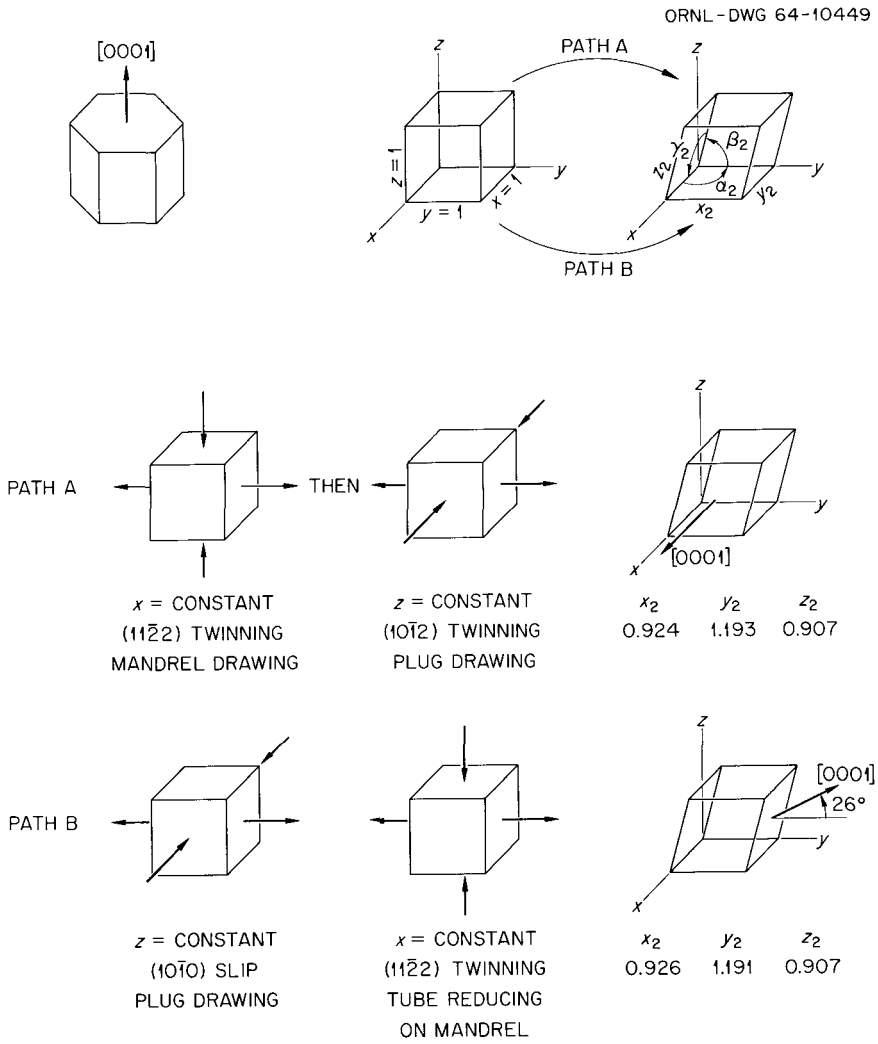

Fig. 21.5. Problem of Producing Different Textures in Zirconium with Same Total Shape Change.

Tube Testing Apparatus

An apparatus was constructed for studying the anisotropy of Zircaloy-2 tubing subjected to biaxial stress. This equipment will allow the simultaneous application of axial stress, torsional stress, and internal pressure. The properties to be measured are axial stress and strain, torsional stress and strain, internal volume change, and uniformity of local strain behavior. Either stress or strain in the axial and torsional directions is programmed, and axial stress, axial strain, torsional stress, torsional strain, and internal volume are continuously recorded. Internal pressure is held constant at some selected level during each test. The uniformity of local strain behavior is determined by photographically recording the distortion of an anodized grid network on the gage section of the specimen. A schematic diagram of the apparatus is given in Fig. 21.6. This apparatus will allow investigation of the stress and strain behavior of Zircaloy-2 tubing as a function of texture and biaxial stress over a region of at least one-half of the biaxial stress circle.

ORNL-DWG 64-11633A

TEST CAPABILITIES
INTERNAL PRESSURE - 3000 psi
TORSION - 7500 lb-in., 360° TWIST
AXIAL - 20,000 lb, 3-in. STROKE

PROPERTY MEASUREMENT	
PROPERTY	MONITOR
AXIAL STRAIN	LVDT, CAMERA
TORSION STRAIN	POTENTIOMETER, CAMERA
AXIAL STRESS	LOAD CELL
TORSION STRESS	LOAD CELL
INTERNAL VOLUME	LVDT

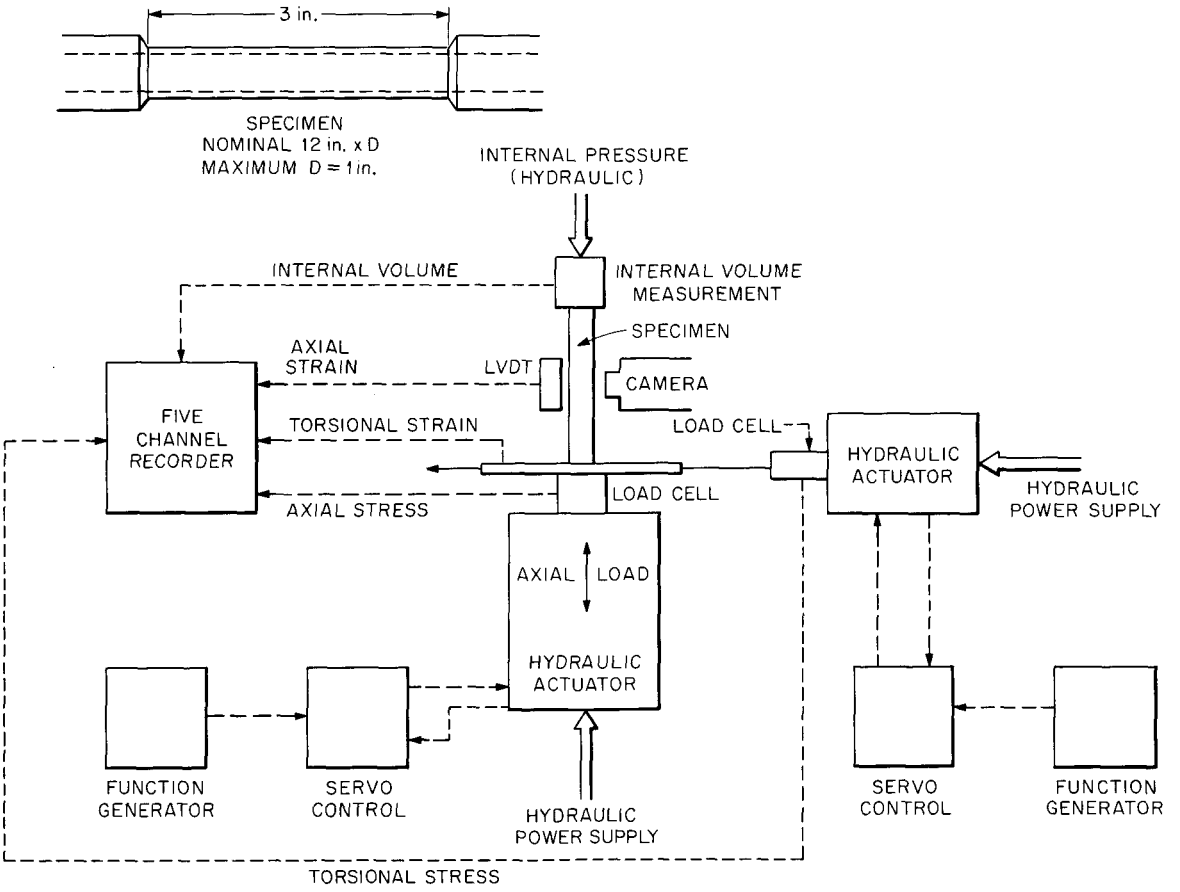

Fig. 21.6. Schematic Diagram of Tube Testing Apparatus.

OXIDE FILM STUDIES

J. C. Banter

Our method[12] for determining the refractive index and thickness of thin anodic oxide films on zirconium was applied to films having thicknesses from 3000 to 5500 A. The refractive index of these films was independent of thickness over this range, but the refractive index measured by this technique on stripped films was different from that of the same oxide film in situ. The removal of the films from the base metal should relieve much of the strain from the film. This relief should affect the optical properties but should not significantly change the film thickness.

[12] J. C. Banter, *Metals and Ceramics Div. Ann. Progr. Rept. June 30, 1964*, ORNL-3670, pp. 154–55.

Therefore, the thicknesses measured by the transmission interference technique were used with reflection interference measurements to calculate the refractive indices of the films in situ.

Interference maxima in the light reflected from the anodized zirconium specimens are described by the equation

$$T\sqrt{n^2 - \sin^2 i} - \delta''\lambda/4\pi = m\lambda/2 , \qquad (1)$$

where n is the refractive index of the film, T is its thickness, i is the angle of incidence of the light, λ is the wavelength at which the maximum occurs, m is the order of the interference, and δ'' is the phase change that occurs upon reflection from the oxide-metal interface. The wavelengths at which the maxima occurred were measured with a spectrophotometer for two films of thicknesses T_1 and T_2, and the quantity $m\lambda/2$ was plotted against wavelength for each specimen. The difference D between the two curves at any given wavelength is then

$$D = (T_2 - T_1)\sqrt{n^2 - \sin^2 i} . \qquad (2)$$

If T_2 and T_1 are determined by the transmission interference technique, n may be calculated for the films in situ if their refractive indices are assumed to be independent of film thickness, as is true for those of the stripped films.

The refractive indices of stripped and in situ films are compared in Fig. 21.7. The refractive indices of the films on the metal are higher than those of the stripped films. Generally, the observed refractive index increases with an increase in density of the material, and the lower index of refraction for the stripped film is consistent with the relief of strain in the films by the removal of the metal.

A series of anodized specimens was exposed to a fast-neutron dose of about 10^{19} neutrons/cm^2 in the ORR, and their reflection spectra were compared to those of unirradiated control specimens. No differences were detected, indicating that irradiation at that level had no effect on the optical properties of these oxide films. An effect would be expected if the irradiation had produced defects on the films. Possibly too few defects were produced to detect by the technique used.

Both the irradiated and control specimens were vacuum annealed at 600°C for 2 hr to partially dissolve the oxide films in the base metal. Again, no difference was apparent between the rates of dissolution or the reflection spectra after partial dissolution. However, reflection spectra in each specimen differed before and after the annealing treatment more than corresponded to the decrease in film thickness due to dissolution. A strong

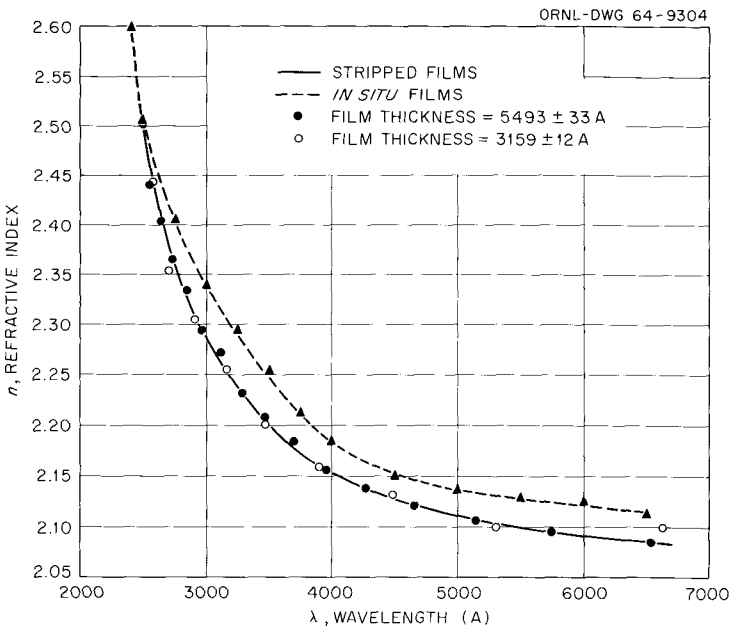

Fig. 21.7. Refractive Indices of Anodized Films in Situ and Stripped from Zirconium.

general absorption of light occurred for the annealed specimens throughout the spectral range studied (visible to ultraviolet). This absorption was not evident for the unannealed specimens.

We attribute the strong absorption after partial dissolution of the oxide film to defects produced by the dissolution process. Further evidence for this view is given by the catastrophic attack of the base metal through the film by the bromine–ethyl acetate solution used to dissolve the metal away from the film. The nature of the defects is not known at the present, and work to characterize them will continue.

PREPARATION OF SINGLE CRYSTALS OF ZIRCONIUM AND ZIRCONIUM ALLOYS

J. C. Wilson

Production of single crystals of zirconium and some of its alloys to meet the needs of the zirconium research program has continued. Most of the single crystals are grown by zone melting[13] with subsequent alpha annealing to perfect their structure. The yield of single crystals in $\frac{3}{8}$-in.-diam bars was almost doubled by seeding. A starting stub for melting was made from a single crystal (only the tip of the stub is melted as it is welded onto the bar to be zoned). Single crystals up to $\frac{3}{4}$ in. in diameter were grown by zone melting directly from as-deposited crystal bar, but the present apparatus must be modified to permit routine production of such large crystals.

We use electrical discharge machining (EDM) to cut single crystals to specific orientations or special shapes with negligible macroscopic deformation of the specimens.[14] The EDM has been particularly useful for producing spherical single crystals for study of the anisotropy of optical properties and oxidation of zirconium. About 10 hr are required to form $\frac{3}{8}$- to $\frac{5}{8}$-in.-diam spheres from zone-melted bars. Chemical polishing of the as-machined surfaces (finish of 50 to 100 μin. rms) smooths the spheres sufficiently to allow metallographic observation at 1000×. The chemical polishing also produces etch pits in regular patterns that can be used to locate the (1010) planes by inspection. The elimination of these etch pits from the specimens used for the study of optical anisotropy has been particularly difficult; the best results have been obtained with a methanol–perchloric acid electropolishing bath[15] operating at 50 v and at −70°C. However, etch pits still exist in two small arcs near $(10\bar{1}0)$ poles. The ability to make single crystal spheres of such large sizes is expected to facilitate many different types of studies. As one example, the habit plane for $ZrH_{1.5}$ in zirconium, (1010), has been confirmed by examination of a hydrided single-crystal sphere.

ZONE REFINING OF ZIRCONIUM

J. C. Wilson

The zone refining apparatus reported previously[13,16] was improved by reducing floor-transmitted vibrations, adding a variable-speed drive system, and changing the operating procedures to produce better vacuum. Early studies had shown carbon contamination to occur; this was reduced by sequential baking and use of a booster pump to isolate the diffusion pump from the mechanical fore pump. The carbon pickup in a single zoning pass has been reduced from about 10 to less than 2 ppm. Oxygen contents have been held to below 20 ppm for 4 passes. The feasibility of floating-zone refining bars up to $\frac{3}{4}$ in. in diameter was demonstrated.

In addition to supplying the requirements of the zirconium metallurgy program with zone-refined and single-crystal materials, we have furnished zone-refined zirconium to other groups for such studies as gettering methods for oxygen analysis in liquid metals and zone-refined titanium for basic studies of corrosion in saline waters for

[13] J. C. Wilson and M. L. Picklesimer, "Variable Gradient Electron-Beam Heating Methods for Growing Single Crystals of Zirconium," pp. 502–20 in *First International Conference on Electron and Ion Beam Science and Technology*, ed. by R. Bakish, Wiley, New York, 1965.

[14] J. C. Wilson, "Electrical Discharge Machining in the Metallurgical Laboratory," paper presented at the 19th AEC Metallographic Group Meeting, April 20–22, 1965 at Oak Ridge National Laboratory, Oak Ridge, Tennessee (proceedings to be published as ORNL-TM-1161).

[15] E. N. Hopkins and D. T. Peterson, "A Universal Electropolishing Method," paper presented at the 19th AEC Metallographic Group Meeting, April 20–22, 1965 at Oak Ridge National Laboratory, Oak Ridge, Tennessee (proceedings to be published as ORNL-TM-1161).

[16] J. C. Wilson, *Metals and Ceramics Div. Ann. Progr. Rept. June 30, 1964*, ORNL-3670, pp. 157–59.

the water desalinization studies. An adaptation of this method to produce extreme purity in small specimens is described in Part I, Chap. 5 of this report.

PROPERTIES OF HIGH-PURITY ZIRCONIUM

J. C. Wilson

We have begun to investigate several of the properties of zirconium that were heretofore difficult to study because of the effects of impurities or of the lack of sufficiently large single crystals. These studies on purified single crystals will serve as points of departure for future studies on the effects of impurities, alloying elements, and polycrystallinity.

Recrystallization

Although the recrystallization of crystal-bar and sponge zirconium has been widely studied, there is yet no clear description of the process, much less an understanding of the mechanisms. We are examining the recrystallization behavior of zone-refined cold rolled zirconium by hardness, x-ray diffraction, and metallographic measurements. The recrystallization temperature of "pure" zirconium was lowered by 200 to 300°C by the removal of several of the relatively insoluble impurities. Other observations include:

1. The recrystallization as detected by optical metallography and x-ray diffraction may begin at 150°C in 24 hr or less. After 100 hr at 175°C the metal is almost completely recrystallized and has a grain size of the order of 10 μ.
2. Although we have had considerable difficulty in etching to allow resolution by optical microscopy of the structures at the start of the recrystallization, it is fairly clear that the nucleation and growth of new grains can occur at these low temperatures in zirconium as in most other metals. Heretofore, the operative process has generally been held to be an in situ recrystallization.[17]
3. The recrystallization of material taken from the head and center of a zone-refined bar is sufficiently different to be immediately apparent under the optical microscope, although the differences in impurity levels are probably less than 50 ppm total.
4. The hardness impressions made on the rolled surface of the cold-rolled single crystals are markedly anisotropic. The diagonal lengths of DPH impressions are less by the equivalent of about 20 DPH numbers in the transverse direction than in the rolling direction for annealing temperatures below 250°C. The difference persists even after the material is well annealed and recrystallized. The difference is not in true hardness but is due to the anisotropy of elastic recovery as the indenter is removed from the impression. The difference is consistent with a high degree of texture in the material.
5. For annealing temperatures below 250°C, the hardness does not decrease monotonically with time; peaks or plateaus of constant hardness are often observed as though age hardening were occurring.

These observations were made on high-purity material rolled directly from zone-refined bar. Each specimen was, in effect, a rolled single crystal in which much of the deformation was by twinning. Experiments in progress with samples recrystallized to a small penultimate grain size may yield information more relevant to the practical working of zirconium.

Oxidation of Single Crystals

The effects of impurity elements on the oxidation of zirconium are not understood. We have begun to measure the oxidation rates of zone refined zirconium to establish a base for future work on the effects of alloying elements.

The first examination has been made of the dependence of oxidation rate on crystallographic orientation by exposing a 0.5-in.-diam single crystal sphere to dry air for 1.5 hr at 350°C. The resultant pattern of interference colors is sketched on a stereographic triangle in Fig. 21.8. The oxide layers in the blue and gold regions are approximately 500 and 250 A thick, respectively, as determined by comparison with reference strips

[17] R. K. McGeary and B. Lustman, *Trans. AIME* **197**, 284 (1953).

made[18] by anodizing in 1% KOH. Thus the oxidation rates for the $(11\bar{2}0)$ and (0001) planes differ by at least a factor of 2. Pemsler[19] and Wanklyn[20] had previously measured the anisotropy of oxidation (in 415°C oxygen and in 500°C steam) using polycrystalline specimens with limited ranges of orientations. The two sets of data agree qualitatively, but our work shows very clearly the variation over the entire set of orientations possible. This clear delineation of the anisotropy of oxidation will permit us to select a small number of orientations of flat single crystals for detailed study with an assurance not available before.

Diffusion rates of oxygen in zirconium have been measured on anodized specimens by several investigators. We are presently performing such experiments on single crystal spheres to determine which crystal orientations deserve more detailed study.

[18]R. D. Misch, *Acta Met.* **5**, 179 (1957).

[19]J. P. Pemsler, *The Diffusion of Oxygen in Zirconium and Its Relation to Oxidation and Corrosion*, NMI-1177 (1957).

[20]J. N. Wanklyn, *Am. Soc. Testing Mater., Spec. Tech. Publ.* **368**, 58 (1964).

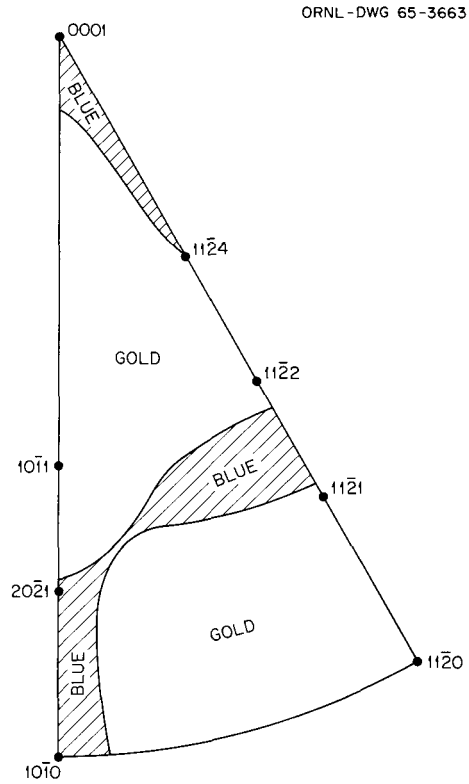

Fig. 21.8. Orientation Dependence of Oxidation on Single-Crystal Zirconium Sphere. Oxidized 1.5 hr at 350°C in dry air. The oxide thickness is approximately 500 A in the blue region and 250 A in the gold region.

Part III.

Reactor Development Support

22. Army Reactors Program

G. M. Adamson, Jr.

During the past year we have been phasing out our work on the Army Reactors Program. The remaining effort has been directed at two problems: (1) completion of the Phase I portion of the study of europium oxide neutron absorbers, and (2) providing general support assistance to the Army Reactor Branch of the AEC. The absorber program has been concerned primarily with studying the stability of europium molybdate compounds. In the support program, we have destructively examined a group of PM-type fuel elements to determine their quality. Other assistance has entailed help in writing specifications and visual examination of various reactor components.

CORROSION RESISTANCE OF EUROPIUM MOLYBDATE AND CHEMICAL COMPATIBILITY WITH IRON, NICKEL, AND CHROMIUM

J. A. Burka C. F. Leitten, Jr.

Work was continued on developing hydration-resistant neutron-absorbing compounds as dispersoids in stainless steel. Studies have centered on evaluating the effect of crystal structure on corrosion resistance and chemical compatibility of europium molybdate. The crystal structure of arc-melted europium molybdate depended on heat-treating temperature and cooling rate. Thus, oxidizing the molybdate in the temperature range 1400 to 1450°C, followed by slow cooling, resulted in the formation of a rhombohedral phase rather than the face-centered cubic phase normally encountered after fast cooling from higher temperatures. The formation of this rhombohedral phase was of concern, since lanthanide structures other than cubic are not normally considered to be hydration resistant.[1]

The europium molybdate used in the corrosion studies was initially prepared by arc melting, oxidizing 16 hr at 1000°C, and then crushing to −325 mesh powder. To form the face-centered cubic structure, pellets of the molybdate were heated to 1650°C and cooled rapidly in air. The rhombohedral structural form was obtained by heating pellets to 1450°C and then slowly cooling them in the furnace. For comparison, pellets of unoxidized as-arc-cast molybdate were also prepared by sintering in vacuum at 1450°C.

Each of these materials was corrosion tested in distilled water at 100 and 250°C for varying times. The results are summarized in Table 22.1. These tests indicate that only small differences in corrosion resistance exist between the face-centered cubic and rhombohedral structures of europium molybdate. In all cases, the face-centered cubic molybdate showed slightly less weight change than the rhombohedral material. The vacuum-sintered molybdate appears stable in the 100°C tests and showed less weight change at 2000 hr than the oxidized materials. However, at 250°C the vacuum-sintered material showed considerably larger changes.

Compatibility in iron, chromium, and nickel was also tested on both the face-centered cubic and rhombohedral molybdates. These tests showed that crystal structure did not significantly affect the chemical compatibility of europium molybdate. As in previous studies, slight swelling and interactions between the molybdate and chromium particles were observed in specimens sintered in both vacuum and argon.[2] These effects were not noted when the compacts were sintered in hydrogen at 1150°C. We feel that the interaction noted in the compacts sintered in vacuum and argon is associated with the oxygen surface contamination of the chromium and not with the reduction of europium molybdate by chromium.

[1] C. F. Leitten, Jr., *Metals and Ceramics Div. Ann. Progr. Rept. June 30, 1964*, ORNL-3670, p. 167.

[2] M. W. Schafer and R. Ray, *J. Am. Ceram. Soc.* **42**(11), 563–70 (1959).

Table 22.1. Corrosion of Europium Molybdates in Distilled Water

Type Molybdate	Weight Change (%)			
	At 100°C		At 250°C	
	1000 hr	2000 hr	190 hr	1000 hr
Face-centered cubic	+0.03	+3.46	+1.28	+2.58
Rhombohedral	+0.24	+3.92	+1.66	+2.79
Vacuum sintered	+0.23	+1.48	+5.59	+6.01

EXAMINATION OF ARMY PM CORE-I TYPE FUEL TUBES

D. O. Hobson

At the request of the Army Reactors Branch of the AEC, we have been determining the quality of fuel elements for the PM-1 and PM-3A reactors. This examination is needed for correlation with performance in developing realistic manufacturing specifications and for comparison with a future examination of an irradiated element. We are evaluating such characteristics as fuel-particle fragmentation and stringering, bonding of the cladding, interface contamination, cladding grain size, and fuel homogeneity and density. The fuel element is a tubular 29% dispersion of 92 to 94% enriched UO_2 in a stainless steel matrix, clad inside and out with stainless steel.

The fuel tubes were visually inspected, radiographed, dimensionally measured, and photographed before being sectioned for further examination. Visual inspection showed the tubes to be in good condition, considering the long storage period and the amount of handling they had undergone. We found that about one-fourth of the tubes had visible indentations in the outer cladding near the end of the fuel section. These will be examined metallographically to ascertain the amount of weakness such defects might cause.

We radiographed 11 tubes to show the interfaces between the fuel and the end caps. Almost all of the fuel ends showed a regularly spaced flash in the shape of a series of circumferential "fish-hooks." We believe that these are the result of the swaging operations in the fabrication procedure. The fuel core ends were found to have a maximum amount of feathering of 0.250 in.

Dimensional measurements of 11 of the fuel tubes showed very few to be outside of specifications. Five of the small-end diameters[3] and one fuel interface-to-tube-end distance were out. This phase of the examination involved 77 measurements.

After nondestructive examination of the tubes was completed, the tubes were sectioned for metallographic examination. Core density was measured and then the sections were mounted for evaluation of fragmentation, stringering, bonding, interface contamination, and cladding grain size.

The fuel core, exclusive of cladding, had an average density of 8.245 g/cm^3. Based on a fuel loading of 29% UO_2, this represents a core density 95.9% of theoretical.

The evaluation of fragmentation and stringering is complete. The fragmentation of the fuel was fairly uniform among the tubes. Chapter 14 of Part II describes our method for characterizing fragmentation in terms of the average number of fragments into which each particle fractures. Table 22.2 lists the results.

The transverse specimens are being examined for interface contamination, clad bonding, and grain size. Each of the 11 tubes was sectioned transversely into from 9 to 12 samples, depending on the length of the fuel element. At least four samples from each tube were examined to determine the amount of interface contamination present.

Both the inner and outer interfaces of 11 tubes were contaminated with a very fine particulate material between the cladding and the foil envelope

[3]The two ends of each element had been reduced by swaging to different diameters for fit in the core structure.

surrounding the fuel core. Table 22.3 lists the results of this examination. The lengths of contamination given in the table do not differentiate between continuous lines of contamination and interrupted lines. Electron microprobe analysis showed that the contamination was not uranium.

Table 22.2. Fragmentation Measured on 11 Army Reactor Fuel Tubes

Specimen Number[a]	Number of Particles	Number of Fragments	Particles per inch of 100× Photograph	Fragments per inch of 100× Photograph	Fragmentation Ratio
X1-KM-4A	584	5503	15.57	146.7	9.423
X1-KM-4B	594	6063	15.55	158.7	10.203
X1-MB-5A	732	6300	19.26	165.8	8.606
X1-MB-5B	655	5539	19.73	166.8	8.456
X1-JT-1A	657	5726	18.25	159.0	8.715
X1-JT-1B	651	5764	18.18	161.0	8.854
X1-CY-1A	614	4248	18.01	124.6	6.918
X1-CY-1B	612	4737	18.16	140.6	7.740
X1-JS-8A	602	4731	17.35	136.3	7.859
X1-JS-8B	589	4446	17.12	129.2	7.548
X1-JP-2A	595	3937	17.45	115.4	6.617
X1-JP-2B	634	4936	18.54	144.3	7.785
X1-EV-8A	583	4335	17.25	128.3	7.436
X1-EV-8B	585	5002	17.11	146.2	8.550
X1-JO-1A	741	5261	21.48	152.5	7.100
X1-JO-1B	638	4622	18.65	135.1	7.244
X1-ET-1A	631	6838	18.29	198.2	10.840
X1-ET-1B	644	6142	18.61	177.5	9.537
X1-DA-3A	673	5676	20.90	176.3	8.434
X1-DA-3B	605	5392	19.14	170.6	8.912
X1-EM-1A	606	5426	17.56	157.3	8.954
X1-EM-1B	642	5333	18.61	154.6	8.307

[a]The tube number is followed by A or B to distinguish two specimens from the same tube.

Table 22.3. Cladding-Core Interface Contamination in 11 Selected Fuel Elements from the Production Run of PM-1 Core 1

Tube Number	Number of Transverse Samples Per Tube	Number of Samples Examined	Length of Interface Examined (in.)		Contamination Observed (in.)		Estimated Percentage of Contaminated Tube Interface	
			Outer	Inner	Outer	Inner	Outer	Inner
X1-CY-1	12	5	7.77	6.74	4.71	4.21	61	62
X1-ET-1	12	12	18.66	16.18	17.20	11.60	92	72
X1-EV-8	12	5	7.77	6.74	6.94	2.74	89	41
X1-EM-1	12	5	7.77	6.74	2.62	0.08	34	1
X1-JP-2	9	9	13.99	12.12	11.65	7.80	83	64
X1-KM-4	12	5	7.77	6.74	4.90	3.85	63	57
X1-JO-1	9	4	6.22	5.39	1.12	3.62	18	67
X1-JT-1	9	5	7.77	6.74	6.26	3.94	80	58
X1-JS-8	9	4	6.22	5.39	6.21	1.09	100	20
X1-MB-5	11	5	7.77	6.74	7.19	4.63	92	69
X1-DA-3	12	5	7.77	6.74	3.16	2.99	41	44

23. Desalination

D. A. Douglas, Jr.

Very large nuclear reactors are attractive as heat sources for water desalination. We are assessing the economics of fuel fabrication for such reactors, developing materials for evaporator-condensers, and evaluating potential fuels for the reactors.

REACTOR FUEL ELEMENT FABRICATION COST ESTIMATES

T. N. Washburn A. L. Lotts

The consideration being given to the desalting of sea water by nuclear power makes very large single-purpose fuel fabrication plants a distinct possibility. Such large fabrication plants would effect substantial economies in the fabrication of fuel and would accordingly lower fuel-cycle costs.

Low-Temperature Reactors

We have assessed the technology and cost of fabricating large quantities of fuel elements for three types of low-temperature reactors: pressurized water, heavy water, and sodium-cooled fast breeder. The first two are fueled with metallic uranium whereas the latter has a core of UO_2-PuO_2, an axial blanket of UO_2, and a radial blanket of uranium metal. With a single fabrication plant supplying the fuel elements required by a 50,000-Mw (thermal) nuclear industry consisting of one reactor type, the optimum fabrication costs for the reference designs were estimated to be: pressurized water, \$6.60/kg of uranium; heavy water, \$9.00/kg of uranium; sodium-cooled fast breeder core (including axial blanket), \$77.00/kg of heavy metal (plutonium plus uranium); and sodium-cooled fast breeder radial blanket, \$11.50/kg of uranium. The applicable production rates in kilograms of heavy metal per day for these four costs are, respectively, 9000, 9000, 660, and 3100.

Heavy-Water Organic-Cooled Reactor (HWOCR)

Costs of remote fabrication for the HWOCR fuel elements proposed by Babcock and Wilcox Company were estimated as follows (\$/kg heavy metal):

Fuel Type	Burnup (Mwd/Tonne)		
	5000	10,000	20,000
Th-U alloy	16.61	18.86	22.37
Th-U oxide			
0.384-in. diam	50.60	58.80	70.13
0.489-in. diam	34.41	40.47	48.98
0.528-in. diam	30.02	35.52	43.19

The Th-U alloy fuel element consists of a center rod surrounded by four concentric fuel tubes. Metal fuel is coextruded with 0.025-in. Zircaloy-4 cladding. The alternate fuel pin designs contain sol-gel ThO_2-UO_2 loaded in Zircaloy-4 tubes by vibratory compaction. This evaluation for both fuel types assumes that 15 reactors, each capable of producing 1000 Mw (electrical), are fueled from one fabrication plant built to produce a single type fuel element. The above costs do not include fertile or fissile material costs, use charges, profit, or shipping costs.

A new computer program, FABCOST 8, was written to calculate fabrication costs of metal fueled elements.

Fast Breeder Reactor with Bare Fuel

A fast breeder reactor has been proposed in which the uranium fuel would be exposed to the

sodium coolant. Irradiated fuel would be melted, cast, and recycled to the reactor without chemical processing for decontamination. Feasibility studies of remote fabrication techniques are currently being outlined.

EVAPORATOR-CONDENSER TUBING

T. N. Washburn D. A. Douglas, Jr.

Major emphasis has been placed upon the evaluation of titanium tubing for use in both the multistage flash and long-vertical-tube evaporator-condenser designs. The primary advantage of titanium is its excellent resistance to corrosion by seawater. A disadvantage is the current price of titanium. However, cost projections by major fabricators of titanium tubing indicate a reduction to approximately $0.40 per linear foot of 1-in.-OD × 0.015-in.-wall seam-welded tubing. This price compares favorably with that of about $\frac{1}{16}$-in.-thick copper-alloy tubing, which would have the same strength. In each case above, the tubing considered has a smooth surface.

The advanced concepts of evaporator-condenser designs would require longitudinal flutes of the tube surface to improve heat transfer. The Materials Processing Group has started to evaluate methods of producing flutes in thin titanium. The most promising method for large-volume production appears to be fluting of thin titanium strip, forming it into a tubular shape, and then welding it. Other fabrication methods to be evaluated include fluting by tube drawing, forming with isostatic pressure, high-energy-rate forming, and press forming. The necessary tooling for each of these processes has been designed or obtained by the Materials Processing Group.

We have just started to investigate the forming of transverse or spiraled flow spoilers on the inner surface of the tubing.

The use of bimetallic tubing was proposed for consideration by the Metals and Controls Company, Inc. A thin layer of titanium would be metallurgically bonded to a much cheaper base material, such as carbon steel. The economics of this proposal are questionable; however, a preliminary evaluation is being conducted to determine its relative merits.

Graphite is being considered as a tubing material because of its excellent resistance to corrosion by seawater and good heat-transfer properties. Five tubes of impervious graphite have been obtained for heat transfer tests. One of these tubes was machined in the Y-12 graphite shop to form longitudinal flutes. Heat-transfer tests are planned in the Reactor Division loops.

Two aluminum tubes were fluted by machining and are being tested in the Reactor Division heat transfer loops to evaluate the effect of extended surface and flute profile upon condensation rates.

Mockup tube-sheet corrosion samples were fabricated by the Welding Group by expanding short lengths of $\frac{1}{2}$-in.-OD × 0.040-in.-wall titanium tubing into each of three $\frac{1}{2}$-in.-thick sections of header plate. Three similar specimens were made in which the expanded tubes were welded to each of the header plates. These specimens are currently being corrosion tested by the Reactor Division in the Freeport demonstration plant.

METAL FUEL EVALUATION

R. E. Adams J. L. Scott

We have surveyed metal fuel performances to assist in defining applications of metal fuels for large desalination reactors.

Recent developments in uranium technology indicate that accelerated "cavitational" swelling in the 375 to 575°C temperature range may be controlled through use of uranium containing minor alloying additions of Fe, Al, Si, or Mo. The data suggest that burnups of 6000 to 7000 Mwd/ton may reasonably be achievable. Research and development will be necessary to define details of fabrication variables and fuel element designs that will allow consistent performance at such burnup levels.

Thorium-base metal fuels inherently exhibit better performance than uranium metal because thorium is not subject to anisotropic growth and does not swell as readily as uranium metal. Burnup of thorium metal fuels must be significantly higher for satisfactory fuel cycle economics. Sufficient data are not yet available to establish the upper limits of burnup and temperature that may be achieved with thorium metal. Successful operation has been demonstrated in pressurized water loops at 10,000 Mwd/ton. Capsule data on alloys containing significant amounts of enriched uranium

suggest that 20,000 or 30,000 Mwd/ton may be feasible at temperatures below 200°C with total swelling in the range of 6 to 10%. Additional data are required to establish performance of thorium metal in which significant burnup of generated ^{233}U is achieved, and a proposal outlining the needed experiments is being prepared.

We have surveyed physical and mechanical data pertinent to nuclear applications[1] and irradiation behavior[2] for thorium, its alloys, and its ceramic compounds.

Potential cladding materials for metal fuels have been briefly considered from the aspect of compatibility with the fuel and with the coolant. Zirconium alloys are preferred for use with metal fuels. Technology has been developed for coextrusion of Zircaloy-2 with both thorium and uranium, and irradiation tests have indicated satisfactory performance. Zirconium-base claddings are being considered for use with organic coolants at temperatures below about 450°C. Embrittlement by hydride formation, however, is reported to be sensitive to coolant impurities, and additional research will be required to establish performance limitations.

The economy of aluminum cladding is attractive, but data indicate that reliable corrosion resistance in water at temperatures above 275°C is likely to be a problem. Operation of aluminum in water at temperatures up to about 300°C might be feasible if the pH is controlled at about 4.5. Although a considerable technology for use of inhibitors based on acidity control exists, the risk and additional problems necessary to ensure unfailing control do not appear justified. Potential new alloys show promise of achievement of higher temperatures. One, containing 12% Si, 1% Ni, 1% Mg, and 0.3% Fe, has shown one-tenth the corrosion of alloy X-8001 at 270°C, but it is still in an early stage of development.

The interaction between aluminum cladding and metal fuels necessitates a barrier to prevent diffusion. Use of nickel barriers approximately 1.5 mils thick has given satisfactory performance up to 375 to 400°C to about 6000 Mwd/ton, but the bond deteriorates under irradiation.

---

[1] S. Peterson, R. E. Adams, and D. A. Douglas, Jr., *Properties of Thorium, Its Alloys, and Its Compounds*, ORNL-TM-1144 (June 1965).

[2] A. R. Olsen, D. B. Trauger, W. O. Harms, R. E. Adams, and D. A. Douglas, Jr., *Irradiation Behavior of Thorium-Uranium Alloys and Compounds*, ORNL-TM-1142 (June 1965).

24. Gas-Cooled Reactor Program

W. O. Harms J. H. Coobs

Our materials effort in support of the Gas-Cooled Reactor Program consists of support for the Experimental Gas-Cooled Reactor (EGCR), development of unclad ceramic fuel elements, and associated supporting research. The significant activities in each of these categories are presented below along with pertinent background information.

EGCR SUPPORT

The EGCR is an outgrowth of conceptual design studies by Kaiser Engineers, Allis-Chalmers, and ORNL. The reactor core consists of 2.46%-enriched UO_2 pellets clad with stainless steel and supported in a graphite moderator structure contained within a carbon-steel pressure vessel. The plant, which is virtually complete, was constructed by the H. K. Ferguson Company and will be operated by the Tennessee Valley Authority. Our major responsibility was the procurement of fuel assemblies and control rods. These components had been completed previously and have now been transferred to the operating contractor in preparation for charging during the coming year. Our continuing efforts in other areas are reported below.

Irradiation Creep of Graphite

C. R. Kennedy

Graphite grades CGB and AGOT have been creep tested under irradiation from 130 to 370°C. Some details of the parabolic beam creep specimens, experimental procedures, and data from creep tests at higher temperatures were reported previously.[1]

The creep curves obtained from this last lower temperature experiment are given in Figs. 24.1 and 24.2. As shown in the figures, the stresses were altered during the experiment to determine the effect of variable stress. The general shape of the curves is much different than those obtained previously;[1] however, the deflection readings obtained from the creep specimens are actually sums of both creep deformation and differential growth. The differential growth, which opposes the creep deformation, was caused by a 10% flux gradient across the creep specimen. While this differential growth was small and insignificant at the higher test temperatures, it is quite large and must be considered at the present test temperatures.

The differential growth was separated from the total deformation curves by two methods. First, the total deformation was plotted vs stress at 100-Mwd/adjacent ton dose intervals. The deformation extrapolated to zero stress was the deflection caused by differential growth. A second method was required after the stress levels were altered in the experiment. This method was essentially the same, except tangent deformation rates were used instead of the total deformation. The tangent deformation rates were also plotted vs stress at 100-Mwd/adjacent ton dose intervals. The slope is the creep coefficient and the zero intercept is the deflection rate due to the differential growth.

The results of these two methods are given in Figs. 24.3 and 24.4. The behavior of the AGOT and CGB grades shows a very marked similarity, the latter having a lower creep rate. The very important difference from previous results is the variation of creep coefficient with dose.

The change in creep coefficient with dose has been predicted by Hesketh[2] using the Cottrell

[1]C. R. Kennedy, *Metals and Ceramics Div. Ann. Progr. Rept. June 30, 1964*, ORNL-3670, pp. 176–78.

[2]R. V. Hesketh, *Phil. Mag.* 11, 917–27 (1965).

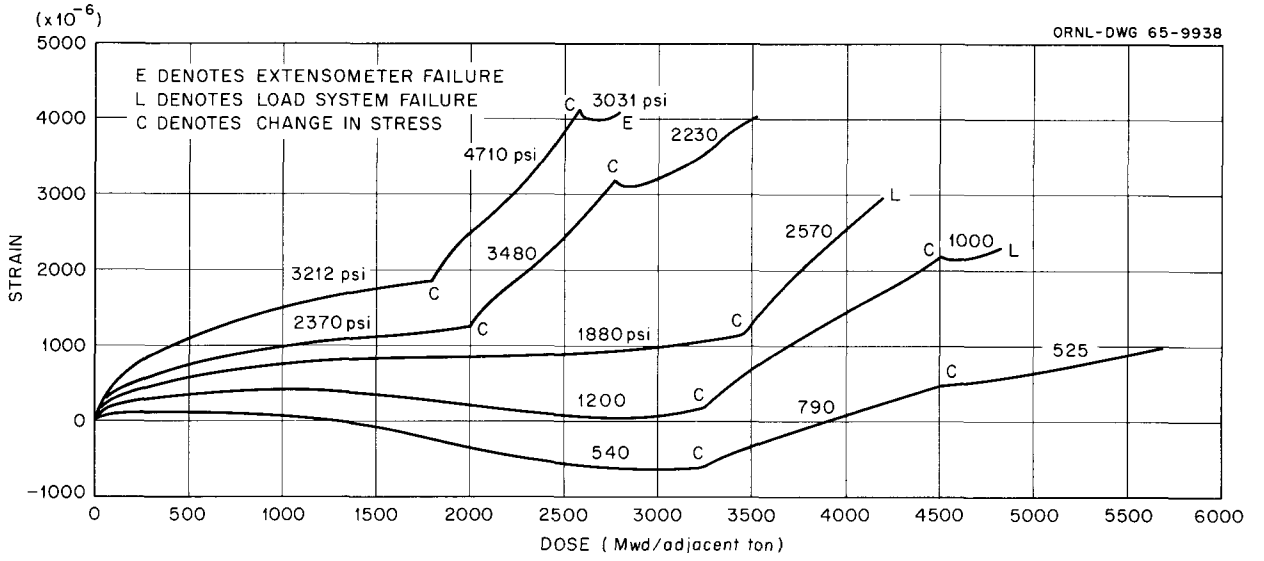

Fig. 24.1. Creep of EGCR-Type AGOT Graphite Under Irradiation at 130 to 180°C.

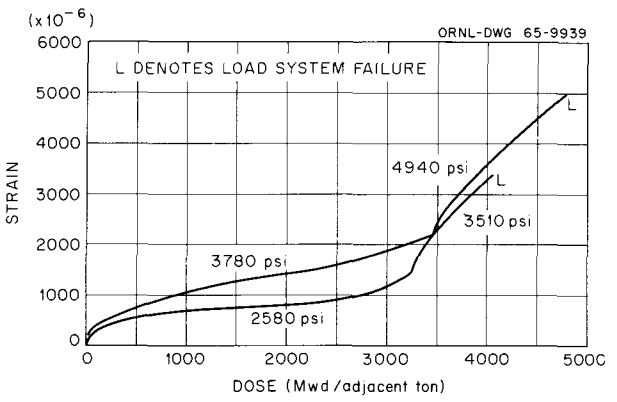

Fig. 24.2. Creep of CGB Graphite Under Irradiation at 150 to 180°C.

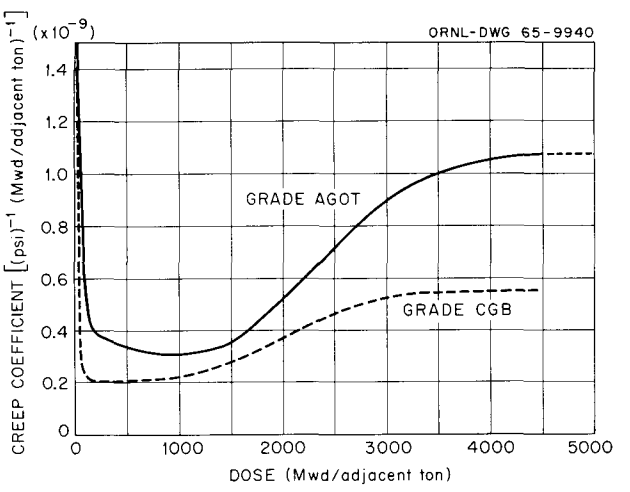

Fig. 24.3. Creep Coefficient of Graphite Under Irradiation at 130 to 180°C.

model of continuous yielding. The implication is that cooling or Mrozowski cracks reduce the internal stress intensity produced by the anisotropic growth of the crystallites. As the cracks are closed, this stress-relaxation process may cease and thus create higher internal stresses, which should increase the creep rate. The dose required to close the cracks will vary with the growth rate of the crystallites and thus with temperature. The dose level required for crack closure equivalent to 2×10^3 Mwd/adjacent ton at 150°C would be about 3×10^4 Mwd/adjacent ton at 400°C and 2.5×10^4 Mwd/adjacent ton at 300°C.

The previous creep tests did not attain neutron dosages of this level and thus did not demonstrate a change in the creep coefficient. There are, however, recent creep results of Gray[3] and Perks[4]

[3]B. S. Gray, J. E. Brocklehurst, and A. A. McFarlane, "Irradiation Induced Plasticity in Graphite," Paper 182, Seventh Biennial Conference on Carbon, June 21–25, 1965, held at the Case Institute of Technology, Cleveland.

[4]A. H. Perks and J. H. W. Simmons, "Dimensional Changes and Radiation Creep of Graphite at Very High Neutron Doses," Paper 188, Seventh Biennial Conference on Carbon, June 21–25, 1965, held at Case Institute of Technology, Cleveland.

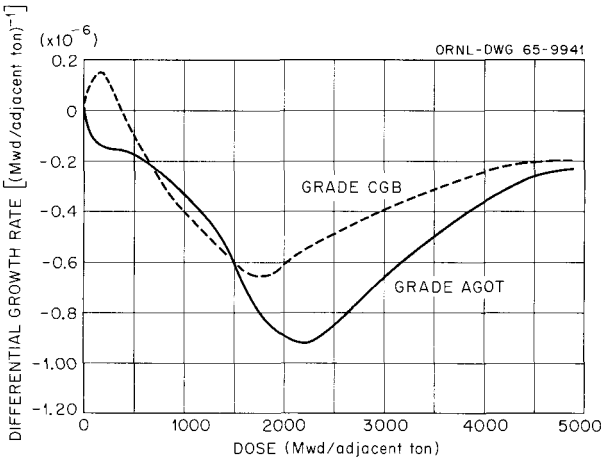

Fig. 24.4. Differential Growth Rate of Creep Specimens at 130 to 180°C.

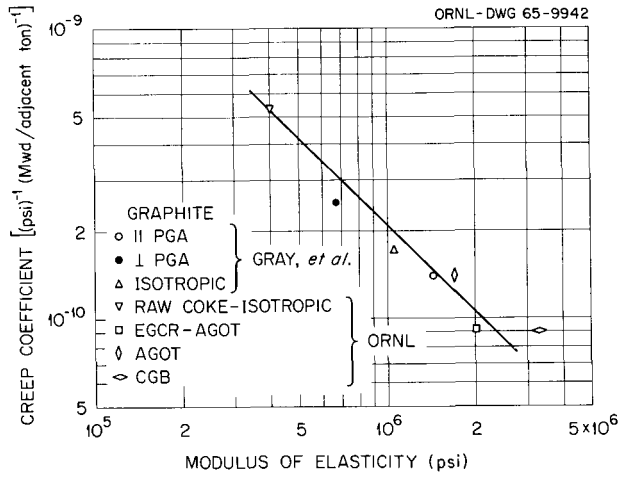

Fig. 24.5. Relationship of the Creep Coefficient of Various Grades of Graphite to Youngs Modulus at 400°C.

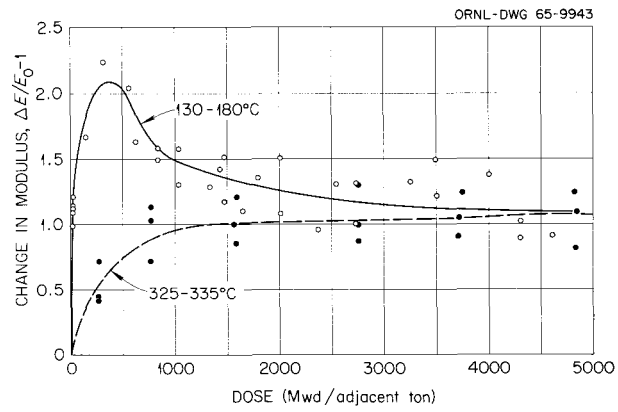

Fig. 24.6. Effect of Irradiation on the Modulus of Elasticity of EGCR-Type AGOT Graphite.

at 400°C to dose levels of 10^5 Mwd/adjacent ton. These creep test data should verify this concept, but on the contrary they indicate a continuous creep-rate coefficient. Also in conflict with this concept are data from thermal cycle tests by Harman, reported in part in the following section, which show a plastic yielding from 1000 to 2000°C without an abrupt change due to crack closure. The explanation of increased creep rate by crack closure does not appear to be verified and is therefore subject to doubt. These results do not detract from the Cottrell model for creep but only cast doubt on the effect of crack closure on stress relaxation.

The concept of the Cottrell model for creep does offer a second possible explanation for the creep rate variation. The rate of continuous yielding or creep depends upon the resistance of the material to deformation. Since the elastic modulus measures the dislocation mobility in graphite, the creep coefficient should be inversely proportional to the elastic modulus. Figure 24.5 demonstrates a very close agreement with this for six grades of graphite. Also, at the lower temperature the elastic modulus increases very sharply with dose and then decreases to a lower value almost equal to the high-temperature value, as shown in Fig. 24.6. We would, therefore, expect that the lower initial creep-rate coefficient is a result of increased strength, as evidenced by the modulus changes. If this is the proper analysis of the variation in creep coefficient, then the later creep coefficient obtained at higher doses is the value that should be compared to the higher temperature data. However, if the proper analysis is based on crack closure, then the initial lower value of the creep coefficient should be compared to the higher temperature data.

The variation of creep coefficient with temperature is shown in Fig. 24.7. This figure includes for comparison both the initial and final values obtained at the lower temperature. Regardless of which values are used, the data do appear to support a Cottrell model for the creep of graphite. If the higher values are used, the Cottrell model appears to be quite accurate; however, if the lower values are used, the Cottrell model will have to be modified to some degree.

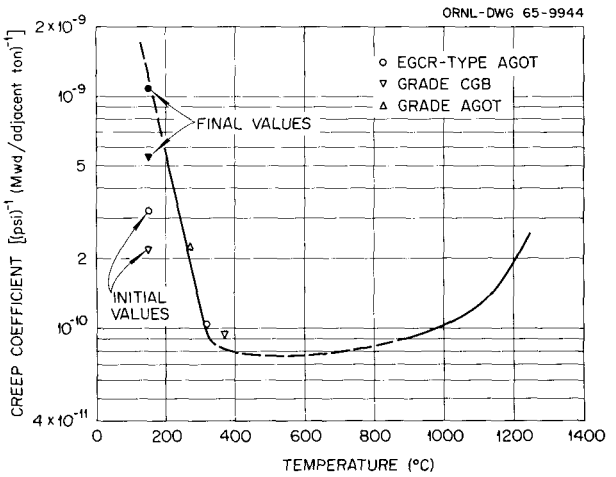

Fig. 24.7. Effect of Temperature on the Irradiation Creep of Graphite. The curve is based on the Cottrell model.

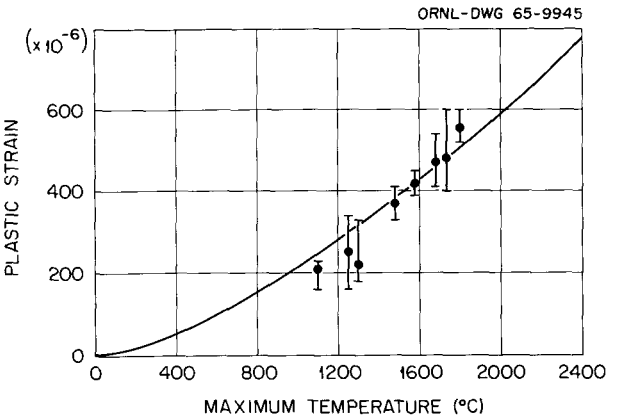

Fig. 24.8. Plastic Strain in AGOT Graphite Due to Thermal Cycling from Room Temperature with 600 psi Applied Stress. Vertical lines indicate data spread and filled circles represent average values; solid line represents theoretical relationship.

These results help relieve our concern over the stress intensity generated by differential growth in moderator structures. That is, as the growth rates increase, the creep rate coefficient also increases, so creep compensates for differential growth by reducing stress intensity. These experiments have also demonstrated a significant increase in the strain absorption without fracture. Several of the specimens have absorbed creep strains of greater than 0.6% and total strain of greater than 0.8%. These values are considerably greater than obtained ex-reactor but are not quite as significant as the 1.5 to 2% tensile strains obtained by Perks and Simmons[4] for PGA graphite. Apparently, strains of this magnitude can be sustained without loss of the mechanical integrity of the material. The strain limit has not been reached as yet.

Dimensional Stability of AGOT Graphite

D. G. Harman

Graphite, because of its pronounced anisotropy, is dimensionally unstable when subjected to thermal cycles. This behavior is related to the anisotropic thermal expansion and to the deformation characteristics of the material.

Type AGOT, a coarse-grained nuclear-grade graphite, has been thermally cycled at temperatures up to 1800°C. A constant tensile stress of 600 psi was applied to a 0.5-in.-diam tensile specimen while it was heated with an induction coil with a tantalum susceptor. The graphite was protected from oxidation by flowing argon. A 10-in. section of the specimen was heated to temperature, held for 15 min, and cooled to room temperature. The strain was continuously monitored by recording the output of a transducer fixed to the bottom pull rod.

The plastic strain due to the thermal cycle was determined by comparing the room-temperature strain measured before the thermal cycle to that measured after the thermal cycle. The plastic strain obtained with a single specimen is shown as a function of maximum temperature in Fig. 24.8. The spread in data is shown by the vertical lines and the filled circles are the average values. The specimen was returned to its initial state by high-temperature anneal after each cycle. Without this anneal, no plastic strain was noted beyond the first cycle.

The macroscopic stress-strain behavior of graphite according to Jenkins and Williamson[5] is given by

$$\epsilon = A\sigma + B\sigma^2 , \qquad (1)$$

where A is the elastic compliance at infinitesimally small stresses (the reciprocal of the elastic modulus) and B is a parameter measuring the extent of the plastic behavior.

[5]G. M. Jenkins and G. K. Williamson, *J. Appl. Phys.* 34, 2837–41 (1963).

By including similar unloading and reloading relationships, the plastic strain due to thermal cycling is predicted by Jenkins and Williamson as

$$\epsilon_{\text{plastic}} = 2\, B\sigma_m \Delta\sigma - B\sigma_m{}^2 \qquad (2)$$

for $\Delta\sigma > 2\,\sigma_m$, where σ_m is the applied stress and $\Delta\sigma$ is the change in local stress due to thermal effects.

For the tensile situation the thermal stress can be approximated as $\Delta\sigma = (\alpha_c - \alpha_a)E\ \Delta T/2$, where α_c and α_a are the expansion coefficients of the individual crystallites in the c and *a* directions, E is the elastic modulus, and ΔT is the temperature cycle.

Using the data of Mason and Knibbs[6] and that tabulated by Carbon Products Division of Union Carbide Corporation[7] $(\alpha_c - \alpha_a)$ is given by $3.0 \times 10^{-6} + 4.45 \times 10^{-10}\ T$ and E is given in psi by $1.5 \times 10^{-6} + 2.0 \times 10^{-4}\ T$. The expansion coefficient data are macroscopic and thus account for the presence of microcracks. The parameter B has been measured[8] to be 0.7×10^{-10} (psi)$^{-2}$ for AGOT graphite.

Using these values with Eq. (2), we obtain the relationship shown as a solid line in Fig. 24.8.

The fact that the data indicate a steeper slope than that of the theoretical curve suggests that the B parameter changes with temperature (which could be caused by crack closure, for example) or that the model proposed by Jenkins and Williamson does not apply.

Graphite Surveillance Program

F. L. Carlsen, Jr.[9]

The specimens for use in the graphite surveillance program[10] are presently being machined.

The melt wires, flux monitor wires, EGCR top spiders, and the EGCR graphite sleeves are being procured for use in the test assemblies. Upon receipt of the specimens and components, the necessary preirradiation measurements will be made prior to assembly and shipment to the EGCR.

Special Fuel Assemblies for Flux Mapping

R. M. Evans E. A. Franco-Ferreira

We assisted the EGCR operating group of TVA in the design and preparation of special fuel assemblies to be used for flux mapping of the EGCR. Standard Core-1 components were used to provide assemblies that can be readily dismantled for remount of the flux sensing elements. The components for ten such special fuel assemblies were modified in accordance with the specifications.

Standard UO_2 pellets (0.707 in. OD × 0.323 in. ID × 0.740 in. long) were sliced by ultrasonic machining techniques to provide half-length and assorted wafer-length pellets for adjusting the fuel column to the specified length. In addition, 50 half-length pellets were drilled ultrasonically to provide 16 axial 0.025-in.-diam holes to support copper flux-monitor wires.

A special technique was developed for drilling these 16 holes simultaneously with a multipronged tool. Ingots of Al–13% U alloy containing highly enriched uranium were prepared by the Metal Forming and Casting Group and extruded into 0.3-in.-diam rods, which will be positioned in the central void region of the fuel pellets. The rods were provided in various lengths to facilitate positioning of copper flux-monitor washers.

Evaluation of Pneumatic Temperature-Measuring Nozzles

N. C. Cole B. Fleischer

As previously reported,[11] we are determining the dimensional stability of nitrided type 304 stainless steel nozzles in slowly flowing helium at 1050°F. The nozzles are thermally cycled from 1050°F to room temperature every 100 hr. The impurity content of the helium approximates that expected

[6] I. B. Mason and R. H. Knibbs, *J. Nucl. Energy: Pt. AB* 18, 311–29 (1964).

[7] *The Industrial Graphite Engineering Handbook*, Carbon Products Div., Union Carbide Corporation.

[8] C. R. Kennedy, this Division, unpublished experiments.

[9] Now with Stellite Division, Union Carbide Corp., Kokomo, Ind.

[10] M. P. Davis, *GCR Program Semiann. Progr. Rept. Mar. 31, 1963*, ORNL-3445, pp. 46–49.

[11] N. C. Cole and B. Fleischer, *GCR Program Semiann. Progr. Rept. Mar. 31, 1964*, ORNL-3619, pp. 22–23.

in the EGCR. During the first 2000 hr the nozzles were removed from the furnace, measured, and calibrated for a flow coefficient at 200-hr intervals. For the last 1200 hr the nozzles have been measured and calibrated only after 400-hr intervals.

After a total of 3200 hr, the nozzles are now registering a possible 95°F temperature error and during the last 800 hr the temperature error has definitely increased. The gradual oxidation of the nozzle throat shrinks the diameter and causes this increasing error. After 3200 hr under the same conditions in the reactor, the nozzles would read a temperature possibly 95°F higher than the actual temperature of the system. Testing of the nozzles is continuing.

DEVELOPMENT OF UNCLAD FUELS

All-ceramic nuclear fuel elements offer the distinct advantages of high-temperature operation and good neutron economy. However, the escape of fission-product activity from them into the coolant system of a power reactor may complicate operation or maintenance. Our program on all-ceramic fuels consists mainly of preparing and testing pyrolytic-carbon-coated carbide and oxide fuel particles and testing of fueled graphite elements containing such particles. Other studies have involved the testing of graphite as a structural material for all-ceramic fuel elements. The results of some related efforts on thorium-containing fuels are reported in Chap. 30 of this report.

Pyrolytic Carbon Coating

R. L. Beatty D. M. Hewette
H. Beutler[12]

The effects of deposition conditions in fluidized beds on the properties of pyrolytic carbon coatings on fuel microspheres are being determined systematically.[13] In a series of coating experiments at temperatures between 1300 and 2000°C, the flow rate of methane relative to the initial surface area of the bed was varied independently while the total gas flow was maintained constant by dilution with helium. Contour plots of the densities and crystallite sizes of all these coatings in Fig. 24.9 show that crystallite sizes varied systematically from approximately 40 to 120 A with increasing temperature and decreasing flow

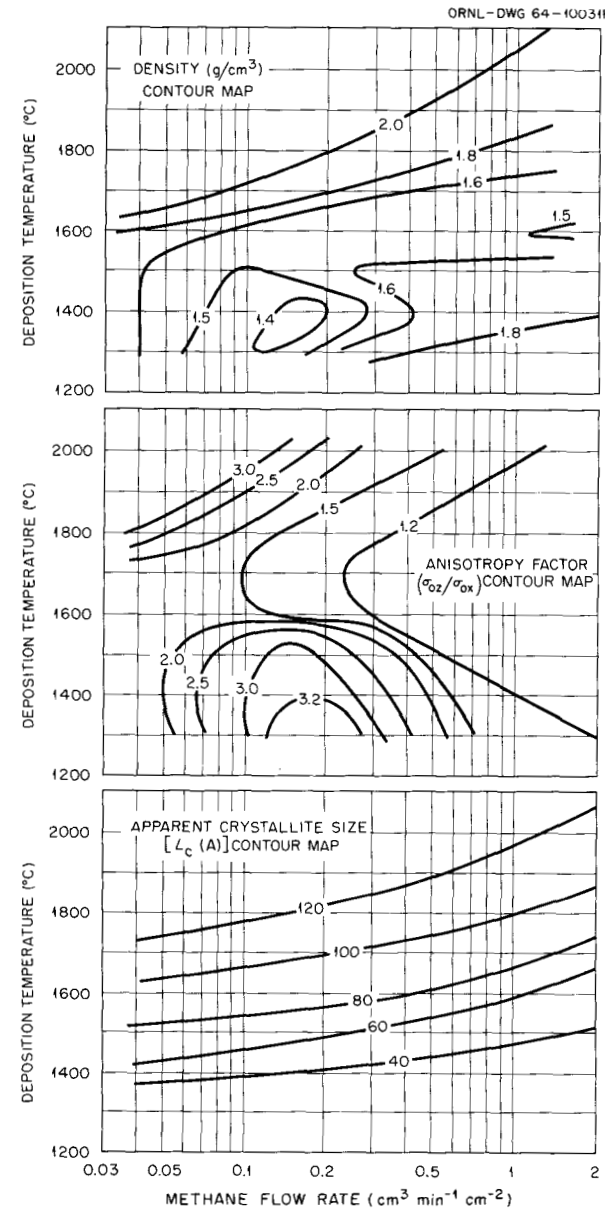

Fig. 24.9. Effect of Deposition Conditions on Properties of 50-μ-thick Pyrolytic Carbon Coatings Deposited in a Fluidized Bed. Methane flow rate is in cm^3/min per square centimeter of particle surface.

[12]Noncitizen employee from Switzerland.

[13]R. L. Beatty, *Metals and Ceramics Div. Ann. Progr. Rept. June 30, 1964*, ORNL-3670, pp. 181–84.

PHOTO 68161A

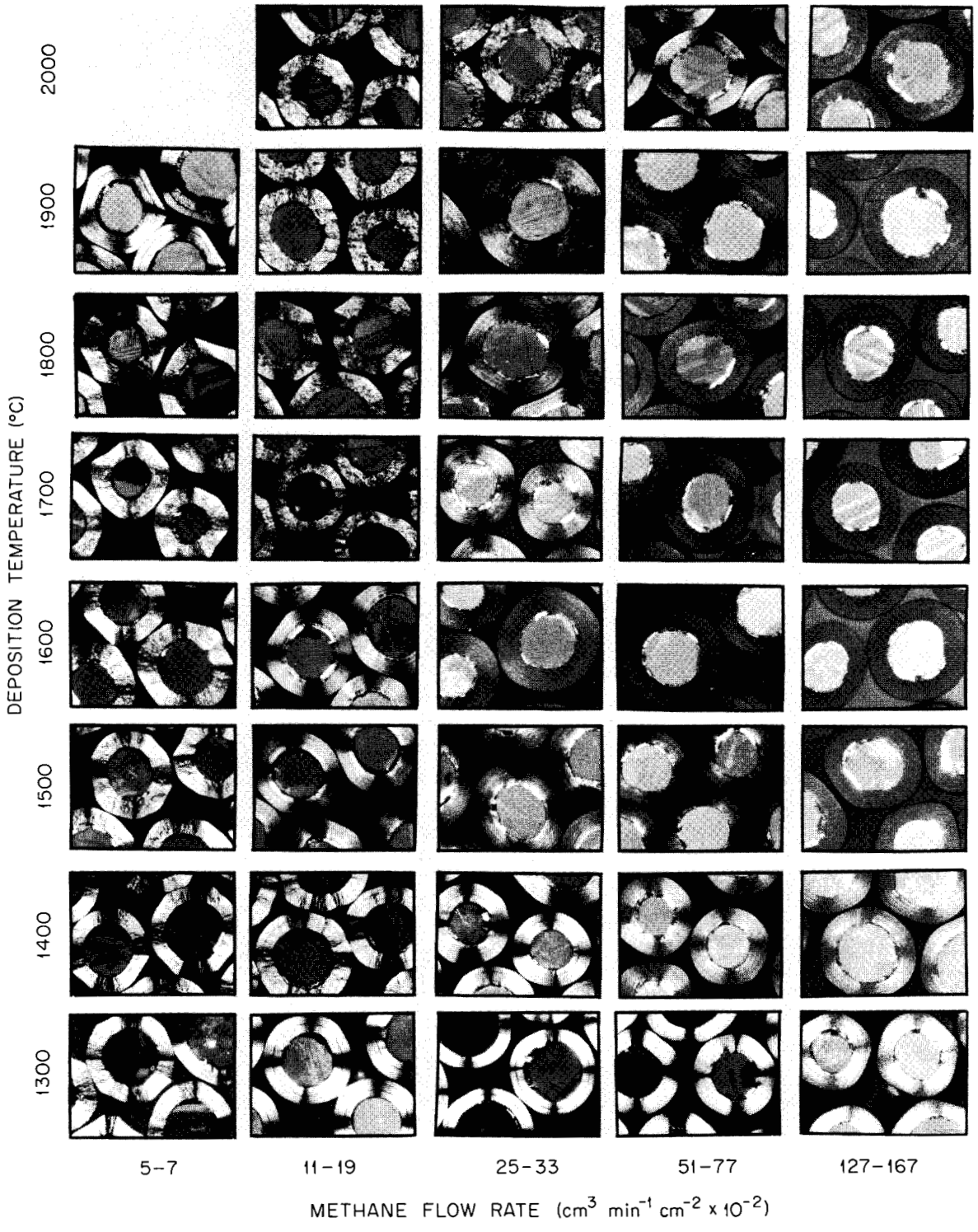

Fig. 24.10. Effect of Deposition Conditions on Microstructure of Pyrolytic-Carbon-Coated UC_2. As polished, polarized light. Methane flow rate is in cm^3/min per square centimeter of particle surface.

rate. Also the density of the coatings behaved similarly above 1600°C, increasing systematically from approximately 1.5 to 2.1 g/cm^3. However, below 1600°C a density minimum extended from 1500 to 1300°C; the density was 1.4 g/cm^3 for 1400°C between 0.13 and 0.2 cm^3/min per square centimeter of particle surface. As the flow rate increased, the density of these low-temperature coatings increased to 1.8 g/cm^3. The third contour plot in Fig. 24.9 shows anisotropy factors. We found two regions of high anisotropy, one at high temperatures and low flow rates and the other coinciding with the low-density region between 1300 and 1500°C. Coating microstructures are correlated with the contour map for anisotropy factors in Fig. 24.10. Because the coatings react to polarized light, these microstructures provide a qualitative correlation with anisotropy factors calculated from x-ray studies.

Additional experiments have been performed at 1300, 1400, and 1600°C with undiluted methane.[14] Under these conditions very high deposition rates were obtained. At a methane flow rate of 3.57 cm^3/min per square centimeter of particle surface, raising the temperature from 1300 to 1600°C increased the deposition rate from 104 to 317 μ/hr respectively. With the same increase in temperature the coating density decreased from 2.1 to 1.5 g/cm^3, the apparent crystallite size increased from 40 to 60 A, and the anisotropy factor decreased slightly from approximately 1.4 to 1.

Coating studies have been initiated on 100-g charges in a 2-in.-diam coating apparatus.[15] The objective is twofold: to study systematically the effect of deposition conditions on coating properties obtained in an apparatus intermediate in size between laboratory and production equipment, and to provide the capability for coating, in single runs, batches of fuel particles large enough for complete evaluation including irradiation testing. Results from preliminary experiments indicate that equivalent deposition rates are produced under deposition conditions selected by extrapolation of data obtained with the smaller coater.

[14] W. O. Harms and J. H. Coobs, *Coated-Particle Fuels Development at Oak Ridge National Laboratory for Period November 15, 1964 to May 15, 1965*, ORNL-TM-1116, pp. 17–21.

[15] D. M. Hewette and R. L. Beatty, *GCR Program Semiann. Progr. Rept. Mar. 31, 1965*, ORNL-3807, pp. 9–10.

Thermal Stability of Pyrolytic-Carbon-Coated Oxide Fuel Particles

R. L. Hamner R. L. Beatty
J. L. Scott H. Beutler[12]

We continued the thermal-stability studies[16,17] of conventionally prepared UO_2 particles and sol-gel ThO_2 particles coated at temperatures of 900 to 1800°C with pyrolytic carbon. The ThO_2 particles were 150 to 250 μ in diameter and the UO_2 particles were 177 to 250 μ in diameter.

Particles with coating thicknesses of at least 85 μ survived short-term ($\leq$ 2 hr) heat treatments at temperatures from 2000 to 2700°C without significant reaction. A batch of particles having a relatively thin coating (40 to 45 μ) survived short-term heat treatments at 2000 and 2200°C but failed after 50 hr at 2000°C. Particles with coating thicknesses of at least 100 μ were heat treated for extended periods (100 to 680 hr) at 1900 and 2000°C without significant reaction with the coating.

Migration of fuel into the coating was observed after heat treatment by radiography only in two batches of UO_2 particles in which each particle had an inner porous layer of pyrolytic carbon; this migration occurred after 680 hr at 1900°C, but extended only about 5 μ into the porous carbon layer.

Examination by microradiography of particles heat treated at 2000°C or higher revealed gaps between fuel particles and some coatings. This gap formation depended upon initial coating properties, which are determined by deposition conditions; for example, the size of the gap was greater for particles having a low-density anisotropic coating. Measurements confirmed the densification and decrease in coating thickness in batches that formed gaps. Also, the crushing strength of the coated particles in which gaps were formed was drastically reduced (up to 57%), probably from lack of support of the coating by the fuel particle. One batch of UO_2 fuel particles having a two-layer coating with such a gap has

[16] R. L. Hamner, R. L. Beatty, and R. E. Meadows, *Metals and Ceramics Div. Ann. Progr. Rept. June 30, 1964*, ORNL-3670, p. 238.

[17] R. L. Hamner, R. L. Beatty, and J. L. Cook, *GCR Program Semiann. Progr. Rept. Mar. 31, 1965*, ORNL-3807, pp. 13–21.

shown[18] very good performance in an irradiation experiment in the ORR.

Mathematical Simulation of Coated-Particle Behavior

J. W. Prados[19] J. L. Scott

A set of mathematical relations was recently developed[20] for predicting stresses and strains in pyrolytic carbon coatings surrounding a fuel particle as a function of geometrical parameters and environmental conditions. These relations provide a mathematical model that can assist the coated-particle developer in the planning and interpretation of irradiation tests and, once confirmed or corrected by experimental comparison, can provide a rational basis for selection of coated-particle dimensions and properties.

Calculations using the model have been performed to investigate the effect of the following coated-particle properties and service conditions on the expected life under irradiation of a two-layer coated particle: fuel-particle diameter, fuel-particle density, fission-gas retention properties of the fuel material, thickness of inner coating layer, void volume provided by inner coating layer, thickness of outer coating layer, degree of anisotropy of outer coating, fuel burnup, fast-neutron dose, and irradiation temperature.

Based on the results of these calculations, we arrive at the following predictions regarding the effect of a coated-particle's configuration and environment on its expected service life.

1. The most important single factor in promoting coating longevity is the provision of adequate free volume for accommodation of fuel-particle swelling and fission gas. A reasonable value for this free volume would be 2% of the fuel-particle volume per atom percent burnup desired in the fuel. Free volume may be provided by use of a low-density fuel particle, a porous inner coating that densifies readily when bombarded by fission recoils, manufacturing techniques that actually provide empty space between fuel and coating, or a combination of these.

2. Primary containment of fission products should be provided by an outer coating whose inner surface is protected against fission recoils. The thickness of this coating should be such that its inside diameter is approximately two-thirds the outside. Thicker coatings do not provide an appreciable increase in strength and may be more subject to failure from anisotropic dimensional change.

3. The release of gaseous fission products from the fuel has a negligible effect on coating life as long as free volumes are provided as specified above. With smaller free volumes, the coating life can be shortened at high fractional release of fission gas only if coating rupture stress is below about 35,000 psi. Hence, the use of a low-density fuel particle to help provide free volume should have no adverse effect on coated-particle life.

4. Two distinct modes of coating failure may occur: failure initiated at the inner coating surface from a combination of fuel particle swelling and fission-gas pressure, and failure initiated at the outer coating surface from anisotropic thermal expansion and fast-neutron damage to the pyrolytic-carbon structure. Failure by the first mode is more likely for coated fuel particles under power-reactor operating conditions. When failure occurs by the first mode, the maximum fuel burnup attained depends primarily on the free volume provided and on the degree of fuel swelling and not greatly on other coated-particle properties.

The preceding results can be employed to arrive at a satisfactory coated-particle configuration with a minimum of information on the properties of the particle and coating materials. Accurate economic optimization of coated-particle design must await critical comparison of the mathematical model's prediction against the results of controlled experimental tests and the development of any necessary corrections.

Coated-Particle Irradiation Tests in the ETR X-Basket

E. E. Bloom J. L. Scott
J. H. Coobs

To meet the need for an inexpensive facility for irradiating several batches of coated particles at one time, we have designed and constructed a

[18] R. M. Carroll *et al.*, *GCR Program Semiann. Progr. Rept. Mar. 31, 1965*, ORNL-3807, pp. 87–101.

[19] On leave from the University of Tennessee.

[20] J. W. Prados and J. L. Scott, *Analysis of Stress and Strain in Spherical Shells of Pyrolytic Carbon*, ORNL-3553 (June 1964).

ORNL-DWG 65-2802

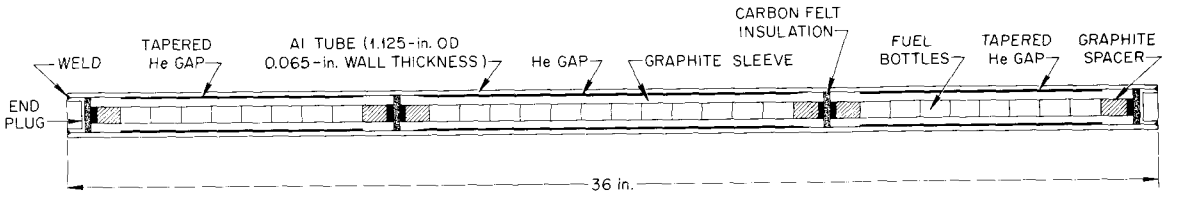

Fig. 24.11. Coated Particle Irradiation Capsule.

new type of irradiation capsule. Because of prohibitive costs, use of thermocouples has been avoided and melt-wires have been used to indicate the maximum temperature reached during irradiation. This approach results in considerable uncertainty in the actual conditions during irradiation, but the experiment will be useful for qualitative comparisons between different types of coated particles in the same capsule and in selecting particles for the more refined and expensive in-reactor sweep capsule tests.

The first capsule in the series has been fabricated and installed in the ETR X-basket facility. Fuel particles consisting of 90%-dense UO_2 and bed-melted UC_2 microspheres approximately 200 μ in diameter were coated with two layers to give a total coating thickness of approximately 120 μ. Samples from 12 different lots of coated particles were distributed in 28 graphite fuel bottles, as shown in Fig. 24.11. Each end compartment contains eight fuel bottles and is designed to operate at a center-line temperature of 400°C. The center compartment contains 12 fuel bottles and will operate at approximately 1400°C center-line temperature. Total neutron exposure is measured by a stainless steel flux monitor contained within the capsule.

Fueled-Graphite Fabrication

A. J. Taylor J. M. Robbins

Fabrication problems were encountered because of inconsistencies in composition of different batches of liquid phenolic resin used as a binder in fueled-graphite fabrication.[21] Heat treating the resin until a predetermined weight loss occurred eliminated those problems and also cracking during baking.

Studies of dimensional changes[22] throughout the various stages of fabrication showed that spherical graphite-matrix elements can be fabricated by a cold-forming and warm-isostatic-molding technique if the cold forming is done in a properly designed die with an elliptical cavity.

We are investigating the problems involved in fabricating an "emitting" type of fuel element, which contains fine-particle-size (about 10 μ) fuel in a fine-grained porous graphite body and is designed so that gaseous fission products can readily escape.[23] Interest in this concept is based on the potential use of fuel elements of this type in a high-temperature gas-cooled breeder reactor. The approach used in preliminary studies was to incorporate the fuel and fertile material as a sol from an intermediate step of the ORNL sol-gel process. Bodies containing up to 40% heavy metal were prepared without cracking by uniaxial cold pressing followed by heating in hydrogen; matrix densities of 1.5 g/cm^3 were readily attainable. Specimens containing sol-derived $(Th,U)O_2$ will be prepared for evaluation by neutron activation and monitoring of ^{133}Xe released during postactivation heat treatments.

Impact Testing of Graphite Spheres

J. M. Robbins C. O. Smith[24]

Graphite fuel spheres for on-stream fueling of gas-cooled reactors of the pebble-bed type must

[21] J. M. Robbins and A. J. Taylor, *GCR Program Semiann. Progr. Rept. Sept. 30, 1964*, ORNL-3731, p. 58.

[22] A. J. Taylor, *Metals and Ceramics Div. Ann. Progr. Rept. June 30, 1964*, ORNL-3670, p. 192.

[23] A. J. Taylor and J. M. Robbins, *GCR Program Semiann. Progr. Rept. Mar. 31, 1965*, ORNL-3807, p. 33.

[24] Education Division; now at University of Detroit.

withstand repeated drops. A program to develop a fuel sphere to meet the requirements for the German Pebble-Bed Reactor (AVR) focused attention on the machined-shell concept, in which a premolded spherical fuel insert containing pyrolytic-carbon-coated $(Th,U)C_2$ particles in a graphite matrix is cemented in a premachined fully graphitized unfueled shell. Two studies were undertaken: evaluation of impact resistance of commercially available graphite for the shell and determination of the minimum shell thickness required and of the effect of gaps that could exist after fabrication or develop there between the insert and the shell during reactor operation. These studies have been completed.[25]

In the initial study, 1.5-in.-diam spheres machined from four grades of extruded graphite and four grades of molded graphite were dropped from 13 m onto a steel plate until they failed. Grade ATJ graphite was clearly the best and was used almost exclusively in further tests.

The results of free-drop tests on ATJ graphite showed:

1. Impact resistance decreases as drop height increases.
2. Impact resistance depends on specimen size and is best for the smallest specimens.
3. Impact resistance varies from one block to another, and the impact resistance of a given sphere cannot be correlated with its original position in the block.
4. Bulk-density variations between 1.65 and 1.80 g/cm^3 have no effect on impact resistance.
5. All damage occurs within the outer 1.1 cm of 6-cm-diam spheres.
6. Thermal cycling in vacuum can have an adverse effect, but similar cycling in helium or hydrogen has none.

In the fueled-sphere tests, simulated elements (the fueled portion simulated by a sphere of solid CS-312 graphite) were dropped from 4 m onto a bed of graphite spheres until they either failed or survived 75 drops. The surviving elements were dropped from 4 m onto a steel plate until they failed. The results are:

1. The effects of preassembly cleaning, variations in plug-closure torques between 15 and 50 in.-lb, and choice of cement (P-514, C-10, or Hexalon) are negligible.
2. Elements with uncemented inserts are clearly inferior to elements with completely cemented inserts.
3. Shells with 0.8-cm-thick walls are satisfactory for nominal radial clearances between insert and shell of 0.005 to 0.010 in., but 1.0- to 1.2-cm-thick shells are needed for clearances of 0.020 to 0.025 in.

Fabrication of In-Reactor Capsules

E. A. Franco-Ferreira

The fabrication of in-reactor irradiation capsules for various aspects of the GCR program has continued.[26] Included in this year's work have been two ORR loop No. 1 elements and four ORR poolside experiments. One of the loop No. 1 capsules, which is of a more complex design than those built previously, is shown in Fig. 24.12. This experiment used a double capsule, and both parts contained coated-particle fuel. Some of the thermocouples that are used to monitor the capsule operating temperatures are seen in the figure.

Fueled-Graphite Irradiation Tests

J. L. Scott

Our irradiation test program on fueled-graphite spheres containing pyrolytic-carbon-coated UC_2, $(U,Th)C_2$, UO_2, or $(U,Th)O_2$ microspheres was completed. Earlier phases of the program were discussed previously.[27] We prepared 23 irradiation capsules and tested 97 spherical fueled-graphite elements. The major areas investigated were irradiation stability and fission-product retention of fueled-graphite spheres, design and fabrication of shells for fuel elements, dimensional stability

[25] C. O. Smith and J. M. Robbins, *Impact Resistance of Fueled Graphite Spheres for Pebble-Bed Reactor Applications*, ORNL-3723 (January 1965).

[26] E. A. Franco-Ferreira, *Metals and Ceramics Div. Ann. Progr. Rept. June 30, 1964*, ORNL-3670, p. 192.

[27] J. L. Scott, C. Michelson, and R. A. Bowman, *Metals and Ceramics Div. Ann. Progr. Rept. June 30, 1964*, ORNL-3670, p. 191.

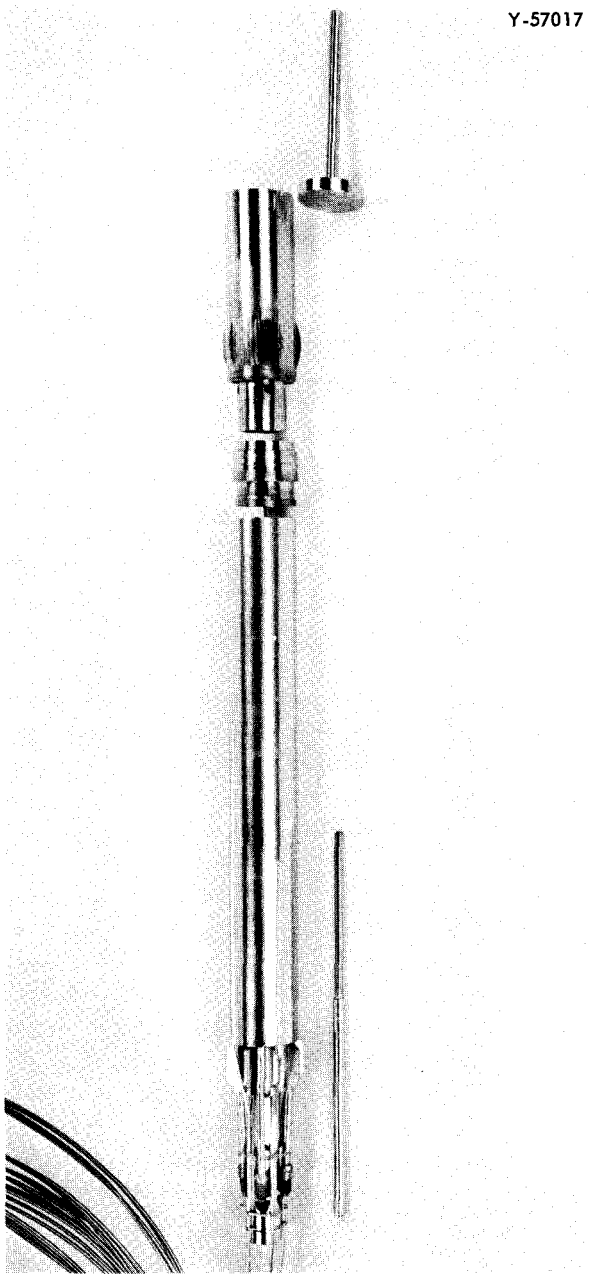

Fig. 24.12. Capsule for Irradiation Studies on Coated-Particle Fuels.

of fuel-element components, thermal conductivity of fuel-element materials and irradiation-induced changes in it, and effects of irradiation on impact and crushing strength of fuel elements fabricated by different processes. Our responsibility was to help in planning the capsule irradiation tests, to load fuel elements into the primary containment, and to aid in the evaluation and interpretation of the results.

Details of the fuel element types, capsule assembly, irradiation testing, and postirradiation examination are reported elsewhere.[28] The highlights of what we learned in this extensive program are briefly summarized below.

Fission-Gas Retention. – Since the fueled-graphite elements are unclad, the coatings on fuel particles must remain intact. Our tests have shown that coated particles made by several commercial vendors and also by ORNL can sustain fuel burnups in excess of 10 at. % of the heavy metal at temperatures as high as 1400°C without coating failures. A few batches of particles have survived burnups in excess of 20 at. % of the heavy metal. When the particle coatings are intact the ratio of the release rate to birth rate of a typical noble gas isotope, such as ^{88}Kr, is about 10^{-4} or less. The source of the observed gas release is uranium contamination rather than broken coated particles. Since there are several ways to reduce contamination levels, we can expect lower release rates from products manufactured in the future.

Thermal Conductivity. – Data from spheres with central thermocouples have been used to calculate effective thermal conductivities for the fueled graphite; these data were central temperature measured as a function of time, temperature adjacent to sphere surface measured as a function of time, and average thermal-neutron flux adjacent to sphere surface. Details have been presented elsewhere.[29] We assumed steady-state spherically symmetrical heat conduction in the sphere and its immediate surroundings and corrected for reduced thermal-neutron flux and altered temperature profile in the sphere due to self-shielding, temperature rise between external thermocouple and the actual outer surface of the fueled graphite, and variation of heat-generation rate during the test.

Calculated thermal conductivities for three instrumented test spheres from irradiation tests

[28] *GCR Program Semiann. Progr. Rept. Sept. 30, 1963*, ORNL-3523; *GCR Program Semiann. Progr. Rept. Mar. 31, 1964*, ORNL-3619; *GCR Program Semiann. Progr. Rept. Sept. 30, 1964*, ORNL-3731; *GCR Program Semiann. Progr. Rept. Mar. 31, 1965*, ORNL-3807.

[29] J. W. Prados, V. A. DeCarlo, and J. L. Scott, *Trans. Am. Nucl. Soc.* 8(1), 37 (June 1965).

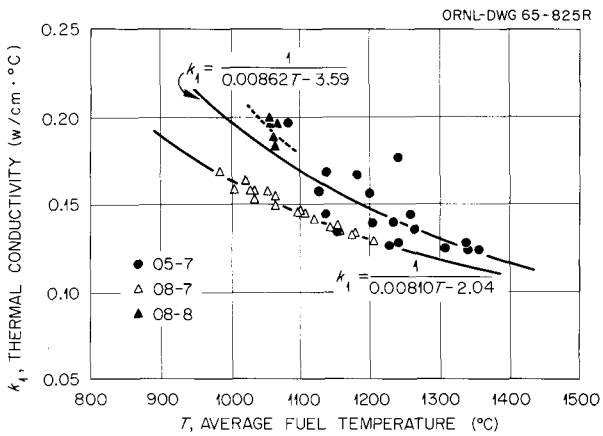

Fig. 24.13. Thermal Conductivity of Fueled Graphite, Derived from Measurements Made During Irradiation.

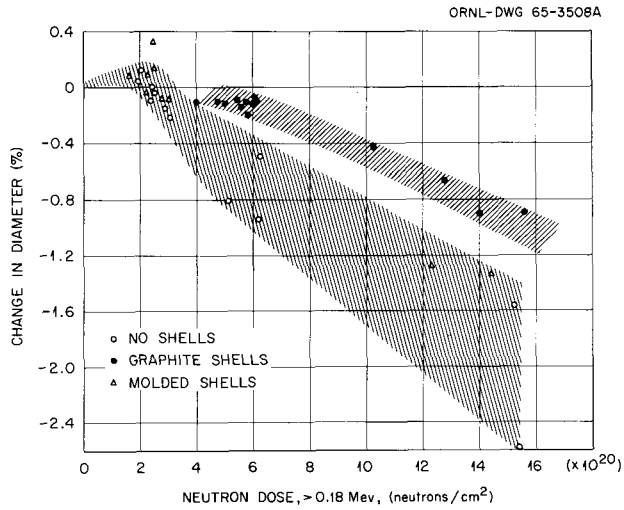

Fig. 24.14. Irradiation-Induced Dimensional Changes of Fueled Graphite Spheres.

designated 05-7, 08-7, and 08-8 are shown in Fig. 24.13 as functions of average fuel temperature. Also shown are least-square curves through the 05-7 and 08-7 points, based on a linear temperature dependence of the reciprocals of the conductivities.

From these results, the thermal conductivities of fueled-graphite bodies are apparently significant functions of temperature and may also depend on materials and fabrication techniques. The results from experiments 08-7 and 08-8 also indicated that the thermal conductivity of fueled graphite is unaffected by irradiation at temperatures above 800°C for thermal-neutron doses of the order of 10^{20} neutrons/cm^2 (approximate conditions for all experiments), since the scatter of the results was random throughout the irradiation tests. This is particularly significant for 08-8, since temperatures were held nearly uniform during its irradiation history. The greater scatter of conductivity values observed with 05-7 suggests an irradiation effect, since the higher values were observed near the start of the irradiation period and the lower values near its conclusion. This we attribute to differential shrinkage of the fueled core relative to the unfueled shell rather than to a change in conductivity of the fueled graphite itself. The separation of shell from core observed during postirradiation examination of the element[30] supports this interpretation.

[30]D. R. Cuneo *et al.*, *GCR Program Semiann. Progr. Rept. Sept. 30, 1964*, ORNL-3731, p. 92.

Dimensional Stability of Fueled Graphite Under Irradiation. – Prompted by the clues in the thermal conductivity data, we undertook a careful analysis of the dimensional changes that resulted in fueled and unfueled graphites from fast-neutron exposure. Pre- and postirradiation dimensions were measured on the fueled-graphite spheres from the various capsules. Data for the 1.5-in.-diam spheres irradiated in the core of the ORR are given in Fig. 24.14. Results showed clearly that molded fueled-graphite bodies shrink at significantly higher rates than do fully graphitized unfueled shells. There were no significant differences between the shrinkage rates of spheres with molded unfueled shells and without unfueled shells. Similar data obtained on 6-cm-diam spheres in ORR poolside capsules indicated a similar differential shrinkage behavior between molded cores and machined shells, except that the shrinkage apparently increased with fast-neutron dose much more for spheres tested above 1000°C than for those tested at 600°C.

The differential shrinkage has two markedly detrimental effects. The resulting gap between the fueled core and the unfueled shell is a thermal barrier so its growth causes the central fuel temperature to rise. Thereby the release of species that diffuse through pyrolytic carbon coatings, such as barium and strontium, is increased. Also, the differential shrinkage markedly reduces the crushing strength and presumably the impact strength of the fuel elements.

From our results one can conclude that a major problem area with spherical fueled-graphite fuel elements has been defined. The solution to the problem lies in the use of more fully graphitized fueled cores or molded unfueled shells. The latter solution was untenable in the core of the AVR reactor, because the abrasion resistance of molded shells is inadequate.

SUPPORTING RESEARCH

Phase Relations in the Pseudobinary UC_2-ThC_2 System[31]

J. L. Cook[32] O. B. Cavin
R. E. Meadows

We have continued our studies of the mixed carbides of thorium and uranium, which have potential use as highly refractory fuel and breeder material for graphite-based gas-cooled reactors.[33,34] This study combined dilatometry, x-ray diffraction, metallography, thermal analysis, and chemical analysis to provide a better understanding of the phase relationships for the UC_2-ThC_2 pseudobinary system. Thermal expansion as a function of temperature up to 1000°C was determined for UC_2, ThC_2, and the $(U,Th)C_2$ alloys using drop-cast and machined specimens.

The microstructural features of all as-cast alloys were similar and all contained excess graphite. Only when annealed above 1500°C for extended periods of time were there significant changes in the microstructure of the carbide or the morphology of the graphite. Microhardness increased slowly with annealing time at 1900°C but did not change significantly at lower temperatures.

Powder x-ray diffraction patterns were generally diffuse and did not improve appreciably with annealing for material that contained much excess graphite. Specimens of ThC_2 that contained only a trace of free graphite gave very sharp diffraction patterns after annealing at 1400°C and below. X-ray diffraction revealed that two distinctly different body-centered tetragonal structures coexisted for alloys in the composition range from 35 to 42 mole % ThC_2.

Dilatometry and thermal analysis clearly showed phase transformations in ThC_2 at 1500 ± 25°C and 1430 ± 10°C. The transformation at the higher temperature was diffusionless. Two similar transformations were observed for ThC_2-rich alloys containing up to 25 mole % UC_2. One phase transformation was observed for UC_2 at 1768 ± 25°C. One solid-state transformation occurred for the $(U,Th)C_2$ alloys in the composition range from 25 to 75 mole % ThC_2. The transformation temperature in this composition range passed through a minimum (approximately 1100°C) at approximately 46 mole % ThC_2.

Two phase diagrams, either of which is consistent with experimental observations, were proposed for the UC_2-ThC_2 pseudobinary system and are shown as Figs. 24.15 and 24.16.

The mean coefficients of expansion for the $(U,Th)C_2$ alloys between room temperature and 1000°C varied from $8.6 \times 10^{-6}/°C$ for ThC_2 to $13.5 \times 10^{-6}/°C$ for UC_2.

Welding of Advanced Alloys

R. G. Gilliland

We have investigated the weldability of two new nickel-chromium alloys strengthened with molybdenum, niobium, and tungsten. These alloys, developed by the International Nickel Company, are designated Inco IN-102 and Inconel 625. Typical chemical compositions of these alloys are as follows:

Element	Analysis (wt %) IN-102	Inconel 625
Chromium	15.50	21.24
Niobium	3.19	3.44
Molybdenum	2.61	9.77
Tungsten	4.04	<0.10
Iron	7.96	3.49
Carbon	0.05	0.02
Nickel	Balance	Balance

These alloys possess properties that make them attractive for application in advanced high-temperature gas-cooled reactors. The results of

[31]Condensed from the University of Tennessee M.S. thesis of J. L. Cook, *Studies of the Thorium-Uranium Dicarbide Pseudobinary System in the Presence of Excess Graphite*, ORNL-TM-1188 (July 1965).

[32]Now with IBM Corp., Lexington, Ky.

[33]N. A. Hill and O. B. Cavin, *Metals and Ceramics Div. Ann. Progr. Rept. June 30, 1964*, ORNL-3670, pp. 192–94.

[34]J. L. Cook *et al.*, *GCR Program Semiann. Progr. Rept. Mar. 31, 1965*, ORNL-3807, pp. 27–33.

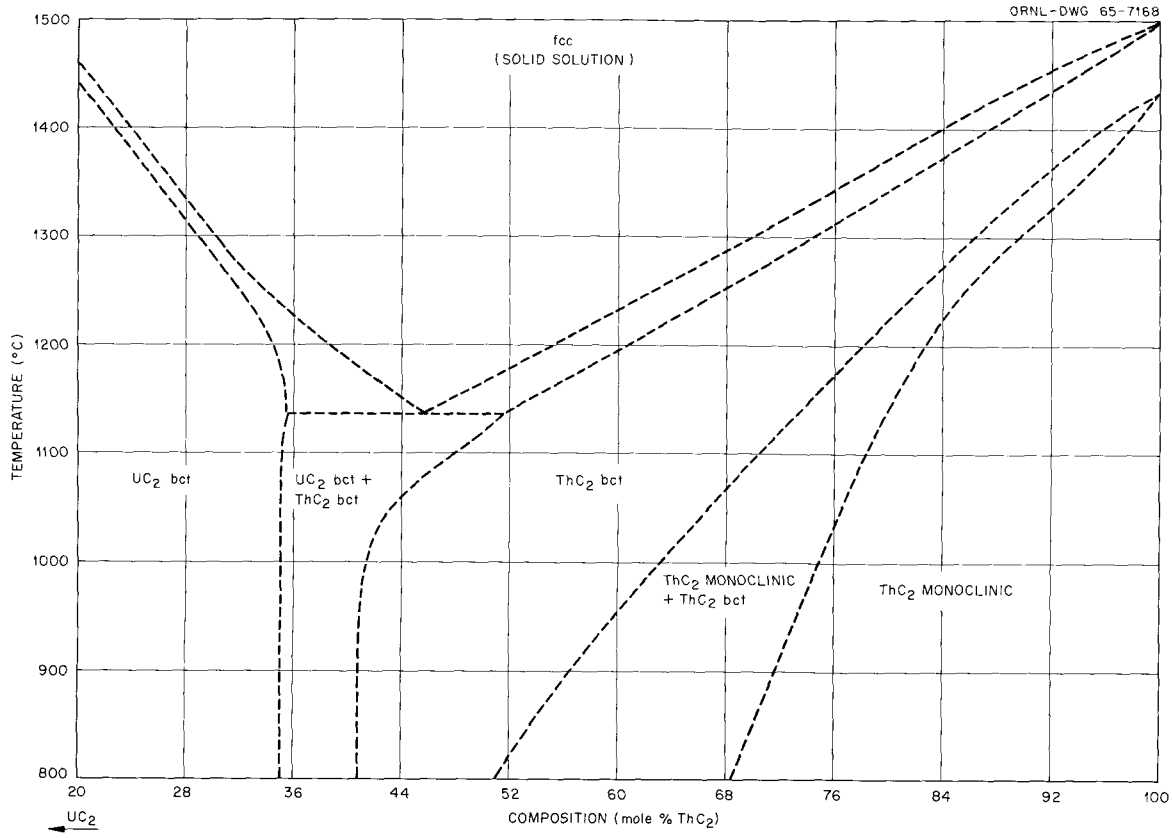

Fig. 24.15. Tentative Equilibrium Phase Diagram for the UC_2-ThC_2 System in the Presence of Excess Carbon.

tensile and stress-rupture properties have already been reported.[35]

Hot-ductility experiments have been performed and the results for Inconel 625 are shown in Fig. 24.17. The data showed the nil-ductility temperatures for these alloys to be 2250°F for Inconel 625 and 2280°F for IN-102. Good recovery of the mechanical properties after heating to the nil-ductility temperature was exhibited for both alloys. Metallographic examination of microstructures of alloys that had been thermally cycled through these temperature ranges did not indicate any apparent liquidation.

In-Reactor Stress-Rupture Testing of Stainless Steel

J. T. Venard J. R. Weir

We performed[36] two types of in-reactor tube-burst tests on a British niobium-stabilized stainless steel containing 20% Cr and 25% Ni. The effect of heat treatment on the stress-rupture properties under constant stress at 650°C is shown in Fig. 24.18. These results show that tubing having a fine-grained structure but with a coarse carbide phase, which was produced by heat treating at 800°C, was unaffected by irradiation but was substantially weaker than solution-annealed tubing. The fracture ductility was improved, however. Although both heat treatments resulted in the same grain size, the tubing annealed at 800°C was more than five times as ductile in out-of-reactor tests and twice as ductile in the irradiation tests.

To study the effect of neutron dose on strength and ductility, we irradiated additional specimens of the solution-annealed tubing at 750°C. The specimens were unstressed at the start of the irradiation. At some time during irradiation, we applied to each specimen a stress that increased

[35] R. G. Gilliland, *Metals and Ceramics Div. Ann. Progr. Rept. June 30, 1964*, ORNL-3670, p. 194.

[36] J. T. Venard and J. R. Weir, *GCR Program Semiann. Progr. Rept. Mar. 31, 1965*, ORNL-3807, pp. 249–53.

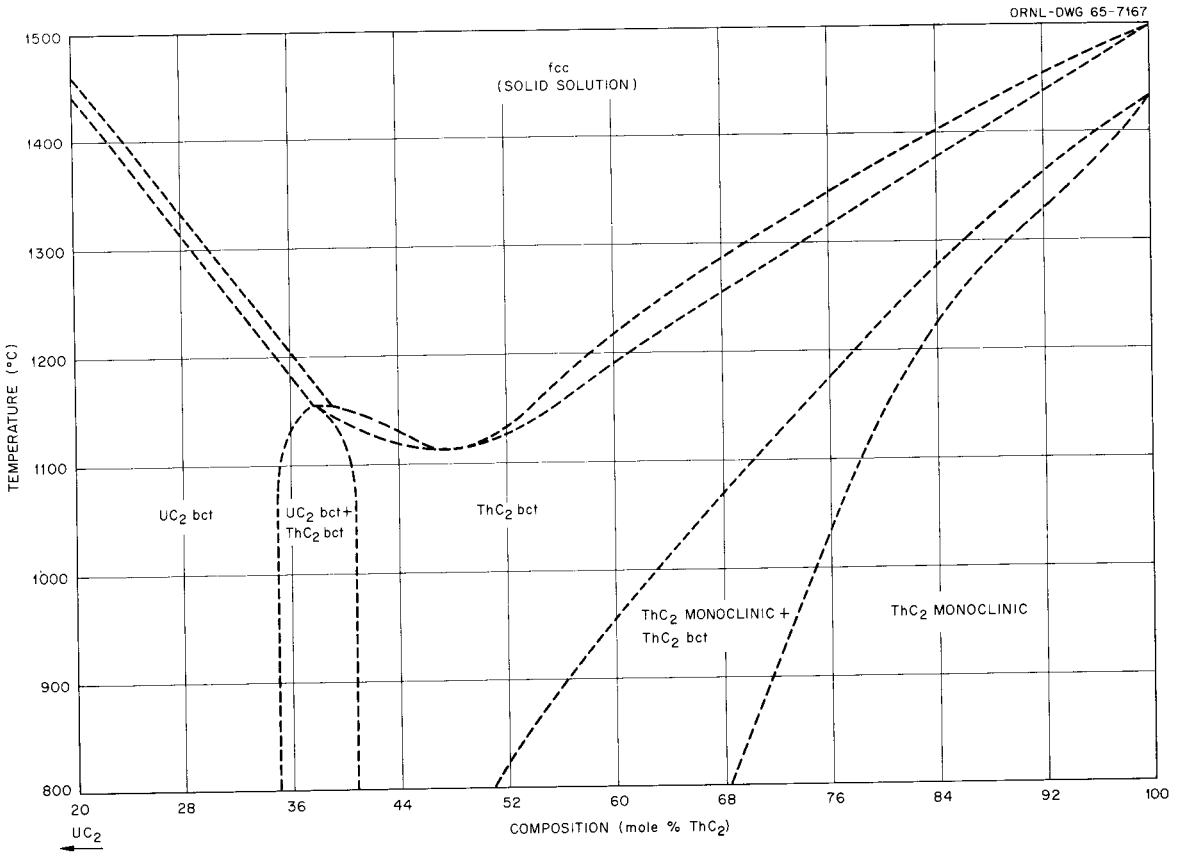

Fig. 24.16. Alternate Equilibrium Diagram for the UC_2-ThC_2 System in the Presence of Excess Carbon.

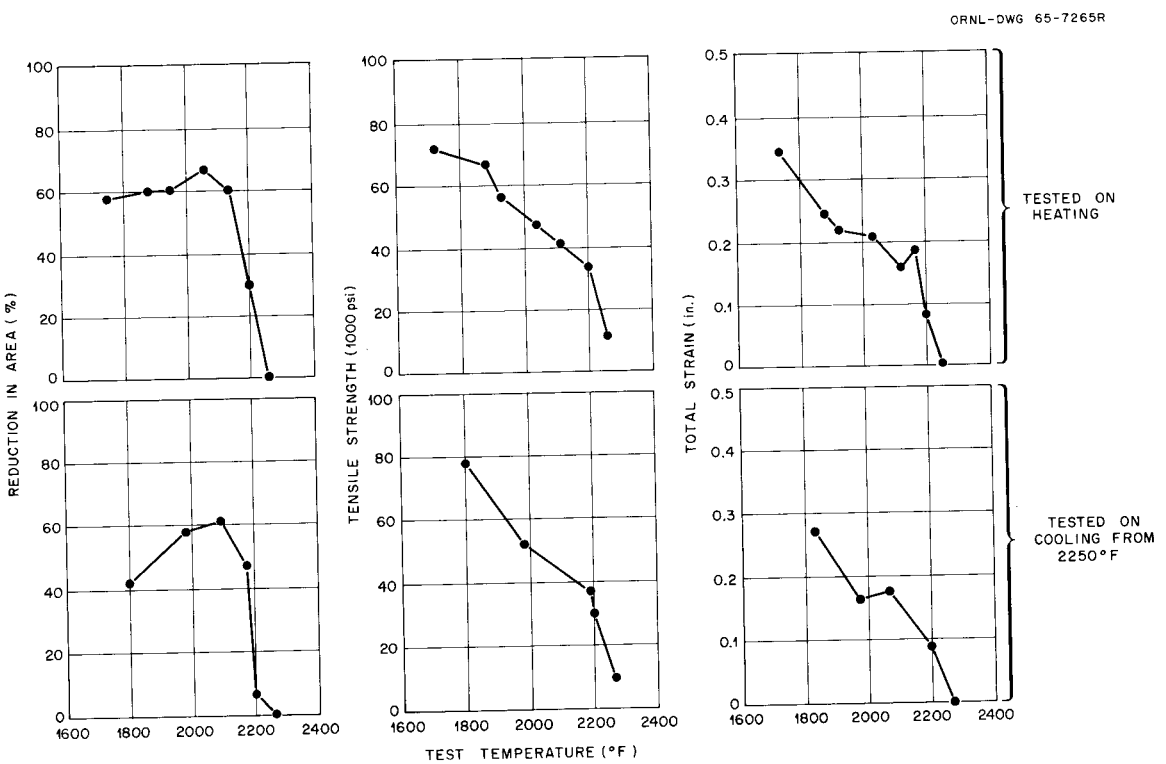

Fig. 24.17. Results of Hot-Ductility Tests on Inconel 625 Alloy. The nil-ductility temperature was found to be 2250°C.

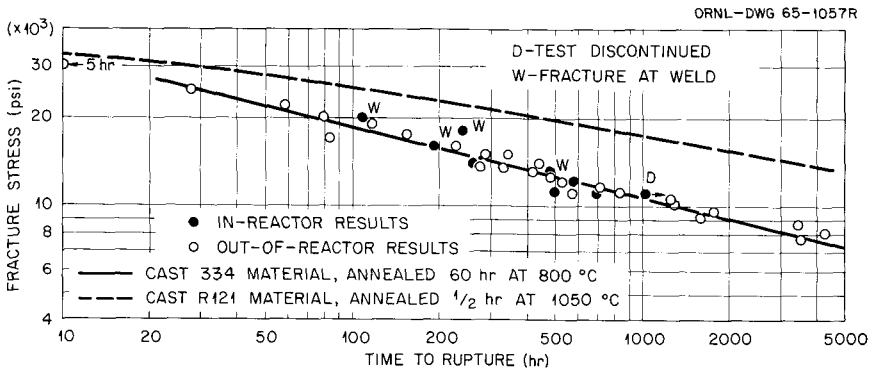

Fig. 24.18. Effects of Heat Treatment and Irradiation on Stress-Rupture Properties of 20% Cr–25% Ni–Nb Stabilized Stainless Steel at 650°C.

with time at a selected constant rate until the specimen failed. The irradiation had no detectable effect on strength, and the fracture ductility was unaffected except at low strain rates on specimens that had received thermal-neutron doses greater than 10^{19} neutrons/cm^2.

An Evaluation of UO_2 Irradiated Above 1600°C

J. L. Scott C. Michelson[37]
E. L. Long, Jr.

We completed[38,39] the examination and evaluation of UO_2 specimens irradiated in four separate capsules at temperatures ranging from 1600 to 2400°C. An analysis of the atmosphere in each capsule indicated that essentially all fission gases formed were released. This was not surprising, since the calculated fuel surface temperature in all capsules exceeded 1900°C.

Metallographic examination revealed[40] that closing of the circumferential and pellet-to-pellet gaps was virtually complete in most regions where the calculated temperature exceeded 1700 to 1750°C. The formation of a dense columnar-grained structure during the first few hours of operation did not appear to retard the subsequent release of fission-product gases. This structure appeared in all specimens where the calculated temperature exceeded 1700 to 1750°C. Numerous lenticular voids were present in these grains in the low-burnup capsule (19 hr in reactor), but none were found in other specimens.

A plot of the maximum grain lengths in the insulating bushings vs the calculated average temperature of the grains, shown in Fig. 24.19, indicates that all specimens had the same general variation in grain size with irradiation temperature. The decrease in the slope of the lines with increasing irradiation time does not appear to have any real significance, although the transition point where the slope of each line changes indicates the temperature at which columnar grain growth predominates. The observed range of 1700 to 1740°C agrees reasonably well with the generally accepted threshold of 1800°C for columnar grain growth in irradiated UO_2.

Thermal Conductivity of AGOT Graphite

J. P. Moore R. S. Graves

Graphite is a useful nuclear material of construction, and, therefore, its high-temperature thermophysical properties are of extreme interest. We are studying some of the numerous types of graphite produced, all of which are anisotropic due to the hexagonal structure and to preferred

[37] On loan from the Tennessee Valley Authority; now at the EGCR site.

[38] J. L. Scott and C. Michelson, *Metals and Ceramics Div. Ann. Progr. Rept. June 30, 1964*, ORNL-3670, pp. 198–99.

[39] J. L. Scott, C. Michelson, and E. L. Long, Jr., *Trans. Am. Nucl. Soc.* 8(1), 37 (June 1965).

[40] C. Michelson *et al.*, *GCR Program Semiann. Progr. Rept. Mar. 31, 1965*, ORNL-3807, pp. 253–62.

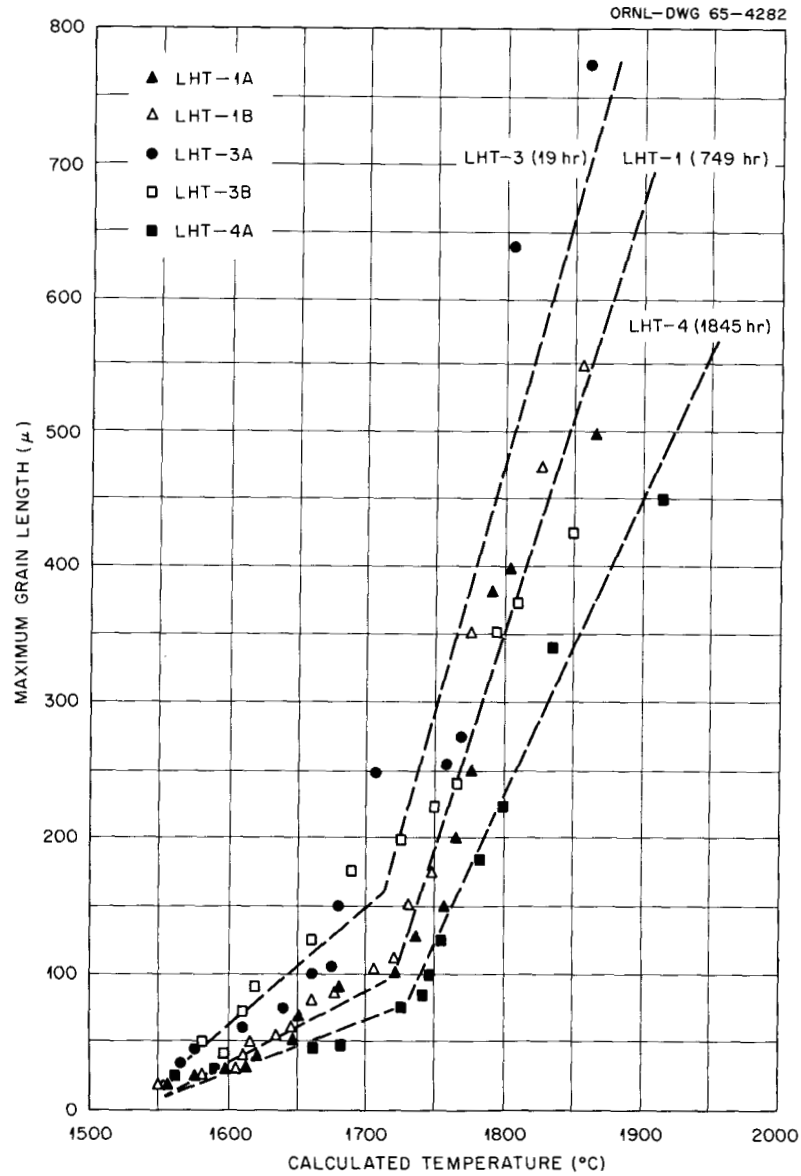

Fig. 24.19. Metallographic Measurements of Maximum Grain Length in Depleted UO_2 Irradiated at High Temperatures.

orientations developed during extrusion. We found that the total thermal resistivity of an AGOT specimen perpendicular to the extrusion direction can be described to ± 0.5% by

$$R = 0.1935 + 1.6246 \times 10^{-3}\, T - 1.229 \times 10^{-7}\, T^2 ,$$

where T is in °K and R is in cm °C w^{-1}. The thermal conductivity of this specimen in this direction was 30% greater at 50°C than that of the CGB graphite that we had previously measured,[41] but it was only 5% greater at 900°C. Since the AGOT specimen was significantly less dense than the CGB, the difference in thermal conductivity must be attributed to a preferred orientation effect. These AGOT graphite results form the base-line comparison for low-temperature thermal-conductivity measurements on the AGOT graphite specimens to be obtained and tested during the EGCR Graphite Surveillance Program.

[41] J. P. Moore and T. G. Godfrey, *Metals and Ceramics Div. Ann. Progr. Rept. June 30, 1964*, ORNL-3670, pp. 199–200.

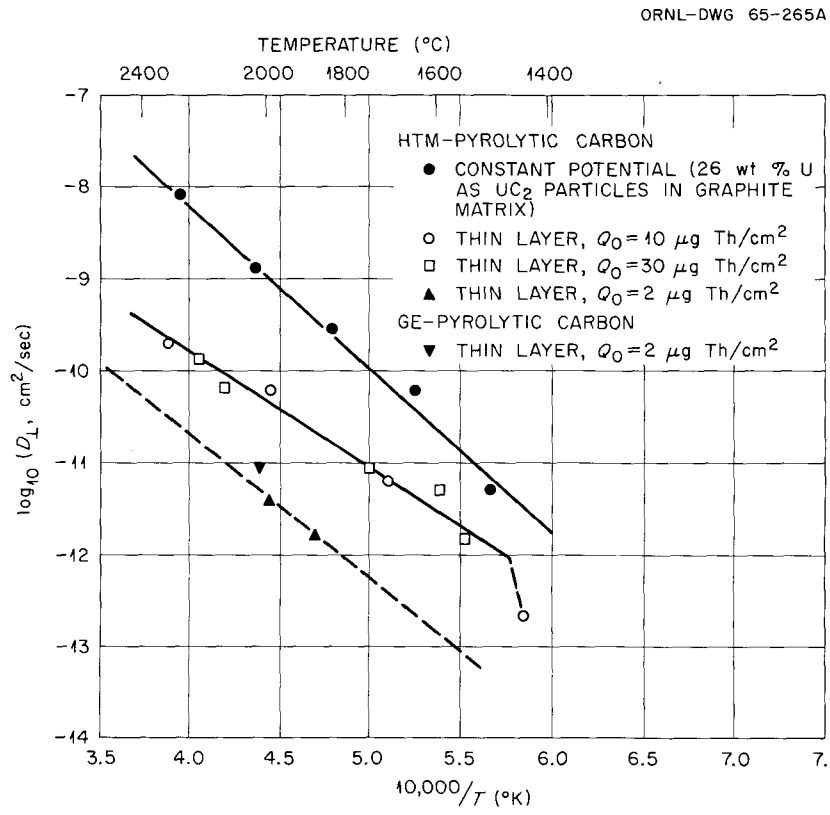

Fig. 24.20. The Effect of Thorium Concentration on the Perpendicular-Direction Diffusion Coefficients in Pyrolytic Graphite. Our measurements with a 2-$\mu g/cm^2$ deposit are compared with measurements by Evans *et al.* for thorium at higher concentrations, and uranium at a still higher concentration.

Effects of Pyrolytic-Graphite Structure on Diffusion of Thorium[42]

F. L. Carlsen, Jr.[43]

Studies of the effects of structure on diffusion of thorium in pyrolytic graphite are of interest in view of the recent development of graphite-matrix fuel elements for nuclear reactors. We have determined diffusion coefficients for thorium in pyrolytic-graphite specimens having a wide range of structural properties in the 1850 to 2000°C temperature range. The specimens included pyrolytic graphites from two sources, both as deposited and heat treated at temperatures of 2200 to 2700°C for times of 1 to 4 hr, and a pyrolytic graphite that had been hot pressed at 3000°C.

Interlayer spacing, crystallite size, preferred orientation of crystallites, microstructure, and porosity were the structural properties considered likely to have the greatest significance and thus emphasized in this research.

The structures of the two as-deposited pyrolytic graphites were very similar. The only significant difference was that one had many microcracks that were parallel to the deposition plane.

The diffusion coefficients for thorium in the direction perpendicular to deposition plane were nearly the same for the two as-deposited pyrolytic graphites, but the pyrolytic graphite with many microcracks had a much higher diffusion coefficient in the direction parallel to the deposition plane.

The structural changes that occurred during heat treatments at temperatures of 2200 to 2700°C did not reduce the diffusion coefficient of either material. The hot-pressed pyrolytic graphite had structural properties that were very close to those of ideal graphite, and the perpendicular diffusion coefficient at 2000°C was less than 9×10^{-14}

[42]Condensed from the University of Tennessee M.S. thesis of F. L. Carlsen, Jr., ORNL-TM-1080 (June 1965).

[43]Now with Stellite Div., Union Carbide Corp., Kokomo, Ind.

cm^2/sec. In this sample, the very large number of microcracks in the parallel direction resulted in a very large parallel diffusion coefficient.

The diffusion process was very dependent upon the concentration of thorium, as shown in Fig. 24.20. The diffusion coefficients measured in the present experiments, in which 2 $\mu g/cm^2$ Th was placed on the samples, were approximately one-tenth those measured in previous experiments.[44,45] This concentration effect resulted in an apparent time dependence of the coefficients measured in thin-layer experiments.

Autoradiographic studies showed that in +c-direction diffusion thorium penetrated slightly deeper into the interior of the growth cones than it did at their boundaries. The penetration depth within the growth cones increased with the diameter of the cones.

A qualitative mechanism that is consistent with the experimental observations was developed for the diffusion of thorium in as-deposited pyrolytic graphite.

Effects of Deposition Conditions and Heat Treatment on the Properties of Pyrolytic Carbon

J. Y. Chang[46] E. E. Stansbury[47]
W. O. Harms

This study was part of the program to provide a better understanding of the effect of deposition conditions and heat treatment on the basic properties of pyrolytic carbon deposited from methane gas. Deposits up to 1 mm thick were formed on direct-resistance-heated graphite substrates (Type ATJ, 1 × 6 × 80 mm) over the temperature range 1400 to 2400°C at deposition rates ranging from 3.2 to 2810 μ/hr. The material deposited at 2200°C was heat treated at 2620°C for periods up to 6 hr. The deposits were characterized by microstructure studies and measurements of density, unit cell height, crystallite size, diamagnetic susceptibility, and preferred orientation (by x-ray diffraction analysis and diamagnetic susceptibility). Details of the experimental procedures and results have been published[48] and are summarized below.

The density of each deposit decreased with increasing distance from the substrate. The values increased with deposition temperature from 1.17 to 1.43 g/cm^3 at 1600°C to 1.96 to 2.21 at 2400°C.

The unit-cell height decreased from 6.846 to 6.740 A as the deposition temperature was increased from 1600 to 2400°C. Heat treatment of the 2200°C deposit at 2620°C for 6 hr changed the unit cell height from 6.778 to 6.738 A.

The crystallite size in the c-axis direction varied from 100 to 245 A over the deposition-temperature range 1600 to 2400°C. For the 2200°C deposit, heating 6 hr at 2620°C changed the crystallite size from 170 to 220 A.

The diamagnetic susceptibility, corrected for ferromagnetic impurities, was measured in directions parallel, χ_{oz}, and perpendicular, χ_{ox}, to the deposition plane. The value of χ_{oz} changed from -4.44×10^{-6} to -18.7×10^{-6} emu as the deposition temperature increased from 1600 to 2000°C; the value then changed to 10.56×10^{-6} emu at 2400°C. Between 1600 and 2000°C, χ_{ox} remained essentially constant at -2.4×10^{-6} emu and changed to 1.32×10^{-6} emu at 2400°C. Heat treatment at 2620°C on specimens deposited at 2200°C changed χ_{ox} smoothly from 1.58×10^{-6} to 1.07×10^{-6} emu in 160 min but changed χ_{oz} little from its value of 12.64×10^{-6} emu for as-deposited material.

Anisotropy factors, determined by x-ray diffraction techniques,[48,49] increased from 2.0 to 14.6 for deposition temperatures from 1600 to 2400°C. The value for the 2200°C specimen was increased from 12.1 to 24.3 by heat treatment for 160 min at 2620°C. Anisotropy factors determined directly from experimental values of χ_{oz}/χ_{ox} showed a similar trend but were somewhat lower than the x-ray diffraction values, ranging from 1.8 to 8 for temperatures of 1600 to 2400°C and including a value of 12.0 for the heat-treated specimen.

---

[44] R. B. Evans III, J. O. Stiegler, and J. Truitt, *Actinide Diffusion in Pyrocarbon and Graphite*, ORNL-3711 (1964).

[45] R. B. Evans III, J. L. Rutherford, J. O. Stiegler, and J. Truitt, *Reactor Chem. Div. Ann. Progr. Rept. Jan. 31, 1965*, ORNL-3789.

[46] On temporary assignment at ORNL under an IAEA Fellowship; now at the University of Tennessee.

[47] Consultant from the University of Tennessee.

[48] University of Tennessee M.S. thesis of J. Y. Chang, *Studies on Effects of Deposition Conditions and Heat Treatment on the Properties of Pyrolytic Carbon*, ORNL-3764 (March 1965).

[49] F. L. Carlsen, Jr., *GCR Program Semiann. Progr. Rept. Sept. 30, 1964*, ORNL-3619, pp. 6–16.

25. High Flux Isotope Reactor

G. M. Adamson, Jr.

The High Flux Isotope Reactor (HFIR)[1] is being constructed at ORNL to provide a high flux density that may be used to provide research quantities of the transplutonium elements. This reactor is designed to produce 5×10^{15} neutrons cm^{-2} sec^{-1} with an average power density of 2000 kw/liter and a total power of 100,000 kw. In spite of the high power density, aluminum is being used as the structural material for both the fuel element and the control rods.

The fuel core for this reactor consists of only two fuel elements containing 171 and 369 plates 0.050 in. thick. Each plate consists of a dispersion of U_3O_8 in aluminum powder and is clad with aluminum. To minimize flux peaking and thereby reduce the hot-spot temperature, the fuel content of each plate is varied nonlinearly across the width. In addition, the plates are formed into an involute configuration so that the coolant channels are equal and uniform in width and thus all surfaces are cooled uniformly. Also, a burnable poison (B_4C) is added to each plate and its concentration varies opposite to that of the fuel. Finally, extremely close tolerances are required for both the fuel concentrations and the dimensions.

The control rods for this reactor are also unique. They consist of eight plates arranged in two cylinders, which fit concentrically around the fuel element; each cylinder is about 18 in. in diameter × 5 ft long. Each plate is unusual in that it contains four regions of different neutron-absorbing characteristics. On each end is a transparent region of all aluminum. In the center are two regions of different "blackness"; these are adjacent dispersions, one of tantalum and the other of europium oxide in aluminum. All parts are clad with aluminum.

[1]F. T. Binford and E. N. Cramer, *The High Flux Isotope Reactor – A Functional Description*, vol. 1, ORNL-3572 (May 1964).

FUEL ELEMENT

The primary effort in the fuel element program has consisted of completion of the first reactor core loading as well as a prototype flow element for use during nonnuclear testing. Assistance and direction were given to the fuel element fabricator, enabling him to start production of fuel plates for later loadings. The fuel element designs have remained essentially the same, with only minor changes in the side plates and combs.

Fuel Element Manufacturing

R. W. Knight G. M. Adamson, Jr.

Through the past year Metals and Controls, Inc.[2] (M&C), working under an ORNL subcontract, has been gearing the HFIR fuel element manufacture to a production basis. Presently, all processes and tooling are ready for production except the fuel plate attachment welds for the outer annulus. This welding development should be completed within the month. As yet, no major changes in the HFIR specifications[3] have been required.

The fuel plate fabrication program was carried through the manufacture of dummy and depleted plates and is presently being tested with enriched material. A qualification run was completed for the inner plates and production has now commenced. The outer plates did not qualify and the die contour is being changed.

Welding procedures developed at ORNL were adapted to M&C operations and successfully qualified for both the end fitting and comb attachment welds. Fuel plate attachment welds are

[2]A division of Texas Instruments, Inc., Attleboro, Mass.

[3]G. M. Adamson, Jr., and J. R. McWherter, *Specifications for High Flux Isotope Reactor Fuel Element (HFIR-FE-1)*, ORNL-TM-902 (August 1964).

being made with fully automated equipment resembling that which we developed. Acceptable procedures for all except those for the large outer tube were achieved. Difficulty with burn-through was encountered with the thick outer tube. Our work indicates that a lower preheat temperature should alleviate this problem.

To assure that the finished fuel element meets the tight specifications, quality control has been carefully factored into all phases of the operation. A quality control program has been set up to statistically analyze the final product data. The information will be used to determine the capabilities of the process and thereby permit the writing of better specifications.

The x-ray attenuation instrument developed for determining homogeneity of the HFIR fuel plates[4] has now been demonstrated on a production basis and turned over to the fabricator for routine operation. The production models are fully automated and transistorized and have been shown[5] to operate satisfactorily at speeds up to 250 in./min. The instrument has sufficient accuracy that it has been used to reveal changes in the uranium loading for the fuel plates.

In the early stages of the development at the fuel fabricator's plant, difficulty arose with the quality of the uranium oxide. The difficulty became apparent through indications on the scanner of excessive fuel loadings. We found (see below under "Uranium Homogeneity" and "Fuel Plate Fabrication") the problem to be excessive fragmentation of the oxide during fabrication. The oxide did not conform to the specifications, and when a satisfactory agreement could not be reached with the producer, a switch was made and oxide fuel produced by the Y-12 Plant of Union Carbide Corporation was adopted for the remainder of the production.

Fuel Plate Fabrication

J. H. Erwin M. M. Martin
W. J. Werner J. P. Hammond
C. F. Leitten, Jr.

Our work has been directed primarily toward the evaluation of fuel plates fabricated for the first reactor core.[6] It culminated with the successful forming of the plates and assembly of the inner- and outer-annulus fuel elements.

The inspection requirements for the fuel plates are set forth in the specification for HFIR fuel elements.[3] They include dimensions and weight of the pressed duplex fuel compacts, core location and dimensions of the machined plates, blister formation, metallurgical bond imperfection, fuel distribution, surface impairment, and formed curvature. Table 25.1 summarizes the data on flat plates and, for comparison, shows similar results for plates made for the third HFIR critical experiment (HFIRCE-3). With the exception of blistering, the rejection rates from the various inspections on fuel plates of reactor core No. 1 increased significantly. Dimensional rejects of inner plates resulted from excessive interference of some fuel compacts during billet assembly and difficulty during rolling with mill conditioning, parallel travel of the billets through the mill, and attempted maximizing of the core length. A single shearing error accounted for 80% of the outer plates rejected for dimensions; however, we successfully held the ±0.024-in. tolerance on the location of the inner and outer edges of the fuel core on the remaining outer plates. Airborne particles of iron oxide that deposited on a few plates during rolling produced the surface rejects. Unfortunately, the inclusions became evident only when the completed plate was etched prior to assembly of the element.

The outer-annulus fuel plates for the first reactor core were inhomogeneous in comparison with similar HFIRCE-3 plates, as indicated in Table 25.1, and more were rejected for ultrasonically detected nonbonds. These problems stem primarily from U_3O_8 buildup, which in many cases exceeded the +27% spot tolerance on uranium. The nonbond indications, which occurred predominantly near the core ends, were under certain conditions related to this clumping of U_3O_8 particles, as described below under "Uranium Homogeneity."

A review of the materials and the production sequences showed that the U_3O_8 and aluminum powders were similar to those used during the HFIRCE-3 production. The compacts were consolidated at 22.5 tsi, which is the same pressure

[4] J. H. Erwin, *Metals and Ceramics Div. Ann. Progr. Rept. June 30, 1964*, ORNL-3670, pp. 206–8.

[5] The instrument work was under the direction of J. Reynolds of the Instrumentation and Controls Division. The scanning was under the direction of K. K. Klindt of the Inspection Engineering Department.

Table 25.1. Summary of HFIR Fuel Plate Fabrication Data

	Inner Element		Outer Element	
	HFIRCE-3	Reactor	HFIRCE-3	Reactor
Number of plates required	187	171	385	369
Duplex powder metal compacts				
Number of compacts pressed	209	216	456	529
U_3O_8 in fuel region, wt %	30.16	30.16	41.44	41.44
B_4C in filler region, wt %	0.39	0.67	0	0
Dimensions of the fabricated plate, in.				
Width	3.562 ± 0.002	3.646 ± 0.002	3.235 ± 0.002	3.215 ± 0.002
Length	24.000 ± 0.010	24.000 ± 0.010	24.000 ± 0.010	24.000 ± 0.010
Thickness	0.050 ± 0.001	0.050 ± 0.0005	0.050 ± 0.001	0.050 ± 0.0005
Dimensions of the fuel region in the fabricated plate, in.				
Width	$3.054^{+0.023}_{-0.016}$	$3.060^{+0.014}_{-0.008}$	$2.773^{+0.013}_{-0.015}$	$2.753^{+0.010}_{-0.013}$
Length	$20.250^{+0.360}_{-0.281}$	$20.273^{+0.745}_{-0.352}$	$19.975^{+0.431}_{-0.412}$	$20.120^{+0.611}_{-0.245}$
Rejection percentage				
Duplex compacts				
Weight	0.5	1.4	0	0
Dimensions	0	0	0	0
Other	1.0	0	0	1.5
Fabricated plate				
Dimensions	0.5	12.7	0.4	8.4
Blisters	0	2.3	4.6	4.4
Nonbond	2.0	6.1	2.9	10.2
Fuel distribution	0	2.8	0	8.4
Surface	0	0.9	0.2	4.0

that was used for the critical-experiment compacts. Use of a pressure of 45 tsi was previously incorrectly reported.[6] During fuel compact production for the outer-annulus plates, however, the building cooling system was out of order and, consequently, the air in the powder metallurgy laboratory was hot and humid. Therefore, we think water condensed in the blending bottles and resulted in clumps of aluminum or U_3O_8 in the blends. We also believe the high end effects in the rolled plates are due to the humidity; that is, the wet powders were more liable to stick to the sides of the die than dry powders.

[6] J. H. Erwin, W. J. Werner, and R. W. Knight, *Metals and Ceramics Div. Ann. Progr. Rept. June 30, 1964*, ORNL-3670, pp. 201–4.

In the light of the high percentage of inhomogeneous outer fuel plates, we determined the critical parameters in the powder metallurgy blending procedures. To simplify the operation, uncontoured fuel compacts of the same volume and composition as the outer-annulus fuel section were studied by visual observation of high-contrast radiographs. First, we concentrated on determining the effect of alcohol addition to the powder mixture. Although good compacts were produced, they were not superior to dry blended compacts made from comparable powders. We then extended the study to include container geometry, particle size distribution, and moisture content of the U_3O_8 and aluminum powders. The two moisture levels tested were 0.08 and 0.003% as determined in vacuum fusion analysis. Parameters held constant were the 24-rpm oblique blending rate, the U_3O_8 particle-size distribution, the 4-oz blending volume, and the 2-hr blending time.

The best blending results used a high-moisture-content U_3O_8. Additionally, the 80% −400 mesh aluminum powder and a spherical blending container produced good homogeneous compacts. The blending procedure for HFIRCE-3 and reactor compacts had called for dry U_3O_8, dry aluminum, cylindrical blending container, and 80% −400 mesh aluminum powder. Under these conditions, the experiment indicated acceptable compacts. The experiment also showed, however, that wet aluminum (the equivalent of wet blending bottles) would increase significantly the degree of segregation. Furthermore, there is good indication that the blending procedure can be optimized with a correct choice of blending container, aluminum particle size distribution, and dispersant blending additives to produce a higher quality compact for plate fabrication.

Table 25.2 summarizes the curvature data obtained from the low-pressure marformed plates and compares them with similar values descriptive of HFIRCE-3 plates. The standard deviations of 2.52 and 4.34 mils, respectively, for the inner and outer plates indicate good forming reproducibility for all the plates. This represents considerable

Table 25.2. Forming Duplication of HFIR Fuel Plates as Shown by Deviation in Curvature Comparator Measurements Taken at the Center of the Involute

	Inner Annulus		Outer Annulus	
	HFIRCE-3	Reactor	HFIRCE-3	Reactor
Number of plates measured	186	171	393	369
Number of plates in statistical sample	20	171	50	369
Duplication of individual measuring points along the line,[a] mils				
Maximum range	6	9	24	17
Average standard deviation[b]	2.82	2.52	7.28	4.34
Range of all measurements,[a] mils	17	21	28	20
Standard deviation[b]	7.64	10.00	9.24	8.56
Curved width (chord), in.				
Top	3.308 ± 0.004	3.388 ± 0.006		3.122 ± 0.006
Center	3.314 ± 0.005	3.395 ± 0.007		3.128 ± 0.006
Bottom	3.307 ± 0.006	3.386 ± 0.009		3.121 ± 0.004

[a]Measurement down line taken at seven equidistant positions.

[b]95% confidence level.

improvement over the standard deviation of 7.28 mils for the outer critical plates. The inner plates require more bending to form the specified involute than do the outer plates. We attribute the significantly small variation of the inner plates to the greater amount of cold work necessary to produce the additional curvature. Differences between the standard deviation for all measuring points along a single traverse and for the individual points are caused by a saddle effect at the center of the fuel plate.[6] The greater chord width shown for the center position in Table 25.2 also indicates this catenary-type curve that exists in the length direction of the plate when the convex side is faced upward. Since this longitudinal curvature has not interfered in assembly of the elements, we did not modify the forming dies to compensate for the springback differences between the fueled and unfueled areas of the plate.

Boron Distribution in HFIR Inner-Annulus Fuel Plates

M. M. Martin C. F. Leitten, Jr.

To minimize the radial peak-to-average powder density ratio in the HFIR, the fuel and poison surface densities in each plate vary nonlinearly across the width, but they are specified to be constant along the length. For maximum effectiveness the ^{10}B, included only in the inner plates in the form of B_4C of natural isotopic content, is added to the aluminum filler piece rather than to the fuel-bearing portion of the duplex core. Previously,[7] the boron distribution was evaluated only at fixed coordinate positions. To conclude the work, we statistically fitted the data to a quadratic equation to permit extrapolation to other regions of the plate. From the data for HFIRCE-3 plates, the derived equation is:

$$Bc = 537.0 - 411.0\,W + 102.6\,W^2 + 0.17\,L^2\,, \quad (1)$$

where Bc is the natural boron content of 0.5-in.-diam punchings in μg, W is the width coordinate ($0.60 \leqq W \leqq 2.85$ in.), and L is the length coordinate measured from the plate center ($L \leqq \pm 8.00$ in.). The 95% confidence interval for the predicted observation is ± 23 μg for an individual value and ± 4 μg for the average of six values.

[7]M. M. Martin, *Metals and Ceramics Div. Ann. Progr. Rept. June 30, 1964*, ORNL-3670, p. 206.

Equation (1) shows that the length coordinate gives a small but significant contribution to the boron content of the punchings. It predicts a gradual increase in boron from the center to the ends of the central 16 in., reaching 9% at $L = \pm 8$ in.

The corresponding relationship derived for the inner plates of the first reactor core is

$$B = 1.724\,Bc\,, \quad (2)$$

where B is the natural boron content in a 0.5-in.-diam punching and Bc is the similar content for the critical-experiment plate given by Eq. (1) for the corresponding location. The multiplier of Bc resulted from a 70.5% increase in boron content specified for these plates and reduction of the experimental error. Equation (2) predicted successfully the boron content in 20 punchings from one reactor plate. In the test, samples were taken randomly from within the coordinate limits $0.60 \leqq W \leqq 2.85$ in. and $L \leqq 8.00$ in. and analyzed chemically for boron. The maximum differences between the analytical results and the predicted values were +5.4% and −4.3%; this excellent agreement attests to the validity of the derived equations. The distribution of boron in this plate appears to be fairly homogeneous within the coordinate limits that were examined. The largest deviations between the analytical results and the specified values were +11.1% and −4.8%.

We could not extend the usable limits of the boron equation to include values of L up to $\pm 9\frac{1}{4}$ in. The boron contents of 0.5-in.-diam punchings decreased significantly beyond $L = \pm 8$ in., while the equation predicts a slight increase. At $L = \pm 9\frac{1}{4}$ in., the average boron content of the punchings was approximately 12% below the expected value. These samples, however, are well within the allowable boron variation of ±35%.

Welding and Machining

J. W. Tackett

During the past year we successfully manufactured two complete fuel assemblies, both by the all-welded concept. This concept, its joint requirements, the welding problems peculiar to it, and the methods developed to evaluate the weld joints in accordance with the HFIR design

requirements have been described.[8] The first fuel assembly was manufactured to check out the complete assembly, welding, and machining procedures and to provide an element for use during preliminary reactor testing. It contained plates fueled with depleted uranium but otherwise met all the basic reactor requirements. The second fuel assembly manufactured is intended to be the first core loading for use during the reactor start-up. The outer element of this assembly is shown in Fig. 25.1 during final inspection.

Very rigid requirements were imposed on the manufactured fuel assemblies by the reactor design specifications. These included the fuel plate spacing, the fuel plate attachment to the support tubes, and the roundness and wall thickness of the support tubes after final machining. Both fuel assemblies manufactured this year satisfied the basic reactor requirements. After assembly and welding of each complete unit, 17,820 plate-spacing measurements were made (5643 on the inner element and 12,117 on the outer element). These were obtained from 33 measuring positions (3 radial and 11 axial) from each water channel. Table 25.3 summarizes the plate-spacing data obtained from both fuel assemblies.

[8]J. W. Tackett, *Metals and Ceramics Div. Ann. Progr. Rept. June 30, 1964*, ORNL-3670, pp. 204–5.

Fig. 25.1. HFIR Outer Element During Dimensional Inspection.

The integrity of the welds joining the fuel plates to the support tubes of the elements was demonstrated with quality control samples welded by procedures identical with those used in manufacturing the elements. The quality control samples were then sectioned through the center line of the weld and prepared for metallographic examination. Typical sectioned samples are shown in Fig. 25.2 and illustrate the excellent attachment achieved. The sample noted as QC-1 was representative of the welds made on the No. 1 support tube (the inside support tube of the inner element) and the No. 3 support tube (the inside support tube of the outer element). Sample QC-2 was representative of the No. 2 support tube (the outside support tube of the inner element) and QC-4 was representative of the No. 4 support tube (the outside support tube of the outer element). We intended originally that only one quality control sample, QC-1, would be required. However, we soon realized that the welds for the inner and outer tubes were significantly different. In addition, a change in design, which simultaneously increased the thickness of the outer tube and decreased the depth of the weld land (both significant changes), required a separate test sample. The 100-lb pullout strength required for the weld joints was demonstrated on mechanical property specimens obtained from a cylindrical No. 1 support tube sample with flat plates protruding radially from its outer surface. Pullout strengths in the 160- to 260-lb range were obtained.

Several assembly, welding, and machining problems were encountered but were satisfactorily solved prior to the manufacture of the first reactor assembly. One of the major welding problems was associated with the inadequacies of the original welding equipment, including welding power supply, the electrode-wire feeding equipment, and the weld programming equipment. The exacting joint requirements and the significant effects of small variations in arc voltage, arc

Table 25.3. Summary of Plate Spacing on HFIR Fuel Assemblies

	Preliminary Fuel Assembly		First Reactor Fuel Assembly		Design Requirements
	Inner	Outer	Inner	Outer	
Number of measurements	5643	12,177	5643	12,177	
Number of channels measured	171	369	171	369	All
Maximum measurement, mils	57	55	56	52	60
Minimum measurement, mils	46	44	44	44	40
Average channel thickness, mils[a]	51.0	48.8	49.9	48.4	50
Maximum average channel cross section, mils	53	52	52	51	56
Minimum average channel cross section, mils	48	47	47	46	44

[a]The average thickness of the channels was calculated at each of the eleven axial measuring positions for every channel.

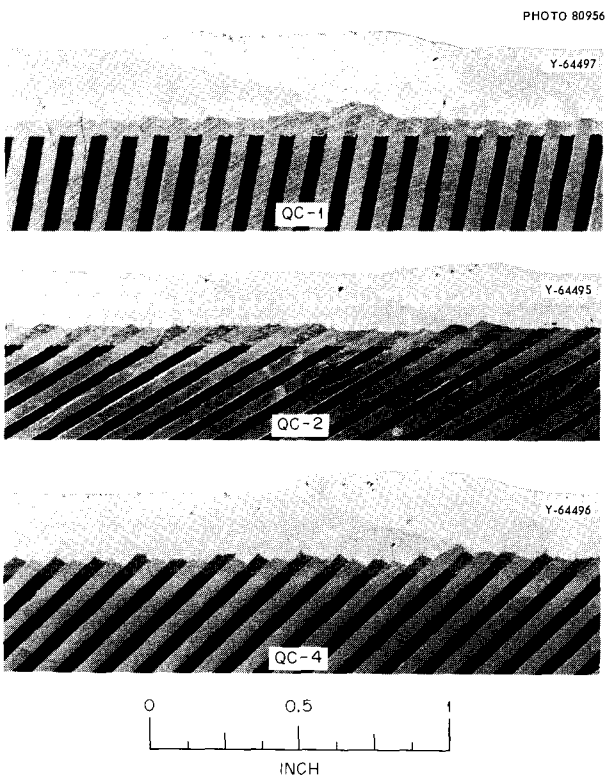

Fig. 25.2. Typical Quality Control Samples for Welds of Fuel Plates to the Support Tube. See text for explanation of specimen numbers.

current, and wire velocity dictate that rigid control over these variables be maintained. We could not accurately control or repeat welding parameters, so special equipment, shown in Fig. 25.3, was acquired. This consists of a commercial power supply and a commercial wire feeder, both built to our specifications, and a welding programmer designed and built at ORNL. Both the power supply and wire feeder had direct-reading high-resolution dials combined with fast-response

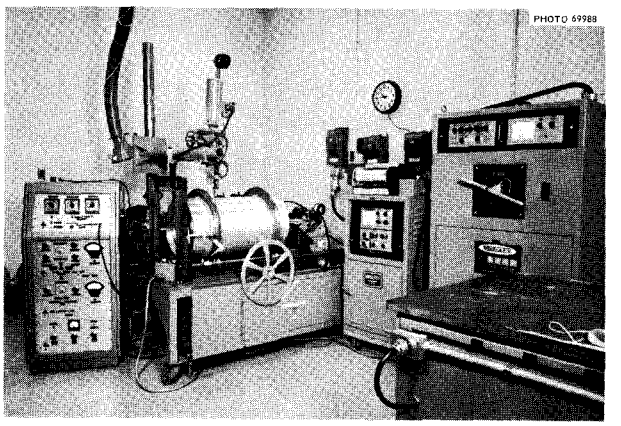

Fig. 25.3. Special Equipment for Welding HFIR Fuel Elements.

self-compensating feedback controls. The welding programmer can integrate and modify the wire speed, the weld travel speed, and the weld current as required for reliable attachment of the fuel plates. With this equipment, the welds could be accurately controlled and reliably repeated. This equipment was essentially duplicated at the plant of the vendor responsible for the manufacture of the first series of reactor fuel elements.

Another problem area involved the machining of the support tubes for the fuel elements and the final machining of the fuel elements to the design configuration. In both cases, rigid control is required during machining to meet the dimensional requirements specified by the design drawings. During the early part of the program, we were plagued with inconsistent results in both machining and inspection of the support tubes. We corrected these inconsistencies by careful programming of the various machine operations and moving the machining and inspection equipment to a temperature-controlled room. During this year, two complete fuel assemblies were finished-machined to the configuration required by the design. The final results were satisfactory for both fuel assemblies; none of the critical dimensions were out of tolerance.

Difficulty was encountered in meeting the roundness required for some of the fuel element surfaces and in meeting some of the surface finish requirements. The weld shrinkage was both greater than expected and nonuniform along the axis of the elements, and the as-welded elements were out of round. To combat the roundness problem, we worked out a special machining procedure, which essentially involved rough machining all surfaces in a restrained condition and finish machining in a nearly unrestrained condition. The finish required for the support tube surfaces was difficult to obtain because weld surfaces alternated with unwelded surfaces and both did not have the same machining characteristics. This problem was corrected, however, when our original "dry-machining" requirement was relaxed to permit a light film of alcohol applied just ahead of the cutting tool.

Uranium Homogeneity

M. M. Martin B. E. Foster S. D. Snyder

The depleted fuel plates produced by Metals and Controls, Inc. (M&C) consistently exhibited excessive fuel concentrations throughout the plate area. Initially we assumed that this was due primarily to incorrect rolled-core dimensions resulting in a fueled core that was too thick. However, determination of total uranium content by analysis of the x-ray attenuation data indicated that those plates fabricated with M&C powders contained approximately 6% too much uranium. Subsequent chemical analysis after total plate dissolution showed that the total uranium content met specifications. We concluded that there was a difference in x-ray attenuation between the ORNL and M&C materials, thus causing a 6% bias.

Several highly enriched fuel plates were then scanned for uranium content analysis. The scans indicated approximately a 3% excess of uranium. Microradiographs of plates containing the M&C depleted material, M&C enriched material, and ORNL enriched material are shown in Fig. 25.4. The radiograph of the depleted material showed a large amount of fragmentation, and the fine particles were interspersed in the matrix, thus increasing the x-ray attenuation. The M&C enriched material did not show as much fine material and ORNL powder showed even less. Longitudinal metallographic sections through these plates are shown in Fig. 25.5.

Clearly, oxide fracturing was causing the bias in uranium content analysis, and to overcome it would require new attenuation standards for the M&C material. A similar bias could be encountered in event of a significant change in the fabrication schedule.

The design of the HFIR requires very tight and complex specifications on uranium homogeneity. We are investigating the uranium distribution in the fuel plates for the dual purpose of elucidating undesirable periodic effects, if any, and defining the degree of uranium homogeneity. We plan to derive statistically the relationships between tolerance limits on uranium segregation and fuel plate rejection rates.

To develop the analysis that will ultimately be applied to the production fuel plates, 25 inner and 50 outer plates, randomly selected from the first ORNL reactor production, were inspected[9] with

[9]The plates were scanned by the Inspection Engineering Division under the supervision of K. K. Klindt.

PHOTO 80957

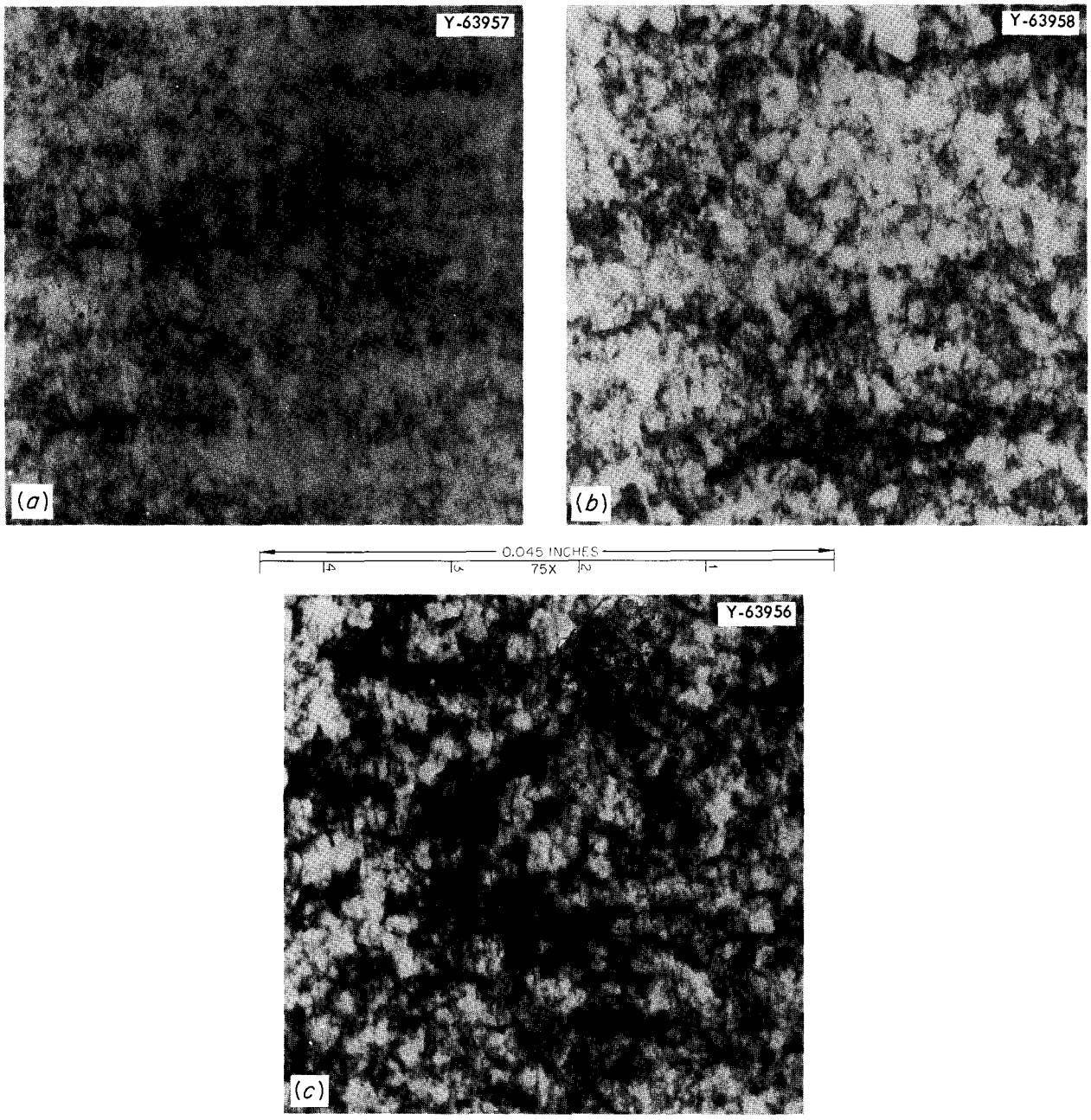

Fig. 25.4. Microradiographs of Fuel Plates Containing (*a*) M & C Depleted, (*b*) M & C Enriched, and (*c*) ORNL Enriched U_3O_8, Showing Fragmentation Differences. 75×.

the homogeneity scanner previously discussed.[10] The instrument completely scanned each plate with a $\frac{5}{64}$-in.-diam x-ray beam at a speed of 240 in./min and monitored the instantaneous (spot) and 0.16-sec RC time constant (average) attenuations at 0.048-in. increments along the length of the fuel core. We recorded approximately 38,000 observations per plate at a combined rate for the

[10]B. E. Foster, S. D. Snyder, and R. W. McClung, *Continuous Scanning X-Ray Attenuation Technique for Detecting Fuel Inhomogeneities in Dispersion Core Fuel Plates*, ORNL-3737 (January 1965).

PHOTO 80958

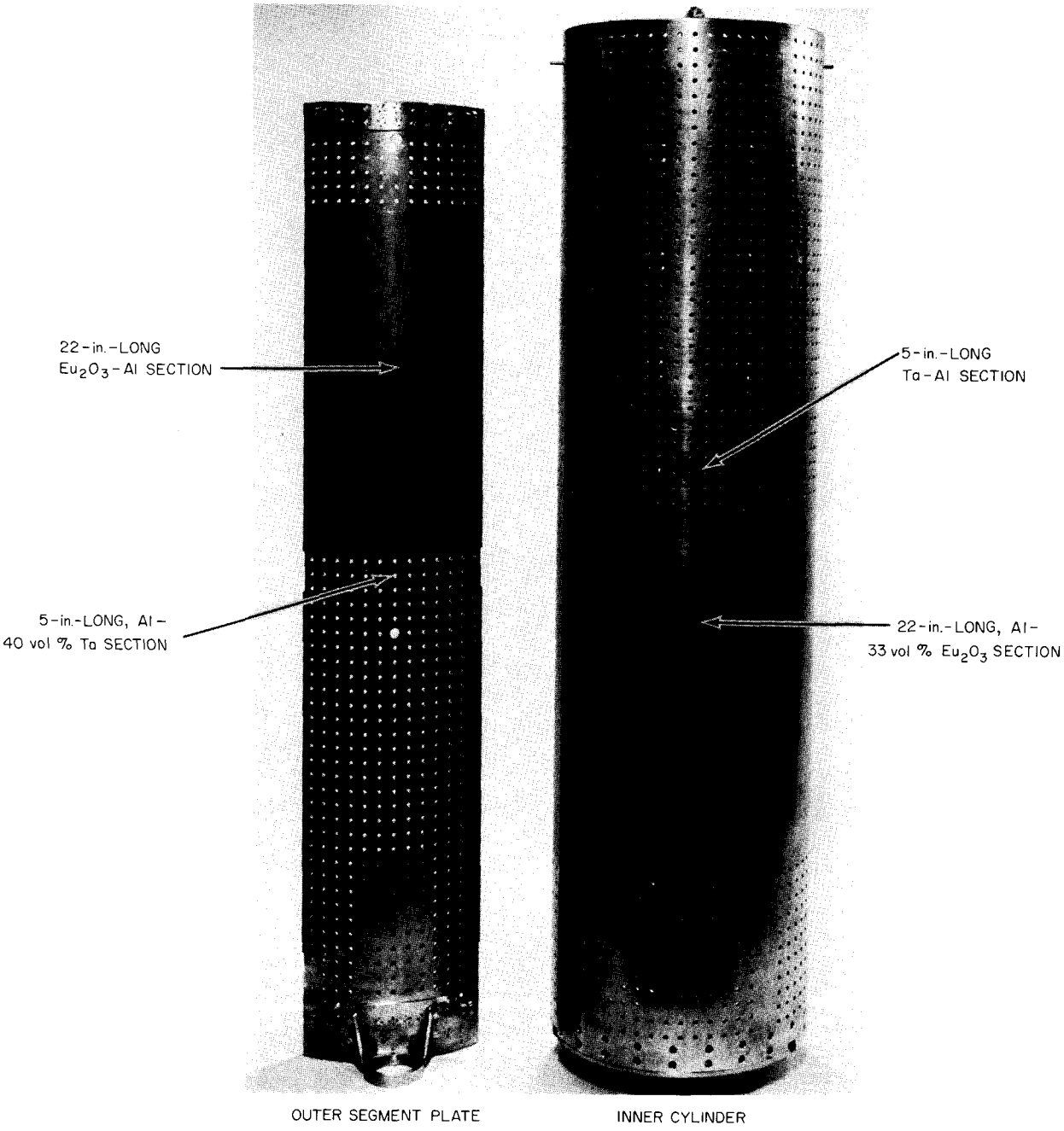

Fig. 25.5. The Inner Cylinder and One of the Four Outer Segment Plates of the HFIR Control Rod.

spot and average of about 165 values per second. The statistical analysis of this mass of data has been programmed for an electronic computer.

Very tentative results for the first reactor plates show no periodicity in the core length direction, more segregation in outer than inner plates, and acceptable production tolerances on homogeneity of 30% for the spot and ±20% for the electronic average. We plan to similarly analyze fuel plates supplied by a vendor for the second reactor core.

Ultrasonic Detection of Nonbonds

K. V. Cook R. W. McClung

In an attempt to correlate results from ultrasonic inspection[11] for nonbond, we have reexamined 22 "rejected" fuel plates using ultrasonic, radiographic, and metallographic techniques. Previous examinations had taken into account only the attenuation of the sound beam by the suspected discontinuity on a go no-go basis. Our studies included monitoring both the amplitude and the area of reduced amplitude, thereby establishing an approximate size of the nonbond. Hence, by using both the area and the signal amplitude as a rejection criterion, we could salvage about 30% of the previously rejected plates.

Because of concern that fuel segregation was causing spurious rejection, metallographic sections were taken to represent ultrasonic indications of nonbond, some of which were associated with segregation. In addition, a section was taken in an area of segregation with no detected nonbond. The results indicated that when severe particle cracking was associated with segregation near core ends, a nonbond indication could be obtained. However, segregation alone did not produce such an indication.

CONTROL ELEMENTS

R. J. Beaver

The HFIR control element is composed of two concentric cylinders, each made up of four curved plates. The inner cylinder consists of four $65\frac{9}{16}$-in.-long plates welded together and explosively sized to 17.842 in. OD. The cylinder surrounds the fuel element and is separated from it by a 0.104-in.-thick water passage. Surrounding it symmetrically and inside the beryllium reflector is the segmented outer cylinder, which comprises four separate curved plates. Water gaps 0.170 and 0.095 in. thick separate the segmented outer cylinder from the inner cylinder and beryllium reflector respectively.

To avoid large pressure differentials in this system, extremely close control of the dimensions of these control pieces must obviously be maintained. Explosive sizing techniques were investigated to achieve this objective. Figure 25.5 illustrates the inner control cylinder and one of the four outer segments, which we successfully made for the first reactor loading. All plates are essentially the same in that they contain 22-in.-long regions consisting of 33 vol % Eu_2O_3 dispersed in aluminum with a 5-in.-long extension of this region that contains 40 vol % Ta dispersed in aluminum. The inner and outer components are positioned in the reactor so that vertical displacement of one relative to the other can result in any combination of europium oxide, tantalum, and aluminum in the active reactor region. The plates are $\frac{1}{4}$ in. thick including a $\frac{1}{32}$-in.-thick cladding over the europium oxide and tantalum-bearing sections. The section containing the europium oxide is readily identified by the absence of holes. All other sections have "radiused" (having edges rounded to $\frac{1}{16}$-in. radius) $\frac{1}{4}$-in.-diam holes to minimize pressure differentials.

In addition to completing the first set of control elements for the reactor, we also produced components for testing in the Critical Test Facility, modifications of these parts for subsequent use in the reactor, and an inner cylinder and four outer segment plates for use during the nonnuclear testing phases of the reactor startup. Including plates for a second production set of control elements, we rolled 28 prototype plates, thereby thoroughly demonstrating fabrication techniques developed in the previous year.

Tests initiated last year to determine the stability of the Al–33 vol % Eu_2O_3 under irradiation were completed. After one year in the ORR at a flux of 1×10^{14} neutrons cm^{-2} sec^{-1}, no dimensional changes were observed.

Control Plate Fabrication and Preforming

M. M. Martin W. J. Werner
C. F. Leitten, Jr.

During the year, major emphasis was placed on producing two sets of inner and outer control plates for use in the reactor and for defining production yields and tolerances. We successfully fabricated these plates to the same specifications and with the identical procedures that were developed for the critical-test components.[12]

[11] R. W. McClung, *Development of Nondestructive Testing Techniques for the High Flux Isotope Reactor Fuel Element*, ORNL-3780 (April 1965).

[12] M. M. Martin *et al.*, *Metals and Ceramics Div. Ann. Progr. Rept. June 30, 1964*, ORNL-3670, p. 210.

The arc-fusing technique for preparing europium oxide for sizing[13] gave a total material loss of only 4.2%. This method yielded economically high-density Eu_2O_3 that was easy to crush, generally producing 70% −100 +325 mesh particles and 30% fines. After disk crushing to −100 mesh, the process yield was 83.4%. However, the material lost in this stage was readily recoverable by subsequent remelting. Compacts containing 33 vol % Eu_2O_3 in aluminum were consolidated at 22.5 tsi. In our previous report,[12] we indicated incorrectly that we were pressing at 45 tsi.

Table 25.4 summarizes the fabrication results for the 28 control plates we produced, including the critical test components and the first two sets for the reactor. The data illustrate our excellent control of rolling parameters, poison loadings, and core dimensions. The two core materials, however, rolled differently, as seen from the variations in average dimensions, rolling parameters, and tolerance limits. The differences in the loading tolerance of the "black" and "gray" sections resulted from variations in the size of the Al–40 vol % Ta compacts caused by machining tolerances.

Of the 28 plates produced, 27 were acceptable for preforming. Previously,[12] gluing a backup plate onto these composite control plates prevented cracking of the brittle Eu_2O_3-Al core section by maintaining it in compression during preforming operations. Twenty-six plates have now been preformed without failure, thoroughly demonstrating the feasibility of this technique.

[13]R. E. McDonald and C. F. Leitten, Jr., *Metals and Ceramics Div. Ann. Progr. Rept. June 30, 1964*, ORNL-3670, p. 166.

Forming Control Element Components

R. J. Beaver

To demonstrate that the techniques reported last year[14] for explosively sizing[15] the outer segments of the control element were feasible, we produced 24 formed plates for the critical

[14]R. J. Beaver *et al.*, *Metals and Ceramics Div. Ann. Progr. Rept. June 30, 1964*, ORNL-3670, pp. 208–15.

[15]Explosive forming by Y-12 Plant under direction of W. T. Carey.

Table 25.4. Summarized Data on HFIR Control Plate Fabrication

Section Tested	Specified Core Dimensions (in.)			Average Measured Core Dimensions (in.)			Core Loading (g)	
	Length	Width	Thickness	Length	Width	Thickness	Specified	Average Found
Outer plates								
Black section[a]	22.00	13.19	0.194	21.97	13.19	0.193	2230	2225
Gray section[b]	5.00	13.19	0.194	4.89	13.16	0.197	1300	1303
Inner plates								
Black section[a]	22.00	13.10	0.194	21.97	13.09	0.193	2215	2212
Gray section[b]	5.00	13.10	0.194	4.89	13.05	0.197	1295	1295
Tolerance limits[c]	±0.50	±0.12	±0.005	±0.30	±0.12	±0.005[d] ±0.009[e]	±22	±3[d] ±10[e]

[a]33 vol % Eu_2O_3.
[b]40 vol % Ta.
[c]Limits cited for measured averages are 95% confidence, 99% distribution.
[d]For black section.
[e]For gray section.

test program, the hydraulic mockup, and the first reactor loading. We first used the previous year's experience to make the components for the critical test No. 3. At that time, we had not completely developed our procedures for making the inner cylinder. Rather than delay the program, we used the techniques developed for outer segments to explosively size plates for the inner cylinder. We then riveted them together to form a cylinder.

Figure 25.6 illustrates the exceptional control of the curvature of the outer segment plates that we achieved by the explosive sizing operation. These typical results were obtained on one of the plates for the first reactor set. The data were obtained by longitudinal scanning at circumferential intervals of $1\frac{5}{8}$ in. for deviations from the nominal 9.300-in. radius and recording a continuous trace with an x-y plotter. Controlling the deviations to within ±0.014 in. of a 9.300-in. radius is an outstanding achievement and demonstrates the advantage of high-energy forming.

We also devoted considerable attention this year to establishing procedures for attaching the end fittings to the outer segment plates. These fittings fix the position of the plates with respect to the adjacent reactor components. It is obvious from the limited space available that a slight deviation in position can have a significant percentage effect on the water passages and, thus, on the hydraulic conditions between these parts. By matching the end fitting exactly to the actual plate radius and using well-designed gages, we were able to position the end fittings remarkably well to the ends of the plate.

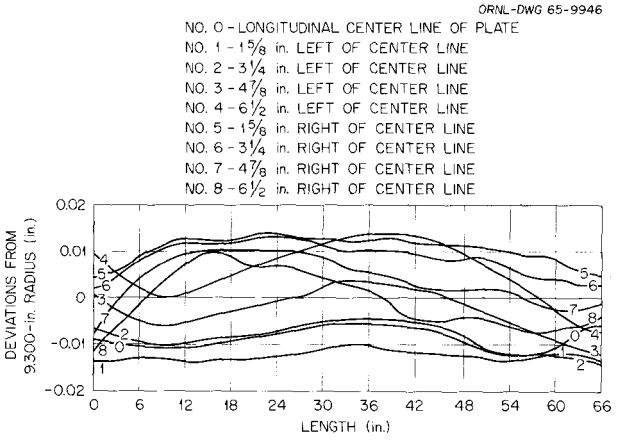

Fig. 25.6. Traces Showing Local Deviations from the 9.300-in. Nominal Radius in Outer Control Plate No. 50.

Our previous work[14] had indicated that we would be able to explosively size the inner control cylinder after welding the four neutron absorber plates to a diameter approximately $\frac{1}{32}$ in. less than the 17.832-in. die diameter. We found, however, that the bond at the interface of the europium oxide dispersion and the aluminum edging of the composite plate failed under the tensile stresses applied in the explosive sizing. We, therefore, resorted to compressive explosive sizing.

In our initial feasibility experiment, we used an all-aluminum cylinder that prior to sizing was in some regions as large as 17.855 in. in diameter. The sizing die is a split die and when closed is 17.832 in. in diameter. We had no unusual difficulty in inserting the part into the split die and closing the die together. Thus, by applying compressive forces, we reduced the diameter of the aluminum cylinder to 17.832 in. prior to detonating the explosive charge. The charge consisted of 50 g per lineal foot of Primacord. The detonation was repeated and the cylinder removed. The diameter measured 17.846 in. With this encouraging result, we started to make the first cylinder for the reactor. However, because of our limited experience, we thought we needed to weld the composite control plates together to form a cylinder that was no smaller than 17.832 in. in diameter and not larger than 17.855 in. in diameter. We established our target for this very precise welding as 17.846 in. in diameter ±0.005 in. By careful fixturing and gaging, we accurately machined three plates to an arc length of 14.041 in. We subsequently machined the fourth plate to 14.118 in., a value based on weld shrinkage data established when the first two plates were welded together. We selected the Pandjiris external seam welder to weld the plates together. Two-pass welds were used. The joint was a butt weld with a 60° included angle and a $\frac{1}{16}$-in. root face. Pertinent welding parameters are listed below.

Pass	Amperage	Voltage	Speed (in./min)		Shielding Gas Rate (cfh)	
			Carriage	Wire	Torch	Backing
1	320	13	6	18	70	None
2	310	15	6	36	70	None

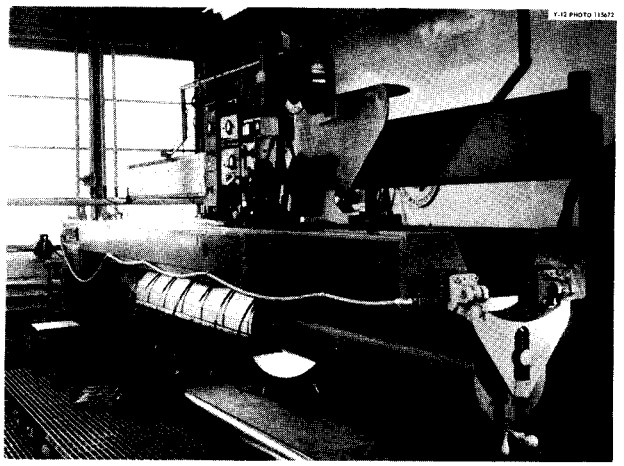

Fig. 25.7. Equipment and Fixturing for Welding Plates Together to Form the HFIR Inner Control Rod Cylinder.

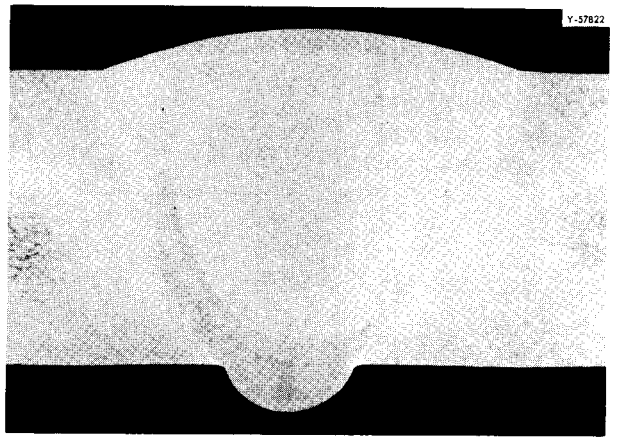

Fig. 25.8. Typical Two-Pass Heliarc Weld Used to Join Plates Together to Form the HFIR Inner Control Cylinder. As polished.

Figure 25.7 shows two plates in the Pandjiris prior to being welded into a half cylinder. The side rails and the bands were used to minimize "gulling" of the welded joint from shrinkage during cooling. Bands also were used to control the symmetry of the part when the two half cylinders were welded together. Figure 25.8 shows the macrostructure of the welded joint. After being welded the joints were all scraped and the first two were also planished. Planishing could be used to increase the arc length of the welded part and enabled us to weld the plates together to form a cylinder whose average diameter was 17.851 in. We also found that we could predict the weld shrinkage per joint to be (0.047 ± 0.005) in.

No difficulty was experienced in squeezing the welded cylinder into the die. The practice for striking the cylinder was again two detonations, each consisting of 50 grains per lineal inch of Primacord. The result was a cylinder with exceptional dimensional control, evidenced by the data presented in Fig. 25.9. The concentricity traces made at 45° intervals and at the stations indicated along the length show that the boundary of the generated surface is within ±0.015 in. of the nominal and well within the allowable ±0.030-in. tolerance. The average diameter values at their specific stations along the length also reveal the close control of the diameter achieved by the high-energy sizing operation.

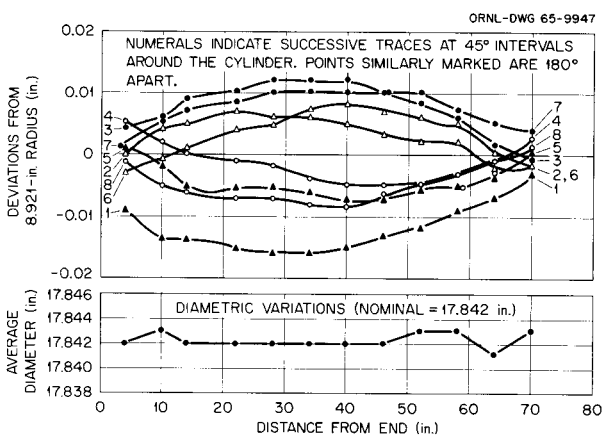

Fig. 25.9. Dimensional Data on HFIR Inner Control Cylinder.

Irradiation Testing of Europium Oxide and Europium Molybdate Dispersions

R. J. Beaver A. E. Richt

During the past year we irradiated in the ORR at 140°F three aluminum-clad coupons, two containing 33 vol % Eu_2O_3 dispersed in aluminum and one containing 38 vol % $Eu_{5.3}MoO_{11}$ in aluminum. These small platelets were illustrated in our previous report.[16] Dimensionally, they

[16] R. J. Beaver and C. F. Leitten, Jr., *Metals and Ceramics Div. Ann. Progr. Rept. June 30, 1964*, ORNL-3670, p. 215.

Table 25.5. Thickness Measurements of Aluminum-Base Specimens Containing Europium Oxide and Irradiated in the ORR at 140°F

Dispersion Concentration (vol %)	Estimated Exposure (neutrons/cm^2)		Average Thickness (in.)	
	Thermal Neutrons	Fast Neutrons	Preirradiation	Postirradiation
	$\times 10^{21}$	$\times 10^{21}$		
33 Eu_2O_3	1.3	0.5	0.2509	0.2508
33 Eu_2O_3	2.0	0.9	0.2502	0.2510
38 $Eu_{5.1}MoO_{11}$	1.3	0.5	0.2499	0.2522

have the same nominal clad-core-clad thickness (0.031-0.188-0.031 in.) as the full-size reactor plate. Knowing from other work that swelling of platelets can be detected readily by monitoring thickness changes, we used this dimension to judge the dimensional stability of these dispersions. Our results after measuring these plates throughout the year are listed in Table 25.5. We found no indications of instability of the Al–33 vol % Eu_2O_3 dispersion after an estimated exposure of 2×10^{21} neutrons/cm^2 (thermal). The specimen containing 38 vol % $Eu_{5.3}MoO_{11}$ increased in thickness 0.9% during an exposure of 4×10^{20} neutrons/cm^2 (thermal). No additional change, however, was observed after a total exposure of 1.2×10^{21} neutrons/cm^3 (thermal).

Mechanical Properties of Control Plate Material

W. R. Martin

We measured the room-temperature elastic moduli and also examined the creep resistance at 300°F and 2000 psi of the europium-bearing and tantalum portions of HFIR control plates. In addition, we tested under irradiation whether stress relaxation occurs in the Al–40 vol % Ta dispersion.

Table 25.6 lists the room-temperature elastic moduli of both dispersions and the all-aluminum sections, measured on specimens cut from full-size plates rolled and heat treated in accordance with HFIR control-plate procedures. For economy, Lindsay Mix (50% Gd_2O_3–50% Sm_2O_3) was substituted in the rare-earth portion for Eu_2O_3.

Creep data for the same three materials, also measured on specimens cut from the rolled full-size composite plate, are also listed in Table 25.6. Of the three materials, Al–40 vol % Ta was the strongest. The 33 vol % Lindsay Mix and the all-aluminum type 6061 portion were comparable to each other but weaker than the tantalum-bearing material.

We tested the Al–40 vol % Ta material to observe the stress relaxation properties of this dispersion under irradiation. Dubrovin *et al.* had previously shown that irradiation can influence the stress relaxation properties of a material.[17] The specimens we used were small plates with overall dimensions $12 \times 1 \times 0.100$ in. and a core $10 \times \frac{1}{2} \times 0.070$ in. These composites and all-aluminum type 6061 plates of the same overall dimensions cut from the ends of the composites were bent to a radius calculated to give an initial stress of 4660 psi on the dispersion and 3680 psi on the aluminum. A fixture held the plates at the desired radius while in test. We conducted the test in the F-7 position of the ORR at the reactor process-water temperature to a dose of 9×10^{20} neutrons/cm^2. After the specimens were removed from the fixture, their radii of curvature were measured. If no stress relaxation had occurred, the radius of curvature would be infinite; however, we found measurable radii. The calculated values of the relaxation strains and stresses for the specimens tested are listed in Table 25.7. Stress relaxation occurred in both the tantalum-aluminum composites and the type

[17] K. P. Dubrovin *et al.*, *Properties of Reactor Materials and the Effects of Radiation Damage*, Butterworths, London, 1961.

6061 aluminum specimens. The average stress decrement for the tantalum-bearing samples is 1410 psi. If the assumption is valid that the magnitude of relaxation is proportional to the stress, our results indicate that stress relaxation in the Al–40 vol % Ta material is about 14% greater than that of the wrought type 6061 alumunium.

Table 25.6. Mechanical Properties of HFIR Control-Element Materials[a]

Material	Elastic Modulus[b] (psi)	Plastic Strain[c] (%) at Times (hr) of							
		1	10	100	250	500	750	1000	2000
6061 aluminum	9.32×10^6		0.04	0.06	0.10	0.11			
Al-Ta[d]	13.3×10^6	0	0	0	0.01	0.02	0.03	0.03	0.03
Al-Lindsay Mix[e]	9.93×10^6	0.04	0.07	0.08	0.09	0.09	0.11	0.12	0.12

[a]Specimens cut from rolled composite plate.
[b]At room temperature.
[c]At 200°F and 2000 psi.
[d]Al–40 vol % Ta, clad with 0.030 in. 6061 aluminum.
[e]Al–33 vol % Lindsay Mix (50% Gd_2O_3–50% Sm_2O_3), clad with 0.030 in. 6061 aluminum.

Table 25.7. Stress-Relaxation in Bending of Aluminum Plates

Material	Relaxation Strain	Relaxation Stress (psi)[a]		
		Initial	Final	Change
	$\times 10^{-4}$			
Al-clad Ta-Al composite	0.96	4660	3380	1280
Al-clad Ta-Al composite	1.28	4660	3210	1450
Al-clad Ta-Al composite	1.12	4660	3160	1500
Aluminum	1.00	3680	2630	1050
Aluminum	1.00	3680	2630	1050
Aluminum	0.72	3680	2920	760

[a]Calculated from an elastic modulus of 10.5×10^6 psi for aluminum and 13.3×10^6 for the dispersion.

26. High Flux Isotope Reactor Target Development

D. A. Douglas, Jr.

The Transuranium Project, in which research quantities of the higher actinide elements will be produced by transmutation, is being carried out in two parts. One is the design and construction of the High Flux Isotope Reactor (HFIR), for which the development of the fuel and control elements is a responsibility of the Metals and Ceramics Division; our efforts in that area are reported in Chap. 25 of this report. The second phase of the program is the development of remote processing and refabrication of the target elements and the requisite equipment. Progress on the fabrication, our part of this phase, is reported below.

The initial targets will contain plutonium oxide. Following their exposure in the reactor, desired isotopes will be chemically separated and processed to provide material for inclusion in new targets for additional exposure. Through these sequential steps, gram quantities of the higher actinide oxides (americium, curium, berkelium, and californium) can be produced. Since the material to be processed will be highly radioactive and toxic, a heavily shielded and contained facility is required for carrying out the chemical processing and fabrication steps.

Our work consists of developing procedures for fabrication of satisfactory target elements, conducting irradiation tests to demonstrate the adequacy of the fabrication techniques, and inventing or adapting equipment to carry out the fabrication in enclosed and shielded cubicles.

A target assembly designed to provide an equivalent cross section is being made for reactor critical experiments, and the plutonium-bearing assembly for the first target loading in the HFIR is being fabricated.

TRANSURANIUM TARGET FABRICATION EQUIPMENT

M. K. Preston, Jr.[1] J. E. Van Cleve
R. I. Deaderick[2] A. L. Lotts

The HFIR target element depicted in Fig. 26.1 consists of a $\frac{3}{8}$-in.-diam intermittently finned rod and a sheath that is mechanically attached to the fins at the bottom of the rod. The sheath, which has a hexagonally shaped top but is otherwise cylindrical, acts as a spacer and coolant channel. The 35-in. element contains 0.250-in.-diam 0.571-in.-long pellets in the 20-in. active length, which will contain transuranium elements. The remainder of the length is occupied by end caps and void space for the accumulation of fission gas. The pellets, which are completely encapsulated in aluminum, are compacts of actinide oxides and aluminum powder pressed to a density 89 to 91% of theoretical.

Equipment is being developed to remotely fabricate these target elements in the Transuranium Process Facility, which is heavily shielded. The basic criteria and methods of operation to be used in the fabrication have not changed substantially from that outlined previously.[3] All equipment has now been designed and fabricated to operate semiautomatically. It requires minimum use of manipulators and it can be removed from the cubicle through the 18- by 35-in. equipment-transfer opening in the roof. In addition, many components, such as motors, cylinders, valve

[1]On loan from General Engineering and Construction Division.

[2]Oak Ridge Gaseous Diffusion Plant.

[3]M. K. Preston *et al.*, *Metals and Ceramics Div. Ann. Progr. Rept. May 31, 1962*, ORNL-3313, pp. 108–11.

ORNL-DWG 65-1383

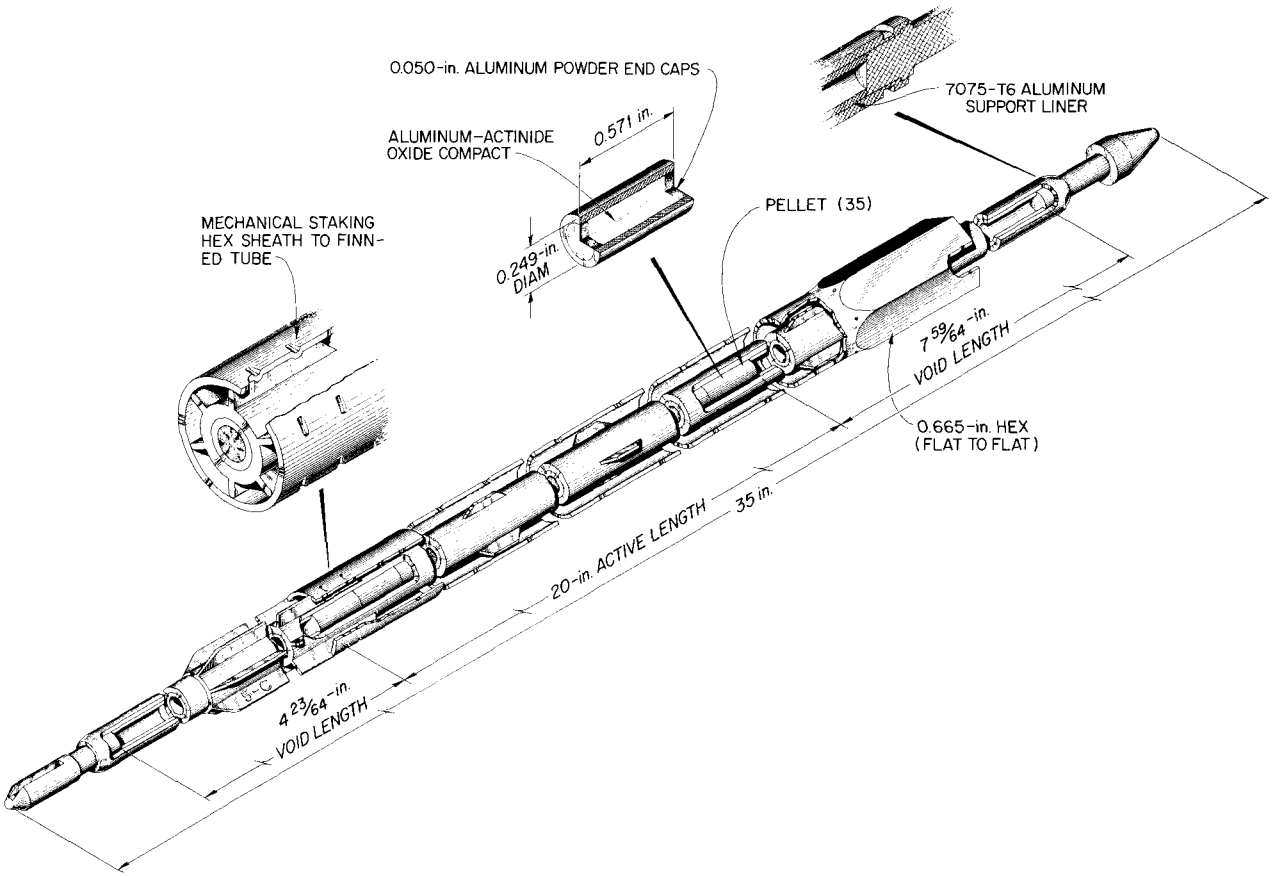

Fig. 26.1. HFIR Target Assembly.

clusters, electrical wiring jumpers, and supporting hoppers or magazines, can be removed from or replaced by the 8-in.-diam by 8-in.-deep intercell conveyor.

The mockup and evaluation of this equipment is well under way. The project is 91% complete. Some effort is being expended on redesign of equipment, including a few major items, as a result of our mockup testing. A resumé of the design, fabrication, and mockup follows; more detailed information on the progress during the past year is reported elsewhere.[4–6]

[4]M. K. Preston, R. I. Deaderick, J. E. Van Cleve, and A. L. Lotts, *Transuranium Quart. Progr. Rept. Aug. 31, 1964*, ORNL-3739, pp. 38–49.

[5]M. K. Preston, R. I. Deaderick, J. E. Van Cleve, and A. L. Lotts, *Transuranium Quart. Progr. Rept. Nov. 30, 1964*, ORNL-3847 (in press).

[6]M. K. Preston, R. I. Deaderick, J. E. Van Cleve, and A. L. Lotts, *Transuranium Quart. Progr. Rept. Feb. 28, 1965* (in press).

Design and Fabrication

Approximately 54 separate items of equipment have been designed and built to fabricate and inspect the HFIR target elements. The redesign of components for Cubicle 3 includes modifications to the calciner and pellet thermal treatment equipment and a new design for the blending and powder-weighing system. Cubicle 2 equipment appears to be satisfactory except that better bearings are needed in the target assembly machine (welder). Cubicle 1 equipment also appears to be satisfactory; however, this equipment has not had the extensive operation needed to find the weak points. Piping manifolds for the two target rod ultrasonic cleaners are being redesigned to incorporate disconnects that can be operated by the manipulators.

Equipment Mockup

A mockup of the three Transuranium fabrication cells has been constructed. The front wall and roof section are mounted on rails so that the wall may be placed in front of each cell as required. The roof section also carries the cubicle crane and the service connectors. We use the mockup test to develop satisfactory operating procedures and to test and modify the equipment in a readily accessible environment. From our experience, operating and maintainance manuals will be developed.

The status of equipment development in the mockup follows.

Cubicle 3. – All the equipment has been received and installed in the mockup. An overall pictorial of the equipment in Cubicle 3 is shown in Fig. 26.2. The preliminary testing is complete and has resulted in a number of minor alterations

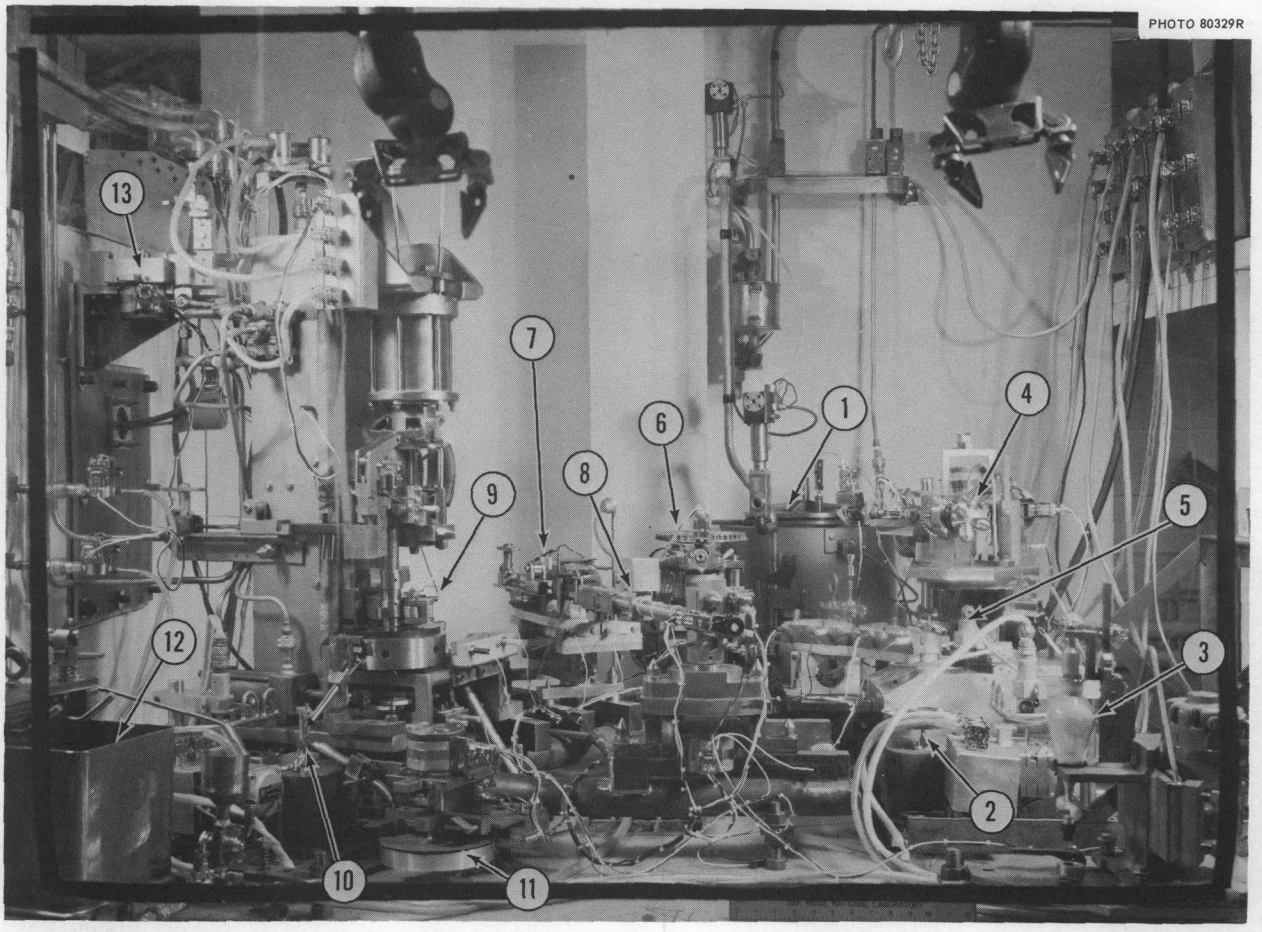

1. CALCINER AND THERMAL TREATMENT FURNACE
2. BATCH SCALE
3. ALUMINUM POWDER ADD STATION
4. BLENDER-DISPENSER
5. PELLET LOAD SCALE
6. CAP POWDER MAGAZINE
7. DIE MAGAZINE
8. TRANSFER ARM
9. PELLET PRESS
10. PELLET WEIGHT AND LENGTH SCALE
11. PELLET MAGAZINE*
12. PELLET ULTRASONIC CLEANER*
13. PELLET DISCHARGE STATION

*SOME COMPONENTS BEING REWORKED AT THE TIME THE PHOTO WAS TAKEN

Fig. 26.2. View of the Equipment in Cubicle 3 Mockup.

involving lifting aids for use with the cell crane and manipulators. We are now determining an optimum set of blending parameters using tungsten carbide as a stand-in for the actinide oxide. This same material will be used throughout the mockup test, since the large density difference between it and the aluminum matrix powder should make this a real test of the system.

Cubicle 2. – The equipment installed in Cubicle 2 of the mockup is shown in Fig. 26.3. All the equipment has been mounted on the equipment base. Each item has been operated independently, and only minor alterations have been necessary to obtain satisfactory performance.

Cubicle 1. – The equipment installed in Cubicle 1 of the mockup is shown in Fig. 26.4. All the equipment has been mounted. The installation of the electrical, instrument, and piping services is nearing completion. Each individual piece has been operated separately and minor alterations have been performed.

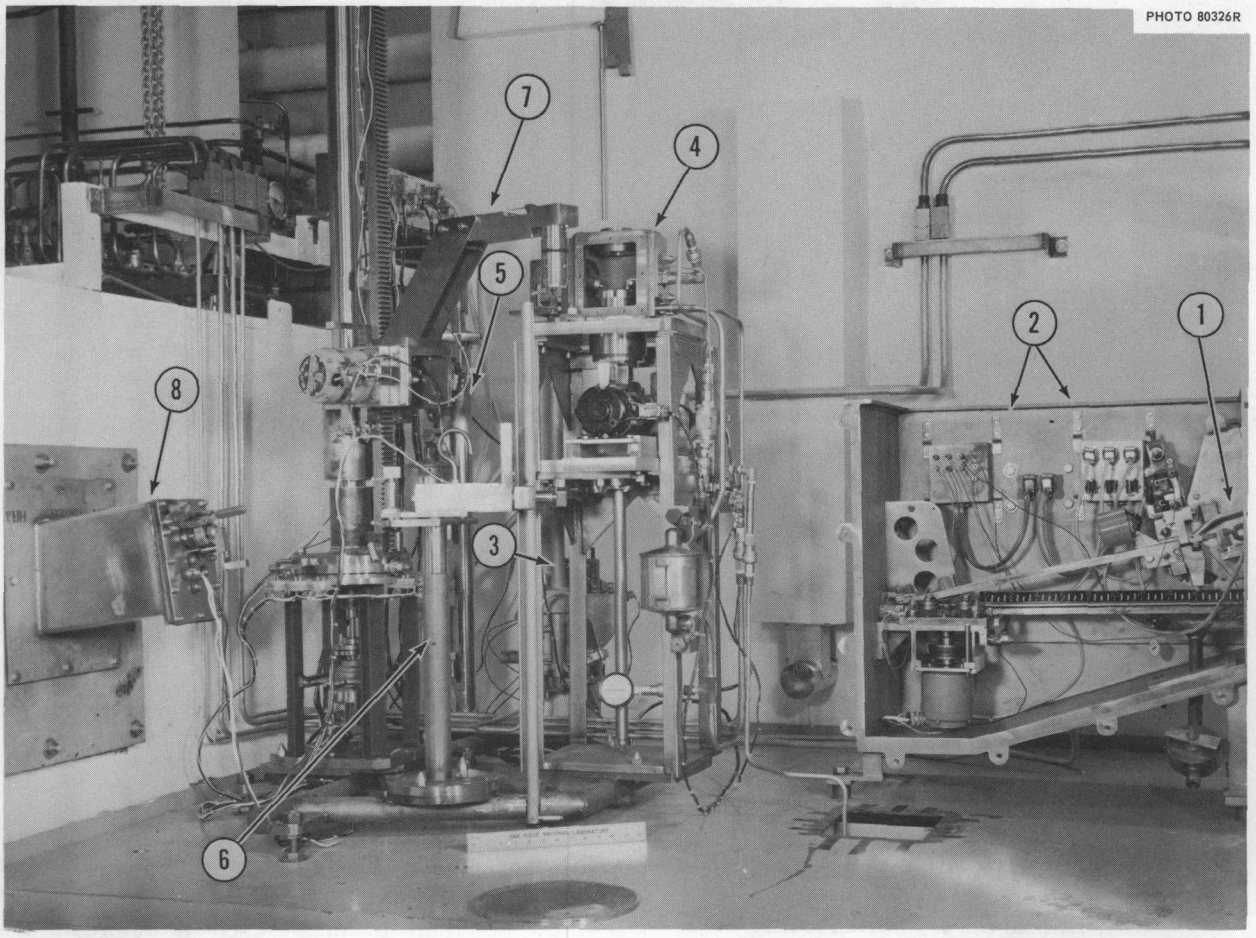

1. PELLET TRANSFER TUBE
2. PELLET INSPECTION AND LOADING EQUIPMENT*
3. TARGET ROD HOLDER AND LOADING STATION
4. TARGET ROD WELDER*
5. HELIUM LEAK TEST CHAMBER
6. TARGET ROD TRANSFER STATION
7. TRANSFER ARM*
8. ULTRASONIC CLEANER

*SOME COMPONENTS BEING REWORKED AT THE TIME THE PHOTO WAS TAKEN

Fig. 26.3. View of the Equipment in Cubicle 2 Mockup.

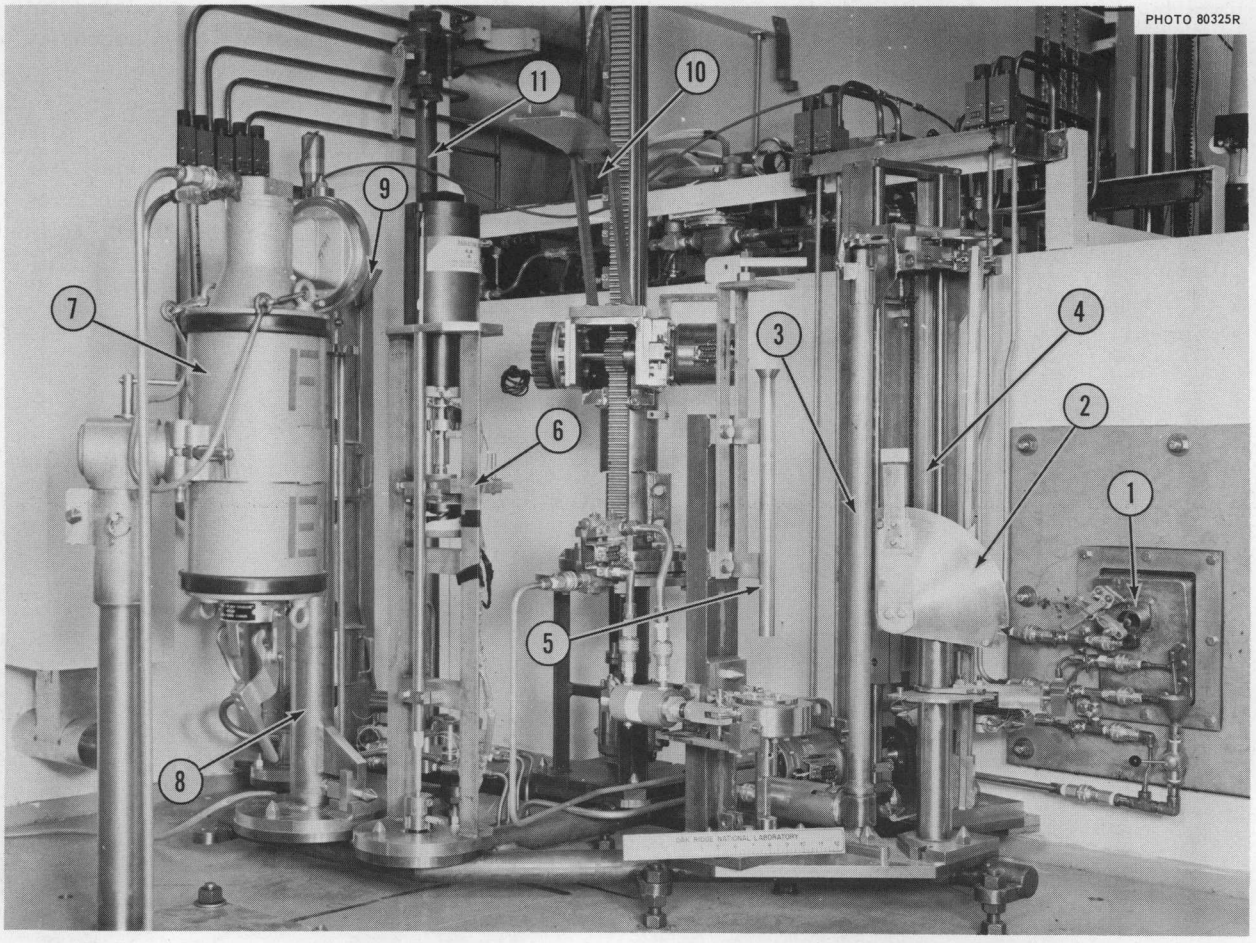

1. ULTRASONIC CLEANER
2. TARGET ROD RECEIVER
3. DRYER AND SURFACE SMEAR STATION
4. DIMENSIONAL INSPECTION STATION
5. HEX CAN PLACEMENT STATION
6. X-RAY FILM STATION
7. X-RAY UNIT
8. HYDROSTATIC COLLAPSE OR HOT ARGON COLLAPSE STATION*
9. ULTRASONIC CLEANER
10. TRANSFER ARM*
11. TARGET ELEMENT DISCHARGE TUBE

*SOME COMPONENTS BEING REWORKED AT THE TIME PHOTO WAS TAKEN

Fig. 26.4. View of Equipment in Cubicle 1 Mockup.

PLUTONIUM TARGET FABRICATION

J. D. Sease A. L. Lotts

Fabrication of ^{242}Pu HFIR Target Elements for Irradiation at Savannah River

We fabricated 18 HFIR target elements, shown in Fig. 26.5, each containing 10 g of ^{242}Pu in the form of PuO_2. They are currently being irradiated in one of the Savannah River reactors to accelerate the Transuranium Program. The procedure that was used to fabricate these elements was essentially identical to those used to fabricate the prototype irradiation target elements[7] and the first Savannah River target elements.[8] The fabrication procedure consisted of pressing pellets

[7] J. D. Sease and D. M. Hewette, *Fabrication and Preirradiation Data for High Flux Isotope Reactor Prototype Target Rods*, ORNL-TM-811 (June 1964).

[8] J. D. Sease, *Fabrication and Preirradiation Data of HFIR Target Elements for Savannah River Irradiation*, ORNL-TM-1095 (June 1965).

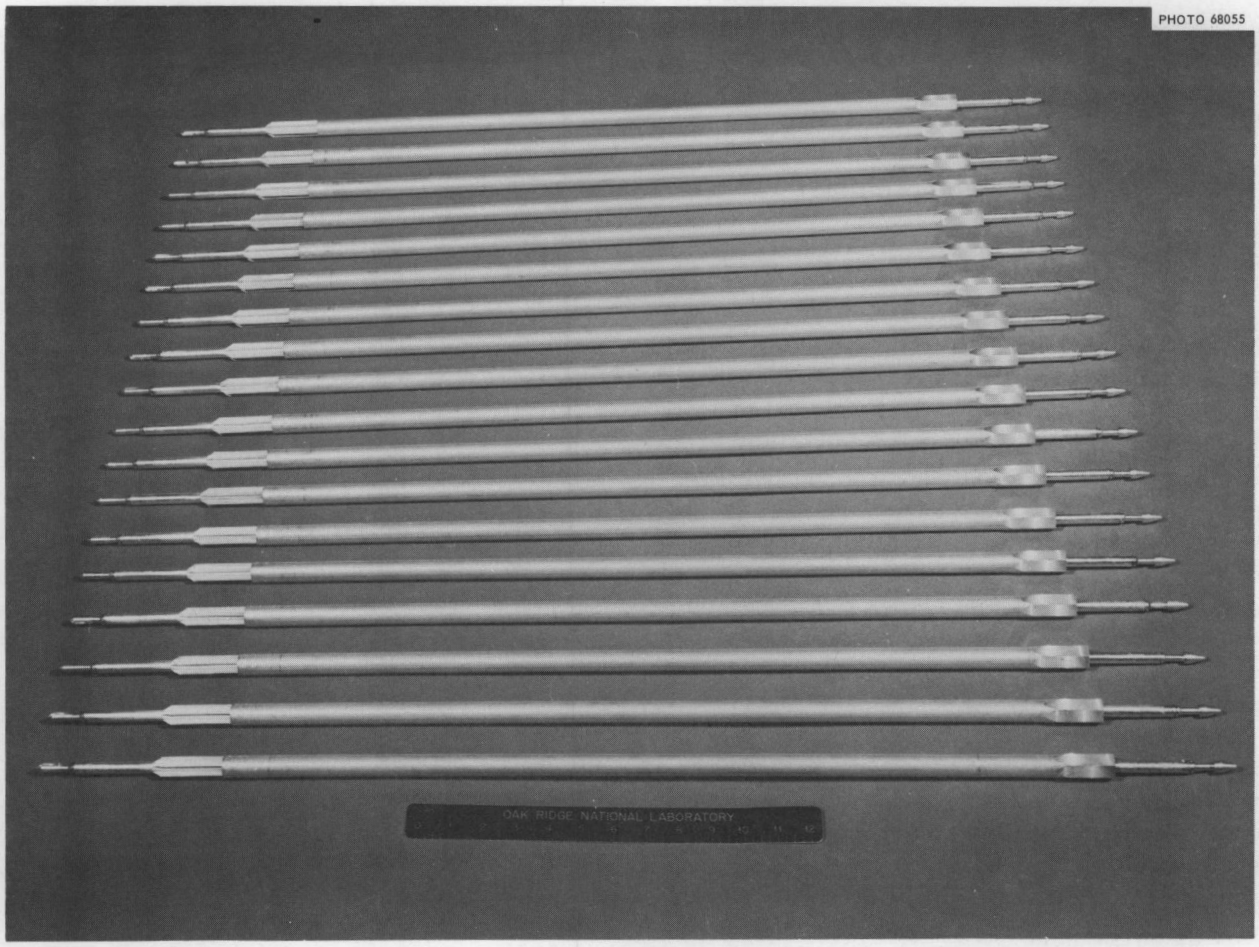

Fig. 26.5. Assembled HFIR Target Elements Currently Being Irradiated at Savannah River Laboratory.

containing $^{242}PuO_2$ in an aluminum matrix (35 separate pellets per element), inserting the pellets into an aluminum tube, end-closure welding, helium leak testing, cold hydrostatic collapse of the cladding onto the pellets, and mechanical attachment of the cover can to the finned cladding tube. The elements were fabricated to the available HFIR target element specifications, since these elements may be used in the HFIR after the initial irradiation at Savannah River.

The fabrication of the elements was completed without major difficulty. The most troublesome problem was in making the PuO_2-containing pellets within the length requirements, a problem attributable to the difficulty of dispensing a homogeneous blend of the aluminum and PuO_2 powders. The collapse fabrication step bowed the rods some, requiring hand straightening.

The preirradiation data included measurement of the rod diameter, rod bow, rod weight, and rod-to-can spacing. Radiographs were taken of the welds (3 planes) and the entire rod assemblies. In addition, the rods were leak checked and the assembled elements were photographed. Complete preirradiation data will be reported elsewhere.[9]

Fabrication of HFIR Target Elements for Flow Testing

We fabricated a flow test assembly of 31 target elements, and it is currently being used by the HFIR designers and operators to establish hydraulic flow parameters in the HFIR. These

[9] J. D. Sease, *Fabrication and Preirradiation Data of Second Series HFIR Target Elements for Savannah River Irradiation* (in preparation).

elements contain no plutonium or transplutonium loading but in every other respect are identical in design to the HFIR target elements shown in Fig. 26.1.

WELDING DEVELOPMENT

J. D. Sease J. W. Tackett

The aluminum-clad HFIR target elements will be seal welded on each end. Many different joint designs were developed and evaluated.[10] Almost all the joint designs appeared satisfactory for sealing the first end of the target elements. All but one of the joint designs developed appeared unsatisfactory for sealing the second end of the target elements. During this weld the end of the tube is heated rapidly, expanding the gas enclosed inside the target element. The expanding gas causes large void areas at the root of the weld joint as it escapes through the liquid weld puddle.

One of the joint designs, described in Fig. 26.6, is unique in the following way. Prior to welding, the end of the tube is roll swaged to the end cap under a reduced pressure, producing a preliminary seal capable of holding the reduced internal pressure during welding. The reduced internal gas pressure during welding essentially eliminated the root porosity. The swaged joint design has been used repeatedly with good results.[8] To date, several hundred closure welds typical of the second end closure have been made satisfactorily. In production, the reduced internal pressures will be obtained for the second weld as follows. The loaded target rod is inserted vertically in the weld chamber. The chamber is evacuated and then partially refilled with helium ($\frac{3}{4}$ to $\frac{1}{2}$ atm). At the reduced pressure, the end cap is inserted and the end of the element is sealed by roll swaging. The chamber is then filled with helium to 1 atm and the closure weld is made.

This joint design is unique also in that the tube material above the swaged joint is used as a filler during welding, as shown in Fig. 26.7. In the first stage of welding, this ring of material melts completely before melting occurs in the end plug. This ring of material during stage 2 flows toward

ORNL-DWG 65-9948

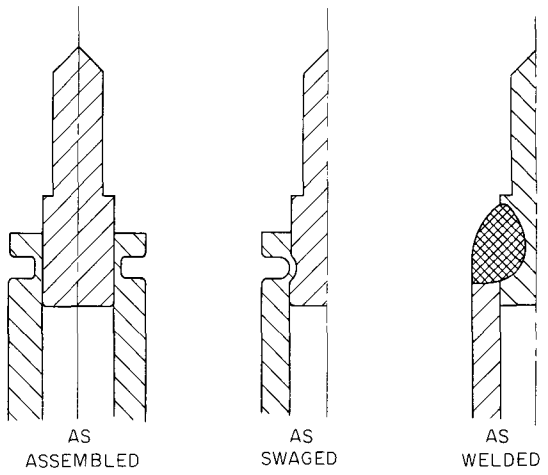

Fig. 26.6. Joint Design Used in Welding Target Rods.

the tube end (below the swage joint), which is preheated and melts faster than the end plug. During the third stage, this ring of material flows up the end plug as weld penetration is achieved. During stage 4, the arc current is tapered to prevent a large weld end crater.

One problem was encountered with this joint design, which appeared to be more pronounced when the tube was welded vertically rather than horizontally. The ring of material caused difficulty during the first and second stages of welding, in which the moving puddle continually changed the arc voltage, causing the arc to become unstable. The ring of molten metal became unbalanced at some time during the first stage of welding; in fact, it sometimes came into contact with the welding electrode and extinguished the arc. The unbalanced ring was seldom corrected and usually resulted in severe rollover on one side of the tube.

Several methods have been found to be useful in limiting this problem. One method that gave excellent control involved the use of an automatic welding head to control the arc length. Another method, which appeared to work reasonably well, involved introducing argon gas instead of helium at the weld start. The lower energy argon arc, which lasted during one to two revolutions of the tube, appeared to stabilize the configuration of the ring. Although the welding equipment proposed for the TRU facility does not have provision for either an automatic head or mixing of the welding

[10] C. H. Wodtke, *Metals and Ceramics Div. Ann. Progr. Rept. June 30, 1964*, ORNL-3670, pp. 271–75.

gas, the later method suggests that an additional limitation of the welding current during the first and second stages might provide sufficient control. Further tests are under way to establish the procedures to be used in the TRU facility.

IRRADIATION TESTING

A. R. Olsen
J. W. Ullmann[11]
J. D. Sease
A. E. Richt

In the first experimental irradiation of HFIR targets, four prototype target elements were exposed in the Engineering Test Reactor. Three have been removed and two examined. The findings on the first rod have been reported.[12]

The second rod was exposed for its final irradiation cycle at an average heat flux of 1×10^6 Btu hr^{-1} ft^{-2}, which is the predicted hot-spot heat flux for the HFIR.[13] It was accidentally subjected to a rather severe mechanical treatment after removal from the reactor. Despite this impact loading, the connections between the rod and the hex can remained intact and the spacing measurements were only slightly changed. This target sustained about 80% burnup of the original plutonium atoms. No gross swelling was seen, even though the PuO_2 particles in the thermal center of each pellet had completely reacted with the aluminum matrix. Since these reaction zones had distinct boundaries of interference with adjacent zones, they apparently were never molten. Attempts to produce a similar reaction out-of-reactor failed even with prolonged heat treatments at 600°C. The reaction in the cooler external portions of the fuel compact showed limited reaction with the matrix, as was seen with the first target, which had been irradiated at 6.4×10^5 Btu hr^{-1} ft^{-2}. Most of the fission gas was retained in the individual pellets. The last two targets are scheduled for examination next year, but the findings to date indicate the target design is adequate for the most severe operating conditions anticipated during the HFIR irradiations.

---

[11] Chemical Technology Division.

[12] A. R. Olson, J. W. Ullmann, and S. D. Clinton, *Transuranium Quart. Progr. Rept. Nov. 30, 1964*, ORNL-3847 (in press).

[13] S. A. Rabin, J. W. Ullmann, S. D. Clinton, and D. A. Douglas, *Metals and Ceramics Div. Ann. Progr. Rept. June 30, 1964*, ORNL-3670, p. 275.

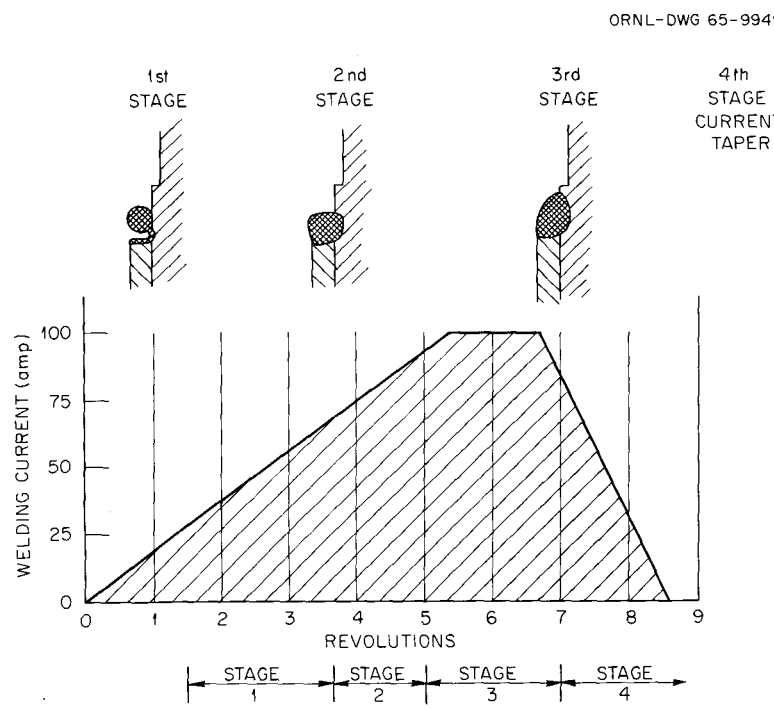

Fig. 26.7. Cycle Used in Welding Target Rods.

27. Medium Power Reactor Experiment

W. C. Thurber G. M. Adamson, Jr.

Our purpose is to provide materials support for the Medium Power Reactor Experiment. This reactor, currently being designed and developed at ORNL, is a single-loop Rankine-cycle system employing boiling potassium as the reactor coolant and thermodynamic working fluid. The reactor system, to be constructed of conventional materials, will operate in the 815 to 870°C temperature range to produce more than 100 kw of electricity to demonstrate its utility for space applications.

The principal materials problems investigated during this period have centered on the performance of various types of materials in liquid metals. This work involves both study of the materials themselves and assistance with fabrication of components for engineering tests. Examples of the latter are the fabrication of turbine pumps and finned tapered-tube radiators, both of which required development of brazing techniques. The materials studies have included the operation and analysis of data on materials performance in natural-circulation loops, refluxing-type loops, and forced-circulation loops.

TURBINE PUMP FABRICATION

C. W. Fox

A major problem in the use of liquid-metal systems is the development of a turbine pump using bearings capable of operating in liquid metals. We are fabricating refractory-metal turbine pumps containing cermet bearings; we fabricated nine during this year, using design details and fabrication procedures similar to those previously reported.[1] To assure the quality of the cermets, they were inspected with penetrant as received, after brazing, after grinding, and after lapping. Although a large number of bearings had pinhole flaws in the as-received condition, in only one case was an additional flaw caused by fabrication. The location and nature of these flaws will be correlated with performance.

To test whether the brazing cycle harmed the TZM (Mo–0.5% Ti–0.08% Zr) structural alloy used in the turbine pumps, we held specimens in vacuum at 1120°C for 10, 20, and 30 min. The specimens were examined metallographically, and no change in microstructure or grain size was evident.

The mechanical properties of the cermet-to-molybdenum brazed joints were determined in a shear testing program. The specimens used were 0.650-in.-diam × 0.125-in.-thick cermet disks brazed to molybdenum pads $1\frac{3}{8} \times 1 \times \frac{1}{4}$ in. The two cermets of principal interest are those in Table 27.1. The strength values for the joints in the as-brazed condition are more than sufficient for the expected stress requirements in service. In addition, the results indicate that the joint will become even stronger during service.

Table 27.1. Shear Strength of Cermet-to-Molybdenum Joints Brazed with Nickel-Silicon-Boron Alloy

Cermet	Condition	Shear Strength[a] (psi)
WC–6% Co	As brazed	28,600
WC–6% Co	Aged 500 hr at 1300°F	40,700
WC–12% Co	As brazed	35,100
WC–12% Co	Aged 500 hr at 1300°F	42,200

[a]Each value is an average of three tests at room temperature.

[1]C. W. Fox, *Metals and Ceramics Div. Ann. Progr. Rept. June 30, 1964*, ORNL-3670, p. 225.

RADIATOR FABRICATION

E. A. Franco-Ferreira

We have fabricated a large finned tapered-tube radiator for an electrically heated test assembly. This unit is similar in configuration to a radiator reported previously.[2] The departure in technique used here was the development of a new method of attachment or positioning for the high-conductivity fins made of copper clad with stainless steel. These fins were substantially thicker than the previous ones and could not be attached the same way.

Prior to brazing, we attached the fins to the radiator tubes by spot welding small angles made of 0.005-in.-thick stainless steel to the fin edge at the tube contact line, as shown in Fig. 27.1. A slurry of nickel-chromium-phosphorus brazing alloy was then applied to the entire length of each tube-to-fin joint. The tubes were then brazed in a hydrogen furnace equipped with a continuously moving hearth. Distortion was thus minimized by limiting to 10 min the time that any portion of a tube was at brazing temperature. Figure 27.2 shows a transverse cross section of a typical tube-to-fin brazed joint. Note that there is a direct metallurgically bonded heat-conduction path from the tube wall through the brazing alloy into the copper core of the fin.

[2]E. A. Franco-Ferreira, *Metals and Ceramics Div. Ann. Progr. Rept. June 30, 1964*, ORNL-3670, p. 226.

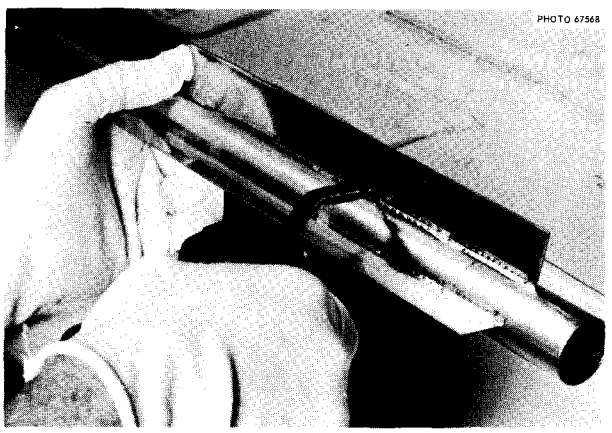

Fig. 27.1. Spot Welding of Small Stainless Steel Angles to Tapered Tubes and to High-Conductivity Fins.

NATURAL-CIRCULATION BOILING-POTASSIUM TEST LOOPS

D. H. Jansen

A summary report[3] was issued describing the results of several loop tests operated to determine the compatibility of conventional nickel-, iron-, and cobalt-base high-temperature alloys with boiling potassium. The studies were conducted in natural-circulation loops, two of which were fabricated from type 316 stainless steel, two from Haynes alloy No. 25, and one from Inconel. Each of the alloys was tested at a maximum boiler-condenser temperature of 870°C for 1500 to 3000 hr, and the Haynes alloy No. 25 was tested also for 3000 hr at 980°C. The potassium condensing rates at the two temperatures were about 175 and 300 g/min respectively.

Results of these loop tests indicated that type 316 stainless steel and Haynes alloy No. 25 resist corrosive attack by boiling potassium at 870°C better than Inconel. The weight losses per unit area in the condenser region were of the same magnitude (8 to 10 mg/in.^{2}) for the stainless steel and the Haynes alloy loops; however, the latter showed less overall corrosive attack in the liquid portion of the boiler region. Typical micrographs from the two surfaces are shown in Fig. 27.3.

Comparing the condenser weight losses of Haynes alloy No. 25 loops operated at 870 and 980°C indicates that dissolutive corrosion of this alloy does not increase inordinately with increasing temperature. Figure 27.4 shows the surface from the higher temperature loop and should be compared with Fig. 27.3*b*. Furthermore, at the higher test temperature, aging, embrittlement, and fatigue cracking were less severe.

Carbon was transferred from the condensing region to the subcooled liquid region in all the loop tests. Attendant with this, the elongation of the material decreased and the tensile strength increased. No evidence of preferential leaching of major metallic constituents of these alloys was detected by electron microprobe analysis of the condenser surfaces. However, limited mass transfer from the hot region to the cold region was noted.

[3]D. H. Jansen and E. E. Hoffman, *Type 316 Stainless Steel, Inconel, and Haynes Alloy No. 25 Natural-Circulation Boiling-Potassium Corrosion Test Loops*, ORNL-3790 (June 1965).

Fig. 27.2. Microsection of Brazed Joint, Showing Stainless Steel Angles and Stainless-Steel-Clad Copper High-Conductivity Fins Brazed to Stainless Steel Tubes.

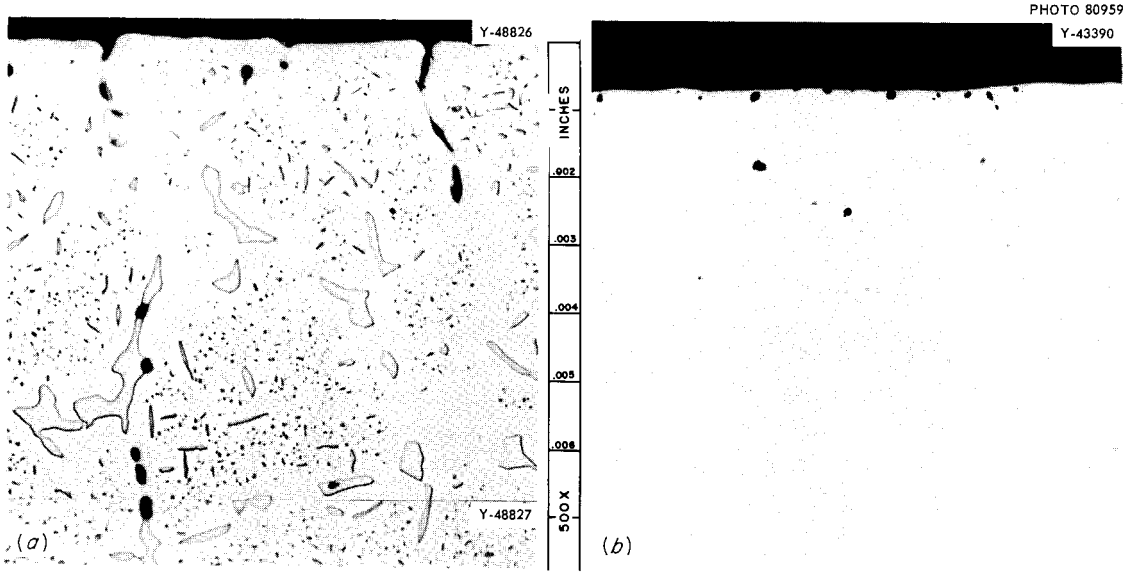

Fig. 27.3. Sections from Condenser Regions of (*a*) Type 316 Stainless Steel and (*b*) Haynes Alloy No. 25 Natural-Circulation Loops, After 3000-hr Exposure to Boiling Potassium at 870°C. Specimen (*a*) etched with aqua regia; (*b*) as polished. 500×.

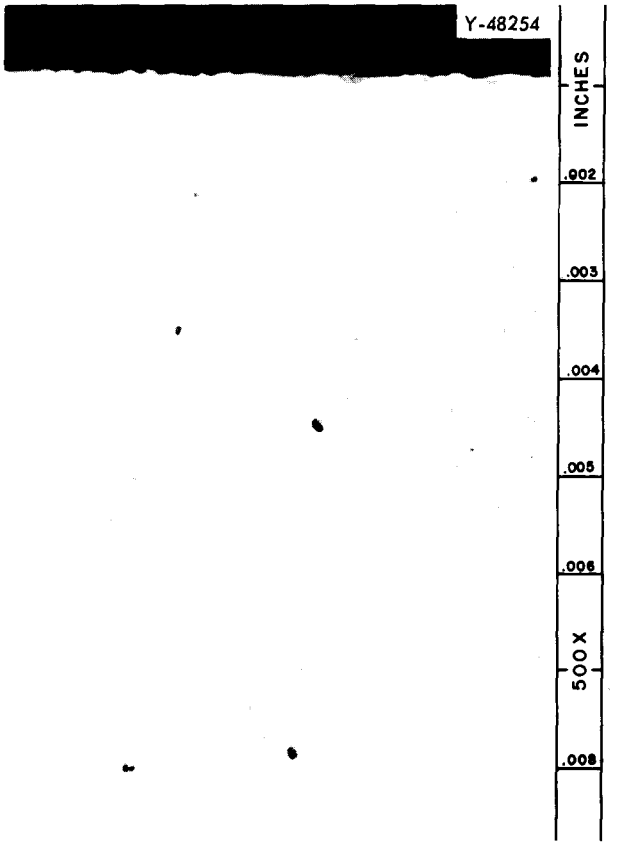

Fig. 27.4. Condenser Region of Haynes Alloy No. 25 Boiling Potassium Loop Operated for 3000 hr at 980°C. 500×. As polished.

Although the two type 316 stainless steel loops in this series had operated under outwardly similar time and temperature conditions, small differences in corrosion rate were noted between the two tests. This effect was attributed to severe boiling instabilities that prevailed in the second of the two loops. Accordingly, a third type 316 stainless steel loop test was recently operated to achieve a longer term evaluation of this alloy with boiling stabilized by the insertion of auto-resistance-heated nucleation sites in the boiler wall. Although scheduled for 5000-hr operation, the test was terminated after 2600 hr by a failure of a $\frac{1}{4}$-in.-OD thermocouple well in the boiler.[4] This failure followed two earlier failures that had also occurred in thermocouple-well closures (a design change has now apparently cured this difficulty). The presence of a relatively large amount of mass-transfer deposit, insert weight changes, and chemical analyses on the inserts indicated a more severe rate of corrosion in this loop than in previous tests. This accelerated attack apparently was the result of air contamination resulting during the thermocouple-well failures. We are now investigating the rate of dissolutive attack on type 316 stainless steel as affected by controlled amounts of oxygen in the potassium.

[4]D. H. Jansen and J. H. DeVan, ORNL-3774, pp. 92–99 (classified).

TYPE 316 STAINLESS STEEL – TZM FORCED-CIRCULATION LOOPS

D. H. Jansen

We are evaluating the corrosion-erosion resistance of candidate nozzle and turbine blade materials in high-velocity potassium vapor.[5,6]

TZM alloy (Mo–0.5% Ti–0.08% Zr) nozzle and turbine blade specimens showed severe cratering and relatively high weight losses after exposure to potassium vapor in a type 316 stainless steel forced-circulation test loop.[7] Reaction products removed from the TZM components showed unusually high concentrations of carbon and oxygen.

To ascertain whether the resultant damage was due to a mass transfer reaction between the dissimilar metals in the system, a type 316 stainless steel capsule with TZM inserts was operated with refluxing potassium for 1000 hr at 870°C. Carefully purified potassium (20 ppm O by the amalgamation method) was used. Alternate TZM and stainless steel sleeve-type inserts (three each) lined the condenser region. Stable boiling was achieved by use of capillary nucleation sites in the lower part of the boiler.

Posttest inspection of the capsule revealed no interaction between the TZM and stainless steel alloys, and metallographic examinations revealed no corrosion or dissimilar-metal mass transfer in any of the components. Slight changes in carbon, oxygen, and nitrogen contents were noted in the insert specimens, but the changes were in the range with those found on all-stainless steel or

[5]R. E. MacPherson, L. C. Fuller, and C. W. Cunningham, ORNL-3571, pp. 173–75 (classified).

[6]J. H. DeVan *et al.*, ORNL-TM-980, p. 65 (classified).

[7]L. C. Fuller, C. W. Cunningham, and D. H. Jansen, ORNL-3683, pp. 226–30 (classified).

all-TZM systems operated for comparable periods in this temperature range.

In view of this test and the lack of any interaction between the alloys, the damage to the TZM test section from the forced-circulation loop discussed above can be attributed to either the erosion and fretting attack of the TZM by high-velocity vapor or to a high oxygen content in the potassium. A forced-circulation system using the same alloys is currently being operated with a full-flow zirconium hot trap incorporated to provide oxygen-free potassium to the TZM test section.

HIGH-EMITTANCE COATINGS FOR METALS

R. M. Evans T. G. Kollie
R. S. Graves

A series of preliminary investigations have been carried out to determine the chemical properties and stability at temperature of a commercial[8] emittance coating designated PT-404. This material was described by the manufacturer as a silicone ceramic material designed for continuous operation at temperatures in the range of 16 to 1100°C.

Initial evaluation of this material included spectrographic analysis of coatings that had been applied to 6061 aluminum, furnace treated for 1 hr at either 260 or 500°C. The analysis revealed very strong evidence of silicon with weak to moderate amounts of Mo, Mn, Fe, Pb, and Ti. The coating treated at the higher temperature showed strong indications of aluminum.

Also, we coated specimens of 0.045-in.-thick type 316 stainless steel sheet. Prior to being coated, the individual pieces of metal were vapor blasted to provide the required roughened surface. A 0.002- to 0.003-in.-thick coating was applied, in accordance with the specifications supplied by the manufacturer, and then cured for 1 hr at 260°C before further testing.

Three series of specimens were open-air furnace treated at temperatures of 260, 537, 815, and 890°C for times of 1, 100, and 1000 hr. In addition, two series of tests were carried out under thermal cycling conditions. One test series was thermally cycled 15 times during a 168-hr period by air cooling to room temperature and reinsertion in the furnace. The other series was similarly tested for 50 cycles and 552 hr.

The coating was quite stable at 269°C. However, inconsistent evidence of flaking was observed at temperatures of 537°C and above. The results of these preliminary tests were too inconclusive to permit establishment of maximum operating conditions for this material. As a result, a second set of tests was initiated with more stringent control of noted variables and the inclusion of specimens made from Alzak, a special one-side-reflective aluminum.

The total hemispherical emittance, E_t, of a type 316 stainless steel strip specimen coated with the PT-404 was measured to 800°C in a vacuum of 1×10^{-6} torr. The specimen was heated for 1 hr at 260°C in air prior to instrumentation with Pt–10% Rh,Pt thermocouples. Data were obtained during two thermal cycles to 800°C and during a 48-hr anneal at 800°C. The results from 200 to 800°C can be expressed to ±2% as a linear function of temperature, t (°C):

$$E_t = 0.880 + 1.1(t - 200) \times 10^{-4} .$$

Previous determinations[9] of the emittance of bright and oxidized type 316 stainless steel had yielded the relations

$$E_t \text{ (bright)} = 0.135 + 1.6(t - 200) \times 10^{-4}$$

and

$$E_t \text{ (oxidized)} = 0.57 + 2.37(t - 200) \times 10^{-4}$$

respectively. Thus the PT-404A coating is an effective means for increasing the total hemispherical emittance of type 316 stainless steel. The 48-hr anneal at 800°C increased E_t 2%.

[8]Produced by Products Techniques, Inc.

[9]T. G. Kollie and D. L. McElroy, *Metals and Ceramics Div. Ann. Progr. Rept. June 30, 1964*, ORNL-3670, p. 109.

28. Molten-Salt Reactor Program

A. Taboada

The Molten-Salt Reactor Program is concerned with research and development for nuclear reactors that use mobile fuels that are solutions of fissile and fertile materials in suitable carrier salts. The program is aimed at the development of reactors for producing low-cost power for civilian uses and ultimately a thermal breeder reactor.

Our major effort is being applied to the development, construction, and operation of the Molten-Salt Reactor Experiment[1] (MSRE). The purpose of this experiment is to test the types of fuels and materials that would be used in thermal breeder and converter reactors and to obtain experience with the operation and maintenance of a molten-salt power reactor. A successful experiment will demonstrate on a small scale the attractive features and the technical feasibility of these systems for large civilian power reactors. The MSRE will operate at 1200°F and atmospheric pressure and will generate 10 Mw of heat. Initially, the fuel will contain 0.9 mole % UF_4, 5 mole % ZrF_4, 29.1 mole % BeF_2, and 65 mole % LiF, and the uranium will contain about 30% ^{235}U. In later operation, highly enriched uranium will be used in lower concentration, and a fuel containing ThF_4 will also be tested.

The fuel will circulate through a reactor vessel and an external pump and heat exchange system. All this equipment is constructed of INOR-8, a Ni-Cr-Mo alloy developed to resist corrosion by molten fluorides and have good strength at high temperatures. The reactor core contains an assembly of low-permeability graphite moderator bars that are in direct contact with the fuel.

Our part of this program is primarily limited to those problems affecting the successful completion and operation of the MSRE. It includes both metallurgical assistance to other divisions working towards this aim and development and testing of reactor materials. We are emphasizing study of effects of irradiation on the elevated-temperature mechanical properties of INOR-8.

[1]R. B. Briggs *et al.*, *MSR Program Semiann. Progr. Rept. July 31, 1964*, ORNL-3708.

EVALUATION OF MSRE GRAPHITE

W. H. Cook

We continued evaluation of the MSRE graphite, grade CGB. Our efforts are directed toward the determination of the acceptability of this material as a moderator in the MSRE and advanced molten-salt reactors.

Grade CGB graphite is not permeated by molten fluoride salts in the MSRE because it is not wetted by the molten fluoride salts and because the pore entrance diameters of the accessible voids in the graphite are so small[2] ($<0.4\ \mu$). We have made additional studies of the accessible voids in CGB graphite with xylene and molten sulfur respectively.[3] The latter showed the configuration of the penetration by a wetting fluid. A soaking technique at room temperature was used to penetrate the graphite with xylene. The sulfur penetration was made with molten sulfur at 150°C under an overpressure of 150 psig. Test specimens were evacuated prior to the penetrations. The results from both tests suggest that a wetting fluid does not penetrate beyond approximately 0.25 in. below an exposed surface, whether external or along a fissure. This is illustrated in Fig. 28.1, which includes a salt-impregnated specimen for comparison.

[2]W. H. Cook, *Metals and Ceramics Div. Ann. Progr. Rept. June 30, 1964*, ORNL-3670, pp. 216–17.

[3]R. B. Briggs *et al.*, *MSR Program Semiann. Progr. Rept. Feb. 28, 1965*, ORNL-3812, pp. 77–80.

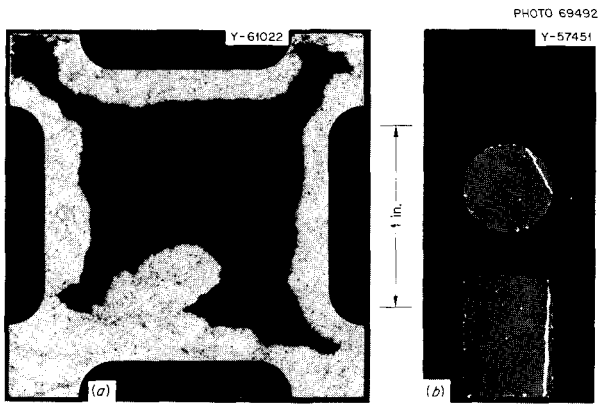

Fig. 28.1. Radiographs of 0.025-in.-thick Sections Machined from Impregnated MSRE Graphite Showing the Penetration by (*a*) a Wetting Fluid, Molten Sulfur, and (*b*) a Nonwetting Fluid, a Molten Fluoride Salt. The white phases are the impregnating fluids.

REACTION OF INOR-8 WITH IMPURE NITROGEN

H. Inouye

The reactor cell atmosphere in the MSRE is designed to be nitrogen containing less than 5% O_2. This atmosphere of low oxygen content eliminates the hazard of explosion that could result from a leakage of oil from the lubricating system of the fuel-salt circulating pump. Since INOR-8, the reactor structural material, will be exposed to this environment at temperatures up to 1300°F, we tested the compatibility of INOR-8 with oxygen-nitrogen mixtures.

The composition of INOR-8 was formulated to resist oxidation and molten-salt corrosion but not nitridation. Furthermore, the possibility existed that the proposed atmosphere could accelerate the oxidation rate of the alloy several orders in magnitude due to "oxygen starvation." Briefly, this surface phenomenon arises from the formation of volatile and corrosive molybdenum oxides rather than the adherent films based on chromium oxide. We expect that the proposed service temperature will be too low for either of these reactions to occur. Our experiments[4] verify this conclusion.

INOR-8 specimens were exposed to oxygen-nitrogen mixtures ranging from 0.03 to 5.6% O_2 for periods up to 700 hr and reaction rates were measured automatically with a recording balance. The reaction rates of the alloy with nitrogen containing three concentrations of oxygen at 1300°F and two concentrations of oxygen at 1400°F are shown in Fig. 28.2. At both temperatures the rate

[4]R. B. Briggs *et al.*, *MSR Program Semiann. Progr. Rept. Feb. 28, 1965*, ORNL-3812, pp. 63–64.

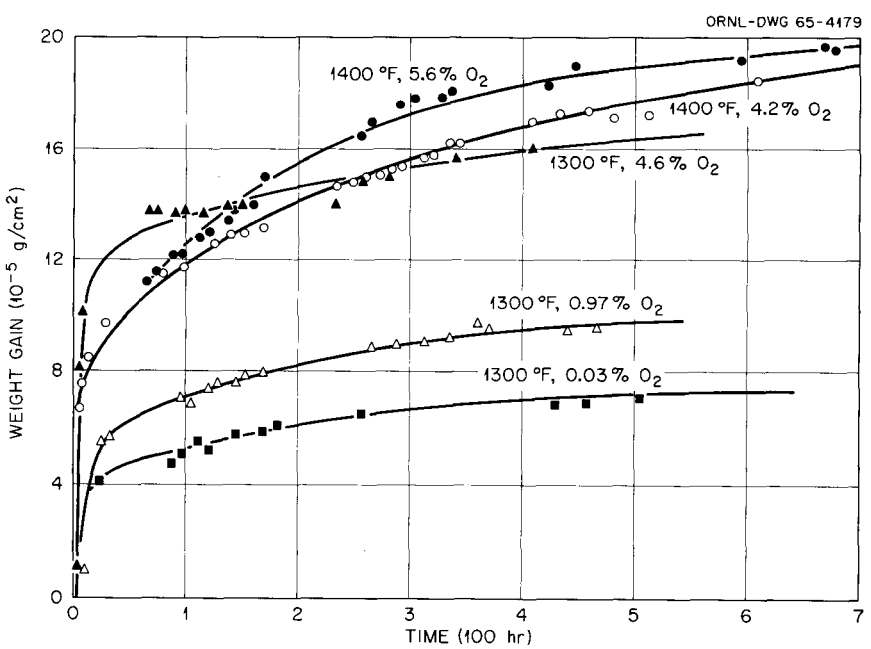

Fig. 28.2. Reaction Rate of INOR-8 with Nitrogen Containing Oxygen.

increased as the oxygen content of the gas increased. The characteristic sharp decrease in the reaction rates after a short exposure time indicated that the reaction product formed an effective barrier between the gases and the alloy.

The above results support our original conclusion regarding resistance of the alloy to the proposed atmosphere. Although the surface films have not been identified, they are expected to be oxides. Based upon our correlations between weight gain and depth of oxidation, the estimated extent of reaction in the worst case amounted to an oxidation depth of about 0.05 mil in 700 hr.

MECHANICAL PROPERTIES OF INOR-8 WELDS

R. G. Gilliland

We have concluded the investigation of the mechanical properties of welds in MSRE-approved heats of INOR-8. Final testing included hot-ductility investigations and stress-rupture studies at 1100, 1300, and 1500°F. The room- and elevated-temperature tensile studies have been reported previously.[5]

The stress-rupture studies were conducted using specimens machined transverse to the INOR-8 weld, which was made under conditions of high restraint. The results of these tests are presented in Table 28.1 for specimens in the as-welded and welded-and-stress-relieved conditions. When compared with base-metal data,[6] the as-welded creep properties of these specimens were equal to wrought metal at all test temperatures. (For behavior of other specimens see below under "Composition Effects in INOR-8.") Stress relief in hydrogen significantly improved creep-rupture properties only at 1300°F; stress-relieved samples tested at 1100 and 1500°F showed little or no improvement over as-welded properties. No improvement resulted from stress relief in argon at 1300°F.

[5]R. G. Gilliland, *Metals and Ceramics Div. Ann. Progr. Rept. June 30, 1964*, ORNL-3670, pp. 217–18.

[6]J. T. Venard, *Tensile and Creep Properties of INOR-8 for the Molten-Salt Reactor Experiment*, ORNL-TM-1017 (February 1965).

Table 28.1. Results of Elevated-Temperature Creep Tests on INOR-8 Transverse Weld Specimens

Test Temperature		Applied Stress	Average Time to Rupture (hr)			Average Elongation (%)			Average Minimum Creep Rate (hr)		
			As Welded	Stress Relieved[a]		As Welded	Stress Relieved[a]		As Welded	Stress Relieved[a]	
(°F)	(°C)	(psi)		H_2	Ar		H_2	Ar		H_2	Ar
1100	594	74,000	1.3	1.7		14.1	13.0		2.6×10^{-3}	1.3×10^{-2}	
1100	594	54,000	197.8	188.3		2.5	8.2		2.3×10^{-5}	1.0×10^{-5}	
1100	594	49,000	308.4	570.5		2.2	5.3		1.4×10^{-5}	3.2×10^{-5}	
1300	704	45,000	3.7	6.4	5.5	3.9	8.2	5.4	4.9×10^{-3}	7.4×10^{-3}	7.0×10^{-3}
1300	704	24,000	158.4	337.8	185.4	3.7	8.8	7.4	1.2×10^{-4}	1.6×10^{-4}	2.2×10^{-4}
1300	704	20,000	472.3	936.7	452.2	4.6	10.8	3.7	3.5×10^{-5}	6.6×10^{-5}	4.4×10^{-5}
1500	816	22,000	12.7	12.1		16.9	20.9		5.8×10^{-3}	7.0×10^{-3}	
1500	816	12,000	172.1	117.5		14.4	9.8		4.8×10^{-4}	4.4×10^{-4}	
1500	816	10,000	446.9	314.5		8.3	8.1		9.8×10^{-5}	2.0×10^{-4}	

[a]Stress relieved 2 hr at 1600°F in atmosphere specified.

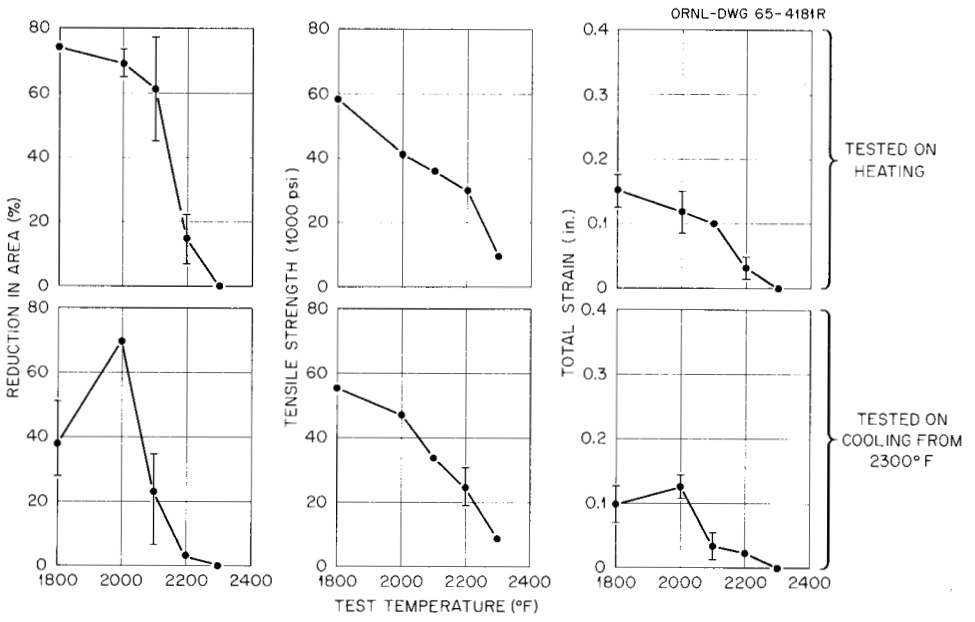

Fig. 28.3. Results of On-Heating and On-Cooling Hot-Ductility Tests on MSRE Reactor-Grade INOR-8. The nil-ductility temperature for the material was found to be 2300° F.

Hot-ductility experiments using Gleeble synthetic heat-affected zone specimens revealed the elevated-temperature nil-ductility point for this material to be 2300°F. Complete data from these studies are presented graphically in Fig. 28.3. Reasonable recovery of the mechanical properties after heating to the nil-ductility temperature was exhibited, although some permanent damage apparently occurred as a result of the welding thermal cycle. Metallographic analysis of alloy microstructures thermally cycled through these temperature ranges revealed some grain-boundary liquation.

MICROSTRUCTURES OF INOR-8 WELDMENTS

R. G. Gilliland

One of the more troublesome problems frequently occurring in nickel-base alloys is that they are, to various degrees, sensitive to damage under conditions of thermal cycling, thermal shock, and thermal fatigue. This type of damage can be a limiting factor in certain areas in reactor design. In the early studies on the original experimental heats of INOR-8 a large number of microfissures were found in the heat-affected zones of highly restrained welds.[7–10] When cracks were observed, they invariably occurred in an eutectic-like structure existing in the grain boundaries. This structure formed during welding and originated from the stringer-type phase existing in the INOR-8 base metal.

Since the thermal damage originates from a brittle structure located in the grain boundaries, the morphology of the INOR-8 heat-affected zone microstructure was of obvious interest. We are conducting a rigorous microstructure analysis on this grain-boundary phase, using simulated heat-affected zone structures produced by the Gleeble hot-ductility machine.[11] The material being used in this study consists of the early experimental SP-type INOR-8 heats, which were found to contain large quantities of the suspect structure in

[7] P. Patriarca and G. M. Slaughter, *MSR Program Progr. Rept. Oct. 31, 1957*, ORNL-2431, pp. 18, 21–23.

[8] G. M. Slaughter, *MSR Program Progr. Rept. Jan. 31, 1958*, ORNL-2474, pp. 65–71.

[9] *MSR Program Progr. Rept. Feb. 28, 1961*, ORNL-3122, pp. 81–86.

[10] *MSR Program Progr. Rept. Aug. 31, 1961*, ORNL-3215, pp. 106–9.

[11] I. F. Nippes *et al.*, *Welding J.* **34**(4), 183–85 (1955).

PHOTO 80960

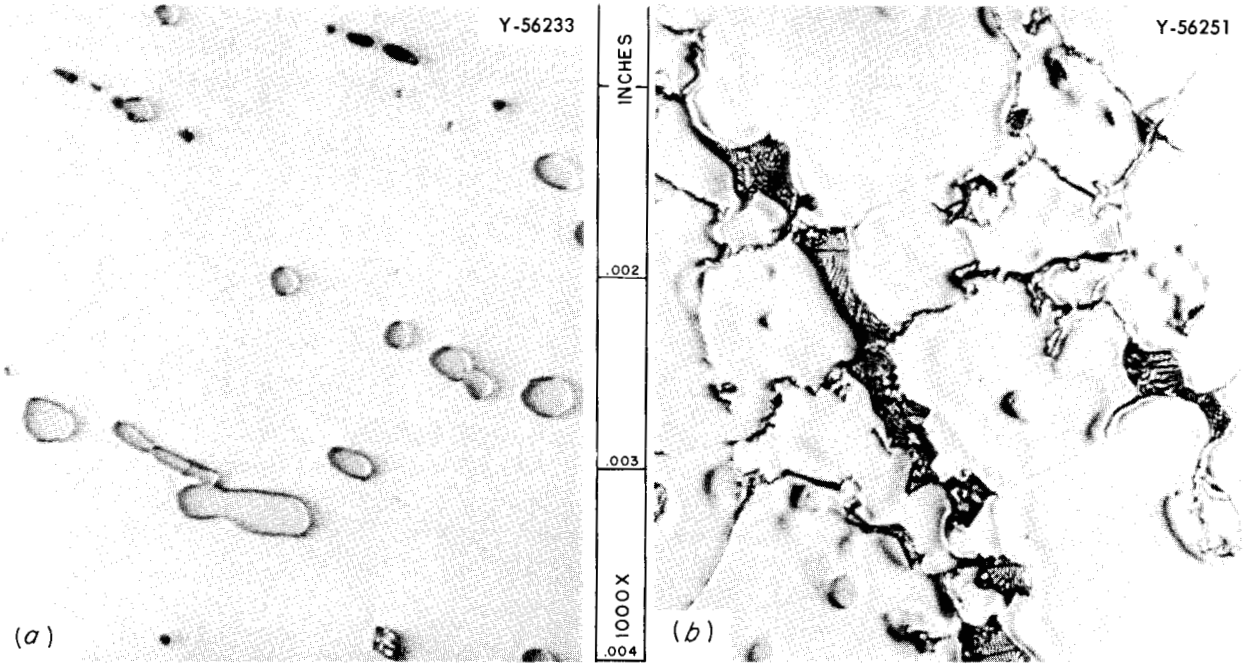

Fig. 28.4. (*a*) Microstructure of Unaffected INOR-8 Base Metal Showing the Stringer-Type Phase; (*b*) Simulated Heat-Affected Zone Microstructure in INOR-8 Heat No. SP-19 Obtained with a Thermal Cycle with a Peak Temperature of 2300°F. Note the eutectic-type structure in the grain boundaries. Electrolytically etched in H_3PO_4 solution. Oblique lighting. 1000×.

Table 28.2. Results of Microprobe Analysis on INOR-8 Heat No. SP-19 (Semiquantitative)[a]

Element	Nominal Composition (wt %)	Approximate Analyzed Composition (wt %)			
		Lamellar Area		Stringer Area	
		Lamellar Product	Matrix	Stringer Phase	Matrix
Ni	69.62	54.6	70.2	29.5	64.5
Mo	16.10	22.4	10.4	46.0	9.5
Cr	7.04	7.5	7.5	6.0	7.5
Fe	4.60	3.9	5.4	1.6	5.3
Mn	0.52	0.7	0.8	0.2	0.6
Al	0.06	0	0	<0.1	<0.1
Ti	0.02	0.5	0.4	0.5	0.5
C	0.024				
Co		0.5	0.6	0.4	0.6
Si	0.16	0.3	0.2	0.6	<0.1

[a]An approximate correction for absorption effects was applied to the semiquantitative results.

heat-affected zone areas. These studies are being supplemented by hot-stage metallography, by the hot-ductility data previously collected for these INOR-8 heats, and by quantitative analysis of the grain-boundary structure using microprobe techniques.

Views of the stringer-type phase in the base metal and the grain-boundary structure in question are shown in Figs. 28.4a and 28.4b respectively. This lamellar-type structure was produced using a simulated welding thermal cycle with a peak temperature of 2300°F in INOR-8 heat No. SP-19. Currently, only preliminary data are available from the microprobe analysis investigation. These studies were performed on the samples shown in Fig. 28.4, and the results are presented in Table 28.2. As shown in these data, the lamellar- or eutectic-type structure is enriched in molybdenum and depleted in nickel when compared with the nominal and matrix compositions. The stringer phase is quite different from the lamellar; molybdenum is its major component.

Further analysis of these data and microstructures is currently under way.

JOINING OF GRAPHITE TO METALS

R. G. Donnelly

The joining of graphite to structural metals such as INOR-8 is of interest for use in advanced molten-salt reactors as well as for general high-temperature engineering systems that might require the use of graphite. The basic obstacle encountered in attempting such a joint is the very large difference between the thermal expansion coefficients of graphite and many metals. Due to this difference, a brazed joint of graphite to INOR-8 cracks upon cooling from the brazing temperature.

Transition Joints

One possible solution to the problem of differential expansion is to introduce one or more materials with expansion coefficients intermediate between those of the graphite and INOR-8 parts. In order to determine optimum techniques for making such a graphite-to-INOR-8 transition joint, INOR-8-to-dissimilar-metal joints and graphite-to-metal joints were brazed with various fluoride-resistant brazing alloys, and T-joints of these combinations were examined metallographically. Details of this work have been reported[12] previously.

The most significant observation from the dissimilar metal joint study is that metals with relatively wide differences in coefficients of thermal expansion exhibited sound joints when brazed with a ductile alloy (gold-nickel or copper), but the joints cracked as expected when brazed with brittle alloys or when brittle phases developed in the braze.

In the tests of graphite-to-metal joints, the ductility of the alloy seemed to make little difference, and the limiting factor was the difference between the coefficients of expansion of the graphite and the metal. Thus, the molybdenum-to-graphite and tungsten-to-graphite joints showed no transverse cracking, while the metals with the higher coefficients, niobium and tantalum, showed considerable cracking across the brazed joints.

As a result of this study, several possibilities for joining graphite to INOR-8 appear to be of interest, and work is currently in progress with those compositions.

Brazing Alloy Development

The most successful alloy that has been developed for brazing graphite and one that is also compatible with molten salts is the 35% Au–35% Ni–30% Mo alloy. This alloy contains a compatible carbide-forming element (molybdenum) added to a corrosion-resistant and reasonably low-melting alloy system (gold-nickel). Since the use of a gold-containing alloy in a high-flux region of a reactor might be inadvisable, we started to develop a gold-free graphite brazing alloy for this application. We selected the palladium-nickel system, which is similar to the gold-nickel system and is expected to be corrosion resistant to fused fluorides. In addition, palladium has the added advantage of a lower thermal-neutron cross section than gold (8 vs 99 barns). Also, the transmutation product of palladium would be silver, which is less objectionable in the molten-salt system than mercury, the transmutation product of gold.

[12] R. B. Briggs *et al.*, *MSR Program Semiann. Progr. Rept. Feb. 28, 1965*, ORNL-3812, pp. 73–76.

MECHANICAL PROPERTIES OF IRRADIATED INOR-8

J. R. Weir W. W. Davis
W. R. Martin H. E. McCoy

We found[13] that the stress-strain relationship of INOR-8 at high temperature was not affected by irradiation but the high-temperature ductility was reduced. This reduction became more severe as the temperature was raised. Ductility also decreased as the strain rate was reduced from 0.2 to 0.002 in./min.

Although the tensile ductilities measured at the MSRE operating temperatures were still adequate to accommodate any tensile-type loading expected in the MSRE, the dependence of ductility on strain rate suggested that additional information was needed on the effects of irradiation on creep properties, particularly on creep ductility. Progress on initial efforts to determine this information is reported below.

Composition Effects in INOR-8

H. E. McCoy

In an accelerated program, we are seeking to (1) evaluate and improve the resistance of INOR-8 to irradiation and (2) improve the basic properties of the alloy. Since both objectives involve the composition of the alloy, we need a thorough knowledge of the physical metallurgy of this alloy and how it varies with changes in composition. The significant findings to date, excluding the irradiation studies, are summarized below.

The various air-melted heats and one vacuum-melted heat had very similar creep strengths. However, the vacuum-melted alloy was more ductile. Studying arc-melted alloys prepared with the addition of elements other than Ni, Mo, Cr, Fe, and C, we found that the strength did not greatly depend upon the "tramp" elements present, such as aluminum, silicon, and manganese.

Welds were prepared from the same heats of base metal and weld wire utilized in the MSRE. At 650°C (operating temperature of the MSRE) test specimens failed in the weld metal. The failure time and rupture ductility were considerably less than that for the base metal. Stress relieving at 871°C significantly improved the rupture life and ductility. A different series of experiments, reported above under "Mechanical Properties of INOR-8 Welds," demonstrated welds with unimpaired mechanical properties. Preliminary evidence indicates that the difference between those results and these arose from differences in the welding wire used.

Metallographic studies showed that welding transforms the large almost spherical precipitate grains to a lamellar phase. Electron microprobe studies have shown that the spherical grains are basically NiMo and that the lamellar phase is Ni_3Mo. These precipitates contain about the same concentration of chromium as the matrix, are deficient in iron and manganese, and are highly enriched in silicon. Independent studies on an alloy containing ^{14}C have shown that both precipitates are deficient in carbon. Hence, these studies have shown that this alloy (as melted in air) contains an intermetallic phase and that large amounts of silicon are associated with this intermetallic. We do not know yet what are the independent effects of the intermetallic compound and the silicon concentration on the weldability and strength.

Experimental alloys have been made to examine the influence of Mo, Mn, Si, Fe, and Al contents on the properties of the basic alloy. We have made two significant observations so far. First, lowering the molybdenum content from the normal 16 to 10% produced a single-phase alloy after a 1-hr anneal at 1177°C. Also, increasing the silicon content made it progressively more difficult to break up the cast structure. An alloy containing 1% Si melted at least 100°C lower than an alloy containing no intentionally introduced silicon. No other elements studied seemed to have any significant effect on the segregation pattern or melting point of the alloy.

Postirradiation Creep of INOR-8

W. R. Martin

Irradiation is known to influence the elevated-temperature mechanical properties of structural materials. The bulk of the data now available is postirradiation tensile data; limited information

[13] W. R. Martin and J. R. Weir, *The Effects of Elevated Temperature Irradiation on the Strength and Ductility of the Nickel-Base Alloy, Hastelloy N*, ORNL-TM-1005 (February 1965).

exists on the in-reactor and postirradiation creep properties. To better assess the lifetime of reactor components designed on the basis of creep data from unirradiated specimens, we need to measure creep of irradiated materials. We are beginning to ascertain the effects of irradiation on the in-reactor and postirradiation creep of INOR-8.

We are determining the dose dependence of the ductility and rupture life of two heats of INOR-8 at several stress levels. These uniaxial creep tests at 650°C will show the influence of irradiation on creep rate, time to rupture, and ductility. Our results to date can be summarized as follows. The time to rupture and ductility are reduced as the irradiation dose is increased, as shown in Table 28.3. For a given time of deformation, the variation in strain among the specimens irradiated to different doses is not significant, as illustrated in Fig. 28.5. The difference in behavior of the two heats is due in part to the boron content. Heat 2477 contained 6.8 ppm B, while Heat 5065 contained approximately 37 ppm.

In-Reactor Creep of INOR-8

W. W. Davis

The first and second ORR poolside creep experiments on INOR-8 are scheduled to be removed from the reactor and a third installed during the second week in July. Each contains five active tensile creep experiments and five postirradiation creep specimens for comparison tests. We have obtained valuable data (mostly on Heat No. 5065) on creep rates, effect of stress on rupture life, and total strain at rupture. Figure 28.6 compares stress and rupture time of three in-reactor creep specimens with data from unirradiated specimens of the same heat. Indicated are the dose at fracture and the creep strain at fracture for the specimens tested in-reactor. These strains may be compared to about 10% creep strain for unirradiated specimens tested in the absence of irradiation.

Table 28.3. Dose Dependence of Elevated-Temperature Embrittlement of INOR-8

Irradiated Dose (neutrons/cm^2)	Stress (psi)	Heat 2477		Heat 5065	
		Time to Rupture (hr)	Elongation[a] (%)	Time to Rupture (hr)	Elongation[a] (%)
	$\times 10^3$				
0	52	~70		52.1	8.2
5.0×10^{16}	52	70.6	3.4	21.2	2.6
1.3×10^{18}	52	57.1	3.3	12.0	2.0
9.0×10^{18}	52	30.4	4.6	5.1	3.4
5.0×10^{19}	52	21.1	4.2	0.4	0.9
0	40			~350.0	
5.0×10^{16}	40			360.0	2.8
1.3×10^{18}	40			147.0	
9.0×10^{18}	40			80.2	2.4
5.0×10^{19}	40			23.5	1.2

[a]Elongation measured during creep. Specimens stressed at 52,000 and 40,000 psi are above the yield strength (~39,000 psi), and approximately 4 and 0.2% strain should be added to the values for the 52,000 and 40,000 psi tests, respectively, to give accurate total strain values.

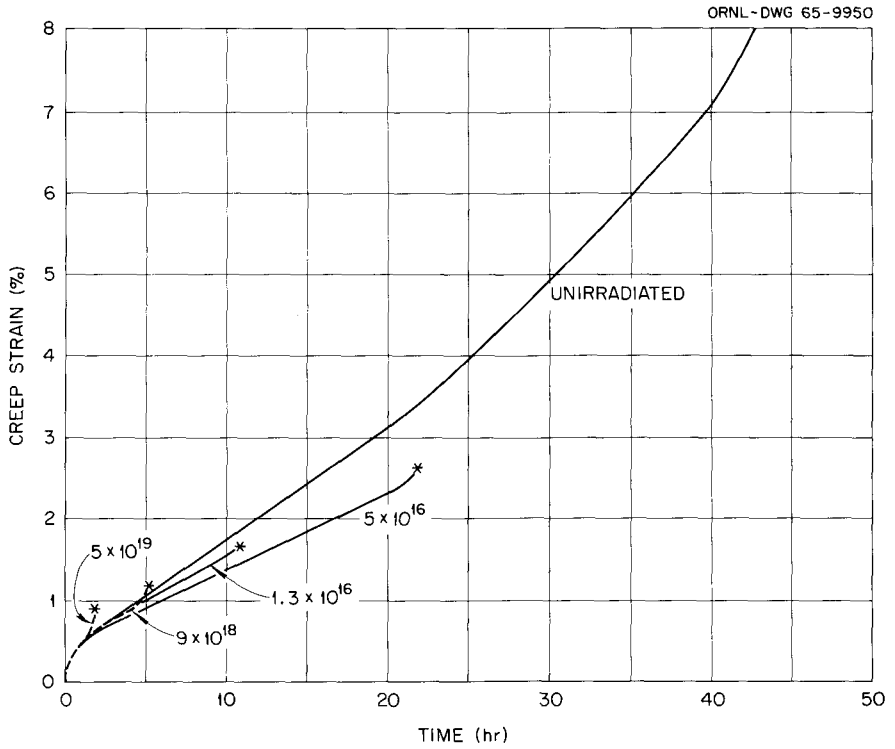

Fig. 28.5. Postirradiation Creep at 650°C of INOR-8, Heat No. 5065, Stressed at 52,000 psi. Total strain at fracture should include 4% deformation that occurred on load application, in addition to the strains given by these curves.

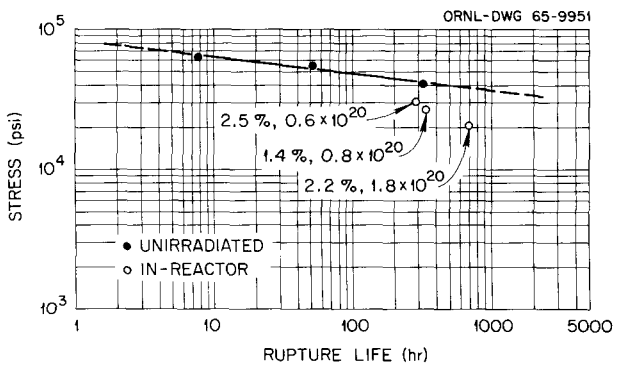

Fig. 28.6. Stress-Rupture Data for INOR-8 Tested at 650°C Both In-Reactor and Unirradiated. The strain and dose (neutrons/cm^2) at rupture are indicated for the in-reactor specimens.

POSTIRRADIATION METALLOGRAPHIC EXAMINATION OF MSRE IN-REACTOR TESTS

E. J. Manthos

We have examined capsule components from two in-reactor experiments, ORNL MTR 47-5 and 47-6.

Experiment ORNL MTR 47-5

Six INOR-8 capsules were irradiated in experiment MTR 47-5. Irradiation conditions and a description of the experiment have been reported.[14]

[14]R. B. Briggs *et al.*, *MSR Program Semiann. Progr. Rept. July 31, 1964*, ORNL-3708, pp. 271–81.

Four types of INOR-8 capsules were irradiated. Two of the capsules, R and F, contained a fuel-impregnated AGOT graphite core that was not in contact with the capsule wall. Capsules 3 and 4 were similar in construction to earlier capsules and contained a graphite core submerged in fuel; the capsules were also equipped with purge lines. Capsule 1 contained a graphite core and a graphite crucible that was in contact with the capsule wall; both the core and the crucible were submerged in fuel. Capsule 2 contained a two-piece INOR-8 core into which a graphite wafer was sandwiched.

Sections of the capsule wall and graphite from all the capsules were examined. A section of the stainless steel reducer from the INOR-8 purge lines of capsules 3 and 4 was also examined.

Fluorine gas was evolved from capsules 3 and 4; a greater amount from 4. The stainless steel reducer from the capsule 4 purge line was severely attacked intergranularly as shown in Fig. 28.7. The attack had occurred adjacent to the weld that joined the stainless steel reducer to the INOR-8 purge line; the INOR-8 line was unaffected and appeared normal. We saw no attack on the stainless steel reducer from capsule 3. The attack on capsule 4 can perhaps be attributed to the greater amount of fluorine. At the liquid-vapor interface, slight surface roughening occurred on capsules 2 and 4, and no evidence of corrosion was seen on capsule 3. The maximum roughening was less than 0.001 in. deep on capsule 4, as shown in Fig. 28.8. There was no difference in attack between the liquid and vapor regions.

We did not examine the walls of capsules R and F. These capsules did not contain free fuel and the capsule walls were not in contact with the fuel-impregnated graphite core. However, we did examine the capsule bottoms and the INOR-8 centering pins that supported and positioned the graphite and saw no evidence of carburization or corrosion. In capsule 1, the surfaces of the INOR-8 core that were in contact with the graphite wafer were carburized to a depth of 0.017 in., as shown in Fig. 28.9. We saw no carburization or corrosion on the surfaces of the INOR-8 core and capsule wall that were exposed to fuel.

We examined at least one graphite section from each capsule, and in most cases the graphite appeared normal. We saw no evidence of salt permeation or film formation on the graphite; however, the specimens were polished in an ethylene glycol slurry that was not inert to the fuel mixture. The graphite from capsules 3 and 4 was cracked and we believe that the fractures may have formed after the fuel solidified or during disassembly, since the crack, as shown in Fig. 28.10, was not filled with salt. We also observed some porous or damaged regions on the surface of the graphite; however, if the graphite was cracked during disassembly, the damaged regions may have been introduced during disassembly. One of the fractures and a damaged region are shown in Figs. 28.10 and 28.11 respectively.

The fuel-exposed surface of the graphite core from capsule 1 appeared normal and is shown in

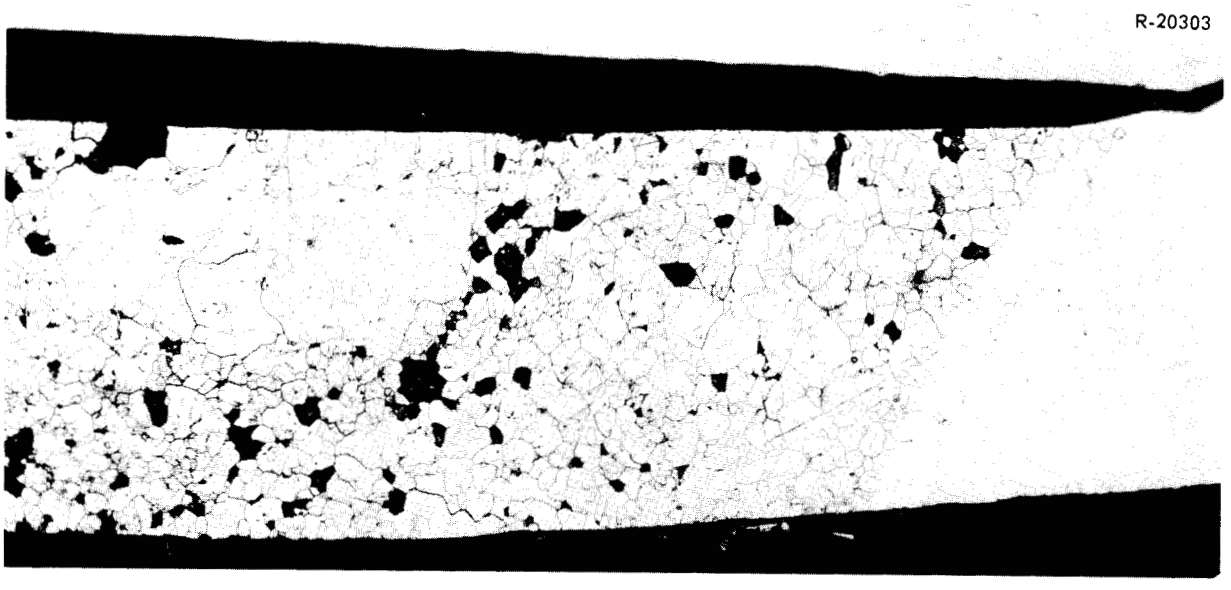

Fig. 28.7. Longitudinal Section of Stainless Steel Reducer Wall on Purge Line Adjacent to INOR-8 to Stainless Weld, Capsule 4 of Experiment 47-5. Intergranular attack was probably caused by fluorine. Unaffected INOR-8 purge line is visible above stainless steel. Etchant: glycera regia. 100×.

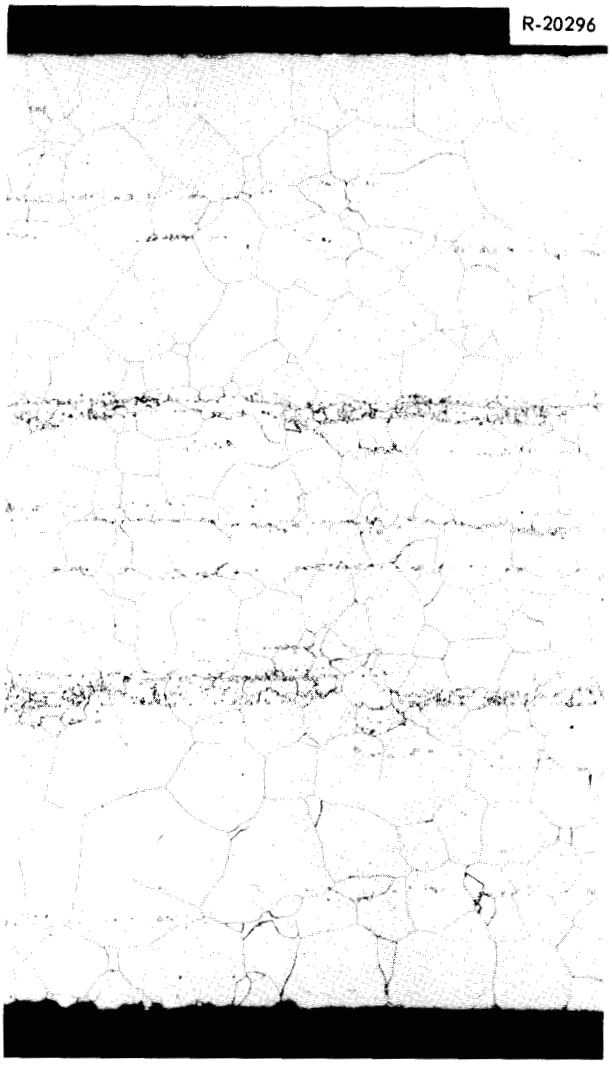

Fig. 28.8. Longitudinal Section of Experiment 47-5 Capsule 4 Wall at Liquid-Gas Interface. Slight roughening less than 0.001 in. deep is visible on inner surface. Etchant: glycera regia. 100×.

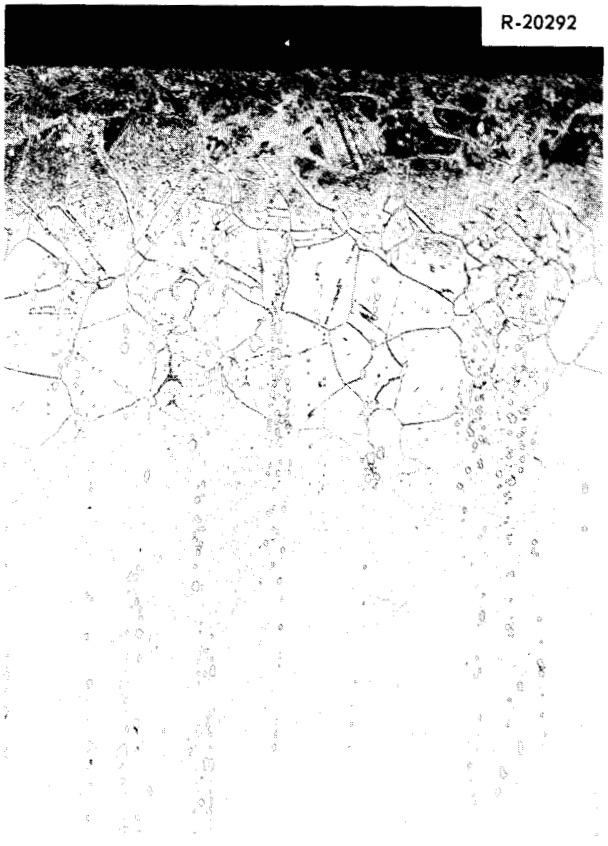

Fig. 28.9. Longitudinal Section of Upper Half of INOR-8 Core Where It Had Been in Contact with Graphite Wafer. INOR-8 had reacted with graphite to a depth of approximately 0.017 in. Capsule 2 of Experiment 47-5. Etchant: picral-HCl. 100×.

Fig. 28.10. Transverse Graphite Core Section Showing Fracture That Formed After Fuel Solidified. Material in fracture is plastic mounting material. Capsule 4 of Experiment 47-5. As polished. 100×.

Fig. 28.11. Transverse Graphite Core Section Showing Damaged Region on Surface. Capsule 4 of Experiment 47-5. As polished. 100×.

Fig. 28.12. Transverse Section of Graphite Core from Capsule 1, Experiment 47-5. As polished. 100×.

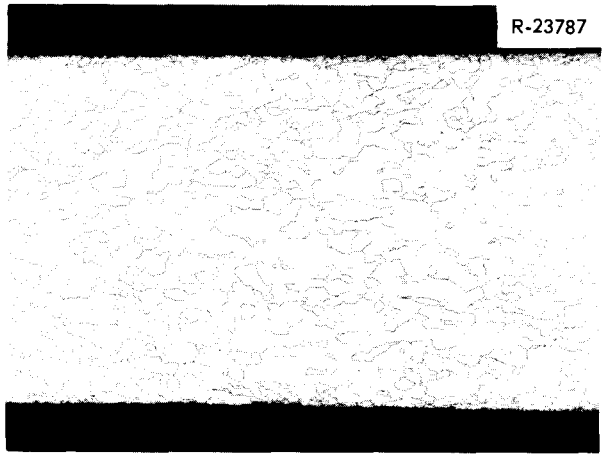

Fig. 28.13. Molybdenum Coupon from Capsule 4 of Experiment 47-6. Etchant: equal parts of 30% H_2O_2 and concd NH_4OH. 100×.

Fig. 28.12. The fuel-impregnated cores from capsules R and F also appeared normal, and we saw no evidence of cracking or swelling of the graphite. The graphite wafer from capsule 1 appeared to have been damaged during disassembly or sectioning, and we could not reach any conclusions regarding the condition of the graphite.

Experiment ORNL MTR 47-6

Four INOR-8 capsules were irradiated in experiment 47-6, and a description of the experiment and operating conditions have been presented.[15] Each capsule contained a graphite core that was submerged in fuel. Two (Nos. 2 and 3) were swept with helium, and the other two (Nos. 1 and 4) were sealed and also contained molybdenum coupons. The capsules were heated to prevent freezing during reactor shutdown. From each capsule, we examined a molybdenum coupon, a graphite section, and a section of the INOR-8 wall at the liquid-vapor interface. Metallographic examination of the capsule walls has not been completed.

We saw no evidence of corrosive attack on the molybdenum coupons examined, as shown in Fig. 28.13. The thicknesses of the coupons were in close agreement with preirradiation measurements.

We prepared the graphite sections under carbon tetrachloride to preserve any fuel or deposits that might have been present. We saw no evidence of fuel permeation, film formation, or corrosive attack on the graphite sections examined. The fuel-exposed surface of a graphite section from capsule 1 is compared to a similar section from an unirradiated control in Fig. 28.14.

[15] R. B. Briggs *et al.*, *MSR Program Semiann. Progr. Rept. July 31, 1964*, ORNL-3708, pp. 281–86.

PHOTO 80961

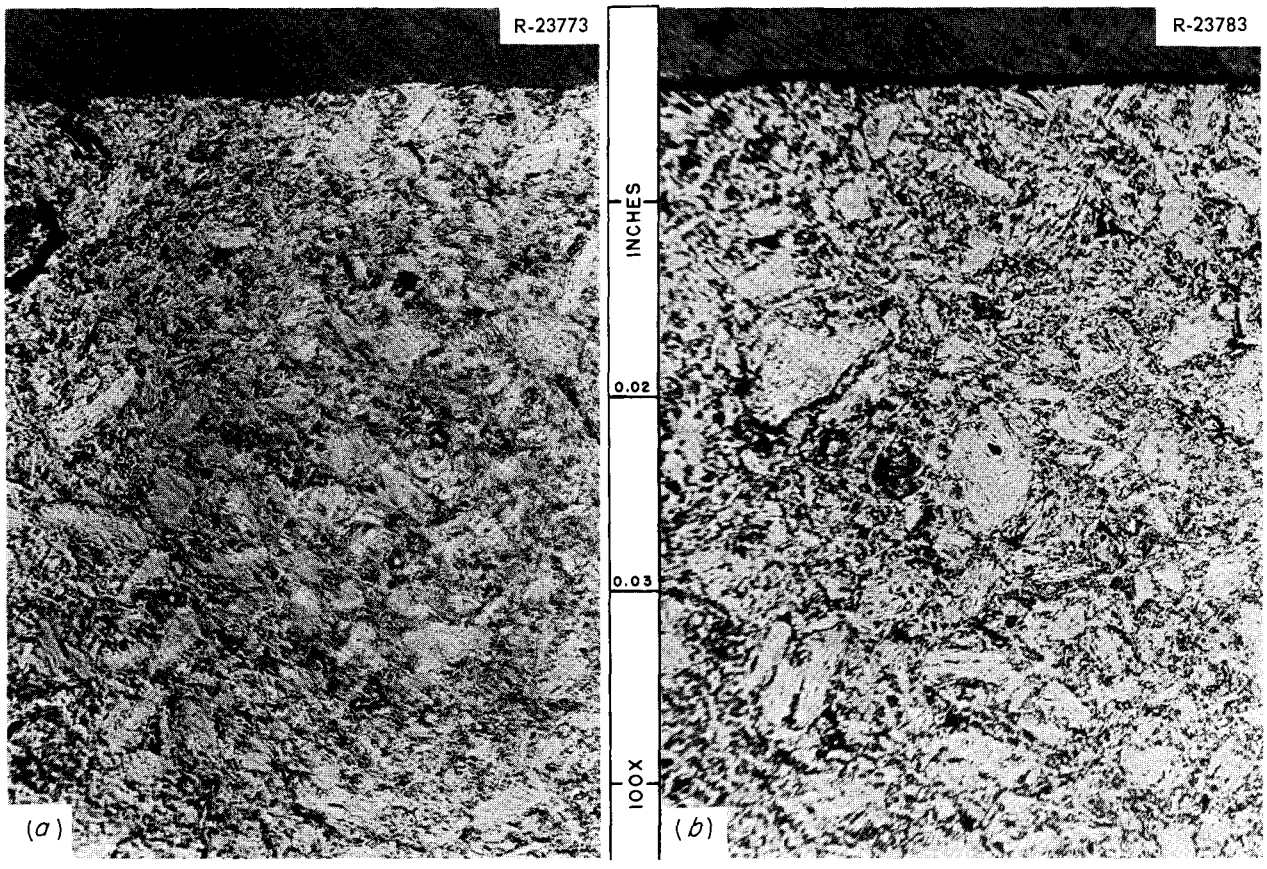

Fig. 28.14. (*a*) Graphite Core from Capsule 1 of Experiment 47-6; (*b*) Unirradiated Graphite Control Specimen. As polished in carbon tetrachloride. 100×.

SURVEILLANCE TESTING

W. H. Cook A. Taboada

Surveillance specimens were fabricated of INOR-8 and type CGB graphite for placement in the central position of the MSRE core. These specimens will be used to survey the effects of reactor operations on the material from which the reactor structure and moderator were constructed.

INOR-8 specimens were made from heats 5081 and 5085 in the shape of miniature tensile bars approximately 2 in. long and with a gage section 1.0 in. long and 0.125 in. in diameter. The tensile bars were welded end to end to form two rods approximately 64 in. long. Included were four tensile bars made with transverse sections of welds in the gage section.

The graphite specimens were made from sections of MSRE moderator bars selected by radiographic methods as being crack free. These specimens were machined into rectangular bars of various dimensions. They will be tested to get data for both the longitudinal and transverse directions of the graphite.

In the final assembly, the graphite specimens will be arranged into a long subassembly having a rectangular cross section of 0.47 × 0.66 in. Three of these graphite subassemblies will be surrounded by six INOR-8 specimen rods and three INOR-8 tubes containing flux monitor wires. The entire assembly will be held in a 1.968-in.-ID perforated tube.

After six months of reactor operation, two INOR-8 specimens, a flux monitor, and one graphite subassembly will be removed from the reactor and

examined, and new specimens will replace those removed. The frequency of removal of additional specimens will be established by the results of the first set of specimens.

The analysis of the INOR-8 specimens will include (1) metallographic examination for structural changes, corrosion effects, and possible layer formations; (2) tensile properties and creep properties, with emphasis on creep ductility; (3) a general check for material integrity and dimensional changes; and (4) chemical analysis for composition changes and fission product deposition.

The graphite specimen analysis will include (1) metallographic examination for structural changes and material deposition; (2) radiographic examination for salt permeation and possible wetting effects; (3) flexural strength tests; (4) dimensional checks for shrinkage; (5) chemical analysis for salt and fission product deposition; (6) a general inspection for integrity; and (7) possibly measurement of physical properties such as electrical conductivity, thermal conductivity, and Hall coefficient.

Control specimens, of shape and source identical to the reactor specimens, will be exposed in fuel salt to the reactor thermal history in a control test rig. The chamber, containing specimens submerged in salt, will be heated by three zones of electric heaters. These will be controlled by signals generated from the inlet and outlet temperature of the reactor through a logger-computer. In this manner, the control test specimens should automatically be exposed to the approximate temperature profile and major temperature fluctuation experienced by the reactor specimens. These specimens will be examined in the hot-cell area at the same time that the reactor specimens are tested.

DYNAMIC CORROSION STUDIES

G. M. Tolson A. Taboada

We are continuing to study the compatibility of coolants and structural materials of interest for molten-salt reactors. Thermal convection loops are generally used for initial screening tests, and forced circulation loops are generally used for proof testing, since they better simulate the engineering parameters that could affect corrosion.

In the past this work was aimed at studying MSRE conditions, but more recently tests have been started to examine potential materials for advanced systems.

Corrosion Loops Circulating Molten Fluorides

Two thermal convection loops have been operating with MSRE reference salt ($LiF-BeF_2-ZrF_4-UF_4$). One loop is constructed of INOR-8 and has included in the hot region INOR-8 specimens modified with 2% Nb because of the interest in this composition for use as weld metal. This loop has operated without incident for over 28,000 hr with a hot-leg temperature of 1300°F and a temperature difference of 160°F. The second loop is constructed of type 304 stainless steel and has operated for over 17,000 hr with a hot-leg temperature of 1250°F and a temperature difference of 180°F. Specimens removed from the stainless steel loop were observed to have intergranular attack to a depth of approximately 0.002 in., as shown in Fig. 28.15.

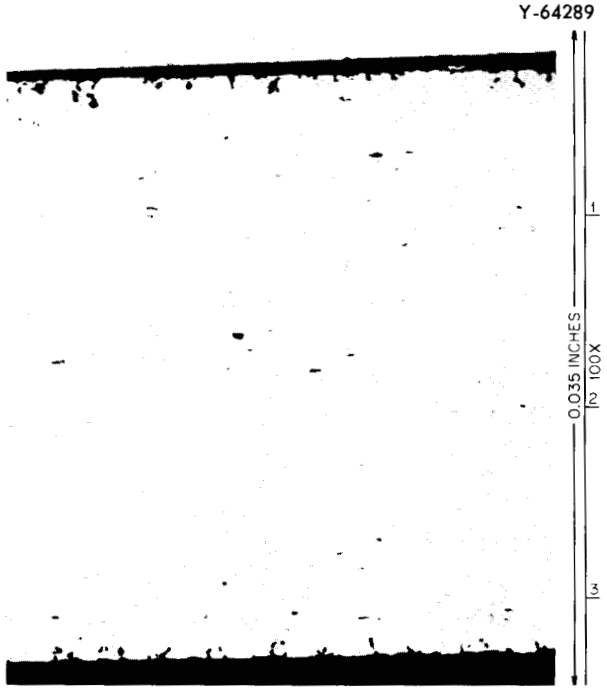

Fig. 28.15. Cross Section of Type 304 Stainless Steel Specimen Removed from Thermal Convection Loop Containing MSRE Salt and Operating at 1250°F Hot Leg with 180°F Temperature Difference. 100×.

Table 28.4. Thermal Convection Loops Using Lead as a Coolant

Loop Material	Maximum Temperature (°F)	Temperature Drop (°F)	Time Operated (hr)	Inhibitors Used	Maximum Depth of Attack (in.)	Average Depth of Attack (in.)
Croloy $2\frac{1}{4}$[a]	1022	221	27,765	25 ppm Mg, Zr	None	None
Croloy $2\frac{1}{4}$	1210	300	266	None	0.001	
Type 410 stainless steel	1215	300	1,346	None	0.002	
Croloy $2\frac{1}{4}$	1100	200	5,156	None	0.008	0.0055
Carbon steel	1100	200	5,064	None	0.010	0.007
Nb–1% Zr	1400	400	5,280	None	0.00	0.00
Croloy $2\frac{1}{4}$	1200	230	1,848	Zirconium	0.0045	0.003

[a]Loop run at Brookhaven, included for comparison.

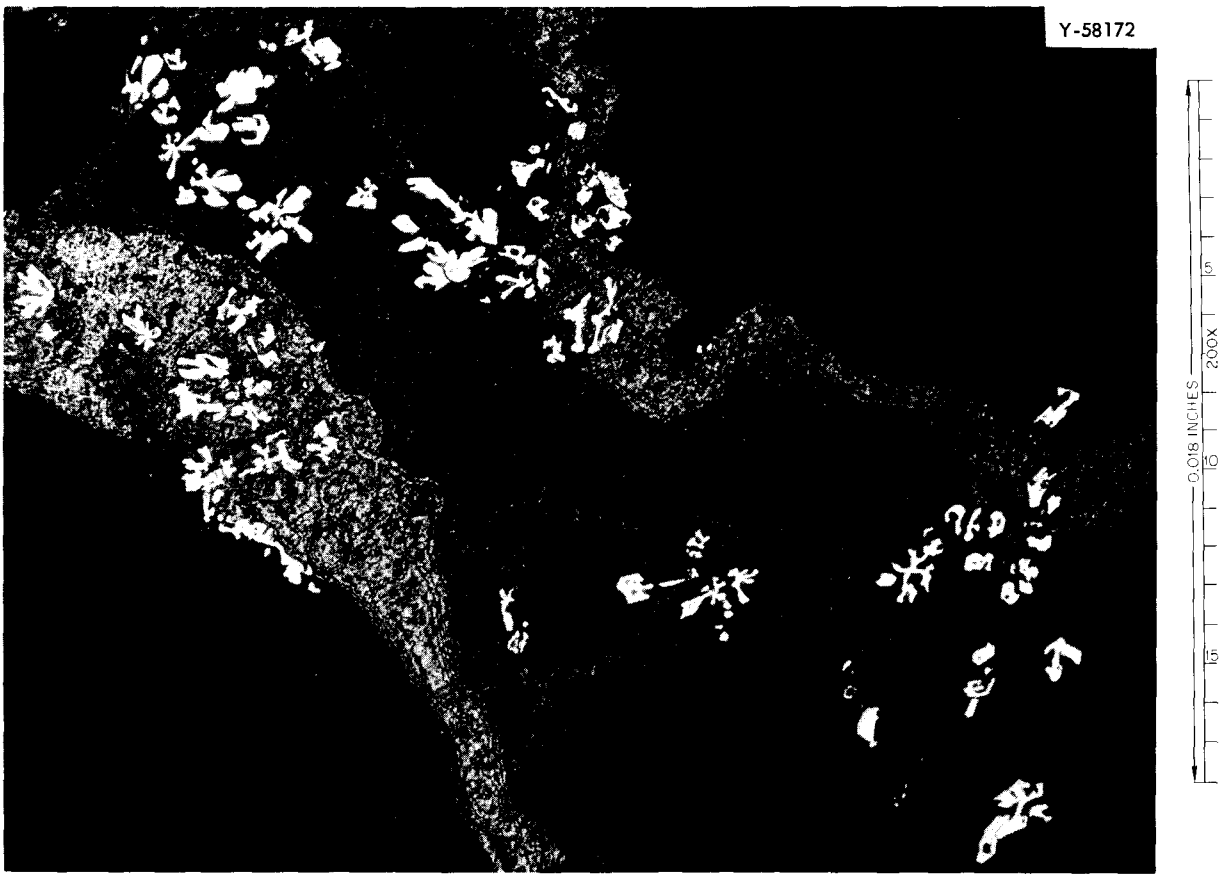

Fig. 28.16. Dendritic Crystals of Iron and Chromium That Formed in the Cold Leg of a Croloy $2\frac{1}{4}$ Loop in Which Lead Circulated 266 hr. Unetched. 200×.

Corrosion Loops Circulating Lead

Thermal convection loop tests were operated that circulated lead because of its attractive properties as a coolant for molten fluoride systems. Screening tests were run in Croloy $2\frac{1}{4}$, carbon steel, type 410 stainless steel, and Nb–1% Zr at conditions described in Table 28.4 along with some results. Two of the tests contained surge tanks in which fluoride salts, Nb–1% Zr alloy, and graphite were placed in contact with the lead to test the compatibility of a direct-cooled lead system.

All the steel loops tended to plug in the cold regions from the formation of dendritic crystals of iron and chromium typically shown in Fig. 28.16. Corrosion of the hot region in general had the appearance seen in Fig. 28.17. General roughening existed with a tendency toward intergranular attack. No effect was seen in the niobium alloy liner examined, shown in Fig. 28.18. This resistance of niobium alloy to corrosion by lead was further strengthened by the Nb–1% Zr loop that operated for 5000 hr with no deterioration of flow.

Presently additional loops are being started to test the effect of inhibitors on lead corrosion and to study Nb–1% Zr at higher temperatures. The new and more versatile loop design is shown in Fig. 28.19. It is more compact, it contains removable samples, and it allows a better control of the temperature profile.

Fig. 28.17. Section of a Croloy $2\frac{1}{4}$ Loop Run with Lead at 1200°F for 266 hr. Unetched. 500×.

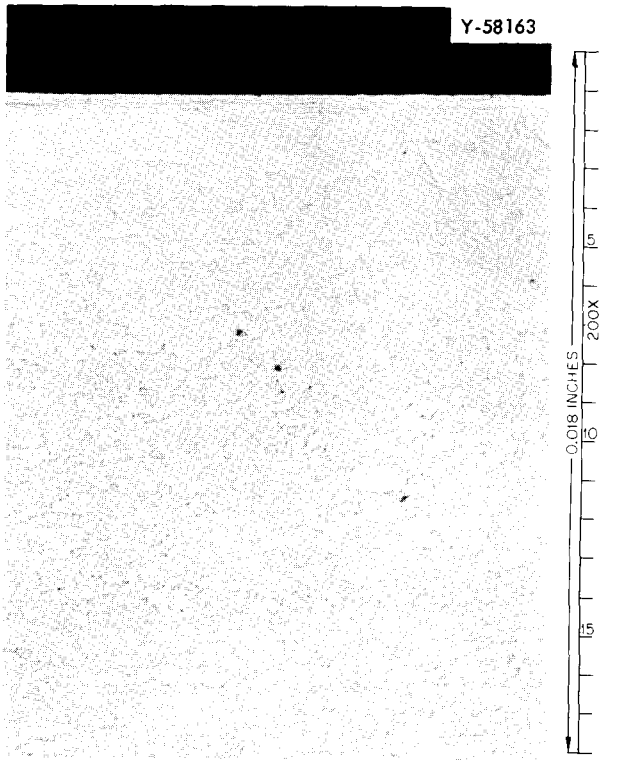

Fig. 28.18. Nb–1% Zr Liner Operated in Lead and Salt for 1349 hr at 1200°F. 200×.

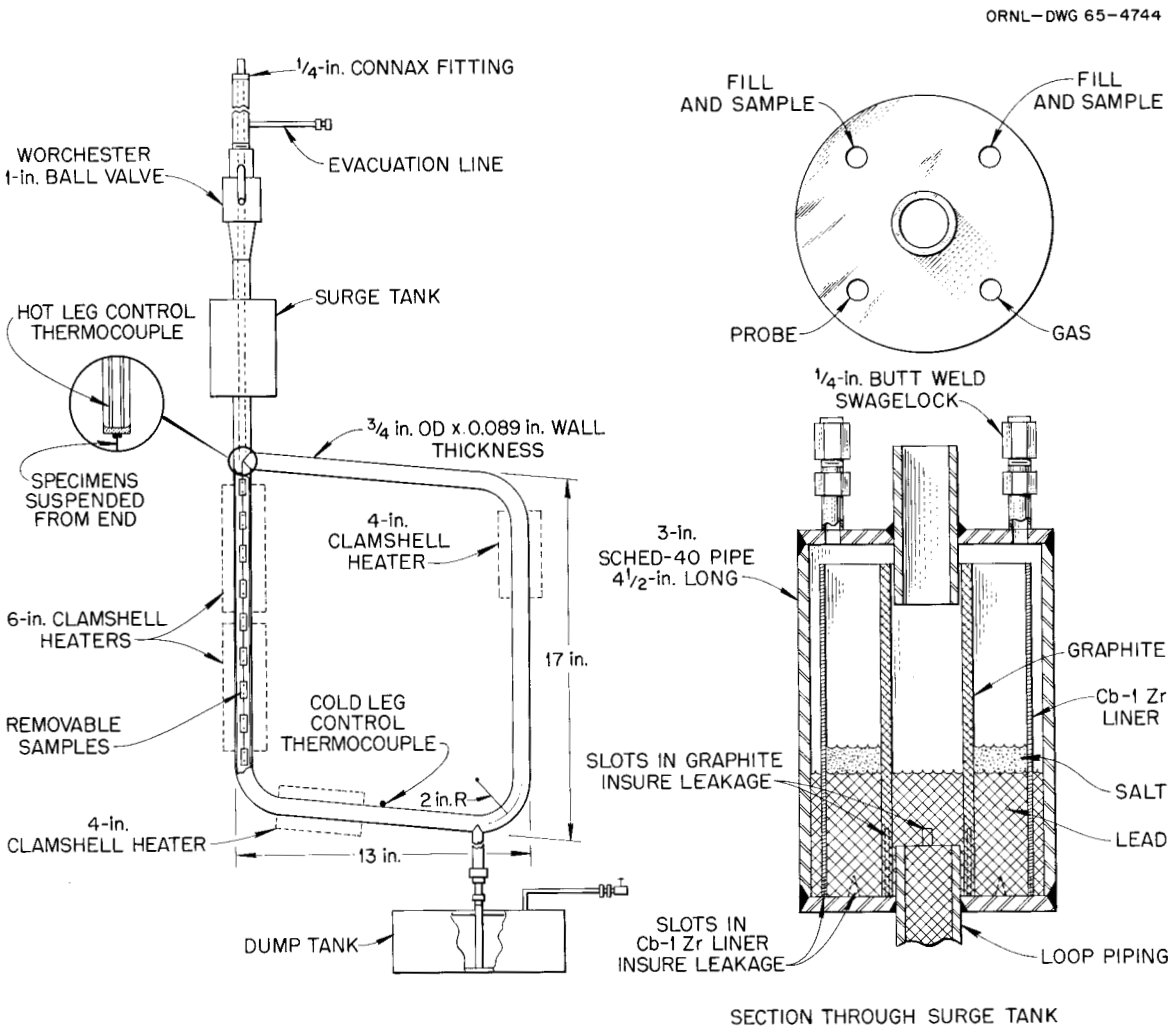

Fig. 28.19. Thermal Convection Loop Used in Lead Corrosion Studies.

29. Reactor Evaluation

D. A. Douglas, Jr.

The total cost of producing heat or power by nuclear energy is composed of a multitude of interacting relationships. Capital costs, operating costs, and fuel cycle costs are some of the general terms used to collectively identify categories. To achieve a meaningful reduction in cost, one must consider the problem in its entirety and recognize the effect that changes made in one area may have on others. ORNL is engaged in studying this general problem, and our role is to examine fabrication costs and fuel element performance as they relate to fuel cycle and other cost areas. Thus, we work in conjunction with chemical processing personnel in the Chemical Technology Division and the physicists and design engineers in the Reactor Division. Thus, we report here fragments of much broader studies.

COMPUTER PROGRAMS FOR CALCULATION OF FUEL FABRICATION COSTS

A. L. Lotts T. N. Washburn

An indispensable factor in the evaluation and comparison of various proposed reactor systems is the cost of fuel element fabrication. Accordingly, we have assisted the evaluation of reactor

Table 29.1. Fuel Element Types for Which a Fabrication-Cost Computer Program is Available

Type Fuel Element	Fuel Material	Fabrication Process	Type Core-to-Cladding Bonding
Rod bundle	Oxide	Vibratory compaction	Gas
Rod bundle	Oxide	Vibratory compaction	Sodium
Rod bundle	Oxide	Pelletization	Gas
Rod bundle	Oxide	Pelletization	Sodium
Rod bundle	Carbide	Slugs	Gas
Rod bundle	Carbide	Slugs	Sodium
Rod bundle	Metal	Extrusion	Diffusion (Ni)
Rod bundle	Metal	Coextrusion	Metallurgical
Nested tubes	Oxide	Vibratory compaction	Gas
Nested tubes	Oxide	Pelletization	Gas
Nested tubes	Carbide	Slugs	Gas
Nested tubes	Metal	Extrusion	Diffusion (Ni)
Nested tubes	Metal	Coextrusion	Metallurgical

concepts by providing extensive studies of the cost of fuel fabrication.

The prediction of fabrication costs involves the selection of the fabrication procedures or flowsheets and the calculation of operating costs, capital costs, and the cost of materials used in the processes. Also, one must apply certain factors such as the fabrication environment, the prospects of success for the process, and the method of financing. Because a large number of variables are involved in calculating fabrication costs, we previously[1] developed three computer programs to perform the calculations on a limited number of fuel element types.

Since writing the initial programs, we have continued to expand the types of fuel elements and flowsheets that can be handled by our computer programs for calculation of fuel fabrication costs. Table 29.1 shows the different fuel element types for which we can now calculate fuel fabrication costs. We have introduced refinements to the programs that allow the calculation of shielding required in remote and semiremote plants and the assessment of the economic penalties associated with the shielding. Some fuel recycle schemes require that part of the fuel be handled in a remotely operated system and part in a direct operation, such as a contact, hooded, or glove-box facility. Therefore, we have incorporated procedures for calculating costs in a single plant having two different modes of operation.

The programs work in the following way. All the information concerning the process and the costs involved in the process are stored in the computer program. When the fuel element, the plant in which it is to be fabricated, and the manner in which the plant is to be operated and financed are described, fuel fabrication costs can be calculated for a number of production rates.

^{233}U VALUE STUDY

A. L. Lotts T. N. Washburn

One of the principal tasks undertaken during the year was to assist in the evaluation[2] of the value of ^{233}U by providing fuel fabrication costs for an advanced high-temperature gas-cooled reactor (HTGR) and for the Spectral Shift Control Reactor (SSCR). We analyzed in detail plants of four capacities (60, 230, 930, and 3700 kg/day) operating 260 days per year three shifts per day and fabricating only one type of fuel. Fissile or fertile material costs and inventory or use charges were not included.

The general procedure used for calculation of the fabrication costs follows. For both the SSCR and HTGR elements, we prepared the fuel fabrication schedules, which establish the sequence of fabrication, uranium concentration, residence time of the material in the plant, and the age of the material at various fabrication steps under the optimum and worse conditions. The material age, quantity, and geometry were then summarized for the recycle ^{233}U with varying amounts of ^{232}U. This information was used to calculate the shielding required in the various plants. Separately, we determined the incremental cost difference between the various types of plants and for varying amounts of shielding. All the information was then used to expand the computer codes that calculate the fabrication costs from the mode of fabrication, the concentration of ^{232}U in the heavy metal, the plant throughput, and other variables.

The calculated shielding requirements for plants fabricating ^{233}U-bearing fuels are shown in Table 29.2. This table shows the shielding for semiremote and remote fabrication for SSCR fuel elements and two types of HTGR fuel elements with different type fuel particles. The first contained pyrolytic-carbon-coated $(U,Th)C_2$ particles and the second, discrete particles of UC_2 and ThC_2, each coated with pyrolytic carbon. The limit of semiremote fabrication was taken as 3.5 in. of steel, since this is the maximum practical working distance for gloved hands or tongs. Also, radiation levels requiring shielding beyond this amount would prohibit, or at least greatly complicate, contact maintenance of the equipment. This chart shows that material containing 1 to 5 ppm ^{232}U in heavy metal can be handled in a semiremote facility. Note that the limit for semiremote fabrication of the discrete particles of UC_2 and ThC_2 is very low because the ^{233}U is handled without the presence of thorium in a number of the operations.

---

[1] A. L. Lotts, *Metals and Ceramics Div. Ann. Progr. Rept. June 30, 1964*, ORNL-3670, pp. 254–55.

[2] M. W. Rosenthal *et al.*, *A Comparative Evaluation of Advanced Converters*, ORNL-3686 (January 1965).

Table 29.2. Shielding Requirements in Plants for Fabrication of ^{233}U-Bearing Fuels

^{232}U[a] (ppm)	Shielding Required for Given Fuel and Plant Capacity (kg heavy metal per operating day)								
	SSCR Fuel			HTGR Fuel – $(U,Th)C_2$ Particles[b]			HTGR Fuel – $UC_2 + ThC_2$ Particles[c]		
	230	930	3700	230	930	3700	230	930	3700
Semiremote Fabrication (in. steel)									
1	0.8	1.2	1.4	1.2	1.9	2.0	2.8	2.8	3.2
2	1.7	2.1	2.3	2.0	2.7	2.9			
5	2.8	3.3	3.5	3.1					
Remote Fabrication (in. concrete)									
2							12.3	12.3	13.5
5					12.8	13.9	15.9	15.9	17.2
10	12.2	13.8	14.8	13.2	15.6	17.0	18.7	18.7	20.0
20	15.0	16.7	17.8	16.0	18.5	20.0	21.4	21.4	22.8
50	18.9	20.6	21.8	19.6	22.2	24.1	25.1	25.1	26.5
100	21.7	23.5	24.8	22.4	25.0	27.2	27.9	27.9	29.3
500	28.4	30.3	31.8	28.8	31.6	34.3	34.3	34.3	35.8
1000	31.2	33.9	34.8	31.6	34.4	37.4	37.0	37.0	38.6
U-Th[d]	36.0	38.5	40.0	36.0	39.0	42.5	41.5	41.5	43.0

[a]Parts per million in heavy metal (U + Th).

[b]Each particle containing a mixture of ^{233}U and virgin thorium.

[c]$^{233}UC_2$ processed alone in parts of the process.

[d]Conditions assumed equivalent to ^{233}U with recycle thorium.

Figures 29.1 and 29.2 show the effect of ^{232}U concentration on the cost of fabricating SSCR and HTGR fuel elements respectively. The cost of refabrication is shown for ^{233}U and virgin thorium.

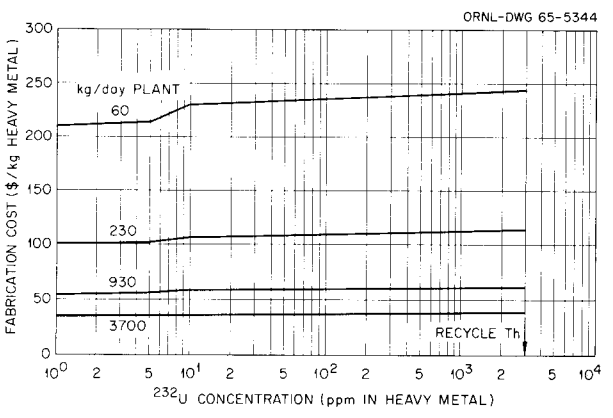

Fig. 29.1. Effect of ^{232}U Concentration on the Cost of Fabricating SSCR Fuel Elements.

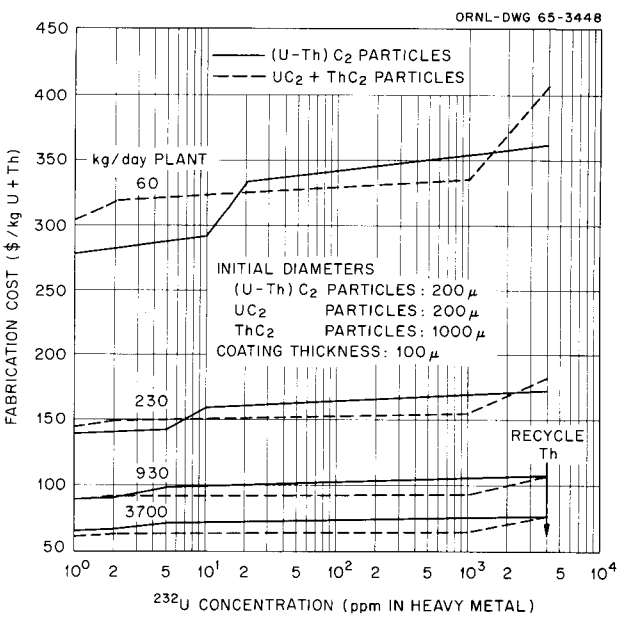

Fig. 29.2. Effect of ^{232}U Concentration on the Cost of Fabricating Fueled-Graphite Elements.

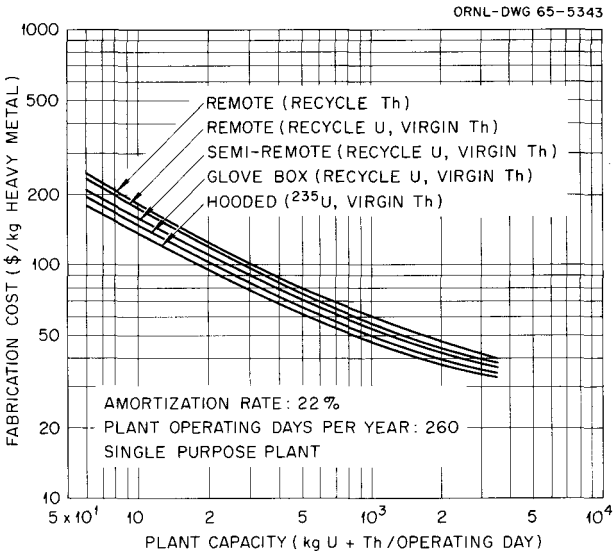

Fig. 29.3. Effect of Production Rate and Mode of Fabrication on the Cost of Fabricating SSCR Fuel Elements.

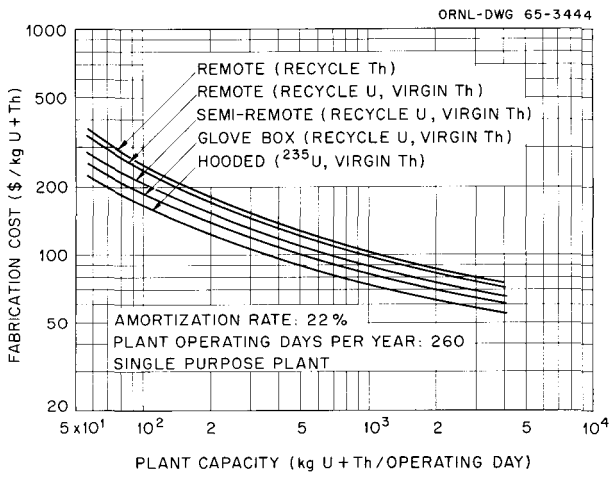

Fig. 29.4. Effect of Production Rate and Mode of Fabrication on the Cost of Fabricating Fueled-Graphite Elements.

The recycle thorium case is depicted as being equivalent to 4000 ppm ^{232}U in heavy metal. We do not know exactly the transition points between semiremote and remote operation, but the curves show that these points need not be determined precisely, since the cost penalty incurred for remote over semiremote fabrication is not substantial.

Figures 29.3 and 29.4 show the effect of production rate and mode of fabrication on the cost of SSCR elements and HTGR elements containing $(U,Th)C_2$ particles.

EFFECT OF VARIABLES UPON FUEL FABRICATION COST

T. N. Washburn D. A. Douglas, Jr.

Our computer code, which we used[2] in reactor-evaluation studies, can also be used to evaluate the effect of significant variables upon fuel fabrication costs. Figure 29.5 illustrates the effects produced by the independent variation of fuel-element design parameters over an extensive range. These curves relate to an advanced pressurized-water reactor fuel element of the rod-bundle design, fueled with low-enrichment UO_2 pellets. Figure 29.6 illustrates the effects of different plant capacities and amortization rates for production of fuel elements of the reference design. These fuel-fabrication costs include operating expenses, capital charges, hardware costs, and conversion of UF_6 to UO_2. Use charges and shipping costs are not included.

Production rate and fuel diameter produce the most marked effect, followed by fuel length, fuel density, and amortization rate. By application of such an analysis to his particular concept, the designer can select parameters resulting in minimum fuel-fabrication costs, which must then be compromised with reactor-design efficiencies to yield the lowest net fuel-cycle costs.

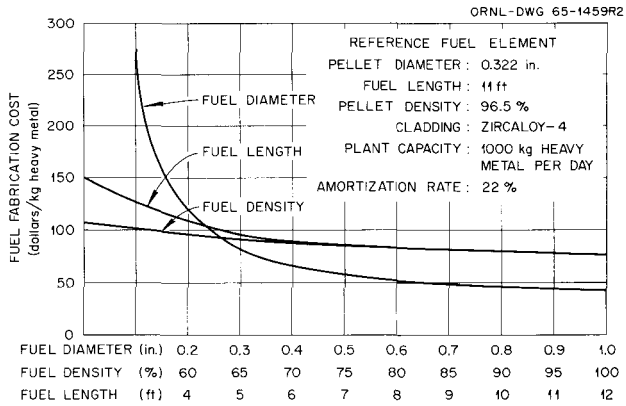

Fig. 29.5. Effect of Fuel Dimensions on Fabrication Cost for an Advanced Pressurized-Water Reactor Fuel Element.

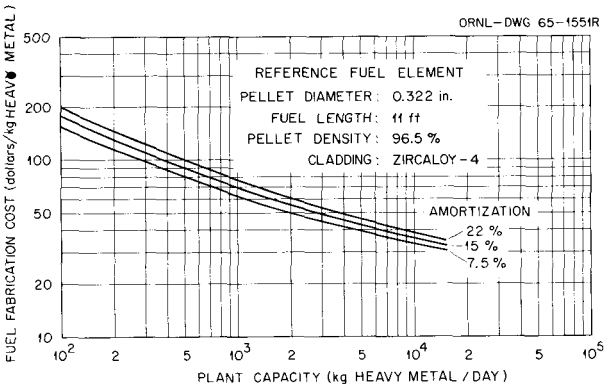

Fig. 29.6. Effect of Fabrication Rate and Amortization Rate on Fabrication Cost for an Advanced Pressurized-Water Reactor Fuel Element.

30. Thorium Utilization

D. A. Douglas, Jr.

Simplification and cost reduction of the fuel cycle as it pertains to bred fuels has been the aim for several years of a joint effort with the Chemical Technology Division. The Th-^{233}U cycle with oxide fuel has received the major attention and we are comprehensively developing processes and equipment. Our work is in three parts: process development, engineering development and demonstration, and product evaluation or irradiation testing.

OPERATION OF A Th-^{233}U FUEL FABRICATION FACILITY

BNL Fuel Rods

J. E. Van Cleve A. L. Lotts

Previously, 1100 specification-grade fuel rods containing (Th–3% ^{233}U)O_2 had been fabricated in the Kilorod Facility for use in critical experiments at Brookhaven National Laboratory. The fuel was vibratorily compacted to an average density of 89.7% of theoretical over the entire 1100 rods.

During the operation of the facility, data were obtained covering the equipment reliability, system operating parameters, utilization of fuel charged to the system, radiation exposure to the operators, fabrication costs, and the productivity of the system. We have completed the analysis of these data and have published final engineering reports.[1–6]

Fabrication of ^{233}U-Bearing Fuel Rods for Irradiation Tests

J. D. Sease A. L. Lotts

The operation of the Kilorod Facility to produce fuel rods containing ^{233}U for critical experiments was successful. Even so, an evaluation of the semiremote fabrication technique employed would not be complete without a demonstration of the fuel rods at power reactor operating conditions. At the conclusion of the production operations of the Kilorod Facility, we fabricated fuel rods for irradiation testing. These rods are currently being irradiated in the ETR.

The irradiation rods for the tests contain (Th–3% ^{233}U)O_2 and are identical to the 18-in. rods fab-

[1] J. D. Sease, A. L. Lotts, and F. C. Davis, *Thorium-Uranium-233 Oxide (Kilorod) Facility Rod Fabrication Process and Equipment*, ORNL-3539 (April 1964).

[2] J. D. Sease, A. L. Lotts, and F. C. Davis, "New Remote Facility and Equipment at the Oak Ridge National Laboratory for Fabrication of Fuel Rods Bearing Uranium-233 and Thorium Oxide," pp. 33–43 in *Proceedings of the 11th Conference on Hot Laboratories and Equipment, ANS Winter Meeting, New York, November 18–21, 1963*, American Nuclear Society, New York (1963).

[3] J. E. Van Cleve and A. L. Lotts, "Operation of a Lightly Shielded Facility at the Oak Ridge National Laboratory for the Fabrication of Fuel Rods Bearing Uranium-233 and Thorium Oxide," paper presented at the *Powder Filled Uranium Dioxide Fuel Element Symposium, Worcester, Mass., November 5–6, 1963* (to be published).

[4] J. E. Van Cleve, Jr., and A. L. Lotts, "Operating Experience in a Semi-Remote Facility for Fabrication of Fuel Rods Containing (U^{233},Th)O_2," pp. 257–71 in *Proceedings of the 12th Conference on Remote Systems Technology*, American Nuclear Society, Hinsdale, Ill. (November 1964).

[5] J. E. Van Cleve, Jr., J. J. Varagona, and A. L. Lotts, *Time Study of Fuel Rod Fabrication in the Kilorod Facility*, ORNL-3740 (in press).

[6] C. C. Haws, J. L. Matherne, F. W. Miles, and J. E. Van Cleve, Jr., *Summary of the Kilorod Project – A Semiremote 10-kg/day Demonstration of 233 UO_2-ThO_2 Fuel Element Fabrication by the ORNL Sol-Gel Vibratory-Compaction Method*, ORNL-3681 (in press).

ricated for the BNL critical experiments. The only change in the fabrication procedure for the irradiation rods compared to the standard Kilorod production rods was the inclusion of radiographic and autoclave inspection steps. A detailed description of the fabrication procedures and results will be reported elsewhere.[7]

THORIUM-URANIUM RECYCLE FACILITY

The thorium fuel cycle development must include reliable economic analyses of the reprocessing and fabrication techniques for various fuel elements. The reliability of such analyses is improved if data are provided at pilot-scale production levels. Current evaluations indicate that an economic advantage results if the fuel is recycled after incomplete decontamination from fission products. Also, the ^{232}U decay in recycled fuel produces increasing radioactivity. Consequently, a heavily shielded facility, the Thorium-Uranium Recycle Facility (TURF)[8] is being constructed to permit the development and evaluation of a variety of integrated fuel reprocessing and fabrication schemes at the necessary pilot-scale production level.

Title II design of the facility was completed in January 1965 and construction started early in May. The final design is essentially the same as that reported previously.[8–10]

Building

A. R. Irvine[11] A. L. Lotts
A. R. Olsen

The facility is under construction in the Melton Valley area near the Transuranium Processing Plant and the High Flux Isotope Reactor. The building will be irregular in shape, approximately 124 ft wide by 162 ft long, and three stories high with a partial basement.

The final plan of the first floor is shown in Fig. 30.1. The second floor provides space for chemical solution makeup, sampling of in-cell processes, cask decontamination, a warm shop, a development laboratory, and building mechanical and electrical equipment. The third floor is a high-bay area, which includes the cell roof area, and is provided with a 50-ton crane for handling casks and with facilities for the introduction of in-cell services. The partial basement provides space for access to the equipment storage cell (F) and support equipment for the chemical cell (G). The building provides a secondary containment shell around the cell complex.

Space for process equipment is provided in cells G, C, D, and E of the complex while cell B serves as a radiation lock and decontamination area. Cell A is an unshielded cell or glove maintenance room and cell F provides storage space for contaminated equipment brought in through the floor hatch in cell B.

Cells C and D will be maintained remotely; that is, all equipment installation, maintenance, and removal will be by remote means. Cells A, B, E, F, and G will initially be contact maintenance cells, but provisions have been made to convert cell G to a remote maintenance cell. The viewing windows, master-slave manipulators, and cell service entries are installed on a modular arrangement to permit flexibility in process equipment arrangement. Sufficient space and shielding is provided for reprocessing and fabricating full assemblies up to 12 ft in length and containing up to 35 kg thorium-uranium fuel irradiated to 25,000 Mwd/tonne and decayed 90 days.

Construction of the special in-cell bridge crane and electromechanical manipulator has started, and the system will be installed after the building has been completed. The building construction is scheduled for completion in December 1966. In the interim, a cell mockup is being used to develop and test processing equipment and remote operational procedures.

---

[7] J. D. Sease and A. R. Olsen, *Fabrication Procedures and Preirradiation Data for $(^{233}U,Th)O_2$-Bearing Irradiation Rods* (in preparation).

[8] A. R. Irvine and A. L. Lotts, "The Thorium Fuel Cycle Development Facility Conceptual Design," pp. 333–50 in *Proceedings of the Thorium Fuel Cycle Symposium, Gatlinburg, Tennessee, December 5–7, 1962*, TID-7650, bk 1 (July 1963).

[9] A. R. Irvine and A. L. Lotts, *Metals and Ceramics Div. Ann. Progr. Rept. May 31, 1963*, ORNL-3470, pp. 198–201.

[10] A. R. Irvine, A. L. Lotts, and A. R. Olsen, *Metals and Ceramics Div. Ann. Progr. Rept. June 30, 1964*, ORNL-3670, pp. 230–31.

[11] Chemical Technology Division.

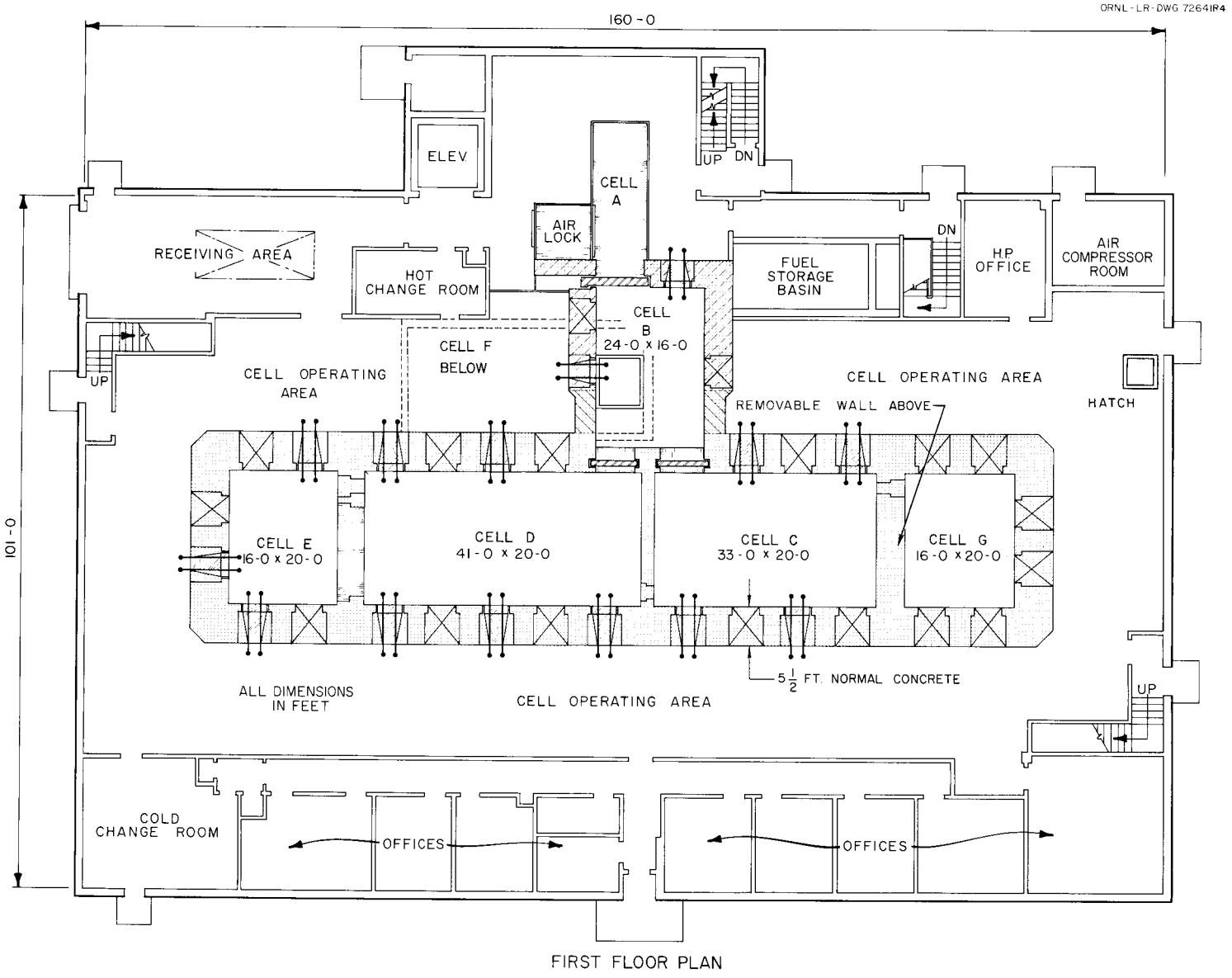

FIRST FLOOR PLAN

Fig. 30.1. Final First-Floor Plan of TURF.

Oxide Fabrication Equipment

J. D. Sease R. B. Pratt
A. L. Lotts

We are developing the oxide fabrication equipment to demonstrate in the TURF the technical and economic feasibility of remote fabrication of metal-clad cluster fuel elements containing (Th, $^{233}U)O_2$. The process for which the equipment is designed is vibratory compaction of bulk oxide into fuel tubes and mechanical assembly of the fuel rods into elements.

The equipment is being designed to process fuel rods at a pilot plant scale of approximately 40 fuel rods per 8-hr shift; however, each equipment item is being designed to operate at its maximum capability to establish criteria for full production facilities. The basic requirement for the equipment is that it be able to accommodate fuel rods 2 to 10 ft long and $\frac{1}{4}$ to $\frac{3}{4}$ in. in diameter. Flexibility of the equipment is gained when possible through minor adjustment of a component, but unit speed will not be sacrificed for flexibility.

The oxide fabrication procedure has changed very little during the year.[12] Simplification of the powder preparation step was the only change made. A revised flow diagram is shown in Fig. 30.2. Most of the design effort during the year has been concentrated in the area of rod fabrication, and most of the equipment in this area is either in a preliminary design stage or completely designed. Design of the element assembly device and associated equipment has not begun because this equipment is almost completely dependent upon the particular element to be fabricated.

Although design of some equipment is being delayed, we are proceeding with fabrication and mock-up testing of two key equipment items, the vibratory compactor and the fuel-blend-transfer device. The fabrication and testing of these devices will give us a basis for evaluating design philosophies and also enable us to evaluate the performance of the vibratory compactor. A pictorial view of the vibratory compaction unit that is currently being fabricated is shown in Fig. 30.3. A complete review of the status of the oxide fabrication equipment is reported elsewhere.[13]

Fueled-Graphite Fabrication Equipment

R. B. Pratt R. L. Pilloton
A. L. Lotts

We are currently conceptually designing equipment to be used for demonstration of refabrication technology for advanced high-temperature gas-cooled reactor (HTGR) fuel elements.[14] The flowsheet that is being used for conceptual design is shown in Fig. 30.4 and a preliminary equipment layout in Fig. 30.5. This equipment occupies half the space in cells D and E.

Production-type equipment will be used for demonstration of refabrication technology for fueled graphite elements, so that information gained will be applicable both technically and economically to a full-scale production facility. The equipment is being sized for a production rate of 35 kg heavy metal per day. The coating process is presently the principal barrier to achieving this goal and, accordingly, a substantial part of our development program is directed toward its development.

To provide a basis for process and equipment design, we are conducting experiments in several areas including spherical particle preparation, conversion of oxide particles to carbide, and coating with pyrolytic carbon. To aid in analyzing process and equipment design requirements, we are currently equipping a pilot-scale coated particle development laboratory (CPDL), which will operate with nonrecycle material. All this work is reported in the subsequent sections.

---

[12] R. B. Pratt, J. D. Sease, and A. L. Lotts, *Metals and Ceramics Div. Ann. Progr. Rept. June 30, 1964*, ORNL-3670, pp. 231–35.

[13] "Oxide Fabrication Equipment," *Status and Progress Report for Thorium Fuel Cycle Development, Dec. 31, 1964*, ORNL-3831 (in press).

[14] *Design Study Report for TARGET. A 1000-Mw(e) High-Temperature Gas-Cooled Reactor*, GA-4706 (1964).

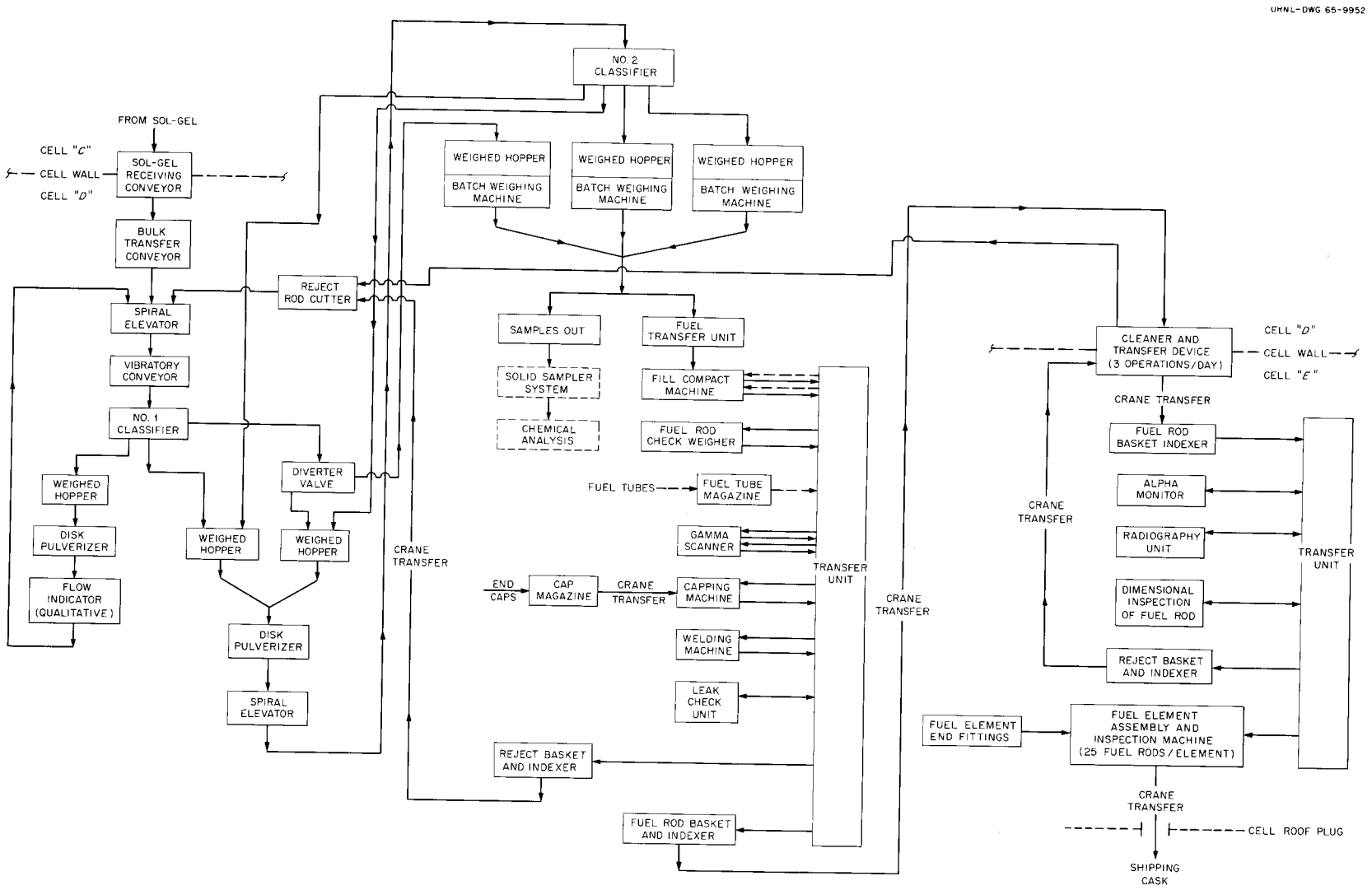

Fig. 30.2. Flowsheet for Oxide Fabrication Line.

ORNL-DWG 65-917

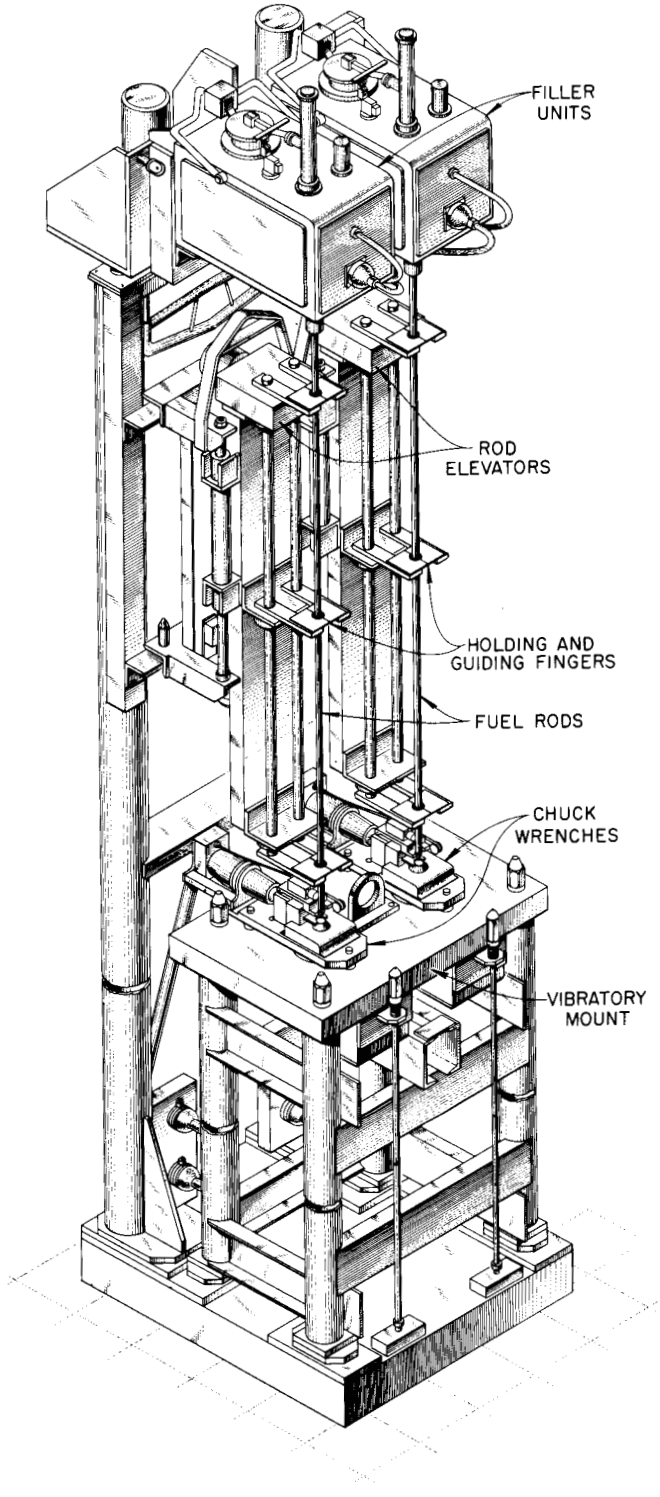

Fig. 30.3. Vibratory Compactor for Remote Fabrication.

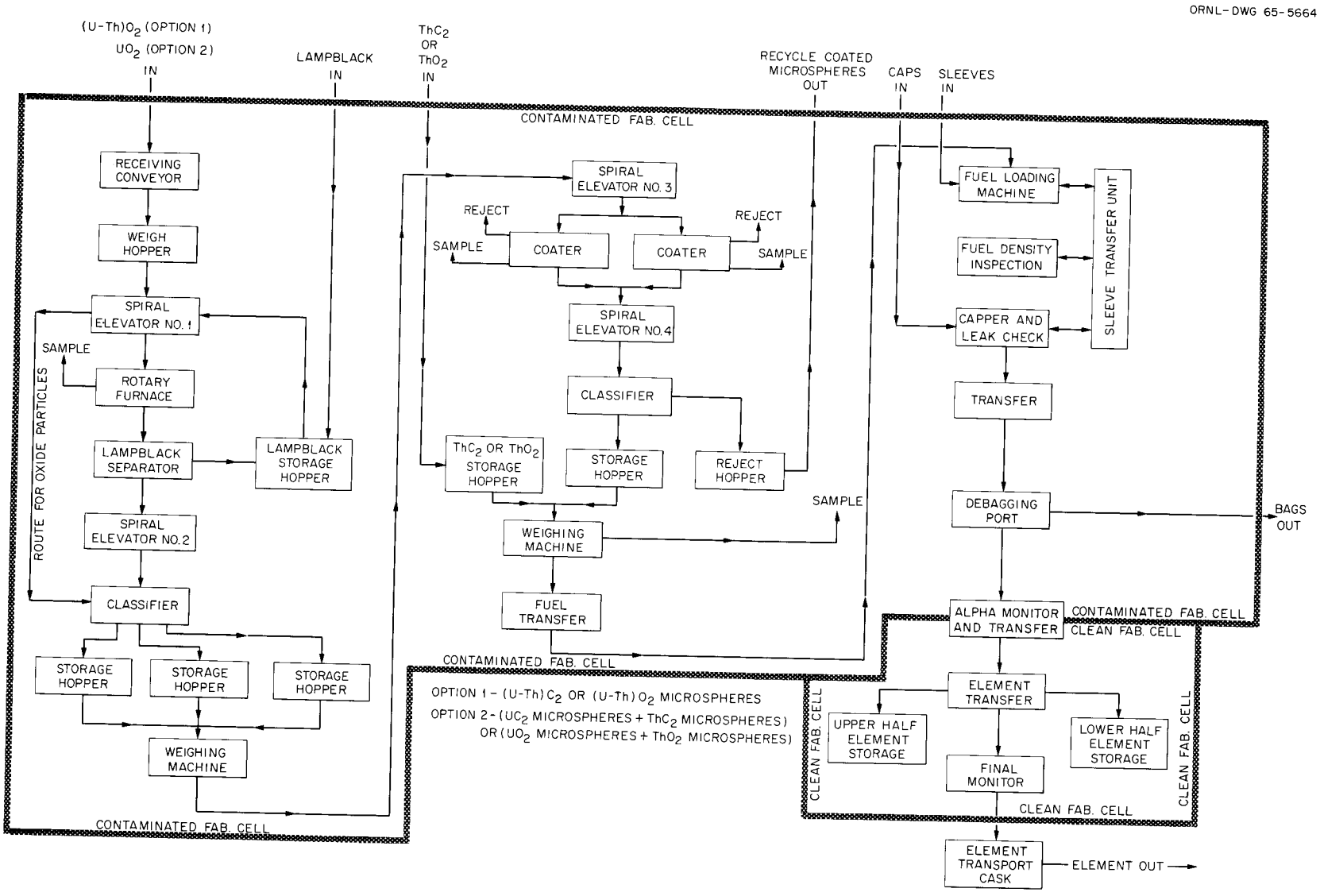

Fig. 30.4. Flowsheet for Fabrication of Fueled Graphite Elements.

ORNL-DWG 65-3442R

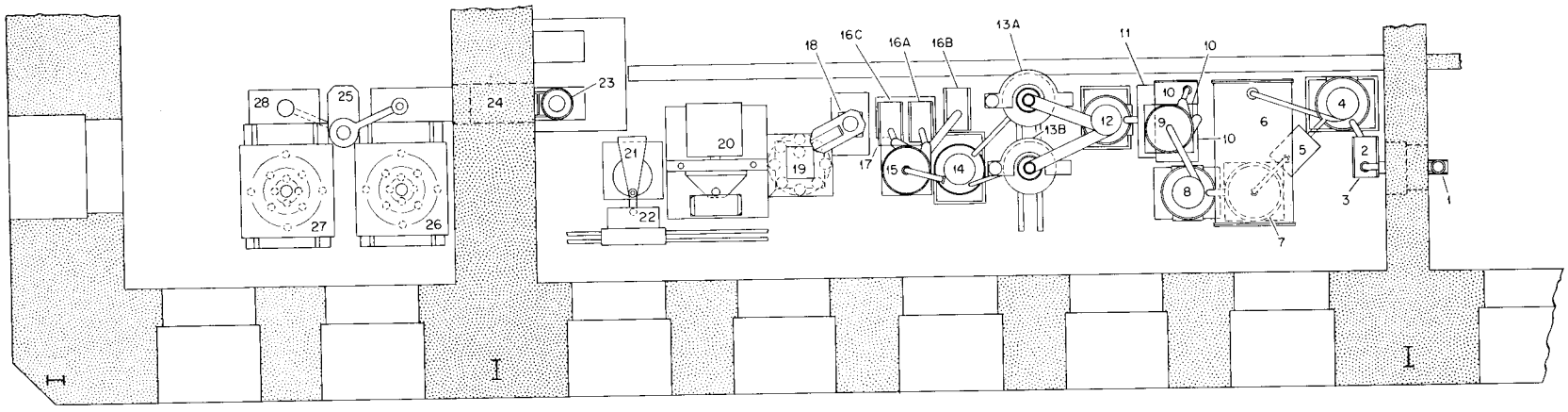

1. TRANSFER CONVEYOR
2. INVENTORY HOPPER
3. BATCH WEIGHING MACHINE
4. SPIRAL ELEVATOR NO. 1
5. LAMPBLACK STORAGE HOPPER
6. ROTARY CONVERTOR FURNACE
7. SEPARATOR
8. SPIRAL ELEVATOR NO. 2
9. AGGLOMERATE SEPARATOR
10. STORAGE HOPPERS (3)
11. BATCH WEIGHING MACHINE
12. SPIRAL ELEVATOR NO. 3
13A. COATER
13B. COATER
14. SPIRAL ELEVATOR NO. 4
15. AGGLOMERATE SEPARATOR
16A. STORAGE HOPPER (USEABLE MATERIAL)
16B. STORAGE HOPPER (REJECT MATERIAL)
16C. STORAGE HOPPER
17. BATCH WEIGHING MACHINE
18. FUEL TRANSFER
19. FUEL LOADING
20. FUEL DENSITY INSPECTION
21. CAP AND LEAK CHECK
22. SLEEVE TRANSFER UNIT
23. DEBAGGING PORT AND TRANSFER
24. ALPHA MONITOR AND TRANSFER
25. ELEMENT TRANSFER
26. UPPER HALF ELEMENT STORAGE
27. LOWER HALF ELEMENT STORAGE
28. FINAL MONITOR

Fig. 30.5. Preliminary Fabrication Equipment Layout for Fueled Graphite Fabrication.

FUELED-GRAPHITE DEVELOPMENT

Carbon-Coated Oxide Fuel Concept

D. A. Douglas, Jr.

Because of the greater simplicity and ease of operation afforded by the use of oxide rather than carbide microspheres, we initiated a program last year[15] to explore the feasibility of a carbon-coated oxide fuel concept. The compatibility experiments have proved very successful, as reported in Chap. 24 of this report. Initial irradiation tests in sweep-capsule experiments[16] encountered experimental difficulties, but the results showed sufficient promise that excellent irradiation performance can be predicted. Thus, we continue to center our main attention on the production and processing of oxide-fueled graphite elements.

[15]R. L. Hamner, R. L. Beatty, and R. E. Meadows, *Metals and Ceramics Div. Ann. Progr. Rept. June 30, 1964*, ORNL-3670, p. 238.

Coated Particle Development Laboratory

R. B. Pratt J. W. Snider[11]
A. L. Lotts

A pilot-scale microsphere fabrication line is currently being installed in the CPDL. During the past year, we have prepared the laboratory and designed, constructed, and installed the process equipment. The purpose of the laboratory is to develop a process suitable for scaled-up use in the TURF for fabrication of fueled graphite elements. Development work will include microsphere preparation, conversion of oxide particles to carbides, and coating of particles with pyrolytic carbon. We shall use natural thorium and uranium of various enrichments. The flow diagram for processing fuels in the CPDL is shown in Fig. 30.6.

[16]P. E. Reagan, O. Sisman, and E. L. Long, Jr., *Coated-Particle Fuels Development at Oak Ridge National Laboratory for Period November 15, 1964 to May 15, 1965*, ORNL-TM-1116, pp. 60–65 (May 1965).

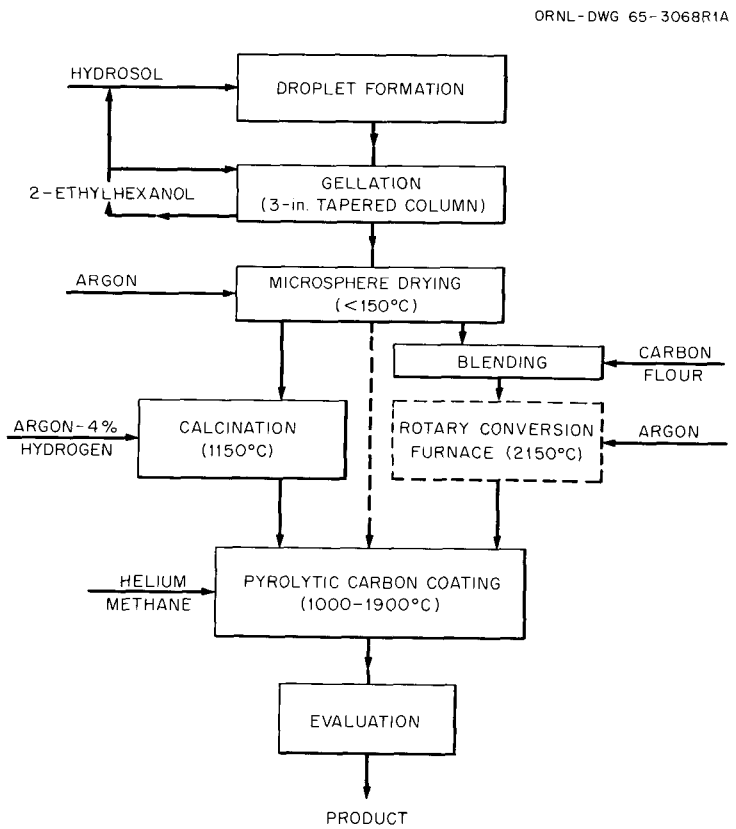

Fig. 30.6. Coated Particle Development Laboratory Process Flow Diagram.

Conversion of Sol-Gel Microspheres from ThO_2 to ThC_2

R. L. Pilloton R. L. Hamner
E. S. Bomar

Other investigators[17,18] make dense particles of ThC_2 or $(U,Th)C_2$ by at least the following four steps: (1) mixing of UO_2, ThO_2, and carbon powders, (2) granulating the mixture, (3) converting the oxides to carbides by heating to 2100°C, and (4) densifying and spheroidizing the carbide particles by heating them to 2500°C in a bed of carbon.

We investigated the feasibility of a process that would be shorter and therefore more amenable to remote operations.[19] At the same time, we sought information for the design and development of equipment that might be used in the TURF for refabrication of gas-cooled reactor fuels containing carbon-coated carbide fuel particles.

Initial feasibility for conversion was established when a dilute dispersion of fully dense sol-gel ThO_2 microspheres[20] in graphite flour (approx 91% graphite) was heated in a stationary graphite crucible for 2 hr at 2200°C and 10^{-2} torr. We showed subsequently that the quantity of graphite required could be reduced to 50% and that the oxide could be converted in a flowing argon atmosphere (approx 3 ft^3/hr). Lampblack was later substituted for graphite because of its greater reactivity.

We finally contained the charge in a horizontal cylindrical graphite crucible rotating at over 15 rpm. The rotation prevented reaction bonding of the ThO_2 particles to the crucible and agglomeration of the particles at temperatures greater than 2000°C. A crucible with one fin for periodic redispersion of the particles during rotation was most satisfactory for prevention of reaction bonding and agglomeration and for completely converting the charge in the shortest time. Time-temperature conversion studies in the single-fin crucible rotating at 44 rpm showed that the conversion of 300- to 400-μ ThO_2 microspheres to ThC_2 required over 5 hr at 2050°C, 3 hr at 2150°C, 2 hr at 2200°C, and at most 1 hr at 2300°C. However, the product converted at 2300°C was badly agglomerated and contained large holes.

Metallographic examination showed the particles converted below 2300°C retained their sphericity and high density, and x-ray diffraction analysis revealed the presence of only ThC_2. Complete conversion to ThC_2 is also shown in Fig. 30.7, a photomicrograph of a typical particle. Based on a 3.8% change in theoretical density in converting ThO_2 (9.62 g/cm^3) we calculated that the volume increase was 0.76% and the diametral increase was 0.26%.

The results of preliminary experiments using conventionally prepared UO_2 particles, 150 to 250 μ in diameter, indicated that UO_2 particles may be converted to the carbide in the same manner as the ThO_2 particles. We demonstrated, however, that temperatures lower than 2150°C are required to prevent reaction-bonding to the crucible and particle agglomeration under the other conditions used in the ThO_2 experiments described above.

The development of equipment necessary for larger scale experiments is in progress.

Gas-Solid Contact Model Studies

R. L. Pilloton H. J. Flamm[21]
A. L. Lotts

A study of gas-solid contact processes is an important part of our program aimed at developing improved carbon coating equipment for the economical refabrication of HTGR fuel[22] in the TURF. In that investigation we have used glass and plastic models to observe the motion of spherical particles in fluidized-bed columns and in rotary drums at room temperature. Direct observation was complemented by a study of slow-motion moving pictures.

---

[17] W. V. Goeddel, *Nucl. Sci. Eng.* **20**, 201–18 (October 1964).

[18] H. G. Sowman, R. L. Surver, and J. R. Johnson, *Nucl. Sci. Eng.* **20**, 227–34 (October 1964).

[19] R. L. Pilloton and R. L. Hamner, "A Method for Preparing Dense Spherical Particles of Thorium and Uranium Dicarbides," paper presented at the *11th Annual American Nuclear Society Meeting, Gatlinburg, Tenn., June 21–24, 1965* (to be published).

[20] D. E. Ferguson, O. C. Dean, and D. A. Douglas, "The Sol-Gel Process for the Remote Preparation and Fabrication of Recycle Fuels," paper presented at *Third United Nations International Conference on the Peaceful Uses of Atomic Energy, Geneva, Aug. 21 to Sept. 9, 1964*, paper A/CONF/28/P./237.

[21] On loan from Euratom.

[22] A. L. Lotts, D. A. Douglas, and R. L. Pilloton, "Refabrication Technology and Costs for High-Temperature Gas-Cooled Reactor Fuels," paper presented at the Euratom Symposium on "Fuel Cycles of High Temperature Gas-Cooled Reactors" at Brussels, Belgium, June 10–11, 1965.

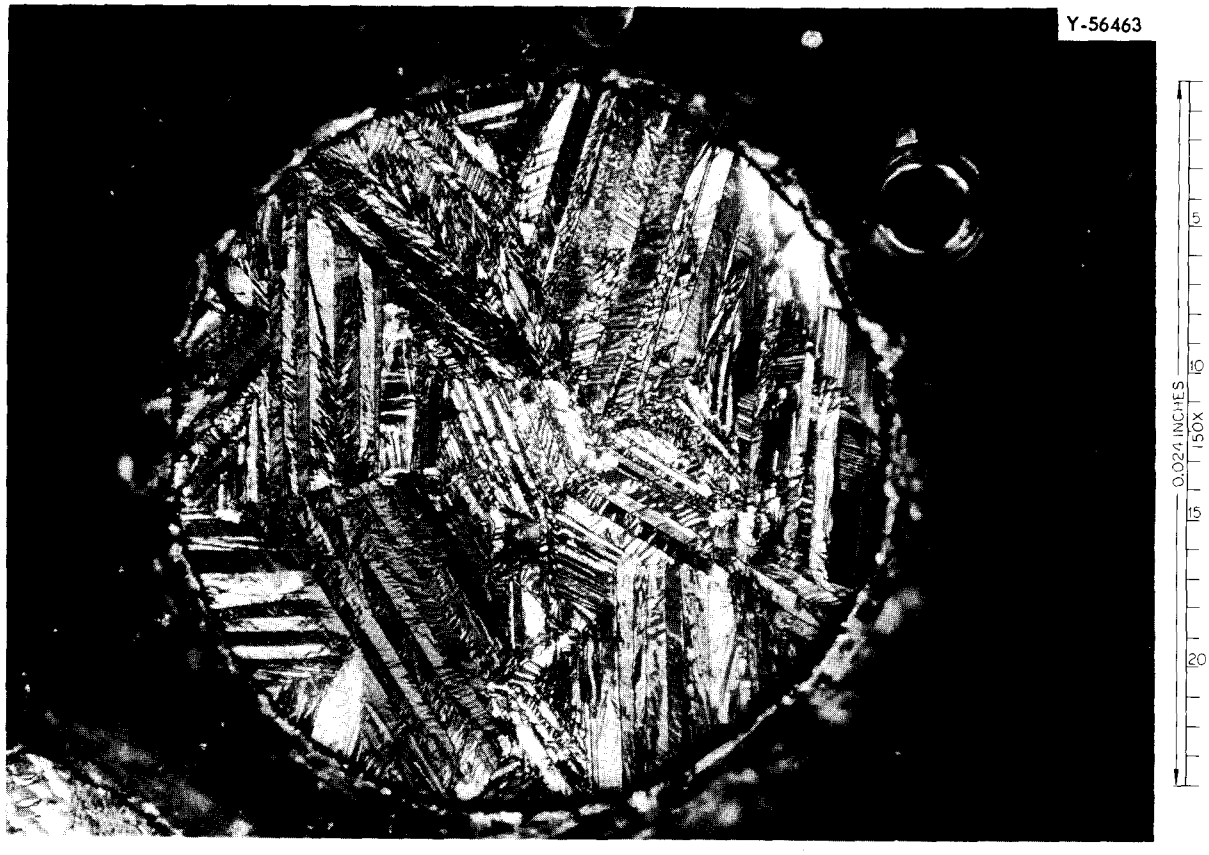

Fig. 30.7. Microstructure of ThC_2 Microsphere Derived from a Sol-Gel ThO_2 Microsphere by Heating at 2200°C for 2 hr at a Pressure of 10^{-2} Torr in a Stationary Crucible with Graphite-to-ThO_2 Weight Ratio of 10. As polished. Polarized light. 150×.

Fluidized-Bed Columns[23]. – In all conical columns with single gas inlets, bubbles formed in rapid succession at the gas entry, expanded while traveling upward, formed a temporary dome at the top of the bed, and finally burst, leaving a thin vertical column of particles that collapsed immediately. In no case could we obtain a perfectly smooth and uniform downward motion of the particles at the periphery where solids were returning to the simulated "coating zone."

Better bed characteristics were observed when the fluidizing gas was introduced through a multiple-orifice gas distributor similar to the one shown in Fig. 30.8 and the bottom part of the column consisted of a 30° contained-angle cone. In this case particles moved smoothly upward in the center of the column and downward at the periphery.

Since in actual coating furnaces particles would be coated mostly at the lower part of the bed where the coating gas is introduced, the "wall velocity" (i.e., the velocity at which the particles travel back to the coating zone along the column wall) is an important factor. Figure 30.9 shows that maximum wall velocity is obtained when the gas distributor plate is a shallow cone with a 120° contained angle.

Rotary Drums. – Since the motion of particles in rotary drums is relatively independent of the gas flow, this means of mechanical particle agitation can, in theory, be more easily applied to pyrolytic carbon coating of larger quantities of fuel particles than can the fluidized-bed methods.

[23]R. L. Pilloton, H. J. Flamm, and A. L. Lotts, "The Development of an Improved Coating Furnace for Nuclear Fuel Particles," paper presented at the *11th Annual American Nuclear Society Meeting, Gatlinburg, Tenn., June 21–24, 1965.*

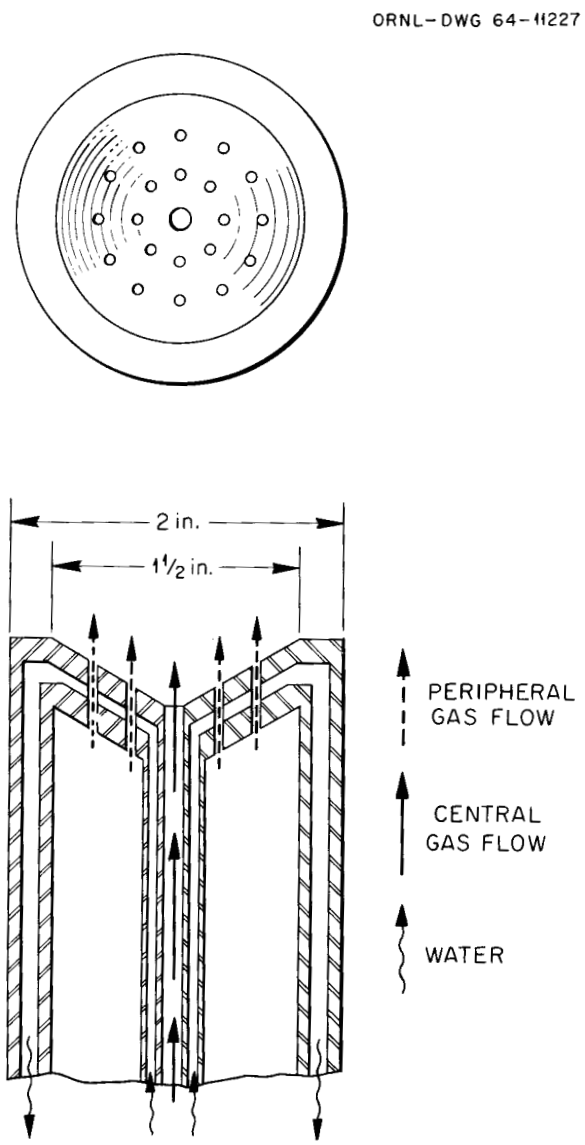

Fig. 30.8. Schematic Cross Section of a Dual-Flow Gas Distributor for Fluidized-Bed Coating of Nuclear Fuel Particles.

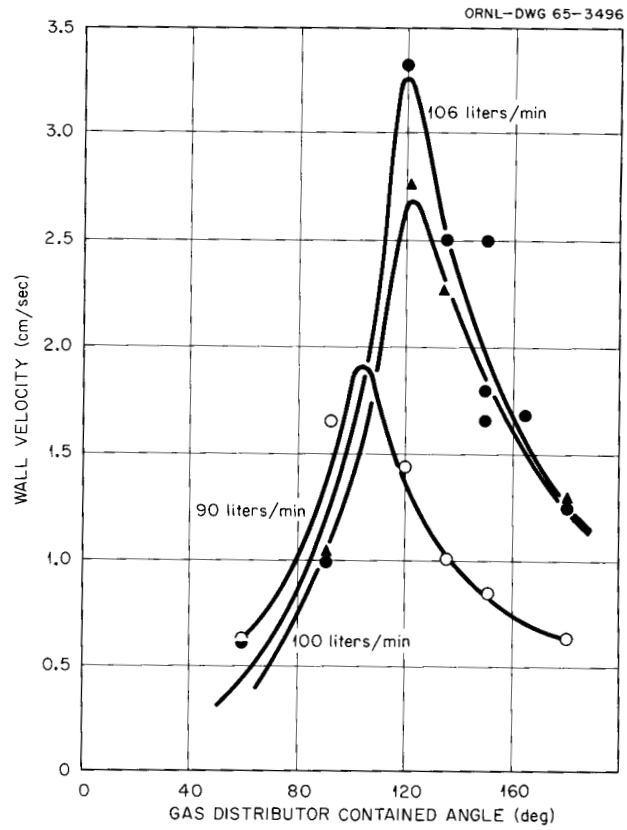

Fig. 30.9. Effect of the Gas Distributor Cone Angle on Particle Wall Velocity.

To study the motion of particles in rotary drum coaters we have simulated the geometrical characteristics of these coaters in glass and plastic models and recorded the patterns of particle movement in the models. We calculated and verified experimentally that nearly spherical particles, such as sol-gel microspheres, would remain practically motionless in a smooth horizontal rotating drum until the charge depth reached a certain value, which depended on the coefficient of friction of the particles on the drum wall. This relation is shown in Fig. 30.10. When the charge depth was sufficient to prevent slippage, the bed had the shape shown in Fig. 30.11. Below the dotted line of the figure particles rotate together in a packed bed; above that line they tumble down in a random motion.

The tendency of particles to remain motionless or to rotate together as packed beds in smooth rotary drums explains some of the difficulties of coating solids uniformly in such drums. The study indicates that baffles must be placed in the drums to increase particle agitation and gas-solid contact. More comprehensive data are reported elsewhere.[24]

[24] R. L. Pilloton and H. J. Flamm, *Motion of Spheres in Smooth Rotating Drums and Applications to the Coating of Nuclear Fuel Particles*, ORNL-3819 (August 1965).

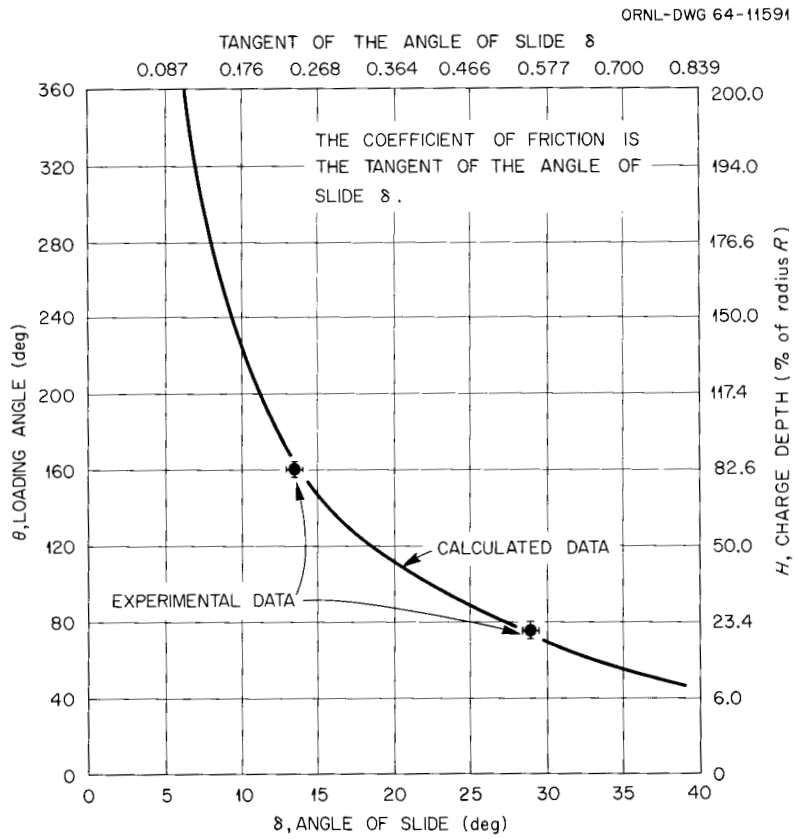

Fig. 30.10. Minimum Loading Necessary to Avoid Slippage of the Charge at Low Angular Speeds as a Function of Friction.

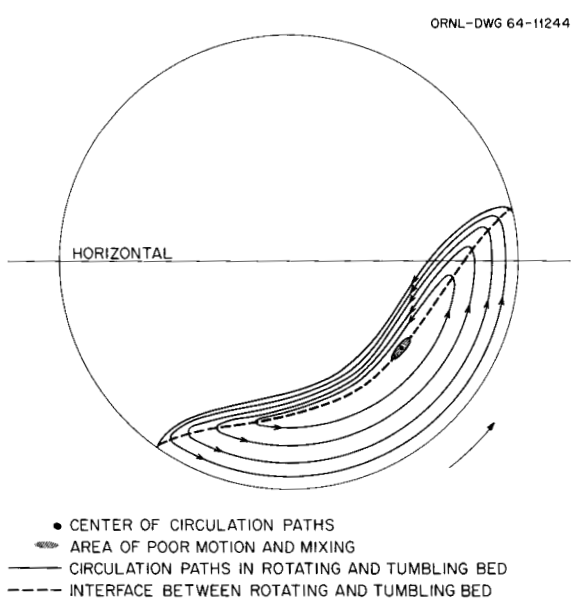

Fig. 30.11. Typical Circulation Path of Particles in a Rotating Drum. Charge depth, 40% of radius; rotation speed, 40 rpm.

Prototype Fluidized-Bed Coater

R. L. Pilloton H. J. Flamm[21]
R. G. Mills[25]

Our theoretical calculations and our model studies on fluidization[24] were used as a basis for the development of a prototype furnace for coating nuclear fuel particles. A cutaway view of this coater is shown in Fig. 30.12. Its main part is a cylindrical 5-in.-ID graphite tube connected by a 30° graphite cone to a 2-in.-ID metal gas distributor. The graphite column is heated by a 70-kw vertical resistance furnace mounted between two upright posts on which it can be raised or lowered. The gas distributor located at the lower end of the furnace is a special water-cooled nozzle with independent central and peripheral gas circuits connected to a series of manifolds and gas metering devices. The upper part of the furnace is a

[25]On loan from the General Atomic Company.

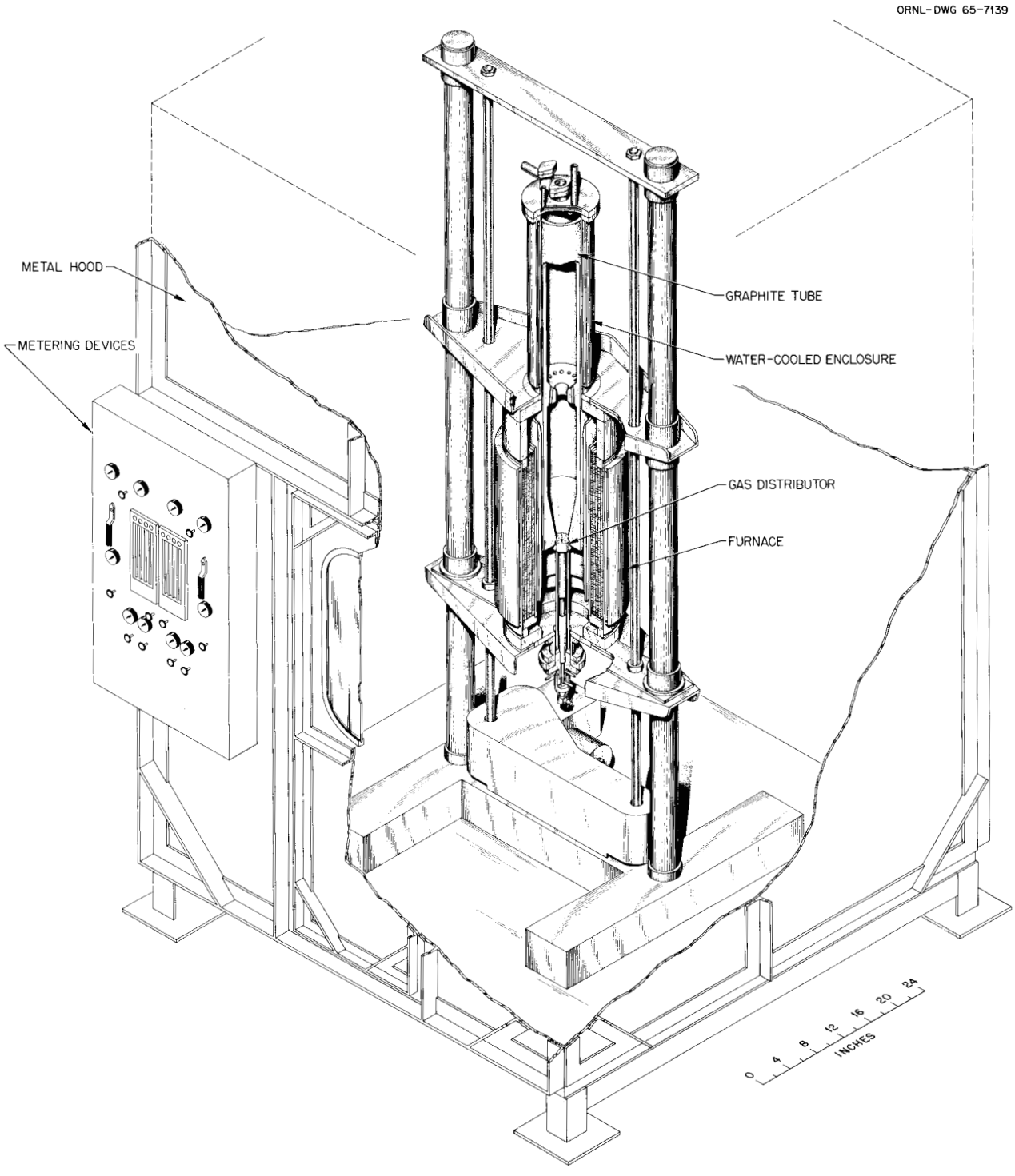

Fig. 30.12. Cutaway View of Coating Furnace Prototype.

water-cooled enclosure, which houses the upper portion of the reaction chamber and contains a sight glass, particle introduction and sample ports, and the connections for off-gas and a safety relief valve. The entire coating apparatus is enclosed in a sheet metal hood, which serves as primary containment for alpha contamination.

This apparatus will be used primarily to coat nuclear particles with pyrolytic carbon by hydrocarbon cracking at temperatures of 1000 to 2000°C. The engineering data thus obtained will be applied to the design of remotely operated fluidized-bed coaters for use in TURF.

Prototype Rotary-Drum Coater

H. J. Flamm[21] R. B. Pratt

The rotary-drum coating process consists of passing a coating gas over a charge of nuclear fuel particles placed in a heated cylindrical drum rotating around a horizontal axis. Based on the observations in studies on the motion of spherical particles in smooth rotary drums[24] and subsequent studies on the effect of baffles and fins in such drums, a prototype rotary-drum coater for operation up to 2200°C has been designed. As shown in the schematic of Fig. 30.13, an induction heating system has been tailored to an existing vacuum chamber. Currently, design is complete and internal components are being fabricated.

Prototype ThO_2-ThC_2 Rotary Conversion Furnace

J. T. Venard R. B. Pratt

The preliminary design of a rotary furnace for conversion of ThO_2 sol-gel microspheres to ThC_2 microspheres is complete and shown in Fig. 30.14. Design criteria were based upon previous conversion studies.[19,26] The principal reason for this prototype furnace is to demonstrate continuous large-scale conversion and to investigate control and remote control problems similar to those that will be encountered in TURF.

The furnace consists of an induction-heated graphite tube placed in a near horizontal position and capable of rotating. A blend of the ThO_2 microspheres and carbon flour is continuously fed to one end of the rotating tube, from which it progresses through the furnace heat zone where conversion takes place. After conversion, the material progresses to the discharge end of the

[26] "Experiments on Conversion of Sol-Gel Microspheres from ThO_2 to ThC_2," *Status and Progress Report for Thorium Fuel Cycle Development*, ORNL-3831 (in press).

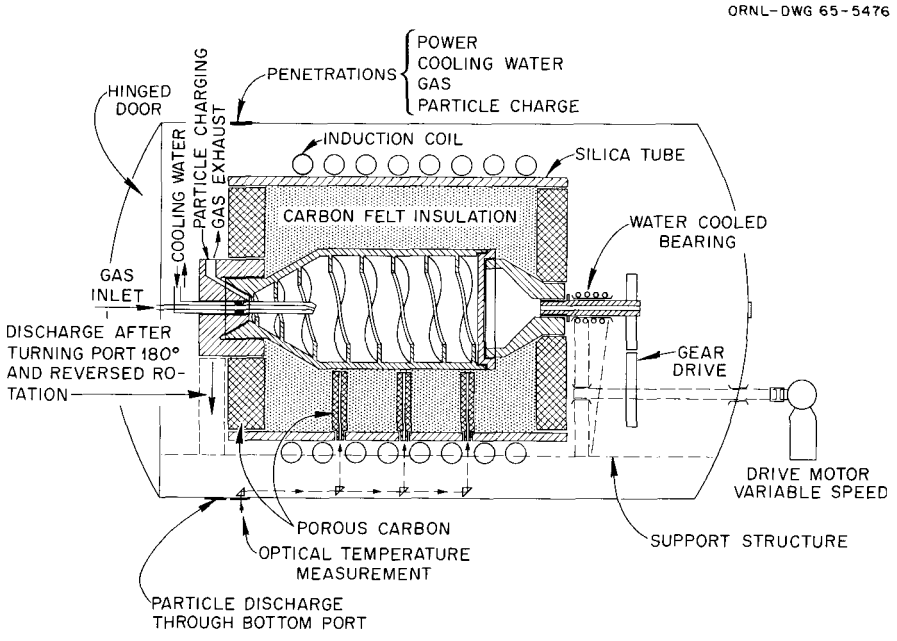

Fig. 30.13. Rotary Drum Coater Prototype.

ORNL-DWG 64-11254

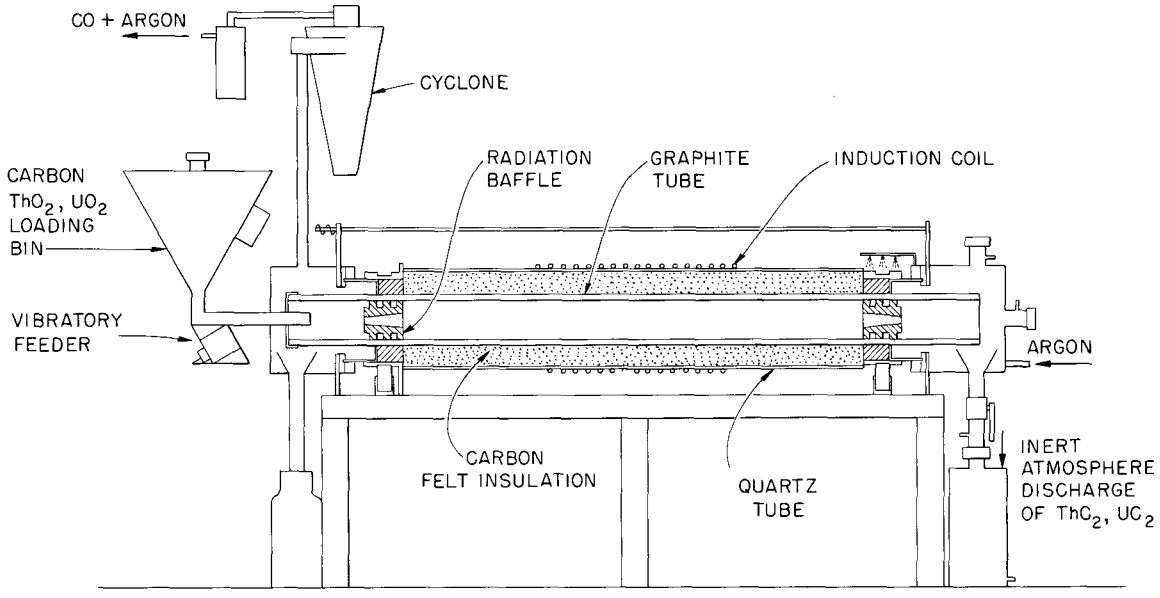

Fig. 30.14. Schematic of Furnace for Conversion of $(U,Th)O_2$ to $(U,Th)C_2$.

tube where it falls into a water-cooled storage hopper. The apparatus is controlled by varying the rotational speed and the elevation of the input end of the graphite tube. We expect that conversion will take place in 5 to 6 hr at approximately 2150°C.

Space and services for the conversion furnace are currently being prepared. During the next year we expect to complete fabrication and installation of this equipment and to begin process development.

VIBRATORY COMPACTION STUDIES

W. S. Ernst, Jr.

Our experimental studies of vibration energy characteristics required for obtaining high bulk densities are essentially complete. Although analyses of these experiments are in progress, some general conclusions are apparent. The most important factor that contributes to a high bulk density of powder-packed fuels is a relatively high radial acceleration level of the tube wall. In addition, the tube must vibrate in a longitudinal mode at a relatively high acceleration level. In this respect, the electrodynamic shaker cannot compare favorably with pneumatic vibrators. Contrary to our previous ideas, compaction is not at all aided by the transmission of an extremely high acceleration pulse directly into the powders. Apparently, densification is achieved by a combination of the radial expansion and contraction of the tube wall and agitation of the powder by the longitudinal mode. The first provides a settling effect and the latter orients the particles into a good geometrical fit.

We also studied the energy transfer mechanics between the anvil, coupling, and tube. These studies led to improved design for off-the-shelf pneumatic vibrators such as the Branford Vibrator Company's VIV and the NAVCO bin hopper type.

A final report covering these aspects, as well as others concerned with vibratory compaction, is being prepared.

SINTERING AND GRAIN GROWTH OF SOL-GEL THORIA AND THORIA-URANIA

M. J. Bannister[27]

Sol-gel thoria and thoria-urania may be sintered to near theoretical density at 1100 to 1200°C. We

[27]On loan from AAEC Research Establishment, Lucas Heights, Australia.

are studying the kinetics of sintering and concurrent grain growth of the dried gels to determine the mechanisms by which these processes occur.

Grain growth during sintering has been studied by differential thermal analysis (DTA). The method depends on detecting the release of surface energy while the gel is heated from room temperature to above 1300°C. The excess energy due to the very fine crystallite size in a typical thoria gel is about 10 cal/g. Thoria gel heated in air at 5°C/min gives the DTA pattern shown in Fig. 30.15*a*. The two endothermic peaks, at 80 and 450°C, are due to the heat absorption accompanying the release of first water and then nitrate from the gel. The broad exotherm extending from 700 to 1250°C is the surface-energy release peak. This peak is shown more clearly in Fig. 30.15*b* for gel calcined at 600°C to remove the nitrate.

This technique shows that crystallite growth begins at very low sintering temperatures. The observed peak profile may be interpreted in terms of a first-order reaction for the rate of decrease of surface area, with an activation energy slightly over 20 kcal/mole. The peak area yields a preliminary value close to 600 ergs/cm^2 for the surface energy of sol-gel thoria at 1000°C.

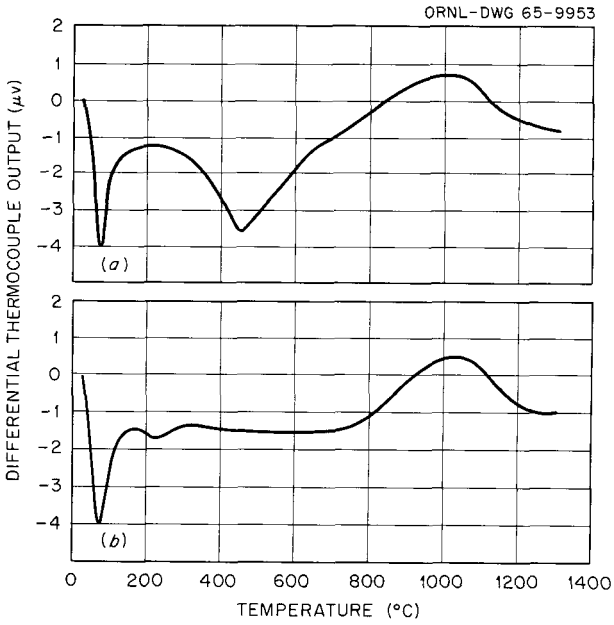

Fig. 30.15. DTA Patterns of Thoria Gel, Heated 5°C/min. (*a*) Air-dried gel. (*b*) Gel calcined 5 hr at 600°C.

We have also set up and calibrated a metallographic hot stage for the determination of shrinkage kinetics of individual gel microspheres. This is a Leitz vacuum heating stage, modified with heaters and shields of platinum to facilitate experiments in either oxygen or hydrogen. Preliminary experiments have confirmed that thoria gel microspheres sinter readily in either atmosphere.

SINTERING OF SOL-GEL OXIDES

J. M. Robbins

We began an investigation of the feasibility of fabricating sol-gel-derived $(Th,U)O_2$ by cold pressing dry powder and sintering.[28] The dried as-received ThO_2–3% UO_2 was crushed, screened to pass 200 mesh, calcined at a temperature in the range 400 to 950°C, cold pressed, and sintered. In the last step, all pellets were heated to 1000°C over a 36-hr period and finally sintered for 2 hr at 1450°C. We studied the effects of isostatic forming pressure, calcination temperature, and sintering atmosphere.

Under the same conditions of temperature and atmosphere, the final densities increased with increasing isostatic forming pressure (up to 35,000 psi). Powder calcined above 650°C was less sinterable than that calcined at lower temperatures. Either calcining the powder or sintering the pellets in hydrogen rather than in air resulted in a lower density. The highest bulk density (~9.4 g/cm^3) was obtained when pellets were isostatically pressed at 35,000 psi from air-calcined powder and sintered in air at 1450°C for 2 hr.

Pellets sintered in hydrogen to only 1000°C cracked on cooling, whereas pellets sintered to 1450°C in one heating cycle did not crack; apparently the pellets heated to only 1000°C were not strong enough to withstand the residual stresses that occurred during cooling.

[28] "Sintering of Sol-Gel Oxides," in *Status and Progress Report for Thorium Fuel Cycle Development Dec. 31, 1964*, ORNL-3831 (in press).

IRRADIATION STUDIES

Powder-Packed Sol-Gel Oxide

A. R. Olsen J. W. Ullman[11]
Y. Hirose[29] E. J. Manthos

The irradiation testing and evaluation of sol-gel oxide as a nuclear fuel is continuing. Previously reported results[30–32] showed that the chemically produced ceramic meets the basic requirements of a nuclear fuel and compares favorably with arc-fused material. Also, vibratorily compacted powder fuel rods performed well when compared with fuel rods containing pressed and sintered pellets at moderate linear heat ratings up to 300 w/cm and burnup levels to 40,000 Mwd/tonne Th + U. Currently we are investigating the effects of extended burnup, higher heat ratings, and sol-gel processing variables, such as calcining atmospheres, on the fuel material. Table 30.1 summarizes the experimental conditions of the irradiation tests in the program to date.

During the past year, two additional fuel rods from the MTR-I group were examined. These rods attained the highest burnup levels yet reached with the vibratorily compacted ThO_2-UO_2 fuels. As can be seen from the data listed in Table 30.2, the fission-gas release rates were moderate. We found no evidence of a saturation phenomenon, such as a sudden increase in gas release or significant changes in the fuel rod dimensions. The gas-release rates appear to be time dependent, indicating a diffusion controlled phenomenon. Other time and temperature controlled phenomena are grain growth and sintering. The development and growth of equiaxed grains were most pronounced in the sol-gel materials in the MTR-I group. The unirradiated material was uniform with no microscopically detectable structure but known to contain submicroscopic porosity. On irradiation this porosity first appeared to agglomerate. Continued irradiation developed a distinct grain structure in the center of the fuel rod with 6- to 8-μ equiaxed grains at 8.2×10^{20} fissions/cm^3 (375 reactor full-power days) and up to 60 μ at 16.5×10^{20} fissions/cm^3 (691 reactor full-power days). A more or less circumferential crack, caused by thermal cycling, was found at different locations, moving with increasing burnup or exposure time from the center toward the outer surface of the fuel. This crack appears to be associated with the extent of fuel sintering at operating temperature and was observed in the pressed and sintered pellet fuels as well as the vibratorily compacted fuels. One additional sol-gel fueled rod in the MTR-I group is still in the reactor and will be exposed to a burnup in excess of 100,000 Mwd/tonne Th + U.

The MTR-III and ETR-I groups contain a single dried sol-gel ThO_2-UO_2 fuel preparation that was divided into three segments that were calcined at 1150°C separately under different atmospheres (air, nitrogen, and the standard Ar–4% H_2). The MTR-III group is still being irradiated but the ETR-I group is being examined. Table 30.3 lists some of the irradiation conditions for this latter group. The experiment was intended to produce central melting in these fuel rods. The postirradiation gamma scans and microstructures indicate this was not achieved, possibly because during the first 9.5 hr of exposure the reactor operated at half power. Such operation would provide an $\int k d\theta$ of 50 w/cm, which the previous ORR loop tests indicated was high enough to produce sintering and columnar grain growth and thus increase the thermal conductivity and lower the central temperature at subsequent full-power operation. Columnar grain growth was extensive, and central voids were formed for the first time in this series of irradiation tests on ThO_2-UO_2. These voids were 3 cm long at the high burnup end of fuel rod 10 and essentially the full fuel length of rods 8, 18, and 20 (27 cm). The composite radial micrographs of three rods are shown in Fig. 30.16. Examination of these microstructures permitted the calculation of $\int k d\theta$ values for columnar grain growth and equiaxed grain growth shown in Table 30.4 together with previously reported data[31] for comparison. These data can be compared with

---

[29] Noncitizen guest from Hitachi Ltd., Japan.

[30] S. A. Rabin, *Metals and Ceramics Div. Ann. Progr. Rept. May 31, 1963*, ORNL-3470, pp. 205–9.

[31] S. A. Rabin, J. W. Ullman, and D. A. Douglas, *Metals and Ceramics Div. Ann. Progr. Rept. June 30, 1964*, ORNL-3670, pp. 238–45.

[32] *Status and Progress Report for Thorium Fuel Cycle Development December 31, 1963*, ORNL-3611, pp. 96–102.

Table 30.1. Summary of Thorium Fuel Cycle Program Irradiations of Powder-Packed Rods[a]

Designation	No. of Rods	Type of Oxide	Density (% of theoretical)	Fuel Rod Dimensions (cm)			Linear Heat Rating (w/cm)	Peak Burnup (Mwd/tonne metal)	Status	Objective
				Length	OD	Wall				
MTR-I	7	Arc-fused and Sol-Gel E	86 to 87	27	0.08	0.06	390	15,000 to 100,000	6 examined; 1 in reactor	Provide base-line data to use in comparing sol-gel and arc-fused oxide
MTR-II	2	Sol-Gel S	88 to 89	57	0.8	0.06	600	100,000	In reactor	Obtain higher heat rating by increasing enrichment
MTR-III	6	Sol-Gel 35	86 to 89	30	1.1	0.06	820	100,000	In reactor	Compare oxide calcining atmospheres and higher heat ratings obtained by increasing diameter
ETR-I	4	Sol-Gel 35	86 to 89	30	1.1	0.06	960	22,000	Being examined	Same as for MTR-III
NRX-I	8	Sol-Gel A and B	86 to 87	27	0.8	0.06	160	16,000	Examined	Provide base-line data
NRX-II	4	Sol-Gel C and arc-fused	83 to 86	57	0.8	0.06	210	5,000	Examined	Study effect of increased length
NRX-III	6	Sol-Gel S	88 to 89	99	0.8	0.06	270	23,000	Examined	Study effect of increased length
NRX-III	3	Sol-Gel ThO_2-PuO_2	74 to 76[b]	29	0.8	0.06	260	22,000	Examined	Study ThO_2-PuO_2 and lower packed density

Table 30.1 (continued)

Designation	No. of Rods	Type of Oxide	Density (% of theoretical)	Fuel Rod Dimensions (cm)			Linear Heat Rating (w/cm)	Peak Burnup (Mwd/tonne metal)	Status	Objective
				Length	OD	Wall				
ORR loop	3	Sol-Gel 26	84 to 85	55	1.2	0.04	500	2,100	Examined	Study in pressurized water at 260°C and 1750 psi
ORR poolside	2	Sol-Gel D	85[b]	18	1.6	0.05	340	5,000	Examined	Measure effective thermal conductivity using a central thermocouple in NaK at 315 psi; 540 and 705°C
ETR-II	6	BNL Sol-Gel	90	48	1.3	0.09	630	30,000 to 100,000	In reactor	Study effects of remote fabrication and oxide recalcining
ETR-III	7	Sol-Gel ThO_2	88	48	1.3	0.09	770	10,000 to 70,000	In reactor	Study ThO_2 blanket material with gradually increasing heat rating, and provide high-protactinium low-fission-product material for chemical processing

[a]All rods were clad with type 304 stainless steel except for groups ETR-II and -III and two of the three ORR loop specimens; these were clad in Zircaloy-2.

[b]Tamp packed.

Table 30.2. Effect of Burnup on Fission-Gas Release of Vibratorily Compacted ThO_2-UO_2 Fuels

Fuel Oxide	Peak Linear Heat Rating Time Averaged (w/cm)	Maximum Burnup (Mwd/tonne Th + U)	Maximum Burnup (Fissions/cm^3)	^{85}Kr Release (%)
			$\times 10^{20}$	
Sol-Gel E	341	14,000	2.9	0.5
Sol-Gel E	286	40,200	8.2	13.2
Sol-Gel E	311	81,000	16.5	17.0
Arc-Fused	299	12,300	2.5	2.4
Arc-Fused	297	42,100	8.6	7.2
Arc-Fused	267	71,000	14.4	6.4

Table 30.3. Conditions for the Irradiation of Vibratorily Compacted Sol-Gel ThO_2–6% UO_2[a] Fuel Rods at Higher Heat Ratings (ETR-I)

Fuel Rod Number	Calcining Atmosphere	Vibrated Density[b] (% theoretical)	Peak Linear Heat Rating[c] (w/cm)	Maximum Burnup (Mwd/tonne Th + U)	Maximum Burnup (Fissions/cm^3)
					$\times 10^{20}$
18	Air	88.1	870	20,400	4.3
10	Ar–4% H_2	88.4	865	20,000	4.3
8	N_2	85.1	910	22,000	4.5
20[d]	Air	88.3			

[a]Uranium enriched in ^{235}U to 93%.

[b]Based on a calculated theoretical density of 10.04 g/cm^3.

[c]Time averaged value for the total exposure of 140.5 test reactor full-power days.

[d]A binary distribution of fuel particle sizes; the other three rods used a ternary mixture.

the performance of vibratorily compacted UO_2 fuel rods,[33] in which voids were formed at an

$$\int_{T_0}^{T_v} k d\theta$$

of approximately 50 w/cm. The fission-gas release based upon the ^{85}Kr analysis is moderate when compared with that from UO_2 at similar heat ratings but indicates a possible effect of calcining atmosphere on the release rates. A final judgement will depend on the examination of the MTR-III group. These tests indicate the vibratorily compacted sol-gel fuels will operate at linear heat ratings up to 1000 w/cm and that the limit has not yet been reached.

Three rods containing sol-gel ThO_2 mixed with PuO_2 before calcining and loaded by tamp packing have been examined after exposure at linear heat ratings up to 245 w/cm to a burnup of 29,000 Mwd/

[33]V. O. Haynes, W. C. Thurber, and E. L. Long, Jr., "Fuel Irradiation Tests," *Maritime Reactor Program Ann. Progr. Rept. Nov. 30, 1963*, ORNL-3775, pp. 61–77.

PHOTO 80962

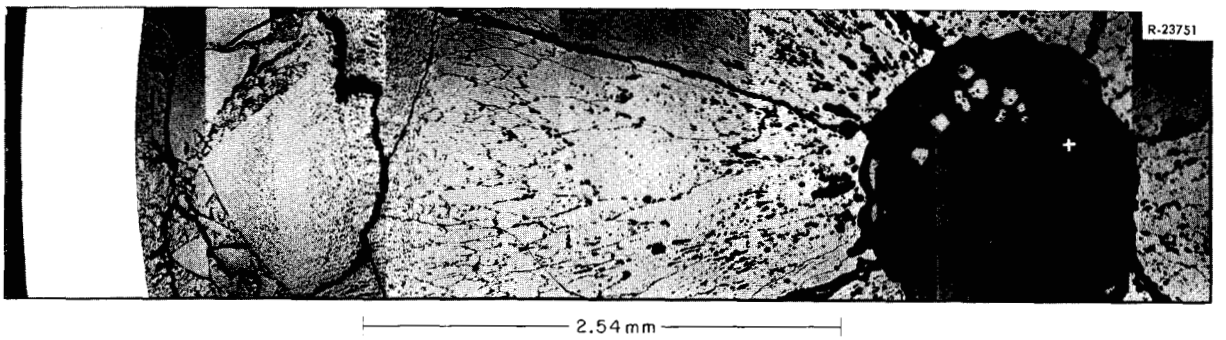

AIR FIRED FUEL IRRADIATED TO 4.3×10^{20} fissions/cm^3 AT A LINEAR HEAT RATING OF 870 w/cm.

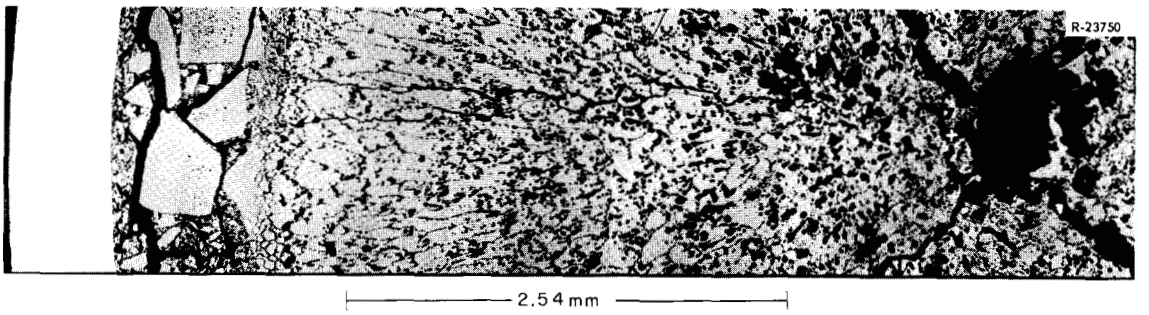

FUEL FIRED IN Ar-4% H_2 AND IRRADIATED TO 4.3×10^{20} fissions/cm^3 AT A LINEAR HEAT RATING OF 865 w/cm.

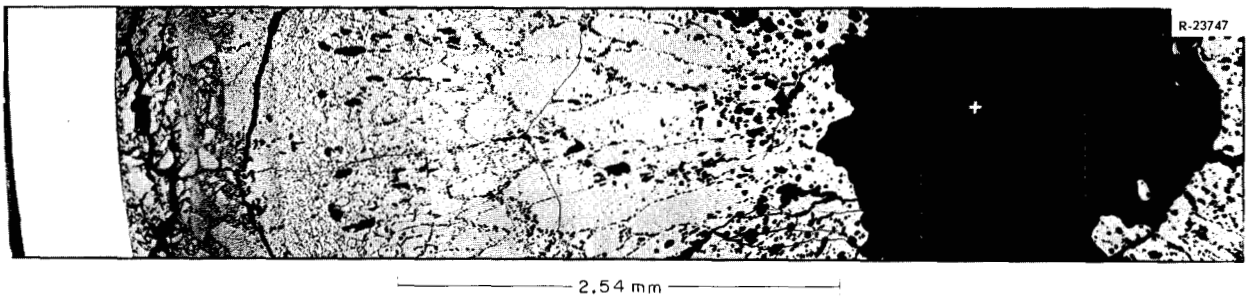

NITROGEN FIRED FUEL IRRADIATED TO 4.5×10^{20} fissions/cm^3 AT A LINEAR HEAT RATING OF 910 w/cm.

Fig. 30.16. Composite Radial Micrographs at Maximum Burnup Locations of Vibratorily Compacted Sol-Gel ThO_2–6% UO_2 Fuel Rods Clad in 304L Stainless Steel.

tonne Th + Pu. The fission-gas release rates were less than 5% and the microstructures were similar to ThO_2-UO_2 exposed under the same conditions.

During the past year, remotely fabricated rods of the ETR-II group containing ThO_2–3% $^{233}UO_2$ in Zircaloy cladding were inserted in the reactor. They are performing without incident after eight months exposure at a linear heat rating greater than 600 w/cm. A similar group of rods containing ThO_2 (ETR-III) are also under irradiation. This group

Table 30.4. Effects of Higher Heat Ratings on Irradiated Sol-Gel ThO_2-UO_2 Fuels

Experiment	Fuel Rod Identification	Cladding Surface Temperature (°C)	Heat Ratings for Various Microstructural Changes[a] (w/cm)				^{85}Kr Release (%)	Burnup (Mwd/tonne Th + U)
			$\int_{T_0}^{T_c} k d\theta$	$\int_{T_0}^{T_v} k d\theta$	$\int_{T_0}^{T_{cg}} k d\theta$	$\int_{T_0}^{T_{eg}} k d\theta$		
ORR loop	L-1-A	260	46.5			31.2	2.3	1600
	L-1-B	260	57.0		54.2	35.4	lost	2100
	L-1-C	260	49.6			38.2	3.9	1230
ORR poolside	03-5	705	58.5			35.5	18.3	5220
	06-5	540	46.7			*b*	lost	4040
ETR-I	18	100		76.5	49.3	48.2	38.6	20,400
	10	100		79.7	38.1	33.3	27.8	20,000
	8	100		75.3	42.2	39.3	21.4	22,000

[a]The heat ratings are time averaged values for the various integrals: T_c is the central temperature limit, T_v is the limit of void formation, T_{cg} is the limit of columnar grain growth, and T_{eg} is the limit of discernible equiaxed grain growth.

[b]Although equiaxed grain growth was observed, the extent has not been clearly defined.

will be subjected to an increasing linear heat rating, which will reach approximately 1000 w/cm after 350 reactor full-power days, when the accumulated burnup will be approximately 28,000 Mwd/tonne. These rods have been in the ETR for one cycle at a maximum unperturbed flux of 2.6×10^{14} neutrons cm^{-2} sec^{-1}.

Fission-Gas Release from Ceramic Fuels

R. B. Fitts

We are studying the release of ^{133}Xe during low temperature (<100°C) neutron activation and the release of this same isotope during postactivation isothermal annealing. The techniques used in these tests have been given in previous reports.[34–36]

Low-Temperature In-Reactor Fission-Gas Release. – We have measured the release of fission gas by thoria, urania, uranium nitride, and V–1% U fuels during low-temperature (<100°C) neutron activation.[37] The results show that the fractional release of fission gas at low temperature and dose is a function only of the surface area of the sample. In other words, the low-temperature neutron activation test yields an accurate measurement of the surface area of a nuclear fuel sample. The relationship between the fraction F of ^{133}Xe released during irradiation and the specific surface area S in cm^{-1} of a sample from our tests is given by:

$$\log F = -6.104 + 0.865 \log S .$$

The method of surface area measurement has several advantages, which are mentioned in an earlier report.[37] The data are being analyzed in detail at present and a report is being prepared for publication.

Elevated-Temperature Postirradiation Release. – We are examining the effects of stress of fission-gas release from ceramic fuels (principally ThO_2–1 or 2% UO_2). The manner in which stress and plastic deformation affect the release rate helps

[34]*GCR Program Quart. Progr. Rept. Dec. 31, 1959*, ORNL-2888, pp. 68–72.

[35]D. F. Toner and J. L. Scott, *Am. Soc. Testing Mater. Spec. Tech. Publ.* **306**, 86 (1961).

[36]R. B. Fitts, J. L. Scott, and C. S. Morgan, *Stress-Induced Release of Fission Gases from UO_2 and ThO_2-UO_2*, ORNL-TM-740 (Jan. 28, 1964).

[37]"Fission-Gas Release from Thoria Fuels," in *Status and Progress Report for Thorium Fuel Cycle Development Dec. 31, 1964*, ORNL-3831 (in press).

to clarify the role of stresses and dislocations in the release of fission gas. Some extension of our previous work[37–39] has shown that there is a strong correspondence between the creep rate of a ThO_2-UO_2 bushing and the observed rate of release of fission gas. In addition, we have shown that a sample under stress and containing a large number of quenched-in dislocations will release much more fission gas during postirradiation heating than will the same sample in the annealed state. These results show that stress, dislocation motion, or both cause enhanced release of fission gas from reactor fuels.

Since we wanted to use the induction-heated carbon dies of our creep apparatus in vacuum, we sought a thermocouple that could measure the sample temperature while in vacuum, in the presence of carbon, and in an induction field. We found no effect of our 10-kc induction field on the reading of a thermocouple by our Brown recorder. Hot carbon strongly affected the performance of most thermocouples. For example, in an 89-hr test, a Pt vs Pt–10% Rh thermocouple in carbon at 1400°C exhibited a spurious drift more than −1°C/hr. A test of four platinum-rhodium alloys and two tungsten-rhenium alloys in carbon and vacuum showed that the platinum-rhodium alloys with higher rhodium contents are the most stable thermoelements of these systems. Also, a small gap between the carbon and the hot junction greatly improved thermocouple performance in vacuum and carbon. We feel that a platinum-rhodium alloy thermocouple with high rhodium content and with a small shield to prevent direct contact with the carbon will perform satisfactorily up to 100 hr in carbon dies at temperatures up to 1500°C.

---

[38]R. B. Fitts, *Metals and Ceramics Div. Ann. Progr. Rept. June 30, 1964*, ORNL-3670, pp. 246–49.

[39]C. S. Morgan, R. B. Fitts, and J. L. Scott, *J. Am. Ceram. Soc.* **48**(3), 166 (1965).

Part IV.

Other Program Activities

31. BONUS Reactor Support Program

J. E. Cunningham

In late November of 1964 we initiated in-cell examination of a superheater fuel assembly that had failed prematurely in the Boiling Nuclear Superheat (BONUS) Reactor. The investigation was undertaken at the request of the U.S. Atomic Energy Commission, Oak Ridge Operations, for the following reasons: (1) to locate the source of fission-product leakage, (2) to establish the nature and extent of damage, (3) to determine the most likely mode or mechanism of failure, and (4) to ascertain the probable cause of failure.

The findings of the examination, as well as follow-up fabrication work to upgrade specifications for future procurement of these components, are reported below.

BACKGROUND ON BONUS REACTOR

During the early morning of November 11, 1964, a reduction-of-coolant-flow accident occurred at the BONUS power station that eventually led to shutdown of the reactor and removal of a damaged superheater fuel assembly. The reactor was in standby operation at a power level of 4.8 Mw (thermal), being readied for additional full-core testing at higher power, when an operator inadvertently closed a by-pass valve through which the bulk of the exit steam from the reactor was being routed. This action reduced steam flow through the superheater assemblies to a value 20% of normal and, although normal flow was restored within 2 to 3 min, the temporary suppression of coolant flow raised the calculated cladding temperature at the steam-cooled surface in the hottest element from 820 to 1400°F. Immediately following the temperature excursion, fission-product activity was detected in the off-gas from the main condenser, indicating probable leakage from one or more of the superheater assemblies. Some leakage was definitely traced to superheater assembly No. 9, located in core position 16D. The defective component was removed from the reactor and shipped to Oak Ridge for examination.

A spare superheater fuel assembly (No. 29) that had not been exposed to reactor service was also included in the examination to provide reference data.

The BONUS power station features a boiling-water-type reactor with integral or nuclear-coupled superheater. The reactor is designed to produce 16.5 Mw net electrical power at the turbogenerator by converting 50 Mw thermal power delivered in the form of steam at 915°F and 915 psi. The reactor core, shown in cross section in Fig. 31.1, consists of two regions: a central boiler region with 64 fuel assemblies in an 8 × 8 array and a peripheral superheater zone with 32 assemblies of rectangular cross section arranged in rows of eight on each side of the square boiler region. The boiler region converts reactor recirculating water at 532°F to saturated steam at 540°F, while the superheater region raises the steam temperature to 915°F. The steam makes a four-pass flow in traversing each superheater assembly.

A perspective drawing of a superheater assembly is shown in Fig. 31.2. The unit stands approximately 7 ft high and weighs about 300 lb. It is composed of 32 fuel rod and coolant tube subassemblies, a shell assembly, the inlet and outlet transition pieces and liners, the upper and lower crossover box liners and covers, lower end fittings, and a protective shroud. The shell forms the basic support structure for the superheater, positions the fuel, and provides a pressure barrier between the moderator and the lower-pressure superheated steam. When a fuel rod and coolant tube subassembly is inserted into a pressure tube and edge welded, as shown in longitudinal view in Fig. 31.2, the resulting annular space between the pressure

ORNL-DWG 65-9954

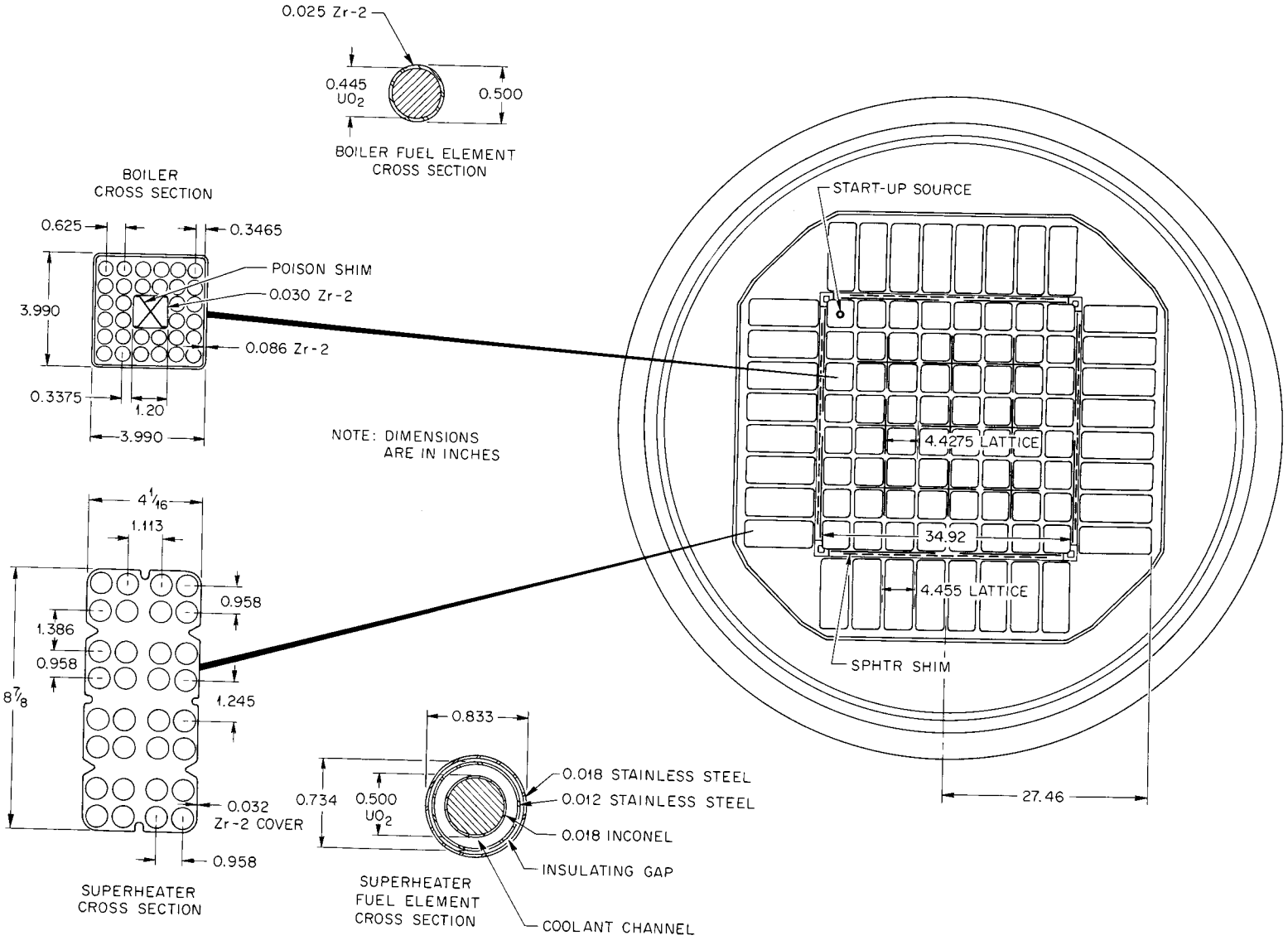

Fig. 31.1. Horizontal Cross Section of the BONUS Core.

ORNL-DWG 65-9955

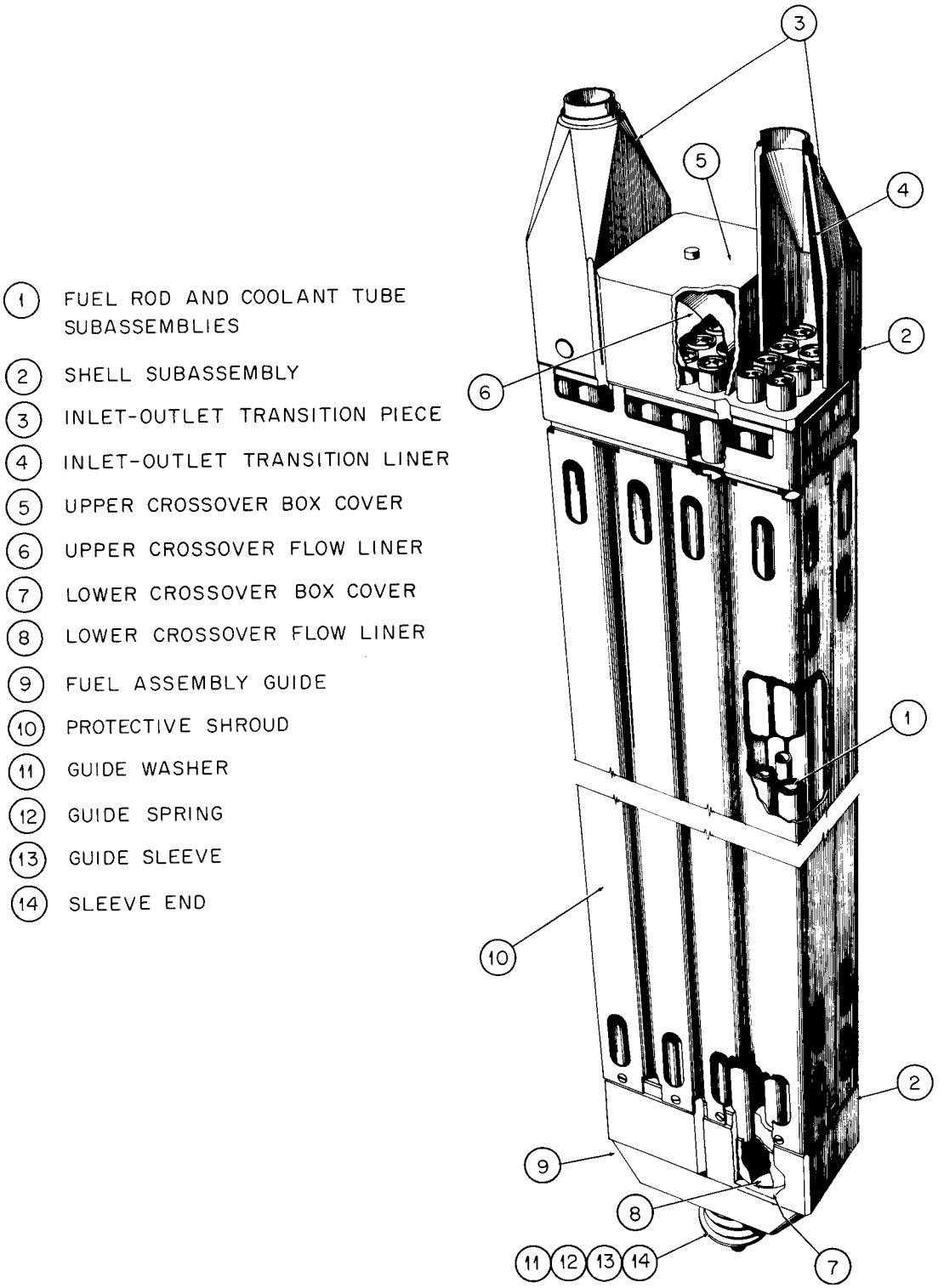

Fig. 31.2. Perspective of BONUS Superheater Fuel Assembly.

and the coolant tubes forms an insulating gap where stagnant steam resides. The other annular space, between fuel rod and coolant tube, serves as the main coolant channel where heat is transferred from fuel to steam. Each fuel rod consists of an Inconel-600 cladding tube, UO_2 fuel pellets, end caps, spacer, and other accessories. Closure between the end caps and cladding tube as well as closure of the two vent holes is accomplished by fusion welding. All weldments were supposedly checked for soundness by dye penetrant and helium leak testing.

IN-CELL EXAMINATION OF SUPERHEATER ASSEMBLIES

E. L. Long, Jr.

Examination of the failed superheater assembly disclosed two major defects. One fuel rod from the third pass had swollen along the entire length of the cladding and had ruptured at the location of maximum neutron flux during service. The rod from the second (and hottest) pass had also swollen along its entire length of cladding but had not ruptured. Leak testing of this rod, however, revealed the presence of two small pin holes at the cladding-to-support cap weldment. Calculation indicated a hole size of 8 μ in diameter, if one assumed that both holes were equal in size. The diameter of the ruptured rod increased a maximum of 15% in the unfailed region, while the other rod showed a maximum diametral increase of about 8%. The remaining 30 rods, however, showed no deviation from the as-manufactured specification.

Gas samples were taken from at least two fuel rods from each of the three material lots used in manufacture of the failed assembly. All analyzed at least 99% He, except that one taken from the swollen rod with pinholes analyzed "wet air."

Metallographic examination of the failed superheater assembly was confined to three rods – the two failed rods and one that showed no unexpected changes as a result of irradiation. The fuel rods used in the superheater assemblies contained four welds, two cladding-to-end-cap welds and two vent-hole welds located in the end caps. Although each of these rods was examined in considerable detail, the most significant results that could be related to failure of the rods were found in the weldments.

A composite overlay of three planes of polish made through the top vent-hole weld from the ruptured rod is shown in Fig. 31.3. A continuous path can be traced from the inside to the outside of the fuel rod, except for 1 to 2 mils. All the vent-hole welds from the three rods examined contained hot-cracks (i.e., cracks that formed during welding), but none were as severely cracked as that shown in Fig. 31.3. This particular weld was leak tested prior to sectioning, but no leak was found. However, this leak test was performed with low internal pressure (He at 20 to 30 psig) while the end cap was held under water.

The two pinholes located in the cladding-to-end-cap weld of the swollen fuel rod were located and examined metallographically. The results of this examination are shown in Fig. 31.4. By successively regrinding and repolishing, we determined that the two holes were about 0.1 in. apart. One extended along the weld for about 0.011 in. and the other for approximately 0.009 in. The maximum size of both openings across the cracks at the outer surface of the weld was 5×10^{-4} in. The holes were the result of insufficient weld penetration and fine hot-cracks in the weld metal. We feel that the holes were enlarged when the cladding swelled.

The findings on examination of the "cold" or spare assembly were similar. All 32 fuel rods were removed from the as-fabricated assembly for examination. We saw a crack in the surface of one of the vent-hole welds. After dye-checking to assure ourselves that a crack did exist, a gas sample was taken from the fuel rod. It analyzed 75% He, which indicated that the crack was quite small, since only 25% of the helium diffused out over a period of about 1.5 years. Another fuel rod from the same welding lot contained an atmosphere of over 99% He.

The most interesting facet of this examination came about as a result of helium leak checking the defective weld. The helium leak test was performed by filling the fuel rod with helium and covering the weld with a mask that was connected to a mass-spectrometer helium leak detector; the mask was then evacuated to 1×10^{-5} torr. The detector was calibrated for a leak rate of 3.8×10^{-10} std cm^3/sec. At an internal pressure of 0 psig the weld did not leak. However, with an internal pressure of 5 psig the weld leaked. The leak rate continued to increase with an increase in internal pressure. We tested this weld further

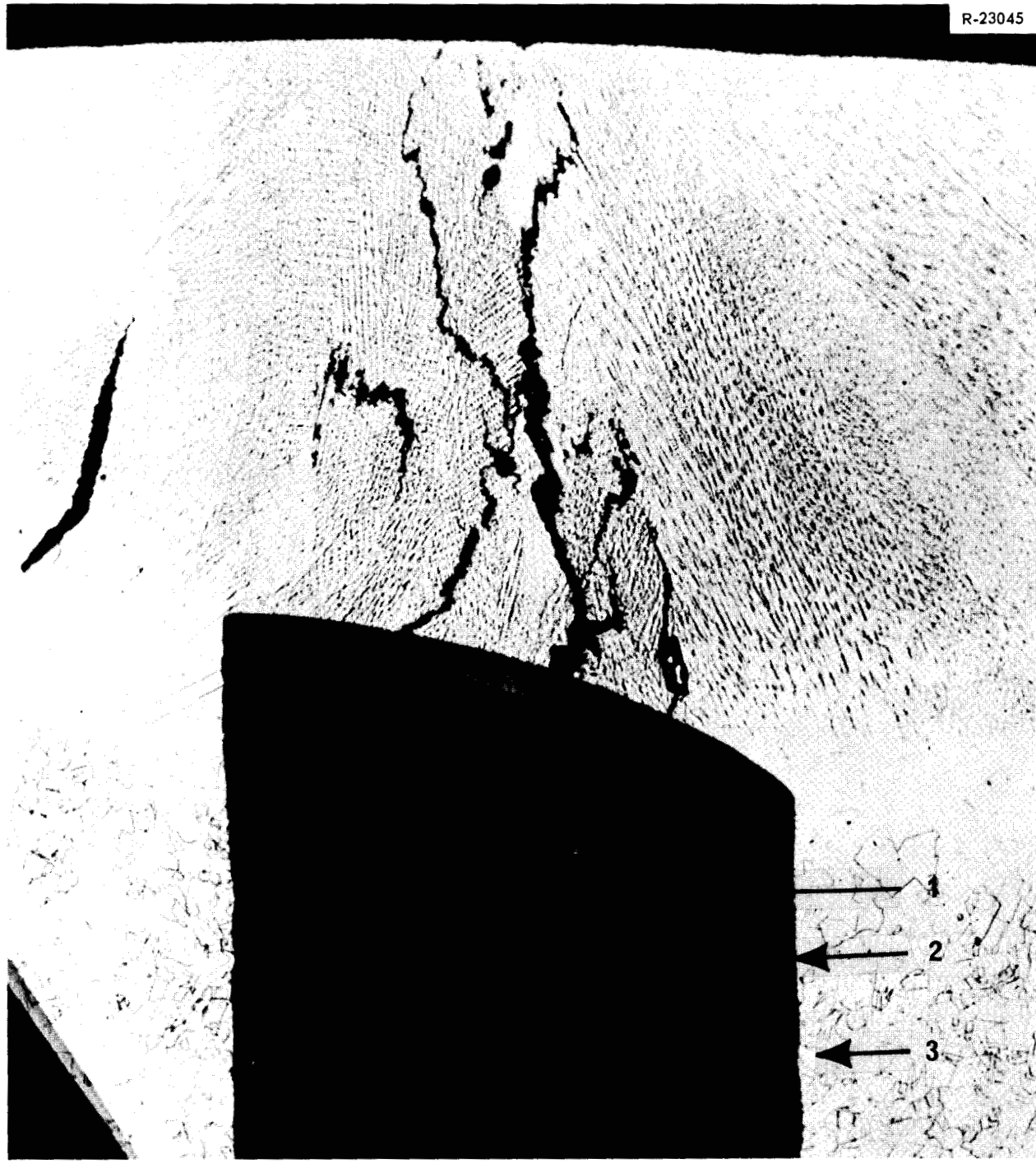

Fig. 31.3. A Composite Overlay Made from Three Planes of Polish on a Transverse Section Through the Top Vent-Plug Weld of the Ruptured Fuel Rod. Etched; 125×.

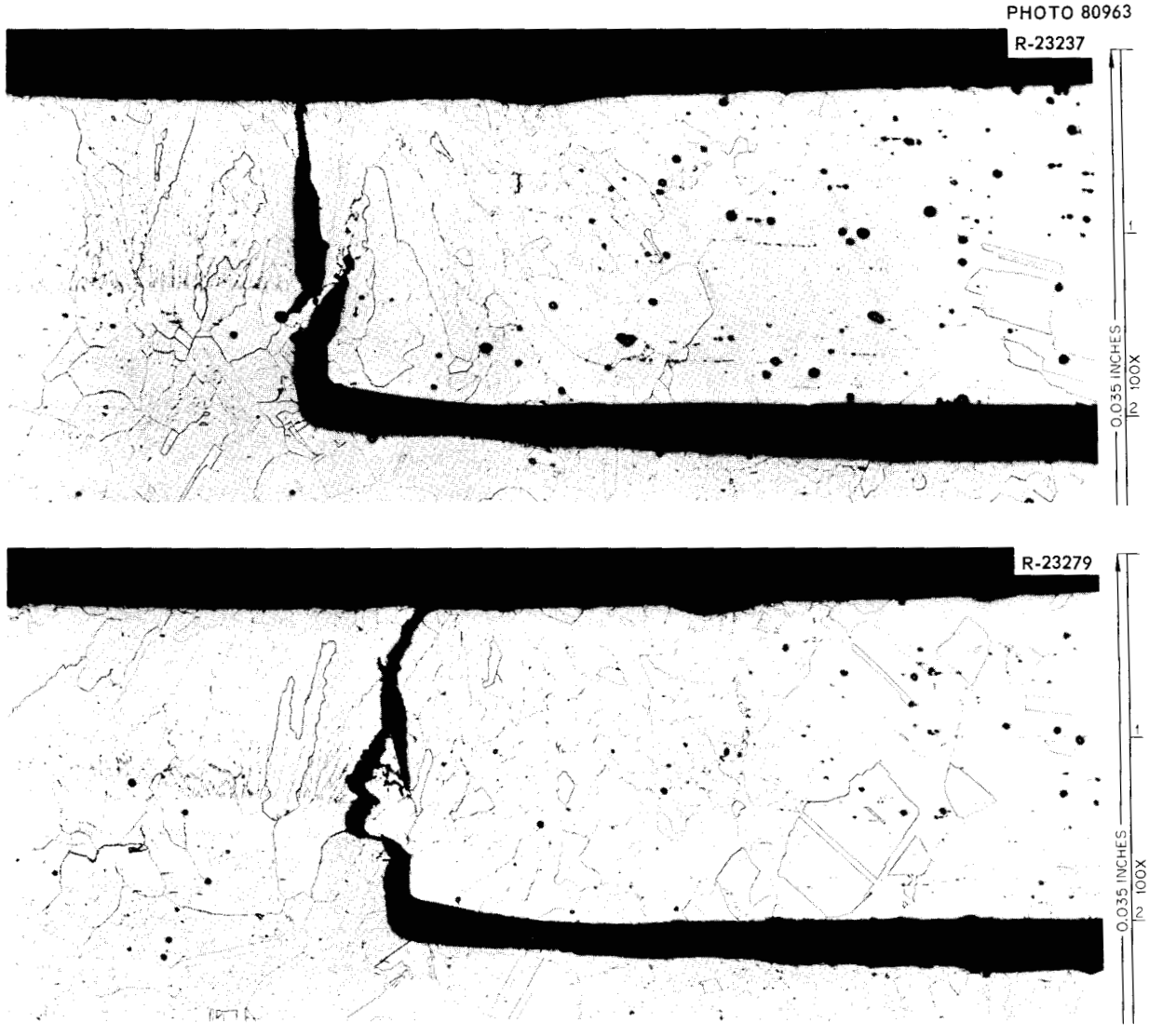

Fig. 31.4. Longitudinal Sections Through the Two Pinholes Found in the Top Cladding-to-End-Cap Weld in the Swollen Fuel Rod from the Failed Superheater Assembly. Etched; 100×.

by internally pressurizing the fuel rod with air and submerging the weld area in liquid Freon. Bubbles emerged from the crack in the weld at a pressure differential of 20 psi. Based on this information, a hole diameter of 0.5 μ was calculated. Metallographic examination of this weld yielded results similar to those shown in Fig. 31.3.

The defective welds found in fuel rods from both a spare superheater assembly and one that had failed in reactor service lead us to conclude that the defects occurred during manufacture. Since these faults afforded continuous paths from the interior to the exterior of the fuel rods, the failures experienced in the superheater region of the BONUS reactor were of a water- or steam-logging type that occurred during the transient. Although the transient resulted in the failures, the actual cause was traced to manufacturing defects. All but two of the 32 rods examined showed no deleterious effects from the transient. There were no indications that the choice of materials or the general design concept played an important role in the failures that occurred in the BONUS superheater fuel assemblies.

FUEL ELEMENT FABRICATION

E. A. Franco-Ferreira

We are currently in the process of developing reliable methods of fabricating fuel rods for superheater elements for the BONUS Reactor. The major aspect has been to devise a design and fabrication method for fuel-rod end closures that is an improvement over that used in the present BONUS core.

The original design uses end caps that are socket-welded into the cladding tube by simple tungsten-arc fusion of the base metal. All components are made of Inconel 600, and the cladding tube is 1/2-in. ID × 0.018-in. wall. The overall length of the fuel rod is approximately 62 in.

The improved end-closure design incorporates an edge fusion weld, which, as previous experience has shown, is a more reliable and inspectable joint than the socket weld. Figure 31.5 shows the sequential steps used in making the fuel-rod top closure. At the left are shown the end cap and cladding tube prior to assembly. In the center is the clad tube with the end cap pressed into place, ready for welding, while the top support hanger is in position to be screwed on. The view at the right shows the weld closure between the cladding and end cap with the support hanger screwed into place. A transverse section of a typical end cap edge weld is shown in Fig. 31.6.

The lower end closure is made similarly. The configurations of both end caps with their respective screwed fittings were chosen so that the overall shape of the fuel rod will conform to the originally designed envelope.

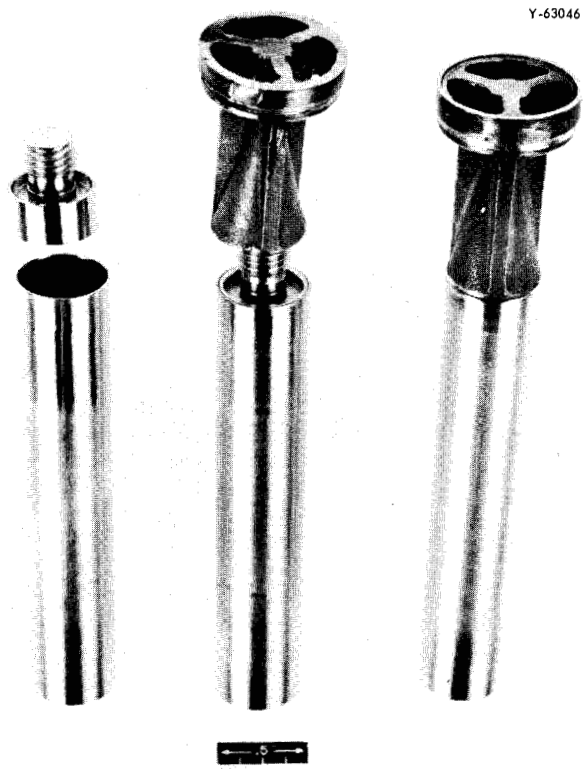

Fig. 31.5. Sequential Steps Used in Making the BONUS Fuel Rod Top Closure.

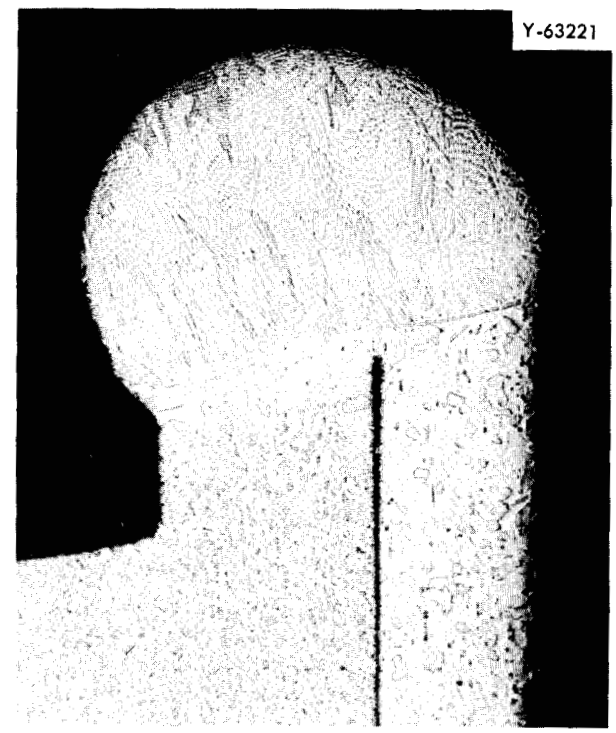

Fig. 31.6. Cross Section of Typical Closure Weld Showing Excellent Joint Quality. Etch: Glycera regia. 39×.

32. Metallography

R. J. Gray

A prime responsibility of the group is to prepare, examine, and help interpret the microstructure of all types of radioactive, toxic, and nonhazardous materials that may be related to fundamental and applied research, development, and reactor programs at Oak Ridge National Laboratory. In addition, we endeavor to keep abreast of improved techniques and equipment in our field and apply them or develop our own as they are needed for us to fulfill our obligations.

An important recent accomplishment, the hot-cell examination of a failed superheater element from the BONUS reactor and discovery of the cause of failure, is reported in Chap. 31 of this report. Other significant accomplishments are reported below.

ELECTRON MICROPROBE X-RAY ANALYSIS

G. Hallerman

The electron microprobe x-ray analyzer is an instrument for qualitative and quantitative analysis of elements on regions as small as 1 μ in diameter on the surface of a specimen. Volumes as small as 10^{-12} cm^3 can be readily analyzed with a relative accuracy of 1% and a limit of detection of 0.1% or less.

A fine beam of high-energy electrons is focused by electromagnetic lenses on a selected area of the specimen surface. The beam excites an x-ray spectrum containing wavelengths that are characteristic of the elements present in the selected area of the sample. By dispersing the x-ray spectrum in a spectrometer and measuring the emitted x-ray intensities, we can make a quantitative analysis, since the intensities of the characteristic wavelengths are proportional to mass concentrations of the elements present in the selected area on the specimen surface.

A Materials Analysis Company model 400 microprobe was put in operation in January 1965. We have used it for the following applications:

1. Analysis of UO_2 fuel particles,
2. Analysis of tungsten carbide–cobalt bearings,
3. Identification of phases in uranium carbide alloys,
4. Analysis of a uranium-thorium alloy,
5. Measurement of grain boundary distribution of calcium in a sample of ThO_2–0.6% CaO,
6. Diffusion studies of uranium nitride–metal alloys,
7. Determination of the distribution of magnesium in an NiO–10 at. % MgO crystal,
8. Measurement of element distribution in Nb–40 at. % V,
9. Analysis of precipitates in INOR-8 alloy.

EXTENDED-TEMPERATURE-RANGE HOT-HARDNESS TESTER

G. Hallerman

The elevated-temperature hardness tester described previously[1] has an upper temperature range of 1000°C. We have installed a new hardness tester, shown in Fig. 32.1, the design characteristics of which are based on concepts developed for the 1000°C tester. Although the temperature capability of the new instrument is extended to 2200°C, the presently available indenter materials limit its usefulness to 1400 or 1500°C. Use of this instrument to evaluate uranium mononitride is described in Part II, Chap. 20 of this report.

[1]G. Hallerman and R. J. Gray, *Equipment for Hardness Testing at Elevated Temperatures*, ORNL-3448 (July 17, 1963).

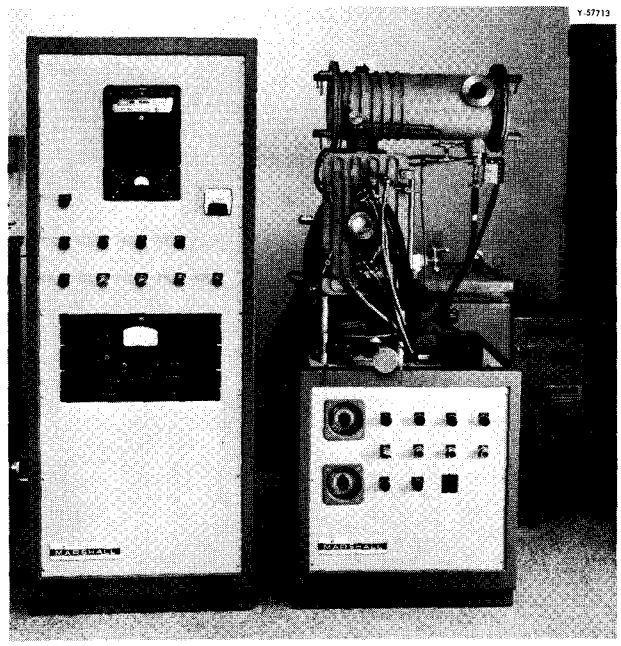

Fig. 32.1. Extended-Temperature-Range Hot-Hardness Tester.

METALLOGRAPHY OF THORIUM CARBIDES

T. M. Kegley, Jr. B. C. Leslie

A study of the microstructure was required to characterize purity of arc-melted thorium carbide samples used in an investigation[2] of the chemical properties conducted by the Chemical Technology Division. Since thorium carbides react readily with moisture in the air, special techniques were required to prepare them metallographically. The techniques developed[3,4] were similar to those we reported previously for preparing thorium-uranium dicarbides.[5,6]

[2]M. J. Bradley and L. M. Ferris, *J. Inorg. Nucl. Chem.* 27, 1021 (1965).

[3]M. B. Sears and T. M. Kegley, Jr., "Correlation of Composition with the Microstructures of Arc-Cast Thorium Carbides," submitted to the *Journal of the Electrochemical Society*.

[4]T. M. Kegley, Jr., and B. C. Leslie, *Metallographic Preparation of Thorium Carbides*, paper presented at the 19th AEC Metallography Group Meeting April 20–22, 1965 at Oak Ridge National Laboratory (proceedings to be published as ORNL-TM-1161).

[5]T. M. Kegley, Jr., and B. C. Leslie, *J. Nucl. Mater.* 13(2), 283 (1964).

[6]T. M. Kegley, Jr., and B. C. Leslie, *Metallographic Preparation of Dicarbides of Thorium and Thorium-Uranium*, ORNL-TM-949 (November 1964).

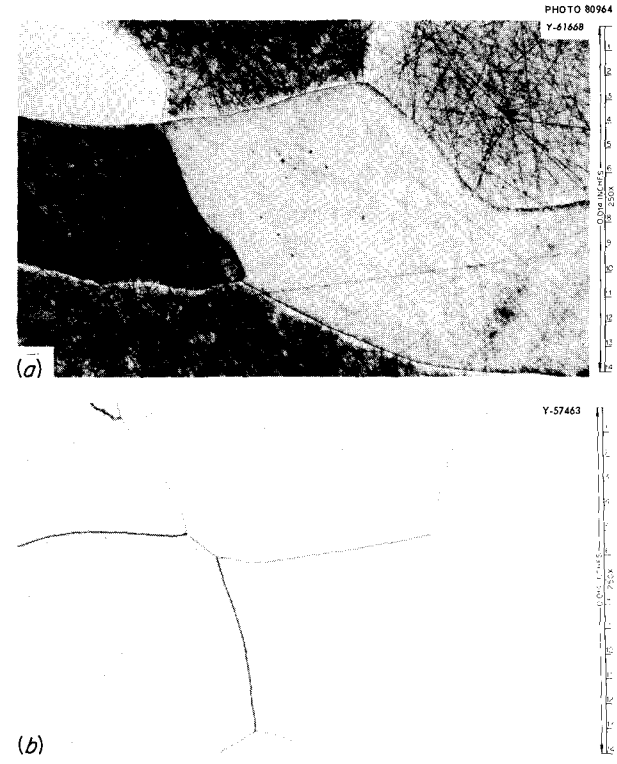

Fig. 32.2. Effect of Air Etching and Etching with a Nitric Acid Solution on a Single-Phase Thorium Monocarbide Specimen (4.00% C). (*a*) Air etched 10 min. Scratches were not evident until specimen was exposed to air. (*b*) Etched by immersing 5 min in a solution of 50 parts concd HNO_3, 50 parts H_2O, and 2 parts concd HCl. 250×.

Air etching has frequently been employed as a means for revealing the microstructures of thorium carbides.[7–9] Air etching results from the exposure of the active polished surface to moisture contained in the ambient air. While air etching reveals some microstructural features, the results are not as clear and distinct as the metallographer sees in the chemical etching of metals. Rather than air etching we etched by immersion in nitric acid solutions. Figures 32.2 and 32.3 illustrate the superiority of the nitric acid etchants over conventional air etching for a single-phase thorium

[7]H. A. Wilhelm and P. Chiotti, *Trans. Am. Soc. Metals* 42, 1295 (1950).

[8]N. Brett, D. Law, and D. T. Livey, *J. Inorg. Nucl. Chem.* 13, 44 (1960).

[9]G. B. Engle, *Metallography of Carbide Fuel Compounds*, GA-2067 (1961).

monocarbide specimen and a thorium dicarbide specimen containing excess graphite.

The microstructure of carbide specimens containing a high percentage of ThC_2 must be observed with polarized light, since the surfaces passivated by immersion in equal parts of water and concentrated nitric acid are essentially featureless when observed in bright field. Figure 32.4 compares the microstructures observed with polarized light for a thorium dicarbide specimen (8.91% C) containing a small amount of monocarbide and a single-phase thorium dicarbide specimen (9.23% C). The monocarbide precipitate shows up cloudy with polarized light; in contrast the structure of the single-phase dicarbide shows up sharply.

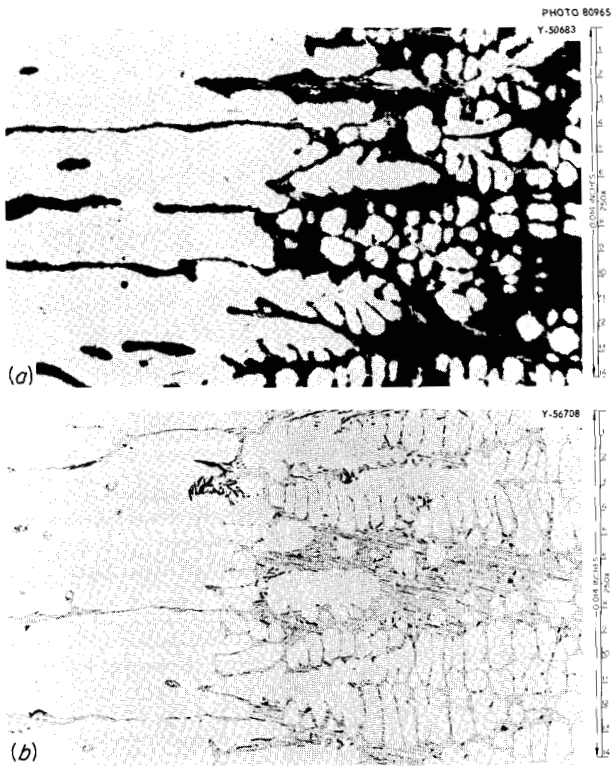

Fig. 32.3. Effect of Air Etching and Passivating with Nitric Acid on a Thorium Dicarbide Specimen (9.98% C) Containing Excess Graphite. (*a*) As air etched. (*b*) As passivated by immersing 1 min in equal parts of concd HNO_3 and water. The thorium dicarbide–graphite eutectic was retained in the passivated specimen but not in the air-etched specimen.

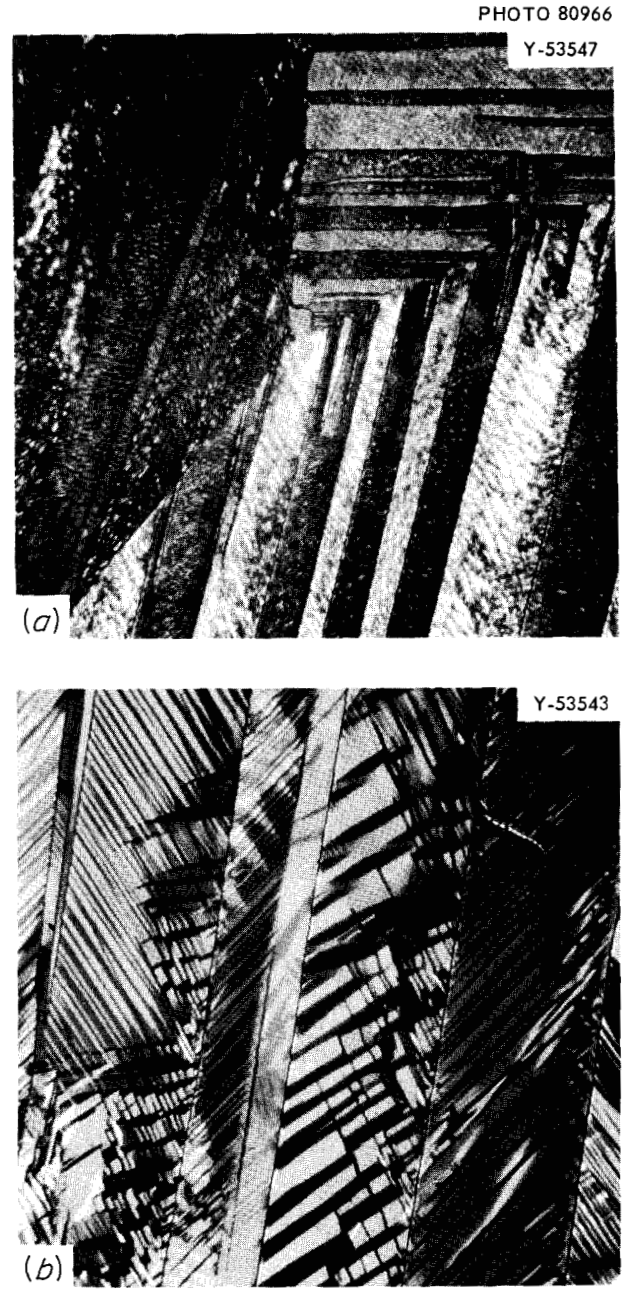

Fig. 32.4. Comparison of the Polarized-Light Microstructures of (*a*) a Thorium Dicarbide Specimen (8.91% C) Containing a Slight Amount of Monocarbide Precipitate and (*b*) a Single-Phase Thorium Dicarbide Specimen (9.23% C). Both specimens were passivated by immersing 1 min in equal parts of concd HNO_3 and water. 1000×.

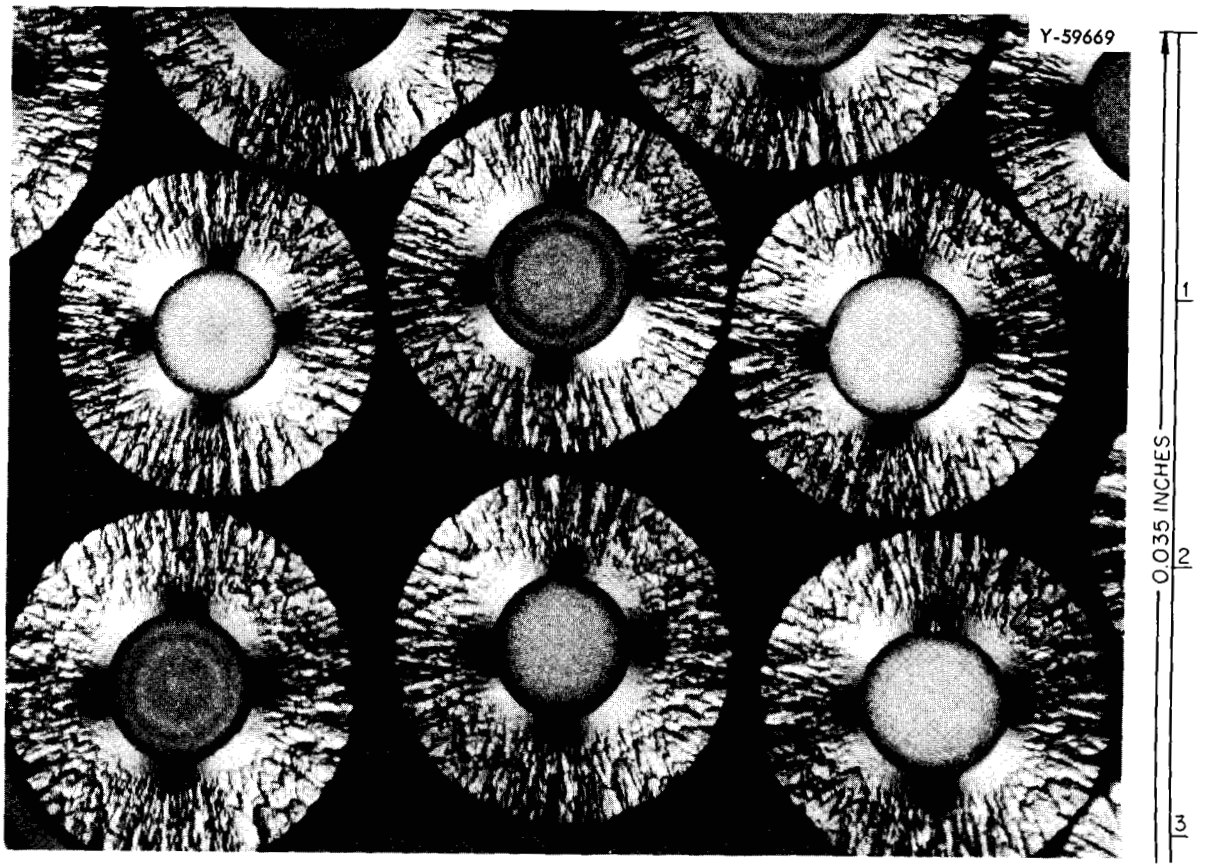

Fig. 32.5. Pyrolytic-Carbon-Coated Thoria.

FRANCIS F. LUCAS AWARD

B. C. Leslie R. J. Gray

The Francis F. Lucas Award and Grand Prize for excellence in metallography was received at the 1964 American Society for Metals Metallographic Exhibit. The color photomicrograph, Fig. 32.5, was made of pyrolytic-carbon-coated thoria spheres. The ThO_2 core particles were prepared by the sol-gel process in the Chemical Technology Division and the pyrolytic carbon coating was deposited at 1400°C by R. L. Beatty in the Ceramics Laboratory.

This award was received previously by the Metallography Group in 1953 and 1958.

POLARIZED-LIGHT MICROSCOPY OF PYROLYTIC CARBON DEPOSITS

R. J. Gray J. V. Cathcart[10]

Polarized-light microscopy has become an extremely powerful tool in the examination of pyrolytic-carbon-coated fuel particles. An unusual optical feature seen in polarized light – the Maltese cross – was explained in terms of the fiber-like texture of the pyrolytic carbon deposits.[11]

[10]Reactions at Metal Surfaces Group.

[11]R. J. Gray and J. V. Cathcart, "Polarized Light Microscopy of Pyrolytic Carbon Deposits," submitted to *Journal of Nuclear Materials*.

IDENTIFICATION OF CARBIDES, NITRIDES, AND OXIDES OF NIOBIUM AND NIOBIUM ALLOYS BY ANODIC STAINING

R. S. Crouse

A method was developed[12] for the identification of some impurity phases in niobium alloys. The procedure is based on the principle that an anodic oxide film formed on niobium produces interference colors. The color is characteristic of the anodic oxide thickness, which in turn depends upon the composition of the substrate. These color differences can be used to identify carbides, nitrides, and oxides.

Using specimens containing known phases, a technique was developed to identify these phases in unknown specimens. Dilute solutions of organic acids were found to be the most satisfactory electrolytes for anodization, although other electrolytes can be used. Clear colors can be produced and good control is possible with individual solutions of lactic, citric, and oxalic acids or mixtures of these.

[12]R. S. Crouse, *Identification of Carbides, Nitrides, and Oxides of Niobium and Niobium Alloys by Anodic Staining*, ORNL-3821 (July 1965).

EXPERIENCE WITH COLOR IN METALLOGRAPHY

R. S. Crouse R. J. Gray

Color reproductions often are a necessity in metallography when staining or anodizing techniques are used to reveal various components in the microstructure. Advancements in color processing techniques have allowed the metallographer to produce color transparancies and prints in his laboratory. Our experiences in the use of Polacolor, Ektachrome, Ektacolor, and the Rapid Color Print Processor have been reported.[13]

[13]R. S. Crouse and R. J. Gray, *Experience with Color in Metallography*, paper presented at the 19th AEC Metallography Group Meeting, April 20–22, 1965 at Oak Ridge National Laboratory (proceedings to be published as ORNL-TM-1161).

ACCELERATED EPOXY MOUNTING USING A RADIO-FREQUENCY FURNACE[14]

R. S. Crouse

By using a radio-frequency furnace in conjunction with a drying oven, we can mount a metallographic specimen in epoxy resin in 20 min. The usual technique requires 3 to 6 hr. The rapid heating promotes both deaeration and impregnation.

[14]R. S. Crouse, paper presented at the 19th AEC Metallography Group Meeting, April 20–22, 1965 at Oak Ridge National Laboratory (proceedings to be published as ORNL-TM-1161).

33. SNAP-8 Corrosion Studies

A. Taboada

The SNAP-8 Corrosion Program is a joint effort between the Metals and Ceramics Division and the Reactor Division to provide a support program for the SNAP-8 electrical generating system. The primary objectives are (1) to evaluate the compatibility of the proposed structural materials with the proposed reactor coolant, eutectic NaK containing hydrogen, and (2) to provide information on the behavior, control, and disposition of the hydrogen present in the primary coolant.

The SNAP-8 system[1] is one of the *Systems for Nuclear Auxiliary Power* being investigated by NASA and the AEC for use in future space vehicles. The primary system incorporates four different structural alloys and a reactor cooled with NaK, fueled with zirconium hydride containing ^{235}U, and reflected with beryllium. The reactor operates with surface temperatures in the range of 590 to 775°C and is designed to supply 35 kw electricity through a boiling-mercury Rankine power-conversion system. All systems are designed for 10,000 hr of unattended operation.

Because the SNAP-8 reactor system represents a relatively complex corrosion circuit, any definitive corrosion study must be based on a relatively complex loop system in which engineering parameters can be adequately reproduced. To reproduce such parameters, a series of forced-flow corrosion loops were operated. These and further information regarding the overall program are described in SNAP-8 Progress Reports.[2–8]

COMPATIBILITY STUDIES OF MATERIALS IN SNAP-8 PRIMARY SYSTEM

B. Fleischer A. Taboada

A series of forced-flow corrosion loop tests was performed to study materials compatibility problems associated with the primary system of the SNAP-8 power package. The structural materials involved in the system are chromized Hastelloy N, types 347 and 316 stainless steel, Hastelloy C, and Croloy 9M. Eutectic NaK (78% K) is the heat transfer medium. The test plan was formulated to enable an evaluation of the effect of oxygen, hydrogen, hot-leg temperature, and time on the compatibility of the above materials. In simulating the SNAP-8 system, we emphasized maintaining NaK velocities and construction material surface area ratios while reducing the mass flow to 2% of that existing in the actual system. Further information and details are reported elsewhere.[2–8]

The information gathered from this program is summarized in Table 33.1. It is apparent from these results that hydrogen did not deleteriously affect corrosion of any of the materials. Increasing oxygen from less than 30 ppm to approximately 80 ppm, however, increased the corrosion rate of the iron-base alloys, type 347 stainless steel and Croloy 9M, but it did not significantly affect the corrosion rate of the nickel-base alloy, Hastelloy N. Corrosion was approximately linear with time for Hastelloy N but somewhat less than linear for type 347 stainless steel. Increasing the hot-leg

[1] *Systems for Nuclear Auxiliary Power*, TID-20079.

[2] H. W. Savage *et al.*, *SNAP-8 Corrosion Program Quart. Progr. Rept. Aug. 31, 1963*, ORNL-3538.

[3] H. W. Savage *et al.*, *SNAP-8 Corrosion Program Quart. Progr. Rept. Nov. 30, 1963*, ORNL-3604.

[4] H. W. Savage *et al.*, *SNAP-8 Corrosion Program Quart. Progr. Rept. Feb. 29, 1964*, ORNL-3618.

[5] H. W. Savage *et al.*, *SNAP-8 Corrosion Program Quart. Progr. Rept. May 31, 1964*, ORNL-3671.

[6] H. W. Savage *et al.*, *SNAP-8 Corrosion Program Quart. Progr. Rept. Aug. 31, 1964*, ORNL-3730.

[7] H. W. Savage *et al.*, *SNAP-8 Corrosion Program Quart. Progr. Rept. Nov. 30, 1964*, ORNL-3784.

[8] H. W. Savage *et al.*, *SNAP-8 Corrosion Program Quart. Progr. Rept. Feb. 28, 1965*, ORNL-3823.

Table 33.1. Effect of Temperature, Time, Presence of Hydrogen, and Oxygen Content on Corrosion of Materials in SNAP-8 Forced-Flow NaK Corrosion Loops

Temperature (°F)	Time (hr)	Hydrogen Present	Oxygen Content (ppm)	Corrosion (mg/cm^2)[a]		
				Chromized Hastelloy N	347 SS	Croloy 9M
1300	2000	No	<30	−3	0.8	+0.1
1400	2000	No	<30	−8	−1	+0.3
1400	2000	No	~80	−8	−3	−1.5
1400	5100	No	<30	−20	−2	−0.3
1300	2000	Yes	<30	−3	0.8	0

[a]23 $mg/cm^2 \cong$ 1 mil of uniform corrosion. Negative values represent weight losses.

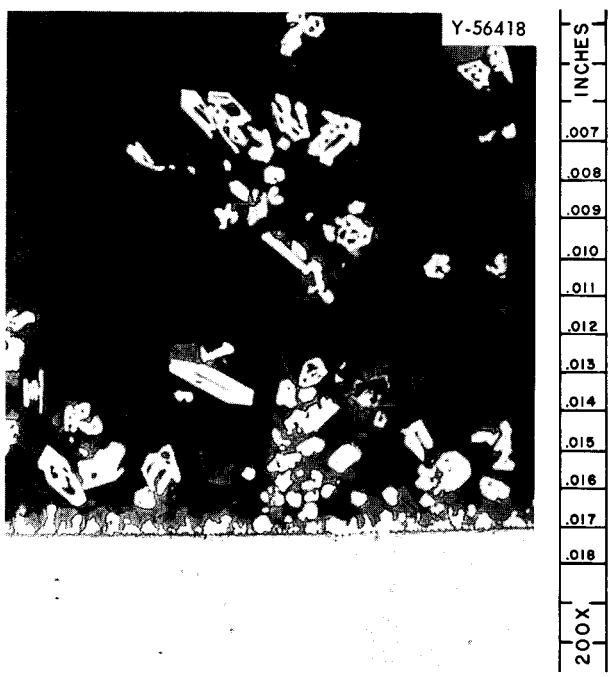

Fig. 33.1. Complex Oxide (Light Gray Material) Mass-Transfer Product Adhering to Metal Surfaces in Deposition Region of High-Oxygen Loop. As polished.

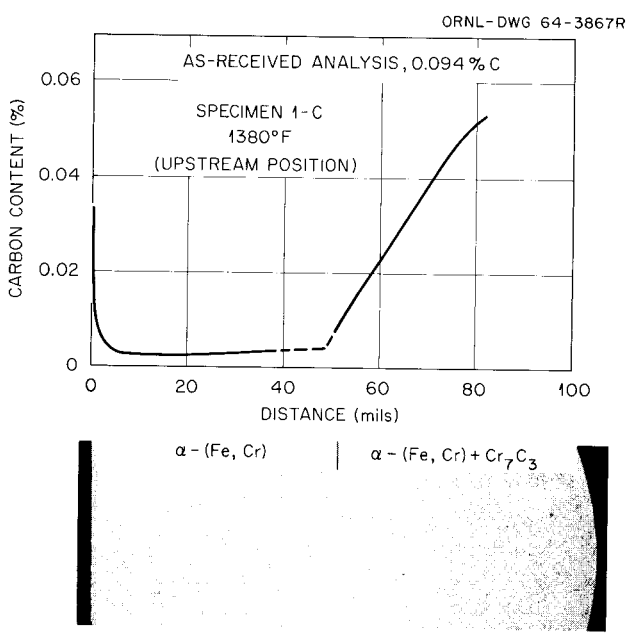

Fig. 33.2. Carbon Profile Across Wall of Croloy 9M Piping.

temperature from 1300 to 1400°F had a significant effect on corrosion of Hastelloy N but only a slight effect on the corrosion of type 347 stainless steel. The slight weight gains shown for Croloy 9M are the result of nickel pickup by dissimilar-metal mass transfer.

Analysis of corrosion mass-transfer products found in the high-oxygen loops revealed the presence of a nonmagnetic complex oxide, shown in Fig. 33.1 and identified as sodium chromite, $NaCrO_2$, by a combination of x-ray diffraction, electron microprobe analysis, and wet chemical analysis. Electron microprobe results also showed that chromium had been selectively leached from all the alloys. The migration of iron was greater than that of nickel in the high-oxygen loops, in-

creasing both the nickel content and the nickel-to-iron ratio of the stainless steels.

Extensive carbon migration was noted in both the 1300 and 1400°F loops. Carbon was removed from the hot portions of the Croloy 9M section, decarburizing it to less than 0.002% C. All other materials were carburized. In the 1400°F loops, the Croloy 9M at the cold end of the heat exchanger was also carburized. Determination of the carbon concentration profile across the wall of decarburized piping (see Fig. 33.2) showed a concentration gradient in the two-phase region [α-(Fe,Cr) + Cr_7C_3], indicating that carbon migration in this alloy under loop conditions is controlled by both the decomposition rate of Cr_7C_3 and the diffusion of carbon.

34. SNAP-50 Corrosion Studies

A. Taboada

We started a corrosion test program[1] using forced-flow loops in support of the SNAP-50 (Systems for Nuclear Auxiliary Power) space-power system. The program is designed to study the nature and extent of corrosion and dissimilar-metal interactions in two of the proposed heat-rejection circuits and thereby assist in determining a suitable design.

The first of the proposed heat-rejection circuits being evaluated consists of four independent radiator loops. Each loop contains the shell side of a potassium condenser, a multitube radiator segment, a pump, an accumulator, and connecting piping. These loops are fabricated entirely of type 316 stainless steel except for the condenser, which is Nb–1% Zr alloy. The coolant fluid is sodium-potassium eutectic (NaK-78).

Our basic objective is to evaluate the soundness of the metallurgical design of the proposed radiator circuit by studying materials compatibility in test loops simulating this circuit. To accomplish this the experimental program has been designed to reflect accurately the expected system parameters and operating conditions. In addition to the lifetime, the system parameters that are considered of primary importance are temperature, material, working-fluid composition and purity, circuit time, surface-area-to-volume ratios, heat flux, fluid velocity, and Reynolds number. We could not duplicate all these parameters concurrently in a reduced-scale mockup. When necessary to depart from the true value of a parameter, we made the test conditions more severe than those expected in the actual system.

A test loop, shown in Fig. 34.1, has been built and operated through approximately 3000 hr of a 6000-hr test. The loop contains a heated section, shown in Fig. 34.2, where the NaK is in contact with Nb–1% Zr alloy, simulating the situation in the SNAP-50 potassium condenser. The remainder of the loop is type 316 stainless steel. The dissimilar metals are attached by extruded joints. The system is operated with a heater outlet temperature of 1257°F and a temperature difference of approximately 175°F.

Metallurgical specimens have been placed in various locations throughout the loop. Some of these specimens in the heated section are removable to provide interim information on the corrosion and mass transfer occurring during loop operation. The remainder are permanently installed for examination upon completion of the test.

Specimens were removed from the loop for examination after approximately 2000 hr of exposure to flowing NaK. These included Nb–1% Zr alloy specimens from the heated part of the loop that were exposed to temperatures ranging from 1080 to 1257°F. Type 316 stainless steel specimens also were removed from the heater inlet (1080°F) and heater outlet (1257°F).

The specimens were weighed, chemically analyzed, and metallographically evaluated. Small quantities of carbon and nitrogen transferred to the Nb–1% Zr alloy from the stainless steel, according to both chemical analysis and metallography. No significant weight changes were observed in the specimens. Metallographic examination revealed a thin (about 0.0001-in.) layer to be present on the surface of all Nb–1% Zr specimens. The appearance of the stainless steel surfaces did not change. A metallographic section of a Nb–1% Zr specimen with a typical layer is presented in Fig. 34.3. This layer was identified by x-ray diffraction techniques to be a mixture of niobium carbides and nitrides.

[1]ORNL-3772 (classified).

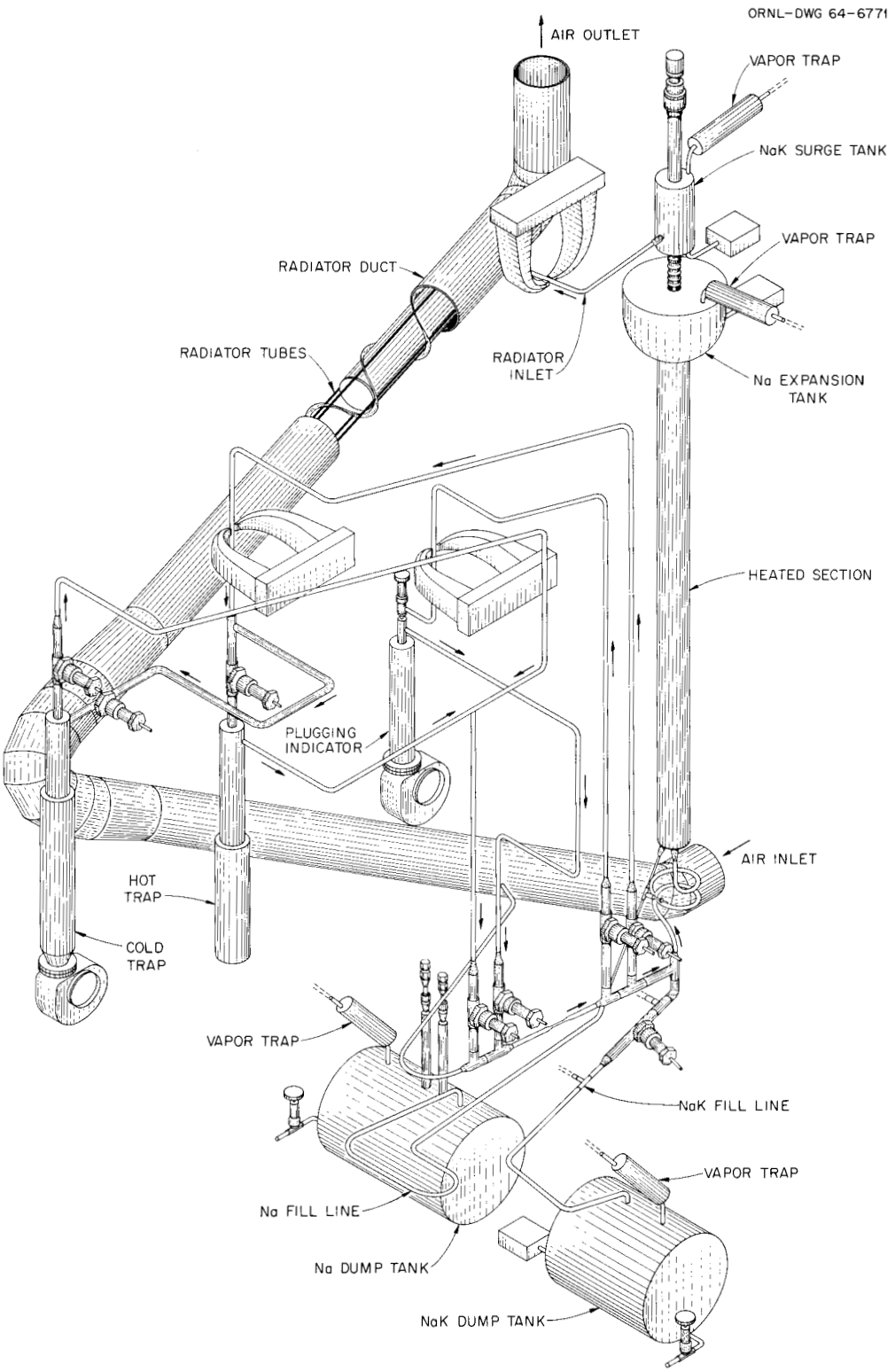

Fig. 34.1. SNAP-50 NaK Radiator Test Loop.

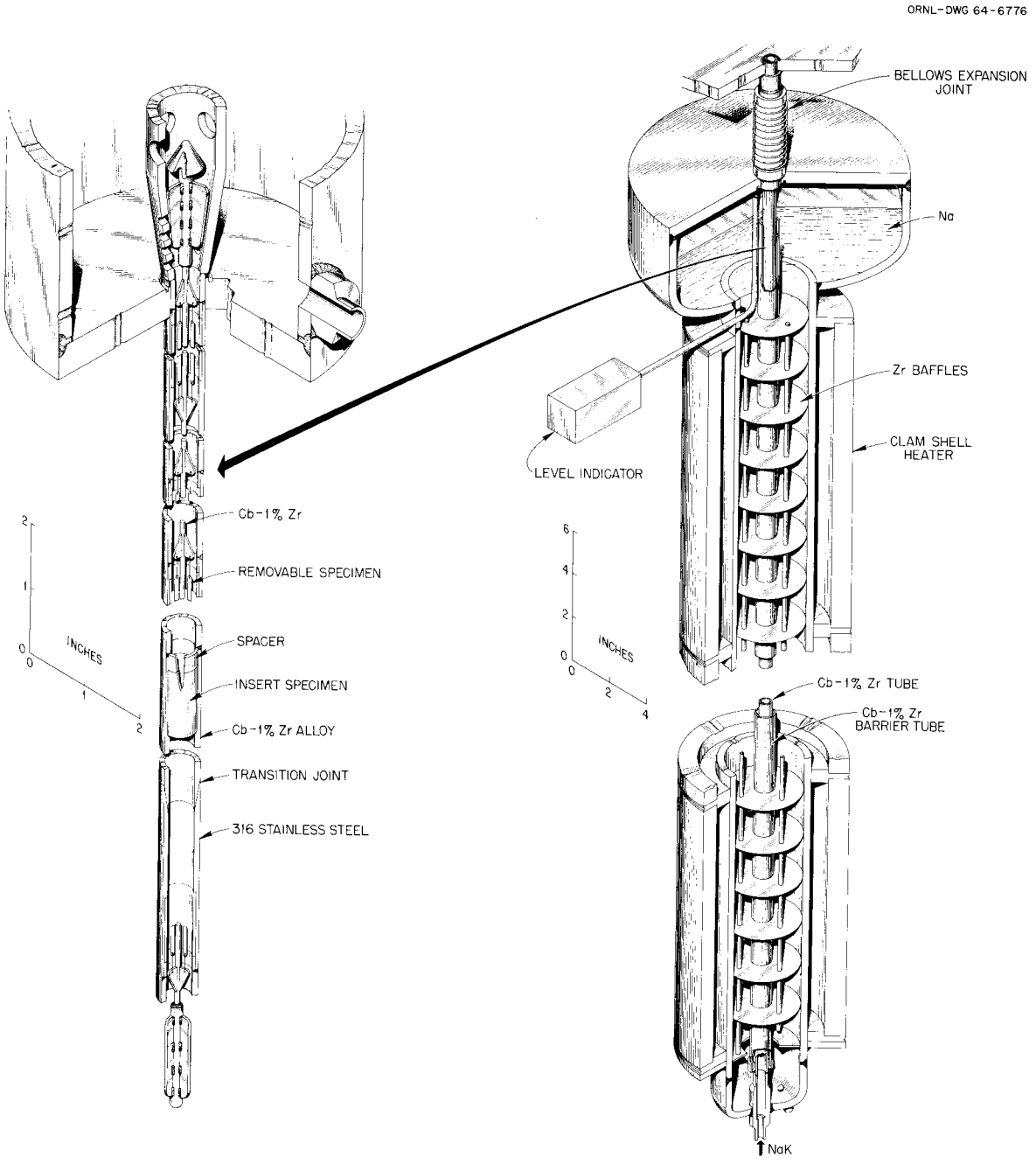

Fig. 34.2. Heated Section Assembly and Details.

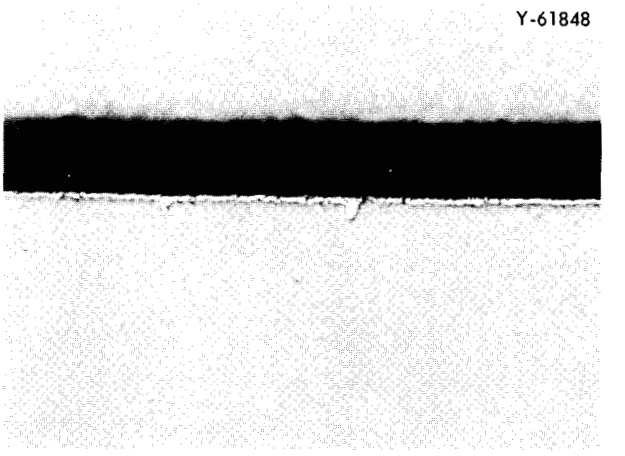

Fig. 34.3. Typical Surface of Nb–1% Zr Alloy Specimen Removed from SNAP-50 Test-Loop Hot Leg After 2000 hr Operation. Layer of niobium carbides and nitrides is evident. 750×.

Papers and Publications

Papers and Oral Presentations

National Physical Laboratory Conference on Thermal Conductivity, Teddington, England, July 15–17, 1964

J. W. Hendricks and D. L. McElroy,* "High-Temperature High-Vacuum Thermocouple Drift Tests"

T. G. Kollie, D. L. McElroy,* R. S. Graves, and W. Fulkerson, "A Thermal Comparator Apparatus for Thermal Conductivity Measurements from 50 to 400°C"

J. P. Moore, T. G. Godfrey, and D. L. McElroy,* "Thermal Properties of Grade CGB Graphite"

J. P. Moore, W. Fulkerson, and D. L. McElroy,* "Comparison of the Thermal Conductivity, Electrical Resistivity, and Seebeck Coefficient of a High-Purity Iron and Armco Iron to 1000°C"

T. G. Godfrey, W. Fulkerson, T. G. Kollie, J. P. Moore, and D. L. McElroy,* "Thermal Conductivity of Uranium Dioxide and Armco Iron by an Improved Radial Heat Flow Technique"

Atomic Energy Commission Nondestructive Testing Meeting, Argonne, Ill., July 22–24, 1964

R. W. McClung, "Discussion of Work in Progress in the Nondestructive Testing Group, Metals and Ceramics Division, Oak Ridge National Laboratory"

American Institute of Mining, Metallurgical, and Petroleum Engineers, Conference on Compounds of Interest in Nuclear Reactor Technology, Boulder, Colo., Aug. 3–5, 1964

Compiled by E. S. Bomar and R. J. Gray, "Thorium-Uranium Carbides for Coated-Particle Graphite Fuels" (presented by W. O. Harms)

R. L. Heestand,* J. I. Federer, and C. F. Leitten, Jr., "Thermochemical Preparation and Properties of Carbides for Nuclear Application"

T. G. Kollie,* D. L. McElroy, R. S. Graves, and W. Fulkerson, "A Thermal Comparator Apparatus for Thermal Conductivity Measurements from 50 to 400°C"

R. A. Potter, R. E. McDonald, and C. F. Leitten, Jr.,* "Preparation and Properties of Lanthanon Molybdates and Tungstenates"

Meeting of Refractory Composites Working Group, Worcester, Mass., Aug. 18–20, 1964

C. F. Leitten, Jr.,* and R. L. Heestand, "Summary of Thermochemical Deposition Studies at Oak Ridge National Laboratory"

United Nations International Conference on the Peaceful Uses of Atomic Energy, 3rd, Geneva, Switzerland, Aug. 31–Sept. 9, 1964

W. P. Chernock,* R. M. Mayfield, and J. R. Weir, Jr., "Cladding Materials for Nuclear Fuels"

D. H. Gurinsky,* J. R. Weeks, C. J. Klamut, L. Rosenblum, and J. H. DeVan, "Corrosion in Liquid Metal Systems"

A. N. Holden,* C. F. Leitten, Jr., and B. Weidenbaum, "Control Rod Materials"

---

*Speaker

J. H. Kittel,* T. K. Bierlein, B. R. Hayward, W. C. Thurber, "Irradiation Behavior of Metallic Fuels"

D. E. Ferguson,* O. C. Dean, and D. A. Douglas, "The Sol-Gel Process for the Remote Preparation and Fabrication of Recycle Fuels"

International Conference on Diffusion in Body-Centered Cubic Materials, Gatlinburg, Tenn., Sept. 16–18, 1964

T. S. Lundy,* J. I. Federer, R. E. Pawel, and F. R. Winslow, "A Summary of ORNL Work on Diffusion in β-Zr, V, Nb, and Ta"

J. F. Murdock, "Diffusion of Titanium-44 and Vanadium-48 in Titanium"

American Ceramic Society, Symposium on Ceramic-to-Metal Seals, Philadelphia, Pa., Sept. 16–18, 1964

C. W. Fox* and G. M. Slaughter, "Ceramic-Brazing Development at Oak Ridge National Laboratory"

Comité International de Thermodynamique et de Cinétique Electrochimiques, London, England, Sept. 21–26, 1964

T. R. Griffiths* and G. P. Smith, "The Identification of Tetrahedral Tetrahalonickel(II) Ions in Molten Organic Halide Salt Melts"

American Vacuum Society Annual Symposium, 11th, Chicago, Ill., Sept. 30–Oct. 2, 1964

R. E. Clausing, "Release of Gases from Surfaces by Energetic Electrons"

American Welding Society, National Fall Meeting, San Francisco, Calif., Oct. 5–8, 1964

R. G. Donnelly* and G. M. Slaughter, "Weldability Evaluation of Selected, Advanced Refractory Alloys"

R. G. Gilliland* and G. M. Slaughter, "The Development of Refractory Metal Brazing Alloys for Very High Temperature Service"

National Academy of Sciences – National Research Council, Conference on Electrical Insulation, Cleveland, Ohio, Oct. 11–14, 1964

J. V. Cathcart, "Parameter Measurements in Thin Dielectric Films"

Electrochemical Society Meeting, Washington, D.C., Oct. 11–15, 1964

J. C. Banter, "Determination of the Refractive Index and Thickness of Oxide Films on Anodized Zirconium from Transmission Interference Measurements"

A. P. Litman* and J. W. Prados, "The Partitioning of Oxygen Between Zirconium and Liquid Potassium"

The British Ceramic Society, Meeting on Fabrication Science, Brighton, England, Oct. 12–14, 1964

C. S. Morgan,* C. J. McHargue, and C. S. Yust, "Material Transport in Sintering"

Thermal Conductivity Conference, San Francisco, Calif., Oct. 13–16, 1964

Compiled by J. W. Hendricks and D. L. McElroy, "High-Temperature High-Vacuum Thermocouple Drift Tests" (presented by W. Fulkerson)

J. P. Moore,* W. Fulkerson, D. L. McElroy, and T. G. Kollie, "Comparison of the Thermal Conductivity, Electrical Resistivity, and Seebeck Coefficients of a High-Purity Iron and Armco Iron to 1000°C"

J. P. Moore,* T. G. Godfrey, D. L. McElroy, N. N. Engel, and W. P. Murray, "Progress Report, Physical Properties Group"

---

*Speaker

American Institute of Mining, Metallurgical, and Petroleum Engineers, Fall Meeting, Philadelphia, Pa., Oct. 18–22, 1964

R. J. Arsenault, "Low-Temperature Deformation of BCC Metals and Alloys"

M. L. Picklesimer* and P. L. Rittenhouse, "Preferred Orientation and Plastic Anisotropy in Zircaloy-2"

R. O. Williams, "Rolling Texture in Copper"

Dragon-Harwell Basic Research Symposium, Harwell, England, Oct. 19–21, 1964

W. O. Harms, "Review of ORNL Materials Development for Graphite-Base, High-Temperature Gas-Cooled Reactors"

Society of Nondestructive Testing, 24th National Fall Meeting, Philadelphia, Pa., Oct. 19–23, 1964

K. V. Cook and R. W. McClung,* "An Ultrasonic Technique for the Evaluation of Heat Exchanger Brazed Joints"

B. E. Foster,* S. D. Snyder, and R. W. McClung, "A Continuous X-Ray Scanning Technique for Determining Minute Inhomogeneities in Solids"

R. W. McClung, "Radiography in the Presence of Background Radiation"

U.S.-Japan Exchange Meeting on Ceramic Nuclear Fuels, Richland, Wash., Oct. 27–30, 1964

W. O. Harms and J. L. Scott,* "Oak Ridge National Laboratory Graphite Fuel Element Development Program for High-Temperature Gas-Cooled Reactors"

High-Temperature Fuels Committee Meeting, 19th, Los Angeles, Calif., Nov. 16–18, 1964

Compiled by Staff Members of the Metals and Ceramics, Reactor Chemistry, and Reactor Divisions, "High-Temperature Fuel Work at the Oak Ridge National Laboratory" (presented by J. L. Scott)

Atomic Energy Commission Coated Particle Working Group Meeting, 8th, La Jolla, Calif., Nov. 17–18, 1964

Compiled by W. O. Harms, "Coated-Particle Fuel Development at Oak Ridge National Laboratory for Period May 15 to November 15, 1964" (presented by W. O. Harms and J. H. Coobs)

American Nuclear Society, Fall Meeting, San Francisco, Calif., Nov. 30–Dec. 3, 1964

J. E. Van Cleve, Jr.,* and A. L. Lotts, "Operating Experience in a Semiremote Facility for Fabrication of Fuel Rods Containing $(^{233}U,Th)O_2$"

R. L. Pilloton* and A. L. Lotts, "Fluidized-Bed Characteristics in the Coating of Nuclear Fuel Particles"

R. L. Beatty,* J. L. Cook, and F. L. Carlsen, Jr., "Techniques for Deposition and Systematic Study of Properties of Pyrolytic Carbon on Ceramic Fuel Particles"

A. Taboada, W. H. Cook,* and P. Patriarca, "Construction Materials for Molten Salt Reactors"

J. I. Federer* and C. F. Leitten, Jr., "Vapor Deposition of Tungsten-Rhenium Alloys"

R. L. Heestand* and C. F. Leitten, Jr., "Thermochemical Reduction of Uranium Halides for the Direct Fabrication of Ceramic Fuels"

W. R. Martin* and J. R. Weir, "Influence of Preirradiation Heat Treatment on the Postirradiation Ductility of Stainless Steels"

J. L. Cook* and R. L. Hamner, "Chlorination as a Means of Removing Uranium and Thorium from Fueled-Graphite Materials"

---

*Speaker

M. F. Osborne,* J. G. Morgan, and E. L. Long, "Effects of Extreme Operating Conditions on Prototype EGCR Fuel"

D. R. Cuneo,* E. L. Long, Jr., and H. E. Robertson, "Hot Cell Techniques for the Evaluation of Fueled Graphite Spheres"

American Institute of Mining, Metallurgical, and Petroleum Engineers, Annual Meeting, Chicago, Ill., Feb. 14–18, 1965

T. K. Roche, "Aging of Columbium Alloy D-43"

C. J. Sparks* and B. Borie, "Methods of Analysis for Local Order"

B. Borie* and C. J. Sparks, "Analysis of Thin Films"

Atomic Energy Commission High-Temperature Thermometry Meeting, Washington, D.C., Feb. 24–26, 1965

Compiled by N. H. Briggs* and D. L. McElroy,* "High-Temperature Thermometry Work at the Oak Ridge National Laboratory"

Atomic Energy Commission Contractors Meeting on Application of X-Ray Diffraction in the Atomic Energy Field, Richland, Wash., Feb. 25–26, 1965

P. L. Rittenhouse* and M. L. Picklesimer, "Comparison of Pole Figure Data Obtained by X-Ray Diffraction and Microhardness Measurements on Zircaloy-2"

Symposium on Thermophysical Properties, Lafayette, Ind., Mar. 22–25, 1965

W. Fulkerson* and D. L. McElroy, "Discussion of 'Thermal Conductivity of Pure and Alloyed Aluminum. I. Solid Aluminum as a Reference Material' by R. W. Powell, R. P. Tye, and M. J. Woodman" and "'II. Molten Aluminum and an Aluminum Alloy' by R. W. Powell, R. P. Tye, and S. C. Metcalf"

D. L. McElroy* and W. Fulkerson, "Discussion of 'Correlation and Prediction of Thermal Conductivity of Metals Through Application of the Principle of Corresponding States' by A. Cezairliyan and Y. S. Touloukian"

American Physical Society Meeting, Kansas City, Mo., Mar. 24–27, 1965

R. J. Arsenault* and G. Czjzek, "The Energy of Formation of a Double Kink"

T. J. Koppenaal* and R. J. Arsenault, "The Activation Energy for Plastic Deformation in Neutron Irradiated Copper Single Crystals"

British Ceramic Society Meeting, Birmingham, England, Apr. 5–7, 1965

C. S. Morgan* and L. L. Hall, "Some Observations on the Creep of Thoria and Thoria-Calcia Solid Solutions"

Conference on Industrial Carbon and Graphite, 2nd, London, England, Apr. 7–9, 1965

Compiled by C. O. Smith and J. M. Robbins, "Impact Resistance of Fueled Graphite Spheres for Pebble Bed Reactor Applications" (presented by C. R. Kennedy)

C. R. Kennedy, "Irradiation Creep of Graphite"

Libby-Cockcroft Meeting on Graphite Physics, Harwell, England, Apr. 12–13, 1965

W. H. Cook* and A. Taboada, "Properties of a Low-Permeation Graphite"

C. R. Kennedy, "Irradiation Creep of Graphite"

---

*Speaker

Meeting of Refractory Composites Working Group, Atlanta, Ga., Apr. 12–14, 1965

R. L. Heestand,* J. I. Federer, F. H. Patterson, C. F. Leitten, Jr., "Summary of Thermochemical Deposition Studies at Oak Ridge National Laboratory, August 1964–March 1965"

Atomic Energy Commission Metallographic Group Meeting, 19th, Oak Ridge, Tenn., Apr. 20–22, 1965

M. L. Picklesimer* and P. L. Rittenhouse, "Hydride and Basal Pole Figures in Zircaloy-2 by Quantitative Metallography"

J. C. Wilson, "Electrical Discharge Machining in the Metallurgical Laboratory"

R. S. Crouse* and R. J. Gray,* "Experience with Color in Metallography"

T. M. Kegley, Jr.,* and B. C. Leslie, "Metallographic Preparation of Thorium Carbides"

R. S. Crouse, "Accelerated Epoxy Mounting Using a Radio Frequency Furnace"

E. L. Long, Jr.,* and R. J. Gray, "Radiation Metallography in the High Radiation Level Examination Laboratory"

AEC-NASA Liquid-Metals Corrosion Meeting, Gatlinburg, Tenn., Apr. 21–22, 1965, Oak Ridge, Tenn., Apr. 23, 1965

A. P. Litman, "Interactions in the Niobium-Oxygen-Potassium System"

K. V. Cook* and R. W. McClung, "Nondestructive Testing of Small-Diameter Tubing"

B. Fleischer,* A. Taboada, W. R. Huntley, H. W. Savage, and R. E. MacPherson, "Compatibility Studies of Materials in SNAP-8 Primary System"

J. R. DiStefano* and D. H. Jansen, "Refractory Metal–Boiling Potassium Compatibility Studies"

J. H. DeVan, "Mass Transfer in Refractory Metal–Conventional Alloys Systems"

C. E. Sessions, "Corrosion of Advanced Refractory Alloys in Lithium"

American Nuclear Society National Topical Meeting on Fast Reactor Technology, Detroit, Mich., Apr. 26–28, 1965

S. H. Bush,* J. Moteff, and J. R. Weir, "Radiation Damage in Fast Reactor Components"

American Welding Society, 46th Annual Meeting, Chicago, Ill., Apr. 26–30, 1965

E. A. Franco-Ferreira* and G. M. Slaughter, "The Welding of Refractory Metal Components for Liquid Metal Service"

G. M. Slaughter,* E. A. Franco-Ferreira, and P. Patriarca, "Welding and Brazing of High-Temperature Radiators and Heat Exchangers"

W. C. Collins, D. G. Scott,* J. W. Tackett, and P. W. Turner, "Welding Control Rods for the High-Flux Isotope Reactor"

American Ceramic Society, Philadelphia, Pa., May 1–6, 1965

J. Truitt,* J. O. Stiegler, and R. B. Evans III, "Actinide Migration in Pyrocarbons as Influenced by Actinide and Defect Concentrations"

A. T. Chapman* and G. W. Clark, "The Growth of UO_2 Single Crystals Using the Floating-Zone Technique"

L. A. Harris,* R. A. Potter, and A. T. Chapman, "An X-Ray Diffraction Investigation of a Phase Transformation in Europium Molybdate ($Eu_{5+x}MoO_{10.5+y}$)"

C. S. Yust* and L. E. Poteat, "Creep of Polycrystalline Thorium Dioxide"

---

*Speaker

Electrochemical Society Annual Spring Meeting, San Francisco, Calif., May 9–14, 1965

G. P. Smith,* T. R. Griffiths, and Samuel von Winbush, "Spectrophotometric Study of Tetrahalonickelate(II) Complex Ions Formed in Molten Organic Salts"

International Atomic Energy Agency Symposium on Non-Destructive Testing in Nuclear Technology, Bucharest, Romania, May 17–21, 1965

D. A. Douglas, Jr., R. W. McClung,* B. E. Foster, and C. V. Dodd, "Nondestructive Testing Techniques for Research and Process Control"

High-Temperature Fuels Committee Meeting, 20th, Cincinnati, Ohio, May 18–20, 1965

Compiled by Staff Members of the Metals and Ceramics, Reactor Chemistry, and Reactor Divisions, "High-Temperature Fuel Work at the Oak Ridge National Laboratory" (presented by J. L. Scott)

Atomic Energy Commission Coated Particle Working Group Meeting, 9th, Oak Ridge, Tenn., May 25–26, 1965

Compiled by W. O. Harms and J. H. Coobs, "Coated-Particle Fuels Development at Oak Ridge National Laboratory for Period November 15, 1964 to May 15, 1965" (presented by contributors)

Atomic Energy Commission Annual Corrosion Symposium, 14th, Aiken, S.C., May 26–28, 1965

G. M. Tolson* and A. Taboada, "Study of the Corrosion Effect of Liquid Lead in Thermal Convection Loops"

G. M. Tolson, N. C. Cole,* and C. W. Fox, "Corrosion Studies of Brazing Alloys in Boiling Potassium"

B. Fleischer,* A. Taboada, W. R. Huntley, H. W. Savage, and R. E. MacPherson, "Compatibility Studies of Materials in SNAP-8 Primary System"

D. H. Jansen* and J. R. DiStefano, "Refractory Metal–Boiling Potassium Compatibility Studies"

A. P. Litman, "The Effect of Oxygen on the Corrosion of Niobium by Liquid Potassium"

Euratom Symposium on Fuel Cycles of High-Temperature Gas-Cooled Reactors, Brussels, Belgium, June 10–11, 1965

A. L. Lotts, D. A. Douglas, Jr., and R. L. Pilloton, "Refabrication Technology and Costs for High-Temperature Gas-Cooled Reactor Fuels" (presented by a rapporteur)

W. O. Harms and D. B. Trauger, "Fabrication Variables, Performance, and Cost Considerations for HTGR Coated-Particle Fuels" (presented by a rapporteur)

International Powder Metallurgy Conference, New York City, N.Y., June 14–17, 1965

J. P. Hammond* and G. M. Adamson, Jr., "Activated Sintering of Uranium Monocarbide"

International Atomic Energy Agency Panel on Utilization of Thorium in Power Reactors, Vienna, Austria, June 14–18, 1965

A. L. Lotts* and D. A. Douglas, Jr., "Refabrication Technology for the Thorium-Uranium-233 Fuel Cycle"

A. R. Olsen, D. B. Trauger,* W. O. Harms, R. E. Adams, and D. A. Douglas, "Irradiation Behavior of Thorium-Uranium Alloys and Compounds"

Compiled by S. Peterson, R. E. Adams, and D. A. Douglas, Jr., "Properties of Thorium, Its Alloys, and Its Compounds" (presented by A. L. Lotts)

---

*Speaker

International Symposium on Working Methods in High Activity Hot Laboratories, Grenoble, France, June 14–18, 1965

R. W. McClung and D. A. Douglas, Jr.,* "Nondestructive Testing of Irradiated Materials in the United States"

Sodium Component Development Performance Meeting, Chicago, Ill., June 16, 1965

W. R. Martin* and J. R. Weir, "Irradiation Effects in Stainless Steels at High Temperatures"

Annual Conference on Vacuum Metallurgy, 8th, New York City, N.Y., June 21–23, 1965

D. T. Bourgette, "High-Temperature Chemical Stability of Refractory-Base Alloys in High Vacuum"

American Nuclear Society, Gatlinburg, Tenn., June 21–24, 1965

W. R. Martin* and J. R. Weir, "Irradiation Embrittlement of Stainless Steel at Very High Temperatures"

H. E. McCoy* and J. R. Weir, "Influence of Neutron Irradiation on the Tensile Properties of the Aluminum Alloy 6061"

C. Michelson,* J. L. Scott, and E. L. Long, Jr., "An Evaluation of UO_2 Irradiated at 1600 to 2400°C"

R. L. Pilloton and R. L. Hamner,* "A Method for Preparing Dense Spherical Particles of Thorium and Uranium Dicarbides"

R. L. Pilloton,* H. J. Flamm, and A. L. Lotts, "The Development of an Improved Coating Furnace for Nuclear Fuel Particles"

T. N. Washburn* and D. A. Douglas, "Controlling Factors in Determining Fabrication Costs of Metal Clad Oxide Fuel Elements"

J. W. Prados,* V. A. deCarlo, and J. L. Scott, "Thermal Conductivities of Fueled Graphite from AVR Fuel Element Irradiation Test Data"

F. R. McQuilkin, N. H. Briggs,* and E. L. Long, Jr., "Summary of Experience with High-Temperature Thermocouples Used in the ORNL-GCR Program Fuel Irradiation Experiments"

Biennial Conference on Carbon, 7th, Cleveland, Ohio, June 21–22, 1965

J. Y. Chang, E. E. Stansbury, and W. O. Harms,* "Effects of Deposition Conditions and Heat Treatment on the Properties of Pyrolytic Carbon"

W. H. Cook* and A. Taboada, "Properties of a Low-Permeation Graphite for Molten-Salt Nuclear Reactors"

C. O. Smith,* and J. M. Robbins, "Impact Resistance of Fueled Graphite Spheres for Pebble Bed Reactor Applications"

J. L. Cook, W. R. Laing, and R. L. Beatty,* "Determination of Density of Pyrolytic-Carbon Coatings on Nuclear Fuel Particles"

J. O. Stiegler, C. K. H. DuBose, and J. L. Cook,* "Electron Microscopy of Pyrolytic Carbon Deposits on Fuel Particles"

Conference on Small-Angle X-Ray Scattering, Syracuse, N.Y., June 24–26, 1965

R. W. Hendricks* and B. S. Borie, "A Note on the Determination of a Metastable Miscibility Gap from Integrated Small-Angle X-Ray Scattering Data"

---

*Speaker

Publications

Abraham, M., R. A. Weeks, G. W. Clark, and C. B. Finch, "Electron Spin Resonance of Rare-Earth Ions in Thorium Oxide: Yb^{3+} and Er^{3+}," *Phys. Rev.* **137**, A138 (1965).

Adams, R. E., and E. S. Bomar, Jr., *Carburization and Chemical Treatments for Recovery of Uranium from Stainless Steel Fuel Elements,* ORNL-2398 (November 1964). Available from CFSTI.

Adamson, G. M., Jr., and J. R. McWherter, *Specifications for High Flux Isotope Reactor Fuel Elements, HFIR-FE-1,* ORNL-TM-902 (August 1964).

Arsenault, R. J., "Effects of Strain Rate and Temperature on Yield Points," *Trans. Met. Soc. AIME* **230**(7), 1570–76 (1964).

Arsenault, R. J., and J. H Frye, Jr., "Effect of Prestrain and Alloying on the Temperature Dependence of Yielding," *Acta Met.* **12**(11), 1303–6 (1964).

Arsenault, R. J., and T. J. Koppenaal, "Thermally Activated Slip in Neutron Irradiated Copper Single Crystals," *Appl. Phys. Letters* **6**, 159 (1965).

Askill, J., *A Bibliography on Tracer Diffusion in Metals: Part I. Self Diffusion in Pure Metals,* ORNL-3795 (May 1965).

Banter, J. C., "Determination of the Refractive Index and Thickness of Oxide Films on Anodized Zirconium from Transmission Interference Measurements," *J. Electrochem. Soc.* **112**(4), 388–90 (1965).

Biermann, W., D. Heitkamp, and T. S. Lundy, "Thermal Diffusion of Antimony and Ruthenium in Silver," *Acta Met.* **13**(2), 71–78 (1965); ORNL-3710 (November 1964).

Bomar, E. S., and R. J. Gray, "Thorium-Uranium Carbides for Coated-Particle, Graphite Fuels," pp. 703–28 in *International Symposium on Compounds of Interest in Nuclear Reactor Technology* (ed. by J. T. Waber, P. Chiotti, and W. N. Miner), AIME Metallurgical Society, New York, 1964.

Borie, B., "Review of 'X-Ray Diffraction in Crystals, Imperfect Crystals, and Amorphous Bodies,' by A. Guinier," *J. Am. Chem. Soc.* **87**(1), 140 (1965).

Borie, B., and C. J. Sparks, Jr., "Special Methods for the Structural Investigation of Thin Films," pp. 45–58 in *Thin Films,* The American Society for Metals, Metals Park, Ohio, 1964.

Borie, B., and C. J. Sparks, Jr., "The Short-Range Structure of Copper–16 at. % Aluminum," *Acta Cryst.* **17**(7), 827–35 (1964).

Boston, C. R., and G. P. Smith, "Furnace for Molten Salt Measurements on the Cary Model 14-H Spectrophotometer Up to 1450°C," *Rev. Sci. Instr.* **36**(2), 206 (1965).

Bourgette, D. T., *Evaporation of Iron-, Nickel-, and Cobalt-Base Alloys at 760 to 980°C in High Vacuums,* ORNL-3677 (November 1964).

Burka, J. A., and J. P. Hammond, *Evaluation of Thorium-Base Alloys for High-Temperature Strength,* ORNL-3777 (April 1965). Available from CFSTI.

Carlsen, F. L., Jr., E. S. Bomar, and W. O. Harms, "Development of Fueled Graphite Containing Pyrolytic-Carbon-Coated Carbide Particles for Nonpurged, Gas-Cooled Reactor Systems," *Nucl. Sci. Eng.* **20**(2), 180–200 (1964).

Carlsen, F. L., Jr., *Effects of Pyrolytic-Graphite Structure on Diffusion of Thorium* (Thesis), ORNL-TM-1080 (June 1965). Available from CFSTI.

Cathcart, J. V., and G. F. Petersen, "Studies on Thin Oxide Films on Copper Crystals with an Ellipsometer," pp. 201–12 in *Ellipsometry in the Measurement of Surfaces and Thin Films, Symposium Proceedings, Washington, D.C., 1963* (ed. by E. Passaglia, R. R. Stromberg, and J. Kruger), National Bureau of Standards, U.S. Government Printing Office, Washington, D.C., 1964.

Cathcart, J. V., "Parameter Measurements in Thin Dielectric Films," pp. 63–66 in *Conference on Electrical Insulation, Natl. Acad. Sci. – Natl. Res. Council, Publ. 1238* (1965).

Cathcart, J. V., G. F. Petersen, and C. J. Sparks, Jr., "Lattice Disregistry in Very Thin Oxide Films on Copper," *Mem. Sci. Rev. Met.* **62**, 11–16 (1965).

Chang, J. Y., *Studies on Effects of Deposition Conditions and Heat Treatment on the Properties of Pyrolytic Carbon* (Thesis), ORNL-3764 (March 1965).

Chapman, A. T., and R. E. Meadows, "Volatility of $UO_{2\pm x}$ and Phase Relations in the System Uranium–Oxygen," *J. Am. Ceram. Soc.* **47**(12), 614–21 (1964).

Cook, K. V., and R. W. McClung, *Nondestructive Evaluation of T-111 and B-66 Alloy Tubing*, ORNL-TM-990 (February 1965). Available from CFSTI.

Cook, K. V., and R. W. McClung, *Feasibility of Ultrasonic Detection of Nonbond in ATR Fuel Plates*, ORNL-TM-888 (August 1964). Available from CFSTI.

Cook, K. V., and R. W. McClung, *An Ultrasonic Technique for the Evaluation of Heat Exchanger Brazed Joints*, ORNL-TM-947 (November 1964).

Crouse, R. S., "Replication of Microstructures Using Silicone Rubber and Epoxy Resin," pp. 60–68 and "A Portable Metallography Laboratory," pp. 129–38 in *Technical Papers of the Seventeenth Metallographic Group Meeting, May 21–23, 1963, Los Alamos Scientific Laboratory, Los Alamos, New Mexico*, NMI-4999 (1965).

Cuneo, D. R., E. L. Long, Jr., and H. E. Robertson, "Hot Cell Techniques for the Evaluation of Fueled Graphite Specimens," pp. 245–56 in *Proceedings of the 12th Conference on Remote Systems Technology*, American Nuclear Society, Hinsdale, Illinois, 1964.

Davis, W. W., and C. R. Kennedy, *Stress-Strain Measuring System for In-Reactor Use in High Neutron Flux*, ORNL-3747 (January 1965). Available from CFSTI.

DiStefano, J. R., and A. P. Litman, "The Effect of Impurities in Some Refractory Metal–Alkali Metal Systems," *Corrosion* **20**(12), 392t (1964).

Dodd, C. V., "Design and Construction of Eddy-Current Coolant-Channel Spacing Probes (1st part)," *Microtecnic (Lausanne)* **18**(5), 286 (1964).

Dodd, C. V., "Design and Construction of Eddy-Current Coolant-Channel Spacing Probes (end)," *Microtecnic (Lausanne)* **18**(6), 369 (1964).

Dodd, C. V., "Recent Eddy-Current Development at the Oak Ridge National Laboratory," pp. 304–8 in *Proceedings of the Fourth International Conference on Non-Destructive Testing*, Butterworths, London, 1964.

Donnelly, R. G., W. C. Thurber, and G. M. Slaughter, *Development of Fabrication Procedures for Core B Fuel Elements for the Enrico Fermi Fast Breeder Reactor*, ORNL-3475 (July 1964). Available from CFSTI.

Donnelly, R. G., *Weldability Evaluation of the Niobium Alloy C-129Y*, ORNL-TM-929 (September 1964). Available from CFSTI.

Donnelly, R. G., *Tube Plugging in the Molten-Salt Reactor Experiment Primary Heat Exchanger*, ORNL-TM-1023 (February 1965). Available from CFSTI.

Ells, C. E., and J. R. Weir, "The Effect of Neutron Irradiation on the Plastic Deformation and Fracture of Beryllium," *J. Nucl. Mater.* **13**(1), 107 (1965).

Evans, R. B., III, J. O. Stiegler, and J. Truitt, *Actinide Diffusion in Pyrocarbons and Graphite*, ORNL-3711 (December 1964). Available from CFSTI.

Faulkner, J. S., "Electronic States of a Kronig-Penney Crystal with Random Atomic Positions," *Phys. Rev.* **135**(1A), A124–30 (1964).

Federer, J. I., and R. A. Padgett, Jr., *Diffusion Studies of ^{95}Nb in Polycrystalline UO_2 Between 1100 and 2100°C*, ORNL-TM-1018 (February 1965).

Federer, J. I., and R. M. Steele, "Identification of a Beta-Tungsten Phase in Tungsten-Rhenium Alloys," *Nature* **205**(4971), 587–88 (1965).

Foster, B. E., S. D. Snyder, and R. W. McClung, "A Continuous X-Ray Scanning Technique for Determining Minute Inhomogeneities in Solids," *Mater. Evaluation* **23**(4), 191–95 (1965).

Foster, B. E., S. D. Snyder, and R. W. McClung, "Measurement and Application of X- and Gamma-Ray Attenuation to Reactor Materials Evaluation," pp. 339–43 in *Proceedings of the Fourth International Conference on Non-Destructive Testing*, Butterworths, London, 1964.

Foster, B. E., S. D. Snyder, and R. W. McClung, *Continuous Scanning X-Ray Attenuation Technique for Determining Fuel Inhomogeneities in Dispersion Core Fuel Plates*, ORNL-3737 (January 1965). Available from CFSTI.

Fox, C. W., *Development of Procedure for Welding Fuel Element End-Closures at Reduced Pressure*, ORNL-TM-1130 (June 1965) (Classified).

Fox, C. W., and G. M. Slaughter, "Brazing of Ceramics," *Welding J. (N.Y.)* **43**(7), 591–97 (1964).

Franco-Ferreira, E. A., "Fabrication of Instrumented Irradiation Capsules for Gas-Cooled Reactor Program at the Oak Ridge National Laboratory," p. 3.7.1. in *Symposium on Problems in Irradiated Capsule Experiments, Germantown, Maryland, October 8, 9, and 10, 1963*, TID-7697 (March 1964).

Godfrey, T. G., W. Fulkerson, T. G. Kollie, J. P. Moore, and D. L. McElroy, "Thermal Conductivity of Uranium Dioxide from −57° to 1100°C by a Radial Heat Flow Technique," *J. Am. Ceram. Soc.* **48**(6), 297–305 (1965).

Hallerman, G., and R. J. Gray, "Instrument for Determining Crushing Strength of Fuel Particles," *Rev. Sci. Instr.* **35**(7), 850–52 (1964).

Hamner, R. L., A. T. Chapman, and W. O. Harms, "Fabrication Development and Irradiation Testing of Fueled Beryllium Oxide," *J. Nucl. Mater.* **14**, 465–72 (1964).

Harms, W. O., and J. H. Coobs, *Coated-Particle Fuels Development at Oak Ridge National Laboratory for Period November 15, 1964 to May 15, 1965*, ORNL-TM-1116 (May 1965).

Harms, W. O., and D. B. Trauger, *Fabrication Variables, Performance, and Cost Considerations for HTGR Coated-Particle Fuels*, ORNL-TM-1123 (Apr. 30, 1965).

Heestand, R. L., J. I. Federer, and C. F. Leitten, Jr., *Preparation and Evaluation of Vapor-Deposited Tungsten*, ORNL-3662 (August 1964). Available from CFSTI.

Heestand, R. L., J. I. Federer, and C. F. Leitten, Jr., "Thermochemical Preparation and Properties of Carbides for Nuclear Applications," pp. 539–45 in *International Symposium on Compounds of Interest in Nuclear Reactor Technology* (ed. by J. T. Waber, P. Chiotti, and W. N. Miner), AIME Metallurgical Society, New York, 1964.

Hendricks, J. W., and D. L. McElroy, *High-Temperature High-Vacuum Thermocouple Drift Tests*, ORNL-TM-883 (August 1964).

Hill, N. A., and O. B. Cavin, "A Monoclinic-Cubic Transformation in Thorium Dicarbide," *J. Am. Ceram. Soc.* **47**(7), 360–61 (1964).

Hill, N. A., and O. B. Cavin, *Phase Equilibrium Studies in the System UC_2-ThC_2*, ORNL-3668 (September 1964).

Hobson, D. O., J. O. Stiegler, and C. J. McHargue, "Twinning in Columbium-Vanadium Alloys," *Trans. Met. Soc. AIME* **233**, 1138–45 (1965).

Hobson, D. O., *Deformation Twinning in the Columbium-Vanadium Alloy System* (Thesis), ORNL-3678 (September 1964).

Hobson, D. O., R. L. Heestand, and C. F. Leitten, Jr., *Fabrication Development of U_3O_8-Aluminum Composite Fuel Plates for the Advanced Test Reactor*, ORNL-3644 (July 1964). Available from CFSTI.

Inouye, H., *Contamination of Refractory Metals by Residual Gases in Vacuums Below 10^{-6} Torr*, ORNL-3674 (September 1964). Available from CFSTI.

Jansen, D. H., and E. E. Hoffman, *Type 316 Stainless Steel, Inconel, and Haynes Alloy No. 25 Natural-Circulation Boiling-Potassium Corrosion Test Loops*, ORNL-3790 (June 1965). Available from CFSTI.

Joy, H. W., L. J. Schaad, and G. S. Handler, "Constant Energy and Minimum Energy Orthogonalization," *J. Chem. Phys.* **41**(7), 2026–31 (1964).

Joy, H. W., and G. S. Handler, "On One-Center Expansions in H_{2+}," *J. Chem. Phys.* **42**(9), 3047–53 (1965).

Kegley, T. M., Jr., and B. C. Leslie, "A New Microhardness Technique," pp. 111–28 in *Technical Papers of the Seventeenth Metallographic Group Meeting, May 21–23, 1963, Los Alamos Scientific Laboratory, Los Alamos, New Mexico, NMI-4999 (1965).*

Kegley, T. M., Jr., and B. C. Leslie, "Metallographic Preparation of Dicarbides of Thorium and Thorium-Uranium," *J. Nucl. Mater.* **13**(2), 283–87 (1964); ORNL-TM-949 (November 1964).

Knight, R. W., and C. F. Leitten, Jr., *Development of the Assembly Method for Fuel Elements for the Advanced Test Reactor*, ORNL-3643 (August 1964). Available from CFSTI.

Kollie, T. G., D. L. McElroy, R. S. Graves, and W. Fulkerson, "A Thermal Comparator Apparatus for Thermal Conductivity Measurements from 50 to 400°C," pp. 651–76 in *International Symposium on Compounds of Interest in Nuclear Reactor Technology* (ed. by J. T. Waber, P. Chiotti, and W. N. Miner), AIME Metallurgical Society, New York, 1964.

Litman, A. P., and J. W. Prados, *The Partitioning of Oxygen Between Zirconium and Liquid Potassium*, ORNL-TM-1039 (April 1965).

Long, E. L., Jr., and C. Michelson, *Some Observations of the Intergranular Corrosion of Irradiated Type 304 Stainless Steel*, ORNL-3684 (November 1964). Available from CFSTI.

Lotts, A. L., D. A. Douglas, Jr., and R. L. Pilloton, *Refabrication Technology and Costs for High-Temperature Gas-Cooled Reactor Fuels*, ORNL-TM-1115 (May 1965).

Lotts, A. L., and D. A. Douglas, Jr., *Refabrication Technology for the Thorium-Uranium-233 Fuel Cycle*, ORNL-TM-1141 (June 1965).

Lundy, T. S., and C. J. McHargue, "Diffusion of V^{48} in Vanadium," *Trans. Met. Soc. AIME* **233**(1), 243 (1965).

Malinauskas, A. P., and F. L. Carlsen, Jr., "Gas Transport Characteristics of Uranium-Fueled Graphites," *Am. Ceram. Soc. Bull.* **44**, 251 (1965).

Manly, W. D., H. Inouye, J. H. DeVan, T. K. Roche, D. A. Douglas, and A. Taboada, "Molten Salt Reactors," pp. 807–23 in *Reactor Handbook*, 2d ed., vol. IV (ed. by S. McLain and J. M. Martens), Interscience, New York, 1964.

Manly, W. D., "Utilization of BeO in Reactors," *J. Nucl. Mater.* **14**, 3–18 (1964).

Manthos, E. J., "Replication of Irradiated Specimens with Room-Temperature Vulcanizing Silicone," pp. 69–77 in *Technical Papers of the Seventeenth Metallographic Group Meeting, May 21–23, 1963, Los Alamos Scientific Laboratory, Los Alamos, New Mexico,* NMI-4999 (1965).

Martin, W. R., and J. R. Weir, "Effect of Elevated-Temperature Irradiation on Hastelloy N," *Nucl. Appl.* **1**(2), 160–67 (1965).

Martin, W. R., and J. R. Weir, "Influence of Chromium Content on Carburization of Chromium-Nickel-Iron Alloys in Carbon Dioxide," *J. Nucl. Mater.* **16**(1), 19–24 (1965); ORNL-TM-965 (November 1964).

Martin, W. R., and J. R. Weir, *Effect of Irradiation Temperature on the Postirradiation Stress-Strain Behavior of Stainless Steel,* ORNL-TM-906 (October 1964).

Martin, W. R., and J. R. Weir, *Effect of Elevated Temperature Irradiation on the Strength and Ductility of the Nickel-Base Alloy, Hastelloy N,* ORNL-TM-1005 (February 1965).

Martin, W. R., and J. R. Weir, *Influence of Grain Size on the Irradiation Embrittlement of Stainless Steel at Elevated Temperatures,* ORNL-TM-1043 (March 1965).

Martin, W. R., H. E. McCoy, and J. R. Weir, *Production of a Low-Boron Heat of Hastelloy N,* ORNL-TM-1146 (June 1965). Available from CFSTI.

Martin, W. R., *Mechanical Cladding-Fuel Interactions During Thermal Cycling of Metal-Clad Fuel Elements,* ORNL-3514 (March 1965). Available from CFSTI.

McClung, R. W., E. S. Bomar, and R. J. Gray, "Evaluating Coated Particles of Nuclear Fuel," *Metal Progr.* **86**(1), 90–93 (1964).

McClung, R. W., and K. V. Cook, "Ultrasonic Detection of Nonbond in Clad Structures," pp. 267–72 in *Proceedings of the Fourth International Conference on Non-Destructive Testing,* Butterworths, London, 1964.

McClung, R. W., "Radiography in the Presence of Background Radiation," *Mater. Evaluation* **23**(1), 41–45 (1965).

McClung, R. W., *Development of Nondestructive Testing Techniques for the High Flux Isotope Reactor Fuel Element,* ORNL-3780 (April 1965). Available from CFSTI.

McCoy, H. E., *Influence of Several Metallurgical Variables on the Tensile Properties of Hastelloy N,* ORNL-3661 (August 1964). Available from CFSTI.

McCoy, H. E., and J. R. Weir, *The Effect of Irradiation on the Bend Transition Temperatures of Molybdenum- and Niobium-Base Alloys,* ORNL-TM-880 (July 1964).

McCoy, H. E., *Studies of British Niobium-Stabilized Stainless Steels,* ORNL-TM-891 (November 1964).

McCoy, H. E., Jr., "Thermal Expansion of Iodide Titanium," *Am. Soc. Metals, Trans. Quart.* **57**(3), 743 (1964).

McCoy, H. E., "Type 304 Stainless Steel vs Flowing CO_2 at Atmospheric Pressure and 1100–1800F," *Corrosion* **21**(3), 84 (1965).

McCoy, H. E., Jr., "Oxidation of Beryllium in CO_2 by Autoradiographic Techniques," *J. Nucl. Mater.* **15**(4), 249–62 (1965).

McCoy, H. E., "Creep Properties of the Nb–1% Zr Alloy," *J. Less-Common Metals* **8**, 20–35 (1965); ORNL-TM-905 (August 1964).

Melton, C. E., and H. W. Joy, "Ionization Potentials and Autoionization Levels of Methyl, Ethyl, *n*-Propyl and *n*-Butyl Free Radicals by an Energy Calibration Molecular Orbital Method," *J. Chem. Phys.* **42**, 1986 (1965).

Melton, C. E., and H. W. Joy, "Calculated Ionization Potential of Chloro- and Fluoromethanes, Tetrafluoromethane (CF_4), Xenon Tetrafluoride (XeF_4), and Xenon Tetrachloride ($XeCl_4$)," *J. Chem. Phys.* **42**(8), 2982 (1965).

Morgan, C. S., R. B. Fitts, and J. L. Scott, "Influence of Stress on Fission-Gas Release," *J. Am. Ceram. Soc.* **48**(3), 166–67 (1965).

Murdock, J. F., T. S. Lundy, and E. E. Stansbury, "Diffusion of Ti^{44} and V^{48} in Titanium," *Acta Met.* **12**(9), 1033–39 (1964).

Ogle, J. C., *Annealing of Deformation Twins in Columbium,* ORNL-TM-904 (September 1964).

Olsen, A. R., D. B. Trauger, W. O. Harms, R. E. Adams, and D. A. Douglas, *Irradiation Behavior of Thorium-Uranium Alloys and Compounds,* ORNL-TM-1142 (June 1965).

Osborne, M. F., E. L. Long, and J. G. Morgan, *Postirradiation Examination of ORR Loop 1 Advanced Fuel Elements,* ORNL-TM-862 (July 1964). Available from CFSTI.

Osborne, M. F., E. L. Long, Jr., and J. G. Morgan, *Postirradiation Examination of EGCR Prototype Capsule 02A-6,* ORNL-TM-877 (July 1964). Available from CFSTI.

Osborne, M. F., and E. L. Long, Jr., *Postirradiation Examination of Maritime-ORR Loop Experiments 5, 7, and 8,* ORNL-TM-921 (October 1964).

Pawel, R. E., "Procedure for Stripping Anodic Oxide Films from Tantalum and Niobium," *Rev. Sci. Instr.* **35**(8), 1066–67 (1964).

Pawel, R. E., and J. J. Campbell, "Electron Microscope Observations of the Crystallization of Anodically Formed Tantalum and Niobium Oxide Films," *J. Electrochem. Soc.* **111**(11), 1230–34 (1964).

Pawel, R. E., and E. E. Stansbury, "The Specific Heat of Copper, Nickel and Copper–Nickel Alloys," *Phys. Chem. Solids* **26**, 607–13 (1965).

Pawel, R. E., and E. E. Stansbury, "Specific Heat Contributions of the Ferromagnetic Transition in Nickel and Nickel–Copper Alloys," *Phys. Chem. Solids* **26**, 757–65 (1965).

Pawel, R. E., and T. S. Lundy, "The Diffusion of Nb^{95} and Ta^{182} in Tantalum," *Phys. Chem. Solids* **26**, 937–42 (1965).

Pawel, R. E., and T. S. Lundy, "Diffusion of Nb^{95} into Tantalum Single Crystals," *Acta Met.* **13**(3), 345–51 (1965).

Peterson, S., "Integrity of Metallic Reactor Fuels," *Nucl. Safety* **6**(1), 38 (1964).

Peterson, S., "Oxidation of Graphite," *Nucl. Safety* **6**(1), 40 (1964).

Peterson, S., "Ignition and Combustion of Fuels and Structural Metals," *Nucl. Safety* **5**(4), 338 (1964).

Peterson, S., "Integrity of Reactor Fuels," *Nucl. Safety* **5**(4), 338 (1964).

Peterson, S., "Metal-Gas Reactions," *Nucl. Safety* **5**(4), 360 (1964).

Peterson, S., R. E. Adams, and D. A. Douglas, Jr., *Properties of Thorium, Its Alloys, and Its Compounds,* ORNL-TM-1144 (June 1965).

Potter, R. A., R. E. McDonald, and C. F. Leitten, Jr., "Preparation and Properties of Lanthanon Molybdates and Tungstates," pp. 547–56 in *International Symposium on Compounds of Interest in Nuclear Reactor Technology* (ed. by J. T. Waber, P. Chiotti, and W. N. Miner), AIME Metallurgical Society, New York, 1964.

Rodriguez, P., *High-Temperature Creep Behavior of Type 304 Stainless Steel in Argon-Oxygen Environment of Different Oxygen Partial Pressures* (Thesis), ORNL-TM-1124 (May 5, 1965). Available from CFSTI.

Rosenthal, M. W., R. E. Adams, L. L. Bennett, W. L. Carter, D. A. Douglas, Jr., R. E. Hoskins, C. G. Lawson, A. L. Lotts, R. C. Olson, A. M. Perry, J. T. Roberts, R. Salmon, and D. R. Vondy, *A Comparative Evaluation of Advanced Converters,* ORNL-3686 (August 1964). Official Use Only.

Sayers, J. B., K. S. B. Rose, J. H. Coobs, G. P. Hauser, and C. Vivante, "The Irradiation Behaviour of Coated Particle Fuel," pp. 919–62 in *Carbides in Nuclear Energy* (ed. by L. Russell), Macmillan, London, 1964.

Sease, J. D., *Fabrication and Preirradiation Data of HFIR Target Elements for Savannah River Irradiations,* ORNL-TM-1095 (June 1965). Available from CFSTI.

Slaughter, G. M., and T. R. Housley, "The Welding of Ferritic Steels to Austenitic Stainless Steels," *Welding J. (N.Y.)* **43**(10), 454-s–460-s (1964).

Slaughter, G. M., "Design of Joints," pp. 43.3–43.9 in *Welding Handbook,* 5th ed., sect. 3 (ed. by A. L. Phillips), American Welding Society, New York, 1965.

Smith, C. O., and J. M. Robbins, *Impact Resistance of Fueled Graphite Spheres for Pebble-Bed Reactor Applications,* ORNL-3723 (January 1965).

Smith, G. P., C. H. Liu, and T. R. Griffiths, "Charge-Transfer and Ligand-Field Spectra of Tetrahedral Tetrahalonickel(II) Ions in Molten Dimethyl Sulfone and Molten Organic Halide Salts," *J. Am. Chem. Soc.* **86**(22), 4796–4802 (1964).

Smith, G. P., D. W. James, and C. R. Boston, "Optical Spectra of Tl^{+}, Pb^{2+}, and Bi^{3+} in the Molten Lithium Chloride–Potassium Chloride Eutectic," *J. Chem. Phys.* **42**(6), 2249 (1965).

Stephenson, R. L., *Comparative Creep-Rupture Properties of D-43 and B-66 Alloys,* ORNL-TM-944 (November 1964).

Stiegler, J. O., C. K. H. DuBose, and J. L. Cook, *An Electron Optical Study of Structural Features of Pyrolytic Carbons,* ORNL-TM-863 (July 1964).

Stiegler, J. O., and C. J. McHargue, "The Effect of Impurities on Mechanical Twinning and Dislocation Behavior in Body-Centered Cubic Metals," pp. 209–36 in *Deformation Twinning,* Gordon and Breach, New York, 1965.

Stiegler, J. O., C. K. H. DuBose, and J. L. Cook, *Effects of Heat Treatment on the Structure of Pyrolytic-Carbon Coatings on Uranium Carbide Particles,* ORNL-TM-876 (July 1964) (Classified).

Swindeman, R. W., "Thermal Shock Tests on Beryllia," *J. Nucl. Mater.* **14**, 405 (1964).

Taylor, A. J., J. H. Cherubini, J. M. Robbins, and M. P. Haydon, *Characterization of Spheroidal UO_2 Particles and Studies of Fabrication Variables for Core B Fuel Plates of the Enrico Fermi Fast Breeder Reactor,* ORNL-3645 (August 1964). Available from CFSTI.

Thurber, W. C., F. R. McQuilkin, E. L. Long, Jr., and M. F. Osborne, *Irradiation Testing of Fuel for Core B of the Enrico Fermi Fast Breeder Reactor,* ORNL-3709 (November 1964). Available from CFSTI.

Van Cleve, J. E., Jr., and A. L. Lotts, "Operating Experience in a Semi-Remote Facility for Fabrication of Fuel Rods Containing $(U^{233}, Th)O_2$," pp. 257–71 in *Proceedings of the 12th Conference on Remote Systems Technology,* American Nuclear Society, Hinsdale, Illinois, 1964.

Vandermeer, R. A., "Dependence of Grain Boundary Migration Rates on Driving Force," *Trans. Met. Soc. AIME* **233**(1), 265 (1965).

Venard, J. T., and J. R. Weir, *In-Reactor Stress-Rupture Properties of a 20 Cr–25 Ni, Niobium-Stabilized Stainless Steel,* ORNL-TM-881 (August 1964).

Venard, J. T., *Stress-Rupture Testing of EGCR Fuel Tubes,* ORNL-TM-1004 (January 1965). Available from CFSTI.

Venard, J. T., *Tensile and Creep Properties of INOR-8 for the Molten-Salt Reactor Experiment,* ORNL-TM-1017 (February 1965).

Weir, J. R., "Argonne Transient Reactor Test Facility," *Nucl. Safety* **6**(2), 169 (1964).

Weir, J. R., "Irradiation of Non-Fissile Materials in the ORR Core and Pool Facilities," p. 1.6.1 in *Symposium on Problems in Irradiated Capsule Experiments, Germantown, Maryland, October 8, 9, and 10, 1963,* TID-7697 (March 1964).

Williams, R. O., "The Stored Energy of Copper Deformed at 24°C," *Acta Met.* **13**(3), 163–68 (1965).

Wilson, J. C., and M. L. Picklesimer, "Variable-Gradient, Electron-Beam Heating Methods for Growing Single Crystals in Zirconium," pp. 502–20 in *First International Conference on Electron and Ion Beam Science and Technology* (ed. by R. Bakish), Wiley, New York, 1965.

Winslow, F. R., "Diffusion 1963," *J. Metals* **16**(7), 589–94 (1964).

Wood, R. F., and H. W. Joy, "On the Theory of the Absorption and Emission of the F Center in Alkali Halides," *Phys. Rev.* **136**, A451 (1964).

Woods, J. W., *Techniques for Performing In-Reactor Stress-Rupture Experiments,* ORNL-3724 (January 1965). Available from CFSTI.

Yust, C. S., and C. P. Haltom, "Comments on Note 'Metallographic Preparation of CeO_2,'" *J. Am. Ceram. Soc.* **48**(4), 216 (1965).

The following quarterly progress reports have been issued during this reporting period:

Patriarca, P., *Fuels and Materials Development Program Quart. Progr. Rept. June 30, 1964,* ORNL-TM-920; *Sept. 30, 1964,* ORNL-TM-960; *Dec. 31, 1964,* ORNL-TM-1000; and *Mar. 31, 1965,* ORNL-TM-1100. Official Use Only.

Thurber, W. C., and W. O. Harms, *High-Temperature Materials Program Quart. Progr. Rept. Oct. 31, 1964,* ORNL-TM-980; *Jan. 31, 1965,* ORNL-TM-1050; and *Apr. 30, 1965,* ORNL-TM-1140 (Classified).

METALS AND CERAMICS DIVISION

DIRECTOR — J. H. FRYE, JR.; BERTIE BYRUM

ASSISTANT DIRECTOR — J. E. CUNNINGHAM; MARGE WHITE

STAFF ASSIGNMENTS
A. R. OLSON[1,*]
S. PETERSON

ADMINISTRATIVE ASSISTANT
L. E. BANKER
MARY YAGGI

FUNDAMENTAL RESEARCH
B. S. BORIE*
WILMA MASON

CRYSTAL PHYSICS
G. W. CLARK
A. T. CHAPMAN
C. B. FINCH
S. D. FULKERSON

DEFORMATION OF CRYSTALLINE SOLIDS
R. O. WILLIAMS
R. ARSENAULT
A. WOLFENDEN[3]

REACTIONS AT METAL SURFACES
J. V. CATHCART
R. E. PAWEL
G. F. PETERSEN
J. J. CAMPBELL

SPECTROSCOPY OF IONIC MEDIA
G. P. SMITH, JR.
N. N. BJERRUM[3]
C. R. BOSTON
J. BRYNESTAD[3]
F. C. GILMORE[4]
W. M. EWING

STRUCTURE OF METALS
C. J. MCHARGUE*
R. E. REED, SR.
R. A. VANDERMEER

THEORY OF ALLOYING
J. O. BETTERTON, JR.
G. V. CZIJZEK
D. S. EASTON
G. R. HADDER[2]
D. OLSON[2]
J. P. PENLAND[2]
J. O. SCARBROUGH

X-RAY DIFFRACTION
H. L. YAKEL, JR.
B. S. BORIE*
O. B. CAVIN
L. A. HARRIS
R. W. HENDRICKS
C. J. SPARKS, JR.
R. M. STEELE

THEORETICAL RESEARCH
J. S. FAULKNER
H. L. DAVIS
H. W. JOY
R. M. RUTLEDGE[3]

APPLIED RESEARCH
C. J. MCHARGUE*
MARY COMBS
DOLORES POE

ELECTRON MICROSCOPY
J. O. STIEGLER
K. FARRELL[2]
B. T. LOH
C. K. H. DUBOSE
J. T. HOUSTON

METALLOGRAPHY
R. J. GRAY
R. S. CROUSE
E. L. LONG, JR.
G. HALLERMAN
T. M. KEGLEY, JR.
H. L. KRAUTWEDEL[3]
E. J. MANTHOS
A. E. RICHT
M. D. ALLEN
L. A. AMBURN
N. M. ATCHLEY
E. D. BOLLING
E. R. BOYD
W. E. DENNY
W. H. FARMER
H. R. GADDIS
J. C. GOWER
E. P. GRIGGS
C. P. HALTOM
T. J. HENSON
C. W. HOUCK
E. H. LEE
B. C. LESLIE
R. J. LOCKETT
Z. R. MCNUTT
L. G. SHRADER
E. D. SIMS
S. E. SPENCER
H. R. TINCH
R. M. WALLACE
M. A. WHEELER
C. E. ZACHARY

METALLURGY OF SUPERCONDUCTING MATERIALS
M. L. PICKLESIMER*
G. R. LOVE
J. A. WHEELER, JR.
J. P. GORDON

PHYSICAL PROPERTIES
D. L. MCELROY
W. FULKERSON
T. G. KOLLIE
J. P. MOORE
R. K. WILLIAMS
R. S. GRAVES
D. W. TRADER[2]
N. D. WOODALL[2]

PHYSICAL CERAMIC STUDIES
C. S. MORGAN, JR.
C. S. YUST
L. L. HALL

SOLID REACTION STUDIES
T. S. LUNDY
J. ASKILL[3]
J. F. MURDOCK
F. R. WINSLOW
L. C. MANLEY
R. A. PADGETT, JR.

ZIRCONIUM ALLOY DEVELOPMENT
M. L. PICKLESIMER*
J. C. BANTER
D. O. HOBSON
P. L. RITTENHOUSE
J. C. WILSON
P. J. JONES
G. C. NELSON

RESEARCH AND DEVELOPMENT
P. PATRIARCA
W. O. HARMS*
R. M. EVANS
ANN HOBBS
EDITH TAYLOR

PROJECT COORDINATION
GCR, HTN, SNPO-C
W. O. HARMS*
J. H. COOBS*
E. A. FRANCO-FERREIRA*

CERAMICS LABORATORY
W. O. HARMS*
M. J. BANNISTER[2]
R. L. BEATTY
H. BEUTLER[3]
E. S. BOMAR
J. H. COOBS*
W. S. ERNST, JR.
T. G. GODFREY, JR.
R. L. HAMNER
D. M. HEWETTE II
J. M. LEITNAKER
D. MATKIN
R. E. MEADOWS
R. A. POTTER
J. M. ROBBINS
J. G. STRADLEY
S. J. ACRES
B. R. CHILCOAT
H. H. DOBASHI[2]
C. M. FITZPATRICK
F. P. JEFFERS
D. V. KIPLINGER[8]
M. PAYNE[2]
J. E. POPE
W. W. PROAPS
D. E. ROSSON
W. H. SMITH, JR.

MATERIALS COMPATIBILITY
J. H. DEVAN
W. H. COOK
J. R. DISTEFANO
D. H. JANSEN
A. P. LITMAN
C. E. SESSIONS
J. L. GRIFFITH
J. W. HENDRICKS
B. W. MCCOLLUM
R. E. POTTER
L. R. TROTTER

PHYSICAL METALLURGY
H. INOUYE
D. T. BOURGETTE
T. K. ROCHE
A. SCHAFFHAUSER
J. F. NEWSOME
R. L. TAYLOR
S. H. WHEELER

DISPERSIONS IN SOLIDS
J. P. HAMMOND
C. HAMBY

RESEARCH AND DEVELOPMENT
G. M. ADAMSON, JR.*
FREDA FINN

PROJECT COORDINATION
TRANSURANIUM, HFIR, MSRP, MPRE, BONUS
G. M. ADAMSON, JR.*
A. TABOADA*

CORROSION ENGINEERING
A. TABOADA*
NANCY C. COLE
B. FLEISCHER
G. M. TOLSON
F. D. HARVEY[6]
E. J. LAWRENCE
J. B. PHILLIPS
M. A. REDDEN

MATERIALS PROCESSING
C. F. LEITTEN, JR.
J. H. ERWIN
J. I. FEDERER
R. L. HEESTAND
R. W. KNIGHT
M. M. MARTIN
R. E. McDONALD
F. H. PATTERSON
G. A. REIMANN
W. C. ROBINSON
W. J. WERNER
L. A. ALLEN[9]
J. K. ALLEY
G. E. ANGEL
T. W. COFFEY
C. E. DUNN
J. B. FLYNN
J. W. GEER
G. D. GOLDSTON
J. N. HIX
C. W. HOLLAND, JR.
R. J. HUNTER
W. R. JOHNSON
L. QUEENER
H. E. REESOR
R. J. SAWYERS[8]
E. R. TURNBILL
H. J. WALLACE
W. H. WARWICK

WELDING AND BRAZING
G. M. SLAUGHTER
D. A. CANONICO
R. G. DONNELLY
C. W. FOX
E. A. FRANCO-FERREIRA
J. M. JONES
W. R. MILLER[10]
J. W. TACKETT
L. G. BRYSON
J. D. HUDSON
H. H. SCOTT[7]
R. G. SHOOSTER
L. C. WILLIAMS
J. J. WOODHOUSE, JR.

RESEARCH AND DEVELOPMENT
D. A. DOUGLAS, JR.*
GENEVA HARRIS
JANE MORRISON
LOUIE MAE PYATT

PROJECT COORDINATION
DESALINATION, SAP, THORIUM UTILIZATION
D. A. DOUGLAS, JR.*
R. J. BEAVER
Y. HIROSE[7]
A. R. OLSEN*
J. T. VENARD
T. N. WASHBURN

FUEL EVALUATION
J. L. SCOTT
R. E. ADAMS
R. B. FITTS
J. W. PRADOS
R. A. BOWMAN
H. G. MOORE

MECHANICAL PROPERTIES
J. R. WEIR, JR.
E. E. BLOOM
W. W. DAVIS
C. W. DOLLINS
D. G. HARMAN
C. R. KENNEDY
R. T. KING
W. R. MARTIN
H. E. McCOY, JR.
R. L. STEPHENSON
R. W. SWINDEMAN
J. W. WOODS
F. L. BEELER
K. W. BOLING
E. BOLLING
V. R. BULLINGTON
D. G. GATES
L. L. HEATHERLY[6]
J. W. KLINE[6]
V. G. LANE
B. McNABB, JR.
E. B. PATTON, JR.
C. K. THOMAS
E. M. THOMAS[6]
R. D. WADDELL, JR.
C. W. WALKER
B. C. WILLIAMS

NONDESTRUCTIVE TESTING
R. W. McCLUNG
W. H. BRIDGES
K. V. COOK
C. V. DODD III
B. E. FOSTER
S. D. SNYDER
L. D. CHITWOOD
O. E. CONNER
R. A. CUNNINGHAM, JR.
R. L. FITZGERALD
D. P. GODSEY
W. J. MASON

REMOTE FABRICATION
A. L. LOTTS
R. L. PILLOTON
R. B. PRATT
R. G. MILLS[10]
H. J. FLAMM[7]
M. K. PRESTON[11]
J. D. SEASE
J. E. VAN CLEVE, JR.
K. P. BAYNE
R. A. BUHL[6]
J. T. EAST
J. E. EVE
C. L. JOHNSON
W. H. MILLER, JR.
C. F. SANDERS
B. J. STRADER

DIVISION SERVICES

COST, BUDGET, AND NUCLEAR MATERIALS
R. G. CARDWELL, JR.
H. W. HOOVER

PROCUREMENT AND MAINTENANCE
R. J. STEERE
RUTH HENGSTLER

REPORTS OFFICE
M. R. HILL
NANCY BOWMAN
JOAN CARDEN
MARJORIE CLARY
FRANCES LOVING
FLORENCE ROBERTSON

SPECIAL ASSIGNMENT
R. E. CLAUSING
R. G. GILLILAND
A. E. GOLDMAN
W. J. LEONARD
J. J. PRISLINGER
C. H. WODTKE
T. L. BOSWELL
J. P. DURR[8]

---

*DUAL CAPACITY
[1]RADIATION CONTROL OFFICER
[2]CO-OP STUDENT
[3]NONCITIZEN EMPLOYEE
[4]GRADUATE RESEARCH STUDENT
[5]POSTDOCTORATE FELLOW
[6]TEMPORARY EMPLOYEE
[7]NONCITIZEN VISITOR
[8]U.S. ARMY PERSONNEL
[9]ON LOAN FROM INSPECTION ENGINEERING DEPARTMENT
[10]ON LOAN FROM GENERAL ATOMIC
[11]ON LOAN FROM GENERAL ENGINEERING AND CONSTRUCTION DIVISION

AUGUST 1, 1965

ORNL-3870
UC-25 – Metals, Ceramics, and Materials
TID-4500 (45th ed.)

INTERNAL DISTRIBUTION

1. Biology Library
2–4. Central Research Library
5. Reactor Division Library
6–7. ORNL – Y-12 Technical Library, Document Reference Section
8–57. Laboratory Records Department
58. Laboratory Records, ORNL R.C.
59. ORNL Patent Office
60. Laboratory Shift Supervisor
61. G. M. Adamson, Jr.
62. L. G. Alexander
63. R. J. Beaver
64. J. O. Betterton, Jr.
65. D. S. Billington
66. A. L. Boch
67. E. G. Bohlmann
68. E. S. Bomar
69. B. S. Borie
70. G. E. Boyd
71. R. B. Briggs
72. J. V. Cathcart
73. C. E. Center
74. G. W. Clark
75. J. H. Coobs
76. J. A. Cox
77. F. L. Culler
78. J. E. Cunningham
79. G. V. Czjzek
80. J. H. DeVan
81. D. A. Douglas, Jr.
82. J. H. Erwin
83. G. W. Flack
84. A. P. Fraas
85. J. H. Frye, Jr.
86. J. H. Gillette
87. A. E. Goldman
88. R. J. Gray
89. W. R. Grimes
90. J. P. Hammond
91. W. O. Harms
92. C. S. Harrill
93–102. M. R. Hill
103. N. E. Hinkle
104. A. Hollaender
105. A. S. Householder
106. A. P. Huber (K-25)
107. H. Inouye
108. R. G. Jordan (K-25)
109. M. T. Kelley
110. E. M. King
111. R. B. Korsmeyer
112. J. A. Lane
113. C. E. Larsen
114. C. F. Leitten, Jr.
115. R. S. Livingston
116. A. L. Lotts
117. T. S. Lundy
118. H. G. MacPherson
119. R. W. McClung
120. H. C. McCurdy
121. D. L. McElroy
122. C. J. McHargue
123. A. J. Miller
124. E. C. Miller
125. C. S. Morgan
126. K. Z. Morgan
127. M. L. Nelson
128. S. M. Ohr
129. A. R. Olsen
130–131. R. B. Parker
132. P. Patriarca
133. S. Peterson
134. M. L. Picklesimer
135. J. W. Prados
136. H. W. Savage
137. A. W. Savolainen
138. J. L. Scott
139. H. E. Seagren
140. G. M. Slaughter
141. G. P. Smith, Jr.
142. P. E. Stein (K-25)
143. J. O. Stiegler
144. A. Taboada
145. E. H. Taylor
146. D. B. Trauger
147. M. S. Wechsler
148. A. M. Weinberg
149. J. R. Weir, Jr.
150. G. D. Whitman

EXTERNAL DISTRIBUTION

151. G. C. Williams
152. R. O. Williams
153. J. C. Wilson
154. H. L. Yakel
155. M. B. Bever (consultant)
156. A. A. Burr (consultant)
157. J. R. Johnson (consultant)
158. A. R. Kaufmann (consultant)
159. C. M. Adams, Jr., MIT
160. M. J. Bannister, MIT
161. R. B. Burlin, AEC, Washington
162. E. D. Calvert, U.S. Bureau of Mines, P. O. Box 492, Albany, Oregon
163–164. D. F. Cope, AEC, ORO
165. J. F. Elliott, MIT
166. N. Engel, Georgia Institute of Technology
167. H. B. Finger, AEC, Washington
168. J. D. Fleming, Georgia Institute of Technology
169. V. D. Frechette, Alfred Univ.
170. Angelo Giambusso, AEC, Washington
171. R. G. Gilliland, MIT
172. J. L. Gregg, Bard Hall, Cornell Univ.
173. E. G. Haas, Dept. of the Navy, Washington
174. R. F. Hehemann, Case Institute of Technology
175. E. E. Hoffman, GE, Cincinnati
176. O. C. Kopp, Univ. of Tenn.
177. J. Korringa, Ohio State Univ.
178. J. J. Lombardo, NASA, Lewis Research Center
179. W. D. Manly, Union Carbide Corp., N.Y.
180. R. S. Mateer, Univ. of Kentucky
181. P. W. McDaniel, AEC, Washington
182. R. W. McNamee, Union Carbide Corp., N.Y.
183. Peter Murray, AERE, Harwell
184. R. R. Nash, NASA, Washington
185. E. F. Nippes, Rensselaer Polytechnic Inst.
186. H. M. Otte, RIAS Research Inst.
187. R. E. Pahler, AEC, Washington
188. R. M. Parke, MAB, National Academy of Science, Washington
189. J. Pheline, Centre d'Etudes Nucleaires de Saclay
190. J. M. Prosser, AEC, Washington
191. H. B. Rahner, Savannah River Operations
192. T. A. Read, Univ. of Illinois
193. R. E. Reed-Hill, Univ. of Florida
194. F. N. Rhines, Univ. of Florida
195. A. F. Saturno, Univ. of Tenn.
196. R. W. Schroeder, NASA, Lewis Research Center
197. F. C. Schwenk, AEC, Washington
198. A. A. Shoudy, Atomic Power Development Associate, Inc.
199. J. Simmons, AEC, Washington
200. E. E. Sinclair, AEC, Washington

201. L. M. Slifkin, Univ. of N.C.
202. E. E. Stansbury, Univ. of Tenn.
203. D. K. Stevens, AEC, Washington
204. Dorothy Smith, AEC, Washington
205. A. Van Echo, AEC, Washington
206. J. B. Wagner, Massachusetts Institute of Technology
207. Watt Webb, Union Carbide Metals
208. J. Weertman, Northwestern Univ.
209. G. W. Wench, AEC, Washington
210. M. J. Whitman, AEC, Washington
211. C. H. T. Wilkins, Univ. of Ala.
212. Research and Development Division, AEC, ORO

213–537. Given distribution as shown in TID-4500 (45th ed.) under Metals, Ceramics, and Materials category (75 copies – CFSTI)